A study on oxy-hydroxide compound mediated fluorometric detection and removal of hexavalent chromium from wastewater and its application in energy harvesting

Thesis submitted to

Jadavpur University

by

Shubham Roy

In partial fulfillment of the requirements for the degree of

Doctor of Philosophy (Ph. D.) in Science

Department of Physics, Jadavpur University

Jadavpur, Kolkata- 700032

India

2022

Certificate from the Supervisor

This is to certify that the thesis entitled "**A study on oxy-hydroxide compound mediated fluorometric detection and removal of hexavalent chromium from wastewater and its application in energy harvesting**" submitted by **Sri Shubham Roy** who got his name registered on 11.11.2019 (Index No.: 126/19/Phys./26 and Registration No.: SOPHY1112619) for the award of Ph. D. (Science) degree of Jadavpur University, is absolutely based upon his own work under the supervision of **Prof. Sukhen Das** and that neither this thesis nor any part of it has been submitted for either any degree / diploma or any other academic award anywhere before.

Prof. Sukhen Das 07/03/202?
Department of Physics, Jadavpur University
Kolkata-700032, India

Prof. Sukhen Das
Department of Physics,
Jadavpur University
Kolkata-700032

Certificate of similarity check

This is to certify that the plagiarism checking for this thesis authored by Shubham Roy has been performed using professional plagiarism prevention software iThenticate. According to the report generated after plagiarism checking there is 08% similarity in this thesis, which is in category "Level 0" (minor similarities) as per the "Promotion of Academic Integrity and Prevention of Plagiarism in Higher Educational Institutions Regulations, 2018" of the University Grant Commission (UGC) of India. The common knowledge or coincidental terms up to 10 (ten) consecutive words (as prescribed in the above said UGC Regulation up to 14 (fourteen) terms for such common knowledge or coincidental terms can be excluded) and own works of the candidate published in various peer-reviewed journals (those are attached in the thesis) are excluded from the similarity checking. It is certified that the present thesis submitted by Shubham Roy is plagiarism free and he has followed standard norms of academic integrity and scientific ethics.

Sukhen Das 07/03/2022

Prof. Sukhen Das
Department of Physics, Jadavpur University
Kolkata- 700032, India

Prof. Sukhen Das
Department of Physics,
Jadavpur University
Kolkata-700032

Declaration

I, hereby, declare that the work embodied in the present thesis has been carried out by me under the supervision of Prof. Sukhen Das at the Department of Physics, Jadavpur University, Kolkata-700032, India. Neither this thesis nor any part thereof has been submitted for any degree whatsoever.

07/03/2022

Shubham Roy
Research Scholar
Department of Physics, Jadavpur University
Kolkata- 700032, India

To my "Ma" & "Baba"

who always picked me up on time

and encouraged me to go on every adventure,

especially this one.

Abstract

A study on oxy-hydroxide compound mediated fluorometric detection and removal of hexavalent chromium from wastewater and its application in energy harvesting

Shubham Roy

Index No.: 126/19/Phys./26   *Registration No.: SOPHY1112619*

Nowadays, unplanned urbanization and rapid industrialization due to the increasing population are causing irreparable damage to the ecosystem. Water is one of the most vulnerable media that introduces such pollution into the environment and leads to severe damage to the ecosystem. Heavy metal contamination into the water and water bodies is considered to be one of the crucial issues to be paid immediate attention because of their high toxicity. The detection and removal of such toxic contaminants from wastewater need immediate attention. Among various heavy metals, hexavalent chromium (Cr(VI)) is contaminating our water bodies rapidly causing numerous carcinogenic diseases. In recent years, the fluorometric detection of heavy metals has gained immense popularity due to their high selectivity, rapid detection and sensitivity. Additionally, adsorption-based removal is found to be an efficient strategy to remove such heavy metals from wastewater. But, a very limited amount of interest has been paid to the field of simultaneous detection and removal of heavy metals from wastewater. Herein, metallic oxy-hydroxide compounds could be a promising candidate having excellent physicochemical properties, such as high adsorption efficacies, biocompatibility, low cost and prominent fluorescence activities. In fact, oxy-hydroxide compounds are having promising energy harvesting properties due to their structural alignment. In the past few decades, substantial efforts have been assigned on the synthesis of these nanostructures that result in various morphologies, such as nanoparticles, nanoflowers, nanofibers and nano-petals. However, a very limited amount of interest has been shown to understand their multifunctional sensing and energy storage properties. This study will be directed towards the investigation of the simultaneous sensing and adsorption of hexavalent chromium in wastewater by using aluminum oxy-hydroxide (boehmite) and its modified forms. Additionally, the bio-sensing of Cr(VI) is performed using these nanostructures to estimate the sensing efficacy in living systems. The fluorometric sensing mechanisms have been substantiated using density functional theory (DFT) and molecular docking simulation, besides several other theoretical techniques. In reality, polymeric boehmite nanocomposite is successfully achieved during this work, which finally leads to a portable device, `Kavach'. This device can efficiently detect Cr(VI) in nanomolar accuracy in real-life wastewater samples and Cr(VI) contaminated living cells. Moreover, Cr(VI) has been successfully removed from wastewater (up to 85%) using boehmite-based nanostructures showing the multifunctional aspects of these materials. The Cr(VI) adsorbed boehmite also shows enhancement in energy storage, which adds another dimension to this study. Henceforth, this work may propel the unlocking of new avenues, which could enlighten the area of application of these novel nanostructures.

Acknowledgments

On a fine summer morning of 2016, I have entered for the first time at the Jadavpur University premises with my Master's project advisor and my well-wisher Dr. Keka Basu Choudhury, Ex-Head, Dept. of Physics, Charuchandra College, Kolkata with a very curious and anxious mind. This journey was not very easy for me until I met Prof. Papiya Nandy, Prof. Ashesh Nandy and Dr. Ruma Basu. Their valuable thoughts and advice finally landed me in the huge facility of the Biophysics Laboratory, Dept. of Physics, Jadavpur University, where I met my Ph. D. supervisor Prof. Sukhen Das and his group for the first time. Prof. Das was very kind to me throughout this journey. His valuable thoughts and vast collaboration helped me a lot to meet various renowned personalities in my field of research. I will remain grateful to him for the rest of my life.

The Physics department of Jadavpur University never allowed me to face any problem and was always very kind to me. Teachers like, Prof. Sanjay Kumar, Prof. Jaydeep Chowdhury, Prof. Partha Pratim Ray, Prof. Debasish Biswas, Dr. Kaustuv Das and Prof. Argha Deb extended their instrumental facilities and their diverse knowledge throughout the process. Their doors were always open for any help and suggestion. Prof. Chiranjib Bhattacharjee, Pro-Vice-Chancellor, Jadavpur University, Prof. Subenoy Chakraborty, Dean, Faculty Council of Science, Jadavpur University and Dr. Rajat Ray, Dean of Students, Jadavpur University helped me in various official matters and encouraged me to participate in numerous national and international competitions. As a result, our team stood second in Anveshan-2019.

I found difficulties during my topic selection process. Seniors like, Biswajoy Da, Nur Da, Swagata Di, Soumya Da, Santanu Da, Tanumay Da, Farha Di, Subrata Da, Somtirtha Di, Bala Da, Srimoyee Di motivated me with their kind advice and vast experiences. I was very fortunate to have such helpful seniors.

From my early childhood days, I was very curious about the instruments. In this extended research facility, I found myself a 'newbie', where skilled machine operators like Nur Da, Arka Da, Biplab Da, Rituparna Di, Joydeep Da trained me to operate various high-end machines. This training process not only developed my research interest but also created a warm relationship with them.

I found my lab mates very friendly and helpful throughout this journey. Shilpa, Anupam, Subha, Debbithi, Dheeraj, Satarupa, Minarul Da and Somen da were always very warm to me and saved me from any difficulties. I am thankful to Paulami Di for enhancing my reading and writing skills. Her immense support and strict nature developed my confidence radically.

My juniors have also become my strong support these days. I would like to thank Dhananjoy, Solanky, Saheli, Aliva, Subhojit, Ishita, Manisha, Prosenjit, Debmalya, Namrata, Indrajit,

Piyali, Shuvronil, Tanmoy, Sanghita, Leenia, Barsha, Kaustav, Shaaista, Shreyashi, Subhankar for staying beside me. I feel very proud for meeting these young talents.

Jadavpur University is always very collaborative and dynamic. I found various people from different departments of this university who were ready to help whenever needed. Panchanan, Kunal, Ishita Di, Chayan, Rajdeep, Saikat, Arnab, Suchi, Swarup, Nirmal, Shaan Da, Bhaskar, Sudip, Mainak, Dhananjay, Animesh Da helped me with their experimental and computational facilities in trying times, which I will never forget. Especially, Dipak da (Dr. Dipak Chanda, CGCRI) was always there for me. I would like to take the opportunity to express my feelings to him.

My instrument and chemical suppliers had never let me down. They met every single criterion and have done their best. I would like to thank Monoranjan babu (Mono Enterprise), my childhood friend Sayak (Equations group) and Kallol da (K. K. Enterprise) for their tremendous support and timely delivery.

I was told to have quality food to get energized for the "Ph.D. battle". Although I am not a foodie, I prefer the sips of tea from Joydeb da, Mama, Hara da and Milan da. The 'oily' snacks of Avijit da and Milan da usually filled our days with great joy.

I am thankful to the Higher Education Department, Govt. of West Bengal, India for providing me the SVMCM fellowship to continue my research work. I would also like to acknowledge the FIST program of DST, India for the XRD and FESEM facilities in the Dept. of Physics, Jadavpur University. Additionally, I want to thank all the office staff and the members of my beloved department and Ph. D. cell of this university for helping me out whenever needed.

One name that I can never forget in this entire journey is my wife and colleague, Souravi. She stayed beside me during my tough times. Her skillful hands taught me various experimental techniques and biological assays. Both in my personal and professional life, I had her immense support.

Most importantly, I want to thank my family members from every corner of my heart. During this journey, I could not manage sufficient time for them due to my busy schedule. I take this opportunity to express my gratitude to my 'Ma' and 'Boni' for accepting me as I am. I have lost my 'Baba' in due course, whose dream was to see me successful in my life. I miss him and want to say a big "Thank you" for his sacrifice.

Love you all…

07/03/2022

(Shubham Roy)
Jadavpur University, Kolkata- 700032

Contents

Chapter 5: Metal ions (Cu^{2+}, Gd^{3+}) doped boehmite nanostructures for Cr(VI) detection in wastewater and their removal from aqueous media………........................ 75

Chapter 6: Nitrogenous carbon quantum dot tailored boehmite nanoparticles for the fluorometric detection of Cr(VI) in wastewater: A sensing probe for early-stage carcinogen detection ……………………...………………………………....... 97

Chapter 7: Polymeric carbon dot/boehmite nanocomposite made portable sensing device (Kavach) for non-invasive and selective detection of Cr(VI) in wastewater and living cells

Thesis publications

Certificates of conferences and seminars

Certificates of awards

Abbreviations

Abbreviation	Expansion
Ac	Alternating current
BET	Brunauer, Emmett, Teller
BJH	Barrett, Joyner, Halenda
Cdot	Carbon dot
Cr(VI)	Hexavalent chromium
Cu(II)	Copper ion
DFT	Density functional theory
DMF	Dimethyl formamide
DTA	Differential thermal analysis
FESEM	Field emission scanning electron microscopy
FRET	Forster resonance energy transfer
FTIR	Fourier transform infrared spectroscopy
FWHM	Full width at half maximum
Gd(III)	Gadolinium ion
γ-AlOOH	Boehmite
IFE	Inner filter effect
JCPDS	Joint Committee on Powder Diffraction Standards
kV	Kilovolt
μM	Micromoles
nM	Nanomoles
PET	Photoinduced electron transfer
PL	Photoluminescence
ppm	Parts per million
PVDF	Poly(vinylidenefluoride)
SV plot	Stern-Volmer's plot
tan δ	Tangent loss
TEM	Transmission electron microscopy
TDDFT	Time dependent density functional theory
TGA	Thermogravimetric analysis
UV-Vis	Ultraviolet visible spectroscopy
XRD	X-ray diffraction

List of publications

This thesis is based on the following publications (1-9)

[1] **Shubham Roy**, Souravi Bardhan, Kunal Pal, Saheli Ghosh, Paulami Mandal, Santanu Das, Sukhen Das, *Journal of Alloys and Compounds* 763 (2018) 749-758.

[2] **Shubham Roy**, Anupam Maity, Paulami Mandal, Dipak Kr. Chanda, Kunal Pal, Souravi Bardhan, Sukhen Das, *CrystEngComm*, 20 (2018) 6338-6350.

[3] **Shubham Roy**, Kunal Pal, Souravi Bardhan, Shilpa Maity, Dipak Kr. Chanda, Saheli Ghosh, Parimal Karmakar, Sukhen Das, *Inorganic Chemistry* (2019) 58, 8369−8378.

[4] **Shubham Roy**, Souravi Bardhan, Dipak Kr Chanda, Anupam Maity, Saheli Ghosh, Dhananjoy Mondal, Subhankar Singh, Sukhen Das, *Materials Research Express* (2020) 7, 025020.

[5] **Shubham Roy**, Souravi Bardhan, Dipak Kr Chanda, Saheli Ghosh, Dhananjoy Mondal, Jhilik Roy, Sukhen Das, *Dalton Transactions* (2020) 49, 6607.

[6] **Shubham Roy**, Souravi Bardhan, Jhilik Roy, Sukhen Das, *Materials Today: Proceedings* (2021) 46, 6223–6229

[7] **Shubham Roy**, Souravi Bardhan, Dipak Kr. Chanda, Jhilik Roy, Dhananjoy Mondal, and Sukhen Das, *ACS Applied Materials & Interfaces* (2020) 12, 43833−43843.

[8] **Shubham Roy**, Souravi Bardhan, Dhananjoy Mondal, Ishita Saha, Jhilik Roy, Solanky Das, Dipak Kr. Chanda, Parimal Karmakar, Sukhen Das, *Sensors & Actuators: B. Chemical* (2021) 348, 130662.

[9] **Shubham Roy**, Souravi Bardhan, Nur Amin Hoque, Sukhen Das, A Brief Review on Carbon-Based Nano-Systems for Detection of Pollutants in Industrial Wastewater and Living Cells and Their Subsequent Removal Strategies in Novel Applications of Carbon Based Nano-materials, *CRC Press, Taylor and Francis*, 2022.

Additional publications
(Not included in the thesis) (11-28)

[10] Kunal Pal, Dipranjan Laha, Pravat Kumar Parida, **Shubham Roy**, Souravi Bardhan, Ananya Dutta, Kuladip Jana, Parimal Karmakar, *Journal of Nanoscience and Nanotechnology*, 19 (2019) 3720–3733.

[11] Kunal Pal, **Shubham Roy**, Pravat Kumar Parida, Ananya Dutta, Souravi Bardhan, Sukhen Das, Kuladip Jana, Parimal Karmakar, *Materials Science & Engineering C*, 95 (2019) 204–216.

[12] Souravi Bardhan, Kunal Pal, **Shubham Roy**, Solanky Das, Abhijit Chakraborty, Parimal Karmakar, Ruma Basu, Sukhen Das *Journal of Nanoscience and Nanotechnology*, 19 (2019) 7112–7122.

[13] R. Majumder, S. Kundu, R. Ghosh, **S. Roy**, U. Guria, M. P. Chowdhury, *Applied Nanoscience* (2019) 9(7), 1553-1563.

[14] R. Ghosh, S. Kundu, R. Majumder, **S. Roy**, S. Das, A. Banerjee, U. Guria, M. Banerjee, M. K. Bera, Kiran M. Subhedar, M. Pal Chowdhury, *Applied Nanoscience* (2019) 9(8), 1939-1952.

[15] Souravi Bardhan, **Shubham Roy**, Dipak Kr. Chanda, Solanky Das, Kunal Pal, Abhijit Chakraborty, Ruma Basu, Sukhen Das, *Crystal Growth & Design* (2019) 19, 4588-4601.

[16] Debbethi Bera, Kunal Pal, Souravi Bardhan, **Shubham Roy**, Rubia Parvin, Parimal Karmakar, Papiya Nandy, Sukhen Das, *Adv. Nat. Sci: Nanosci. Nanotechnol.* (2019) 10(4), 045017.

[17] Rahul Majumder, Soumalya Kundu, Ria Ghosh, Monalisa Pradhan, Dibyendu Ghosh, **Shubham Roy**, Subhadip Roy, Manish Pal Chowdhury, *SN Applied Sciences* (2019) 2, DOI: 10.1007/s42452-019-1799-z.

[18] Anupam Maity, Subha Samanta, **Shubham Roy**, Debasish Biswas, and Dipankar Chakravorty, *ACS Omega* (2020) 5, 12421−12430.

[19] Abdulla Al Masum, Kunal Pal, Ishita Saha, Deblina Ghosh, **Shubham Roy**, Sougata Ghosh Chowdhury, Md Maidul Islam, Parimal Karmakar, *Adv. Nat. Sci.: Nanosci. Nanotechnol.* (2020) 11, 025020.

[20] Souravi Bardhan, **Shubham Roy**, Dipak Kr. Chanda, Saheli Ghosh, Dhananjoy Mondal, Solanky Das, Sukhen Das, *Dalton Transactions* (2020) 49, 10554.

[21] Subha Samanta, Anupam Maity, **Shubham Roy**, Saurav Giri, Dipankar Chakravorty, *The Journal of Physical Chemistry:C* (2020) 124, 21155−21169.

[22] Souravi Bardhan, **Shubham Roy**, Dipak Kr. Chanda, Dhananjoy Mondal, Solanky Das, Sukhen Das, *Microchimica Acta* (2021) 188, 134.

[23] Saheli Ghosh, **Shubham Roy**, Souravi Bardhan, Nibedita Khatua, Barsha Bhowal, Dipak K. Chanda, Solanky Das, Dhananjoy Mondal, Ruma Basu, Sukhen Das, *Journal of Electronic Materials* (2021) 50, 3836- 3845.

[24] Anupam Maity, Subha Samanta, **Shubham Roy**, Debasish Biswas, Dipankar Chakravorty, *Journal of Non-Crystalline Solids* (2021) 569, 120997.

[25] Dhananjoy Mondal, **Shubham Roy**, Souravi Bardhan, Jhilik Roy, Ishita Kanungo, Ruma Basu, Sukhen Das, *Dalton Transactions* (2022) 51, 451.

[26] Souravi Bardhan, **Shubham Roy,** Mousumi Mitra, Sukhen Das, Metal oxide/ graphene nanocomposites and their biomedical applications, in Metal Oxides for Biomedical and Biosensor Applications pp. 569 *Elsevier*, 2021.

[27] Souravi Bardhan, **Shubham Roy,** Sukhen Das, Carbon Dots: Fundamental Concepts and Biomedical Applications, in Nanotechnology for Biomedical Applications, *Springer-Nature*, 2021.

[28] Solanky Das, Dhananjoy Mondal, Souravi Bardhan, **Shubham Roy**, Dipak Kr. Chanda, Anupam Maity, Subhojit Dutta, Kamalakanta Mukherjee, Kaustuv Das, *Journal of Materials Science: Materials in Electronics* (2022) DOI: 10.1007/s10854-022-07894-7.

[29] Souravi Bardhan, **Shubham Roy**, Sanghita Das, Ishita Saha, Dhananjoy Mondal, Jhilik Roy, Dipak Chanda, Solanky Das, Parimal Karmakar, Sukhen Das, *Spectrochimica Acta Part A: Molecular and Biomolecular Spectroscopy* (2022) 273, 121061.

List of conferences/ seminars presented

Oral

[1] *"Natural plant resin gum acacia based multifunctional nano-device for heavy metal detection and remediation: From the nature, for the nature"*, ANVESHAN: National Student Research Convention: 2018-2019, Ganpat University, Gujarat, March 12-14, 2019.

[2] *"Natural plant resin gum acacia based multifunctional nano-device for heavy metal detection and remediation: From the nature, for the nature"*, ANVESHAN: National Student Research Convention: 2018-2019, Central University of Jharkhand, February 18-19, 2019.

[3] *"Multifunctional Nanosensors",* One Day Workshop on Material Synthesis & Characterization Techniques, Jadavpur University, February 29, 2020.

Poster

[4] "*Multifunctional fluorescence-based nano sensor for detection and removal of Cr(VI)"*, New Directions in Physical Sciences-2020 (NDPS-2020), Jadavpur University, Kolkata, February 25, 2020.

[5] *"Waste capacitor: A fresh approach to detect and remove Cr(VI) from water and making it an energy harvesting material"*, Third International Conference on Material Science (ICMS-2020), Tripura University (A Central University), India March 04-06, 2020.

[6] *"Boehmite based "MFNS" for fluorescent sensing and removal of hexavalent chromium: A waste to wealth conversion"*, National Seminar on Physics at Surfaces and Interfaces of Soft Materials-2019 (CMPRC), Jadavpur University, Kolkata, September 26-27, 2019.

[7] *"A polymer-nanocomposite based multifunctional material for fluorescent sensing and removal of heavy metals and energy storage applications"*, Young scientists Colloquium (MRSI) 2019, Saha Institute of Nuclear Physics, Kolkata, September 17, 2019.

[8] *"Hydrothermal synthesis of boehmite (γ-AlOOH) nanoparticles, nanoneedles and nanoflowers: A brief comparison in dielectric properties",* International Conference on Emerging Trends in Chemical Sciences, Dibrughar University, February 26-28, 2018.

[9] *"Preparation of Copper Oxide Nano-Flowers Using High Energy Electron Beam"*, Nanotechnology: From Materials to Medicines and their Social Impact, BITM, Kolkata, March 25, 2017.

List of awards/ achievements

[1] Young Achievers Award (2020) INSC, Bangalore for the publication in ACS Applied Materials & Interfaces.

[2] 2nd place for Innovative Research (Basic Sciences, 2019), Anveshan-Student Research Convention (National Level), UGC-AIU, India.

[3] 1st place for Innovative Research (Basic Sciences, 2019), Anveshan-Student Research Convention (Eastern Zone), UGC-AIU, India.

List of figures

Chapter 4

Chapter 5

Chapter 6

Chapter 7

Appendix 1

Appendix 2

Appendix 3

List of tables

Chapter 1

Introduction

Chapter 1

Introduction

1.1 Historical Development of the Wastewater Treatment Technology

In ancient days, people were aware of water pollution. Shreds of evidence suggest that Indus Valley (26-1700 BC) was far advanced in wastewater management [1]. They used separate channels for drainage water, which was passed through tapered terra-cotta pipelines into small sumps [2]. The sumps were used to collect the solid wastes using the sedimentation process and the freshwater was further used from the above. Similarly, Egyptian, Greek, and Roman civilizations were also equipped with their wastewater management systems [3]. The taste and odor are the key parameters to ensure the water quality back then.
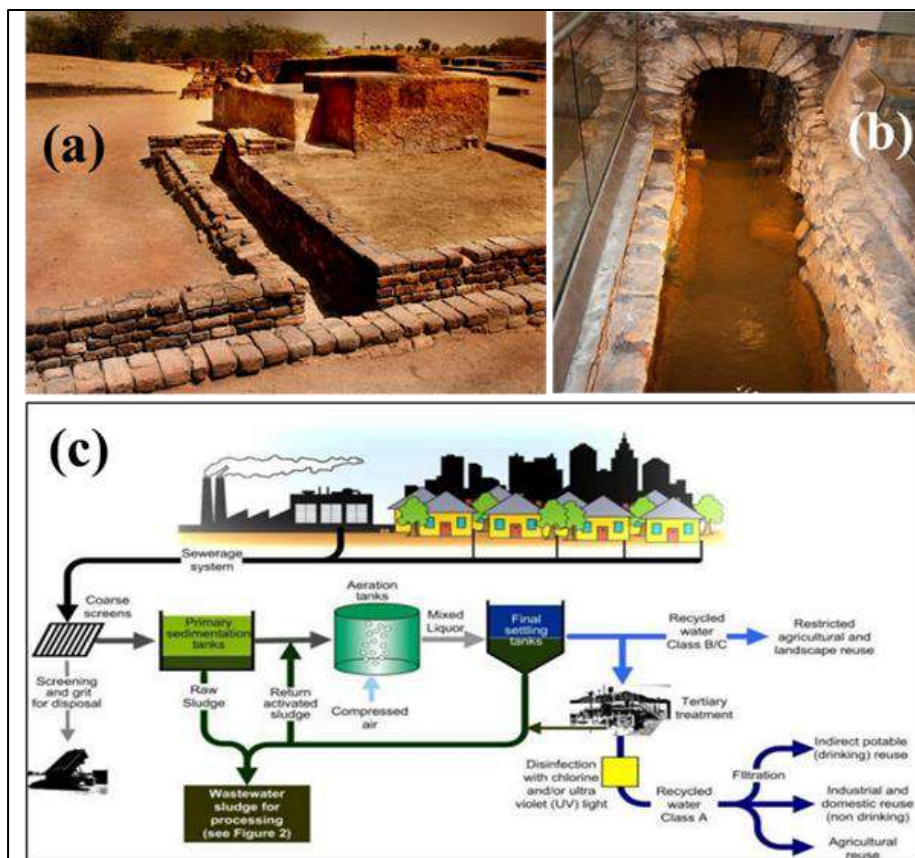
Figure 1.1 *Water monitoring and treatment technologies in ancient days*

The Greek people used charcoal to eliminate harmful products from the drinking water. Coagulants like alum were used by ancient Egyptians to achieve clean water. The positive

surface charge of alum was responsible to adsorb negatively charged molecules and compounds.

The world's first water filter, Hippocratic sleeves was fabricated in 500 BC. It is a fabric to filter boiled water for drinking. Hippocrates, a Greek physician invented such a fabric to remove sediments from drinking water. Similarly, Aqueducts have gained immense popularity around 200 BC as they can transport clean water from one area of plentiful water supply to areas of high population. These aqueducts are revolutionary and the foundation of bigger cities at that time.
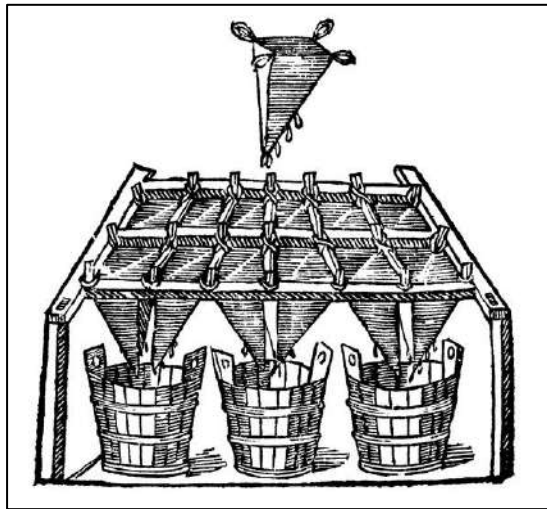
Figure 1.2 A schematic diagram of Hippocratic sleeves

Things were changed when the Roman era collapsed. It is known as the sanitary Dark Age (476-1800 AD) [1]. During this period, the culture of wastewater treatment and water resource management was abandoned [4]. Lack of concern regarding hygiene and health with lots of rumors and convictions probably caused this.

In the year 1627, Sir Francis Bacon invented the desalination process, which has become a futuristic way to combat the clean water crisis. In reality, extensive research is going on the desalination process until now. In the early 18th century, Robert Thom built the world's first water treatment plant in Scotland. The treatment plant used slow sand filters for water purification and distributed the water through early sewer systems to everyone within the city limits.

Urbanization and the evolution of technology during the 19th century brought industrial wastes and microbial contamination into the picture [5]. In 1854, chlorine disinfection was introduced to prevent cholera in European countries. Arden and Lockett (1913) introduced the 'activated sludge process' to reduce biological oxygen demand (BOD) and ammonia levels in the water.
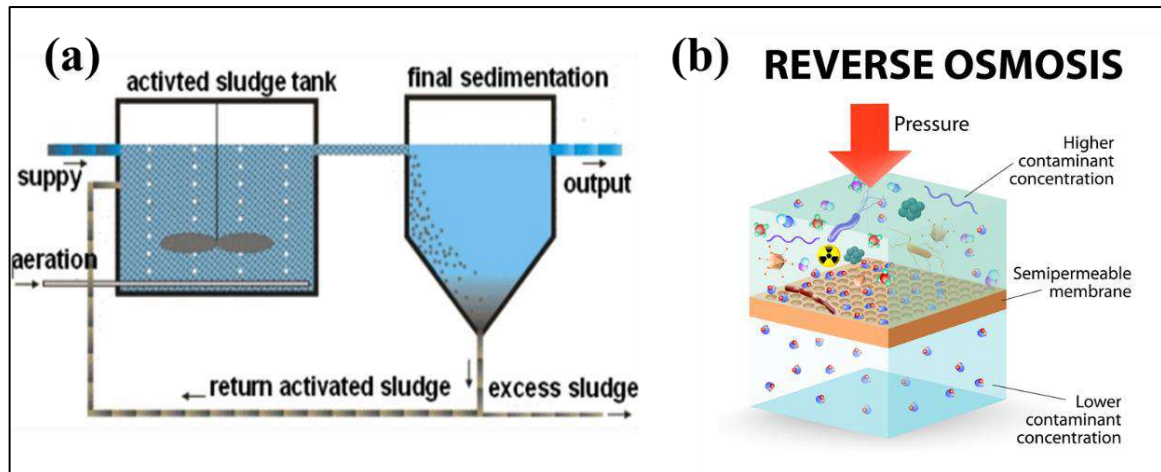
Figure 1.3 *The activated sludge process (a) and the reverse osmosis process (b) for water treatment*

The idea behind this process is to cultivate microorganisms to consume organic wastes and oxidize ammonium to nitrate and nitrite. In the late 1970s, UV disinfection and reverse osmosis (RO) processes were introduced. These advanced technologies can easily disinfect water and remove hazardous pollutants in a very facile way.

Nowadays, water pollution is occurring in numerous pathways, among them, industrial water pollution is causing severe harm to the environment. Various industries like textile, leather, steel, chemical, fertilizer, etc. are discharging hazardous contaminants directly into the water through pipelines and small canals [6]. Industrial contaminants, such as chromium, arsenic, lead, mercury is enormously harmful to human health even at lower doses [7] and some of them, iron, nitrate, and sulphate can also damage water bodies above a critical limit [8]. Long-time exposure to these contaminants results in various diseases such as chronic diarrhea, various bowel syndromes, improper pigmentation of skin [9] beside several carcinogenic diseases [10] like cirrhosis of the liver, lung cancer, skin cancer, etc., which could be minimized if the proper wastewater management system is employed. Thus, wastewater monitoring and treatment in a proper way is much needed.

1.2 Wastewater monitoring and treatment in India

In a country like India, where basic sanitation is a difficult task to maintain due to the massive population (~138 crore, 2020), it is quite challenging to impose advanced sensors and wastewater monitoring systems in households. Urbanization and growing population restrict the overall cleanliness in the urban region of the country. Whereas, villagers are reluctant and somewhat bound to use untreated water for different purposes. It is also very difficult to ensure water safety in most cases due to such an escalated population. Most wastewater monitoring systems are equipped with multiple sensors and filtration systems,

which increases their cost and complexity [11]. Such complexities might be an issue for untrained people to handle these devices. Cost is also an important factor to procure such systems. Being a growing economy, it is difficult for the Indian mass to purchase and maintain these costly devices in their household. Thus, it seems very difficult to use clean water in India. Sometimes strong conviction against the traditional approach plays an important role to reject modern water remediation systems in rural areas.

Despite these facts, the growing economy and proper education lead to follow newer approaches nowadays. Technological advancements also play a role to minimize the cost of productivity growth. The young generation seems to be health-conscious, which might be another reason for the increasing demand for portable and handheld water filtration systems in recent years [12].

Various river safety projects and centralized action plans have been carried out by the state and the central government to resolve wastewater issues in India. Ganga action plan is quite a directional project among such river safety policies [13]. According to a World Bank 2010 report [14], an improved policy about potable water with standard guidelines has been proposed. This report depicts the functions to support drinking water safety. These river safety projects have been pursued on a large scale and local wastewater issues sometimes cannot be resolved by implementing such large-scale projects and policies. Thus, several NGOs and private organizations are working hard on local wastewater treatment projects [15]. These organizations provide education and awareness among the people and train them to implement central policies in the locality.

Numerous central funding agencies, such as the Department of Science and Technology (DST), Department of Biotechnology (DBT), University Grants Commission (UGC) and Council of Scientific and Industrial Research (CSIR) are providing funds and infrastructure to develop novel research ideas and nurture young minds through various central and state universities and research institutes. These funds and infrastructures have been utilized among the research students and scientists for the training and development of modern wastewater monitoring technologies and devices for the Indian population. Such research projects have introduced modern technologies (like nanoscience and nanotechnology) and become very useful in recent years.
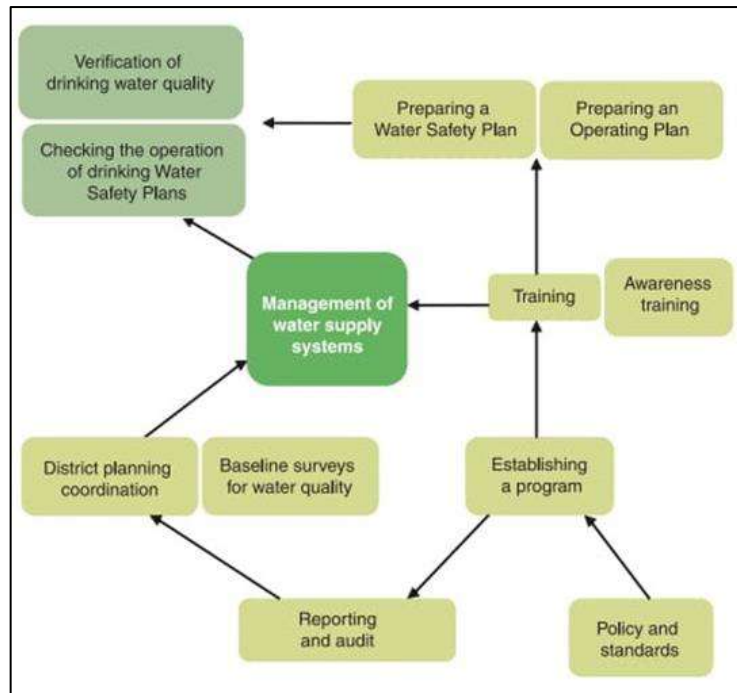
Figure 1.4 *Functions to support the drinking water safety planning*

1.3 Emergence of nanotechnology in wastewater treatment

Nanotechnology is one of the newest branches of material science. It deals with various physicochemical aspects of fine nanomaterials (~10-100 nm) and their applications in different fields. Recently, nanomaterials have been employed in numerous wastewater-related problems, especially in the detection of hazardous contaminants and their removal from the wastewater. Globally, researchers are focused to detect and measure the level of contamination through various fluorometric and colorimetric assays. These detection methods are relatively new and enormously sensitive.
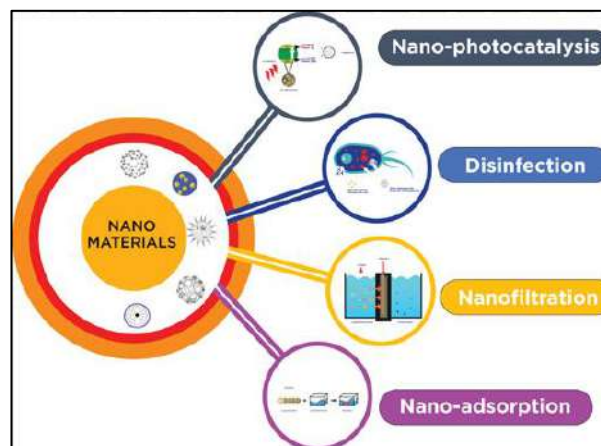
Figure 1.5 *Application of nanomaterials in wastewater treatment*

Fluorescent nanomaterials and quantum dots have emerged as promising candidates in this field due to their biocompatibility and extreme sensitivity. On the other hand, the high aspect ratio (surface to volume) of fine nanomaterials makes them preferable for the adsorption-mediated removal of contaminants. Due to the biocompatible nature and rapid response of these nanoprobes, these functional materials have been used in different biological experiments, such as bio-sensing and studying the bioaccumulation of hazardous contaminants.

1.3.1 Fluorometric detection of contaminants

Fluorometric detection techniques involve two main pathways, namely, energy transfer and charge/electron transfer. When fluorophores of the sensor molecule find a contaminant molecule/ion in its close vicinity, it can either collide with the contaminant or may interact by donating/accepting charge carriers. Such interaction results in three main pathways of fluorometric detection, namely, Inner Filter Effect (IFE) [16], Photoinduced Electron Transfer (PET) [17], and Förster Resonance Energy Transfer (FRET) [18].

It is observed that when fluorophores interact with foreign elements, such as ions, molecules, complexes with a relatively higher concentration, some of those 'block' the emission of the fluorophore [19]. In this case, some fluorophores are less accessible than others and result in fluorometric quenching (turn off). In other words, fluorescence quenching suggests the presence of the targeted quencher in the sample. IFE is a steady-state phenomenon that usually occurs in the ground state. Studies suggest that carbon dot undergoes IFE in various cases to detect silver nanoparticles in cosmetics, biomarkers like alkaline phosphatase, hexavalent chromium, and ascorbic acid in wastewater [20]. IFE can happen in other nanostructures like CNT and graphene quantum dot (GQD). Zhao et al., 2010 [21] reported the behavior of Bovine Serum Albumin adsorbed onto CNT through IFE. Similarly, GQD depicts its efficacy in detecting artemisinin, cyanide, and blood glucose using the inner filter effect [22].

In PET, donors are nearby (<10 nm) with acceptors get excited when photons are irradiated [23]. This donor-acceptor pair in an excited state collides with each other and electrons get transported to the acceptor moiety causing a rapid alteration in the fluorescence intensity. This phenomenon is known as photoinduced electron transfer. Fluorescence lifetimes get changed in this phenomenon as the PET occurs in the excited state. Lan et al. in their 2015 paper [24] proposed a carbon dot-based turn-on sensor (sensitivity 84 nM) for hydrogen peroxide following the PET mechanism. In this case, the

carbon dot acts as an electron acceptor. A similar phenomenon has been reported by Pan et al. [25] showing detection of mercury ions using PET-based technique. Carbon nanotube undergoes PET as well [26]. Phthalocyanines-CNT complex shows significant photoinduced electron transfer as reported by Ballesteros et al. in their 2007 paper [27].
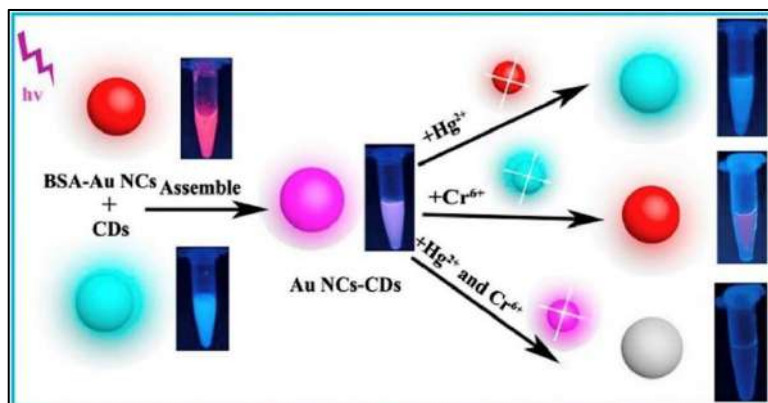
Figure 1.6 A typical fluorometric sensing process. (Source: Li et al., Nanophotonics, 10(2), 2021, pp. 877-908)

FRET is the radiation-less energy transmission from the donor molecule to the acceptor molecule. The donor molecule is the fluorophore that initially absorbs the energy and the acceptor is the molecule to which the energy is subsequently transferred. To achieve a decent FRET system, the distance between the donor and the acceptor must be less than 5-10 nm [28]. The efficacy of this energy transfer is inversely proportional to the sixth power of the distance between donor and acceptor, which makes FRET extremely sensitive to a little alteration in distance [29]. Currently, FRET-based sensing probes are quite popular due to their sensitivity. Bu et al. [30] developed a carbon dot-gold nanoparticle FRET system for polybrominated biphenyl detection with a sensitivity of 0.039 µg/ml. FRET-based ammonia sensor with carbon dot as a sensing probe [31] has also been reported recently showing a 3 ppm detection limit.

1.3.2 Adsorption: the cheapest way of contamination removal

The enhanced surface area and porosity greatly influence the overall sorption capacity of a nanomaterial. In reality, nanomaterials have meso/microporous pores on their surface, which makes them promising industrial adsorbent materials. If the sorption occurs by weak Van der Waals forces, it is called physical adsorption. If the adsorption is related to chemical bonding, the sorption is referred to as chemisorption. The adsorption mechanism of a specific interaction could be validated broadly by using three unique models (isotherms), namely, the Langmuir model, Freundlich model and BET adsorption model.
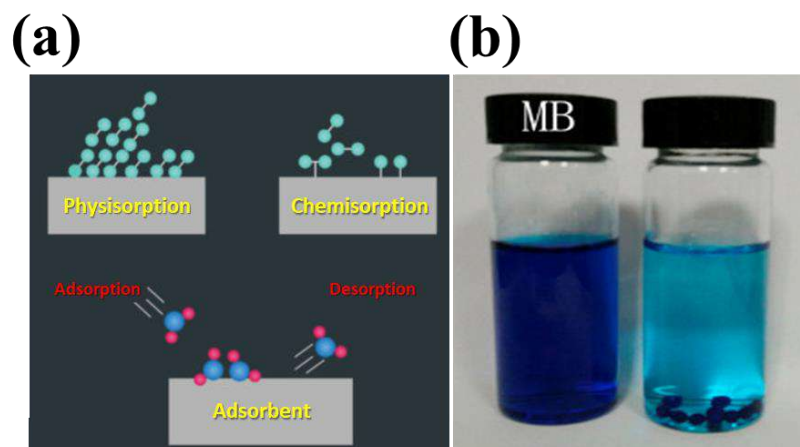
Figure 1.7 *(a)Different types of adsorption processes, (b) adsorption of methylene blue dye using a core-shell nanosystem (Source: Chen et al., Journal of Environmental Chemical Engineering, 5(2), 2017, 1732-1743)*

Langmuir (1918) considered monolayer adsorption of gases/vapors having an identical and fixed number of pores. But in most cases, the active adsorption sites are energetically heterogeneous. Such deviation leads us to the Freundlich model in which, energetically adsorption takes place on a heterogeneous surface. The Freundlich model is not a physical model, rather a mathematical tool to interpret sorption experiments. Unlike the Langmuir model, the Freundlich isotherm does not approach linearity at low concentrations.

The Brunauer-Emmett-Teller (BET) model (1938) deals with the multilayer adsorption theory. This model was developed to interpret submonolayer to multilayer sorption of vapor onto solid surfaces. The BET theory is the backbone of porosity and surface area measurements of solids.

In reality, these models are equally valid for any solute from a solution and have enormous potential in determining the adsorption-based removal mechanism of a toxic solute onto the surface of a solid nanostructure.

1.4 Hexavalent chromium: detection and removal

1.4.1 Why hexavalent chromium is a persistent threat to the environment?

Hexavalent chromium (Cr(VI)) is a well-known carcinogen. It can spread through soil and water bodies from various industries like leather tanning, pigment production, metallurgy, electroplating causing various diseases such as nasal and dermal irritation, ulcer, eardrum perforation, and lung cancer. Because of its extremely harmful nature to human health and the environment, various regulating agencies limited its exposure to the environment. The

current federal drinking water standard (the United States Environmental Protection Agency) for total chromium is 0.1 mg/L or 100 ppb, whereas, in India, it is 0.5 mg/L or 500 ppb (IS 10500).
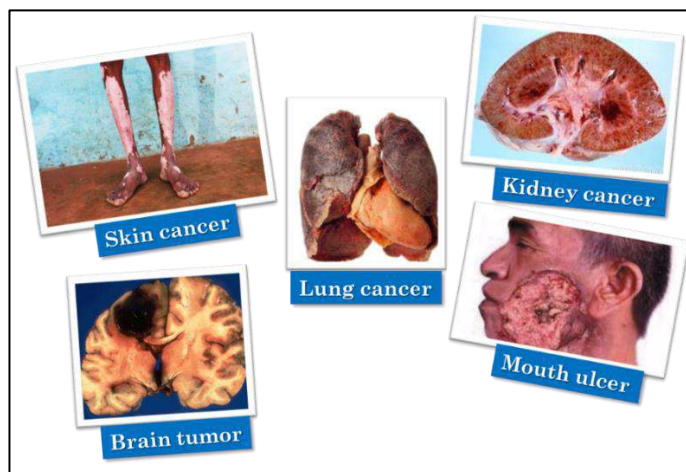
Figure 1.8 *Various diseases due to the hexavalent chromium contamination*

Whereas, the World Health Organization (WHO) restricts the maximum limit of hexavalent chromium in wastewater and soil is 0.05 ppm and 0.1 ppm respectively. The detection and segregation of hexavalent chromium from water streams are immensely challenging. Apart from these, the accumulation of Cr(VI) in aquatic living varieties can cause biomagnifications. Therefore, developing selective and sensitive methods to detect and remove Cr(VI) ions for environmental monitoring, medical diagnostics and food safety is having considerable importance.

1.4.2 Fluorometric sensing of hexavalent chromium

Globally, heavy metal pollution is a burning issue. Various approaches have been utilized in the past few decades to get rid of this [32-34]. Numerous conventional detection methods have been used to quantify heavy metals in water. Techniques like ICP-AES, ICP-MS and AAS have been employed for such quantification studies [35-37]. The limit of detection (LOD) of these conventional methods lies between a few millimolar and micromolar ranges [38-39]. According to the World Health Organization (WHO), sometimes these contaminants are present below a few nanomolar range in water and causes enormously harmful effects in local biota [40]. Thus, a more sensitive detection technique is required.

Initially, it was found that the electrochemical technique [41-42] could be used as an alternative for those conventional detection mechanisms. But bulk instrumentation and

costly sample preparation made this electrochemical technique [43] obsolete in the following years. Relatively a simpler fluorometric approach [44-45] was developed by scientists all over the world to minimize the detection cost with simultaneously improved LOD values.

Various inorganic and organic compounds and interfaces have been initially employed in heavy metal sensing. Hassan et al. [46] in their 2005 paper initially proposed a Rhodamine-B based fluorometric sensor for chromium ion detection. The sensor exhibits a micromolar LOD value when exposed to hexavalent chromium. This is probably the first time when quantitative fluorometric detection of hexavalent chromium was done using some fluorophore. The sensitivity of the sensing probe was further increased by scientists in the following decades, which make this fluorometric approach popular. Lin et al. in their 2017 [47] paper reported a Zr-based metal-organic framework having an exceptional LOD value (1.8 µM). This MOF is quite stable and biocompatible according to their report. Additionally, Cao and his group [48] reported two solvent-stable MOFs as a recyclable luminescent probe for hexavalent chromium. The detection limit, in this case, is found to be 2 µM.

The discovery of carbon dot and graphene quantum dot unlocked new avenues of fluorometric sensing after 2010. The biocompatible nature of these quantum dots makes them promising sensor materials [49]. Scientists used the enhanced and tunable fluorescence of these quantum dots [50-51] to detect various heavy metals. Zhang et al. (2018) [52] suggested a novel carbon dot-based fluorometric sensor for Cr(VI). The quantitative detection of Cr(VI) was realized through Cr(VI) acting as a quencher to quench the fluorescence of carbon dots by inner filter effect (IFE) and static quenching effect. Under the optimal conditions, the LOD was found to be 5 nM, which was indeed a great achievement. In later years, Lu and his group (2019) [53] and Xu et al. [54] proposed quantum dot-based nanosystems of Cr(VI) probing in water. Zhang et al. [55] alternatively co-doped nitrogen and sulfur into the quantum dot matrix to enhance the fluorescence as well as the sensitivity of the probe. In 2018, Mutuyimana and his team [56] successfully synthesized yellow emissive carbon dots for chromium detection. The synthesized structure is stable in an aqueous medium and the recovery rate is significantly high in this case. In reality, the discovery of fluorescent compounds like carbon dots, paved the path for fluorometric detection in a facile manner [57].

Polymers and nanoparticle encapsulated polymer matrices have also gained importance in recent years. Vallejos and co-workers (2012) [58] reported a fluorogenic sensory film made of bulk radical polymerization of different comonomers, one of which contained a piperazinedione motif as a sensory fluorophore. This film is capable to detect hexavalent chromium in water. The LOD value, in this case, lies around 1 ppb, which is quite low compared to other chromium sensors. Similarly, polyaniline (PANI) coated ethyl cellulose shows promising affinity towards chromium sensing as stated by Qui et al. in their 2014 paper [59]. Polymer-coated gold nanoparticles also showed promising chromium sensing efficacy. Wang et al. (2018) [60] stated this newer sensing approach with a LOD value of 0.63 µM.

Additionally, several research works have been carried out by other research groups and individuals in the past few years that made a global impact on water research. Bardhan et al. recently reported a few papers [61-62] on natural nanomaterial-based fluorometric sensing of multiple heavy metal ions (iron and chromium). According to their study, the LOD values are significantly low for these green nanostructures, namely microcline. They made a polymeric alternative [61] of such fluorometric sensors for on-site studies. Similarly, Rapti et al. [63] fabricated a Zirconium doped metal-organic framework for hexavalent chromium removal and detection. The detection limit is found to be 4 ppb in this case. Another major advancement has been proposed by Sompalli and co-workers [64] on solid-state detection of heavy metal through fluorescence alteration method. They used tailor-made porous polymer and silica monolithic designs for this purpose. Biopolymeric gum acacia has also been used in chromium sensing by Shahnaz et al. (2020) [65] recently.

1.4.3 Removal of hexavalent chromium

On the other hand, the removal of contaminants from water is also required. There are several techniques to remove hexavalent chromium from wastewater [43-44]. Among them, adsorption, piezocatalysis, electrocatalysis and photocatalysis have gained importance in the past few decades [45-47]. Adsorption is a classical approach to eliminate any impurity from water. Progress of modern nanotechnology results in various types of adsorption mechanisms [48], such as chemisorption and physisorption. Single and multilayered adsorption models have also been tested based on different sorption isotherms, like the Langmuir model and Freundlich model [49]. In reality, the enhanced

aspect ratio of nanoparticles enables capture of contaminants into their pores and remove them from the wastewater [50].

This adsorption technique using maghemite nanoparticles was implemented by Hu et al. (2005) [51] to remove hexavalent chromium from water. In the same year, Niu and co-workers [52] presented iron nanoparticles as hexavalent chromium adsorbents. Later on, magnetic nanoparticles show promising chromium adsorption efficacy. Montmorillonite-supported magnetite nanoparticles for the removal of hexavalent chromium was reported by Yuan et al. (2009) [53].

Table 1.1 *Summary of a few adsorbent materials recently reported for Cr(VI) removal*

Adsorbent Material	Maximum Sorption Capacity	Isotherm	Kinetics	Optimum pH	Ref
Algae, *Sargassum dentifolium*	1.5g/100 mL	Langmuir	---	7.0	[72]
Algae, *S. bevanom*	100 mg/L	Langmuir & Freundlich	Pseudo second	3.0	[73]
Algae, *Sargassum sp. (brown marine algae)*	6.877 mg/g	Langmuir	Pseudo second	2.0	[74]
Fungal, *Phanerochaete chrysosporium*	344.8 mg/g	Langmuir	Pseudo-first	3.0	[75]
Fungal, *A. fumigatus* Fresenius	50 mg/L	Langmuir & Freundlich	Pseudo-second	5.5	[76]
Fungal, *Aspergillus niger*	97.1 mg/g	Langmuir	Pseudo-second	2.0	[77]
multi-walled carbon nanotube (MWCNTs)	16.23 mg/g	Langmuir	Pseudo-second	3.0	[78]
MWCNTs	37 mg/g	Langmuir & Freundlich	Pseudo-second	4.0	[79]
Functionalized MWCNTs	270.27 mg/g	Langmuir	---	6.0	[80]
Carbon-Microsilica Composite	18.9 mg/g	Langmuir	Pseudo-second	2.0	[81]
Graphene oxide	49 mg/g	Langmuir	Pseudo-second	3.0	[82]
Graphene oxide/NiO NCs	198 mg/g	Langmuir	Pseudo-second	4.0	[83]
Graphene oxide-Fe_3O_4	3.197 mg/g	Langmuir	Pseudo-second	2.0	[84]
Fe_3O_4/Graphene/PANI	155.54 mg/g	Langmuir	Pseudo-second	2.0	[85]
PANI/Ag(AMPSA)/GO QDs NC	59.96 mg/g	---	Pseudo-second	2.0	[86]
Oxidized and Unoxidized Activated Carbon (AC)	30.84 and 27.51 mg/g	Langmuir	Pseudo-second	2.0	[87]
mFeOOH@AC	28.1 mg/g	Langmuir	Pseudo-second	3.0	[88]
Silica-AC	60.9 mg/g	Freundlich	---	---	[89]
TSA-Polyaniline @CNT NC	158 mg/g	Langmuir	---	2.0	[90]

The adsorption efficiency, in this case, was found to be 15.3 mg/g. A chitosan-based iron nanoparticle was used by Geng and co-workers (2009) [54]. Such biocompatible adsorbents tremendously enhance the applicability of adsorption-based removal techniques. Recently, NiO/ Ni nanoparticles [55] and mesoporous silica [56] have emerged as Cr(VI) adsorbents. A detailed description of such adsorbent has been illustrated in Table 1.

1.5 Outline of the present work

1.5.1 Origin of the problem

In early 2018, numerous reports have pointed out that a village near Kolkata (Bantala, East Kolkata suburban area, West Bengal, India) and its surroundings were suffering from hexavalent chromium mediated diseases. Endless efforts have been made to get rid of such chromium contamination. Closer observation revealed that the contamination was coming from various water bodies. Initially, it was hard to find the cause, but a proper investigation indicated that some local tanneries were mistakenly spreading their dangerous chromium contained end-products into a local canal. The water of that canal was tested through conventional methods, such as inductively coupled plasma (ICP-AES), mass spectrometry and a high percentage of chromium (~20 ppm) was found. But these conventional detection methods are costly and the sample preparation is difficult. Such traditional methods are inefficient to resolve the problem by removing the contaminants from the water.

Figure 1.9 Photograph of the Bantala leather complex area, Kolkata and the original photograph of the wastewater collection from the contaminated canal

Additionally, during the literature review, it was found that an insufficient amount of research has been paid on simultaneous detection and removal of hexavalent chromium in wastewater and living systems. The removed chromium is also a threat to the environment if improperly handled. Thus, a proper elimination/ reuse of the removed chromium is required.

Henceforth, a goal was set to fix this problem by employing efficient and cost-effective multifunctional materials.

1.5.2 Aims and objectives

Recent advancements in nanotechnology equipped us with several nanostructured materials capable of determining contaminants rapidly and removing them from any medium in a facile manner [66]. Hence, such real-life problems could be addressed by employing efficient, handheld, rapid and multifunctional devices that can detect and remove hexavalent chromium from the contaminated wastewater. Not only simultaneous detection and removal of hexavalent chromium from wastewater but also converting it into a dielectric separator for energy harvesting applications. These smart, multifunctional materials can detect the presence of the targeted heavy metal in the wastewater and can entrap it by using a facile adsorption process [5]. Thereafter, it changes the microstructure and results in enhanced dielectric properties, which could be useful in fabricating dielectric separators for energy harvesting applications. Hexavalent chromium sensing in living cells will be another major aspect of this work. This study will be pursuing the bio-transmission pathways and most importantly detection of an early stage of heavy metal-induced carcinogenesis.

After considering recent developments and previous works on wastewater treatment, it has been noted that there is a discrepancy in the implementation of low-cost and multipurpose devices in water treatment. Globally such multifunctional devices and materials are needed to combat water pollution. Keeping this in mind, the entire work has been divided into six distinct clusters,

- Preparation of cost-effective and biocompatible compounds using the facile cost-effective technique.
- Comprehensive and meticulous characterization of the nanostructured samples using various characterizations. Particularly, emphasis will be given to Rietveld

refinement-based crystallographic studies to validate the primary reason behind crystal defects.

- Study of basic optical properties of the materials by using absorption, emission and excitation spectroscopy methods. Time-Dependent Density functional calculations (TDDFT) could be utilized here to estimate electronic transition probabilities between different molecular orbitals.

- Fluorometric detection of hexavalent chromium using synthesized nanostructures. Emphasis will be given on quantitative analysis of the detection in all water types and detection pathways. Fabrication of some solid-state sensing devices could be done in this section of the work. The sensing pathways could be computed using the theoretical DFT approach and verified experimentally by estimating the fluorescence lifetimes of the fluorophores.

- Adsorption-based removal of the toxic hexavalent chromium. Adsorption capacity, isotherm, kinetics and pathways will be studied in a detailed manner.

- After completion of the removal process, chromium adsorbed adsorbent will be used in energy storage applications. Especially, the adsorbed materials will be used as dielectric separators for energy harvesting.

1.5.3 Selection of nanomaterials

Material selection and cost-effective synthesis are the key parameters to minimize the production cost. In reality, metallic oxyhydroxide compounds are exceptionally well when it comes to the surface adsorption of metal ions [67-68]. These highly stable compounds are having a high surface area with significant mesoporosity (5-50 nm) [69]. Generally, these compounds are biocompatible and they have prominent crystal defects, which is responsible for their enhanced electrical permittivity and defect-mediated fluorescence [70]. Despite having such promising properties, a very limited amount of interest has been paid on oxyhydroxide compounds. Synthesis of such compounds is relatively easier. These materials generally require solvothermal and sol-gel-based techniques to prepare, which minimizes the cost of production. These methods consist of one or two-step processes that also reduce the complexity of production. As mentioned previously, proper detection and removal of contaminants could be possible if a material with a large surface area and 'sponge-like' porosity is employed. Binding affinity is also an important feature that might do well in sensing hexavalent chromium. Keeping these in mind, boehmite (γ-AlOOH), an oxy-hydroxide phase of aluminum is selected for this purpose. Boehmite is a

non-toxic and biocompatible material with a wide band gap (more than 2.5 eV) [15]. It has high porosity (3-5 nm) and surface area (~100 m^2/g) [16], which is required for the adsorption-mediated removal of toxic hexavalent chromium. Briefly, the following features of boehmite will be used in this work.

Figure 1.10 *The orthorhombic structure of boehmite (Source: Vatanpour et al., J. Membrane Sci., 401, 2012 pp.132-143)*

- High surface area (above 50-100 sq.m/g) with enhanced porosity
- Non-toxic, Low-cost and biocompatible
- Impressive structure-property correlation
- A wide band semiconductor with a tunable band gap
- Water soluble and easy to use
- Stability

Although structural and numerous synthesis processes have been well established for this material [71], the application of this nanostructure in wastewater treatment is still an unexplored avenue. Modified boehmite with various quantum dots, polymers, metal ions to enrich its effectiveness towards multifunctional wastewater treatment and monitoring approach would surely unlock new avenues.

1.5.4 Organization of the thesis

Chapter 1:

Introduction

Chapter 2:

Methodology

Chapter 3:

Synthesis & characterization of boehmite (γ-AlOOH) nanoparticles of different particle sizes to study their growth mechanisms for validating their optical activities and energy storage capacities

Chapter 4:

Synthesis & characterization of boehmite (γ-AlOOH) nanostructures of different morphologies and their application in detection, removal of Cr(VI) and using it as a 'Waste capacitor'

Chapter 5:

Metal ions (Cu^{2+}, Gd^{3+}) doped boehmite nanostructures for Cr(VI) detection in wastewater and their removal from aqueous media

Chapter 6:

Nitrogenous carbon quantum dot tailored boehmite nanoparticles for the fluorometric detection of Cr(VI) in wastewater: A sensing probe for early-stage carcinogen detection

Chapter 7:

Polymeric carbon dot/boehmite nanocomposite made portable sensing device (Kavach) for non-invasive and selective detection of Cr(VI) in wastewater and living cells

Chapter 8:

Conclusion and outlook

References

[1] Lofrano, G. and Brown, J., 2010. Wastewater management through the ages: A history of mankind. Science of the Total Environment, 408(22), pp.5254-5264.

[2] De Feo, G., Antoniou, G., Fardin, H.F., El-Gohary, F., Zheng, X.Y., Reklaityte, I., Butler, D., Yannopoulos, S. and Angelakis, A.N., 2014. The historical development of sewers worldwide. Sustainability, 6(6), pp.3936-3974.

[3] Angelakis, A.N. and Spyridakis, D.S., 2010. A brief history of water supply and wastewater management in ancient Greece. Water Science and Technology: Water Supply, 10(4), pp.618-628.

[4] Yannopoulos, S., Yapijakis, C., Kaiafa-Saropoulou, A., Antoniou, G. and Angelakis, A.N., 2017. History of sanitation and hygiene technologies in the Hellenic world. Journal of Water, Sanitation and Hygiene for Development, 7(2), pp.163-180.

[5] Geels, F.W., 2006. The hygienic transition from cesspools to sewer systems (1840–1930): the dynamics of regime transformation. Research policy, 35(7), pp.1069-1082.

[6] Yadav, V.B., Gadi, R. and Kalra, S., 2019. Clay based nanocomposites for removal of heavy metals from water: a review. Journal of environmental management, 232, pp.803-817.

[7] Duruibe, J.O., Ogwuegbu, M.O.C. and Egwurugwu, J.N., 2007. Heavy metal pollution and human biotoxic effects. International Journal of physical sciences, 2(5), pp.112-118.

[8] Du, L., Wu, A., Liu, G., Li, H., Yu, B. and Wang, X., 2020. Green autofluorescence eleocytes from earthworm as a tool for detecting environmental iron pollution. Ecological Indicators, 108, p.105695.

[9] Fernandez-Luqueno, F., López-Valdez, F., Gamero-Melo, P., Luna-Suárez, S., Aguilera-González, E.N., Martínez, A.I., García-Guillermo, M.D.S., Hernández-Martínez, G., Herrera-Mendoza, R., Álvarez-Garza, M.A. and Pérez-Velázquez, I.R., 2013. Heavy metal pollution in drinking water-a global risk for human health: A review. African Journal of Environmental Science and Technology, 7(7), pp.567-584.

[10] Fasinu, P.S. and Orisakwe, O.E., 2013. Heavy metal pollution in sub-Saharan Africa and possible implications in cancer epidemiology. Asian Pacific journal of cancer prevention, 14(6), pp.3393-3402.

[11] Massoud, M.A., Tarhini, A. and Nasr, J.A., 2009. Decentralized approaches to wastewater treatment and management: applicability in developing countries. Journal of environmental management, 90(1), pp.652-659.

[12] Capitan-Vallvey, L.F. and Palma, A.J., 2011. Recent developments in handheld and portable optosensing—A review. Analytica chimica acta, 696(1-2), pp.27-46.

[13] Trivedi, R.C., 2010. Water quality of the Ganga River–an overview. Aquatic Ecosystem Health & Management, 13(4), pp.347-351.

[14] World Bank, 2010. World development indicators 2010. The World Bank.

[15] Agarwal, R., Chaudhary, M. and Singh, J., 2015. Waste management initiatives in India for human well being. European Scientific Journal.

[16] Huangfu, X., Shen, Y., Yang, A., Liu, L., Luo, W. and Zhao, W., 2020. Synthesis of water soluble CuGaS2/ZnS quantum dots for ultrasensitive fluorescent detection of alkaline phosphatase based on inner filter effect. Colloids and Surfaces B: Biointerfaces, 191, p.110984.

[17] Fegade, U., Attarde, S. and Kuwar, A., 2013. Fluorescent recognition of Fe^{3+} ion with photoinduced electron transfer (PET) sensor. Chemical Physics Letters, 584, pp.165-171.

[18] Miao, S., Liang, K. and Kong, B., 2020. Förster resonance energy transfer (FRET) paired carbon dot-based complex nanoprobes: versatile platforms for sensing and imaging applications. Materials Chemistry Frontiers, 4(1), pp.128-139.

[19] Wang, N., Wang, L., Yang, H., Xiong, T., Xiao, S., Zhao, J. and Du, W., 2019. Fluorescent Sensors Based on Organic Polymer-Capped Gold Nanoparticles for the Detection of Cr (VI) in Water. International journal of analytical chemistry, 2019.

[20] Owlad, M., Aroua, M.K., Daud, W.A.W. and Baroutian, S., 2009. Removal of hexavalent chromium-contaminated water and wastewater: a review. Water, Air, and Soil Pollution, 200(1), pp.59-77.

[21] Li, H., Li, Z., Liu, T., Xiao, X., Peng, Z. and Deng, L., 2008. A novel technology for biosorption and recovery hexavalent chromium in wastewater by bio-functional magnetic beads. Bioresource Technology, 99(14), pp.6271-6279.

[22] Tian, W., Qiu, J., Li, N., Chen, D., Xu, Q., Li, H., He, J. and Lu, J., 2021. Efficient piezocatalytic removal of BPA and Cr(VI) with SnS_2/CNFs membrane by harvesting vibration energy. Nano Energy, 86, p.106036.

[23] Qiu, H., Lv, L., Pan, B.C., Zhang, Q.J., Zhang, W.M. and Zhang, Q.X., 2009. Critical review in adsorption kinetic models. Journal of Zhejiang University-Science A, 10(5), pp.716-724.

[24] Chen, X., 2015. Modeling of experimental adsorption isotherm data. Information, 6(1), pp.14-22.

[25] Kim, J. and Van der Bruggen, B., 2010. The use of nanoparticles in polymeric and ceramic membrane structures: review of manufacturing procedures and performance improvement for water treatment. Environmental Pollution, 158(7), pp.2335-2349.

[26] Hu, J., Chen, G. and Lo, I.M., 2005. Removal and recovery of Cr (VI) from wastewater by maghemite nanoparticles. Water research, 39(18), pp.4528-4536.

[27] Niu, J., Ding, P., Jia, X., Hu, G. and Li, Z., 2019. Study of the properties and mechanism of deep reduction and efficient adsorption of Cr (VI) by low-cost Fe_3O_4-modified ceramsite. Science of The Total Environment, 688, pp.994-1004.

[28] Yuan, P., Fan, M., Yang, D., He, H., Liu, D., Yuan, A., Zhu, J. and Chen, T., 2009. Montmorillonite-supported magnetite nanoparticles for the removal of hexavalent chromium [Cr (VI)] from aqueous solutions. Journal of hazardous materials, 166(2-3), pp.821-829.

[29] Geng, B., Jin, Z., Li, T. and Qi, X., 2009. Kinetics of hexavalent chromium removal from water by chitosan-Fe^0 nanoparticles. Chemosphere, 75(6), pp.825-830.

[30] Abukhadra, M.R., Sayed, M.A., Rabie, A.M. and Ahmed, S.A., 2019. Surface decoration of diatomite by Ni/NiO nanoparticles as hybrid composite of enhanced adsorption properties for malachite green dye and hexavalent chromium. Colloids and Surfaces A: Physicochemical and Engineering Aspects, 577, pp.583-593.

[31] Jang, E.H., Pack, S.P., Kim, I. and Chung, S., 2020. A systematic study of hexavalent chromium adsorption and removal from aqueous environments using chemically functionalized amorphous and mesoporous silica nanoparticles. Scientific reports, 10(1), pp.1-20.

[32] Vardhan, K.H., Kumar, P.S. and Panda, R.C., 2019. A review on heavy metal pollution, toxicity and remedial measures: Current trends and future perspectives. Journal of Molecular Liquids, 290, p.111197.

[33] Vareda, J.P., Valente, A.J. and Durães, L., 2019. Assessment of heavy metal pollution from anthropogenic activities and remediation strategies: A review. Journal of environmental management, 246, pp.101-118.

[34] Zamora-Ledezma, C., Negrete-Bolagay, D., Figueroa, F., Zamora-Ledezma, E., Ni, M., Alexis, F. and Guerrero, V.H., 2021. Heavy metal water pollution: A fresh look about hazards, novel and conventional remediation methods. Environmental Technology & Innovation, p.101504.

[35] Moor, C., Lymberopoulou, T. and Dietrich, V.J., 2001. Determination of heavy metals in soils, sediments and geological materials by ICP-AES and ICP-MS. Microchimica Acta, 136(3-4), pp.123-128.

[36] van de Wiel, H.J., 2003. Determination of elements by ICP-AES and ICP-MS. National Institute of Public Health and the Environment (RIVM). Bilthoven, The Netherlands, pp.1-19.

[37] Yayintas, O.T., Yılmaz, S., Turkoglu, M. and Dilgin, Y., 2007. Determination of heavy metal pollution with environmental physicochemical parameters in waste water of Kocabas Stream (Biga, Canakkale, Turkey) by ICP-AES. Environmental monitoring and assessment, 127(1), pp.389-397.

[38] Guo, X., He, M., Chen, B. and Hu, B., 2012. Solidified floating organic drop microextraction combined with ETV-ICP-MS for the determination of trace heavy metals in environmental water samples. Talanta, 94, pp.70-76.

[39] Sereshti, H., Heravi, Y.E. and Samadi, S., 2012. Optimized ultrasound-assisted emulsification microextraction for simultaneous trace multielement determination of heavy metals in real water samples by ICP-OES. Talanta, 97, pp.235-241.

[40] Zeitoun, M.M. and Mehana, E.E., 2014. Impact of water pollution with heavy metals on fish health: overview and updates. Global Veterinaria, 12(2), pp.219-231.

[41] Aragay, G. and Merkoçi, A., 2012. Nanomaterials application in electrochemical detection of heavy metals. Electrochimica Acta, 84, pp.49-61.

[42] Pujol, L., Evrard, D., Groenen-Serrano, K., Freyssinier, M., Ruffien-Cizsak, A. and Gros, P., 2014. Electrochemical sensors and devices for heavy metals assay in water: the French groups' contribution. Frontiers in chemistry, 2, p.19.

[43] Jain, R., Thakur, A., Kaur, P., Kim, K.H. and Devi, P., 2020. Advances in imaging-assisted sensing techniques for heavy metals in water: Trends, challenges, and opportunities. TrAC Trends in Analytical Chemistry, 123, p.115758.

[44] Rasheed, T., Bilal, M., Nabeel, F., Iqbal, H.M., Li, C. and Zhou, Y., 2018. Fluorescent sensor based models for the detection of environmentally-related toxic heavy metals. Science of the Total Environment, 615, pp.476-485.

[45] Liu, Y., Deng, Y., Dong, H., Liu, K. and He, N., 2017. Progress on sensors based on nanomaterials for rapid detection of heavy metal ions. Science China Chemistry, 60(3), pp.329-337.

[46] Hassan, S.S., El-Shahawi, M.S., Othman, A.M. and Mosaad, M.A., 2005. A potentiometric rhodamine-B based membrane sensor for the selective determination of chromium ions in wastewater. Analytical sciences, 21(6), pp.673-678.

[47] Lin, Z.J., Zheng, H.Q., Zheng, H.Y., Lin, L.P., Xin, Q. and Cao, R., 2017. Efficient capture and effective sensing of $Cr_2O_7^{2-}$ from water using a zirconium metal–organic framework. Inorganic chemistry, 56(22), pp.14178-14188.

[48] Cao, C.S., Hu, H.C., Xu, H., Qiao, W.Z. and Zhao, B., 2016. Two solvent-stable MOFs as a recyclable luminescent probe for detecting dichromate or chromate anions. CrystEngComm, 18(23), pp.4445-4451.

[49] Das, R., Bandyopadhyay, R. and Pramanik, P., 2018. Carbon quantum dots from natural resource: A review. Materials today chemistry, 8, pp.96-109.

[50] Himaja, A.L., Karthik, P.S. and Singh, S.P., 2015. Carbon dots: the newest member of the carbon nanomaterials family. The Chemical Record, 15(3), pp.595-615.

[51] Chen, J., Yu, Y., Zhu, B., Han, J., Liu, C., Liu, C., Miao, L. and Fakudze, S., 2021. Synthesis of biocompatible and highly fluorescent N-doped silicon quantum dots from wheat straw and ionic liquids for heavy metal detection and cell imaging. Science of The Total Environment, 765, p.142754.

[52] Zhang, Y., Fang, X., Zhao, H. and Li, Z., 2018. A highly sensitive and selective detection of Cr (VI) and ascorbic acid based on nitrogen-doped carbon dots. Talanta, 181, pp.318-325.

[53] Lu, K.H., Lin, J.H., Lin, C.Y., Chen, C.F. and Yeh, Y.C., 2019. A fluorometric paper test for chromium (VI) based on the use of N-doped carbon dots. Microchimica Acta, 186(4), pp.1-7.

[54] Xu, W., Yu, L., Xu, H., Zhang, S., Xu, W., Lin, Y. and Zhu, X., 2019. Water-dispersed silicon quantum dots for on-off-on fluorometric determination of chromium (VI) and ascorbic acid. Microchimica Acta, 186(10), pp.1-8.

[55] Zhang, H., Huang, Y., Hu, Z., Tong, C., Zhang, Z. and Hu, S., 2017. Carbon dots codoped with nitrogen and sulfur are viable fluorescent probes for chromium (VI). Microchimica Acta, 184(5), pp.1547-1553.

[56] Mutuyimana, F.P., Liu, J., Nsanzamahoro, S., Na, M., Chen, H. and Chen, X., 2019. Yellow-emissive carbon dots as a fluorescent probe for chromium (VI). Microchimica Acta, 186(3), pp.1-9.

[57] Kumar, A., Chowdhuri, A.R., Laha, D., Mahto, T.K., Karmakar, P. and Sahu, S.K., 2017. Green synthesis of carbon dots from $Ocimum\ sanctum$ for effective fluorescent sensing of Pb^{2+} ions and live cell imaging. Sensors and Actuators B: Chemical, 242, pp.679-686.

[58] Vallejos, S., Muñoz, A., García, F.C., Serna, F., Ibeas, S. and García, J.M., 2012. Methacrylate copolymers with pendant piperazinedione-sensing motifs as fluorescent chemosensory materials for the detection of Cr (VI) in aqueous media. Journal of hazardous materials, 227, pp.480-483.

[59] Qiu, B., Xu, C., Sun, D., Yi, H., Guo, J., Zhang, X., Qu, H., Guerrero, M., Wang, X., Noel, N. and Luo, Z., 2014. Polyaniline coated ethyl cellulose with improved hexavalent chromium removal. ACS Sustainable Chemistry & Engineering, 2(8), pp.2070-2080.

[60] Zhang, Y., Li, Q., Tang, R., Hu, Q., Sun, L. and Zhai, J., 2009. Electrocatalytic reduction of chromium by poly (aniline-co-o-aminophenol): an efficient and recyclable way to remove Cr (VI) in wastewater. Applied Catalysis B: Environmental, 92(3-4), pp.351-356.

[61] Bardhan, S., Roy, S., Chanda, D.K., Mondal, D., Das, S. and Das, S., 2021. Flexible and reusable carbon dot decorated natural microcline membrane: a futuristic probe for multiple heavy metal induced carcinogen detection. Microchimica Acta, 188(4), pp.1-12.

[62] Bardhan, S., Roy, S., Chanda, D.K., Ghosh, S., Mondal, D., Das, S. and Das, S., 2020. Nitrogenous carbon dot decorated natural microcline: an ameliorative dual fluorometric probe for Fe^{3+} and Cr^{6+} detection. Dalton Transactions, 49(30), pp.10554-10566.

[63] Rapti, S., Sarma, D., Diamantis, S.A., Skliri, E., Armatas, G.S., Tsipis, A.C., Hassan, Y.S., Alkordi, M., Malliakas, C.D., Kanatzidis, M.G. and Lazarides, T., 2017. All in one porous material: exceptional sorption

and selective sensing of hexavalent chromium by using a Zr^{4+} MOF. Journal of Materials Chemistry A, 5(28), pp.14707-14719.

[64] Sompalli, N.K., Mohan, A.M., Rao, C.B., Nagarajan, S. and Deivasigamani, P., 2019. Tailor-made porous polymer and silica monolithic designs as probe anchoring templates for the solid-state naked eye sensing and preconcentration of hexavalent chromium. Sensors and Actuators B: Chemical, 298, p.126896.

[65] Shahnaz, T., Patra, C., Sharma, V. and Selvaraju, N., 2020. A comparative study of raw, acid-modified and EDTA-complexed Acacia auriculiformis biomass for the removal of hexavalent chromium. Chemistry and Ecology, 36(4), pp.360-381.

[66] Malik, L.A., Bashir, A., Qureashi, A. and Pandith, A.H., 2019. Detection and removal of heavy metal ions: a review. Environmental Chemistry Letters, 17(4), pp.1495-1521.

[67] Roy, S., Pal, K., Bardhan, S., Maity, S., Chanda, D.K., Ghosh, S., Karmakar, P. and Das, S., 2019. Gd (III)-doped boehmite nanoparticle: an emergent material for the fluorescent sensing of Cr (VI) in wastewater and live cells. Inorganic chemistry, 58(13), pp.8369-8378.

[68] Roy, S., Bardhan, S., Chanda, D.K., Ghosh, S., Mondal, D., Roy, J. and Das, S., 2020. Development of a Cu (II) doped boehmite based multifunctional sensor for detection and removal of Cr (VI) from wastewater and conversion of Cr (VI) into an energy harvesting source. Dalton Transactions, 49(20), pp.6607-6615.

[69] Roy, S., Bardhan, S., Roy, J. and Das, S., 2020. Waste capacitor: A fresh approach to detect and remove Cr (VI) from water and making it an energy harvesting material. Materials Today: Proceedings.

[70] Roy, S., Bardhan, S., Pal, K., Ghosh, S., Mandal, P., Das, S. and Das, S., 2018. Crystallinity mediated variation in optical and electrical properties of hydrothermally synthesized boehmite (γ-AlOOH) nanoparticles. Journal of Alloys and Compounds, 763, pp.749-758.

[71] Karger-Kocsis, J. and Lendvai, L., 2018. Polymer/boehmite nanocomposites: A review. Journal of Applied Polymer Science, 135(24), p.45573

[72] Husien, S., Labena, A., El-Belely, E.F., Mahmoud, H.M. and Hamouda, A.S., 2019. Adsorption studies of hexavalent chromium [Cr (VI)] on micro-scale biomass of *Sargassum dentifolium*, Seaweed. Journal of Environmental Chemical Engineering, 7(6), p.103444.

[73] Javadian, H., Ahmadi, M., Ghiasvand, M., Kahrizi, S. and Katal, R., 2013. Removal of Cr (VI) by modified brown algae *Sargassum bevanom* from aqueous solution and industrial wastewater. Journal of the Taiwan Institute of Chemical Engineers, 44(6), pp.977-989.

[74] Esmaeili, A. and Ghasemi, S., 2012. Investigation of Cr (VI) adsorption by dried brown algae *Sargassum* sp. and its activated carbon.

[75] Chen, G.Q., Zhang, W.J., Zeng, G.M., Huang, J.H., Wang, L. and Shen, G.L., 2011. Surface-modified *Phanerochaete chrysosporium* as a biosorbent for Cr(VI)-contaminated wastewater. Journal of Hazardous Materials, 186(2-3), pp.2138-2143.

[76] Dhal, B. and Pandey, B.D., 2018. Mechanism elucidation and adsorbent characterization for removal of Cr (VI) by native fungal adsorbent. Sustainable Environment Research, 28(6), pp.289-297.

[77] Ren, B., Zhang, Q., Zhang, X., Zhao, L. and Li, H., 2018. Biosorption of Cr (VI) from aqueous solution using dormant spores of *Aspergillus niger*. RSC advances, 8(67), pp.38157-38165.

[78] Ghasemi, R., Sayahi, T., Tourani, S. and Kavianimehr, M., 2016. Modified magnetite nanoparticles for hexavalent chromium removal from water. Journal of Dispersion Science and Technology, 37(9), pp.1303-1314.

[79] Alguacil, F.J. and Lopez, F.A., 2019. Removal of Cr (VI) from waters by multi-walled carbon nanotubes: Optimization and kinetic investigations. In Water and Wastewater Treatment. IntechOpen.

[80] Moosa, A.A., Ridha, A.M. and Abdullha, I.N., 2015. Chromium ions removal from wastewater using carbon nanotubes. International Journal for Innovative Research in Science & Technology, 4(2), pp.275-282.

[81] Zhang, D., Ma, Y., Feng, H. and Hao, Y., 2012. Adsorption of Cr (VI) from aqueous solution using carbon-microsilica composite adsorbent. Journal of the Chilean Chemical Society, 57(1), pp.964-968.

[82] Zhang, Q., Hou, Q., Huang, G. and Fan, Q., 2020. Removal of heavy metals in aquatic environment by graphene oxide composites: a review. Environmental Science and Pollution Research, 27(1), pp.190-209.

[83] Zhang, K., Li, H., Xu, X. and Yu, H., 2018. Synthesis of reduced graphene oxide/NiO nanocomposites for the removal of Cr (VI) from aqueous water by adsorption. Microporous and Mesoporous Materials, 255, pp.7-14.

[84] Neolaka, Y.A., Lawa, Y., Naat, J.N., Riwu, A.A., Iqbal, M., Darmokoesoemo, H. and Kusuma, H.S., 2020. The adsorption of Cr (VI) from water samples using graphene oxide-magnetic (GO-Fe$_3$O$_4$) synthesized from natural cellulose-based graphite (kusambi wood or Schleichera oleosa): Study of kinetics, isotherms and thermodynamics. Journal of Materials Research and Technology, 9(3), pp.6544-6556.

[85] Harijan, D.K. and Chandra, V., 2016. Magnetite/graphene/polyaniline composite for removal of aqueous hexavalent chromium. Journal of Applied Polymer Science, 133(39).

[86] Shokry, A., El Tahan, A., Ibrahim, H., Soliman, M. and Ebrahim, S., 2019. The development of a ternary nanocomposite for the removal of Cr (vi) ions from aqueous solutions. RSC Advances, 9(67), pp.39187-39200.

[87] ALOthman, Z.A., Naushad, M. and Ali, R., 2013. Kinetic, equilibrium isotherm and thermodynamic studies of Cr (VI) adsorption onto low-cost adsorbent developed from peanut shell activated with phosphoric acid. Environmental Science and Pollution Research, 20(5), pp.3351-3365.

[88] Su, M., Fang, Y., Li, B., Yin, W., Gu, J., Liang, H., Li, P. and Wu, J., 2019. Enhanced hexavalent chromium removal by activated carbon modified with micro-sized goethite using a facile impregnation method. Science of the total environment, 647, pp.47-56.

[89] Karnib, M., Kabbani, A., Holail, H. and Olama, Z., 2014. Heavy metals removal using activated carbon, silica and silica activated carbon composite. Energy Procedia, 50, pp.113-120.

[90] Kumar, R., Ansari, M.O., Alshahrie, A., Darwesh, R., Parveen, N., Yadav, S.K., Barakat, M.A. and Cho, M.H., 2019. Adsorption modeling and mechanistic insight of hazardous chromium on para toluene sulfonic acid immobilized-polyaniline@CNTs nanocomposites. Journal of Saudi Chemical Society, 23(2), pp.188-197.

Chapter 2

Methodology

Chapter 2

Methodology

2.1 General synthesis procedure of boehmite (γ-AlOOH) nanocrystal

Oxyhydroxide nanomaterials are quite easy to prepare. They require a simple two-step hydrothermal route. Musić et al. in their 1999 paper reported hydrothermal crystallization of boehmite from aluminum hydroxide, which is adopted widely to prepare boehmite nanocrystals [1]. Researchers have synthesized hybrid boehmite nanoparticles for better performances in different fields in the following years. Mathieu et al. (2007) reported boehmite nanostructures of different morphologies in their work [2]. They used aluminum chloride as a starting material and sodium polyacrylate (NaPa) 2100 to control morphology [2]. These works have influenced researchers a lot in synthesizing boehmite nanocrystals.

Figure 2.1 *General synthesis procedure of boehmite nanoparticles*

In a typical process, aluminum nitrate produces Al^{3+} ions. These cations initiate the olation reaction when added with amines (such as ethylenediamine, hexamine, and ammonia) at high pH values (~9-12). At this high pH, thick and white precipitation of the solution occurs, which confirms the production of aluminum hydroxide.

Initially, the aluminum nitrate dissolute in water as $[Al\,(H_2O)_6]^{3+}$ ions and then produces $[Al\,(H_2O)_5OH]^{2+}$. During this reaction, one proton (H^+) generates and reduces the pH of the medium. After the addition of the amine $(R\text{-}NH_2)$ containing precursor, this proton is accepted and in turn, delivers the $R\text{-}NH_3^+$ group. This is when the pH of the medium increases and starts the Ostwald ripening [3]. This process forms the white precipitates of aluminum hydroxide. The $R\text{-}NH_3^+$ are further adsorbed by the $[Al\,(H_2O)_5OH]^{2+}$ ions, which can be validated by the rise of the pH of the medium. A higher pH level indicates the formation of more adsorption of the $R\text{-}NH_3^+$ ions.

$$Al\,(NO_3)_3 + H_2O \longrightarrow [Al\,(H_2O)_6]^{3+}$$

$$[Al\,(H_2O)_6]^{3+} \longrightarrow [Al\,(H_2O)_5OH]^{2+} + H^+$$
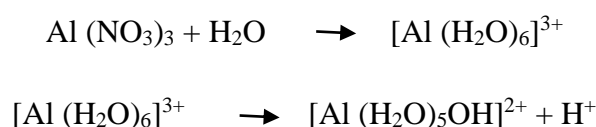
During the hydrothermal treatment, aluminum hydroxide releases one molecule of water from its structure and forms boehmite $(\gamma\text{-}AlOOH)$.

$$Al\,(OH)_3 \longrightarrow AlOOH + H_2O$$
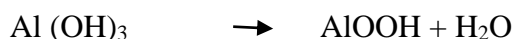
The doping of impurity atoms into the orthorhombic facet of boehmite could be performed during the nucleation process. The rest of the synthesis process remains the same. It is very important to calculate the exact ratio of doping before the experimental synthesis. Here, a minute amount of error could lead to a radical change in the physicochemical properties.

2.2 Characterizations of the synthesized samples

2.2.1 Structural, morphological and elemental characterizations

X-ray powder diffraction (XRD) is a useful tool to characterize the crystallinity of a material [4]. The crystalline defects could also be verified by using this method. Initially, the diffraction patterns are obtained by using a D8, Bruker AXS, Wisconsin, USA diffractometer equipped with Cu-Kα target of 1.5418 Å and operated at 35 kV, 35 mA bias with a scan speed of 2 sec/step. The diffractograms have been matched with the Joint Committee on Powder Diffraction Standards (JCPDS) card of boehmite (no. 21-1307) to verify the formation and purity of the materials [5]. The detection of any unwanted phases like $Al(OH)_3$ or Al_2O_3 could also be possible using this technique. The Debye-Scherrer equation reveals the crystallite sizes of nanocrystalline boehmite from the broadening of (020) peak as follows [6],
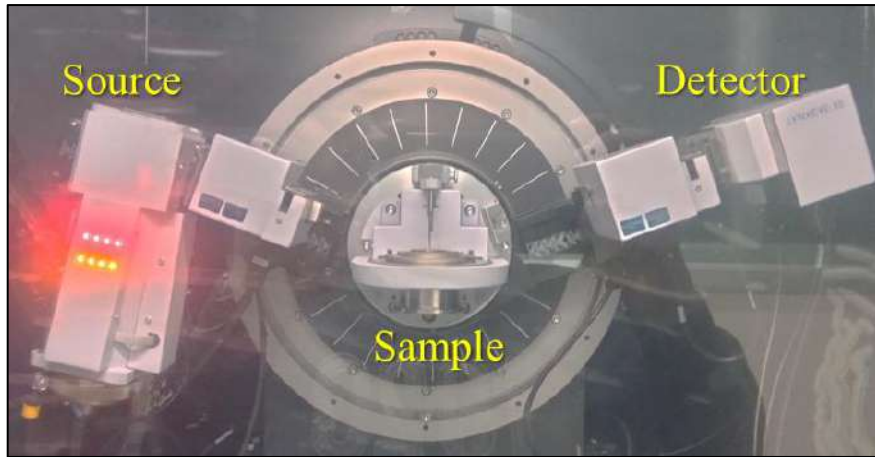
***Figure 2.2** The Bruker D8 Advance XRD machine situated at the Dept. of Physics, JU*

$$<\text{D}>_{(020)} = \frac{0.9\lambda}{\beta_{1/2}\,cos\theta} \qquad\qquad (1)$$

Where $<\text{D}>$, λ, $\beta_{1/2}$, θ are the average crystallite size, the wavelength of the incident X-ray radiation, the full width at half maximum (FWHM) of the (020) peak, and the corresponding Braggs angle respectively. In our earlier works, the Scherrer equation has been used to evaluate the crystallite sizes of the synthesized boehmite nanostructures, but this equation is insufficient to estimate other microstructural parameters. Thus, Rietveld refinement has been adopted to analyze the microstructural parameters in a detailed manner [7].

The XRD diffractograms have been refined by using the Rietveld-based software package MAUD (v2.9) and the lattice parameters along with other crystallographic parameters have been calculated [8]. First, the instrument's broadening parameters and the Caglioti-PV functions were refined. Then the refinement of the atomic positions and cell parameters were conducted for a reasonable theoretical model. Finally, the texture parameters, size, and microstrain parameters were refined. In each case, at least fifteen iterations were visualized by using the VESTA v3.5.2 program [9]. The bond lengths and bond angles were calculated to estimate the crystal defects and capture the theoretical model of the synthesized nanostructure.
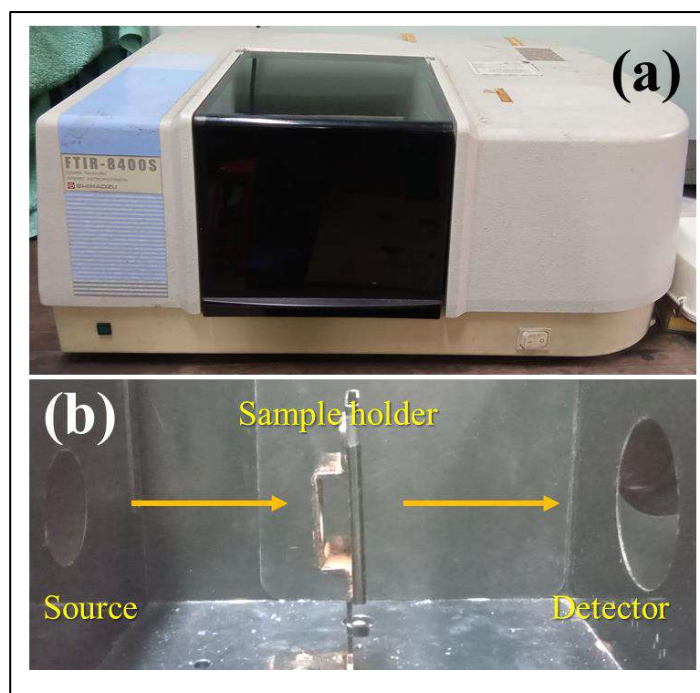
Figure 2.3 *(a) FTIR 8400S, Shimadzu situated at the Dept. of Physics, JU, (b) sample compartment of the instrument*

The purity and bonding network of the as-synthesized samples were further characterized by using Fourier transform infrared spectrometry (FTIR) [10]. It is a great tool to assess the rotational and vibrational spectra. The synthesized powders were mixed with potassium bromide (KBr) (1:50 sample to KBr ratio) and solid pellets were made using a hydraulic pressing machine. These pellets were exposed to infrared radiation of varying wavenumber (400-4000 cm^{-1}) in a FTIR-8400S, Shimadzu for analyzing the spectra. Boehmite nanoparticles are having -OH groups facing outwards from their orthorhombic structure. Thus, a broad IR peak between 3000-3500 cm^{-1} is observed in the FTIR spectrum of nano-boehmite. As the KBr powder is prone to adsorb ambient moisture, it is directed to use dried KBr powders (HPLC grade) for making pellets for FTIR study. In our studies, pre-heating of the pellets was done at 80 ºC to avoid such issues.

Morphological investigation of the synthesized nanostructures has been executed by using scanning and transmission electron microscopy (FESEM, TEM) [11-12]. The powdered samples were ground in an agate mortar and dispersed in HPLC grade acetone to make them diluted. A rigorous sonication of these suspensions was performed by using an ultrasonic bath (~20 kHz) to break the agglomeration of the nanostructures. The suspensions were then directly cast on the glass slides (for FESEM) and carbon-coated copper mesh (for TEM) and dried in a vacuum.
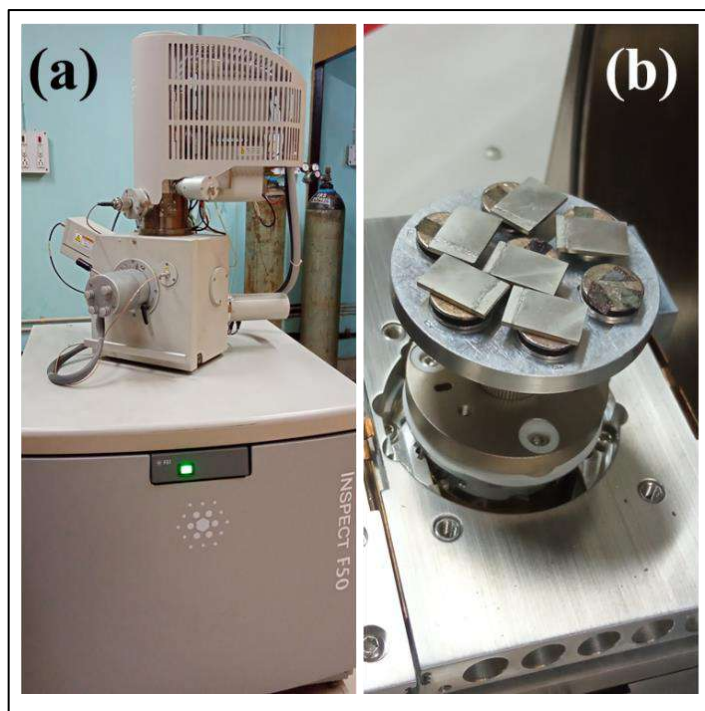
Figure 2.4 *The FESEM facility of the Dept. of Physics, JU, (b) the samples placed inside the sample chamber*

In FESEM analysis, the dried samples were further placed on carbon grids and sputter-coated with gold to restrict charge accumulation during the experiment. The gold-coated samples were then examined under the microscope (Inspect F50, FEI) in an operating voltage of 10-30 kV with a chamber pressure of at least 2×10^{-3} Pa.

The TEM micrographs were taken in a JEOL JEM-2000 transmission electron microscope. The samples on the carbon-coated copper grids were directly placed into the instrument under a high vacuum before the experiment. Both FESEM and TEM micrographs were further analyzed using the ImageJ program (v1.52p) to calculate the particle sizes.

Apart from the structure and morphology, it is very important to obtain the elemental composition of a sample before any application. Energy Dispersive X-Ray Analysis (EDX) is one of such techniques to characterize the elemental composition [13]. Herein, an Inspect F50, FEI Scanning Electron Microscope equipped with Bruker Quantax EDS analyzer was used to estimate the EDX data of boehmite and its derivatives. The sample preparation for EDX is similar to that of the FESEM. The filament operating was set at 20 kV voltage. In some of our works, elemental mapping was performed similarly, showing better agreement with other characteristics of the as-prepared samples.

Figure 2.5 The HR-TEM facility of IACS, Kolkata used to obtain the TEM micrographs

2.2.2 Estimation of the surface properties

Nanoparticles have excellent surface features due to their high aspect ratio. Sometimes these surface features control the structure-property correlation of the system. Moreover, a high surface with promising porosity is required in the adsorption experiment. These surface phenomena could influence the overall fluorometric sensing performance of sensor material. Thus, it is recommended to characterize the surface properties of nanosystems like boehmite to validate its applicability in wastewater treatment and monitoring.

The mean porosity and surface area of the samples were evaluated by employing the Brunauer–Emmett–Teller (BET) and Barrett–Joyner–Halenda (BJH) methods respectively [14-15]. Herein, a Twin Surface Area Analyzer from Quanta-chrome Instruments (USA) was used. The adsorption-desorption isotherms were studied using nitrogen (N_2) gas. The N_2 gas adsorption-desorption isotherms were studied at -196 ℃ with a degassing temperature set at 200 ℃ for 1 h.
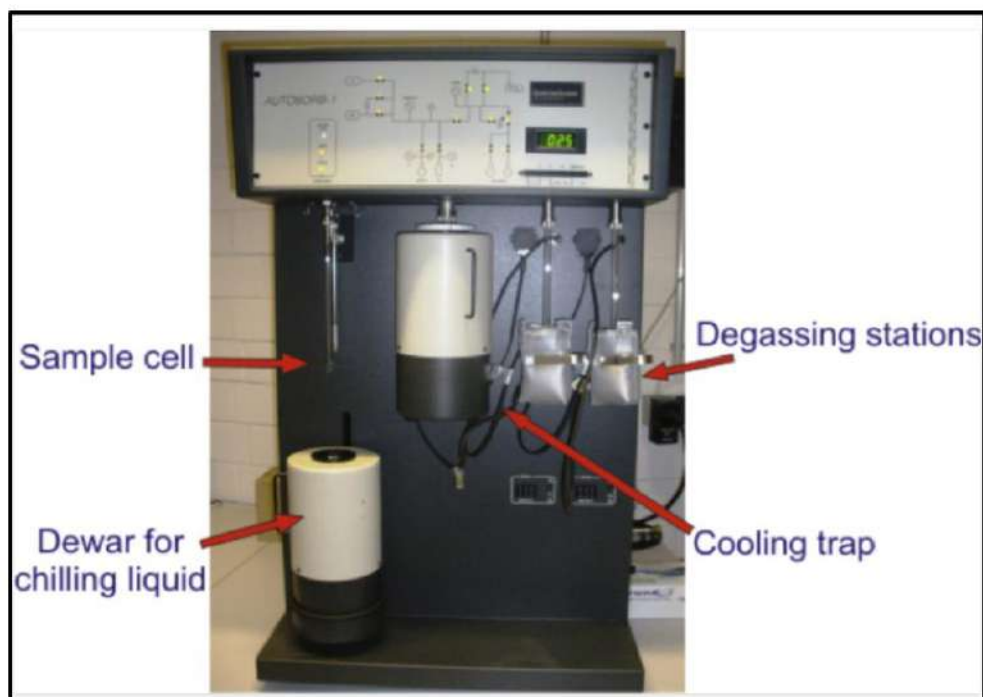
Figure 2.6 *The BET-BJH analyzer facility of IACS, Kolkata used for the porosity studies*

Boehmite nanocrystals normally follow a type-IV isotherm, which validates the slit-like mesopores on the surface. This type of isotherm is quite useful for industrial adsorbents and making boehmite nanocrystals a promising agent for adsorption-based removal of hexavalent chromium.

2.2.3 Thermal stability of the materials

Various literature suggests that boehmite is a starting precursor of alumina (Al_2O_3). Paglia et al. (2004) [16] suggested γ-Al_2O_3 from boehmite over 500 ºC. A similar observation has been made by other researchers, which confirms the fact that boehmite could be transferred into alumina at higher temperatures. Thus, it is quite necessary to estimate the thermal stability of boehmite nanoparticles up to a certain temperature range (depending upon the application).

Herein, thermogravimetric (TGA) and differential thermal analyses of the samples were performed to check the temperature stability. A DTG-60H, Shimadzu was used in broad temperature ranges with 5-10 ºC/min heating rate under nitrogen atmosphere (flow rate 50 cc/ minute).

Figure 2.7 *The DTA-TGA instrument of Dept. of Physics, JU showing the furnace, reference (R) and the sample (S) stages.*

Very small amounts of samples (~10-15 mg) were placed over platinum sample holders before each experiment. The mass losses and corresponding differential data were collected from the TA-60 program connected to the instrument. To avoid any irregularity in data, the samples were kept in vacuum for at least 48 h before each experiment. As boehmite is a highly porous sample, such vacuum treatment restricts the ambient moisture adsorption.

2.2.4 Assessment of optical properties and their validation using density functional theory

It is essential to have promising optical qualities along with fluorescence stability in a dedicated fluorometric sensor. In reality, absorbance and emission spectroscopies are two major characterization tools for estimating the optical quality of a material [17-18]. The absorption spectrum also helps to calculate the optical band gap of a molecule whereas, the emission spectrum shows the fluorescence quality and predicts the defect states of the molecule. Both of these spectroscopic techniques require very low concentration solutions of the sample (preferably 100-500 µM).
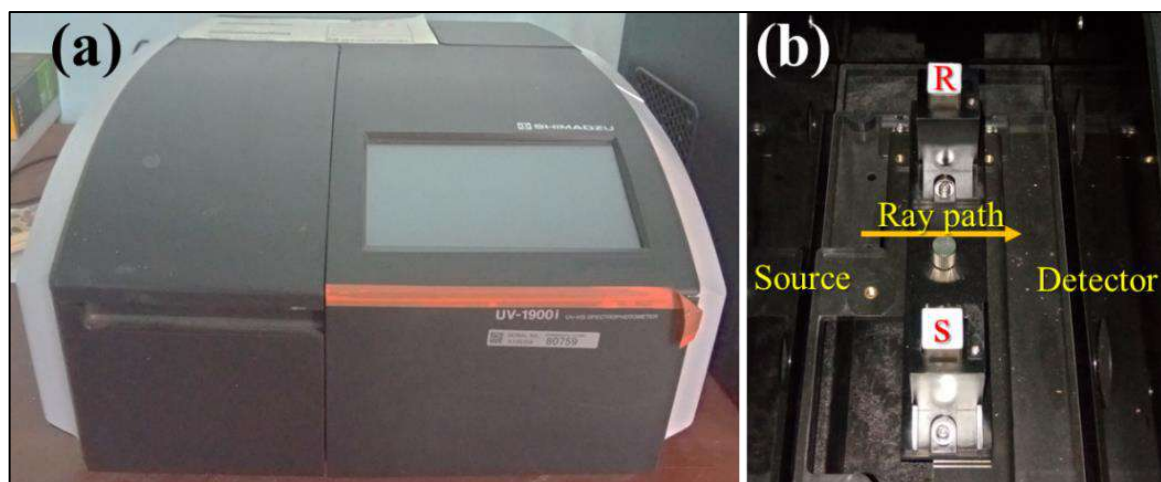
Figure 2.8 *(a) The UV-Vis spectrometer facility of the Dept. of Physics, JU, (b) the sample compartment with ray diagram of the instrument*

Absorbance spectrometry follows Beer-Lambert's law [19], which suggests the dependence of material's absorbance on the thickness and the concentration. The absorbance experiments have been performed in a UV-1900i, Shimadzu in the wavelength ranging between 200-800 nm. the primary absorbance peaks were located in each case to excite the sample while taking the fluorescence data. Moreover, the absorbance characteristics conversely predict the optical band gap using Tauc's relation [20],

$$\alpha E = A(E - E_g)^n \qquad (2)$$

Here, E, E_g, α, and A are the photon energy, the optical band gap energy, absorption coefficient, and a constant term respectively. In this equation, the value of n varies between 2 and ½ for direct and indirect band gaps respectively. As boehmite has a direct band gap, in the Tauc plot, $(\alpha h\nu)^2$ is plotted against photon energy $h\nu$ and the band gap energy was calculated by extrapolating the linear region and intersecting the linear portion of the curve to the energy axis. Absorption spectroscopy has also been used in adsorption experiments. The sorption kinetics and uptake studies of nanostructured boehmite have been performed using this tool.

Apart from absorption, emission spectra could also be useful in determining the fluorescence quality. A Cary Eclipse, Agilent Technologies has been used with a 5 nm slit opening (both emission and excitation slits) for this purpose.
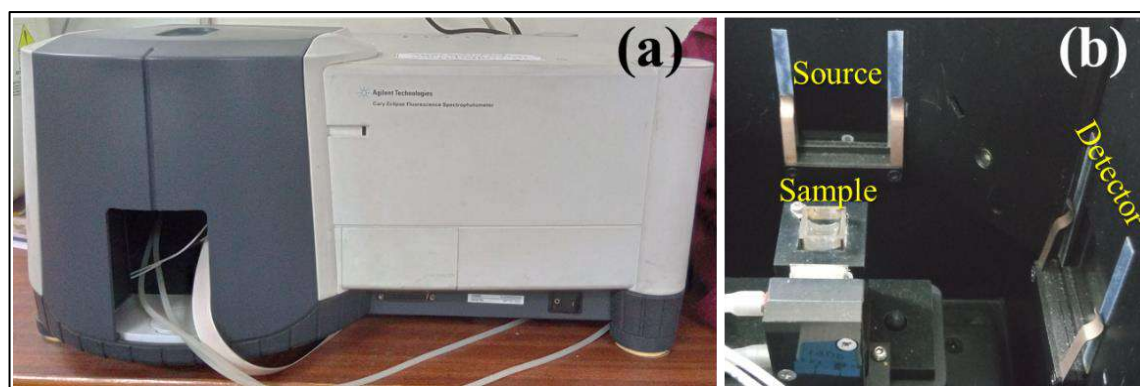
Figure 2.9 *(a) The Fluorescence spectrometer facility of the Dept. of Physics, JU, (b) the sample chamber of the instrument*

Additionally, the fluorescence stability of the samples has been measured by varying the ambient conditions. The fluorescence stability of the samples has been measured by fluctuating the temperature by using a Cary Single Cell Peltier Accessory, Agilent equipped with the fluorescence spectrometer. The temperature varied between 10-80 ºC in such experiments. the steady-state sensing experiment has also been performed in a similar setup by varying the chromium concentration.

Fluorescence lifetimes have also been measured in our works to validate the fluorometric detection mechanism of hexavalent chromium [21] These experiments were carried out in a time-resolved spectrofluorometer from IBH, UK. Different excitation energies were used to excite the samples and the photon counts were performed to estimate the fluorescence lifetimes.

The fluorometric detection mechanisms and electronic transitions have been validated using the density functional theory (DFT) and time-dependent density functional theory (TDDFT) [22]. The theoretical calculations were performed by imposing Becke, 3-parameter, Lee-Yang–Parr (B3LYP) hybrid functional in Orca v4.2 software. The molecular modeling has been conducted in the Avogadro v1.2 program [22-23]. The 6-31G** basis set was used to describe the elements before the calculation. Before the time-dependent calculations (TDDFT), the geometry and vibrational modes were optimized. Finally, the TDDFT method was executed to evaluate the theoretical absorbance spectra and electronic transitions. [24].

2.2.5 Electrical properties of the synthesized sample

Apart from fluorometric sensing, boehmite is chiefly known for its adsorption property. It has a good affinity towards hexavalent chromium due to its ionic radius. This type of physical adsorption not only treats the wastewater but also influences the structure of the chromium adsorbed boehmite. In such cases, more interfaces have been generated resulting in higher amounts of interfacial polarization. This type of polarization greatly enhances the dielectric constant of the adsorbed sample compared to the pristine one. Boehmite is already known for its high dielectric constant at lower frequencies. Therefore, the adsorption of contaminants elevates this value, which could be used as a 'waste capacitor'.

Figure 2.10 (a) The Agilent impedance analyzer set up of the Dept. of Physics, JU, (b) the electrode system with the contacts of the instrument

Grain and grain boundaries are determining factors for the electrical properties of a material, especially dielectric permittivity and tangent loss. These properties could be measured in a standard LCR meter or impedance analyzer. Before opting for such measurements, it is important to fabricate the electrical contacts carefully as they influence the electrical properties significantly. Dielectric properties of the nanomaterials depend on many parameters such as frequency of the external applied electric field, temperature during measurement, chemical composition, grain structure, sample preparation technique, etc. The real part contributes to the amount of energy stored in a dielectric material due to polarization whereas the imaginary part is generally associated with the dissipation of energy within the dielectric materials.

Herein, an Agilent 4294A Precision Impedance Analyzer operating at 0.5 V bias voltages set at a frequency ranging between 40 Hz to 10 MHz was used to measure the electrical characteristics of synthesized nanostructures. The solid pellets of the samples were

prepared in a hydraulic press system the electrical contact was made using copper tapes. In the case of temperature-dependent measurements, a hot air oven has been employed to calibrate the temperature at a rate of 2 ℃/min. The ac conductivities and conduction mechanisms have also been established using the same instrumental setup.

2.2.6 Biological assays and molecular docking simulation

The biological studies (mainly, MTT assay and bio-sensing of chromium) have been initiated to ensure the biocompatibility of the synthesized samples. Additionally, the bio-sensing platform delivers a focused approach for detecting hexavalent chromium in living systems. In these works, human cervical cancer cells (HeLa), MDA-MB 468 triple-negative breast cancer cells, and WI38 human fibroblast cells were purchased from National Centre for Cell Science (NCCS Pune, India).

Figure 2.11 The fluorescence microscope facility of the Dept. of Physics, JU

To conduct the bio-sensing study, the cells were cultured in DMEM (Dulbecco's modified eagle's medium) medium and treated with 5 % FBS (fetal bovine serum) followed by incubation at 37 ℃ in a 5 % CO_2 atmosphere for 24 h. Further, the cells were washed with 1x PBS (phosphate buffer saline) buffer to avoid any contamination. The fresh medium was then added to the washed cells and incubated again at 37 ℃ with a 5 % CO_2 atmosphere. The cells were then divided into two parts that have already been mounted over cell culture plates and sent for overnight incubation (37 ℃ with 5 % CO_2

atmosphere). On the very next day, one part of the sample was treated with a small drop of Cr(VI) solution of 50 µM and incubated for another 2 h to interact. After incubation, the samples were sent for microscopy under a fluorescence microscope (Leica, Germany).

Molecular docking studies have been performed to substantiate the bio-sensing capabilities of the sensor materials [25]. Autodock Tools v.1.5.6 was used to create the proteins and the ligand [26]. The water molecules of the protein have been removed and polar hydrogen bonds and Kollman charges were added to the protein structures. Autodock vina v.1.1.2 was employed to estimate the binding affinities between the protein-ligand complexes [27]. The binding pockets were identified and visualized using PyMol v.2.0.7 program [28].

References

[1] Musić, S., Dragčević, Đ. and Popović, S., 1999. Hydrothermal crystallization of boehmite from freshly precipitated aluminum hydroxide. Materials Letters, 40(6), pp.269-274.

[2] Mathieu, Y., Lebeau, B. and Valtchev, V., 2007. Control of the morphology and particle size of boehmite nanoparticles synthesized under hydrothermal conditions. Langmuir, 23(18), pp.9435-9442

[3] Voorhees, P.W., 1985. The theory of Ostwald ripening. Journal of Statistical Physics, 38(1), pp.231-252.

[4] Notten, P.H.L., Daams, J.L.C., De Veirman, A.E.M. and Staals, A.A., 1994. In situ X-ray diffraction: a useful tool to investigate hydride formation reactions. Journal of alloys and compounds, 209(1-2), pp.85-91.

[5] Lepot, N., Van Bael, M.K., Van den Rul, H., D'Haen, J., Peeters, R., Franco, D. and Mullens, J., 2008. Synthesis of platelet-shaped boehmite and γ-alumina nanoparticles via an aqueous route. Ceramics international, 34(8), pp.1971-1974.

[6] Holzwarth, U. and Gibson, N., 2011. The Scherrer equation versus the the'Debye-Scherrer equation'. Nature nanotechnology, 6(9), pp.534-534.

[7] McCusker, L.B., Von Dreele, R.B., Cox, D.E., Louër, D. and Scardi, P., 1999. Rietveld refinement guidelines. Journal of Applied Crystallography, 32(1), pp.36-50.

[8] Saville, A.I., Creuziger, A., Mitchell, E.B., Vogel, S.C., Benzing, J.T., Klemm-Toole, J., Clarke, K.D. and Clarke, A.J., 2021. MAUD Rietveld refinement software for neutron diffraction texture studies of single-and dual-phase materials. Integrating Materials and Manufacturing Innovation, 10(3), pp.461-487.

[9] Momma, K. and Izumi, F., 2008. VESTA: a three-dimensional visualization system for electronic and structural analysis. Journal of Applied crystallography, 41(3), pp.653-658.

[10] Griffiths, P.R. and De Haseth, J.A., 2007. Fourier transform infrared spectrometry (Vol. 171). John Wiley & Sons.

[11] Deng, H., Hu, X., Li, H.A., Luo, B. and Wang, W., 2016. Improved pore-structure characterization in shale formations with FESEM technique. Journal of Natural Gas Science and Engineering, 35, pp.309-319.

[12] Barsukov, P.O., Fainberg, E.B. and Khabensky, E.O., 2015. Shallow investigations by TEM-FAST technique: methodology and examples. In Electromagnetic sounding of the Earth's interior (pp. 47-78). Elsevier.

[13] DeGaetano, D., Siegel, J.A. and Klomparens, K.L., 1992. A comparison of three techniques developed for sampling and analysis of gunshot residue by scanning electron microscopy/energy-dispersive X-ray analysis (SEM-EDX). Journal of Forensic Science, 37(1), pp.281-300.

[14] Naderi, M., 2015. Surface Area: Brunauer–Emmett–Teller (BET). In Progress in filtration and separation (pp. 585-608). Academic Press.

[15] Villarroel-Rocha, J., Barrera, D. and Sapag, K., 2014. Introducing a self-consistent test and the corresponding modification in the Barrett, Joyner and Halenda method for pore-size determination. Microporous and Mesoporous Materials, 200, pp.68-78.

[16] Paglia, G., Buckley, C.E., Rohl, A.L., Hart, R.D., Winter, K., Studer, A.J., Hunter, B.A. and Hanna, J.V., 2004. Boehmite derived γ-alumina system. 1. Structural evolution with temperature, with the identification and structural determination of a new transition phase, γ '-alumina. Chemistry of materials, 16(2), pp.220-236.

[17] Bennett, G.E. and Johnston, K.P., 1994. UV-visible absorbance spectroscopy of organic probes in supercritical water. The Journal of Physical Chemistry, 98(2), pp.441-447.

[18] Bergmann, U. and Glatzel, P., 2009. X-ray emission spectroscopy. Photosynthesis research, 102(2), pp.255-266.

[19] Calloway, D., 1997. Beer-lambert law. Journal of Chemical Education, 74(7), p.744.

[20] Jubu, P.R., Yam, F.K., Igba, V.M. and Beh, K.P., 2020. Tauc-plot scale and extrapolation effect on bandgap estimation from UV–vis–NIR data–a case study of β-Ga2O3. Journal of Solid State Chemistry, 290, p.121576.

[21] Noomnarm, U. and Clegg, R.M., 2009. Fluorescence lifetimes: fundamentals and interpretations. Photosynthesis research, 101(2), pp.181-194.

[22] Gross, E.K. and Maitra, N.T., 2012. Introduction to TDDFT. In Fundamentals of Time-Dependent Density Functional Theory (pp. 53-99). Springer, Berlin, Heidelberg.

[23] Jacobsen, E. and Lyons, R., 2003. The sliding DFT. IEEE Signal Processing Magazine, 20(2), pp.74-80.

[24] Cornard, J.P., Dangleterre, L. and Lapouge, C., 2006. DFT and TD-DFT investigation and spectroscopic characterization of the molecular and electronic structure of the Zn (II)–3-hydroxyflavone complex. Chemical physics letters, 419(1-3), pp.304-308.

[25] Morris, G.M. and Lim-Wilby, M., 2008. Molecular docking. In Molecular modeling of proteins (pp. 365-382). Humana Press.

[26] Morris, G.M., Goodsell, D.S., Huey, R., Hart, W.E., Halliday, S., Belew, R. and Olson, A.J., 2001. AutoDock. Automated docking of flexible ligands to receptor-User Guide.

[27] Trott, O. and Olson, A.J., 2010. AutoDock Vina: improving the speed and accuracy of docking with a new scoring function, efficient optimization, and multithreading. Journal of computational chemistry, 31(2), pp.455-461.

[28] DeLano, W.L., 2002. PyMOL.

Chapter 3

Synthesis & characterization of pure boehmite (γ-AlOOH) nanoparticles of different particle sizes to study their optical activities and energy storage capacities

Chapter 3

Synthesis & characterization of pure boehmite (γ-AlOOH) nanoparticles of different particle sizes to study their optical activities and energy storage capacities

3.1 Introduction

Nowadays, an intense amount of research activities are being performed to study the synthesis and characteristics of numerous nanocrystals [1]. The technological development escalates the high demand for high-performance materials creating a pressing need for the fabrication of hybrid composites than single metal, polymer, or ceramic owing to their limited performance in different applications [2]. However, advanced nanotechnology paved the path for single materials and compounds due to their excellent physicochemical properties [3]. These unique properties of nanocrystals are closely related to their phases, shapes, sizes, crystallinities and therefore it would be very useful to prepare these materials with controllable characteristics [4].

This work reports the successful synthesis of boehmite (γ-AlOOH) nanoparticles of varying sizes using a facile time varied and cost-effective hydrothermal technique. The as-prepared nanocrystals have been characterized by using basic characterizing techniques to validate their purity and other physicochemical activities. The synthesized samples depict fairly high fluorescence emission and dielectric constant (3.71×10^6 for BH12 sample) with a nominal dielectric loss. This study also substantiates the temperature-dependent dielectric property and ac conductivity of these samples. The influence of particle size and crystallinity in the optical and electrical assays has been illustrated with proper analytical details. Not only high emission intensity in the blue and green region of the spectrum makes our sample a strong candidate for bio-imaging and bio-sensing applications, but also high dielectric constant makes them desirable for cost-effective dielectric separators for energy harvesting applications.

3.2 Experimental details

3.2.1 Materials

The precursors like aluminum nitrate nonahydrate [Al(NO$_3$)$_3$.9H$_2$O] and aqueous ammonia solution (25%) were purchased from Merck, India. All the reagents were used without further purification. Millipore water was used throughout the experiments with a resistivity of at least 18.2 MΩ-cm. The glass-wares used in these experiments were cleaned with aqua regia solution followed by rinsing with ultrapure water.

3.2.2 Synthesis method

Boehmite nanoparticles were prepared by a simple two-step hydrothermal method as previously reported by Music´ et al. (1999) [5] with some major modifications. Initially, the aluminum nitrate powder was first dissolved uniformly in Millipore water till the complete dissolution of the salt was achieved. The ammonia solution was then added drop-wise in the salt solution to initiate the co-precipitation process and the final pH of the solution was maintained at 9. The vigorous stirring was continued for another 3 h at room temperature to complete the reaction process. The resultant milky white solution was then transferred into a Teflon-lined stainless-steel autoclave and placed in a dust-free hot air oven at 160 ºC for 12 h. The solid white precipitates were collected from the bottom of the Teflon jacket and washed several times by water till the pH reaches a neutral value (~6-7). The washed precipitate was further dried in a vacuum desiccator at room temperature first and then at 60 °C for another 12h.

Maintaining all other parameters constant, boehmite nanoparticles were also synthesized by varying the hydrothermal treatment time for 18 and 24 h to understand the growth mechanism of the nanostructure. The synthesized boehmite nanoparticles were marked according to the hydrothermal reaction times (BH12, BH18, and BH24 respectively) and sent for further characterizations.

3.3 Results and discussion

3.3.1 Structural and morphological analysis of the nanoparticles

In order to ascertain the purity and the crystallinity, XRD patterns of as-synthesized nanostructures of boehmite have been obtained (Figure 3.1). The diffractograms show the

crystalline nature of the boehmite sample. Further, these diffraction maxima are indexed to the orthorhombic phase of boehmite (JCPDS card no. 21-1307) showing the absence of any unwanted diffraction planes. This also reveals that the synthesized nanostructures are phase pure. No unreacted phases (such as aluminum hydroxide) are present in the systems. Thus, it can be argued that the entire Al(OH)₃ precursor had been completely transformed into boehmite after the hydrothermal treatment.
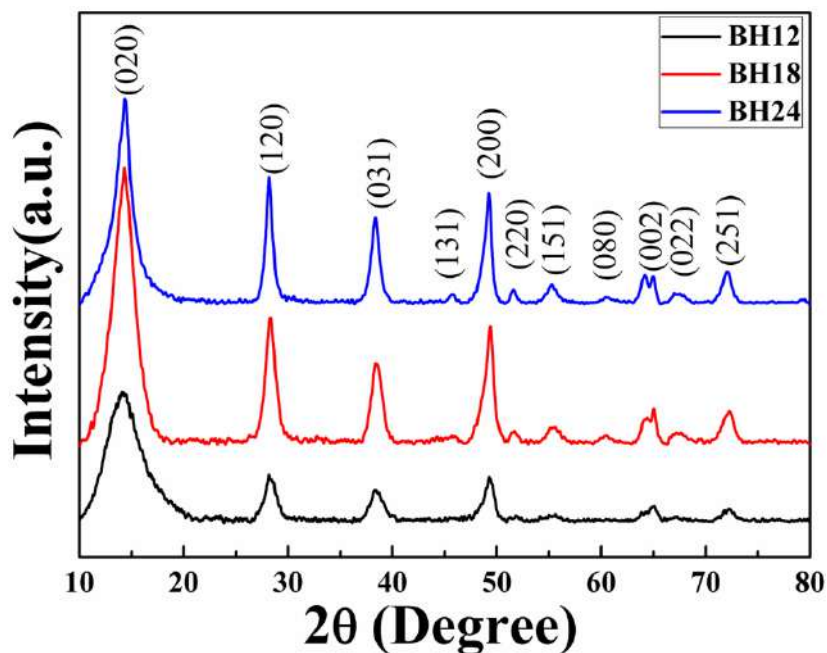
Figure 3.1 *XRD patterns of the synthesized samples*

Interestingly, the strong diffraction maxima corresponding to the (020) plane gets sharper with increasing hydrothermal treatment time, which implies the growth units of boehmite nanostructures are abundant along (020) facets [6].

Table 3.1 *Microstructural parameters calculated from the diffractograms*

Sample	D (nm)	FWHM (rad)	a(Å)	b(Å)	c(Å)	d-spacing (Å) [020]
BH12	2.11	0.0664	3.6939	12.3029	2.8683	6.1546
BH18	3.536	0.0395	3.6875	12.3328	2.8653	6.1663
BH24	4.926	0.0281	3.6965	12.4539	2.8676	6.2257

Similarly, the calculated full width at half maxima (FWHM) (Table 3.1) taking the (020) plane for the entire sample set shows more crystallinity in the BH24 sample among the

three samples. The crystallite sizes of the samples have been estimated by the Debye-Scherrer equation using the following equation [7],

$$<D>_{(020)} = \frac{0.9\lambda}{\beta_{1/2}\,cos\theta}$$
(1)

Here, D is the average crystallite size, λ is the wavelength of the incident X-ray beam, θ is the corresponding Braggs angle, $\beta_{1/2}$ is the full width at half maximum (FWHM) of the (020) peak. It is observed that the average crystallite size of the boehmite samples varies slightly from 2.11 nm to 4.93 nm depending on the hydrothermal reaction time.
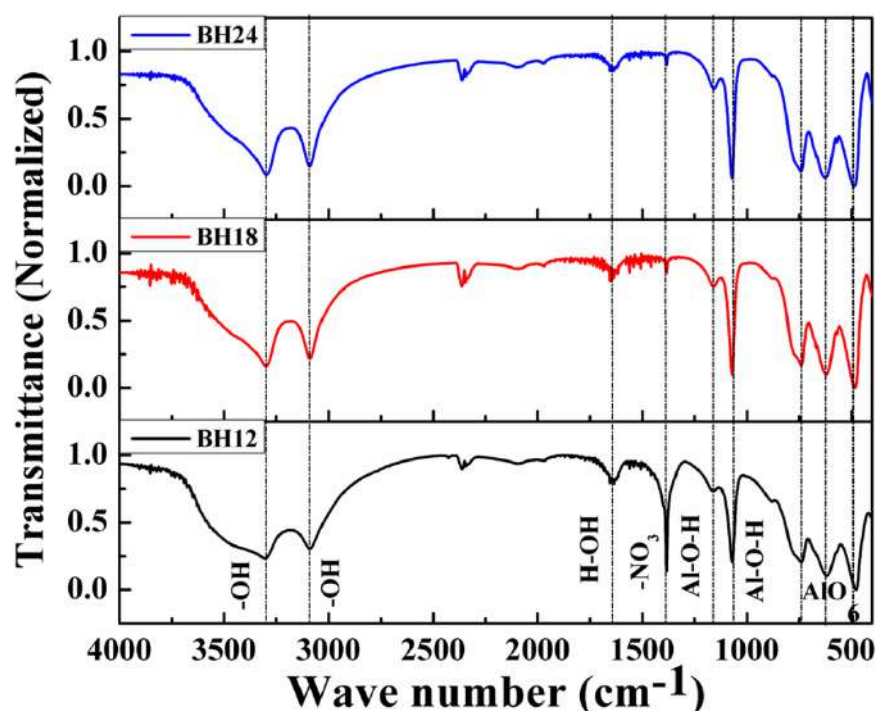
Figure 3.2 FTIR spectra of the samples

The bonding networks of the samples were investigated by using FTIR spectrometry (Figure 3.2). It is observed that the absorption bands are located at 3392, 3099, 1635, 1159, 885, 752, 629, and 478 cm^{-1} are in good agreement with the reported literature and further confirm the formation of boehmite nanocrystals. In reality, the absorbance band present at 1384 cm^{-1} is attributed to the stretching vibration of the nitrate [8]. Two separate strong bands located at 3300 and 3103 cm^{-1} are assigned to the asymmetric and symmetric vibration of O-H respectively [9]. Similarly, the absorbance maxima present at 1072 and 1159 cm^{-1} are attributed to the symmetric and asymmetric modes of Al–O–H and Al–O–H respectively [6]. The torsional modes situated at 740, 617 and 478 cm^{-1} substantiate the AlO$_6$ vibration [6]. Traces of some surface adsorbed moister have also

been found at 1636 and 3853 cm^{-1} [10]. Therefore, the FTIR data is consistent with the XRD results revealing the formation of the pure boehmite nanocrystals.
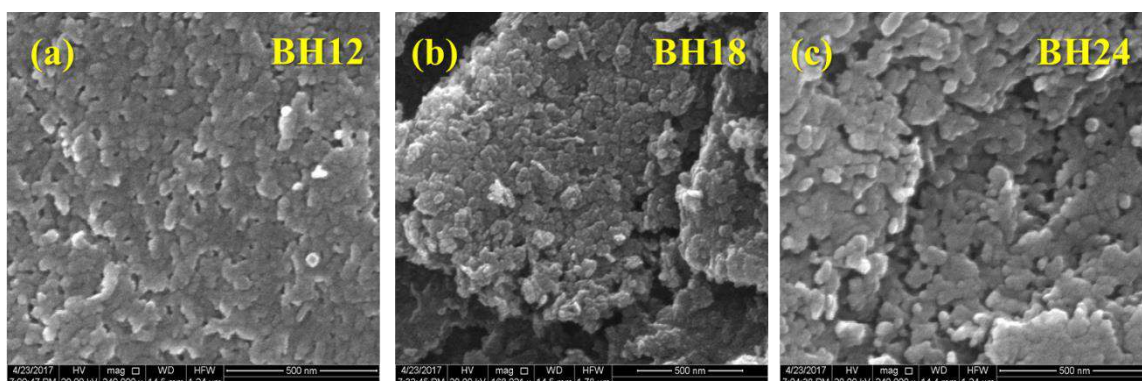
Figure 3.3 *FESEM images of the synthesized nanostructures*

The morphology and particle sizes of the synthesized samples were investigated by FESEM and TEM characterizations. The FESEM micrographs of all the samples have been depicted in Figure 3.3 showing agglomerated globular structures. The hydrothermal reaction time significantly enhanced the particle size of the boehmite nanoparticles, which is visible in the TEM micrographs (Figure 3.4).
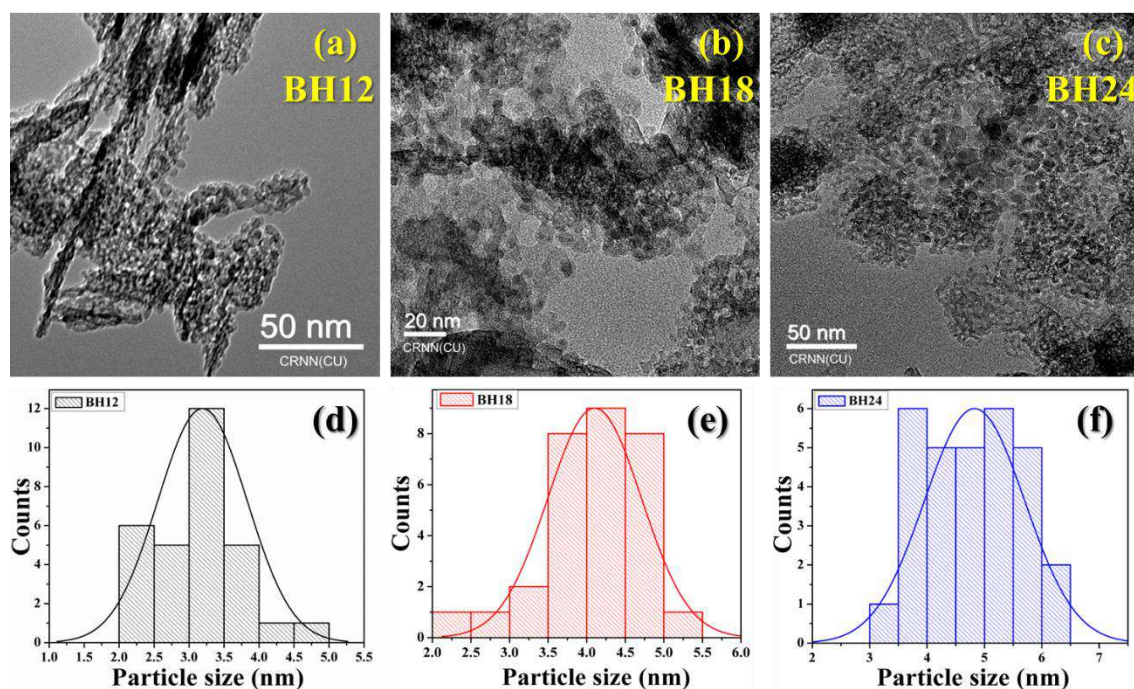
Figure 3.4 *(a-c) TEM images and (d-f) corresponding size distribution plots of the samples*

The average particle sizes of the boehmite samples are found to be 3.2, 4.1, and 4.8 nm for BH12, BH18, and BH24 respectively, which corroborate the XRD results.

3.3.2 Optical properties of the nanostructures

Initially, the absorption spectra of boehmite nanoparticles were obtained (Figure 3.5) to ascertain the optical band gap and excitation wavelengths. It is evident from the absorption spectra that two prominent electronic transitions have occurred around 206 and 265 nm during the process. The 206 nm transition originates from O_2^- to Al_3^+ charge transfer [11].
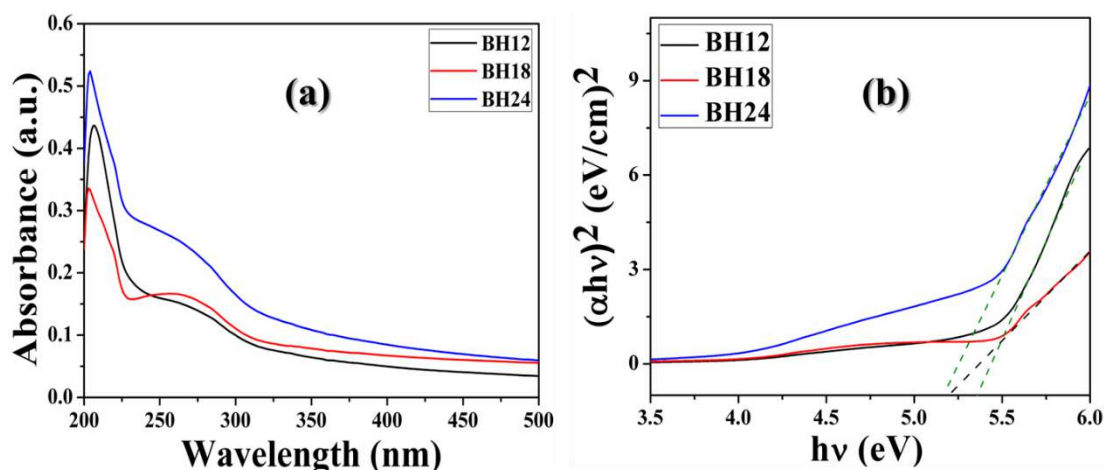
Figure 3.5 *(a) Absorbance spectra and (b) corresponding Tauc plots of the samples*

The optical band gap of the samples was calculated using the Tauc plot relation [12] given as,

$$\alpha E = A(E - E_g)^n \qquad (2)$$

Where E, E_g, α and A are the photon energy, the optical band gap energy in eV, absorption coefficient, and a constant term respectively. In the Tauc plot (Figure 3.5), $(\alpha h\nu)^2$ is plotted against photon energy $h\nu$ and the band gap energy is calculated by extrapolating the linear region and intersecting the linear portion of the curve to the energy axis. The band gap energy is seemed to decrease with hydrothermal reaction time and achieved a minimum value of 5.17 eV in the BH24 sample. The smaller-sized particles accommodate a small number of molecules or atoms. The number of overlapping orbitals in such cases quenches the width of the energy level, which in turn creates a large band gap. Such tunability of band edges (and overall band gap maneuvering) would be useful for different optical applications.

The emission spectra of the synthesized samples at the excitation wavelength 389 nm are represented in Figure 3.6. A few strong emission bands of boehmite have been achieved, which are located at 439, 486, and 530 nm for all the samples. Such emission bands

indicate different defect states in the orthorhombic phase of boehmite crystals that occurred during the crystal growth [13]. Normally, these crystal defects promote the entrapment of photo-generated carriers during their transitions from the higher energy level to the lower ones. Previous studies suggest that non-bridging oxygen hole center can take a significant role to originate emissions within the range of 467 nm to 576 nm [14] which is visible in emission spectra of the samples.
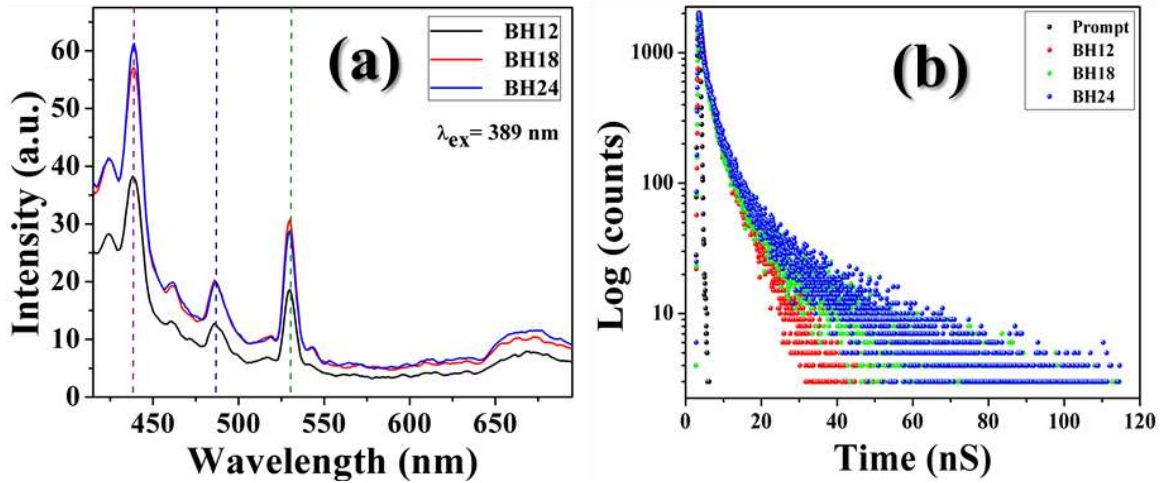
Figure 3.6 (a)Emission spectra and (b) fluorescence lifetimes of the boehmite nanostructures

Moreover, the variation in emission intensities could be substantiated using defect-mediated emission theory. Briefly, the smaller surface area possesses fewer defects, thus, BH24 has a lesser number of defects than the rest of the samples as it has the lowest surface area due to its largest dimension among the three samples. Similarly, BH12 possesses the highest surface area and results in its lowest emission intensity due to the charge entrapment mechanism. Thus, it is evident that the surface defects can greatly influence the emission intensity of a material.

Table 3.2 Fluorescence lifetime data of the samples excited at 389 nm

Sample	τ_1 (ns)	f_1	τ_2 (ns)	f_2	Average lifetime $<\tau>$ (ns)	χ^2
BH12	5.6657	100	0	0	5.666	1.1789
BH18	2.6336	62.91	11.25	37.09	5.783	1.0158
BH24	3.0896	61.77	14.69	38.23	7.527	1.2330

It is very interesting to observe the fluorescence lifetimes of such defect-induced fluorescence. Thus, the fluorescence lifetime experiment for three boehmite nanoparticles was carried out (Figure 3.6, Table 3.2). It is found that the lifetime decay profiles are in the nanosecond range, which is useful in various fluorometric applications. It could be

seen in the fitted fluorescence decay profiles that the BH12 sample has the lowest fluorescence lifetime (5.666 ns), whereas the average lifetimes of the two other samples BH18 and BH24 are seemed to be 5.783 and 7.527 ns respectively. Nonetheless, these values of lifetimes of our three samples also hint at the probable use of these three boehmite nanostructures in the field of bio-imaging and biosensing [15].

3.3.3 Investigation of the electrical properties

The energy storage capacities of the synthesized nanostructures have been estimated by the dielectric response of the samples. The real part of the dielectric constant subsidizes the amount of energy stored in a material due to polarization. The real part of the dielectric constant (ε') can be evaluated using the relation [16],

$$\varepsilon' = \frac{C.d}{\varepsilon_0 \, A} \quad (3)$$

Here, C, d and A are the capacitance, thickness, and area of the sample respectively of the pellet, and ε_0 is the free space permittivity (8.85×10^{-12} F/m). The real part of dielectric constant (ε') for all the samples with the applied field frequency (ranging from 40 Hz to 2 MHz) at different temperatures (from 30°C to 200°C) have been shown in Figure 3.7. The particle size has a significant impact on the dielectric behavior as the crystallinity gets increased with the reaction time. The BH12 sample possesses the highest permittivity (3.71×10^6) at room temperature and 40 Hz field. Similarly, the permittivity value for BH24 attains the lowest (1.43×10^6) in similar ambient conditions. The temperature response of the dielectric constants has also been recorded from 30 ^{0}C to 200 ^{0}C at different frequencies from 40 Hz to 10 MHz (Figure 3.8) showing that the permittivity of the samples is increasing with the temperature up to 50 ℃, and beyond 50 ^{0}C the dielectric constants decrease gradually with the increasing temperature. This type of dielectric relaxation is analogous to the Maxwell-Wagner interfacial polarization phenomenon [17-18], which is in good agreement with Koop's theory [19]. According to this theory, the free charge carriers are accumulated at the resistive grain boundaries [20-21] in dielectric materials and behave like dipoles [22]. Smaller-sized BH12 sample has a larger surface area among the three samples accommodating a higher number of such dipoles and resulting in higher dielectric permittivity. However, at relatively high frequencies, this polarization cannot withstand and the permittivity gradually decreases.
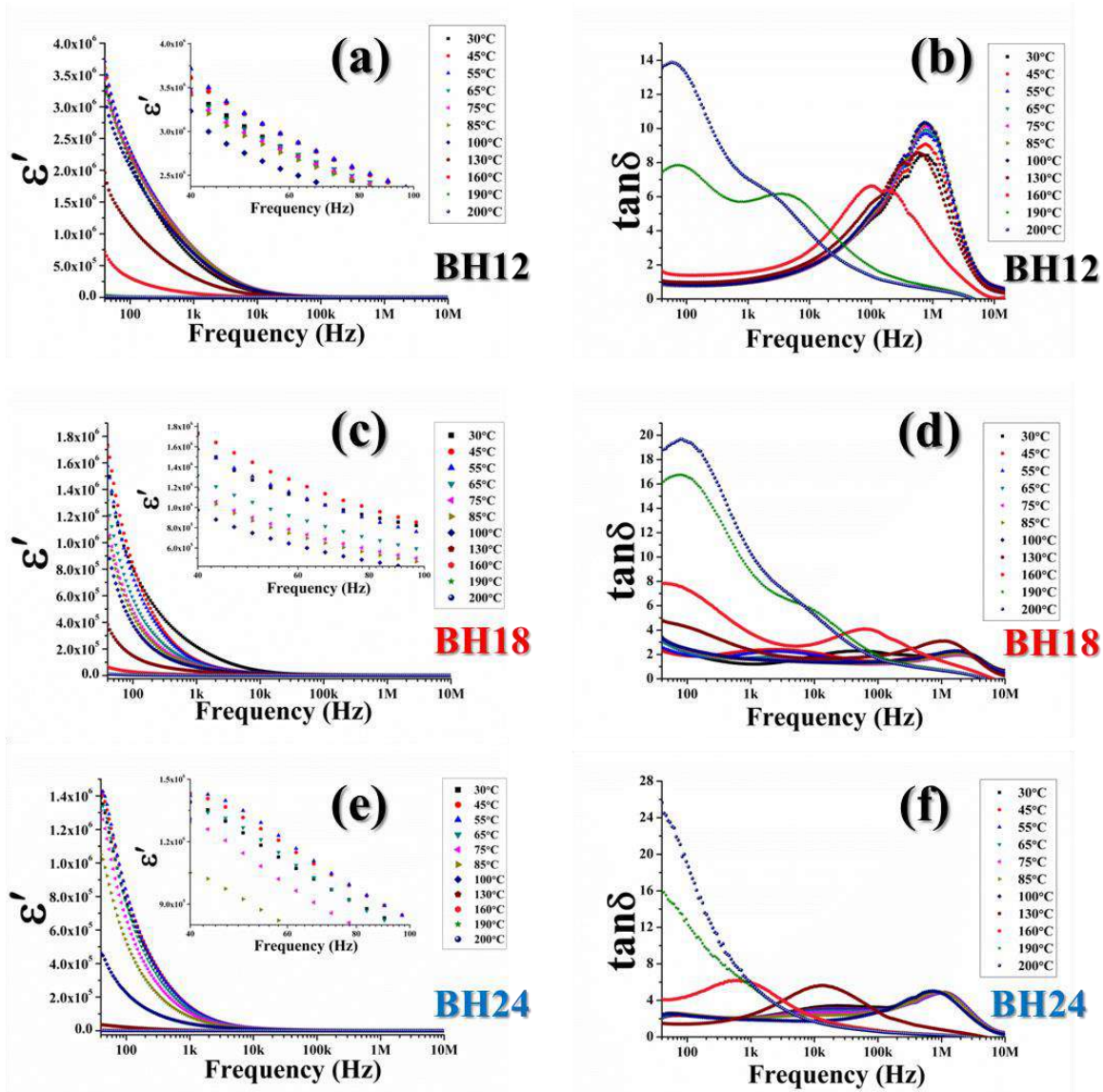
Figure 3.7 (a, c, e) Electrical permittivity and (b, d, f) corresponding tangent losses of the samples

The dielectric tangent loss varies significantly with the particle size of the samples (Figure 3.7). The samples depict less lossy nature at the low-frequency regime at lower temperatures, whereas a high loss tangent is found at low frequency at higher temperatures. Thermally agitated charge carriers cause this type of dielectric relaxation in the entire sample set as the dipoles cannot change their orientation with the changing external field at such a rapid speed [17]. Nonetheless, these nanostructures could be considered as good energy storage materials as they have high dielectric permittivity with a nominal loss.
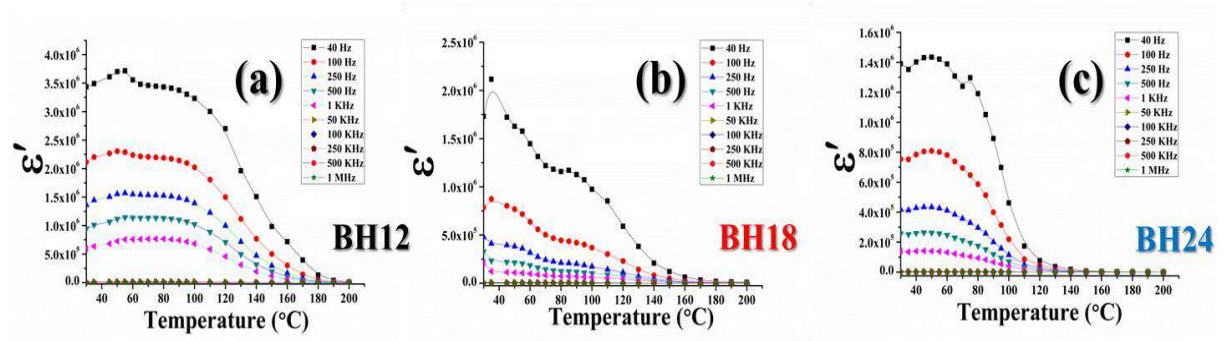
Figure 3.8 Dielectric constants of the samples as a function of the temperature

During the conductivity study, low values and almost frequency independent nature of ac conductivities (σ_{ac}) are found (Figure 3.9). In reality, resistive grain boundary normally restricts charge hopping below a certain excitation of the external field. Beyond that critical limit, the external field excites the carriers and the charge conduction occurs with increasing frequency, which results in the elevated values of ac conductivity at the high-frequency region [23-24]. Herein, a similar observation can be made at different temperatures above 10^4 Hz frequency for the entire sample set.
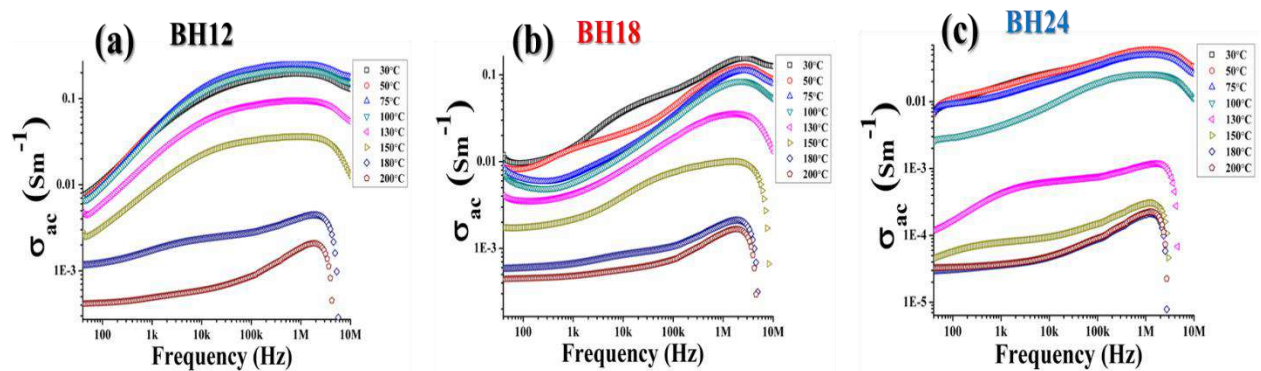
Figure 3.9 Ac conductivity of the samples at different temperatures

At lower temperatures (below 75°C), the ac conductivity of the BH12 sample increases with temperature, whereas it gets quenched gradually beyond 75°C. Such a phenomenon supports the presence of cationic/anionic vacancy defects in the sample. The carriers get trapped in these defect zones very easily causing such quenching of the conductivity. Moreover, at higher temperature γ- AlOOH transforms into γ*- AlOOH having more oxygen vacancies than that of γ- AlOOH and results in a decreased ac conductivity [25].

The dependence of ac conductivity on frequency has also been studied by using Jonscher's power law [26]

$$\sigma_{ac} = B\omega^n \qquad (4)$$

where B, n are constant terms. B has the units of conductivity and n is a dimensionless number. The values of n have been calculated for the entire set of samples by plotting $\ln\sigma$ vs $\ln\omega$ (Figure 3.10). The calculated n values of the samples are found to vary between 0.4499 to 0.1875 indicating the non-Debye type diffusion-limited hopping of the charge carriers [27-29].
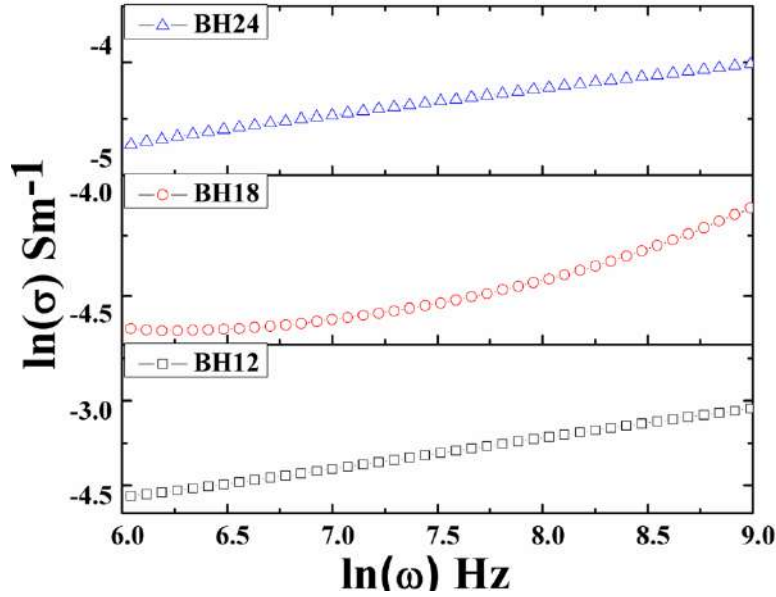
Figure 3.10 *Jonscher's plot of the samples*

Further, the activation energies of the samples at different frequencies have been evaluated by the Arrhenius equation [30].

$$\sigma = \sigma_0 \exp \frac{-E_a}{K_B T} \qquad (5)$$

Here, σ_0, E_a, K_B, T are the pre-exponential factor, the activation energy for conduction, Boltzmann's constant and absolute temperature respectively.
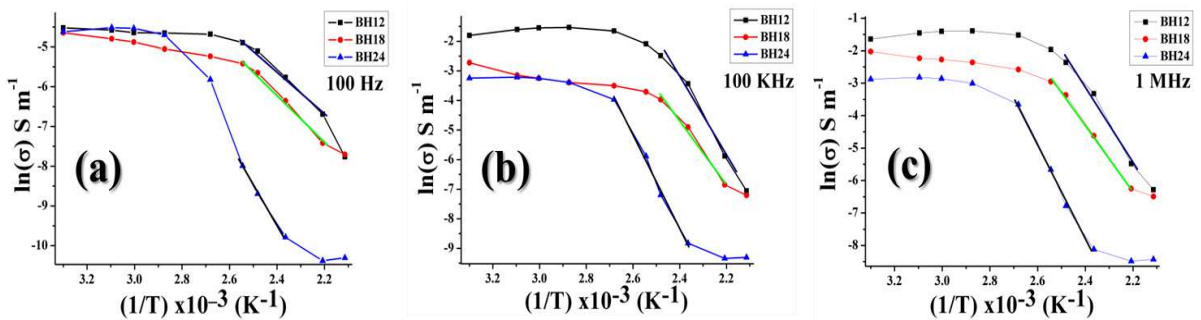
Figure 3.11 *Arrhenius plots of the samples at different frequencies*

Table 3.3 *Activation energies calculated from the Arrhenius plots*

Sample	Frequency	Activation Energy (eV)
BH12	100HZ	0.5540
	100KHZ	1.1402
	1MHZ	1.0061
BH18	100HZ	0.5023
	100KHZ	0.9261
	1MHZ	0.8829
BH24	100HZ	0.8938
	100KHZ	1.3555
	1MHZ	1.2383

The Arrhenius plots are calculated at frequencies 100 Hz, 100 kHz, and 1 MHz of the external field and have been presented in Figure 3.11. The activation energy is found to increase with the increasing frequency due to the charge mobility. Table. 3.3 depicts a detailed description of the activation energies. Henceforth, the crystal defect, more precisely the crystallinity of the nanostructures plays a dominating role in substantiating their numerous electric properties.

3.4 Summary

This work substantiates that the effect of particle size, more precisely the crystallinity, has a prominent impact on the optical and electrical properties of boehmite nanoparticles. Various physicochemical properties of this novel nanostructure have also been evaluated in due course. The hydrothermal-based synthesis procedure has been standardized, which shows how the reaction time can influence the morphology and the particle size of the system. Optical band gap can also be maneuvered, if a controlled reaction process is achieved. Such band gap tuning could be useful in different optical applications. Meanwhile, the defect-mediated fluorescence of the boehmite nanocrystal is achieved, which could be further enhanced and applied in numerous fluorometric assays. Here, crystallinity plays a pivotal role in determining the electrical characteristics of the boehmite nanostructures. The lower crystalline sample exhibits higher charge storage capacity with a minimal dielectric loss. Such features make this nanostructure a potential candidate for energy storage applications.

References

[1] Carolan, D., 2017. Recent advances in germanium nanocrystals: Synthesis, optical properties, and applications. *Progress in materials science*, *90*, pp.128-158.

[2] Reddy, L.H., Arias, J.L., Nicolas, J. and Couvreur, P., 2012. Magnetic nanoparticles: design and characterization, toxicity and biocompatibility, pharmaceutical and biomedical applications. Chemical reviews, 112(11), pp.5818-5878.

[3] Kulp, K. and Lorenz, K., 1981. I. Physicochemical Properties'. Cereal chem, 58(1), pp.46-48.

[4] Leung, A.C., Hrapovic, S., Lam, E., Liu, Y., Male, K.B., Mahmoud, K.A. and Luong, J.H., 2011. Characteristics and properties of carboxylated cellulose nanocrystals prepared from a novel one-step procedure. Small, 7(3), pp.302-305.

[5] S. Music´, O. Dragc̆evic´, S. Popovic, Hydrothermal crystallization of boehmite from freshly precipitated aluminium hydroxide, Materials Letters, 40 (1999) 269–274.

[6] Liu, X., Niu, C., Zhen, X., Wang, J. and Su, X., 2015. Novel approach for synthesis of boehmite nanostructures and their conversion to aluminum oxide nanostructures for remove Congo red. Journal of colloid and interface science, 452, pp.116-125.

[7] Holzwarth, U. and Gibson, N., 2011. The Scherrer equation versus the'Debye-Scherrer equation'. Nature nanotechnology, 6(9), pp.534-534.

[8] S. Das, S. Das, A. Roychowdhury, D. Das, S. Sutradhar, Effect of Gd doping concentration and sintering temperature on structural, optical, dielectric and magnetic properties of hydrothermally synthesized ZnO nanostructure, Journal of Alloys and Compounds, 708 (2017) 231-246.

[9] A. Zirehpour, A. Rahimpour, F. Seyedpour, M. Jahanshahi, Developing new CTA/CA based membrane containing hydrophilic nanoparticles to enhance the forward osmosis desalination, Desalination 371 (2015) 46–57.

[10] W. Brostow, T. Datashvili, Chemical Modification and Characterization of Boehmite Particle, CHEMISTRY & CHEMICAL TECHNOLOGY, 2 (2008) 27-32.

[11] A. Alemi, Z. Hosseinpour, M. Dolatyari, A. Bakhtiari, Boehmite (γ-AlOOH) nanoparticles:Hydrothermal synthesis, characterization, pH-controlled morphologies, optical properties, and DFT calculations, Phys. Status Solidi B, 249 (2012) 1264–1270.

[12] S. Das, S. Das, A. Roychowdhury, D. Das, S. Sutradhar, Effect of Gd doping concentration and sintering temperature on structural, optical, dielectric and magnetic properties of hydrothermally synthesized ZnO nanostructure, Journal of Alloys and Compounds, 708 (2017) 231-246.

[13] Wang, J.A., Bokhimi, X., Morales, A., Novaro, O., Lopez, T. and Gomez, R., 1999. Aluminum local environment and defects in the crystalline structure of Sol− Gel alumina catalyst. The Journal of Physical Chemistry B, 103(2), pp.299-303.

[14] Z. Q. Yua, C. X.Wanga, X. T. Gub, C. Li, Photoluminescent properties of boehmite whisker prepared by sol-gel process, Journal of Luminescence 106 (2004) 153–157.

[15] K. Okabe, N. Inada, C. Gota, Y. Harada, T. Funatsu, S. Uchiyama, Intracellular temperature mapping with a fluorescent polymeric thermometer and fluorescence lifetime imaging microscopy, Nat Commun., 3 (2012) 705-714.

[16] Szigeti, B., 1949. Polarisability and dielectric constant of ionic crystals. Transactions of the Faraday Society, 45, pp.155-166.

[17] S. Das, S. Das, S. Sutradhar, Effect of Gd3+ and Al3+ on optical and dielectric properties of ZnO nanoparticle prepared by twostep hydrothermal method, Ceramics International, 43 (2017) 6932-6941.

[18] J. Liu, C.G. Duan, W.G. Yin, W.N. Mei, R.W. Smith, J.R. Hardy, Phys. Rev. B 70 (2004) 144106.

[19] C.G.Koops, On the Dispersion of Resistivity and Dielectric Constant of Some Semiconductors at Audiofrequencies, Phys. Rev. 83 (1951) 121.

[20] L. Singh, W. Kim, B. C. Sin, K. D. Mandal, U. S. Rai, A. Ullah, H. Chung, Y. Lee, Dielectric studies of a nano-crystalline $CaCu_{2.90}Zn_{0.10}Ti_4O_{12}$ electro-ceramic by one pot glycine assisted synthesis from inexpensive $TiO_2$for energy storage capacitors, , RSCAdv. 4 (2014) 52770-52784.

[21] P. K. Ghosh, M. K. Mitra, K. K. Chattopadhyay, ZnS nanobelts grown in a polymer matrix by chemical bath deposition, Nanotechnology, 16 (2005) 107–112.

[22] K. Tsuji, H.Su Han, S. Guillemet-Fritschc, C. A. Randall, Dielectric relaxation and localized electron hopping in colossal dielectric (Nb,In)-doped TiO2 rutile nanoceramics, Phys.Chem.Chem.Phys., 19 (2017) 8568.

[23] W. Ling, L. Hongxia, J. Peihai, W. Tinga, L. Lizhu, The effects of TiC@AlOOH core shell nanoparticles on the dielectric properties of PVDF based nanocomposites, RSC Adv., 6 (2016) 25015.

[24] S.Kabashima, T.Kawakubo, High Frequency Conductivity of NiO, Journal of the Physical Society of Japan, 24 (1968) 493-497.

[25] J. A. Wang, X. Bokhimi, A. Morales, O. Novaro, T. Lo´pez, R. Go´mez, Aluminum Local Environment and Defects in the Crystalline Structure of Sol-Gel Alumina Catalyst, J. Phys. Chem. B, 103 (1999) 299-303.

[26] A.K.Jonscher, A new understanding of the dielectric relaxation of solids, Journal of Materials Science 16 (1981) 2037-2060.

[27] S.R. Majid, A.K. Arof, Electrical behavior of proton-conducting chitosan-phosphoric acid-based electrolytes, Physica B 390 (2007) 209–215.

[28] Sudha L. K., S.Roy, and K. Uma Rao, Evaluation of Activation Energy (E_a) Profiles of Nanostructured Alumina Polycarbonate Composite Insulation Materials, International Journal of Materials, Mechanics and Manufacturing, 2 (2014) 96-100.

[29] S.K.Saha, M.A.Rahman, M. R. H. Sarkar, M. Shahjahan, M. K. R. Khan, Effect of Co doping on structural, optical, electrical and thermal properties of nanostructured ZnO thin films, Journal of Semiconductors, 36 (2015) 033004.

[30] Laidler, K.J., 1984. The development of the Arrhenius equation. Journal of chemical Education, 61(6), p.494.

Chapter 4

Synthesis & characterization of boehmite (γ-AlOOH) nanostructures of different morphologies and their application in detection, removal of Cr(VI) and using it as a 'Waste capacitor'

Chapter 4

Synthesis & characterization of boehmite (γ-AlOOH) nanostructures of different morphologies and their application in detection, removal of Cr(VI) and using it as a 'Waste capacitor'

4.1 Introduction

In the previous chapter, the hydrothermal synthesis route of the boehmite nanocrystal has been successfully optimized. Moreover, the size-dependent characteristics of the boehmite have been discussed in a detailed manner. It showed enhanced fluorescence and the highest energy storage capacity in the nano-sized boehmite (BH12). Henceforth, nano-boehmite has been selected for further applications. Previously, various groups have studied different morphologies of boehmite for their purposes. Interestingly, the physicochemical properties have been greatly influenced when the morphology is varied. In reality, various morphologies of boehmite nanostructures, such as nanofibers, nanoparticles, nano-flowers, nanobelts, nanoflakes have been synthesized until now [1-2]. However, their application is limited in the field of energy storage and wastewater treatment.

Herein, the present work reports the successful synthesis of three distinct morphologies of boehmite nanostructures, spherical (EBH), flower-like (UBH), and needle-shaped (HBH). Moreover, a novel synthesis route for spherical (EBH) boehmite nanostructures using ethylenediamine has been reported here for the first time. After studying various physicochemical properties, these three nanostructures have been further employed to detect hexavalent chromium (Cr(VI)) in wastewater by using a facile fluorometric method. The simultaneous removal of the chromium ion using the adsorption-based technique makes boehmite nanostructures multifunctional. Apart from that, this material can change its microstructure after adsorbing the chromium ions directly from the wastewater, which further enhances its dielectric permittivity and ac conductivity. Such an increment in energy harvesting property makes boehmite a useful 'Waste capacitor'. In reality, nano-boehmite uses hexavalent chromium ions from wastewater and converts them into a superior dielectric separator. Hence, these chromium adsorbed samples could be highly beneficial for capacitor industries and different energy harvesting applications.

4.2 Experimental details

4.2.1 Materials

Aluminum nitrate nonahydrate [$Al(NO_3)_3.9H_2O$], Urea crystal extra pure [CH_4N_2O], and Ethylenediamine [$C_2H_8N_2$] were purchased from Merck, India. Hexamine (99% extra pure) was purchased from Loba Chemie Pvt. Ltd. The reagents were used without further purification. Millipore water was used throughout the experiment with a resistivity of at least 18.2 MΩ-cm. All glassware used in our experiments was cleaned with aqua regia solution followed by rinsing with ultrapure water.

4.2.2 Synthesis of nanostructures

Boehmite of different morphologies has been synthesized using a hydrothermal route. In a typical protocol, 0.1(M) aluminum nitrate nonahydrate was dissolved in Millipore water to form a transparent solution [3-4]. The transparency of the solution indicates the formation of Al^{3+} ions. Later, it had been basified using different precursors to achieve different nanostructures of boehmite. The solution was divided into three parts, namely part-A, part-B, and part-C.

Ethylenediamine was added drop-wise until the pH of the solution reached 9 and marked as part-A, which results in thick white precipitation. The part-B solution was treated with hexamine under vigorous stirring conditions maintaining a pH value of 5. Urea crystals were added to the part-C solution and the pH was adjusted to 7 to start flower-like nucleation. These solutions were stirred for another 3 h for complete reaction.

All three treated solutions were then transferred into three different Teflon-lined stainless-steel autoclaves and kept in a dust-free oven at 160 ℃ for 16 h. After completion of the hydrothermal reaction, the autoclaves were then allowed to cool naturally to room temperature, and white precipitates were obtained in every case which indicates the formation of boehmite nanostructures. Hydrothermally treated part-A sample was found in spherical nanostructure and was named as EBH, whereas, nano-needle (part-B) and nanoflower (part-C) morphologies were achieved in HBH and UBH samples respectively. The precipitates were collected by centrifugation at 10,000 RPM for 10 minutes washed several times with distilled water and then dried in a vacuum for 24 h to develop dry powders of various morphologies. The samples were then marked and sent for further characterizations.

4.3 Results and discussion

4.3.1 Structural and morphological analyses of the nanostructures

The X-ray diffraction studies (Figure 4.1) have been carried out to substantiate the phase purity and successful synthesis of the boehmite nanostructures of different morphologies. Additionally, the crystallite dimensions have been calculated using this technique to ascertain any alterations in the orthorhombic structure of the boehmite nanocrystals due to morphological variation. The diffractograms of the boehmite nanocrystals have been matched with the JCPDS card no. 21-1307 suggesting the high purity of the samples. This also validates the complete transformation of the precursors to aluminum oxy-hydroxide phases in each case. The diffraction maxima located at 14.5 ° corresponds to the (020) plane of the boehmite, which also suggests the abundance of the growth units in this direction.
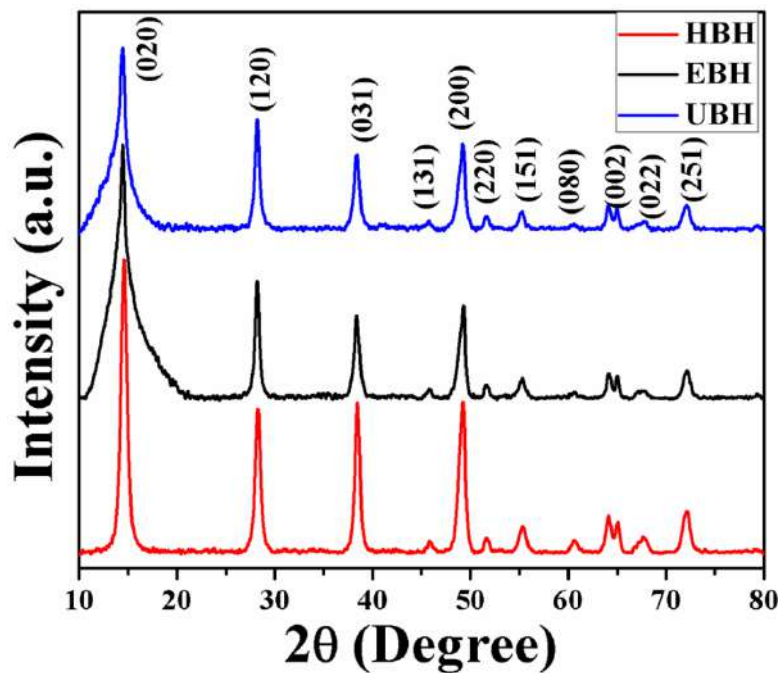
Figure 4.1 *XRD patterns of the samples*

Moreover, the crystallite sizes have been calculated using the Scherrer equation as mentioned below [5]

$$<\text{D}>_{(020)} = \frac{0.9\lambda}{\beta_{1/2}\, cos\theta} \qquad (1)$$

Here, λ, D, θ, and $\beta_{1/2}$ are the wavelength of the X-ray, mean crystallite sizes, Braggs angle, and the full width at half maximum (FWHM) of the (020) peak respectively. The calculated crystallite dimensions have been illustrated in Table 4.1 showing that the morphology greatly influences the crystallite diameter.

Table 4.1 Microstructural parameters from XRD analysis

Sample	FWHM corresponding to (020) plane (rad)	Crystallite diameter (nm)
EBH	0.0297	4.7
HBH	0.0126	11.1
UBH	0.0191	7.3
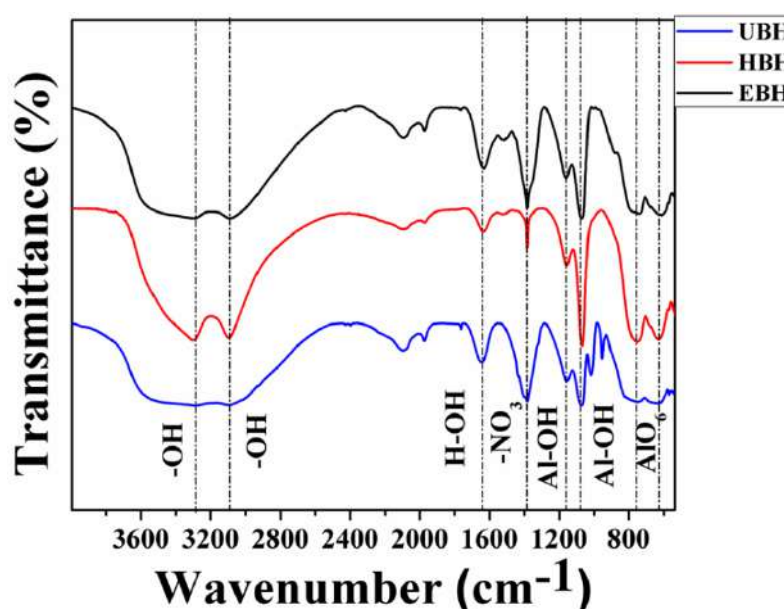
Figure 4.2 FTIR spectra of the samples EBH, UBH and HBH

The bonding network analysis has been performed by using FTIR spectrometry (Figure 4.2). All the three morphologies of boehmite depict their AlO_6 characteristics vibrations at 889, 758 and 629 cm^{-1} confirming the successful synthesis of the nanostructures [6]. The asymmetric (Al)O–H and symmetric (Al)O–H stretching vibrations have also been located at 3286 and 3090 cm^{-1} respectively [7]. The vibrational modes centered at 1071 and 1159 cm^{-1} are also found in the spectra confirming the symmetric and asymmetric Al–O–H modes of boehmite respectively [8]. The surface adsorbed moisture and -OH vibrations have been located at 1640, 3286 and 3090 cm^{-1} respectively confirming the presence of the oxy-hydroxide phase of alumina. Such characteristics vibrations are consistent with the diffraction data and denote the successful preparation of the samples.
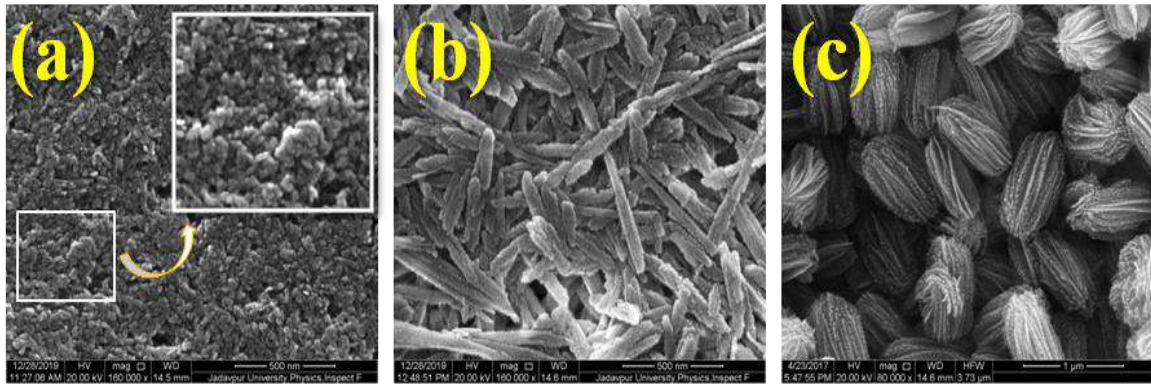
Figure 4.3 *FESEM micrographs of the synthesized (a) EBH, (b) HBH, and (c) UBH samples*

The morphological characteristics of the three boehmite nanostructures have been estimated by using FESEM and TEM techniques. The FESEM micrographs (Figure 4.3) depict three distinct architectures of boehmite. The EBH sample shows spherical morphology, whereas the needle-like and nanoflower morphologies are obtained for HBH and UBH samples respectively.
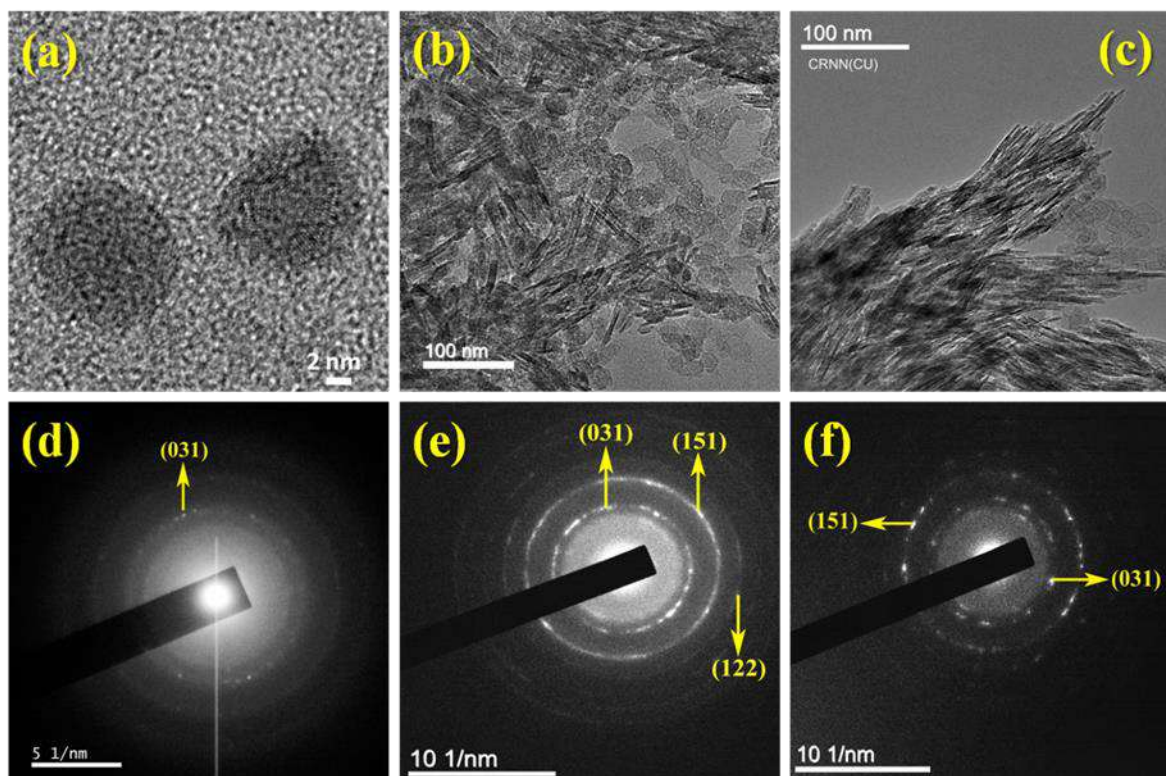
Figure 4.4 *The TEM images of (a) EBH, (b) HBH, and (c) UBH and their corresponding SAED patterns (d-f)*

The TEM images (Figure 4.4) show that the spherical EBH nanoparticles are having a diameter of ~8-10 nm. These spheres are quite agglomerated, probably due to the inter-particle cohesive forces between the particles of boehmite. The needles are quite sharp

having an average length and breadth of ~45-50 nm and ~8-10 nm respectively. The nanoflower morphology of boehmite is fairly unique. The surface roughness is visible in this morphology, which could be ascribed to the aggregation of the smaller-sized particles to form the hierarchical nano-flower structure of boehmite. Each of these nanoflowers is consists of nano-petals having an average thickness of ~15-20 nm.
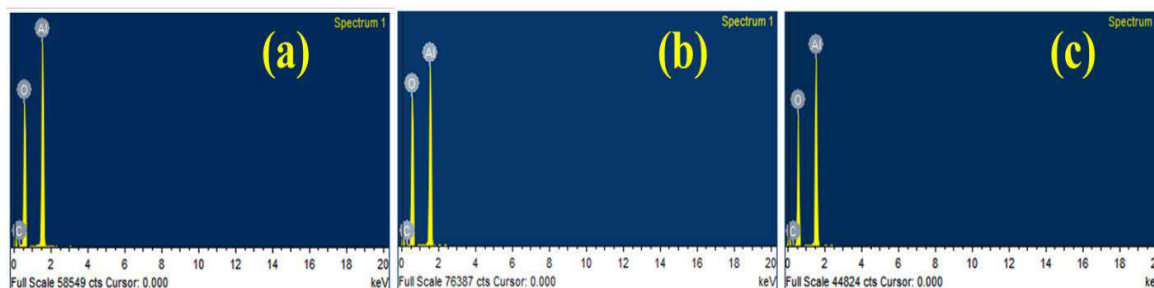
Figure 4.5 EDX spectra of the synthesized samples

The elemental analyses of these three boehmite nanostructures have been performed by using EDX (Figure 4.5), showing the presence of aluminum and oxygen in all three samples. The absence of any impure traces further validates the purity of these nanostructures.

4.3.2 Surface characteristics of the nanostructures
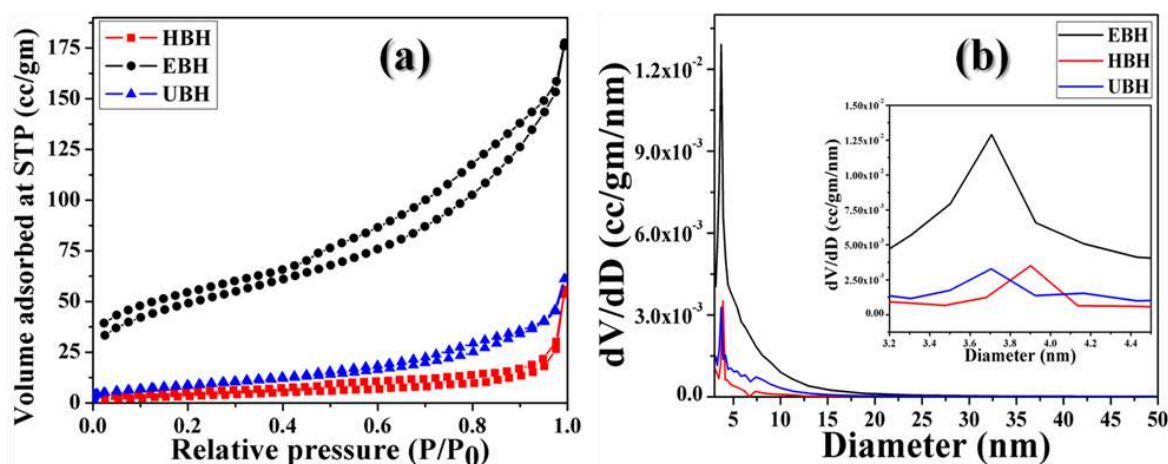
Figure 4.6 *Surface area and porosity studies of the boehmite samples*

Previously, it has been observed that boehmite has mesopores and the porosity is found to be uniform. In this case, the nitrogen (N_2) adsorption-desorption isotherms (Figure 4.6) suggest an almost similar amount of adsorption and desorption of the gas in all the cases. Such results yield type IV isotherms for our samples, which leads to the mesoporous surface of the nanostructures [9-10]. The corresponding H4-type hysteresis loop also

suggests the presence of narrow slit-like pores over the surfaces of these nanostructures confirming that these samples could be used as adsorbents [9-10].

Table 4.2 *Estimated BET surface area, pore radius, and pore volume data of different boehmite samples*

Sample name	Surface area (m²/g)	Pore size (nm)	Pore volume (cc/g)
HBH	12.81	3.9	8.628×10^{-2}
EBH	176.8	3.8	2.746×10^{-1}
UBH	31.64	3.7	9.486×10^{-2}

It is observed that the EBH and HBH nanostructures are having average porosity of ~3.9 and 3.8 nm respectively, while UBH has ~3.7 nm pore diameter on average. The surface area is found to be highest in the EBH sample ($176.8 \ m^2g^{-1}$), whereas it is 12.81 and 31.64 m^2g^{-1} for HBH and UBH respectively.

4.3.3 Qualitative model for the different nano-architecture formation of boehmite

In order to substantiate the morphological evolution of the boehmite nanostructures, XRD, FTIR, and FESEM characterizations were employed (Figure 4.7). The physical characteristics of the formation have been estimated especially at three different points of the growth. These are nucleation, growth, and self-assembly of the nanostructures [11-12]. Based on the characterizations, it is observed that the three basifying agents namely, ethylenediamine, hexamine, and urea were not only controlled the pH of the reaction but also results in three different morphologies of boehmite.

In the case of ethylenediamine, the reaction found no preferential growth in any direction as it is the simplest amine. Thus, it creates a spherical morphology after the complete reaction.

Interestingly, the needle-shaped HBH sample possesses less precipitation during the nucleation process. But, at high pressure and temperature (during the hydrothermal reaction) the thick and white precipitates form. This could be reasonably due to the less adsorption of the $R-NH_3^+$ ions at normal ambient conditions. When the pressure is employed at the hydrothermal chamber, the adsorption takes place and results in the white precipitate of the boehmite. The time varied FESEM data suggests that the hydrothermal

reaction time influences the growth of the needles remarkably. A similar observation could be made by using the time varied XRD data of the sample (Figure A1.2).

Moreover, covalently bonded urea is unable to split in the aqueous medium [13]. Hence, during the hydrothermal reaction, rod-shaped structures of boehmite are formed due to the strong cationic environment and excess pressure [14-15]. As a chelating agent, the electronegative moiety of urea (C=O) chelates with the aluminum ions for unidirectional growth. During the hydrothermal process, such nanorods are agglomerated to form nano-petals and the self-assembly process finally yields the nanoflower morphology of the system.
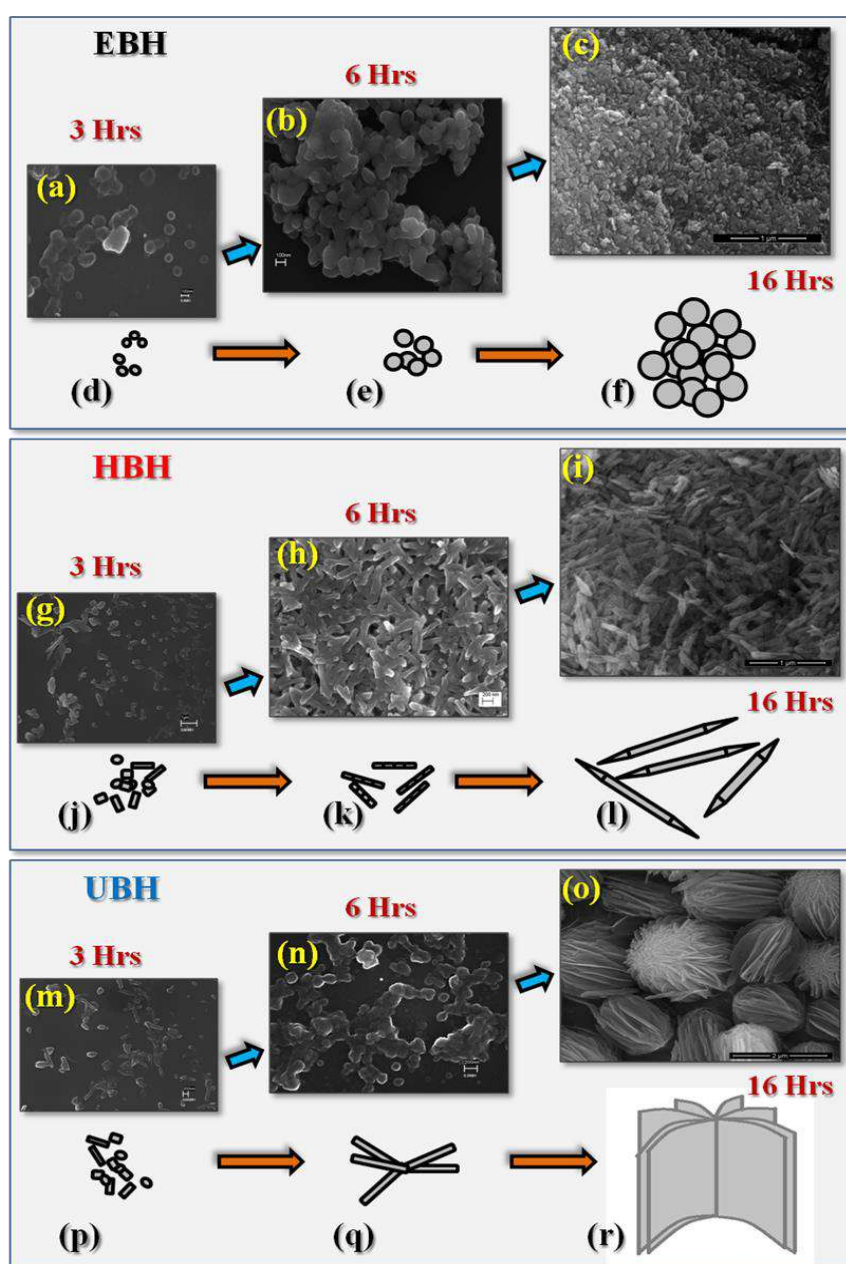
Figure 4.7 Mechanisms of formation of different boehmite nano-architectures

4.3.4 Optical properties of the synthesized nanostructures

Initially, the absorbance spectra of the samples were recorded to estimate the optical band gap and any alteration in the absorbance maximum due to the morphological variation of the samples (Figure 4.8).
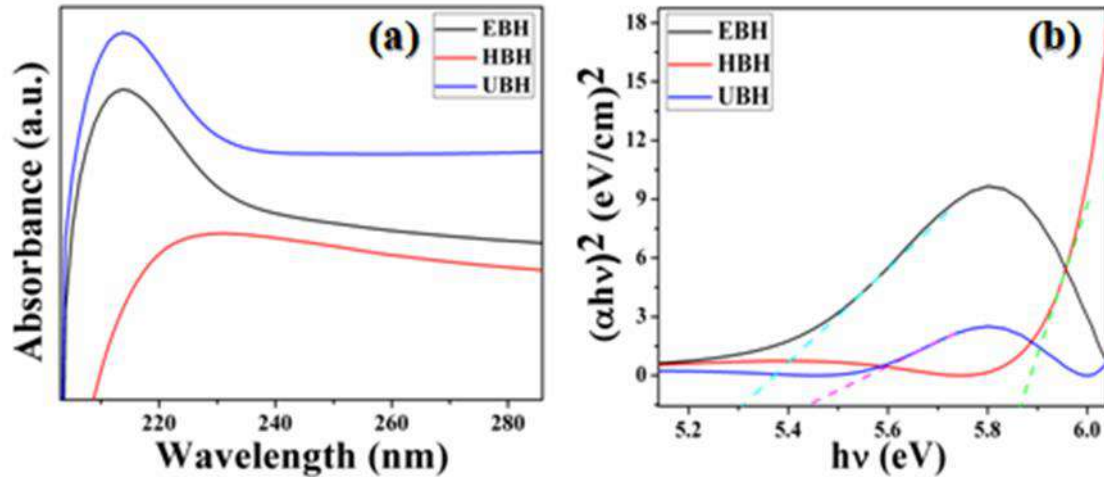
Figure 4.8 Absorbance spectra (a) and corresponding Tauc plots of the samples

The spectra yield a gradual shift in the absorbance maximum with varying morphology. It is observed that the absorbance peak of needle-like HBH is situated at 226 nm, whereas it is blue-shifted to 214 and 213 nm for UBH and EBH respectively. Such a blue shift also alters the optical band gap of the samples. The Tauc relation is used to estimate the band gap as follows [16],

$$\alpha E = A(E - E_g)^n \qquad (2)$$

Where E, E_g, α and A are the photon energy, optical band gap energy, absorption coefficient, and a constant term respectively. The optical band gap changed radically with the varying morphology of boehmite. Typically, the band gap energies for EBH, UBH, and HBH are 5.30 eV, 5.44, and 5.87 eV respectively. Such alteration validates the influence of the morphology on the optical property of the sample.

Further, the nanostructures were exposed to the ultraviolet energy of 375 nm wavelength for studying their emission properties. The emission intensity (centered at 428 nm) is found to be highest in the needle-shaped HBH sample and it is lowest for the spherical EBH (Figure 4.9). In reality, the BET measurement suggests that the HBH has the lowest and EBH has the highest surface area among the three samples. As the surface area

66

increases, the number of defects also increases and those are responsible for the non-radiative recombination of the photo-generated electrons.
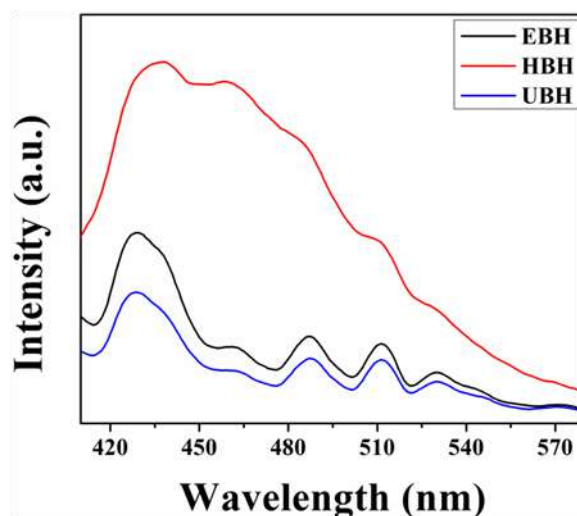
Figure 4.9 *Fluorescence spectra of the synthesized boehmite samples*

Such recombination quenches the emission intensity drastically, which has been found in the case of the EBH sample. Due to the highest emission intensity in the blue/ violet region of the spectrum, a needle-shaped HBH sample is selected for further fluorometric applications.

4.3.5 Fluorometric detection of hexavalent chromium (Cr(VI)) using needle-shaped boehmite (HBH)
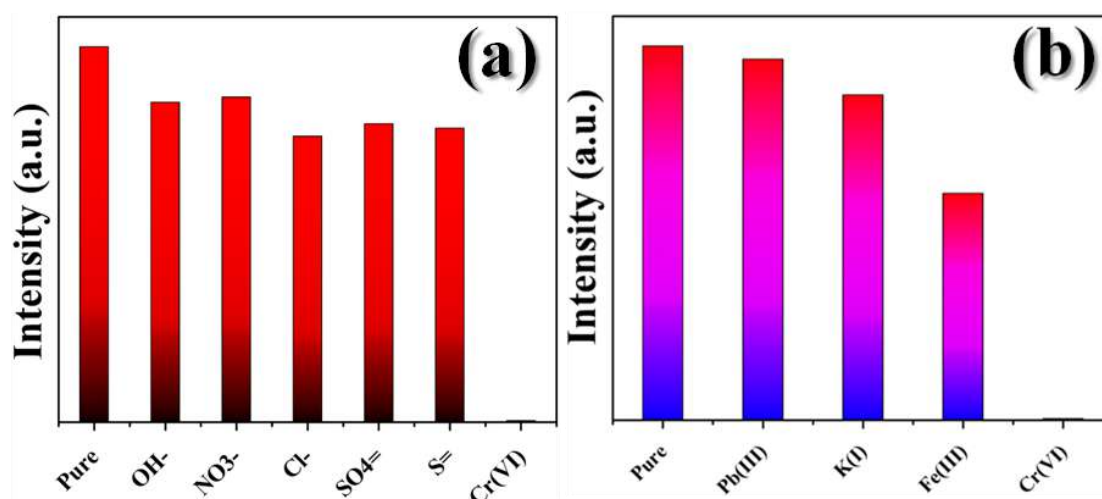
Figure 4.10 *Selectivity analysis of the HBH sample*

Initially, the selectivity and the sensitivity experiments of the detection have been performed. A range of various cations and anions were exposed separately to the HBH

sample (500 µM concentration of the HBH in water) and each time the fluorescence level of the sample was checked at 428 nm (Figure 4.10). It is observed that there is a drastic quenching in the fluorescence level of HBH when Cr(VI) is added to the solution. Otherwise, no such alteration is found when other ions are exposed to the system. The hexavalent chromium quenches the fluorescence level of the HBH is about 99% of its primary intensity, which makes HBH a potential sensor for Cr(VI).
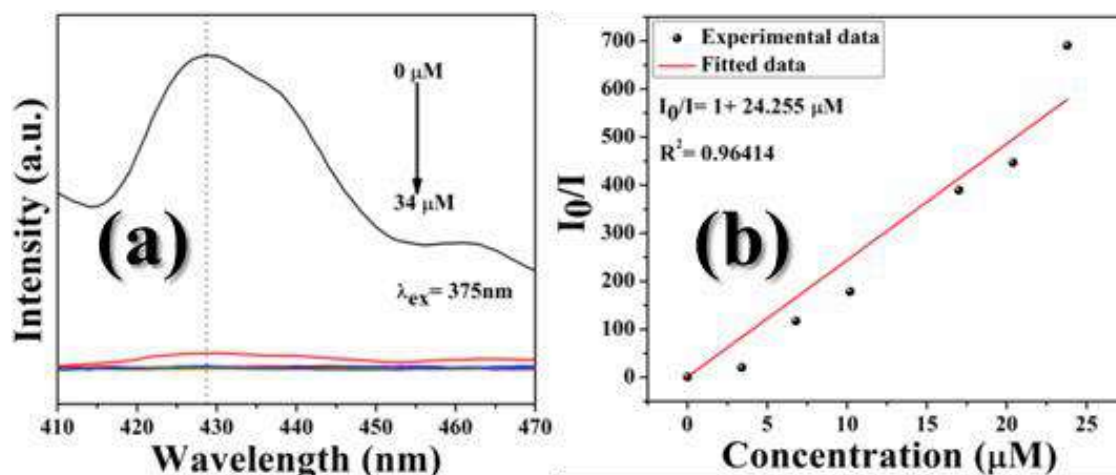
Figure 4.11 *(a) Concentration-dependent fluorometric quenching and (b) the Stern-Volmer plot of the sample*

The sensitivity of the sensing probe (HBH) has been analyzed based on the limit of detection (LOD). The relative fluorescence intensity (I_0/I) has been plotted against the concentration of the quencher ion (here Cr(VI)) and fitted with the Stern-Volmer's equation, as mentioned here [17-18],

$$\frac{I_0}{I} = 1 + K_{SV} \, [M] \tag{3}$$

Here, I_0, I, and K_{SV} are fluorescence intensities of pure HBH, HBH with Cr(VI) at various concentrations of Cr(VI), and the Stern-Volmer coefficient respectively.

The fitted parameters suggest a high K_{SV} value (24.255×10^6) with a fitting coefficient of 0.96414 (Figure 4.11). Such a high quenching constant yields a very low detection limit (only 0.42 nM) in this case suggesting the sensor material (HBH) is tremendously sensitive and selective towards hexavalent chromium.

The real-life extent of this fluorometric sensor has also been evaluated. The tannery wastewater sample has been collected from a local tannery industry and the amount of total chromium was tested using the ICP-AES method.
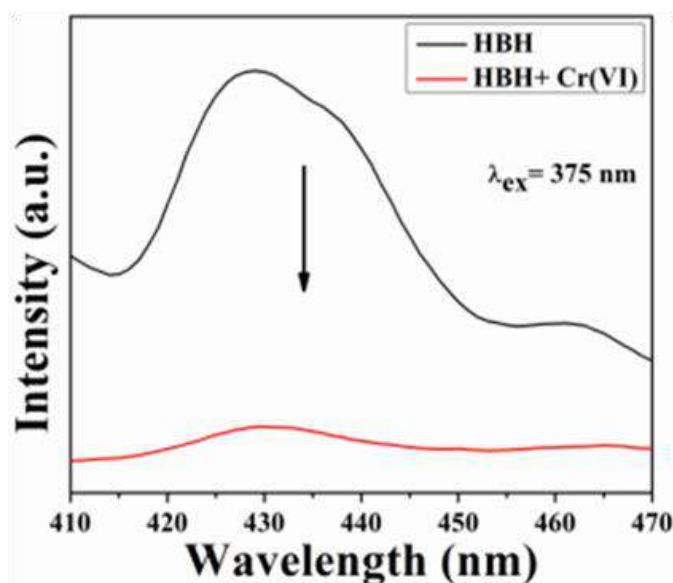
Figure 4.12 *Fluorometric quenching of the sensor material in the tannery wastewater sample*

The ICP-AES data depicts 23.4 ppm of chromium in the wastewater sample, which was further filtered using a Whatman filter paper and preserved at 4 ºC temperature before use. When the wastewater sample is exposed to the sensor material, the fluorescence intensity of the material suddenly quenches (Figure 4.12). Such a rapid quenching detects the presence of Cr(VI) in the wastewater making the sensor a good alternative for real-life applications.

4.3.6 Removal of hexavalent chromium from wastewater
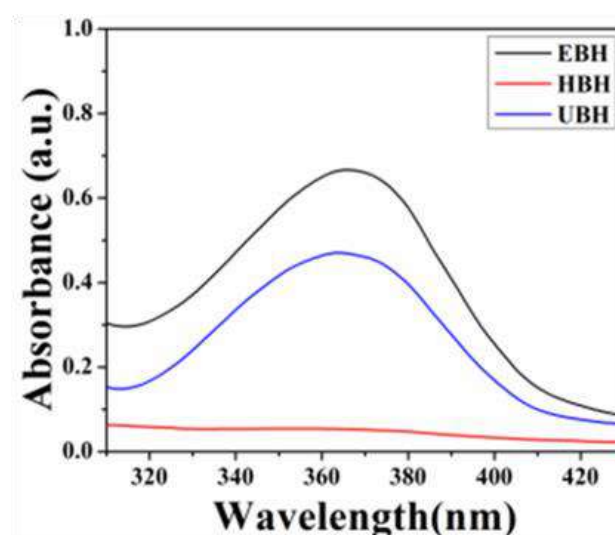
Figure 4.13 *Adsorption uptake of the boehmite samples*

Removal of hexavalent chromium from water is not an easy task. Various methods have been applied until now to eliminate the Cr(VI) contamination. Herein, a facile adsorption-

based removal approach is adopted to minimize the contamination level. Initially, all the three nanostructures of boehmite, namely HBH, EBH, and UBH was employed to study the chromium uptake. The uptake study was performed by taking 500 µM concentrations of each adsorbent separately into the 100 ppm solution of hexavalent chromium. Before taking the uptake data, the suspensions were stirred gradually for at least 6 h and then the absorption characteristics were recorded (Figure 4.13). The characteristics peak of chromium (351 nm) gets quenched when exposed to the adsorbents. The highest amount of quenching is obtained for the needle-shaped HBH sample. The sorption uptakes have been calculated using the following relation [19],

$$\text{Uptake (\%)} = \frac{C_0 - C_e}{C_0} \; x \; 100 \qquad (4)$$

Here, C_0 and C_e are initial and equilibrium concentrations of Cr(VI) ions in the media. The percentage uptake is found to be highest for the HBH sample (~76%), whereas it is 48% and 64% for EBH and UBH respectively. According to the surface characteristics of these three morphologies of boehmite, the HBH has the highest surface area among other nanostructures. The porosity is also highest for this need-like morphology, which could be the rationale for the highest uptake of HBH. Such a high uptake of HBH makes this needle-shaped boehmite (HBH) a potential adsorbent for hexavalent chromium and thus selected for further adsorption experiments.
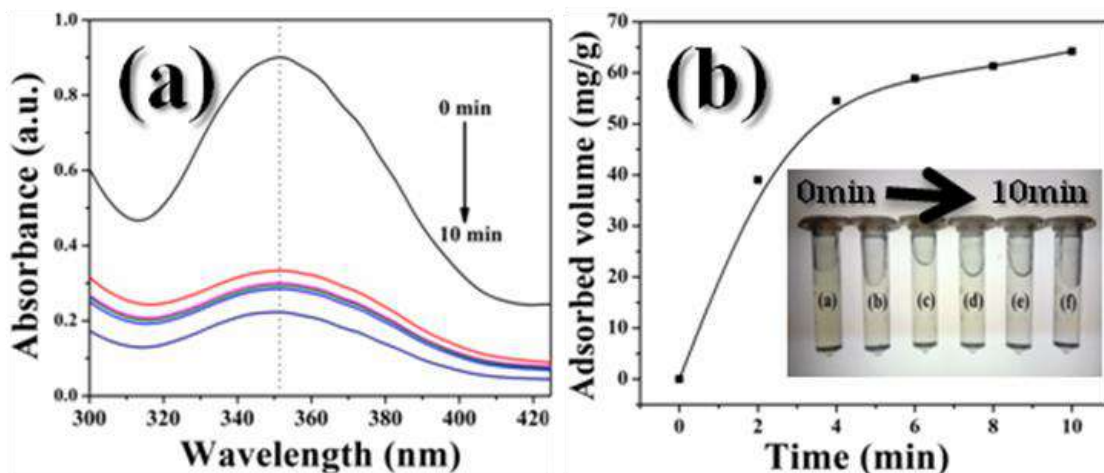
Figure 4.14 Adsorption kinetics study for needle-like HBH sample

The adsorption kinetics of HBH has also been studied to estimate the overall removal performance of the sorbent. Typically, a chromium solution of 80 ppm was exposed to the adsorbent and the spectra were recorded up to 10 minutes in every 2 minutes interval

(Figure 4.14). It is found that the characteristic peak of hexavalent chromium (351 nm) gradually quenches with time. The change in the color of the solution is visible through naked eyes (Figure 4.14).

4.3.7 Boehmite (HBH) as the 'Waste capacitor'

The dielectric permittivity of a sample denotes the charge storage capacity of a material. Herein, the dielectric property of pristine HBH and Cr(VI) adsorbed HBH (HBH+Cr(VI)) have been evaluated to observe any change in the energy storage property of the samples.
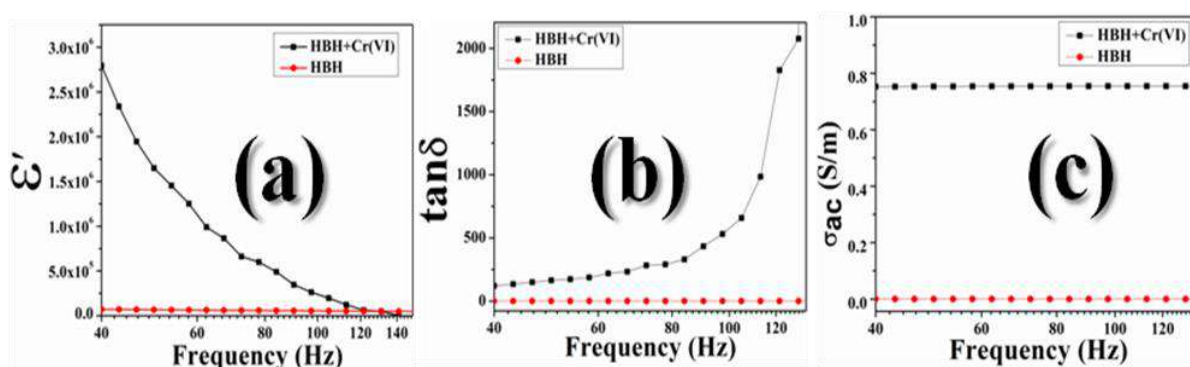
Figure 4.15 Electrical properties of the pure and Cr(VI) adsorbed HBH samples

The permittivity of HBH is found to be 6.2×10^4 at 40 Hz field frequency at room temperature, whereas the Cr(VI) adsorbed sample possesses an elevated dielectric constant of 2.7×10^6 at the same ambient condition. The dielectric constant of the adsorbed HBH sample is nearly ~43 times higher than that of its pure fraction (HBH). Such an augmented electrical permittivity corresponds to Maxwell-Wagner's interfacial polarization effect [20]. The number of conductive grains is increased in the Cr(VI) adsorbed HBH sample, which results in an enhanced number of grain-grain boundaries. As mentioned previously (Section 3.3.3), such grain-grain boundary polarization can contribute to the dielectric value of a sample. Thus, chromium adsorbed HBH depicts a higher dielectric constant than its pure counterpart.

The ac conductivity of the Cr(VI) adsorbed boehmite is also greater than its pure fraction, which could be due to the augmentation in the number of charge carriers. After getting released from their potential barrier, these free charge carriers initiate hopping from one-grain boundary to another and improve the conductivity of the sample [21], which in this case is pronounced in the chromium adsorbed sample.

The augmented dielectric constant and ac conductivity make the chromium adsorbed sample a potential candidate for energy storage applications, more precisely, the separator layer of any capacitor. Henceforth, this material could be regarded as a potential 'Waste capacitor'.

4.4 Summary

In this work, three different nanostructures of boehmite, namely nanoneedles, nanoparticles, and nanoflowers have been synthesized successfully using three different basifying agents. A detailed nucleation and growth mechanism has been delivered showing how these nanostructures are formed. In order to analyze phase purity and morphological characteristics, XRD, FTIR, FESEM, TEM, and EDS measurements have been performed showing the successful formation of the nanostructures. The BT-BJH analyses of the nanostructures revealed the highest surface area and porosity in the needle-shaped HBH nanostructure, which also has promising fluorescence and adsorption properties and is thus selected for further applications. The Cr(VI) sensing efficacy of the HBH sample is quite high and rapid. The S-V fitting suggests a detection limit of 0.42 nM, which is extremely low as compared to the previous studies. This HBH sample is capable to eliminate the Cr(VI) ion from wastewater using a facile adsorption technique. Almost 76% of chromium has been removed from the medium using this sample in just 10 minutes. Adsorbed chromium ions onto the porous structure of boehmite are not only used for sensing and removal applications but also this phenomenon drastically changes the dielectric permittivity and ac conductivity of the chromium adsorbed sample. At least ~43 times increment in dielectric constant makes our multifunctional needle-shaped boehmite nanostructure a budding candidate for fabricating 'waste capacitors'.

References

[1] J. Yang and R. L. Frost, *Research Letters in Inorganic Chemistry*, 2008, **1**, 1-4.

[2] X. Y. Chen, H. S. Huh and S. W. Lee, *Nanotechnology*, 2007, **18**, 285608 (5pp).

[3] J. R. Wen, M. H. Liub and C. Y. Mou, *CrystEngComm,* 2015, **17**, 1959.

[4] M. A. Pagano, C. Forano and J. P. Besse, *J. Mater. Chem.*, 2003, **13**, 1988–1993.

[5] Das S., Das S., Roychowdhury A., Das D., Sutradhar S. Effect of Gd doping concentration and sintering temperature on structural, optical, dielectric and magnetic properties of hydrothermally synthesized ZnO nanostructure. J. Alloys Compd. 708 (2017) 231-246.

[6] A. Dandapat and G. De, *J. Mater. Chem.*, 2010, **20**, 3890–3894.

[7] W. Brostow and T. Datashvili, *Chemistry & Chemical Technology*, 2008, **2**, 27-32.

[8] B. J. Saikia and G. Parthasarathy, *J. Mod. Phys.*, 2010, **1**, 206-210.

[9] D. K. Chanda, P. S. Das, A. Samanta, A. Dey, A. K. Mandal, K. D. Gupta, T. Maitya and A. K. Mukhopadhyay, *Ceramics International*, 2014, **40**, 11411–11417.

[10] D. K. Chanda, A. Samanta, A. Dey, P. S. Das and A. K. Mukhopadhyay, *J. Mater. Sci.*, 2017, 101007/s10853-016-0728-4

[11] H. Cao, H. Zheng, K. Liu and J. H. Warner, *J. Chem. Phys. Chem.*, 2010, **11**, 489.

[12] X. L. Li, C. X. Wang and G. W. Yang, *Prog. Mater. Sci.*, 2014, **64**, 121-199.

[13] C. Fong, D. Wells, I. Krodkiewska, P. G. Hartley and C. J. Drummond, Chem. Mater. 2006, **18**, 594-597.

[14] Z. G. Zhao and M. Miyauchi, *J. Phys. Chem. C,* 2009, **113**, 6539–6546.

[15] D. Ma, G. Shi, H. Wang, Q. Zhang and Y. Li, *J. Mater. Chem. A*, 2013, **1**, 684.

[16] S. Das, S. Das, A. Roychowdhury, D. Das and S. Sutradhar, *J. Alloys Compd.*, 2017, **708**, 231-246.

[17] Hussain S., Malik A. H., Afroz M. A., Iyer P. K. Ultrasensitive Detection of nitroexplosive-Picric Acid Via a Conjugated Polyelectrolyte in Aqueous Media and Solid Support. Chem. Commun. 51 (2015) 7207−7210.

[18] Lin Z. J., Zheng H. Q., Zheng H. Y., Lin L. P., Xin Q., Cao R. Efficient Capture and Effective Sensing of $Cr_2O_7^{2-}$ from Water Using a Zirconium Metal-Organic Framework. Inorg. Chem. 56 (2017) 14178-14188.

[19] Vijayakumar G., Tamilarasan R., Dharmendirakumar M. Adsorption, Kinetic, Equilibrium and Thermodynamic Studies on the Removal of Basic Dye Rhodamine-B from Aqueous Solution by the use of Natural Adsorbent Perlite. J. Mater. Environ. Sci. 3 (1) (2012) 157−170.

[20] Bardhan S., Roy S., Chanda D. K., Das S., Pal K., Chakraborty A., Basu R., Das S. Microstructure and Dielectric Properties of Naturally Formed Microcline and Kyanite: A Size-Dependent Study. Crystal Growth & Design 19(8) (2019): 4588-4601.

[21] Das S., Das S., Sutradhar S. Enhanced dielectric behavior and ac electrical response in Gd- Mn-ZnO nanoparticles. J. Alloys Compd. 726 (2017) 11-21.

Chapter 5

Metal ions (Cu^{2+}, Gd^{3+}) doped boehmite nanostructures for Cr(VI) detection in wastewater and their removal from aqueous media

Chapter 5

Metal ions (Cu^{2+}, Gd^{3+}) doped boehmite nanostructures for Cr(VI) detection in wastewater and their removal from aqueous media

5.1 Introduction

It was observed in the previous works that the particle size and morphology have a significant influence in creating the defect states in boehmite nanostructures [1]. These defects are capable to trap free-charge carriers, which in turn changes the optical and electrical properties of this system [2]. Thus, controlled creation of these defect states is necessary to obtain promising applicability in various aspects [3]. Crystal defects could be originated by adding impurities in crystals [4].

Herein, a facile strategy of initiating crystal defect has been discussed by doping transition metal copper (Cu(II)) and rare-earth metal gadolinium (Gd(III)) into the orthorhombic sites of boehmite nanocrystals. Such metal ion doping causes crystal defects, leading to the doped samples' defect-mediated fluorescence [5]. The fluorescence of the doped samples was used to detect hexavalent chromium ions in wastewater by a simple and cost-effective 'turn off'-based fluorometric technique. The detection limit of these fluorometric sensors is found to be very low (a few µM) besides their remarkable selectivity. These fluoro-sensors gain multifunctionality when they are used to remove Cr(VI) from aqueous media. The samples show tremendous efficacy in removing the contaminant (80-85% removal in a few minutes).

Moreover, copper (CBH) doped boehmite samples show excellent charge storage ability when it adsorbs Cr(VI) from wastewater. The storage efficiencies have been measured using dielectric constant and corresponding loss tangent. Approximately, 10 times increment of the dielectric constant has been observed in this chromium treated CBH sample. Due to the remarkable multifunctionality of these synthesized materials, they are regarded as 'Multifunctional fluorescent Nano-Sensors' (MFNS).

5.2 Experimental details

5.2.1 Materials

Aluminum nitrate nonahydrate, ammonia solution (25%), copper acetate, acetone, and ethanol were purchased from Merck, India. The gadolinium oxide was purchased from SRL, India. All the reagents used were of analytical grade and were used without any further purification. Millipore water with a resistivity of at least 18.2 MΩ-cm was used throughout the experiments.

5.2.2 Synthesis of the nanostructures

The samples were synthesized by a facile hydrothermal process. In a typical synthesis process, aluminum nitrate was added into 70 ml Millipore water under stirring. Gadolinium oxide and copper acetate were additionally mixed in the solution separately maintaining the 1% (w/w) ratio to the aluminum nitrate. After proper dissolution, ammonia solution was added drop-wise to the suspensions until the pH reached 10.

The entire set of the solution was then stirred vigorously for another 3 h and then placed separately in Teflon-lined stainless-steel autoclaves. These autoclaves were heated at 180 ⁰C for 18 h in a dust-free hot air oven. After the completion of the reaction, the solid precipitates were collected from the bottom of the Teflon container washed several times with water, and finally dried in a vacuum. The dried samples were then ground and marked as GBH (gadolinium doped boehmite), and CBH (copper doped boehmite).

5.3 Results and discussion

5.3.1 Structural and microstructural analyses

Initially, the microstructural features of the synthesized nanostructures have been estimated by using the X-ray crystallography method [6]. The XRD patterns have been illustrated in Figure 5.1 showing the characteristic diffraction maxima for all the samples. The absence of any undesired peak substantiates the purity of the nanocrystals. The Rietveld refinement of the diffractograms was further performed to ascertain the changes in the microstructural features due to the doping of foreign metals like Cu and Gd [7]. It is found that doping does not alter the orthorhombic phase of the boehmite. However, the microstrain value significantly increased in the doped boehmite samples (CBH, GBH). In

reality, larger-sized Cu^{2+} (0.71 Å) and Gd^{3+} (0.94 Å) ions substitute smaller Al^{3+} ions (0.53 Å), which might create this enhanced microstrain in the doped boehmite crystals [8].
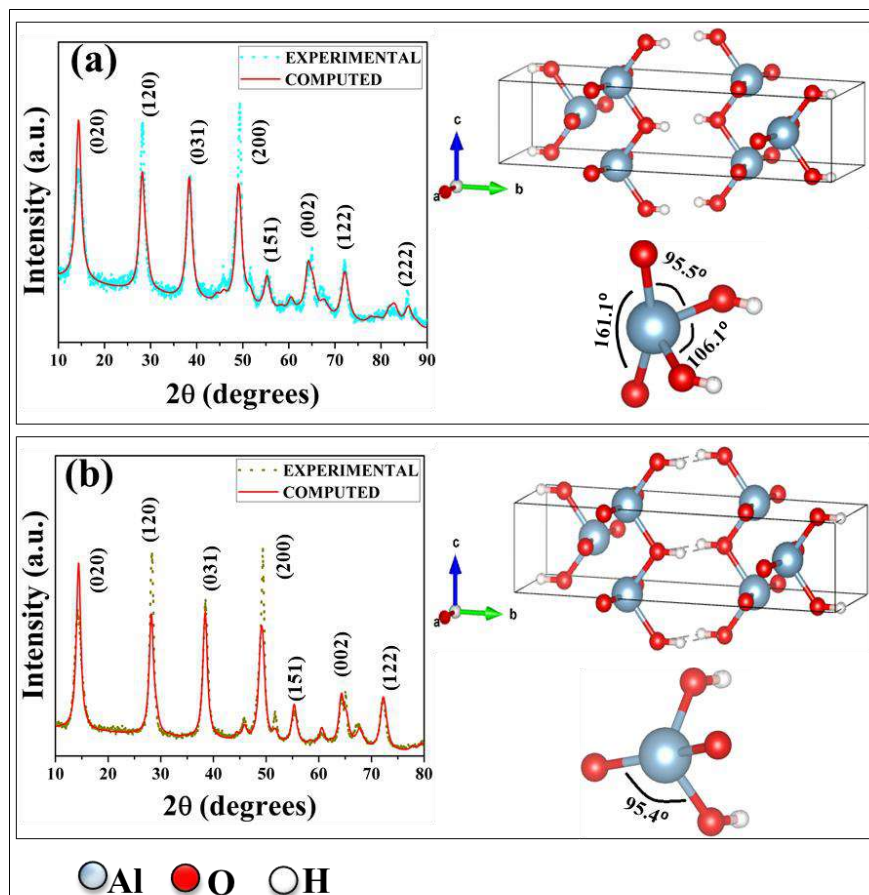
Figure 5.1 *Diffraction data and corresponding microstructure of (a) GBH and (b) CBH*

Table 5.1 *Microstructural parameters of the doped boehmite nanocrystals*

Parameters	GBH	CBH
a (Å)	3.694±0.0013	3.688±8.923 x10^{-4}
b (Å)	12.242±0.0064	12.226±0.0049
c (Å)	2.8607±0.0010	2.859±7.333 x10^{-4}
Crystallite size (nm)	7.787±0.7237	11.013±1.0858
Strain	1.731 x10^{-5}	4.678 x10^{-6}
χ^2	1.768	1.698
R_p (%)	0.094	0.127
R_{wp} (%)	0.126	0.166

Besides, the characteristic diffraction peaks have been slightly shifted to the higher diffraction angle due to this additional strain [9]. Such increased microstrain leads to crystal defects, which have been captured in this work (Table 5.1) [10]. These defects would be beneficial for various applications in the real world [11].
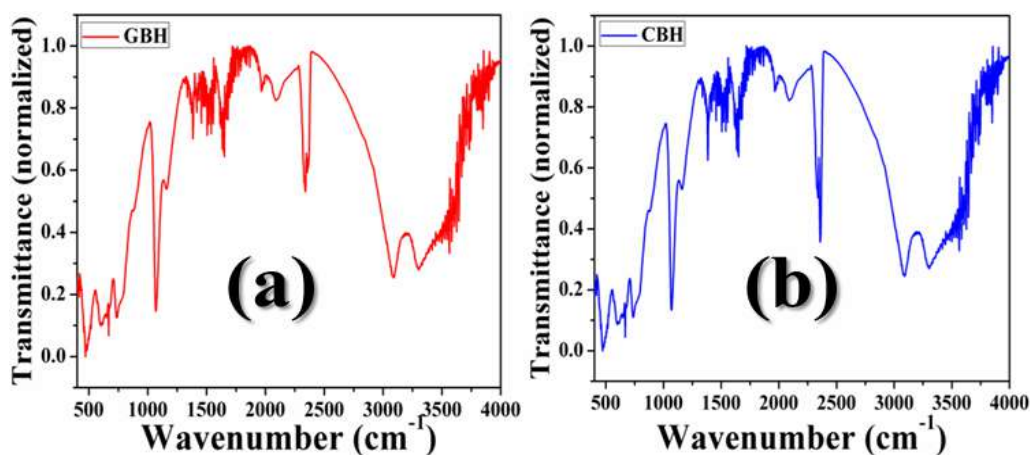
Figure 5.2 *FTIR spectra of the samples*

The FTIR study has been carried out to estimate the bonding networks of the synthesized samples (Figure 5.2) [12]. This characterization also ensures the incorporation of Gd^{3+} and Cu^{2+} into the orthorhombic sites of boehmite. The FTIR spectra depict the characteristic vibrations of the nanostructures at 480, 758, and 634 cm^{-1} due to the AlO_6 deformation [13]. The Al-O-H vibrations have also been observed at 1069 and 1158 cm^{-1} confirming the orthorhombic boehmite phases [14]. The symmetric and asymmetric O-H vibrations have also been located at 3095 and 3305 cm^{-1} respectively in the spectra [15]. Another characteristic vibration of boehmite has been found in 1634 cm^{-1} depicting the presence of surface adsorbed moisture and confirming the existence of surface porosity in the synthesized samples [16]. However, neither Gd^{3+} nor Cu^{2+} creates any bond with the boehmite phase, which corroborates with the XRD data.

The particle morphologies of the doped boehmite nanocrystals have been envisaged by transmission electron microscopy (TEM) (Figure 5.3) [17]. The copper doped CBH shows porous rhomboidal particles with a 2-5 nm mean pore diameter. The sides of this rhomboid are approximately 12-16 nm. Nonetheless, the synthesized GBH sample's morphology and particle size drastically changed. It is showing rod-shaped particles having an average length of 40-60 nm. Such morphological changes could be ascribed to the doping-induced enhancement of the microstrain [18]. As the microstrain is found to be

the highest in the GBH sample, the morphological features evolved maximum in this case [19].
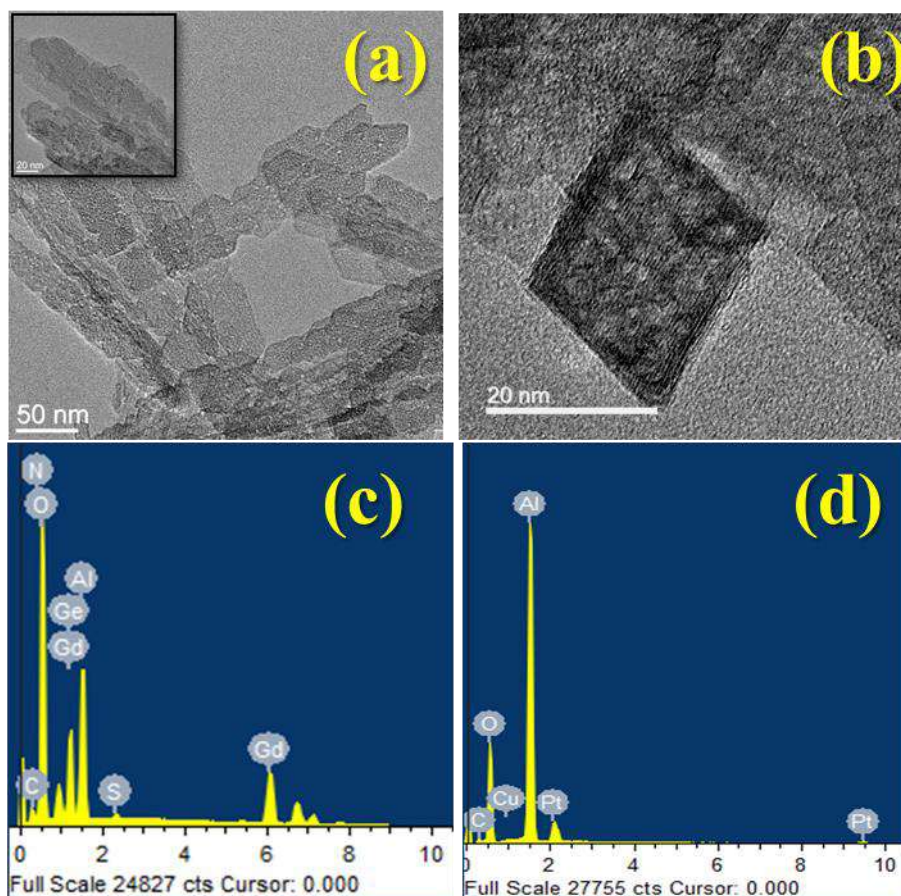
Figure 5.3 TEM images and corresponding EDX spectra of GBH (a,c) and CBH (b,d) respectively

Additionally, traces of copper and gadolinium along with oxygen and aluminum have been found in the EDX spectra of CBH and GBH samples respectively (Figure 5.3), which validates the successful incorporation of the foreign cations into the phases of orthorhombic boehmite.

5.3.2 Analyses of the surface properties

The Brunauer-Emmett-Teller (BET) and Barrer-Joyner-Halenda (BJH) methods have been utilized to estimate the surface area and porosity of the synthesized samples (Figure 5.4) [20]. The samples show type-IV isotherm indicating the presence of mesopores on the surfaces [21-22]. The mean pore diameters have been estimated using the BET method and it is found to be 5.03 and 3.91 nm for GBH and CBH respectively. Similar porosity has been observed in the TEM micrographs, which might be caused due to the defects during the incorporation of the foreign cations. The H4- type hysteresis loops suggest the

formation of slit-shaped pores on the surfaces of these nanostructures, which could be beneficial in making industrial adsorbents [21-22].
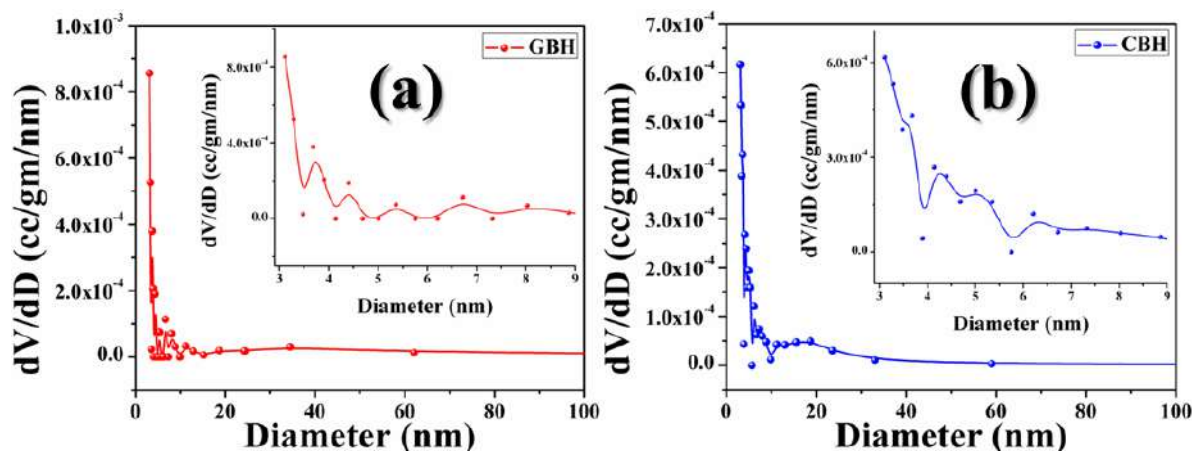
Figure 5.4 BET-BJH plots of the samples

Table 5.2 Surface properties of the metal ions doped boehmite samples

Sample name	Surface area (m²/g)	Pore size (nm)	Pore volume (cc/g)
GBH	92.174	5.03	9.532×10^{-2}
CBH	15.297	3.91	4.514×10^{-2}

Moreover, the surface areas have been calculated from the BJH method depicting the highest surface to volume ratio in the GBH sample (92.174 m²/g), while it is lower in the CBH (15.297 m²/g). A table (Table 5.2) has been constructed to feature the surface properties of the samples.

5.3.3 Thermal stability of the samples

Sensor materials must have significant thermal stability up to a certain critical limit, which makes them usable in any condition [23]. The thermal stability of the synthesized nanostructures has been assessed by differential thermal analysis (DTA) and thermo-gravimetric analysis (TGA) (Figure 5.5) [24]. The thermograms show very nominal mass losses for the CBH (7.45%) and GBH (11.16%) samples when they are exposed to 150 ℃.

Typical endothermic peaks were observed in the differential thermogram for both CBH (at 67.17 ℃) and GBH (79.92 ℃) suggesting the release of surface adsorbed moisture. Thus, these doped boehmite samples could be considered as thermally stable up to 150 ℃ making them potentially useful for sensing applications.
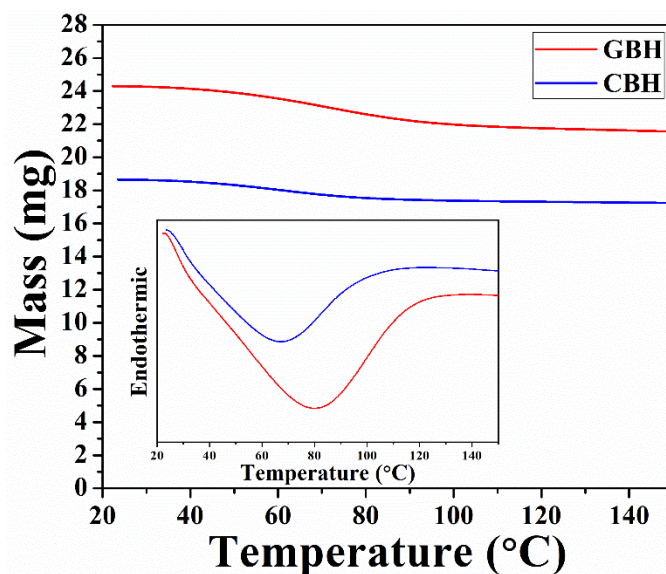
Figure 5.5 DTA (inset) and TGA thermograms of the synthesized samples

5.3.4 Optical properties of the synthesized nanostructures

Herein, the emission properties of both CBH and GBH have been evaluated. Previously, the absorption and emission properties of pure boehmite samples of different morphologies and sizes have been evaluated (Chapter 4), which shows 375 nm is the optimum excitation wavelength for boehmite samples. Thus, in this work, both CBH and GBH have been excited at 375 nm wavelength to achieve fluorescent emission.
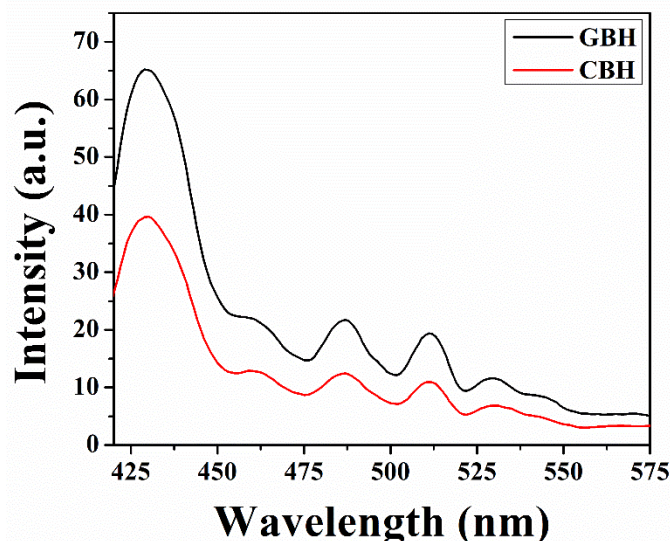
Figure 5.6 Emission spectra of the samples

The emission characteristics show a promising blue emission centered at 430 nm in both cases (Figure 5.6). Although both the samples show promising fluorescence intensities, the intensity of GBH is found to be slightly higher than that of the CBH sample. This could be

ascribed to the presence of a higher number of defect states in the GBH as compared to the CBH sample [25].

5.3.5 Detection of Cr(VI) using the doped boehmite samples
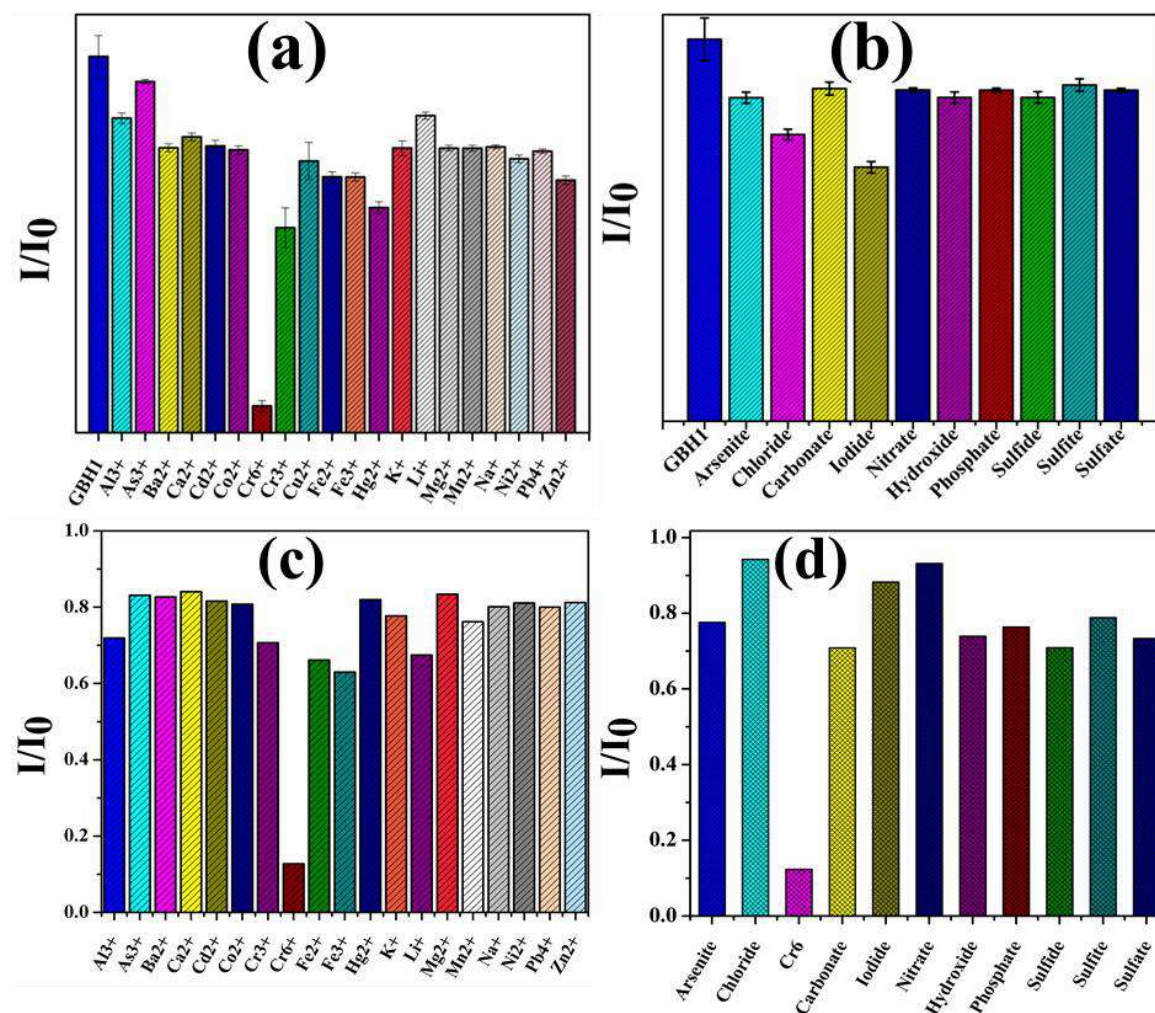
Figure 5.7 Selectivity analysis of the sensor materials

Initially, the selectivity and sensitivity of the samples (CBH and GBH) have been studied. The selectivity of the materials has been examined by exposing them separately in different ionic environments at a concentration of 500 µM. Then the UV-radiation of 375 nm have been irradiated and the fluorescence has been monitored at 430 nm (Figure 5.7). In both cases, the fluorescence intensities of the doped boehmite samples have been greatly quenched upon the Cr(VI) addition. However, no significant changes in the spectra have been observed in the rest of the cases, which make these doped materials dedicated Cr(VI) sensors.

The sensitivities of these materials have been examined by calculating the limit of detections (LOD) using the liner Stern-Volmer equation as stated below [26],

$$\frac{I_0}{I} = 1 + K_{SV}[M] \qquad (1)$$
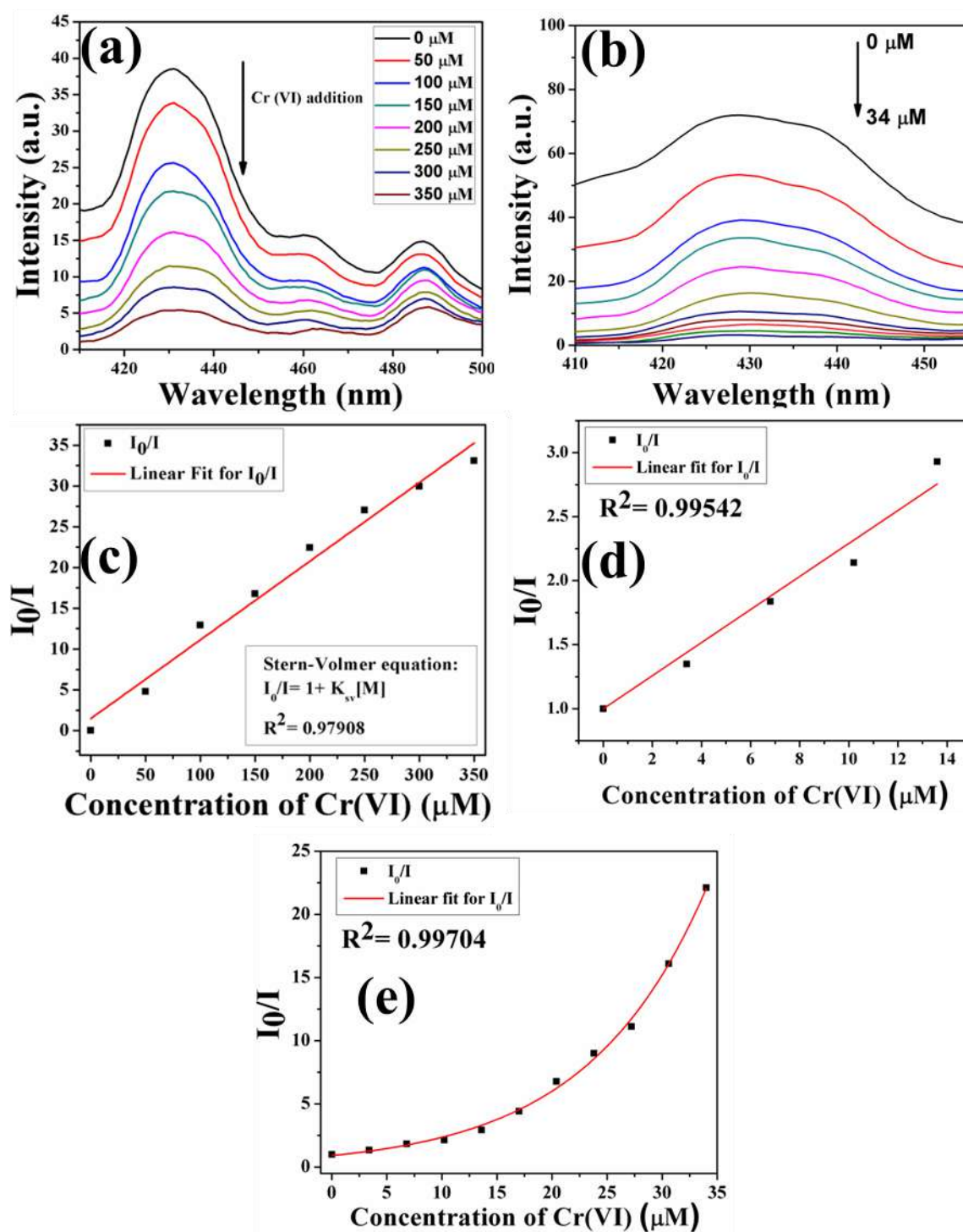
Figure 5.8 *(a-b) Fluorometric decay of GBH and CBH respectively upon Cr(VI) addition, (c-d) linear S-V plots of GBH and CBH respectively, (e) exponential fitting of the S-V plot for CBH*

Here, I_0/I represents the relative fluorescence intensities, K_{SV} and M imply the Stern-Volmer quenching constants and the concentrations of the hexavalent chromium respectively. The linearity of the fitting is very crucial in order to obtain the LOD value of the sensor material. Herein, the linearity of the fitting for the GBH sample is found to be up to 350 µM with a fitting coefficient of 0.979 (Figure 5.8). Whereas, the CBH sample provides linearity only up to 14 µM (fitting coefficient 0.997), beyond which an exponential fluorometric decay has been observed (Figure 5.8). The detection limits have been calculated based on the K_{SV} values of the sensing probes as mentioned below [27],

$$LOD = \frac{3\sigma}{K_{SV}} \quad (2)$$

Here, σ is the standard deviation of the fluorescence intensities of the sensor material without the presence of Cr(VI). The detection limit in the case of GBH is found to be 10.5 µM, whereas it is 6.24 µM for the copper doped CBH sample.

Table 5.3 ICP-AES data of the collected wastewater sample

Constituents	Amount (ppm)
Cadmium (Cd)	Not detected
Lead (Pb)	0.10
Chromium (Cr)	20.58
Iron (Fe)	4.84

Additionally, the sensing probes were employed to measure the contamination levels in real-life industrial wastewater. The elemental composition of the wastewater sample was initially examined by the ICP-AES (inductively coupled plasma atomic emission spectroscopy) technique (Table 5.3), which shows an alarming level of chromium concentration (~20 ppm) besides several other heavy metals. After collecting the water sample, it was passed through a filter membrane (porosity 11 µm) and then kept at 4 ℃ before the experiment.

When the wastewater sample is exposed to the sensor materials (CBH and GBH), the fluorescence intensity of the materials gets quenched remarkably (Figure 5.9). Such rapid decay of fluorescence intensities validates the synthesized sensing probes to be promising chromium sensors in the real world.
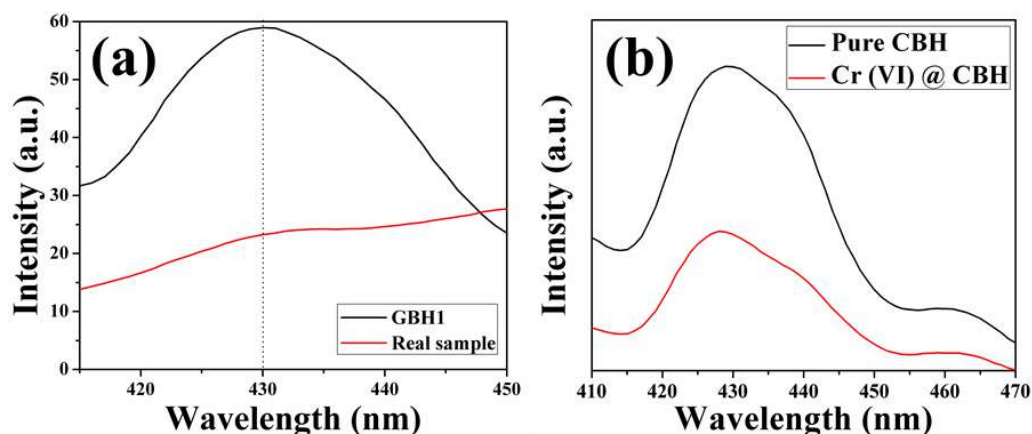
Figure 5.9 *Detection of Cr(VI) in real-life industrial wastewater sample using (a) GBH and (b) CBH*

As mentioned previously, traces of some other heavy metals have also been found during the ICP-AES measurements. Although, no interference has been observed due to those unwanted metal ions, which reveals that these materials are capable to detect hexavalent chromium in all water types.

5.3.6 Mechanism behind the fluorometric detection of Cr(VI)

In order to substantiate the sensing mechanism of the probes, fluorescence lifetimes of the sensor materials have been studied with different concentrations of Cr(VI) (Figure 5.10). It is observed that the fluorescence lifetimes get quenched in both cases, which suggests the fluorometric quenching happens in the excited state of the fluorophores [28]. Besides, the steady-state fluorescence for both the samples are found to be linear (for CBH the linearity is up to 14 µM). these two results suggest the photoinduced electron transfer is primarily responsible for such drastic fluorometric quenching for both CBH and GBH [29].

Precisely, the fluorophores of the sensor materials absorb the energy (375 nm) in the ground state and jump into the excited state where they collide with the quencher (Cr(VI)), which results in nonradiative decay [30]. Interestingly, in the case of CBH, the linearity of the S-V plot has been found only up to 14 µM, beyond which exponential decay occurs. This phenomenon could be ascribed to the inner filter effect at higher Cr(VI) concentrations besides the electron transfer [31]. In reality, at higher quencher concentrations, the fluorophores get trapped by the quencher molecules/ions, which blocks the fluorescence emission.
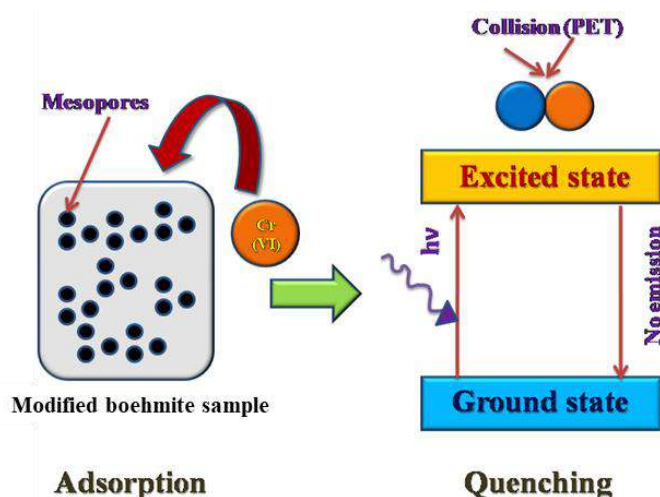
Figure 5.10 *Fluorescence quenching mechanism of the modified boehmite samples*

5.3.7 Removal of hexavalent chromium
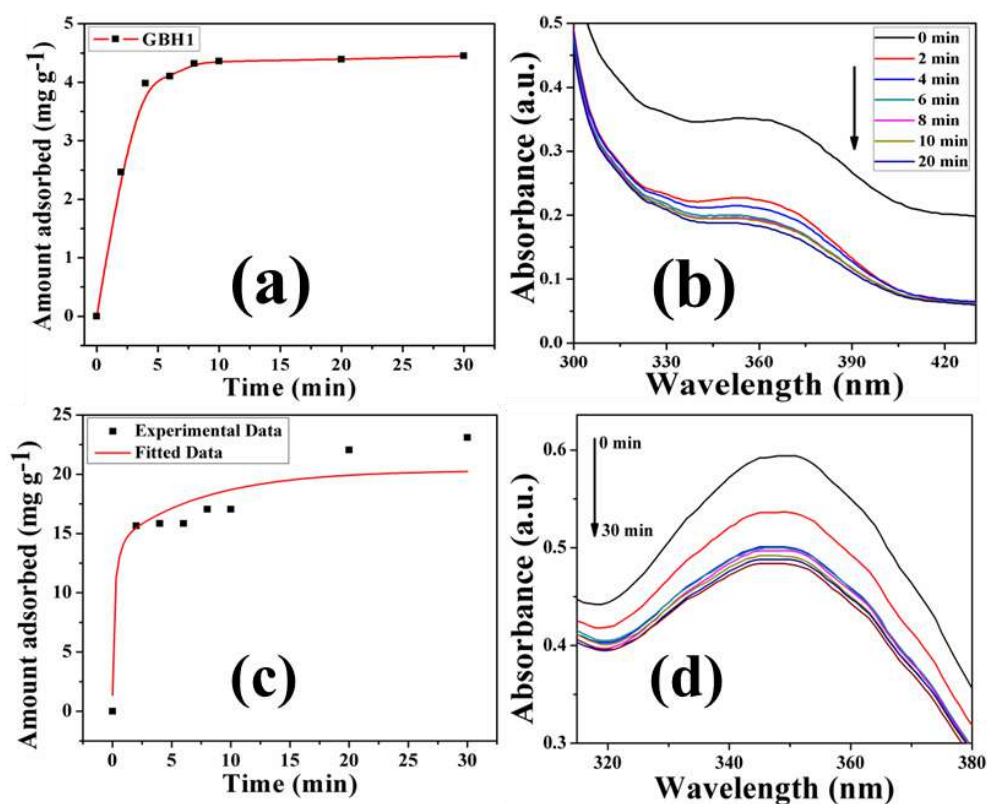
Figure 5.11 *Adsorption uptakes (a, c) and adsorption kinetics (b, d) of GBH and CBH respectively*

The synthesized nanostructures of modified boehmite samples gain multifunctionality when they are employed to remove Cr(VI) from water based on a facile adsorption process. In reality, adsorbents need porosity and high surface area in order to entrap the contaminants [32]. Previously, it was noted that boehmite has a significant binding affinity towards hexavalent chromium. Thus, in this work, the modified boehmite samples have been employed to adsorb the Cr(VI) contamination from wastewater.

Initially, the adsorption uptake of CBH and GBH was studied. Precisely, 10 mg of each adsorbent was added to the 50 ppm Cr(VI) solution separately and then stirred slowly for 2 h to reach the equilibrium. The spectrometry was then performed to evaluate the percentage uptake using the following relation [33],

$$\text{Uptake (\%)} = \frac{C_0 - C_e}{C_0} \times 100 \qquad (3)$$

where C_e and C_0 are equilibrium and initial concentrations of Cr (VI) in water. The uptake data shows around ~80% uptake capacity of the GBH sample, whereas it is found to be ~85% for the CBH sample. The EDX spectra of the chromium adsorbed samples show the traces of chromium (Figure 5.11), which also confirms the successful adsorption of Cr(VI) into the slit-shaped pores of both CBH and GBH.

Further, the adsorption kinetics were studied to optimize the time to reach the equilibrium state. It also ensures the rapidity of the sorption process [34]. The spectrometric data shows a remarkable reduction of absorbance in a very short duration (Figure 5.11). Both CBH and GBH show similar phenomena and reach the equilibrium state within 5 minutes. Although 20 minutes is selected here to ensure the complete sorption in both cases.
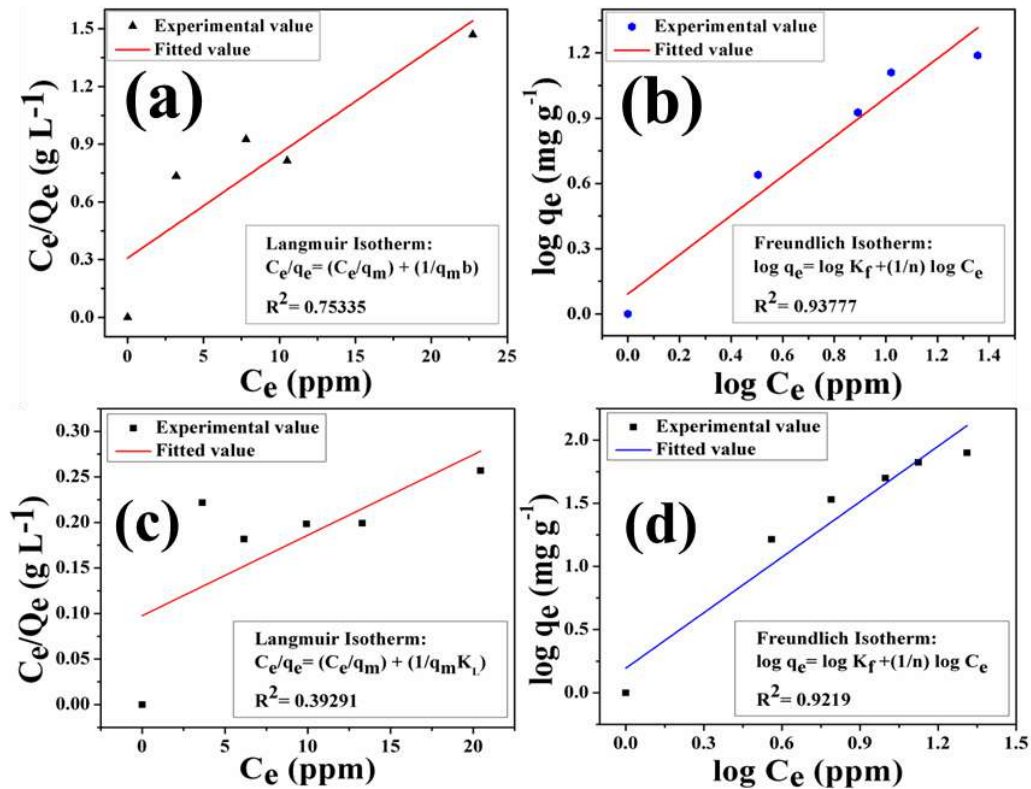
Figure 5.12 *(a, c) Langmuir and (b, d) Freundlich isotherms of the GBH and CBH samples respectively*

After the successful optimization of the adsorption uptakes and equilibrium times, the adsorption isotherms have been studied to ensure the sorption mechanism and capacities [35]. The isotherm data were studied at 25°C temperature and fitted with standard Langmuir and Freundlich isotherms (Figure 5.12) [35-38]. The linear forms of these equations are given as follows,

$$\frac{C_e}{q_e} = \frac{C_e}{q_m} + \frac{1}{q_m K_L} \qquad (4)$$

$$\log q_e = \log K_F + \frac{1}{n}\log C_e \qquad (5)$$

Here, C_e is the equilibrium concentration in the solution, q_e is the amount of Cr(VI) adsorbed at equilibrium, q_m sensors is the maximum adsorption capacity, and K_L and K_F are Langmuir and Freundlich constants respectively.

Table 5.4 Cr(VI) adsorption capacities of the modified boehmite samples

Sample name	Adsorption capacity (mg/g)
CBH	10.902
GBH	5.151

The linear fitting coefficients in both cases suggest that the adsorption specifically follows the Freundlich model (fitting coefficient for GBH= 0.9378 and CBH= 0.9219). According to this model, sorption takes place on a heterogeneous surface. In reality, multilayered adsorption occurs in such cases [39]. As these boehmite samples (CBH and GBH) have significant porosity (as seen in the BET study), multilayered adsorption is found to occur in these cases, which in turn is responsible for such a quick removal of Cr(VI). The adsorption capacities of the synthesized samples have been calculated and given in Table 5.4.

5.3.8 Copper doped boehmite (CBH) as a 'Waste capacitor'

It has been observed that copper doped boehmite (CBH) has a grater Cr(VI) uptake quality compared to the gadolinium doped GBH sample. Almost 5% higher uptake has been found in this work. Thus, the capacitive features of this copper doped sample have been studied before and after adsorbing the hexavalent chromium ions. In this case, the CBH sample is mixed with the Cr(VI) solution (500 µM) and stirred slowly for 2 h to reach the

sorption equilibrium. After reaching the equilibrium the Cr(VI) adsorbed CBH was collected and dried in a vacuum. A small pellet of this sample was made using a hydraulic press and sent for measuring the electrical properties.

Electrical properties of both the treated (Cr(VI) adsorbed CBH) and untreated (pristine CBH) pellets were measured to compare their dielectric properties. The frequency-dependent dielectric data of both the samples show a radical enhancement in the dielectric permittivity in the treated CBH sample (Figure 5.13). At a low-frequency regime (~100 kHz), this dielectric enhancement has not been found, rather when the external field approaches the high-frequency domain (~1MHz), the permittivity of the treated sample gets enhanced compared to its untreated counterpart. Such an augmented permittivity at the high-frequency domain is related to the electronic polarization of the system [40]. In reality, the adsorbed Cr(VI) ions at this frequency region get polarized and elevate the permittivity value. the overall permittivity at 1 MHz frequency is found to rise around 10 times compared to the pristine CBH sample. The loss tangent of the samples is also in good support with the high dielectric data.
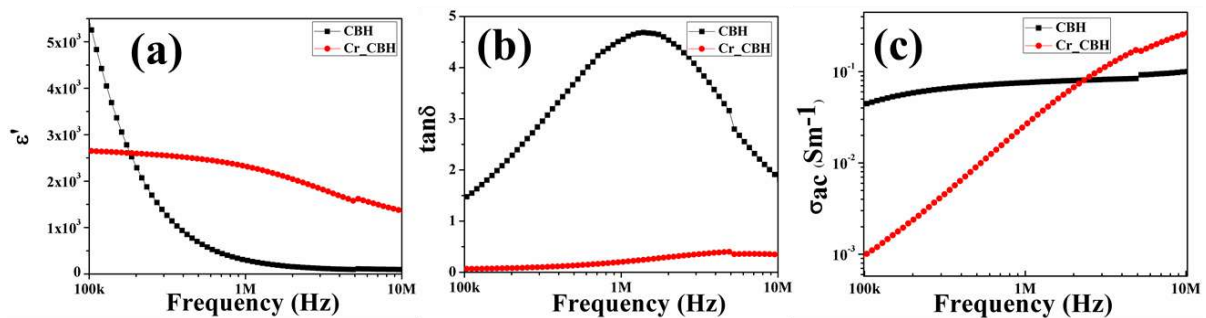
Figure 5.13 Comparative analysis of (a) dielectric constant, (b) tangent loss, and (c) ac conductivity of pure CBH and Cr(VI) adsorbed CBH

The ac conductivity of the samples has also been studied (Figure 5.13). It shows a drastic enhancement of the conductivity of the treated sample beyond 1 MHz frequency. Such relaxation could be ascribed to the excitation of free charge carriers at a high-frequency domain [41]. The Cr(VI) adsorbed sample has more free ionic charge transport units than the pure CBH which causes this type of drastic increment of ac conductivity in the higher frequency side.

5.4 Summary

This work reports a facile strategy to increase the defect states of boehmite nanostructure by incorporating cations like Cu(II) and Gd(III). Such defects also augment their fluorescence properties, which becomes useful in detecting hexavalent chromium ions in wastewater. Both the samples show excellent fluorometric 'turn off' phenomena when exposed to chromium ions. Additionally, the sensing performance of these two materials has been validated in real-life tannery wastewater samples. These photoinduced electron transfer-based sensing probes are exceptionally selective and depict promising detection limits (6-10 µM) making them dedicated chromium sensors.

Moreover, these synthesized materials are capable to remove the Cr(VI) ions from the wastewater using a facile adsorption method. The removal process is rapid and these nanomaterials can remove 80-85 % of chromium within 5 minutes. Such a rapid sorption method has been validated using the standard Freundlich model. Particularly, the copper doped CBH sample, after adsorbing Cr(VI) show remarkable augmentation in its dielectric constant at the high-frequency region. In reality, electronic polarization is responsible for such an enhancement. Henceforth, these doped boehmite samples could be considered as multifunctional nanostructures, or in other words, 'multifunctional fluorescent nano-sensors'.

References

[1] Bai, X., Caputo, G., Hao, Z., Freitas, V.T., Zhang, J., Longo, R.L., Malta, O.L., Ferreira, R.A. and Pinna, N., 2014. Efficient and tuneable photoluminescent boehmite hybrid nanoplates lacking metal activator centres for single-phase white LEDs. Nature communications, 5(1), pp.1-8.

[2] Alemi, A., Hosseinpour, Z., Dolatyari, M. and Bakhtiari, A., 2012. Boehmite (γ-AlOOH) nanoparticles: Hydrothermal synthesis, characterization, pH-controlled morphologies, optical properties, and DFT calculations. physica status solidi (b), 249(6), pp.1264-1270.

[3] Alemi, A., Hosseinpour, Z., Dolatyari, M. and Bakhtiari, A., 2012. Boehmite (γ-AlOOH) nanoparticles: Hydrothermal synthesis, characterization, pH-controlled morphologies, optical properties, and DFT calculations. physica status solidi (b), 249(6), pp.1264-1270.

[4] Zhang, J., Liu, S., Lin, J., Song, H., Luo, J., Elssfah, E.M., Ammar, E., Huang, Y., Ding, X., Gao, J. and Qi, S., 2006. Self-assembly of flowerlike AlOOH (boehmite) 3D nanoarchitectures. The Journal of Physical Chemistry B, 110(29), pp.14249-14252.

[5] Yoo, J., Han, S., Park, W., Lee, T., Park, Y., Chang, H., Hahn, S.K. and Kwon, W., 2018. Defect-induced fluorescence of silica nanoparticles for bioimaging applications. ACS applied materials & interfaces, 10(51), pp.44247-44256.

[6] Bunaciu, AA, UdriŞTioiu, EG and Aboul-Enein, HY, 2015 Crit. Rev. Anal. Chem.45(4), 289-299.

[7] Serafini, A, Lutterotti, L, Gross, S and Gialanella, S, 2017 Powder Diffr.32(S1), S63-S68.

[8] Das, S, Das, S, Roychowdhury, A, Das, D and Sutradhar, S, 2017 J. Alloys Compd.708, 231-246.

[9] Ateia, EE, Ahmed, MA, Salah, LM and El-Gamal, AA, 2014 Phys B445, 60-67.

[10] Roy, S., Bardhan, S., Chanda, D.K., Maity, A., Ghosh, S., Mondal, D., Singh, S. and Das, S., 2020. Cu (II) and Gd (III) doped boehmite nanostructures: a comparative study of electrical property and thermal stability. Materials Research Express, 7(2), p.025020.

[11] Roy, S., Pal, K., Bardhan, S., Maity, S., Chanda, D.K., Ghosh, S., Karmakar, P. and Das, S., 2019. Gd (III)-doped boehmite nanoparticle: an emergent material for the fluorescent sensing of Cr (VI) in wastewater and live cells. Inorganic chemistry, 58(13), pp.8369-8378.

[12] Zhang, Y., Zhang, T., Huo, F., Wang, Y., Li, X. and He, H., 2020. Structure and interaction properties of MBIL [Bmim][FeCl4] and methanol: a combined FTIR and simulation study. Journal of Molecular Liquids, 309, p.113061.

[13] Zirehpour, A, Rahimpour, A, Seyedpour, F and Jahanshahi, M, 2015 Desalination, 371, 46-57.

[14] Brostow, W and Datashvili, T, 2008 Chem. Chem. Technol. 2, 27-32.

[15] Dandapat, A and De, G, 2010 J. Mater. Chem.20(19), 3890-3894.

[16] Zhang, J, Liu, S, Lin, J, Song, H, Luo, J, Elssfah, EM, Ammar, E, Huang, Y, Ding, X, Gao, J and Qi, S, 2006 J. Phys. Chem. B 110(29), 14249-14252.

[17] Liu, Y., Ma, D., Han, X., Bao, X., Frandsen, W., Wang, D. and Su, D., 2008. Hydrothermal synthesis of microscale boehmite and gamma nanoleaves alumina. Materials Letters, 62(8-9), pp.1297-1301.

[18] Mathieu, Y., Lebeau, B. and Valtchev, V., 2007. Control of the morphology and particle size of boehmite nanoparticles synthesized under hydrothermal conditions. Langmuir, 23(18), pp.9435-9442.

[19] Roy, S, Pal, K, Bardhan, S, Maity, S, Chanda, DK, Ghosh, S, Karmakar, P and Das, S, 2019 Inorg. Chem.58, 8369-8378.

[20] Maji, S.K., Mukherjee, N., Mondal, A. and Adhikary, B., 2012. Synthesis, characterization and photocatalytic activity of α-Fe2O3 nanoparticles. Polyhedron, 33(1), pp.145-149.

[21] Chanda, DK, Das, PS, Samanta, A, Dey, A, Mandal, AK, Gupta, KD, Maity, T and Mukhopadhyay, AK, 2014 Ceram. Int.40(7), 11411-11417.

[22] Chanda, DK, Samanta, A, Dey, A, Das, PS and Mukhopadhyay, AK, 2017 J. Mater. Sci.52(9), 4910-4922.

[23] Meixner, H., Gerblinger, J., Lampe, U. and Fleischer, M., 1995. Thin-film gas sensors based on semiconducting metal oxides. Sensors and Actuators B: Chemical, 23(2-3), pp.119-125.

[24] Lassoued, A., Dkhil, B., Gadri, A. and Ammar, S., 2017. Control of the shape and size of iron oxide (α-Fe2O3) nanoparticles synthesized through the chemical precipitation method. Results in physics, 7, pp.3007-3015.

[25] Roy, S., Bardhan, S., Chanda, D.K., Ghosh, S., Mondal, D., Roy, J. and Das, S., 2020. Development of a Cu (II) doped boehmite based multifunctional sensor for detection and removal

of Cr (VI) from wastewater and conversion of Cr (VI) into an energy harvesting source. Dalton Transactions, 49(20), pp.6607-6615.

[26] Z. J. Lin, H. Q. Zheng, H. Y. Zheng, L. P. Lin, Q. Xin and R. Cao, Inorganic chemistry, 2017, 56, 14178-14188.

[27] J. Mandal, P. Ghorai, K. Pal, P. Karmakar and A. Saha, Journal of Luminescence, 2019, 205, 14-22.

[28] Lakowicz, J.R., Gryczyski, I., Kuba, J. and Bogdanov, V., 1994. Light quenching of fluorescence: a new method to control the excited state lifetime and orientation of fluorophores. Photochemistry and photobiology, 60(6), pp.546-562.

[29] Roy, S., Bardhan, S., Chanda, D.K., Roy, J., Mondal, D. and Das, S., 2020. In situ-grown Cdot-wrapped Boehmite nanoparticles for Cr (VI) sensing in wastewater and a theoretical probe for chromium-induced carcinogen detection. ACS Applied Materials & Interfaces, 12(39), pp.43833-43843.

[30] Berezin, M.Y. and Achilefu, S., 2010. Fluorescence lifetime measurements and biological imaging. Chemical reviews, 110(5), pp.2641-2684.

[31] Kubista, M., Sjöback, R., Eriksson, S. and Albinsson, B., 1994. Experimental correction for the inner-filter effect in fluorescence spectra. Analyst, 119(3), pp.417-419.

[32] Lin, Z. J.; Zheng, H. Q.; Zheng, H. Y.; Lin, L. P.; Xin, Q.; Cao, R. Efficient Capture and Effective Sensing of $Cr_2O_7{}^{2-}$ from Water Using a Zirconium Metal−Organic Framework. Inorg. Chem. 2017, 56, 14178-14188.

[33] A. Hassan, G. M. Mustafa, S. K. Abbas, S. Atiq, M. Saleem, S. Riaz and S. Naseem, Ceramics International, 2019, 45, 14576-14585.

[34] H. K. Chung, W. H. Kim, J. Park, J. Cho, T. Y. Jeong and P. K. Park, Journal of Industrial and Engineering Chemistry, 2015, 28, 241-246.

[35] J. N. Putro, S. P. Santoso, S. Ismadji and Y. H. Ju, Microporous and Mesoporous Materials, 2017, 246, 166-177.

[36] G. Vijayakumar, R. Tamilarasan and M. Dharmendirakumar, J. Mater. Environ. Sci, 2012, 3, 157-170.

[37] N. Nasseh, L. Taghavi, B. Barikbin and M. Khodadadi, International journal of environmental science and technology, 2017, 14(2), 251-562.

[38] N. Nasseh, L. Taghavi, B. Barikbin and A. R. Harifi-Mood, Journal of Water Reuse and Desalination, 2017,7(4), 449-460.

[39] T. Karthikeyan, S. Rajgopal and L. R. Miranda, Journal of hazardous materials 2005, 124, 192-199.

[40] X. Qi, E. Sun, R. Zhang, B. Yang, S. Li and W. Cao, Ceramics International, 2017, 43, 16819-16826.

[41] S. Kabashima and T. Kawakubo, Journal of the Physical Society of Japan, 1968, 24, 493-497.

Chapter 6

Nitrogenous carbon quantum dot tailored boehmite nanoparticles for the fluorometric detection of Cr(VI) in wastewater: A sensing probe for early-stage carcinogen detection

Chapter 6

Nitrogenous carbon quantum dot tailored boehmite nanoparticles for the fluorometric detection of Cr(VI) in wastewater: A sensing probe for early-stage carcinogen detection

6.1 Introduction

Previously, crystal defects were used to generate fluorescence emission to detect contaminants in wastewater. Such defect-mediated fluorescence has been generated either by modulating the morphology of the system or doping some impurities (i.e., Gd(III) and Cu (II)) in the orthorhombic boehmite crystals. Another way to increase the fluorescence of a material is to conjugate any fluorescent material with the system [1]. The interplay of such conjugated systems is very interesting and gives rise to several outstanding problems [2].

Carbon quantum dot (cdot) is a fluorescent quantum mechanically confined nanosystem known for its remarkable physicochemical properties [3-4]. The size-dependent tunable emission along with the highest degree of biocompatibility makes this zero-dimensional semiconductor a potential contender for numerous imaging and sensing applications [5-6,7]. The synthesis of cdot is not very costly and even quite easy. But, due to its smaller size (<10 nm), this nanostructure is prone to get agglomerated, which not only affects its physicochemical properties but also quenches its fluorescence level [8-9]. Recently, a few research works have been carried out to get rid of this agglomeration by grafting the cdot over the porous surfaces of various polymers, nanoparticles and composites [10-12]. Mostly these grafting procedures are of *ex-situ* type, which is time-consuming and costly.

In this work, an *in-situ* grafting strategy of the carbon dot is reported over the porous boehmite nanoparticle's surface. Such conjugation not only restricts the agglomeration of the cdot but also improves the fluorescence quality of boehmite nanoparticles. The formation of the boehmite-cdot nanocomposite has been confirmed by the Rietveld refinement-based x-ray crystallography method. Further, the FTIR and the TEM characterizations substantiate the bonding networks and the morphology of the system respectively. The nanocomposite is found to detect hexavalent chromium in an aqueous medium by altering its fluorescence level.

Initially, the selectivity and the sensitivity of the sample have been measured showing only 58 nM of the detection limit. Such a low detection limit makes this nanocomposite a promising chromium sensor. The density functional theory has been applied over the system to substantiate the sensing mechanism. It is found that the sensing probe specifically follows the photoinduced electron transfer mechanism in order to detect chromium ions.

Moreover, the sensor material is exposed to the chromium-containing HeLa cells to ascertain its efficacy in detecting the contaminant in living cells. The results show a drastic turn-off of the fluorescence of the probe when exposed to the contaminated cells. Such turn-off-based sensing activity has been validated by molecular docking studies. In reality, Cr(VI) is a well-known carcinogen and the synthesized sensor material is capable to detect it in the living cells, which makes this nanocomposite a truly early stage chromium mediated carcinogen detector.

6.2 Experimental details

6.2.1 Materials

Aluminum nitrate nonahydrate and Ethylenediamine, the main two precursors of boehmite were purchased from Merck, India. The anhydrous citric acid was used as the starting material of cdot was also collected from Merck, India. Potassium bromide, ethanol and hydrochloric acid solution (5%) were collected from Sigma Aldrich. The chemicals were of analytical grades and were used without further purification. Millipore water (resistivity at least ~18.2 MΩ-cm) was used throughout the experiments.

6.2.2 Synthesis method

Typically, 3.56 gm of aluminum nitrate along with 0.096 gm of citric acid were dissolved in 70 ml Millipore water and stirred slowly until a transparent solution was achieved. the ethylenediamine was then added to the solution dropwise until the pH reached 12. The stirring was continued for another 3 h to complete the reaction and then the solution was transferred into a Teflon lined stainless steel autoclave and placed in a dust-free hot air oven for 20 h at 170 ℃. After completing the hydrothermal treatment, the autoclave chamber was naturally cooled down to room temperature and the precipitates were collected from the bottom of the Teflon container. The collected precipitates were washed

several times with distilled water and finally dried in a vacuum for 48 h. The dried clusters were then ground in an agate mortar and sent for characterizations.

6.3 Results and discussion

6.3.1 Microstructure and morphological features of the sample

Herein, X-ray crystallography has been employed to analyze the purity and other microstructural properties of the synthesized sample (Figure 6.1) [13]. The Rietveld refinement of the sample was carried out by superposing the obtained diffractogram of the sample over the COD file no. 9015088 (crystallographic open database) [14].

Parameters	CDBH
a (Å)	3.6862557
b (Å)	12.160722
c (Å)	2.8536618
V (Å^3)	127.9243
Size (Å)	68.23992
Microstrain	1.4809×10^{-4}
R_p (%)	7.745
R_{wp} (%)	9.751
χ^2	1.59
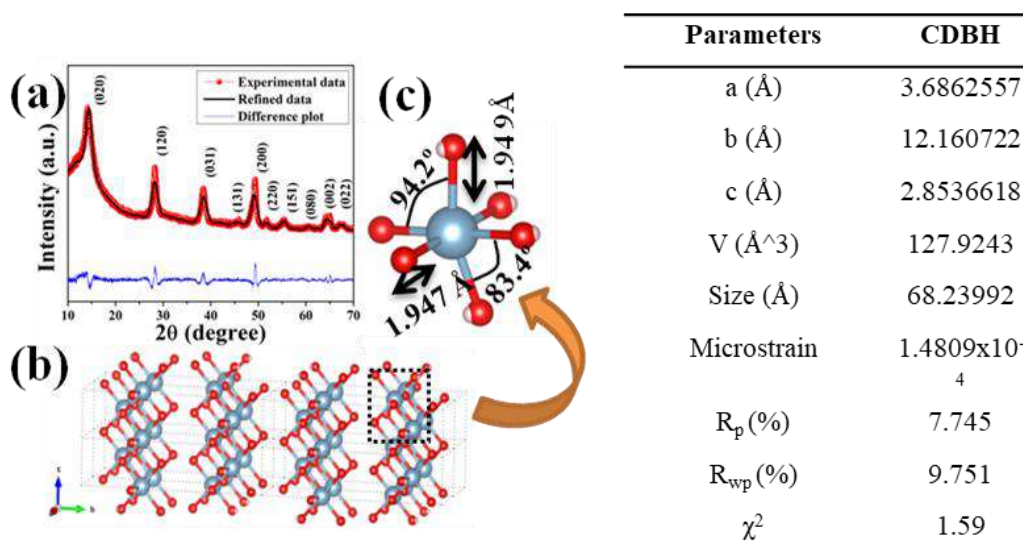
Figure 6.1 *Rietveld refinement of the diffraction pattern (a), the microstructure of the sample (b) bond angles and bond lengths of the synthesized sample (c) and corresponding microstructural parameters in the table*

Initially, the refinement of the instrumental parameters was done, thereafter the phase parameters, size, and microstrain values were refined. The fitting coefficient is found to be $\chi^2 = 1.59$ validating the reasonable fitting of the diffraction pattern (Figure 6.1). The microstructural data depicts the presence of AlO_6 polyhedra with -OH groups facing outwards. The polyhedra are stacked together to form the orthorhombic phase of the boehmite nanocrystals. In some parts, the orthorhombic phases are distorted due to the incorporation of the cdot. The average Al-OH and Al-O distances are around 1.949 and 1.947 Å respectively causing an angular displacement of 94.2º (O-Al-OH) and 83.4º (OH-Al-OH) respectively. Hence, a significant microstrain has been developed (1.481×10^{-4})

inside the system that validated the formation of the boehmite-cdot nanocomposite (CDBH).

Further, the bonding characteristics of the composite have been estimated by using the FTIR spectroscopy method (Figure 6.2). The characteristic AlO_6 vibrations are visualized between 590-780 cm^{-1} along with the OH deformation linked to aluminum ions at 896 cm^{-1} [13-15].
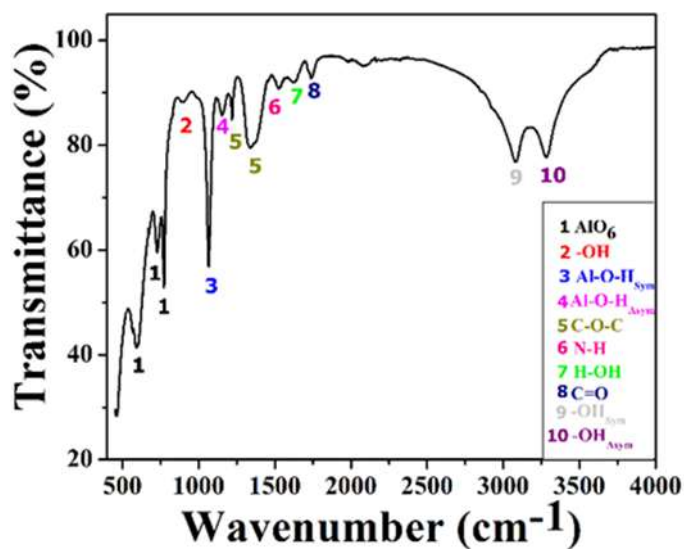
Figure 6.2 The FTIR spectrum of the synthesized nanostructure

Another two important characteristic modes of boehmite are present at 1071 and 1154 cm^{-1} substantiating the symmetric and asymmetric vibrations of the Al-O-H respectively [13]. The formation of the nitrogenous carbon dots has been confirmed by using the modes located at 1223, 1336, and 1746 cm^{-1} those are formed due to the C-O-C stretching and C=O vibration respectively [16-17]. The N-H vibration situated at 1526 cm^{-1} validates the presence of nitrogen in the cdot moiety [18]. The -OH vibrations are present in the spectrum (3081 and 3285 cm^{-1}) are also corroborating the successful formation of the boehmite-cdot nanocomposite [15].

The morphological features of the nanocomposite have been assessed by using the transmission electron microscopy method (TEM) (Figure 6.3). The overall morphology of the nanocomposite is seen to be spherical (particle size ~80-100 nm) with a very rough surface. Such surface roughness comes from the tiny cdot particles having an average diameter of 3-5 nm. In reality, the surface of the entire nanocomposite is wrapped with such tiny cdot particles causing the surface roughness.
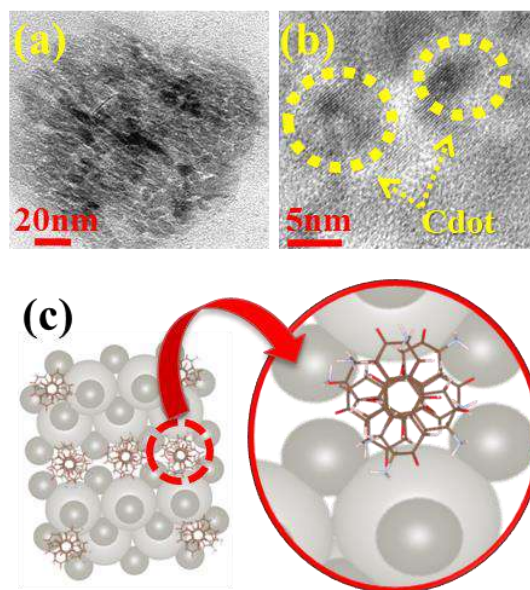
Figure 6.3 (a) TEM and (b) HR-TEM micrographs, (c) plausible structure of the sample showing cdot captures the pores of boehmite on its surface

A schematic diagram is given herein for the understanding of the entire structure of the synthesized nanocomposite (Figure 6.3).

Previously, it has been mentioned that aluminum nitrate in water produces H^+ ions due to the hydrolysis of the -OH bonds (Section 2.1). This H^+ ion chelates with the amine (herein, ethylenediamine) to produce aluminum hydroxide. Similarly, citric acid in water releases an extra proton (H^+) as follows,

$$C_6H_8O_7 + H_2O \rightarrow C_6H_5O_7^{-3} + H^+ \qquad (1)$$

Individually, the nucleation starts for both aluminum nitrate and citric acid in water by the transfer of these extra protons to the amine side. During the hydrothermal treatment, both of these two nuclei grow, and due to the lack of preferential growth (as ethylenediamine is the simplest amine) the shape of the composite becomes spherical. Meanwhile, the porous boehmite substrate accommodates the cdot particles (3-5 nm) into its pores (porosity ~3-8 nm) and finally forms the nanocomposite.

6.3.2 Optical properties of the synthesized sample

The optical quality of the synthesized sample has been assessed by absorption and emission spectra [19]. Initially, the absorption spectrum was taken (Figure 6.4) showing the characteristic absorption maximum at 352 nm with an optical bandgap of 5.52 eV. The bandgap has been calculated by Tauc's method (Equation 2) as shown,

$$\alpha E = A(E-E_g)^n \tag{2}$$

where E, E_g, α and A are the photon energy, optical band gap energy in eV, absorption coefficient, and a constant term respectively.

The emission and excitation spectra of the sample (CDBH) were estimated to observe the fluorescence quality of the sample. It is found that the emission maximum of the sample is located at 462 nm having a broad emission curve in the blue-green region of the spectrum. In reality, the excitation-dependent emission spectra were initially collected showing the most probable excitation lies in the region between 370-380 nm (Figure A2.1). Then the excitation spectrum was taken for 462 nm wavelength depicting the broad peak at 375 nm.
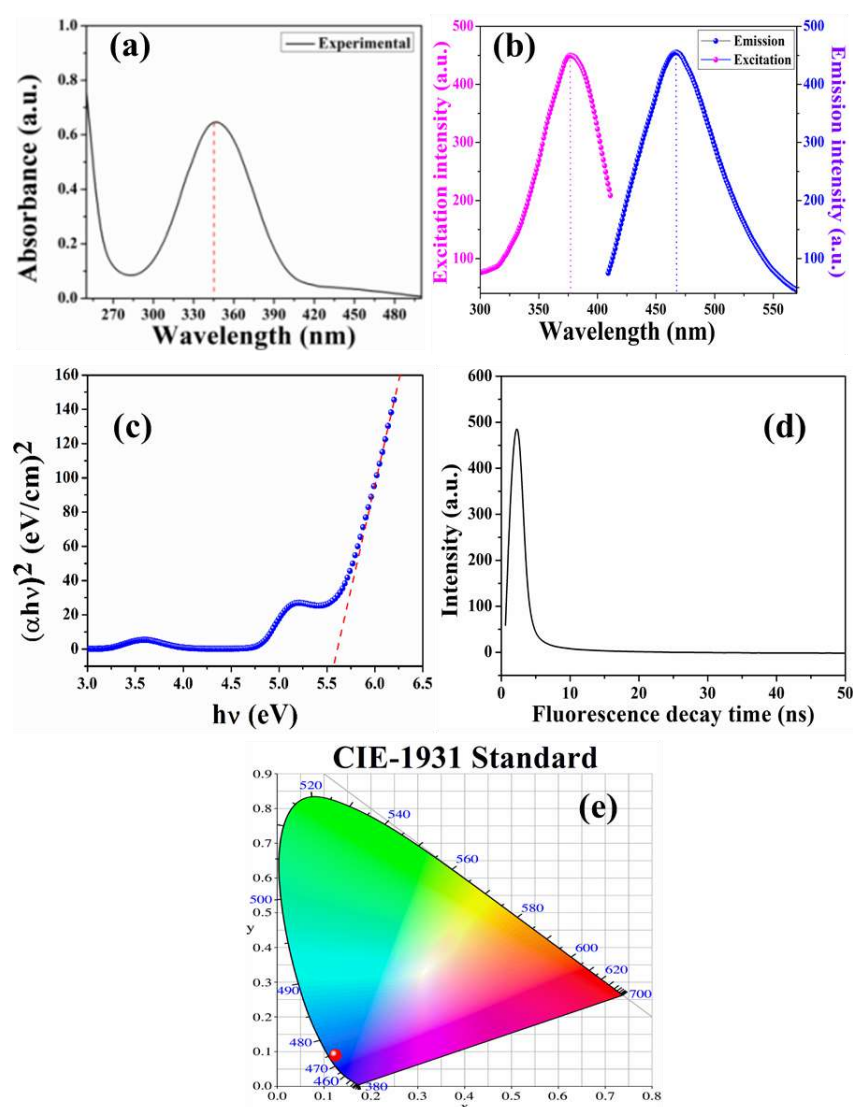
Figure 6.4 *(a) Absorbance spectrum of the probe; (b) excitation and emission spectra of the sample; (c) Tauc plot of the probe; (d) time-resolved fluorescence decay pattern and (e) CIE-1931 color space analysis of the sensor material*

The colorimetric assay was further performed by using the CIE-1931 method (Figure 6.4) to confirm the color coordinates and color temperature of the emission [19]. The emission color coordinates are found to be x= 0.12484, y= 0.09432, which lie in the blue region of the spectrum with a color temperature of 3372 K.
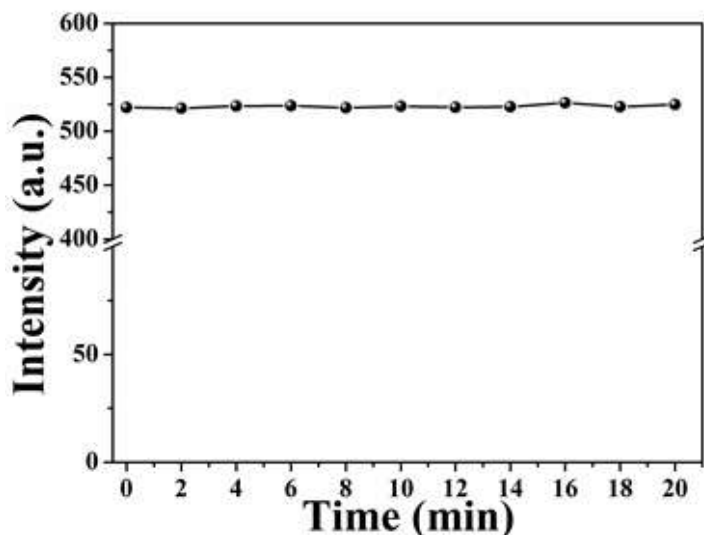
Figure 6.5 Stability of the fluorescent emission with respect to the time

Moreover, the stability of the fluorescence emission has been estimated by varying the time (Figure 6.5). Normally, cdot molecules can agglomerate rapidly resulting in fluorescence quenching after a few minutes, but in this case, no such quenching has occurred up to 20 minutes of exposure to the ambient conditions. This reveals that the boehmite nanoparticles successfully separate the cdot molecules by trapping the molecules into their pores.

The time-resolved fluorescence decay profile of the nanocomposite is showing a promising decay time of 3.58 ns at 462 nm (Figure 6.4), which is reasonably high and makes this composite a capable alternative for fluorometric applications.

Additionally, the theoretical density functional approach (DFT) studies have been conducted to substantiate the origin of the fluorescence and the electronic transitions of the fluorophores [20-22]. The nitrogenous carbon dot moiety of the sample was taken to perform the DFT studies as it accommodates the fluorophores [23]. After optimizing the geometry and vibrational modes the TDDFT studies have been performed on the system to achieve the electronic transitions that occurred during the absorption and emission processes. The frontier molecular orbitals have been illustrated in Figure 6.6 shows a

HOMO-LUMO gap of 5.59 eV, which is quite near to the experimental band gap of the sample (5.52 eV). Moreover, the theoretical absorbance spectrum depicts four distinct transitions (278, 291, 305, and 323 nm), among them 323 nm transition is considered to be the characteristic transition (λ_{max}) of the fluorophores. This particular transition has occurred between the HOMO (-6.074 eV) and LUMO (-0.482).
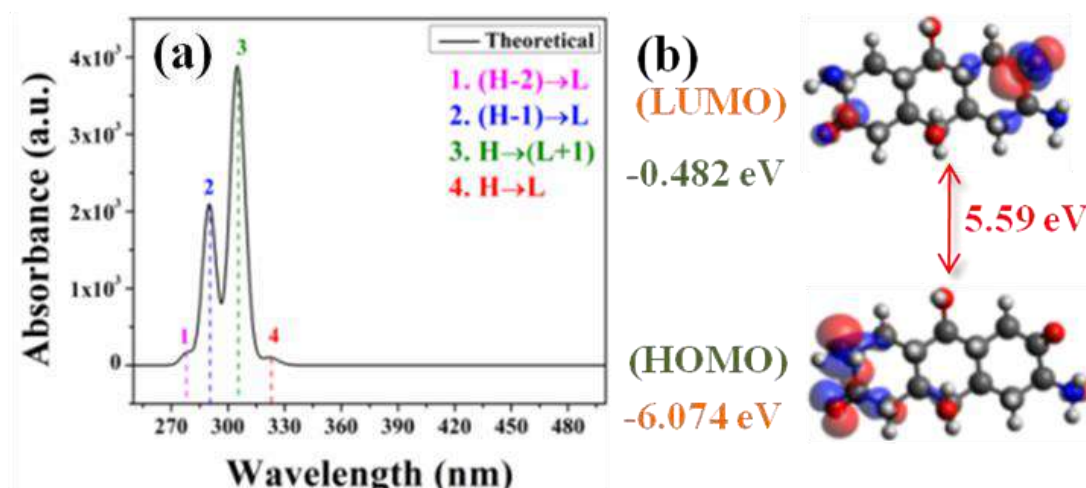
Figure 6.6 *(a) Theoretical absorbance spectrum of the sample calculated from TDDFT study and (b) TDDFT based electronic transition pattern of the fluorophores for CDBH sample*

The origin of the fluorescence in cdot is very difficult to understand. Previously, researchers showed that the C-N moiety of the cdot molecule initiates the charge dislocation and endorses charge transfer causing the enhanced fluorescence [24].

6.3.3 Selectivity and sensitivity experiments of the sensor material

Initially, the prepared sensor material was exposed to the Cr(VI) solution of 50 µM and the fluorescence data was taken. The fluorescence data shows a drastic quenching of the fluorescence intensity compared to the fluorescence of the pristine CDBH sample. In a similar way, solutions of various cations and anions (50 µM) were prepared and they are separately added to the sensor material prior to the fluorescence experiments. The results of this selectivity test are depicted in Figure 6.7 showing that the fluorescence of the sensing probe (CDBH) specifically quenches upon Cr(VI) addition. Otherwise, no fluorescence quenching is observed for other ions. This implies the fact that the prepared sensing probe is selective toward hexavalent chromium only.

Besides, the sensitivity of the probe has been estimated by the linear Stern-Volmer's equation (Figure 6.7) [25],

$$\frac{I_0}{I} = 1 + K_{SV}[M] \qquad (3)$$

Where, I_0, I, [M], and K_{SV} are the fluorescence intensities before and after the addition of Cr(VI), the concentration of the ions, and the Stern-Volmer quenching constant respectively.
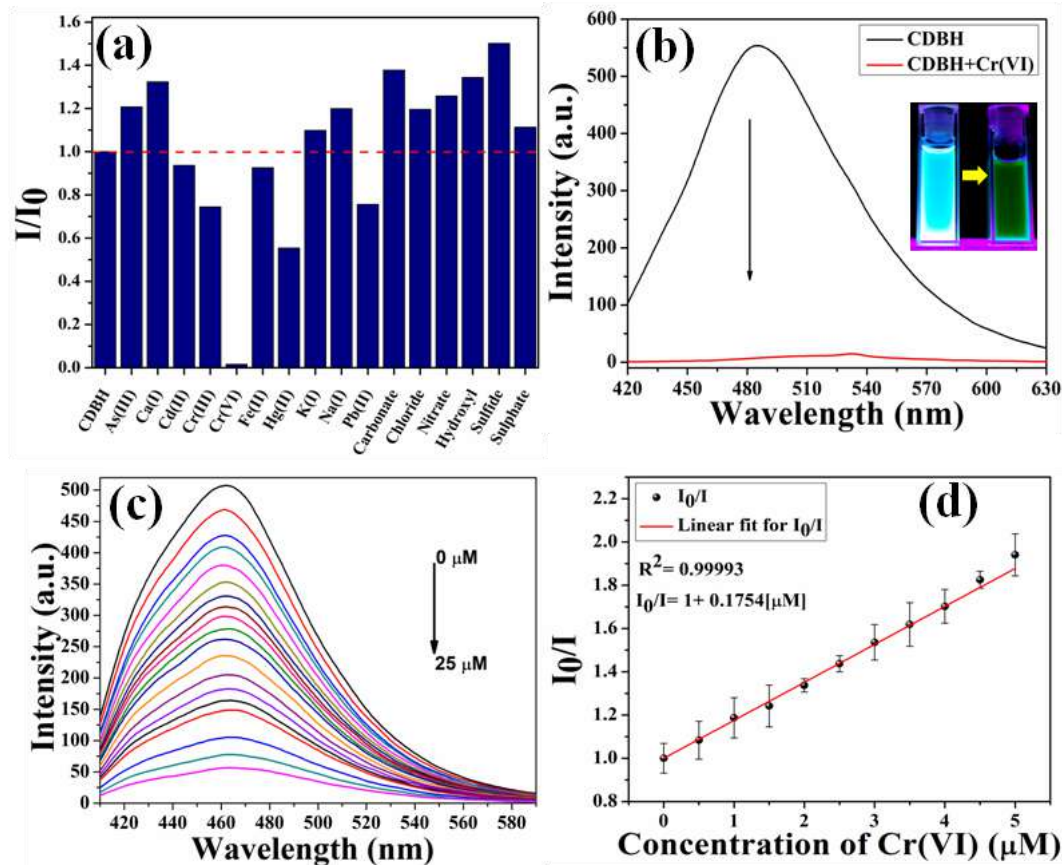
Figure 6.7 *(a) Selectivity study of the sensor among various anions and cations; (b) fluorescence quenching experiment of CDBH upon 50μM Cr(VI) addition and (inset) naked-eye detection of the fluorescence quenching; (c) concentration-dependent fluorescence quenching of the sensor; (d) linear Stern-Volmer plot of the probe*

The SV plot shows linearity up to 5 µM concentration of Cr(VI) having a fitting coefficient (R^2) of 0.99993 (Figure 6.7). Beyond this, the graph shows an upward increment (Figure A2.2) which is reasonably due to the inner filter effect (IFE) [26].

The limit of detection (LOD) of the system is found to be 58.1 nM, which is calculated by using the following formula (Equation 4), [25]

$$LOD = \frac{3\sigma}{K_{SV}} \qquad (4)$$

Where σ and K$_{SV}$ are the standard deviations by taking at least ten measurements of the fluorescence intensities of the pristine sensor material without any quencher and the quenching constant respectively.

Such fluorophore-quencher interaction in the excited state has been studied by employing time-resolved fluorescence decay measurements (Figure A2.3). It is observed that the fluorescence lifetime reduces tremendously upon chromium addition. The quenching of the fluorescence lifetime is found to be greatly dependent upon the concentration of the quencher. Thus, it can be said that the fluorescence 'turn off' quenching has occurred in the excited state of the system.

6.3.4 Detection mechanism of the sensor

There are various ways for the fluorophores to interact with the quencher. Among them, energy transfer, electron transfer, and inner filter effect are quite common [27-28]. The electrostatic potential mapping of the fluorophore (cdot) enables us to determine the negatively charged surface of the fluorophore (Figure A2.4), which might be the reason for its tremendous selectivity towards cationic chromium ions. Moreover, the mesoporous porosity of the boehmites surface is another major cause of trapping the smaller-sized chromium ions (~0.4 Å) on its surface.
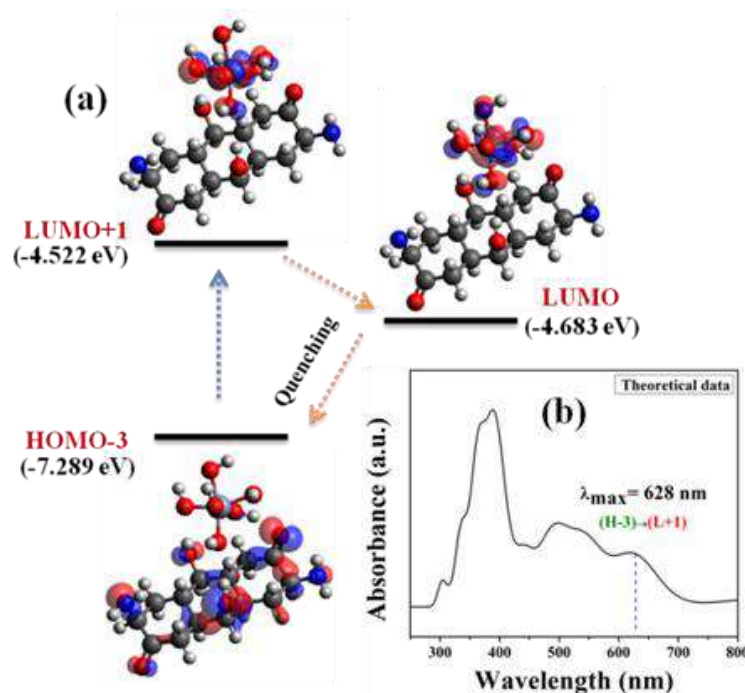
Figure 6.8 *(a) PET-based fluorescence 'turn off' mechanism analysis for CDBH using TDDFT; (b) TDDFT based theoretical absorbance spectrum of CDBH*

Previously, the fluorescence lifetime data suggest that the quenching interaction between fluorophore and quencher is taking place at the excited state. A theoretical model has been developed using the standard DFT formalism to validate this fact. Precisely, the quencher is placed in close proximity to the fluorophore (~4 Å) in the theoretical model (Figure 6.8). After optimizing the geometry and frequencies, the TDDFT formalism has been imposed on the system, which shows an electronic transition between HOMO-3 (-7.289 eV) and LUMO+1 (-4.522 eV). Interestingly, the molecular orbitals have been completely shifted from the fluorophore to the quencher moiety during this transition (Figure 6.8). Further, internal conversion is occurred from LUMO+1 to LUMO (-4.683 eV) causing a non-radiative transfer of the charges at the excited state. Finally, the charges reach the ground state. As there are a charge transfer takes place in the excited state, this phenomenon could be considered as the photoinduced electron transfer (PET), which initiates the quenching process upon chromium addition.

6.3.5 Detection of Cr(VI) at different ambient conditions
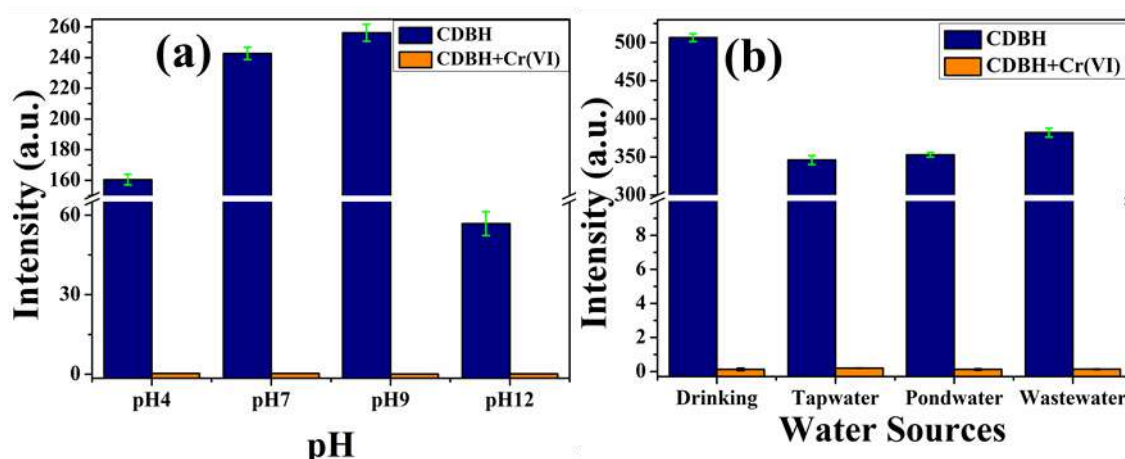
Figure 6.9 Detection efficacies testing for (a) varying pH and (b) different water conditions

The sensing efficacy of the sensor material has been examined by varying the pH and other physical parameters of the water and depicted in Figure 6.9. The pH of the medium varied from a very low pH (4) to a relatively higher pH (12). It is observed that the varying pH has almost no contribution to the sensing efficiency of the probe. Although, at neutral pH (7-9) the fluorescence intensity is found to be highest, otherwise, there is a very minute quenching of the fluorescence intensity of the pristine sensor material has been observed at extreme pH conditions. At these extreme pH values, more H^+ and OH^- ions are present in the medium causing obstruction of the fluorescence path and resulting in fluorescence

quenching. This phenomenon is known as the inner filter effect. However, the contribution of the inner filter effect is negligible in our case.

Table 6.1 *Physical parameters of the collected water samples*

Type of water	pH	TDS (ppm)
Drinking	6.53	41
Tap	7.44	>2000
Pond	8.29	1012
Waste	3.05	1996

Besides, the total dissolved solids (TDS) effect on the sensing efficacy has also been noted. In reality, water samples from different sources, such as laboratory tap water, pond water, drinking water, and wastewater from drainage have been collected and filtered (0.45 µm membrane filter) prior to the experiment. Half portion of each water sample was then spiked with hexavalent chromium (50 µM) and the TDS have been measured by using a portable pH/TDS/Temperature Meter, Hanna (HI991300) (Table 6.1). The water samples were then separately added to the sensor and the fluorescence intensity was recorded in each case (Figure 6.9). It is found that the TDS quenches the intensity of the pristine sensor sample a little bit due to the inner filter effect. However, the gross sensing efficacy remains unaltered in every water sample. Henceforth, it can be argued that the sensitivity and the selectivity of the sensing probe are quite stable and the sensor could be employed in any type of water sample.

6.3.6 Detection of Cr(VI) in real life tannery wastewater

The tannery wastewater was collected from a canal adjacent to a tannery factory near Bantala leather complex area, Kolkata, India.

Table 6.2 *ICP-AES data of the collected wastewater sample*

Constituents	Amount (ppm)
Arsenic (As)	Not detected
Lead (Pb)	0.31
Chromium (Cr)	18.24
Iron (Fe)	5.94
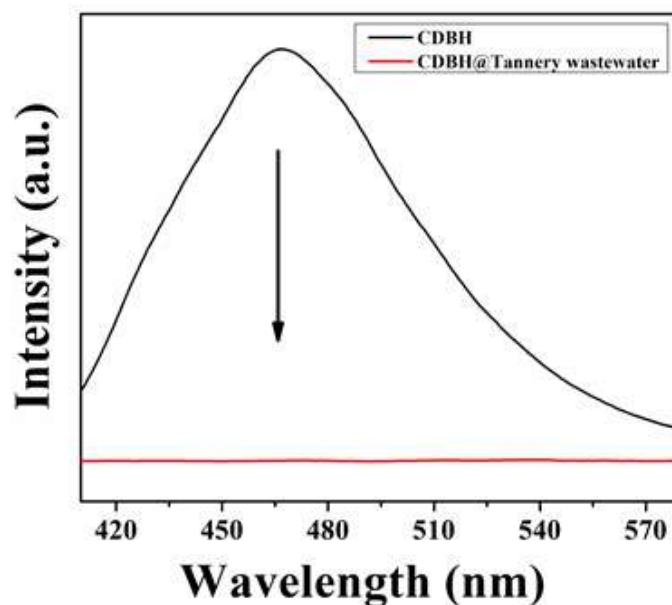
Figure 6.10 *Detection of Cr(VI) in real life tannery wastewater sample*

The collected wastewater was filtered using a membrane filter (0.45 µm) the inductively coupled plasma atomic emission spectroscopy (ICP-AES) was performed to determine the chromium contamination level (Table 6.2). The total chromium content was found to be 18 ppm, which was then added to the sensor material for our study. After adding the wastewater to the sensing probe, the fluorescence intensity rapidly drops (Figure 6.10). Besides chromium, several other metallic contaminations have been found in the ICP-AES result. However, the sensitivity of the sensing probe remains unaltered in this case approving the applicability of the sensor in real-life conditions.

6.3.7 Detection of Cr(VI) in living cells

Due to the genotoxicity and cytotoxicity of hexavalent chromium, insertion and accumulation of this contaminant into the living cell is detrimental [29]. Cr(VI) directly binds with various enzymes, such as glutathione, cytochrome-b$_5$, cytochrome-P$_{450}$ which are available in almost every prokaryotic and eukaryotic cell. Specifically, glutathione is an antioxidant capable of preventing heavy metal-mediated cellular damage [30]. Surprisingly, Cr(VI) initially transformed into Cr(III) through numerous reactive intermediates (Cr(IV) and Cr(V)) in presence of enzymes like glutathione and cytochrome-b$_5$ [31]. The trivalent chromium deposit forms reactive oxygen species through 'Fenton- like' reactions and leading to DNA damage. Such DNA damage finally causes cancer development [32]. Therefore, detection of hexavalent chromium in living cells could be beneficial for early-stage cancer detection.
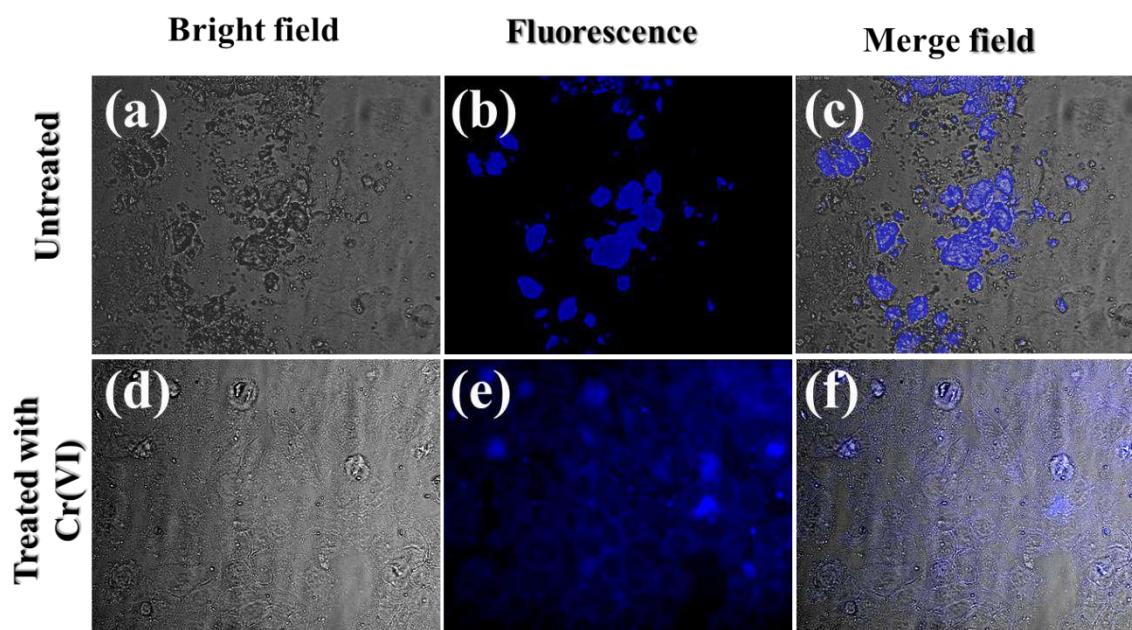
Figure 6.11 *Fluorescence microscopy showing the Cr(VI) treated cells (d-f) suffering from fluorescence quenching compared to the untreated cells (a-c)*

Herein, HeLa cells were used to check whether the sensing probe is capable to detect the presence of Cr(VI) in living cells. Half of the cells were treated with hexavalent chromium and the rest was remained untreated. Both the treated and untreated cells were then exposed to the sensor material and fluorescence microscopy was performed, which is depicted in Figure 6.11. The micrographs show that the untreated samples are glowing with vibrant blue color, whereas the blue fluorescence is missing in the Cr(VI) treated sample. This phenomenon substantiates that the fluorometric probe is capable to penetrate the cell membrane and it binds well with the cellular enzymes mentioned previously.

Henceforth, the molecular docking simulation between the fluorophore (cdot) and one of such Cr(VI) binding enzymes, glutathione (PDB ID: 1PKW) has been conducted to observe the biding affinity between these two (Figure 6.12). The docking study predicted nine possible poses of binding between glutathione and the fluorophore of CDBH, among which the first pose has been selected as it has the minimum binding affinity (-8.7 kcal/mol) (Table A2.1). Moreover, the binding pocket has been identified, which shows the formation of weak hydrogen bonds between amino acids like serine (SER-18) and isoleucine (ILE-96) with the C-O and N-H moiety of the fluorophore. Thus, the bio-sensing of Cr(VI) using the synthesized fluorometric probe has been successfully demonstrated using the molecular docking simulation.
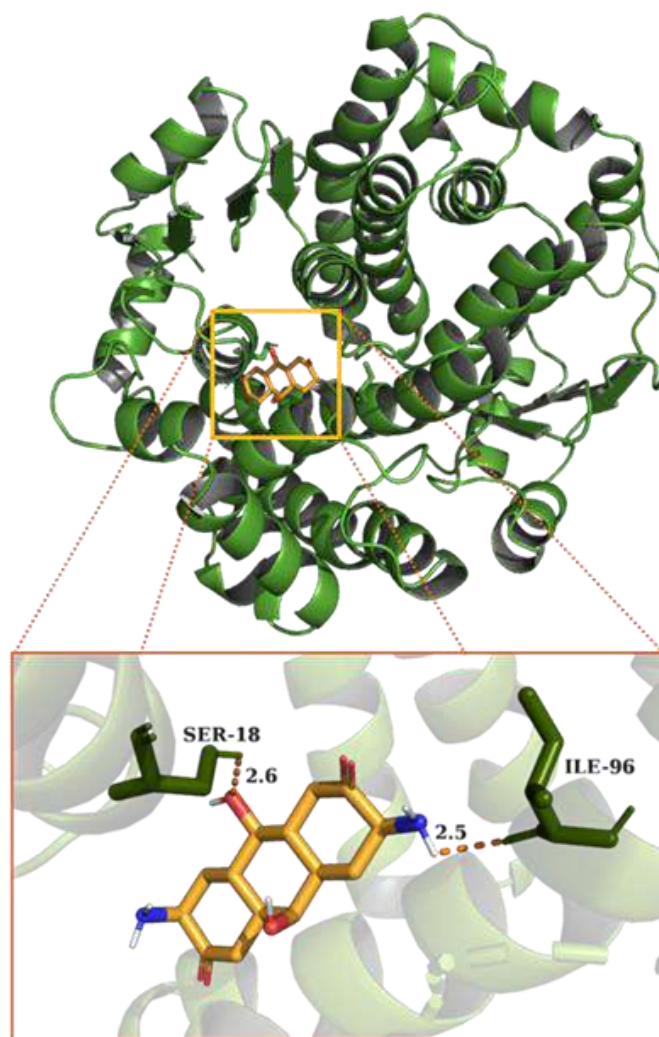
Figure 6.12 *Molecular docking simulation showing cdot binds with glutathione*

6.4 Summary

This work reports for the first time the *in-situ* growth of cdot into the orthorhombic boehmite phase that renders the successful detection of Cr(VI) in wastewater and in living cells. The synthesized sample has been well characterized using various characterization techniques that reveal the purity, morphology and overall growth mechanism of the nanocomposite. The promising fluorescence emission of the material leads to the sensing studies, which show a drastic quenching of the fluorescence when the sensor material is exposed to hexavalent chromium. The sensitivity of this 'turn off' sensing has been calculated using Stern-Volmer's equation showing ~58.1 nM detection limit. The sensing mechanism has been substantiated by using the theoretical DFT approach, which depicts the occurrence of photoinduced electron transfer at the excited state causing dynamic quenching of the fluorescence of the probe upon Cr(VI) addition. The sensing probe is found to be very stable and effective even in real-life tannery wastewater samples. The

fluorescence microscopy along with the molecular docking studies reveal the bio-sensing capability of this sensing probe, which could be beneficial for the detection of Cr(VI) mediated cancer at an early stage.

References

[1] Thomas, S.W., Joly, G.D. and Swager, T.M., 2007. Chemical sensors based on amplifying fluorescent conjugated polymers. Chemical reviews, 107(4), pp.1339-1386.

[2] Sun, X., Wang, Y. and Lei, Y., 2015. Fluorescence based explosive detection: from mechanisms to sensory materials. Chemical Society Reviews, 44(22), pp.8019-8061.

[3] Bhattacharya, S.; Phatake, R. S.; Nabha Barnea, S.; Zerby, N.; Zhu, J. J.; Shikler, R.; Lemcoff, N. G.; Jelinek, R. Fluorescent Self-Healing Carbon Dot/Polymer Gels. *ACS Nano* **2019**, *13(2),* 1433-1442.

[4] Kalytchuk, S.; Wang, Y.;Poláková, K. i.; Zbořil, R. Carbon Dot Fluorescence-Lifetime-Encoded Anti-Counterfeiting. *ACS Appl. Mater. Interfaces* **2018**, *10(35),* 29902-29908.

[5] Wang, C.; Lin, H.; Xu, Z.; Huang, Y.; Humphrey, M. G.; Zhang, C. Tunable Carbon-Dot-Based Dual-Emission Fluorescent Nanohybrids for Ratiometric Optical Thermometry in Living Cells. *ACS Appl. Mater. Interfaces* **2018**, *8(10),* 6621-6628.

[6] Tian, Y.; Ran, Z.; Yang, W. Carbon Dot-Silica Composite Nanoparticle: An Excitation-Independent Fluorescence Material with Tunable Fluorescence. *RSC adv.* **2017**, *7 (69),* 43839-43844.

[7] Li, H.; Yan, X.; Lu, G.; Su, X. Carbon Dot-Based Bioplatform for Dual Colorimetric and Fluorometric Sensing of Organophosphate Pesticides. Sens. Actuators, B2018, 260, 563-570.

[8] Rezaei, B.; Hassani, Z.; Shahshahanipour, M.; Ensafi, A. A.; Mohammadnezhad, G. Application of Modified Mesoporous Boehmite (γ-AlOOH) with Green Synthesis Carbon Quantum Dots for a Fabrication Biosensor to Determine Trace Amounts of Doxorubicin. Luminescence 2018, 33(8), 1377-1386.

[9] Zhai, Y.; Bai, X.; Cui, H.; Zhu, J.; Liu, W.; Zhang, T.; Dong, B.; Pan, G.; Xu, L.; Zhang, S. Carbon Dot/Polyvinylpyrrolidone Hybrid Nanofibers with Efficient Solid-State Photoluminescence Constructed using an Electrospinning Technique. Nanotechnology 2017, 29(2), 025706.

[10] Zhang, D.; Jiang, W.; Zhao, Y.; Dong, Y.; Feng, X.; Chen, L. Carbon Dots Rooted PVDF Membrane for Fluorescence Detection of Heavy Metal Ions. Appl. Surf. Sci. 2019, 494, 635-643.

[11] Bardhan, S.; Roy, S.; Chanda, D. K.; Ghosh, S.; Mondal, D.; Das, S.; Das, S. Nitrogenous Carbon Dot Decorated Natural Microcline: An Ameliorative Dual Fluorometric Probe for Fe3+ and Cr6+ Detection. Dalton Trans., 2020, 49, 10554-10566.

[12] Unnikrishnan, B.; Wu, C.-W.; Chen, I.-W. P.; Chang, H. T.; Lin, C.-H.; Huang, C. C. Carbon Dot-Mediated Synthesis of Manganese Oxide Decorated Graphene Nanosheets for Supercapacitor Application. ACS Sustainable Chem. Eng. 2016, 4(6), 3008-3016.

[13] Roy, S.; Maity, A.; Mandal, P.; Chanda, D. K.; Pal, K.; Bardhan, S.; Das, S. Effects of Various Morphologies on the Optical and Electrical Properties of Boehmite Nanostructures. CrystEngComm 2018, 20(40), 6338-6350.

[14] Roy, S.; Bardhan, S.; Chanda, D. K.; Maity, A.; Ghosh, S.; Mondal, D.; Singh, S.; Das, S. Cu (II) and Gd (III) Doped Boehmite Nanostructures: A Comparative Study of Electrical Property and Thermal Stability. Mater. Res. Express 2020, 7(2), 025020.

[15] Roy, S.; Bardhan, S.; Pal, K.; Ghosh, S.; Mandal, P.; Das, S.; Das, S. Crystallinity Mediated Variation in Optical and Electrical Properties of Hydrothermally Synthesized Boehmite (γ-AlOOH) Nanoparticles. J. Alloys Compd. 2018, 763, 749-758.

[16] Zhao, L.; Di, F.; Wang, D.; Guo, L.-H.; Yang, Y.; Wan, B.; Zhang, H. Chemiluminescence of Carbon Dots under Strong Alkaline Solutions: A Novel Insight into Carbon Dot Optical Properties. Nanoscale 2013, 5(7), 2655-2658.

[17] Ma, Z.; Ming, H.; Huang, H.; Liu, Y.; Kang, Z. One-Step Ultrasonic Synthesis of Fluorescent N-Doped Carbon Dots from Glucose and their Visible-Light Sensitive Photocatalytic Ability. New J. Chem. 2012, 36(4), 861-864.

[18] Su, Y.; Zhou, X.; Long, Y.; Li, W. Immobilization of Horseradish Peroxidase on Amino-Functionalized Carbon Dots for the Sensitive Detection of Hydrogen Peroxide. Microchim. Acta 2018, 185(2), 114

[19] Janke, E. M.; Williams, N. E.; She, C.; Zherebetskyy, D.; Hudson, M. H.; Wang, L.; Gosztola, D. J.; Schaller, R. D.; Lee, B.; Sun, C. Origin of Broad Emission Spectra in InP Quantum Dots: Contributions from Structural and Electronic Disorder. J. Am. Chem. Soc. 2018, 140(46), 15791-15803.

[20] Zhou, T.; Wang, M.; Zang, Z.; Fang, L. Stable Dynamics Performance and High Efficiency of ABX3-type Super-Alkali Perovskites First Obtained by Introducing H5O2 Cation. Adv. Energy Mater. 2019, 9(29), 1900664.

[21] Zhou, T.; Zhang, Y.; Wang, M.; Zang, Z.; Tang, X. Tunable Electronic Structures and High Efficiency Obtained by Introducing Superalkali and Superhalogen into AMX3-type Perovskites. J. Power Sources 2019, 429, 120-126.

[22] Yan, D.; Shi, T.; Zang, Z.; Zhou, T.; Liu, Z.; Zhang, Z.; Du, J.; Leng, Y.; Tang, X. Ultrastable CsPbBr3 Perovskite Quantum Dot and their Enhanced Amplified Spontaneous Emission by Surface Ligand Modification. Small 2019, 15(23), 1901173.

[23] Gross, E.K. and Dreizler, R.M. eds., 2013. Density functional theory (Vol. 337). Springer Science & Business Media.

[24] Schneider, J.; Reckmeier, C. J.; Xiong, Y.; von Seckendorff, M.; Susha, A. S.; Kasák, P.; Rogach, A. L. Molecular fluorescence in citric acid-based carbon dots. J Phys Chem C2017, 121(3), 2014-2022.

[25] Roy, S.; Pal, K.; Bardhan, S.; Maity, S.; Chanda, D. K.; Ghosh, S.; Karmakar, P.; Das, S., Gd (III)-Doped Boehmite Nanoparticle: An Emergent Material for the Fluorescent Sensing of Cr(VI) in Wastewater and Live Cells. Inorg. Chem2019, 58(13), 8369-8378.

[26] Kubista, M.; Sjöback, R.; Eriksson, S.; Albinsson, B. Experimental Correction for the Inner-Filter Effect in Fluorescence Spectra. Analyst 1994, 119(3), 417-419.

[27] Slocum, J. D.; Palmer, A. E.; Jimenez, R. Intramolecular Fluorescent Protein Association in a Class of Zinc FRET Sensors Leads to Increased Dynamic Range. J Phys Chem B 2019, 123(14), 3079-3085.

[28] Mohandoss, S.; Stalin, T. A New Fluorescent PET Sensor Probe for Co2+ Ion Detection: Computational, Logic Device and Living Cell Imaging Applications. RSC adv 2017, 7(27), 16581-16593.

[29] Speer, R. M.; Wise, S. S.; Croom-Perez, T. J.; Aboueissa, A.-M.; Martin-Bras, M.; Barandiaran, M.; Bermúdez, E.; Wise Sr, J. P. A Comparison of Particulate Hexavalent Chromium Cytotoxicity and

Genotoxicity in Human and Leatherback Sea Turtle Lung Cells from a One Environmental Health Perspective. Toxicol. Appl. Pharmacol. 2019, 376, 70-81.

[30] Grahn, E.; Novotny, M.; Jakobsson, E.; Gustafsson, A.; Grehn, L.; Olin, B.; Madsen, D.; Wahlberg, M.;Mannervik, B.; Kleywegt, G. J. New Crystal Structures of Human Glutathione Transferase A1-1 Shed Light on Glutathione Binding and the Conformation of the C-Terminal Helix. Acta Crystallogr. Sect. D. Biol. Crystallogr. 2006, 62 (2), 197-207.

[31] DesMarias, T. L.; Costa, M. Mechanisms of Chromium-Induced Toxicity. Current opinion in toxicology 2019, 14, 1-7.

[32] Mazzer, P. A.; Maurmann, L.; Bose, R. N. Mechanisms of DNA Damage and Insight into Mutations by Chromium (VI) in the Presence of Glutathione. J. Inorg. Biochem. 2007, 101(1), 44-55.

Chapter 7

Polymeric carbon dot/boehmite nanocomposite made portable sensing device (Kavach) for non-invasive and selective detection of Cr(VI) in wastewater and living cells

Chapter 7

Polymeric carbon dot/boehmite nanocomposite made portable sensing device (Kavach) for non-invasive and selective detection of Cr(VI) in wastewater and living cells

7.1 Introduction

In the previous chapter (Chapter 6) a strategy to grow fluorescent carbon dots over the boehmite nanoparticle's surface has been discussed. The synthesized compound shows effective fluorometric detection of hexavalent chromium in wastewater and living cells. However, after careful evaluation for a prolonged duration, it is observed that the cdot molecules have been leached out from the boehmite's surface in the aqueous medium. Although the leaching percentage is very nominal, one needs to restrict such leaching to stabilize the system for better applicability. Similar studies have been performed by various other groups and it was observed that due to weak bonding between cdot and the host surface or perhaps the uncontrolled grafting caused such leaching [1-3].

Thus, this work is directed to restrict such leaching of cdot by encapsulating the CDBH nanocomposite into a polymeric substrate, poly (vinylidene fluoride-co-hexafluoropropylene) (PVDF-HFP). PVDF-HFP is a synthetic and porous fluoropolymer known for its excellent piezoelectric property [4]. This novel polymeric nanocomposite restricts the cdot leaching and acts as the solid substrate of the sensor material and makes it flexible [5]. Such a flexible sensing probe is much needed in devising the fluorometric probe. Herein, a handheld device is made up of this flexible sensor material and named 'Kavach'. Kavach can detect the presence of hexavalent chromium in wastewater and living cells with high accuracy (LOD ~ 66 nM). This fluorometric device is reusable, non-invasive, and made for on-site studies.

7.2 Experimental details

7.2.1 Materials

Aluminum nitrate nonahydrate, poly (vinylidene fluoride-co-hexafluoropropylene) (Avg. Mw 4,55,000), ethylenediamine, dimethylformamide, and anhydrous citric acid were purchased from Sigma-Aldrich, Germany. Aqua regia, hydrochloric acid (5%), acetone,

and ethanol (Merck) were used to clean the glassware and sample holders. All the reagents were of analytical grades and were used without further purification. Millipore water having a resistivity of at least 18.2 MΩ-cm was used throughout the experiments.

7.2.2 Synthesis of the flexible PV/BH@CD membrane

The synthesis of the cdot doped boehmite nanoparticles was initially done by the method mentioned previously (Chapter 6, Section 6.2). The as-synthesized cdot/boehmite nanocomposite (7.5 mg) was then suspended in 15 ml DMF along with 150 mg PVDF-HFP polymer under continuous stirring (900 RPM) for 12 h (at 60 ℃). After the complete dissolution of the polymer, the yellow-colored solution was poured into a petri dish and placed in a dust-free oven at 70 ℃. finally, the dried thick film was peeled off and marked as PV/BH@CD.

7.2.3 Fabrication of 'Kavach'
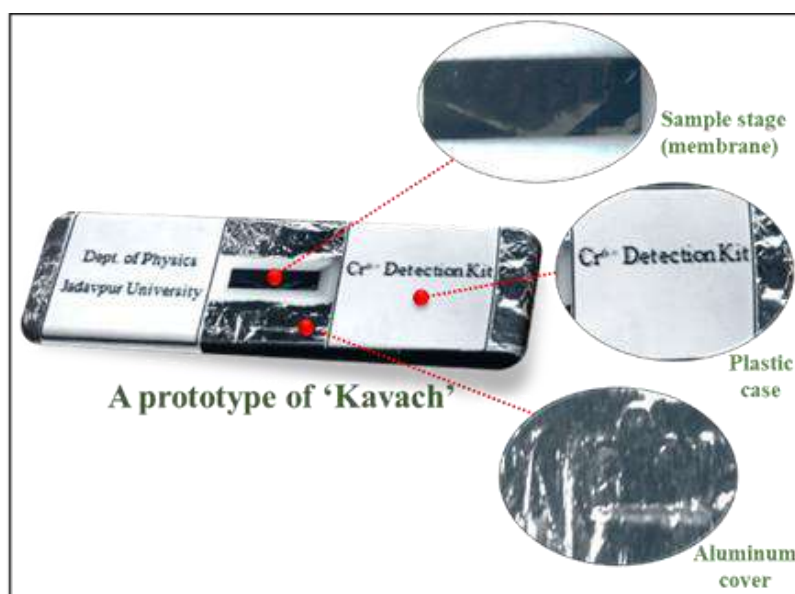
Figure 7.1 A single prototype of Kavach with its various parts

The synthesized membrane (1 mm thick) was initially cut into pieces (2x4 cm) and attached to a plastic frame having a hole at its center. The hole is termed the 'sample stage'. The rest part of the plastic frame was covered by an aluminum sheet to restrict any unwanted light (Figure 7.1). The device is made in such a way that a small drop of test sample into the sample stage could be able to detect the presence of Cr(VI) if the stage is illuminated by UV rays (~340-370 nm).

7.3 Results and discussion

7.3.1 Structure and morphology analyses of the sensing probe
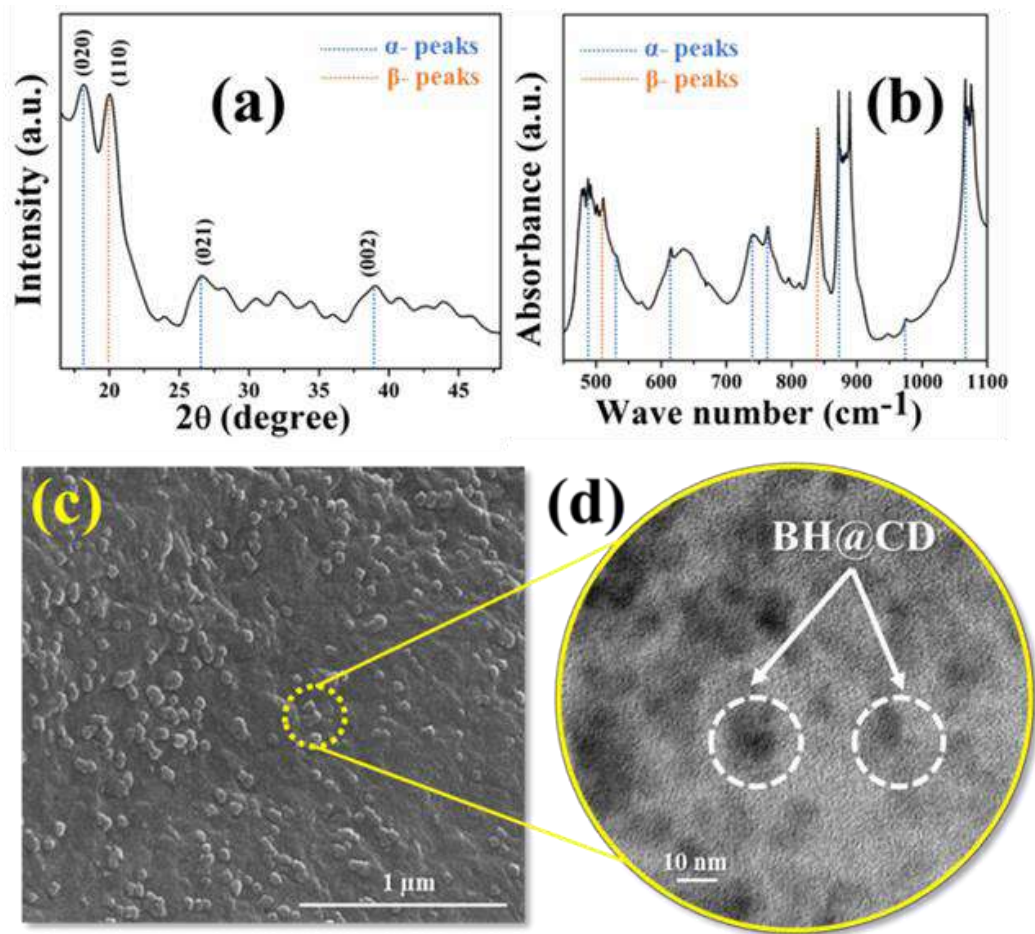
Figure 7.2 (a) XRD, (b) FTIR, and (c) FESEM of the membrane sample; (d) TEM micrograph of BH@CD

The XRD pattern of the synthesized membrane has been obtained to validate the structure and purity of the sample. The diffractogram of the sample shows a semi-crystalline pattern (Figure 7.2). The peak positions are located at 17.9 °, 26.6 °, and 38.9 ° are linked to the non-polar α-phase of PVDF-HFP [6]. Additionally, the 20.2 ° diffraction peak corroborates the formation of the polar β-phase [7], which also illustrates the successful incorporation of the BH@CD nanocomposite into the polymeric PVDF-HFP.

The vibrational modes of the membrane have been estimated by using FTIR spectrometry (Figure 7.2). The characteristic α-bands of the sample have been observed in the spectrum. Precisely, 488 cm^{-1} (-CF2 wagging), 532 cm^{-1} (-CF2 bending), 635 cm^{-1} (skeletal bending), 763 cm^{-1} (-CF2 bending), 871 cm^{-1} (-CF2 stretching), 1072 cm^{-1} (C-O-C stretching), and 976 cm^{-1} (-CH2 twisting) these α-modes are representing the purity of the

sample [8-10]. Moreover, two vibrational bands are found at 840 cm^{-1} (related to skeletal C-C stretching and -CF2 asymmetric stretching) and 511 cm^{-1} (-CF2 stretching) are representing the β-phase of the polymer [11]. In reality, the β-phase generates when the polymer rearranges itself due to the incorporation of any dopant [12]. Herein, both XRD and FTIR data suggest the formation of the polar β-phase, which is due to the incorporation of the BH@CD nanocomposite.

In order to study the re-arrangement of the polymer due to the BH@CD doping, it is important to evaluate the surface charge of the dopant. Thus, the zeta potential of the dopant has been studied using a Zetasizer, Malvern. The zeta potential of the sample depicts a positive surface charge (38.7 mV) of the sample, which validates the stability of the sample (Figure A3.1). Apart from the stability, such a positive surface of the dopant can attract the -CF$_2$ moiety of the PVDF-HFP to its side making it polar [13]. This polarity alternatively enhances the β-phase of the polymer, which has already been substantiated by XRD and FTIR data.

The surface features of the membrane have been envisaged by the FESEM technique (Figure 7.2). In the FESEM micrograph, nanoparticles of the cdot doped boehmite are visible quite uniformly over the polymeric surface of PVDF-HFP. The nanoparticles are rigidly attached to the membrane and are fairly distant from each other. Hence, less agglomeration is seen, which will increase the fluorescence quality of the sample. Moreover, the TEM study reveals the microstructure of the BH@CD nanocomposite (Figure 7.2). As seen previously (Chapter 6), the nanocomposite shows nearly spherical morphology having a rough surface. Such surface roughness is due to the presence of cdot particles having an average diameter of 4-6 nm.

The element mapping has also been performed to analyze the purity of the membrane (Figure A3.2). The mapping data shows the presence of carbon, hydrogen, and fluorine in the polymeric part of the micrograph, whereas traces of aluminum and oxygen has been found in the dopant part. Such mapping data validate the successful formation of the carbon dot doped boehmite nanocomposite in the polymeric backbone of the PVDF-HFP.

7.3.2 Optical properties of the membrane

Initially, the absorption spectrometry of the membrane has been carried out in order to achieve the excitation wavelength of the sample. The spectrum shows a broad

characteristic peak ranging between 300 and 360 nm (Figure 7.3). The peak is centered at 325 nm, which originates probably due to the π-electron stacking of the fluorophores (cdot) [15].
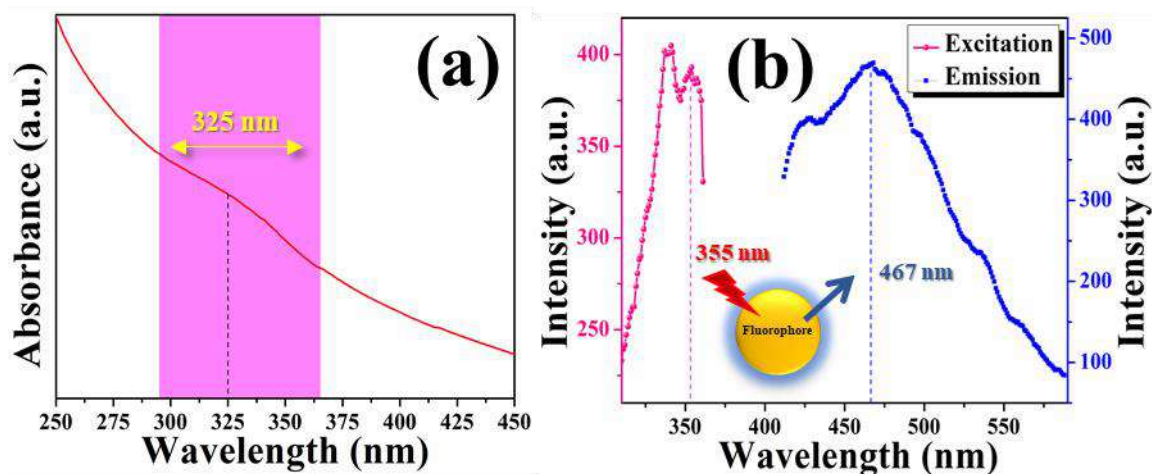
Figure 7.3 *(a) Absorbance and (b) excitation and emission spectra of the sample*

The excitation wavelength-dependent emission spectra of the membrane have also been evaluated (ranging from 340-375 nm excitation wavelength) to locate the exact excitation energy (Figure A3.3). It is observed that the excitation energy corresponding to 355 nm wavelength is originating the highest fluorescence intensity, which is also in good agreement with the absorption data. Meanwhile, a separate excitation spectrum has also been recorded (Figure 7.3), which shows that the sample could be excited in a broad excitation range (340-360 nm). Henceforth, 355 nm wavelength is selected as the optimum excitation wavelength for the membrane sample.

The membrane when exposed to the 355 nm excitation, produces a promising blue fluorescence signal centered at 467 nm (Figure 7.3). Such fluorescence emission is visible through naked eyes and is essential for various sensing applications.

7.3.3 Effect of various conditions on the fluorescence stability of the membrane

In order to establish the fluorescence stability of the membrane with time, a time-dependent fluorometric study has been performed for hundred days (Figure 7.4). In this experiment, the same part of the membrane was used for the entire study, and the sample was kept at normal room temperature and pressure without any extra care. Surprisingly, the fluorescence intensity of the membrane remains unaltered even after hundred days of

rigorous experiments. Previously, it was found that the fluorescence of carbon dots greatly quenches due to moisture adsorption [16]. However, polymeric support of the PVDF-HFP restricts such moisture adsorption.
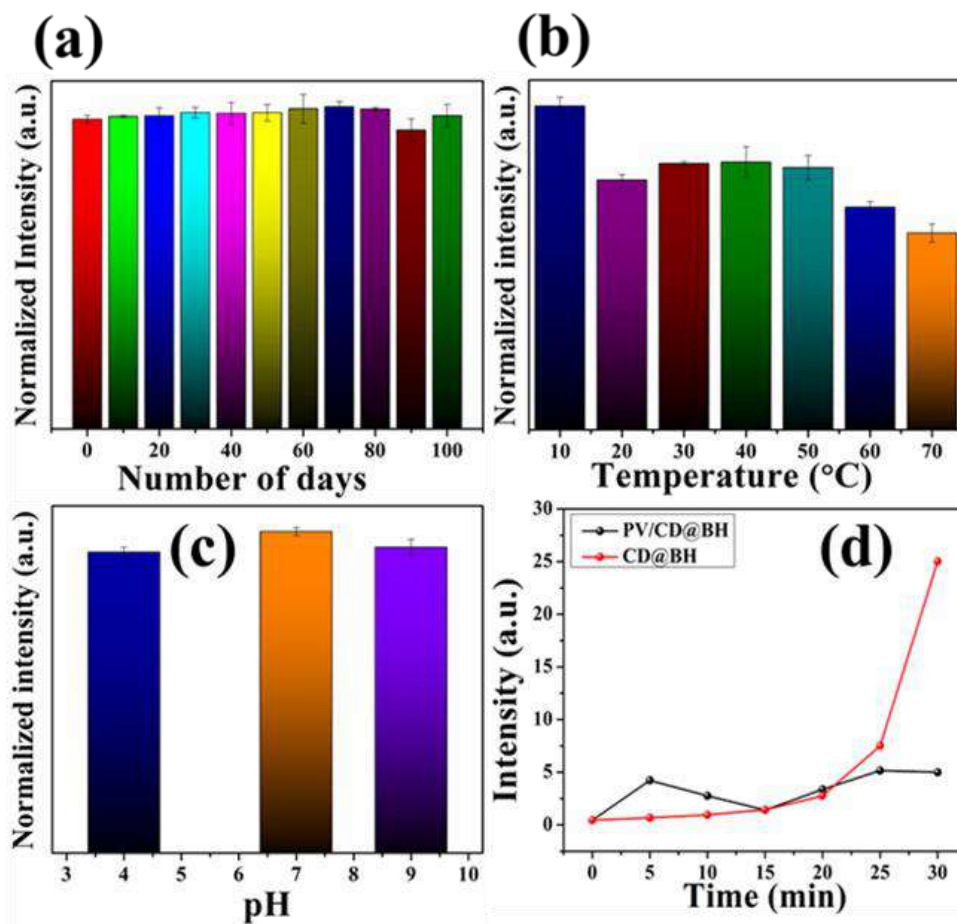
Figure 7.4 *Fluorescence stability of the sample as functions of (a) time, (b) temperature, and (c) pH; (d) c-dot leaching from the bare BH@CD and PVDF modified BH@CD as a function of time*

Additionally, the temperature-dependent fluorescence stability of the membrane has been studied. The DTA-TGA data suggests the chemical stability of the membrane up to 153 ℃ (Figure A3.4). Beyond this temperature, an endothermic transition occurs due to the melting of the membrane. The TGA data depicts a minute mass loss up to 200 ℃ temperature (~0.66 %), which validates the chemical stability of the sample up to such a higher temperature. Besides, the fluorometric stability of the fluorophores has been assessed (Figure 7.4) showing a gradual quenching of fluorescence intensity beyond 50 ℃. Such quenching may occur due to the collision between the fluorophores at higher temperatures [17].

The pH of the medium has also been varied to assure the stability of the fluorophores (Figure 7.4). In reality, the pH was varied in a wide range (4-9) by adding HCl and NaOH in a controlled way. The fluorescence intensity of the membrane gets slightly reduced in extreme pH levels as stated earlier (Chapter 6). This is because of the presence of excess H^+ and OH^- ions [18], which block the optical path of the fluorophores and create an inner filter effect. However, the quenching is very low compared to the fluorescence intensity itself (only 3-4 %).

Previously, it has been mentioned that the carbon dots are very prone to get leached out from any surface if improperly grafted. Although boehmite-carbon dot nanocomposite is a futuristic probe for detecting hexavalent chromium, the leaching of cdot restricts its reusability. Herein, a comparative leaching study has been performed to substantiate the efficacy of involving the PVDF-HFP matrix in the system (Figure 7.4). It is found that the polymeric BH@CD leaches only 3.7 % of its total fluorophores in 30 minutes, whereas the bare BH@CD leaches around 11.2 % at the same time interval. Such a leaching experiment implies that the PVDF-HFP coating successfully reduces the cdot leaching from its structure, which makes this polymeric nanocomposite a promising and reusable fluorescent material.

7.3.4 Selectivity and sensitivity assays of the sensor

The selectivity of the sensor membrane was obtained by immersing it into various cationic and anionic solvents separately (500 µM) and exposing them to 355 nm UV-excitation. The fluorescence of each solution was collected separately (at 467 nm) and plotted in Figure 7.5. Although no fluorometric alterations have been observed in the dataset but in the case of hexavalent chromium, the fluorescence intensity of the membrane quenched tremendously. Moreover, an anti-interference study was performed using some common ions (Figure 7.6). The presence of such interfering ions does not alter the selectivity of the membrane. Similar characteristics have been found in our previous works, which suggests the membrane to be a selective Cr(VI) sensor.

During the selectivity experiment, it was observed that the color of the fluorescence is changed quite a bit after the Cr(VI) addition. Thus, the CIE-1931 color coordinates were imposed to study such colorimetric variation (Figure 7.5) [19]. The pristine membrane emits a blue fluorescence (x= 0.2342, y= 0.14505) upon UV irradiation, whereas the Cr(VI) addition changes its color coordinates to x= 0.50548, y= 0.26047, which suggests

an dark orange emission. Such color change would make this sample usable in the real world.
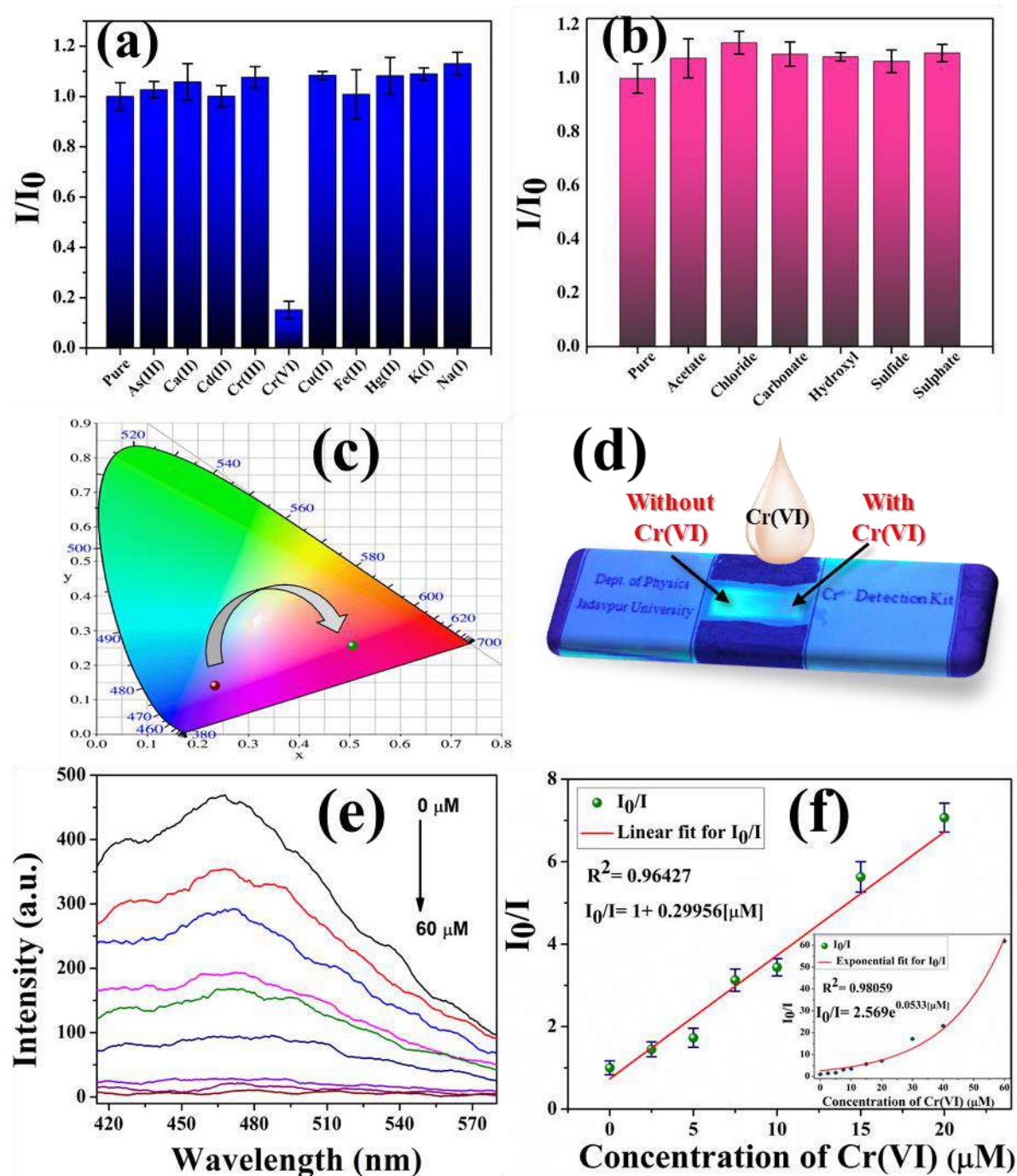
Figure 7.5 *Selectivity study of the probe among various (a) cations and (b) anions; (c) CIE-1931 plot of the probe showing color difference upon chromium addition; (d) naked eye visualization of the device under UV rays upon partial Cr(VI) addition on its sample stage; (e) UV fluorescence quenching experiment of the sensor upon Cr(VI) addition; (d) subsequent linear Stern-Volmer plot of the probe with exponential S-V plot (inset)*

In order to estimate the sensitivity of the probe, the limit of detection (LOD) and limit of quantitation (LOQ) were calculated by using Stern-Volmer's equations (Figure 7.5) [20-21].

$$\frac{I_0}{I} = 1 + K[M] \qquad (1)$$

$$\frac{I_0}{I} = Ae^{K[M]} \qquad (2)$$

Here, I_0, I, and K are the fluorescence intensities before and after the addition of Cr(VI) and the Stern-Volmer quenching constant respectively, [M] is the concentration of Cr(VI) and A is a constant term. This time two types of fitting have been done. The linear part of the fitting has been performed for the low Cr(VI) concentrations (0-20 µM), whereas beyond 20 µM concentration of Cr(VI) exponential decay of the fluorescence has been observed. This exponential decay has been fitted with the exponential S-V equation depicted in equation 2.
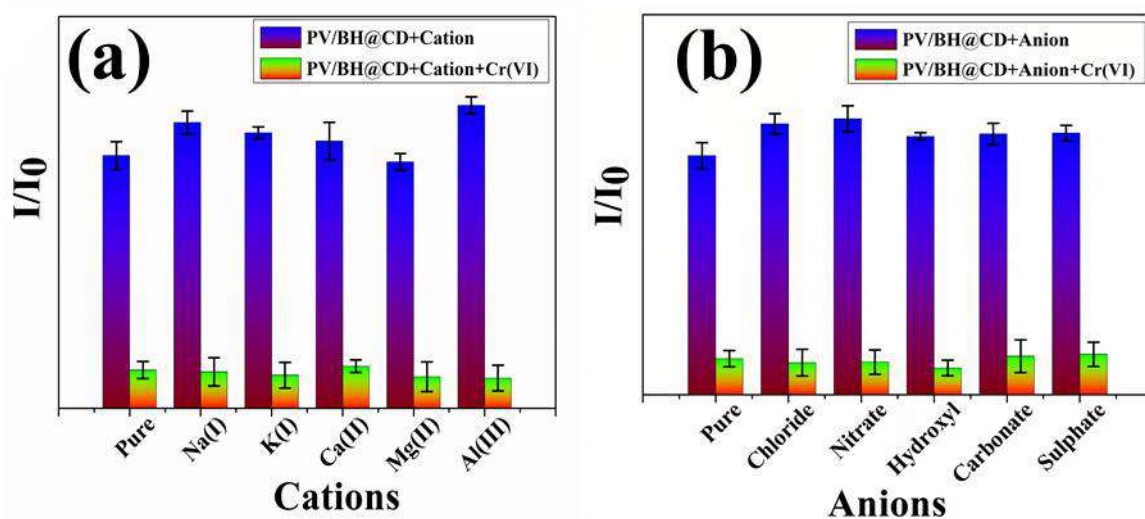
Figure 7.6 *Interference of various common (a) cations, (b) anions upon Cr(VI) sensing efficacy of the sensor*

The linear plot yields a quenching constant of 0.29956×10^6 M^{-1} with a fitting coefficient of 0.96427. Similarly, the exponential plot shows a quenching constant of 0.0533×10^6 M^{-1} with a fitting coefficient of 0.98059. These quenching constants are further used to calculate the LOD and LOQ values as follows [22],

$$LOD = \frac{3\sigma}{K} \qquad (3)$$

$$LOQ = \frac{10\sigma}{K} \quad (4)$$

Here, σ and K are the standard deviations by taking at least ten measurements of the normalized fluorescence intensities of the pristine sample and the quenching constant respectively. The LOD and LOQ of the sensing probe are found to be 66 and 220 nM respectively. Such low detection limits are quite significant and depict the sensitivity of the detection.

Table 7.1 *Recovery study of the sensing probe at different Cr(VI) concentrations*

Amount spiked (µm)	Recovered amount (µm)	Recovered (%)
1.5	1.39	92.67
5.0	5.06	101.2
20.0	19.07	95.35

The quantitative detection of hexavalent chromium has also been carried out by computing the recovery percentages. In this study, the linear S-V plot has been used as the calibration curve of the sensor material. Moreover, separate chromium solutions were prepared to have 1.5, 5, and 20 µM concentrations and further tested using the sensor material to validate their concentration (Table 7.1). The recovery rates are found quite significant illustrating the successful quantification of the contaminant.

7.3.5 Establishing the detection mechanism

The Cr(VI) detection mechanism of the probe has been established by involving the density functional theory and experimental fluorescence lifetime assay. Initially, the lifetime profiles of the sensor have been analyzed by exposing the sensor to Cr(VI) at a varied concentration of the contaminant (Figure A3.5). A gradual reduction in fluorescence lifetime has been obtained, which substantiates the sensing to take place at the excited state of the system [23].

Further, to obtain the electronic transitions involved in the excited state of the fluorophore (cdot), the time-dependent density functional theory has been applied (Figure 7.7). The quencher (Cr(VI)) has been placed nearby (5 Å) of the fluorophore to construct the model. The TDDFT study offers an electronic transition from HOMO-5 to the LUMO+2 state of the fluorophore through energy absorption.
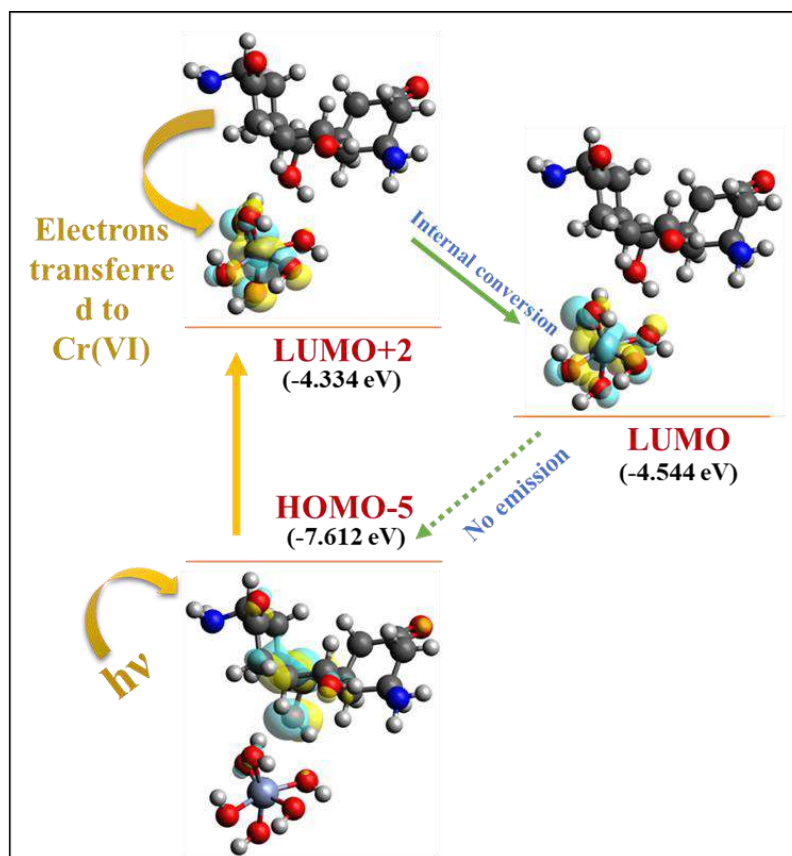
Figure 7.7 *(a) PET-based fluorescence 'turn off' mechanism analysis using TDDFT formalism*

During this transition, the molecular orbital of the fluorophore has completely been shifted to the quencher suggesting an electron transfer phenomenon. After a non-radiative internal conversion process (LUMO+2 to LUMO), the system brings itself to the ground state. This part of the electronic transition offers no radiation, as the electron has already been transferred to the quencher moiety at the excited state. Such phenomenon is known as photoinduced electron transfer offers radical fluorescence quenching in systems [24]. Besides, the S-V plots of the system are showing two different phenomena at different concentration domains. This could be probably due to the synergistic effect of the static and dynamic quenching at the excited state of the system at a higher concentration domain (>20 µM) [25]. However, at lower quencher concentrations, the system strictly follows static quenching.

7.3.6 Detection of hexavalent chromium varying the external parameters

The sensing efficacy of the membrane has been verified by varying the pH of the medium. The pH varied between 4 and 9 to observe the sensing stability. The fluorometric data at varied pH conditions suggest that the sensing efficacy remains unaffected even at extreme pH levels (Figure 7.8).
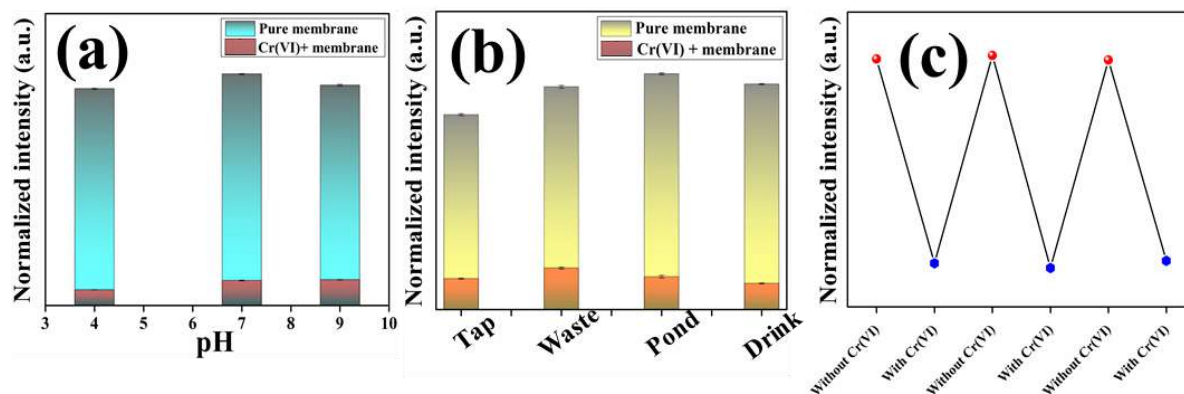
Figure 7.8 Detection efficacies of the sensing probe at (a) various water qualities and (b) different pH; (c) reusability study of the sensor

Additionally, water samples from different sources have been used to study the sensing efficacy of the probe. The water samples were collected from the laboratory tap (tap water), a nearby pond (pond water), a water purifier (drinking water), and from a nearby canal connected to a local tannery (wastewater). These samples were initially filtered through a 0.45 µm filter membrane and then the TDS was measured (Table 7.2).

Table 7.2 Physical parameters of collected water samples from numerous sources

Type of water	pH	TDS (ppm)
Drinking	8.02	99
Tap	8.36	740
Pond	7.66	933
Waste	3.80	1923

Each water sample was divided into two parts, among which one part was spiked by Cr(VI) maintaining a 500 µM concentration. The samples were then exposed to a 355 nm wavelength for fluorometric study. It is observed that in all the cases Cr(VI) successfully decays the fluorescence intensity of the sensor (Figure 7.8). Such fluorometric sensing data reveals the efficiency of the sensing probe in real-life studies as it does not affect water qualities. Further, inter-day and intraday batch studies on different water qualities have been performed (Table 7.3). Promising recovery rates (87-108 %) have been found in this batch experiments validating the applicability of the sensor in different environments.

The reusability study has also been performed by repetitively using the sensor membrane. The sensor membrane maintains its efficacy even after three complete cycles (Figure 7.8). Henceforth, it can be argued that the sensitivity of the sensor remains unaffected even when the external parameters are varied. Such a stable sensing efficiency would make it a dedicated chromium sensor in the real world.

Table 7.3 *Detection and sensing performance in various water samples*

Water Type	Intraday (n=3)				Interday (n'=3)			
	Added amount (µM)	Recovered amount (µM)	Recovery (%)	RSD (%)	Added amount (µM)	Recovered amount (µM)	Recovery (%)	RSD (%)
Drinking water	5.0	4.77	95.40	1.12	5.0	4.81	96.20	1.08
	10.0	9.85	98.50	1.08	10.0	9.69	96.90	1.71
	15.0	15.56	103.73	1.72	15.0	16.16	107.73	2.03
Tap water	5.0	15.56	87.20	1.06	5.0	4.41	88.20	1.99
	10.0	4.36	90.10	2.03	10.0	9.10	91.04	1.27
	15.0	9.01	91.60	1.8	15.0	13.27	88.47	3.11
Pond water	5.0	4.60	92.00	1.6	5.0	4.54	90.80	1.39
	10.0	9.52	95.20	2.81	10.0	9.20	92.00	1.57
	15.0	16.27	108.47	2.48	15.0	16.01	106.73	2.65
Wastewater	5.0	4.56	91.20	0.8	5.0	4.46	89.20	1.14
	10.0	8.91	89.07	1.75	10.0	9.09	90.90	2.37
	15.0	13.63	90.87	2.91	15.0	13.33	88.87	3.19

7.3.7 Detection of 'early-stage Cr(VI) induced carcinogenic effect' in living cells

Previously in Chapter 6 the genotoxicity and cytotoxic effects of hexavalent chromium have been discussed. Moreover, the contamination pathways have also been illustrated, which makes this toxic effluent a potential carcinogen. It has also been reported that Cr(VI) uses a sulphur transport channel to enter into a cell and produces various reactive oxygen species in presence of enzymes like glutathione and cytochrome b5 [26]. These reactive species suppress cellular activities and lead to DNA damage [27]. This work aims to detect the hexavalent chromium in the cell membrane as well as in the interior of the living cell to fetch an alarm at an early stage of cancer development.
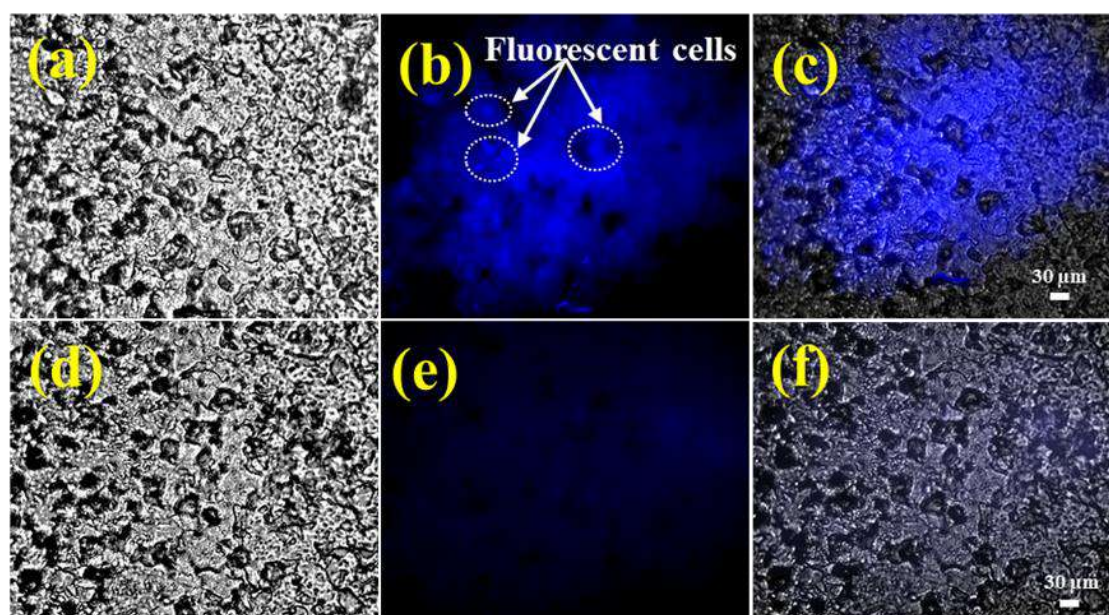
Figure 7.9 *Sensing of Cr(VI) ion in HELA cells by using the sensing probe showing excellent fluorescence quenching upon Cr(VI) addition, where, (b) fluorescent cells turn off their fluorescence (e) upon Cr(VI) addition. (a), (d) and (c), (f) are showing bright and merged fields*

Thus, fluorescence microscopy has been carried out before and after the Cr(VI) addition to the HeLa cells (Figure 7.9) in order to observe the bio-sensing activity of the synthesized sensor. The protocol of fluorescence microscopy and cellular adhesion have been discussed earlier (Chapter 2, Section 2.2.6). It is found that the Cr(VI) contaminated cells show no fluorescence signal, whereas the untreated cells emit bright blue fluorescence.

To substantiate this phenomenon, molecular docking simulation has been employed (Figure 7.10). In this theoretical study, mainly two proteins have been selected for the docking analysis with the fluorophores of the sensor (cdot), namely SLC26Dg transporter protein (PDB: 5IOF) and glutathione (PDB: 1PKW). SLC26Dg transporter protein normally creates the sulphur transport channel of the cells and glutathione acts as a chromium receptor [28].

In both cases, strong binding affinities have been found between the protein and the fluorophore (Table 7.4). The binding affinity between the fluorophore and the glutathione is found to be -8.3 kcal/M, whereas it is -7.0 for SLC26Dg transporter protein and the fluorophore. Such high binding affinities suggest that the sensor is capable to bind with the cells and it can detect hexavalent chromium in living cells as seen in the fluorescence microscopy data.
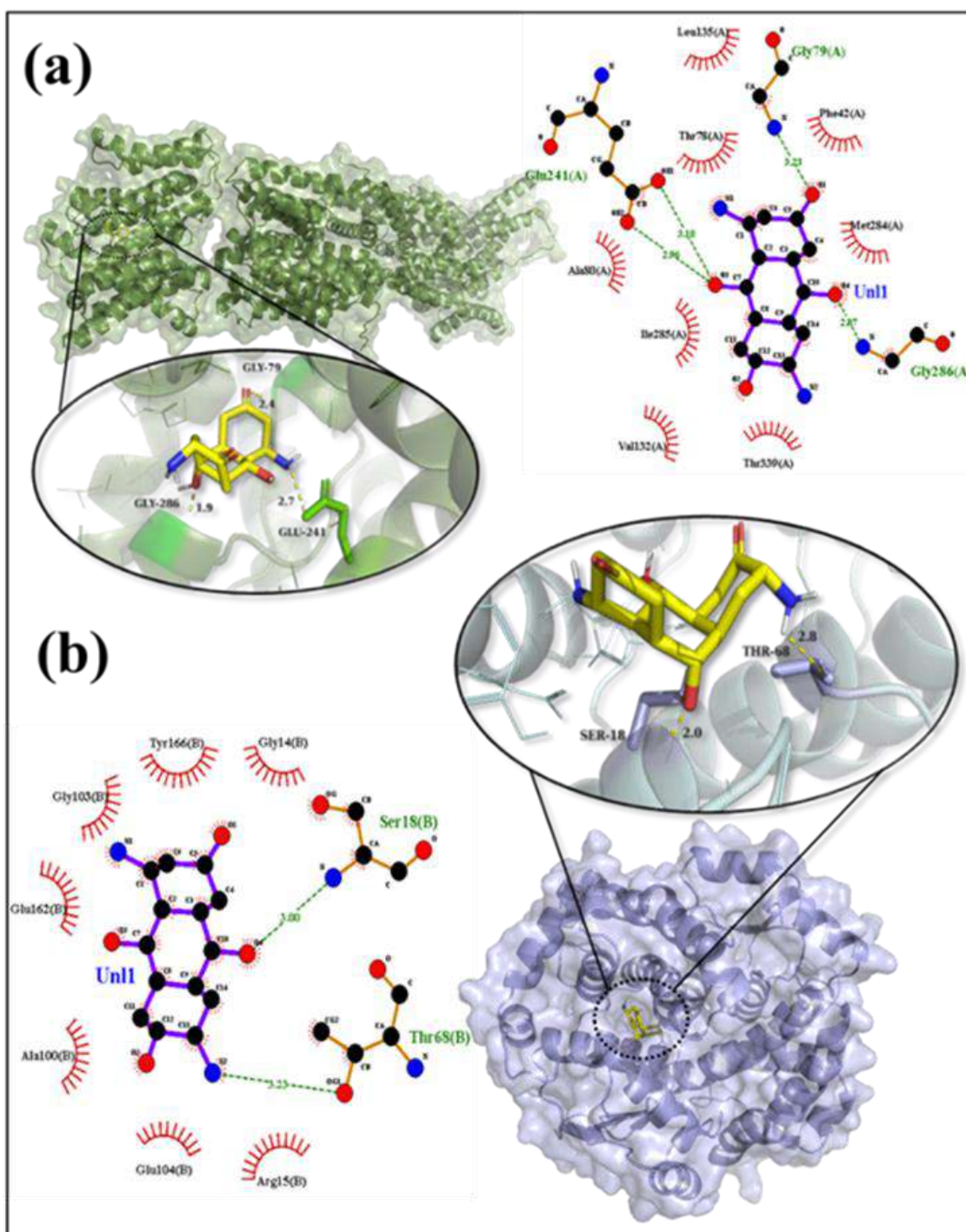
Figure 7.10 *Molecular docking analyses of the sensing probe showing interactions between fluorophore of the probe and (a) sulphur channel protein (5IOF), (b) glutathione (1PKW)*

Table 7.4 Molecular docking results showing various poses between the sensing probe and different proteins

Protein	Pose	Binding affinity (kcal/mol)	Distance from best mode	
			rmsd l.b.	rmsd u.b.
	1	-7.0	0.000	0.000
	2	-6.8	2.663	4.535
5IOF	3	-6.6	3.164	6.144
	4	-6.6	3.079	5.751
	5	-6.5	2.606	3.889
	6	-6.3	2.779	4.681
	7	-6.3	1.492	5.475
	8	-6.2	11.366	12.748
	9	-6.2	5.885	8.113
	1	-8.3	0.000	0.000
	2	-7.8	2.369	4.132
1PKW	3	-7.7	2.605	5.412
	4	-7.7	15.959	19.443
	5	-7.6	2.331	3.559
	6	-7.6	7.704	10.123
	7	-7.2	24.963	27.581
	8	-7.0	2.617	4.101
	9	-6.9	25.881	27.933

7.4 Summary

This study reports a low-cost reusable fluorometric sensor device, Kavach for hexavalent chromium detection. This device can detect hexavalent chromium in all types of water irrespective of their source, pH, TDS, and other physical parameters. This sensing probe has a great potential to detect chromium in living cells as well. The device is made of cdot tailored boehmite nanoparticles wrapped in the polymeric substrate of PVDF-HFP. Such polymeric encapsulation reduces the cdot leaching from its structure making it more stable compared to other available cdot based fluorometric sensors. Kavach is highly selective towards chromium with a very low detection limit (66 nM). it can quantify the level of contamination, which has been examined in this work. The sensing mechanism of this device has been substantiated by using TDDFT and fluorescence lifetime experiment, which shows that the photoinduced electron transfer is responsible for such rapid turn-off sensing. The molecular docking analysis along with the fluorescence microscopy study reveals the bio-sensing capability of this smart sensing probe making it an early-stage chromium-induced carcinogen sensor.

References

[1] S. Bardhan, S. Roy, D. K. Chanda, S. Ghosh, D. Mondal, S. Das, S. Das, Nitrogenous Carbon Dot Decorated Natural Microcline: An Ameliorative Dual Fluorometric Probe for Fe3+ and Cr6+ Detection, Dalton Trans. 49 (2020) 10554-10566

[2] H. Liu, J. Yang, Z. Li, L. Xiao, A.A. Aryee, Y. Sun, R. Yang, H. Meng, L. Qu, Y. Lin, X. Zhang, Hydrogen-bond-induced emission of carbon dots for wash-free nucleus imaging, Anal. Chem. 91(14) (2019) 9259-9265.

[3] C.M. Carbonaro, D. Chiriu, L. Stagi, M.F Casula, S.V. Thakkar, L. Malfatti, K. Suzuki, P.C. Ricci, R. Corpino, Carbon dots in water and mesoporous matrix: chasing the origin of their photoluminescence, J. Phys. Chem. C 122(44) (2018) 25638-25650.

[4] Wadhai, S.M., Sawane, Y.B., Limaye, A. and Banpurkar, A.G., 2021. Large tuning in the electrowetting behaviour on ferroelectric PVDF-HFP/Teflon AF bilayer. Journal of materials science, 56(28), pp.16158-16166.

[5] Willinger, K. and Thelakkat, M., 2011. Photosensitizers in solar energy conversion. In Photosensitizers in medicine, environment, and security (pp. 527-617). Springer, Dordrecht.

[6] T.U. Patro, M.V. Mhalgi, D.V. Khakhar, A. Misra, Studies on poly (vinylidene fluoride)–clay nanocomposites: effect of different clay modifiers, Polymer 49(16) (2008) 3486-3499.

[7] S. Roy, P. Thakur, N.A. Hoque, B. Bagchi, S. Das, Enhanced electroactive β-phase nucleation and dielectric properties of PVdF-HFP thin films influenced by montmorillonite and Ni(OH)2 nanoparticle modified montmorillonite, RSC Adv. 6(26) (2016) 21881-21894.

[8] X. Cai, T. Lei, D. Sun, L. Lin, A critical analysis of the α, β and γ phases in poly (vinylidene fluoride) using FTIR, RSC Adv. 7(25) (2017) 15382-15389.

[9] P. Mondal, M.K. Purkait, Effect of Polyethylene glycol methyl ether blend Humic acid on poly(vinylidene fluoride-co-hexafluropropylene) PVDF-HFP membranes: pH responsiveness and antifouling behavior with optimization approach, Polym. Test. 61 (2017) 162-176.

[10] X.T. Qiao, L. Gong, S.H. Chen, S.P. Zhan, X.D. Sun, Isothermal Crystallization Behavior of Poly(vinylidene fluoride) Based Membrane with Graphene Oxide, Int. Polym. Process 35(4) (2020) 398-407.

[11] T.M.W.J. Bandara, A.M.J.S. Weerasinghe, M.A.K.L. Dissanayake, G.K.R. Senadeera, M. Furlani, I. Albinsson, B.E. Mellander, Characterization of poly(vinylidene fluoride-co-hexafluoropropylene)(PVdF-HFP) nanofiber membrane based quasi solid electrolytes and their application in a dye sensitized solar cell, Electrochim. Acta 266 (2018) 276-283.

[12] Lolla, D., Pan, L., Gade, H. and Chase, G.G., 2018. Functionalized Polyvinylidene Fluoride Electrospun Nanofibers and Applications. In Electrospinning Method Used to Create Functional Nanocomposites Films (pp. 69-89). IntechOpen.

[13] X. Tian, X. Jiang, Poly(vinylidene fluoride-co-hexafluoropropene)(PVDF-HFP) membranes for ethyl acetate removal from water, J. Hazard. Mater. 153 (2008) 128-135.

[14] R. Jalili, A. Khatae, M.R., Rashidi, R. Luque, Dual-colored carbon dot encapsulated metal-organic framework for ratiometric detection of glutathione, Sensor Actuat B-Chem 297(2019) 126775.

[15] Guo, Z., Zhang, Z., Zhang, W., Zhou, L., Li, H., Wang, H., Andreazza-Vignolle, C., Andreazza, P., Zhao, D., Wu, Y. and Wang, Q., 2014. Color-switchable, emission-enhanced fluorescence realized by engineering C-dot@ C-dot nanoparticles. ACS applied materials & interfaces, 6(23), pp.20700-20708.

[16] [24] M.J. Molaei, Principles, mechanisms, and application of carbon quantum dots in sensors: a review, Anal. Methods 12(10) (2020) 1266-1287.

[17] C. Pérez-Rodríguez, L.L. Martín, S.F. León-Luis, I.R. Martín, K.K. Kumar and C.K. Jayasankar, Relevance of radiative transfer processes on Nd3+ doped phosphate glasses for temperature sensing by means of the fluorescence intensity ratio technique, Sens. Actuators B Chem. 195 (2014) 324-331.

[18] G. Gabor, D.R. Walt, Sensitivity enhancement of fluorescent pH indicators by inner filter effects, Anal. Chem 63(8) (1991) 793-796.

[19] T. Liang, P. Yang, T. Wu, M. Shi, X. Xu, T. Qiang, X. Sun, A general strategy to quantify analytes through fluorescence chromaticity and luminosity, Chin. Chem. Lett. 31(11) (2020) 2975-2979.
[20] S. Roy, S. Bardhan, D.K. Chanda, S. Ghosh, D. Mondal, J. Roy, S. Das, Development of a Cu (II) doped boehmite based multifunctional sensor for detection and removal of Cr (VI) from wastewater and conversion of Cr(VI) into an energy harvesting source, Dalton Trans. 49(20) (2020) 6607-6615.

[21] J. Carvalho, P. Nottelet, J.L. Mergny, J.A. Queiroz, G.F. Salgado, C. Cruz, Study of the interaction between indole-based compounds and biologically relevant G-quadruplexes, Biochimie. 135 (2017) 186-195.

[22] M. Pajewska-Szmyt, B. Buszewski, R. Gadzała-Kopciuch, Sulphur and nitrogen doped carbon dots synthesis by microwave assisted method as quantitative analytical nano-tool for mercury ion sensing, Mater. Chem. Phys. 242 (2020) 122484.
[23] M. van de Weert, L.V. D. Stella, Fluorescence Quenching and Ligand Binding: A Critical Discussion of a Popular Methodology, J. Mol. Struct. 998 (2011) 144-150.

[24] Z. J. Lin, H. Q. Zheng, H. Y. Zheng, L. P. Lin, Q. Xin, R. Cao, Efficient Capture and Effective Sensing of $Cr_2O_7^{2-}$ from Water Using a Zirconium Metal-Organic Framework, Inorg. Chem. 56 (2017) 14178-14188.

[25] Dhenadhayalan, N., Lin, K.C. and Saleh, T.A., 2020. Recent advances in functionalized carbon dots toward the design of efficient materials for sensing and catalysis applications. Small, 16(1), p.1905767.

[26] S. Mishra, R.N. Bharagava, Toxic and genotoxic effects of hexavalent chromium in environment and its bioremediation strategies, J. Environ. Sci. Health C 34(1) (2016) 1-32.

[27] X. Shi, Reduction of chromium(VI) and its relationship to carcinogenesis, J Toxicol Environ Health B Crit Rev 2(1) (1999) 87-104.
[28] P. Ruzza, A. Calderan, Glutathione transferase (GST)-activated prodrugs, Pharmaceutics 5(2) (2013) 220-231.

Chapter 8

Conclusion and outlook

Chapter 8

Conclusion and outlook

Our world is presently going through a huge crisis in the energy and environment sectors. While the limited amount of fossil fuel encourages us to invest in alternative energy sources, the waste products from the heavy and medium scale industries contaminate our environment drastically. Besides alternative energy sources, such as hydel power, nanogenerators, solar-thermal power, researchers are nowadays focusing on smart materials for harvesting the generated energy for future use.

Further, industrial contamination, especially water pollution from heavy metal discharge is considered a global dispute by various international organizations. In order to prevent heavy metal contamination, detection of the metal ions in wastewater and their removal is necessary. Numerous nanomaterials have been employed to do these tasks in the recent past, but the lack of sensitivity in detection and poor stability of these materials restricted their use in the real world. Simultaneous detection and removal in a single compound are still not achieved in real-life.

Herein, fluorescent nanostructures of oxy-hydroxide compounds have been successfully utilized to detect and remove heavy metal (Cr(VI)) from industrial wastewater. Additionally, the removed hexavalent chromium is further processed and employed as 'waste capacitors' to harness the electrical energy.

Initially, nanoparticles of aluminum oxy-hydroxide, namely boehmite (γ-AlOOH) of different sizes have been synthesized and characterized in *Chapter 3*. It has been observed that hydrothermal reaction time greatly modifies the crystallinity and particle size of boehmite nanostructures. The absorbance and the emission spectra are also found to be altered due to this size variation. Blue fluorescence of these boehmite samples has been observed, which is due to the defect-induced emission of these samples. Moreover, the electrical properties have been measured in each case showing a radical increment in the dielectric constant and corresponding ac conductivity of the smaller-sized BH12 sample. The dielectric constant is found to be 3.71 x 10^6 at the 40 Hz frequency. These electrical properties have been further studied by varying the temperature up to 200 °C showing a stable character of the sample up to a certain limit.

138

In *Chapter 4*, the primary focus has been given to understanding the influence of morphology on the emission and electrical properties of boehmite nanostructures. Particularly three distinct morphologies of boehmite have been synthesized (nanoparticles, nanoneedles, and nanoflowers) and characterized before checking their optical and electrical properties. It is found that the samples are providing defect-mediated fluorescence, especially the needle-shaped HBH sample that shows the highest fluorescence intensity and is selected for fluorometric sensing applications. The limit of detection, in this case, is found to be ~0.42 nM. This needle-shaped nanostructure of boehmite is also capable to remove hexavalent chromium from industrial wastewater using a simple surface adsorption technique. The removal process is quick and almost 76% of total chromium has been removed in 10 minutes. The removed chromium occupies the pores of the boehmite sample and results in an increased dielectric constant (~43 times), which is suitable to harvest electrical charge and make it a 'waste capacitor'.

Later, in *Chapter 5* the crystal defects in boehmite nanostructures have been enhanced by incorporating metal ions (i.e., copper and gadolinium) in order to enhance the fluorescence of the samples. Not only the emission properties have been enriched, but also the morphology and other physicochemical properties of boehmite have been altered. This time the detection limit of the fluorometric sensing of Cr(VI) is found to be varied between 6-10 µM with promising removal efficacies (80-85% removal of Cr(VI) within 5 minutes). Moreover, the sensing and adsorption mechanisms have been discussed. The copper doped boehmite sample shows better surface adsorption compared to the rare earth gadolinium doped boehmite. Thus, the copper doped sample has been used to study the dielectric properties before and after adsorbing the hexavalent chromium. It is found that the dielectric constant is increased remarkably in the high-frequency domain making the sample a potential waste capacitor.

Besides defect-induced fluorescence, carbon quantum dot has been incorporated into boehmite nanoparticles as a fluorophore. This incorporation drastically enhances the fluorescence emission of the sample, which has been utilized further to detect hexavalent chromium in wastewater and living cells. The detection limit reduces quite radically (58.1 nM) in this work. The detection mechanism has been substantiated by using the fluorescence lifetime experiment and theoretical TDDFT methods. This emerging fluorometric probe is used in different water samples to justify its efficacy in real-life. It

has been used to detect Cr(VI) in living cells by fluorescence microscopy and the detection mechanism has been validated by molecular docking simulation.

It has been realized that the carbon dots have a tendency to leach out from the surface of boehmite. Although the leaching rate is very nominal, it has been restricted by wrapping the nanocomposite into the polymeric matrix of PVDF-HFP. This work is reported in *Chapter 7* showing that the leaching of carbon dot has been successfully controlled. Furthermore, the chromium sensing efficacy has been limited to about 66 nM. The polymeric encapsulation provides us a thick film, which has been used to fabricate a fluorometric sensing device for Cr(VI), namely 'Kavach'.

Kavach is capable to detect chromium in living cells, which has been validated by molecular docking and TDDFT. This device has all the properties of bare carbon dot loaded boehmite nanostructure. Additionally, it provides a longer lifetime and rigidity, which makes it a dedicated chromium sensor for industrial use.

Appendices

Appendix 1

Supporting information of Chapter 4
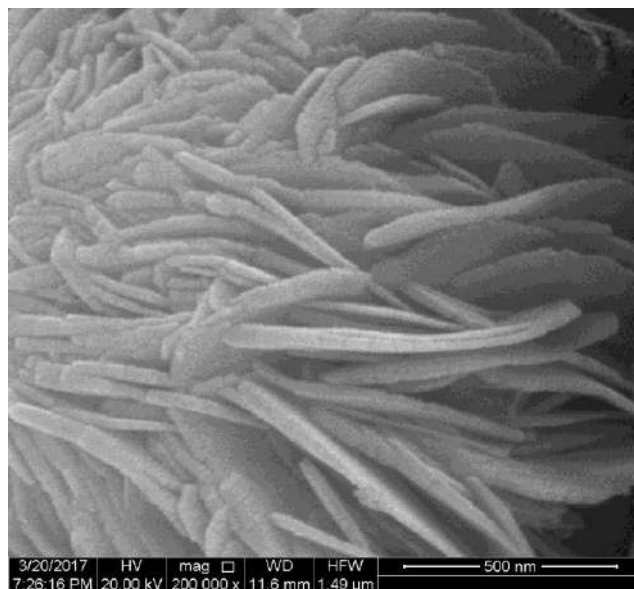
Figure A1.1 *High-resolution FESEM image of the UBH sample*
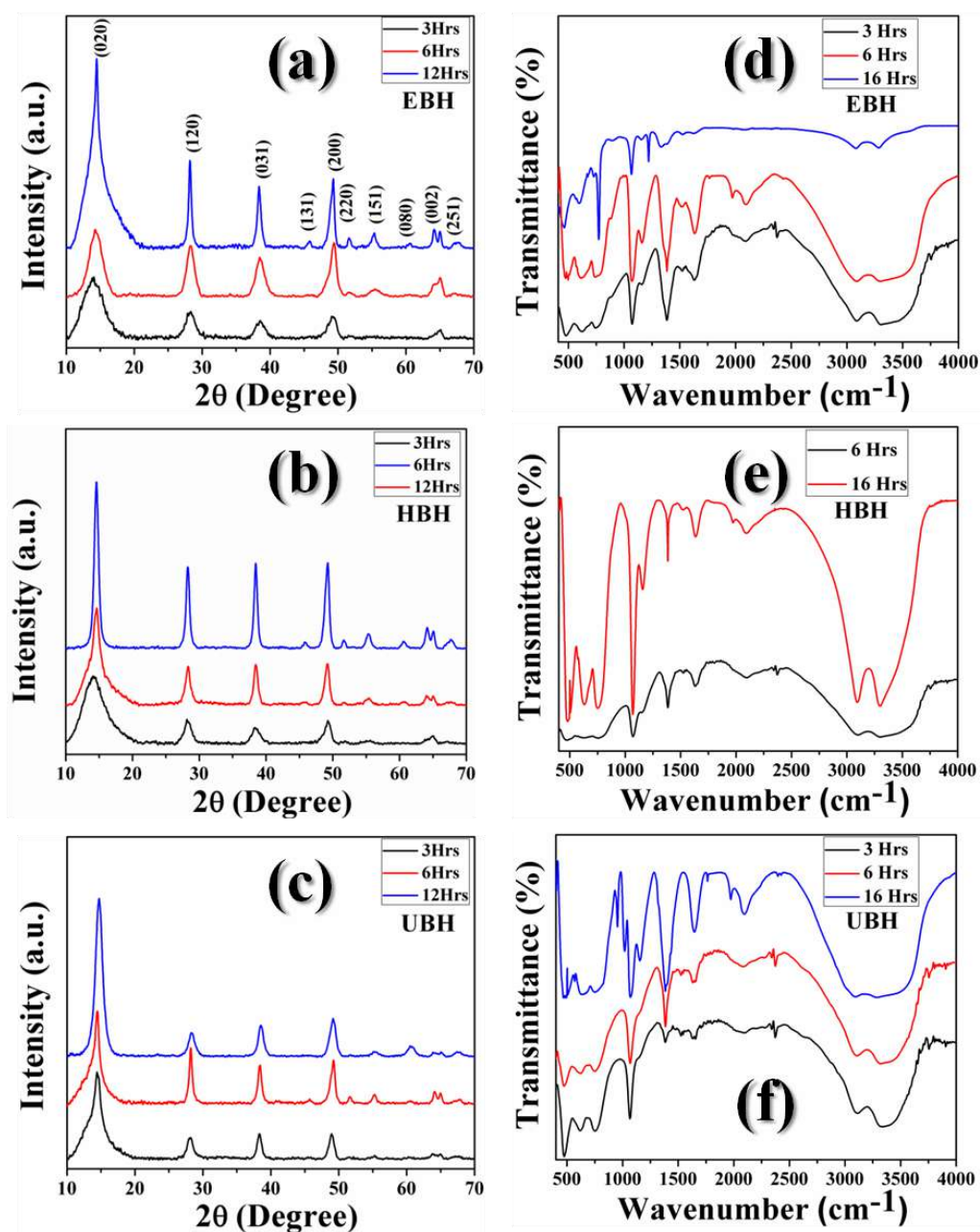
Figure A1.2 *X-Ray Diffractograms (a-c) and FT-IR spectra (d-f) of EBH, HBH, and UBH samples*

after 3, 6, and 16 h of hydrothermal reaction

Appendix 2

Supporting information of Chapter 6
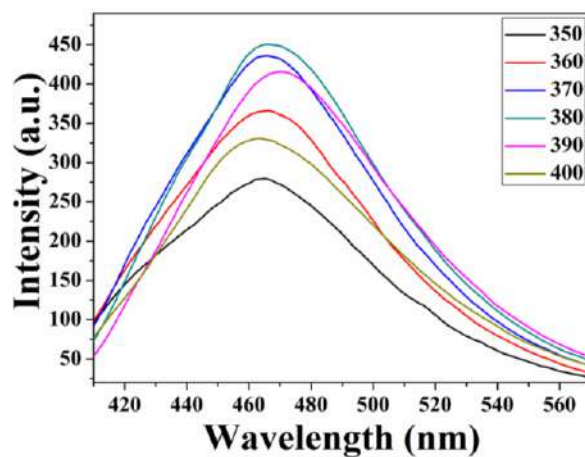
Figure A2.1 *Excitation wavelength dependent emission spectra*
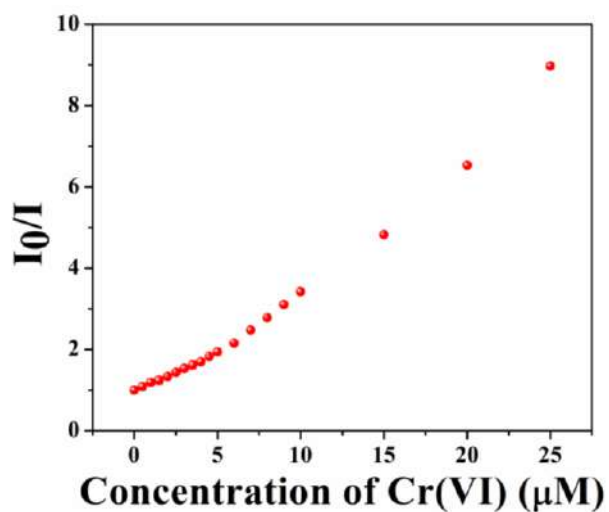
Figure A2.2 *Stern-Volmer plot for CDBH (0-25 µM) showing an exponential decay*
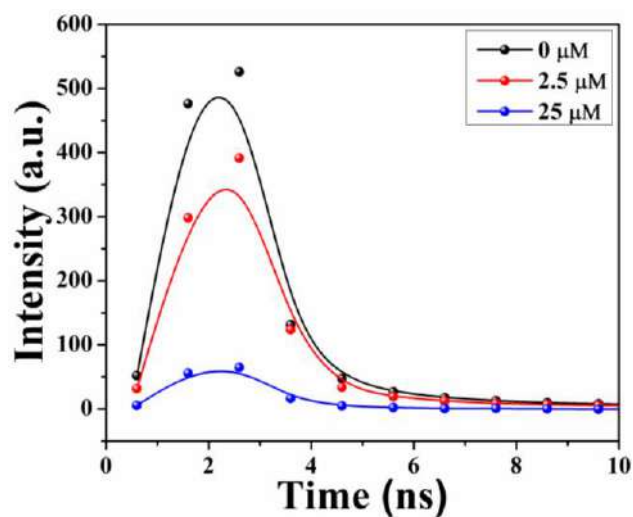
Figure A2.3 *Time resolved fluorescence decay of CDBH upon Cr(VI) addition*
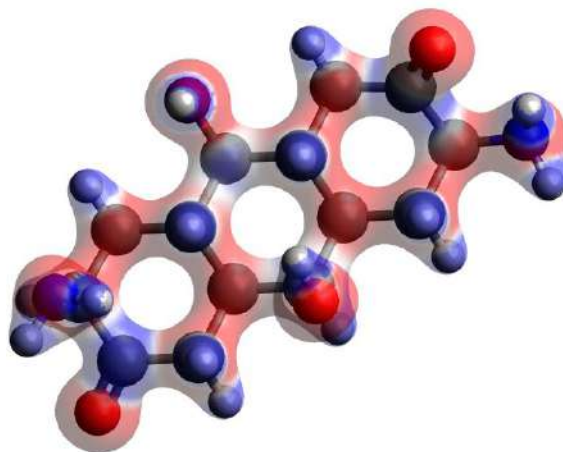
Figure A2.4 *Electrostatic potential mapping diagram of CDBH computed from the DFT study (red region is negative and blue is positive in the map)*

Pose	Binding affinity (kcal/mol)	Distance from best mode	
		rmsd l.b.	rmsd u.b.
1	8.7	0.000	0.000
2	8.7	19.023	20.878
3	8.3	16.982	19.333
4	8.2	1.980	2.954
5	8.1	17.372	19.649
6	8.0	17.484	19.628
7	8.0	20.981	22.772
8	7.9	2.042	2.964
9	7.8	5.788	8.736

Table A2.1 *Molecular docking results showing various poses between CDBH and glutathione*

Crystallographic refinement data (.cif file) of CDBH

data_Bohmite

_audit_creation_date 'Sat Jul 11 10:22:24 IST 2020'
_audit_creation_method 'Maud, version 2.94'
_audit_update_record 'Sat Jul 11 10:40:52 IST 2020'
_computing_structure_refinement 'Maud, version 2.94'
_refine_ls_R_factor_all 0.056968044
_refine_ls_wR_factor_all 0.07805589
_refine_ls_goodness_of_fit_all 0.04005924
_publ_contact_author_name 'S.Das'
_publ_section_title 'CDBH'

_chemical_name_common Bohmite
_chemical_formula_sum 'Al H0.08 O2'
_symmetry_cell_setting orthorhombic
_symmetry_space_group_name_H-M Amam:-cba
_cell_formula_units_Z 1
_refine_ls_d_res_low 0
_refine_ls_d_res_high 5000
_reflns_d_resolution_low 0.7
_reflns_d_resolution_high 50
_maud_sg_centering_type P
_chemical_name_mineral Bohmite
_chemical_name_systematic Unknown
_cell_length_a 3.6863(9)
_cell_length_b 12.161(4)
_cell_length_c 2.8536(7)
_cell_angle_alpha 90
_cell_angle_beta 90
_cell_angle_gamma 90

loop_
_symmetry_equiv_pos_site_id
_symmetry_equiv_pos_as_xyz
0 'x, y, z'
1 '-x, -y, z'
2 'x+0.5, -y, -z'
3 '-x+0.5, y, -z'
4 '-x, -y, -z'
5 'x, y, -z'
6 '-x+0.5, y, z'
7 'x+0.5, -y, z'
8 'x, y+0.5, z+0.5'
9 '-x, -y+0.5, z+0.5'
10 'x+0.5, -y+0.5, -z+0.5'
11 '-x+0.5, y+0.5, -z+0.5'
12 '-x, -y+0.5, -z+0.5'
13 'x, y+0.5, -z+0.5'

14 '-x+0.5, y+0.5, z+0.5'
15 'x+0.5, -y+0.5, z+0.5'

loop_
_atom_site_label
_atom_site_type_symbol
_atom_site_occupancy
_atom_site_fract_x
_atom_site_fract_y
_atom_site_fract_z
_atom_site_B_iso_or_equiv
_atom_site_calc_flag
Al_Al Al 1.0 0.24999909 0.682342 0.9999988 0.3(1) .
O1_O O 1.0 0.25000218 0.2915999 0.99997133 0.3(2) .
O2_O O 1.0 0.25000182 0.07330115 9.957081E-7 0.3(1) .
H_H H 1.0 0.75256 0.6924094 4.177863E-4 0.0(23) .

DFT optimized Cdot structure

Cartesian coordinates (Å)

C	-1.311858	-3.353203	0.458573
C	-2.576506	-2.621320	0.960550
C	-2.290660	-1.161413	1.357714
H	-1.539525	-1.131615	2.157749
C	-3.569057	-0.415528	1.832175
C	-4.135732	-1.230238	2.993365
H	-4.301539	-0.475515	1.008924
N	-3.382671	0.970853	2.221528
C	-4.509584	-2.656416	2.638706
O	-4.179506	-0.796857	4.130081
C	-3.257093	-3.399637	2.112618
H	-5.278030	-2.652193	1.852425
H	-4.921919	-3.159688	3.515514
C	-3.593683	-4.840942	1.687767
H	-2.547332	-3.459410	2.959142
H	-3.283770	-2.611576	0.114902
C	-2.348596	-5.593035	1.176872
H	-4.331903	-4.796458	0.874220
O	-4.267317	-5.553445	2.720969
C	-1.643550	-4.806900	0.047454
O	-0.230161	-3.283691	1.393192
C	-0.387137	-5.556665	-0.442449
H	-2.352069	-4.739245	-0.793900
C	-2.712368	-7.012784	0.704252
H	-1.645732	-5.670479	2.028635
C	-1.514993	-7.817100	0.178556
H	-3.454315	-6.924034	-0.102902
H	-3.189852	-7.572727	1.513903
C	-0.665340	-7.008920	-0.814942
H	-1.878988	-8.699851	-0.357041
N	-0.679617	-8.312084	1.293254
H	0.359834	-5.530187	0.364174
O	-0.187921	-7.523610	-1.810473
H	-0.202346	-7.540191	1.757732
H	0.053577	-8.913397	0.918151
H	-3.641376	-5.690971	3.451888
H	-2.558257	1.372479	1.783473
H	-3.272818	1.019054	3.233605
H	0.069039	-5.065957	-1.308507
H	-0.927416	-2.825094	-0.422329
H	-1.860039	-0.621388	0.502956
H	-0.543056	-3.608666	2.251647

Appendix 3

Supporting information of Chapter 7
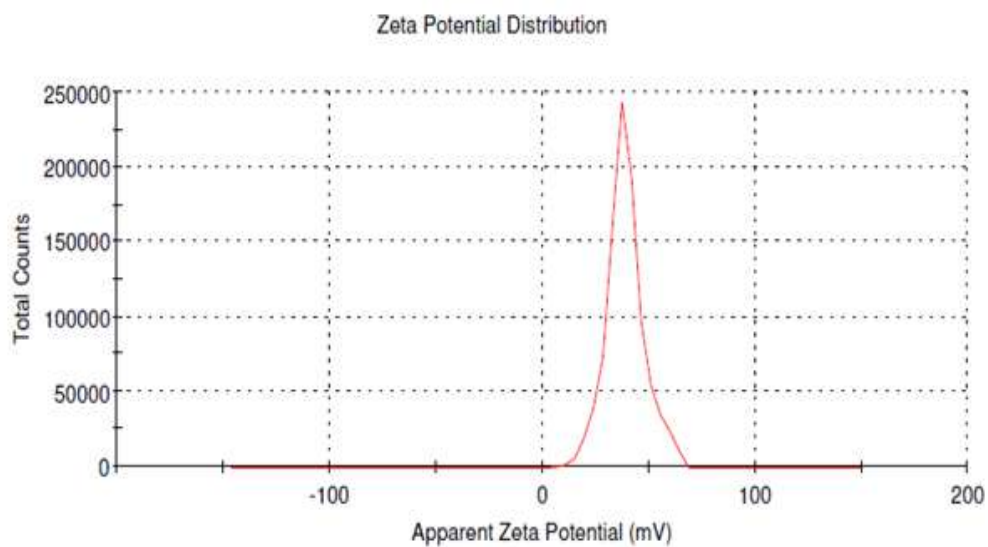
***Figure* A3.1** *Zeta potential of the BH@CD nanocomposite*
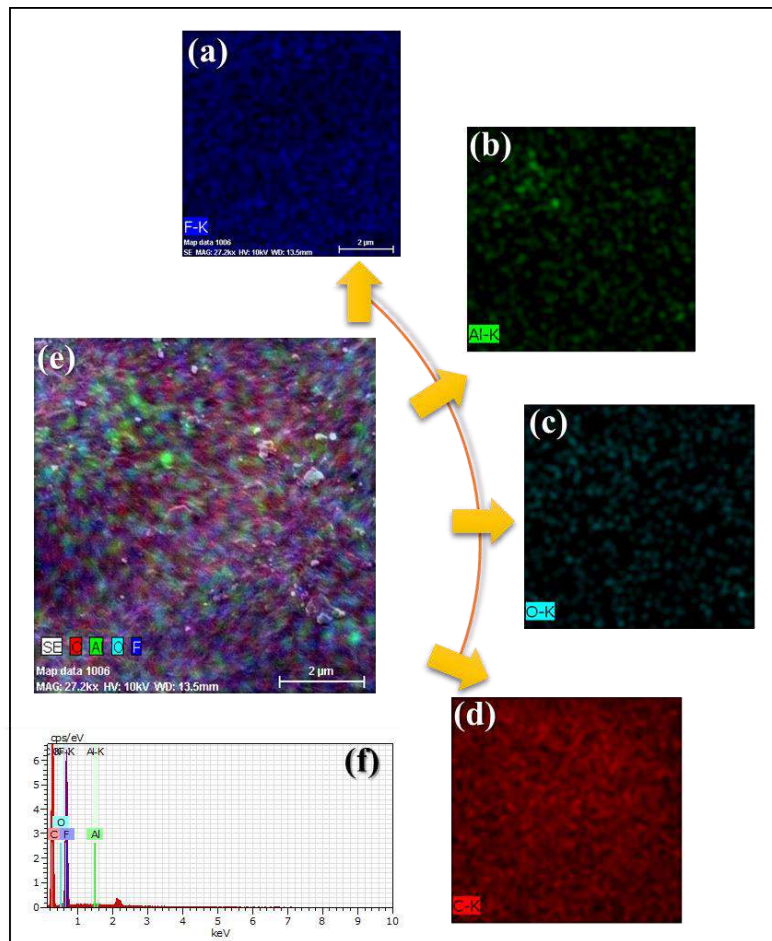
Figure A3.2 *Elemental mapping data of the membrane showing (a) fluorine, (b) aluminum, (c) oxygen, (d) carbon contents and (e) the merged image; (f) shows the elemental composition from EDX analysis of the membrane sample*
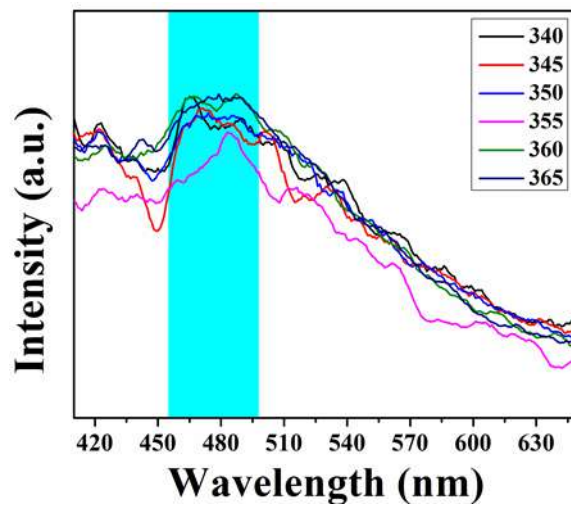
Figure A3.3 *Fluorescence intensities of the PV/BH@CD membrane at different excitation energies*
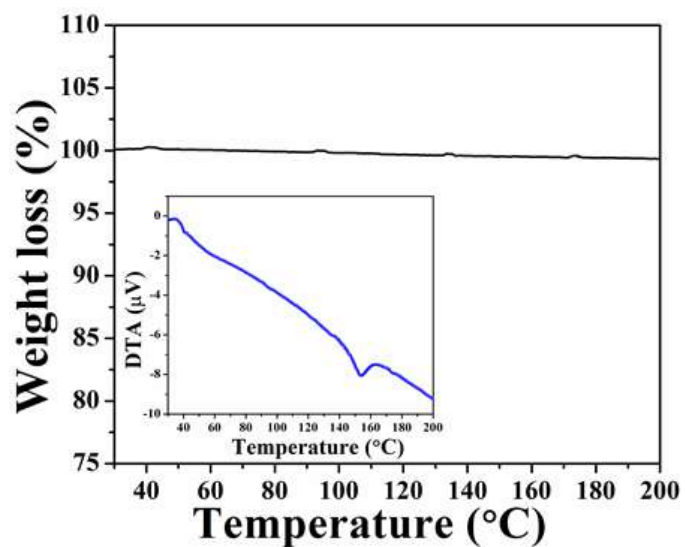
Figure A3.4 TGA and DTA (inset) thermograms of the membrane sample showing the temperature stability
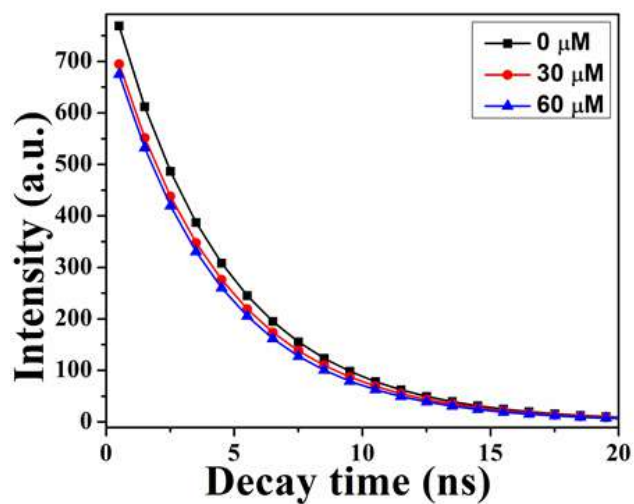
Figure A3.5 Fluorescence lifetimes of the sensing probe when exposed to different concentrations of Cr(VI) solutions

m

DFT optimized structure of the fluorophore-quencher conjugate

C	-1.04307701668065	-0.14860556080456	0.70482822669436
C	0.20156349447232	-1.03492508784661	0.42973544708199
C	-0.26256481673789	-2.48751833095940	0.11759814127173
C	-1.27490065899133	-3.06784301800174	1.14323751570102
C	-2.36141347020786	-2.09231540262625	1.57452134792816
H	-0.76453422975804	-3.37692876197619	2.06373874961654
H	-1.75962893831887	-3.96108563235211	0.73705749049440
C	-1.87598647894216	-0.68480030102595	1.88427553278808
O	-3.52894659740989	-2.41756006017702	1.67081652796110
H	-1.25723856171152	-0.69620592408470	2.79230985102600
H	-2.75025028668409	-0.05471189016699	2.08080355708109
N	-0.66480126381768	1.25294333961757	0.98542740284549
H	-1.48899060659186	1.78363407176764	1.26566529201368
H	-0.30753918170844	1.69419712449319	0.13774847735590
H	-1.68318427137706	-0.21239918257599	-0.19440889622532
C	1.30329829851752	-0.96476819083367	1.52098723836848
H	0.67995264935780	-0.64204626020525	-0.48083538150159
C	2.49699956452880	-1.85736102940315	1.13412377113941
H	0.88766749533367	-1.30763589406559	2.48630904809724
O	1.80061168998021	0.35612408691444	1.65054937172839
C	2.08705112010304	-3.32900617088821	0.91006317095756
C	0.92751279929861	-3.45164227710303	-0.10700264488069
H	0.54388297659016	-4.48031785804104	-0.08528231943061
O	1.45513242014472	-3.28444291312080	-1.44405495351889
H	-0.80507424596361	-2.45501633671637	-0.83932498271890
C	3.66967879025441	-1.75039744999480	2.14111916535413
H	2.87518182106381	-1.46480080677743	0.18207629209522
C	3.45376135103176	-2.55570890857707	3.40792927146599
H	3.86007545892437	-0.70841759149780	2.40461538193422
H	4.56044639406447	-2.16395958872676	1.64950798110628
C	3.04426619724939	-4.02186477587964	3.19013159196595
O	3.60235356345034	-2.10871117936452	4.53063536854106
C	1.83168459568184	-4.07145289071593	2.24034824067179
N	4.19375160061352	-4.72672123996309	2.59893180431135
H	0.98689949231149	-3.63953618875277	2.78738939636221
H	1.56889406597566	-5.12120283208854	2.04127257070450
H	2.93993978666837	-3.83755822693187	0.44347375453564
H	3.94692555905513	-5.70175046662177	2.43040950827488
H	4.96542736132695	-4.73586196901432	3.26513035583071
H	1.01211064575815	0.93567280098827	1.74635473101081
H	1.19741629306277	-2.43143176692982	-1.84857359729178
H	2.74137926578573	-4.41556901578248	4.17350459018976

O 3.64758699206922   -2.87275859510907   -2.78110899449477
H 2.98092601070398   -3.16524653840539   -2.07680371299037
H 4.76554220228322   -1.21883568512374   -5.29608869944807
H 5.96006213668842   -0.68969011956529   -2.67347657793387
O 5.53815690550633   -0.72519740263877   -3.55120238652882
O 3.86040756909322   -1.37242485228686   -4.96199016495587
O 4.34849045027314   -0.99732625100614   -1.45175952910305
Cr 3.76709925731204   -1.22453220372556   -3.20950230609128
O 1.94142180417438   -1.16525184860977   -3.10003108028166
H 4.22390047689882   -0.03788508841616   -1.31372486898680
O 3.41939077281543   0.63615049003504   -3.09964800365286
H 4.22015160891972   1.04559365649643   -3.47434219762344
H 1.70616968755767   -0.23266600483222   -3.26690486684648

Thesis publications

Crystallinity mediated variation in optical and electrical properties of hydrothermally synthesized boehmite (γ-AlOOH) nanoparticles

Shubham Roy [a], Souravi Bardhan [a], Kunal Pal [b], Saheli Ghosh [a], Paulami Mandal [a], Santanu Das [a], Sukhen Das [a, *]

[a] *Department of Physics, Jadavpur University, Kolkata, 700032, India*
[b] *Department of Life Science and Biotechnology, Jadavpur University, Kolkata, 700032, India*

ABSTRACT

In this article, nanostructures of boehmite (γ-AlOOH) have been successfully synthesized in a time varied, facile and cost effective hydrothermal route. The samples have been characterized by using X-Ray Diffraction (XRD), Field Emission Scanning Electron Microscopy (FESEM), Transmission Electron Microscopy (TEM) and Fourier Transform Infrared (FTIR) spectroscopy. Our samples exhibit remarkably high photoluminescence emission intensity and dielectric constant (3.71×10^6 for BH12 sample) with a nominal dielectric tangent loss. A detailed growth mechanism including the nucleation and self assembly of our nanomaterial has been discussed. Moreover, we are the first to report here the electrical properties of the boehmite nanoparticles. Present investigation also explores temperature dependent dielectric property and ac conductivity of these samples. The role of crystallinity in the optical and electrical enhancement of our samples has been illustrated with proper analytical details. Not only high emission intensity in the blue and green region of the spectrum makes our sample a strong candidate for bio-imaging and bio-sensing applications, but also high dielectric constant makes them desirable for cost-effective energy storing devices, such as supercapacitors and solar cells.

© 2018 Elsevier B.V. All rights reserved.

1. Introduction

Since past few decades an intense amount of research activity has been carried out in the fundamental study of synthesis and photo-physical properties of nanocrystals. Due to the rapid development in technology and industry there is always a high demand for high performance material which in turn creates a pressing need for the fabrication of inorganic-organic hybrid material than single metal, polymer or ceramic owing to their limited performance in different technological applications. However, advanced nanotechnology provides us the unique features of single materials and compounds due to their smaller sizes. Nanocrystals are class of materials possessing intermediate size between the molecular and bulk materials. The unique properties of nanocrystals such as high dielectric constant, increased surface to volume ratio etc. are currently known to be closely related to their sizes, phases, shapes, crystallinities and therefore it would be very meaningful to prepare

these materials with controllable characteristics. Size and morphology control of inorganic nanoparticles is therefore very important since it provides unique physicochemical properties which have wide and promising applications: photovoltaic, photo conducting devices, electroluminescence devices, solid-state lasers, and energy storage devices, biological and medical applications [1,2]. During the last few years, considerable efforts have been focused on the synthesis of boehmite nanostructures (γ-AlOOH) [3—5]. As a typical oxyhydroxide compound and owing to high surface area (90—246 m²/g), boehmite is also extensively used as an adsorbent material with photoluminescence property, catalyst, filler in membrane, optical material, coating, composite reinforcement material in ceramics [6,7]. Boehmite also has a significant role in the field of orthopedic and dental science due to its biocompatibility [8]. Because of these applications, a great amount of research has been devoted to study the relation between the synthesis of boehmite nanocrystals and its chemical and physical properties. However till date, a very limited investigation has been made upon electrical conductivity and dielectric response of boehmite nanoparticle. In general, nano-crystalline materials have high specific surface area and large grain boundary compared to the

bulk [9]. Moreover, if these grain boundaries consist of a number of microstructural defects, these can able to induce pronounced variation in dielectric properties [10] of the target nanocrystal. Keeping this in mind, study of the optical and electrical properties of boehmite nanoparticles could able to open up an avenue to the use of this material in the field of biotechnology and industry.

There were mainly two routes for boehmite synthesis: (a) the hydrolysis of aluminium alkoxides and (b) precipitation from inorganic salts in an aqueous medium. Synthesis of boehmite nanoparticle hydrothermally [11−14] requires critically maintained experimental parameters such as pH of the solution, temperature, ionic strength etc. During sample preparation, it is essential to take an extra precaution to avoid the formation of aluminum hydroxides (i.e. gibbsite or bayerite). Nonetheless, smallest deviation from the synthesis procedure and grade of the reactants may lead to the formation of undesired aluminum hydroxide polymorphs.

Here in our study, we have employed simple hydrothermal technique [6] for large scale production of boehmite nanoparticle with controlled size and morphology. Corresponding qualitative model of particle formation and self assembled growth mechanism has been depicted in this article. In our investigation, characterization of our synthesized nanostructure have been made by using X-Ray Diffraction (XRD), Field Emission Scanning Electron Microscopy (FESEM), Transmission Electron Microscopy (TEM) and Fourier Transform Infrared Spectroscopy (FTIR). In addition, optical quality of our nano-materials has been estimated by measuring UV−Vis absorption (UV−Vis), Photoluminescence (PL) and time resolved fluorescence spectroscopy showing strong luminescence emission with different intensities which could be potentially applied in the field of bio-imaging and bio-sensing. Here we are the first to report the temperature dependent electrical characteristics of boehmite nanoparticles. Therefore, our present endeavor on synthesis and characterization of boehmite nanostructure with extensive study of the optical and electrical properties could be helpful in designing cost effective energy storage devices, bio-imaging and bio-sensing devices which further creates new paths towards its applications in the advancement of biotechnology and industry.

2. Experimental details

2.1. Materials

Aluminum nitrate nonahydrate [$Al(NO_3)_3 \cdot 9H_2O$], acetone (HPLC grade), ethanol (HPLC grade) and aqueous ammonia solution (25%) were purchased from Merck, India. All the reagents were used without further purification. Deionised (Millipore) water was used throughout the experiment with resistivity at least 18 MΩ-cm. All the glass-wares used in our experiments were cleaned with aqua regia solution followed by rinsing with ultrapure water.

2.2. Synthesis method

Nanoparticle of γ −AlOOH was prepared by a simple hydrothermal method as reported by S. Music' et al. [6] with some major modifications. In a typical synthesis process, $Al(NO_3)_3 \cdot 9H_2O$ was first dissolved uniformly in Millipore water using magnetic stirrer under vigorous stirring condition. After complete dissolution of the aluminum salt in the water, ammonia solution was added drop wise in the salt solution to initiate co-precipitation process and the final pH of the solution was maintained at 9. Stirring was continued for another 3 h at room temperature to complete the reaction process. The resultant milky white solution was then transferred into a Teflon lined autoclave which was then placed in an oven at 160 °C for 12 h. The solid white precipitates were collected from the

bottom of the Teflon jacket and washed several times with water. The washed precipitate was dried in vacuum at room temperature first and then at 60 °C for another 12 h. Keeping all other parameters constant, boehmite nanoparticles were also synthesized by varying the hydrothermal treatment time for 18 and 24 h to understand the growth mechanism of the nanostructure. Synthesized boehmite nanoparticles were named according to hydrothermal reaction times which were BH12, BH18 and BH24 respectively.

2.3. Characterization techniques

The XRD of all the samples were recorded using powder X-Ray Diffractometer, Model D8, BRUKER AXS, with Cu-Kα radiation (λ = 1.5405 Å) in the range of 2θ from 10° to 80°.

The Fourier transform infrared spectroscopy study was done using FTIR-8400 S, Shimadzu in the wave number range of 400 cm^{-1} to 4000 cm^{-1}.

INSPECT F50 (FEI, Netherland) Field emission scanning electron microscope (FESEM) was employed to analyze the morphology of our nano-powders. Very small amount of nano-powders were directly casted on carbon grids and sputter coated with gold to obtain the FESEM micrographs.

The TEM characterization of our boehmite samples was done using JEOL JEM-2000 transmission electron microscope (operated at 200 KV). Small amount of samples were first dissolved in acetone and then ultra-sonicated to form a homogenous solution. The solution was then casted drop wise on the carbon coated copper mesh and dried in ultra high vacuum for further analysis.

Spectroscopic studies were carried out by dissolving boehmite nanopowders directly in ethanol at a concentration of 1 mg/ml. Ultraviolet−visible spectra (UV−Vis) of the samples were recorded using Perkin Elmer Lambda-365 Spectrophotometer.

The photoluminescence spectroscopy study was done using Cary Eclipse Fluorescence Spectrophotometer, Agilent Technologies with an excitation wavelength (λ_{ex}) of 389 nm. Fluorescence lifetime of our samples was measured using a time-resolved spectrofluorometer from IBH, UK. The samples were excited at 389 nm. The channel width is 56 ps/channel.

Dielectric measurement and electrical conduction mechanisms were investigated using Agilent 4294 A Precision Impedance Analyzer.

3. Result and discussion

3.1. Structural and morphological analysis of the nanoparticles

X-Ray Diffraction (XRD) is an important characterization tool to determine the crystallographic structure and crystallite size of the samples. This tool also provides us with the information regarding the crystal growth and purity of the samples. In this article, Fig. 1 shows the XRD patterns of our synthesized γ-boehmite nanostructures. The XRD peaks of all boehmite nanostructures are in good accordance with the orthorhombic phase of γ-AlOOH (JCPDS card no. 21-1307). Absence of any unwanted peak confirms that there is no other aluminum-induced phase such as $Al(OH)_3$ or Al_2O_3 in our samples. Hence, it could be assumed that the entire $Al(OH)_3$ precursor has been completely transformed into γ-AlOOH after the hydrothermal treatment. As per previous reports nano boehmite adopts lamellar structure within an orthorhombic symmetry [15]. This nano γ-AlOOH is basically a type of layered material where each layer constitutes the (OAlOH−HOAlO) stacking sequence in the x- and z-direction. Four tetrahedral oxygen and two hydroxyl groups are bounded around octahedral aluminum AlO_6 of γ-AlOOH. These stacked layers are connected by hydrogen bonds of hydroxyl group to construct the zig-zag chain along Z-direction [16]. In our
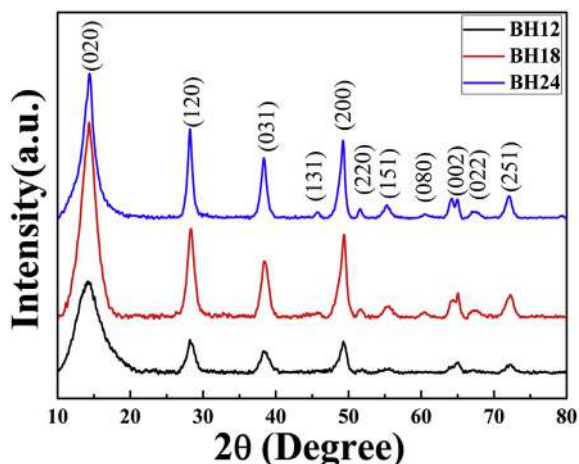
Fig. 1. XRD pattern of the samples BH12, BH18 and BH24.

Fig. 2. Normalized FTIR spectra of the samples BH12, BH18 and BH24.

case, strong diffraction peak corresponding to (020) plane implies that the growth units of boehmite nanostructures are abundant along (020) facets. Full width at half maxima (FWHM) (depicted in Table 1) was calculated for the (020) plane for the three samples which indicates highest crystallinity in BH24 sample among the three samples. FWHM is a measure of crystallinity as well as directional growth of a sample. Lower FWHM value corresponds to the higher crystallinity. We have obtained sharpest peak at (020) for BH24. Calculated value of FWHM for this peak is 0.0281 rad which is quite lower than that of BH12 (0.0664 rad) and BH18 (0.0395 rad) respectively. These values of FWHMs imply that, BH24 is much more crystalline than the other two boehmite samples. Thus, it can be concluded that with the increment in hydrothermal reaction time crystallinity of our boehmite sample get enhanced. The nano-crystallite sizes of our samples are estimated by Debye-Scherrer equation (Eq. (1)) from the broadening of (020) peak as observed in the diffraction pattern [17].

$$<D>_{(020)} = 0.9\lambda \big/ \left(\beta_{1/2} \cos\theta \right) \qquad (1)$$

Here, D is the average nanocrystallite size, λ is the wavelength of the incident X-ray beam, θ is the corresponding Braggs angle, $\beta_{1/2}$ is the full width at half maximum (FWHM) of the (020) peak. The average crystalline size of γ-AlOOH varies slightly from 2.11 nm to 4.93 nm depending on the hydrothermal reaction time. These lattice parameters have been displayed in Table 1. From Fig. 1 it is also apparent that the diffraction peaks are getting sharper with the increasing hydrothermal reaction time indicating change in degree of crystallinity along with the directional growth.

FTIR measurements are performed to investigate the presence of the bonds i.e. the structure and the purity of the synthesized γ-AlOOH nanoparticles (Fig. 2). In Fig. 2 absorption bands at 3392, 3099, 1635, 1159, 885, 752, 629, and 478 cm^{-1} are observed which confirm the formation of γ-AlOOH. The peak present at 1384 cm^{-1} is attributed to the stretching vibration of the nitrate [18]. The
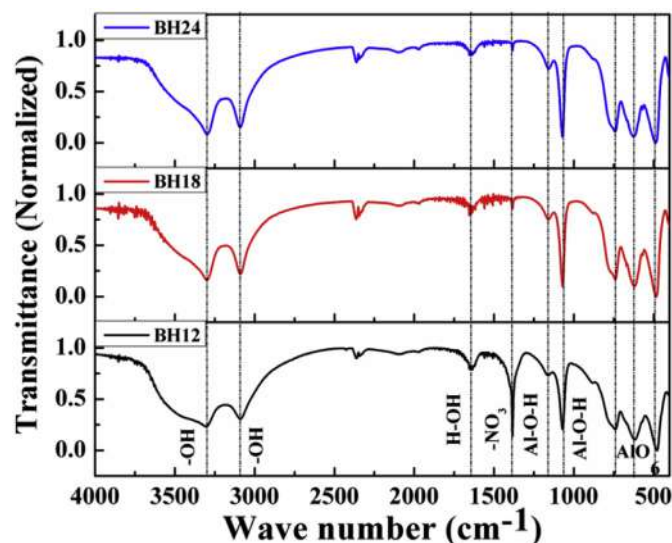
strong bands located at 3300 and 3103 cm^{-1} can be assigned to the asymmetric and symmetric vibrations of O–H respectively [19]. Bands located at 1072 and 1159 cm^{-1} are attributed to the symmetric and asymmetric modes of Al–O–H respectively [6]. The torsional modes present at 740, 617 and 478 cm^{-1} are occurred due to the vibration of AlO$_6$ [6]. Two large bands around 1636 cm^{-1} and 3853 cm^{-1} can be assigned to the stretching and bending modes of the surface adsorbed moister [20]. For BH18 and BH24, the bands located at 1636 and 1383 cm^{-1} get shortened possibly due to the release of absorbed moister and nitrate impurity respectively. However for BH24 sample these two peaks do not undergo such changes indicating more pure and crystalline nature of BH24 than the other two samples. Thus, our FTIR analysis is quite consistent with the XRD results revealing the formation of pure boehmite crystalline nanostructures.

To further investigate the morphology and particle size of our synthesized boehmite nanoparticles, Field Effect Scanning Electron Microscopy (FESEM) was performed. FESEM micrographs of all the samples are presented in Fig. 3. It is observed from the micrographs that all the synthesized nanoparticles are similar in morphology and also all of them get agglomerated. The sizes of our samples increase gradually with the increasing hydrothermal reaction time which is in good agreement with our XRD results. Hakuta et al. [21] have reported that no particle formation occurs at higher pH in the starting solution probably due to the high solubility of boehmite particle at the higher pH values [22]. However, we have obtained boehmite nanoparticles at pH value of 9 in a surfactant-free hydrothermal technique.

In order to confirm further the size and the morphology of the nano-structured boehmite samples more precisely we have taken TEM micrographs of all of our samples. In the TEM image (Fig. 4) spherical particle shape are observed for BH12 whereas mixture of both nanosphere and cubic particle shapes are obtained for BH18

Table 1
Structural parameters calculated from XRD data are nanocrystallite size (D), Full width at half maximum (FWHM), lattice parameter (a, b, c) and d-spacing for [020] plane of the corresponding boehmite samples.

Sample	D (nm)	FWHM (rad)	a(Å)	b(Å)	c(Å)	d-spacing (Å) [020]
BH12	2.11	0.0664	3.6939	12.3029	2.8683	6.1546
BH18	3.536	0.0395	3.6875	12.3328	2.8653	6.1663
BH24	4.926	0.0281	3.6965	12.4539	2.8676	6.2257
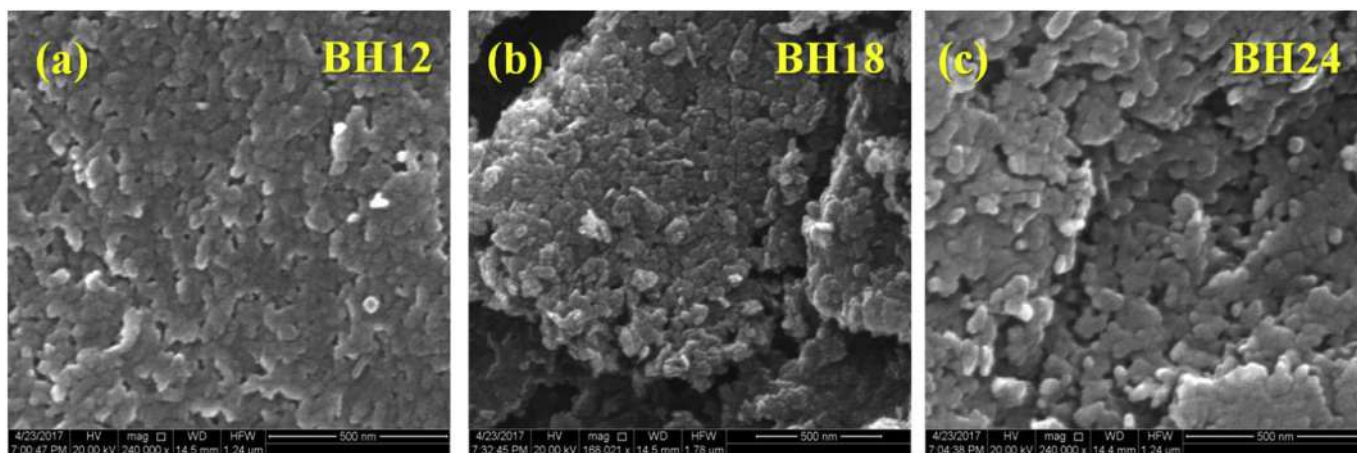
Fig. 3. FESEM image of the samples (a) BH12, (b) BH18 and (c) BH24.
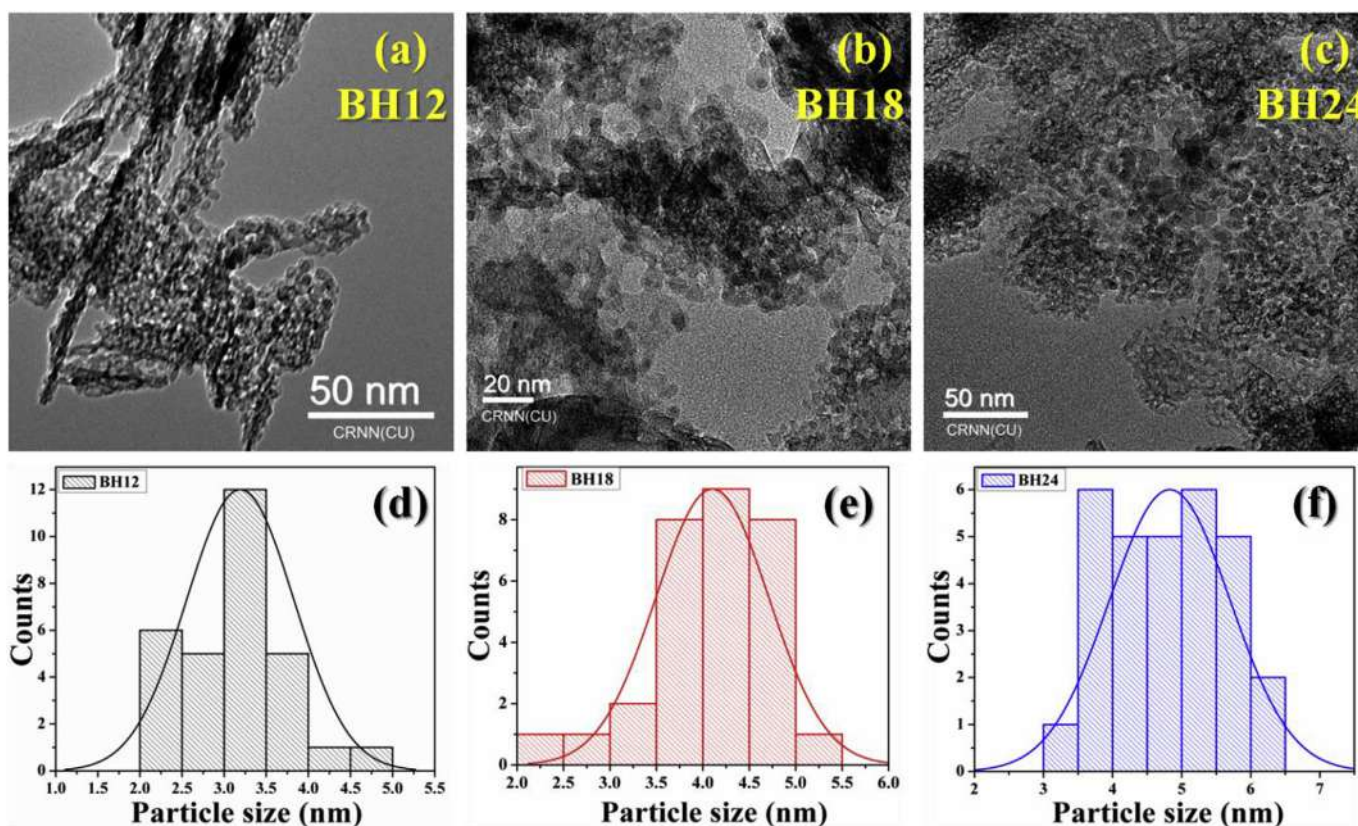
Fig. 4. TEM micrographs of the boehmite samples (a–c), corresponding size distribution plots from the TEM images (d–f).

and BH24. From TEM micrographs mean particle sizes are found to be 3.2, 4.1 and 4.8 nm for BH12, BH18 and BH24 respectively which corroborate our XRD results very well.

3.2. Qualitative model for nanostructure formation

Here we are demonstrating the possible growth mechanism for self-assembled boehmite nanoparticle (Fig. 5) depending upon the results of XRD, FTIR, FESEM and TEM studies. There are three stages in the formation of a nanostructure: (i) Nucleation, (ii) growth, and (iii) self assembly to produce the final nanostructure [23,24]. In our case, nucleation initiates with the reaction between Al^{3+} ions and

hydroxyl ions (OH^-). Aluminum nitrate salt dissolute in water producing $Al(OH)_2^-$ and an extra proton (H^+). With the addition of ammonia (NH_3) precursor, this proton is 'accepted' by ammonia which further produces $H-NH_3^+$. However, after accepting this proton, the pH of the solution increases rapidly leading to the formation of aluminum hydroxide $Al(OH)_3$ as white precipitate. In a typical hydrothermal condition, one water molecule has been released by $Al(OH)_3$ to produce boehmite nanostructure followed by the growth of nuclei. This is the probable reason behind the formation of the spherical shape of the BH12 and BH18 samples. After 24 h of hydrothermal reaction, boehmite nanoparticles get agglomerated which is supported by the XRD results.

For BH24 sample there is formation of nano-cubes along with nanospheres due to the surface energy minimization [25]. Actually, in the process of reducing the surface energy, smaller nanospheres get agglomerated which further form hierarchical nanocubes. This result is well supported by our XRD results.

3.3. Optical properties of the nanostructures

Absorption and emission are two important qualitative data to analyze the optical quality of a material. The absorption spectra of boehmite nanoparticles obtained through time varied hydrothermal process were recorded and have been displayed in Fig. 6 (a). From the absorption spectra two prominent absorption bands around 206 nm and 265 nm are observed. The absorption band at 206 nm originates from O_2^- to Al_3^+ charge transfer [26]. However, BH12 has the absorbance maxima at around 206 nm, BH18 and BH24 have their corresponding absorbance maxima slightly blue shifted at 204 and 203 nm respectively. The optical band gap of the samples (Fig. 6 (b)) was estimated using the Tauc plot relation [17] given below

$$\alpha E = A(E - E_g)^n \tag{2}$$

where E, E_g, α and A are the photon energy, the optical band gap energy in eV, absorption coefficient and a constant term respectively. In the Tauc plot (Fig. 6 (b)), $(\alpha h\nu)^2$ is plotted against photon energy $h\nu$ and the band gap energy is calculated by extrapolating the linear region and intersecting the linear portion of the curve to the energy axis. Band gap energy is found to decrease with hydrothermal reaction time and achieved minimum value up to 5.17 eV in BH24. This band gap energy varies due to the variation in particle size. Due to the small dimension of our nano size particle it consists of very small number of molecules or atoms. Thus, the number of overlapping orbital and width of the energy level decreases which in turn creates large band gap. However, in our case, the band gap values are slightly higher than that of the previously reported value of 4.67 eV by Alemi et al. [26]. This deviation of band gap energy might be due to difference in pH of precursor solution, nanocrystallite size etc.

Fig. 7 (a) presents PL emission spectra of synthesized samples at the excitation wavelength 389 nm. We have obtained strong emission bands located at 439, 486 and 530 nm whereas; relatively low emission intensity is observed at 461 nm for all the samples. The emission bands indicate different defect states in the

Fig. 5. Mechanisms of formation of different boehmite nanostructure.

orthorhombic phase of boehmite crystal structure which occurred during the crystal growth in hydrothermal reaction. Normally, these crystal defects promote entrapment of excited charge carriers during their transition from the higher energy level to the lower energy level. Previous experimental studies suggest that non-bridging oxygen hole center can take a prime role to originate emissions within the range of 467 nm–576 nm [27] which is clearly visible in our PL spectra.

Variation in emission intensities is another commendable phenomenon which could be explained in terms of defect states. Smaller surface area possesses fewer defects, thus, BH24 has lesser amount of defects than the rest of the samples as it has lowest surface area due to its largest dimension among the three samples. This, in turn, produces highest emission intensity for this sample. Similarly, BH12 has the highest surface area due to its smallest size among the three samples, so in this case, the number of the defect is highest which results in its lowest emission intensity due to charge entrapment mechanism. Thus, surface with fewer defects can greatly enhance the optical quality of a material, which is in proportional relation with the crystal growth/crystallinity of the samples.

Fluorescence lifetime experiment for three boehmite nanoparticles BH12, BH18 and BH24 are carried out at room temperature (26 °C). From the time-resolved lifetime measurements (Fig. 7(b)) it is found that the lifetime decay profile of BH12 follows single exponential fitting whereas BH18 and BH24 both the nanostructures follow a double exponential fitting. The fitted values of the fluorescence decay curves are presented in Table 2. From Table 2 it could be seen that for BH12 the fluorescence lifetime is found to be 5.666 ns The average lifetime of the two other morphologies BH18 and BH24 are observed to be 5.783 ns and 7.527 which are indicative of the presence of two types of morphologies: (i) spherical and (ii) nanocubes arising from aggregation in both the cases. Henceforth, our fluorescence lifetime results match very well with our TEM data. Nonetheless these values of lifetimes of our three samples also hint probable use of these three boehmite nanostructures in the field of bio-imaging and biosensing [28] (see Table 2).

3.4. Investigation of the electrical properties of boehmite nanoparticles

Dielectric properties of the nanomaterials depend on many parameters such as frequency of the external applied electric field, temperature during measurement, chemical composition, grain structure, sample preparation technique etc. The dielectric response is described by expressing relative dielectric constant i.e. $\varepsilon = \varepsilon' + j\,\varepsilon''$. Where, ε' and ε'' are the real and imaginary part of the relative dielectric constant respectively. The real part contributes to the amount of energy stored in a dielectric material due to polarization whereas the imaginary part is generally associated with the dissipation of energy within the dielectric materials. The real part of the dielectric constant can be calculated using the relation

$$\varepsilon' = (C \cdot d)/(\varepsilon_0 A) \tag{3}$$

C is the capacitance of the sample, d and A are thickness and area respectively of the pellet and ε_0 is the free space permittivity (8.85×10^{-12} F/m). Observed Variations of the real part of dielectric constant (ε') with the applied electric field frequency (ranging from 40 Hz to 2 MHz) for all the samples at different temperatures (from 30 °C to 200 °C) have been shown in Fig. 8 (a, c, e). It is apparent from the figure that the hydrothermal reaction time has a great influence on the dielectric behavior of our samples as the crystallinity gets increased with the hydrothermal reaction time. The real
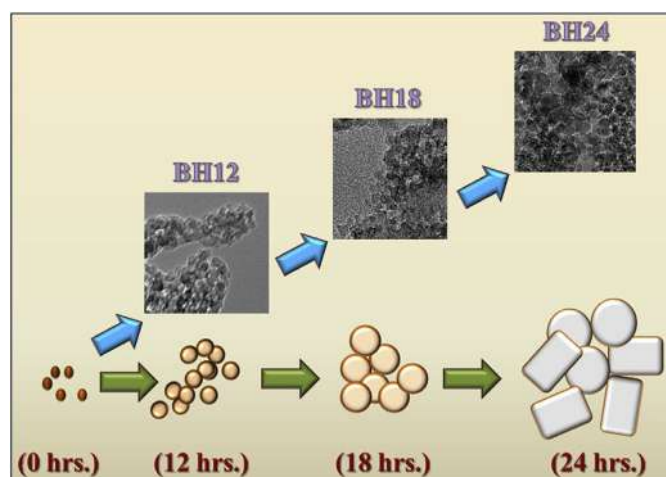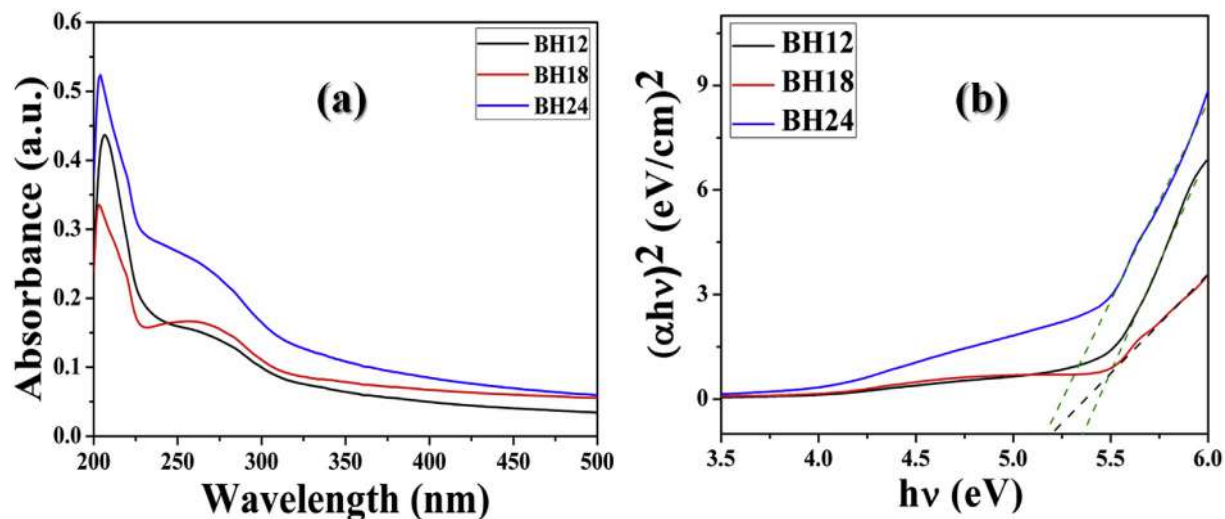
Fig. 6. (a) UV–Vis spectra of BH12, BH18 and BH24, (b) Tauc plot (band gap) of the boehmite samples.
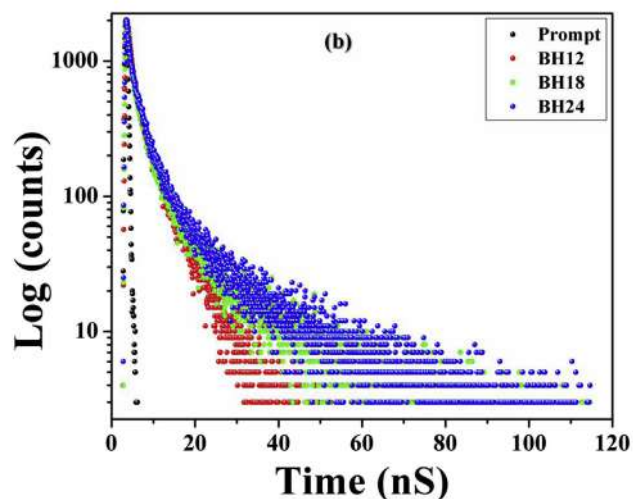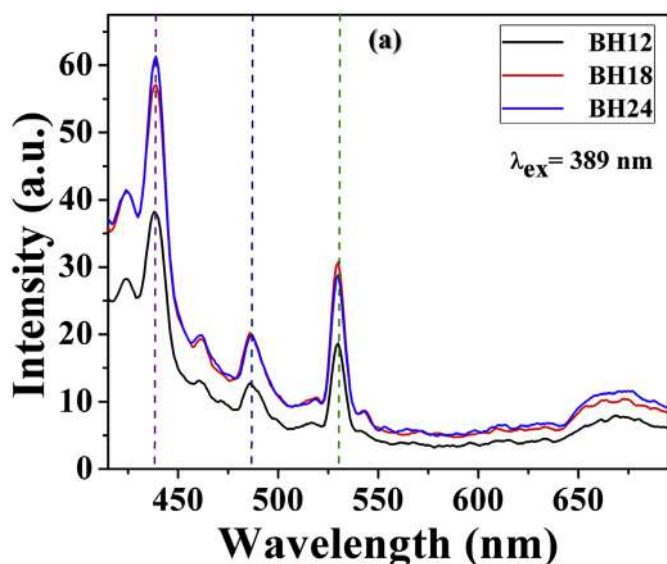
Fig. 7. (a) Photoluminescence spectra of boehmite nanostructures, (b) Fluorescence life time data of boehmite nanostructures.

Table 2
Fluorescence life time data of the synthesized boehmite samples excited at 389 nm. The emission measurement has been done at 438 nm.

Sample	τ_1 (ns)	f_1	τ_2 (ns)	f_2	Average lifetime $<\tau>$ (ns)	χ^2
BH12	5.6657	100	0	0	5.666	1.1789
BH18	2.6336	62.91	11.25	37.09	5.783	1.0158
BH24	3.0896	61.77	14.69	38.23	7.527	1.2330

Table 3
Calculated activation energies from Arrhenius plots at different frequencies.

Sample	Frequency	Activation Energy (eV)
BH12	100 HZ	0.5540
	100 KHZ	1.1402
	1 MHZ	1.0061
BH18	100 HZ	0.5023
	100 KHZ	0.9261
	1 MHZ	0.8829
BH24	100 HZ	0.8938
	100 KHZ	1.3555
	1 MHZ	1.2383

part of the relative dielectric constant is found to be highest for BH12 (3.71×10^6) at 40 Hz frequencies and lowest (1.43×10^6) in case of BH24 at the same frequency among the three samples when crystal growth attains the maximum value. Fig. 9 depicts the variation of the dielectric constants of the three samples with the increasing temperature from 30 °C to 200 °C at different frequency from 40 Hz to 10 MHz. Interestingly, from Fig. 9 it is observed that the dielectric constants (ε') of all the samples are increasing with the increase of the temperature from 30 °C to 50 °C and after 50 °C the dielectric constants decreases with the increasing temperature. Above mentioned variation in dielectric constants with temperature is observed at 40 Hz–10^3 Hz frequency of the external field. Thereafter, with the increasing setting frequency the dielectric value gradually decreases with the increasing temperature. However, this type of behavior can be interpreted by Maxwell-Wagner interfacial polarization phenomenon [29,30], which is in good agreement with Koop's theory [31a]. It is known that interfacial polarization occurs when free charge carriers are accumulated at the highly resistive grain boundary [31b,31c]. Actually, within the dielectric material conducting grains are separated by insulated

grain boundaries which can trap the free charge carriers and create a number of dipoles during their hopping through the grain [32]. Our XRD analysis reveals that average particle size of boehmite nanoparticle increased with the hydrothermal reaction time from 2.11 nm to 4.93 nm which causes a reduction in the grain boundary. Hence average dipole moment per unit volume gradually decreases and consequently loss in dielectric data is found. Moreover, polarization mechanisms such as dipole orientation polarization and electronic displacement polarization are very crucial in the improvement of the degree of polarization [29–33]. But as in the high-frequency range, all kind of polarization cannot withstand the electrical field frequency variation the value of dielectric constant

rapidly decreases [29].

Variation in dielectric loss tangent of our samples is in good support with our high dielectric data (Fig. 8 (b, d, f)). Low losses at the low-frequency region at low temperature for the three samples contribute towards high dielectric constant. In addition, high loss at low frequency at higher temperatures is also observed for our samples. These observations can be interpreted on the basis of the thermal agitation of the dipoles due to their orientation which cannot easily follow the frequency variation of the externally applied electric field [17]. Nonetheless, as our three nanomaterials are with high dielectric constant and low dielectric loss these materials could be considered as good capacitive materials. In
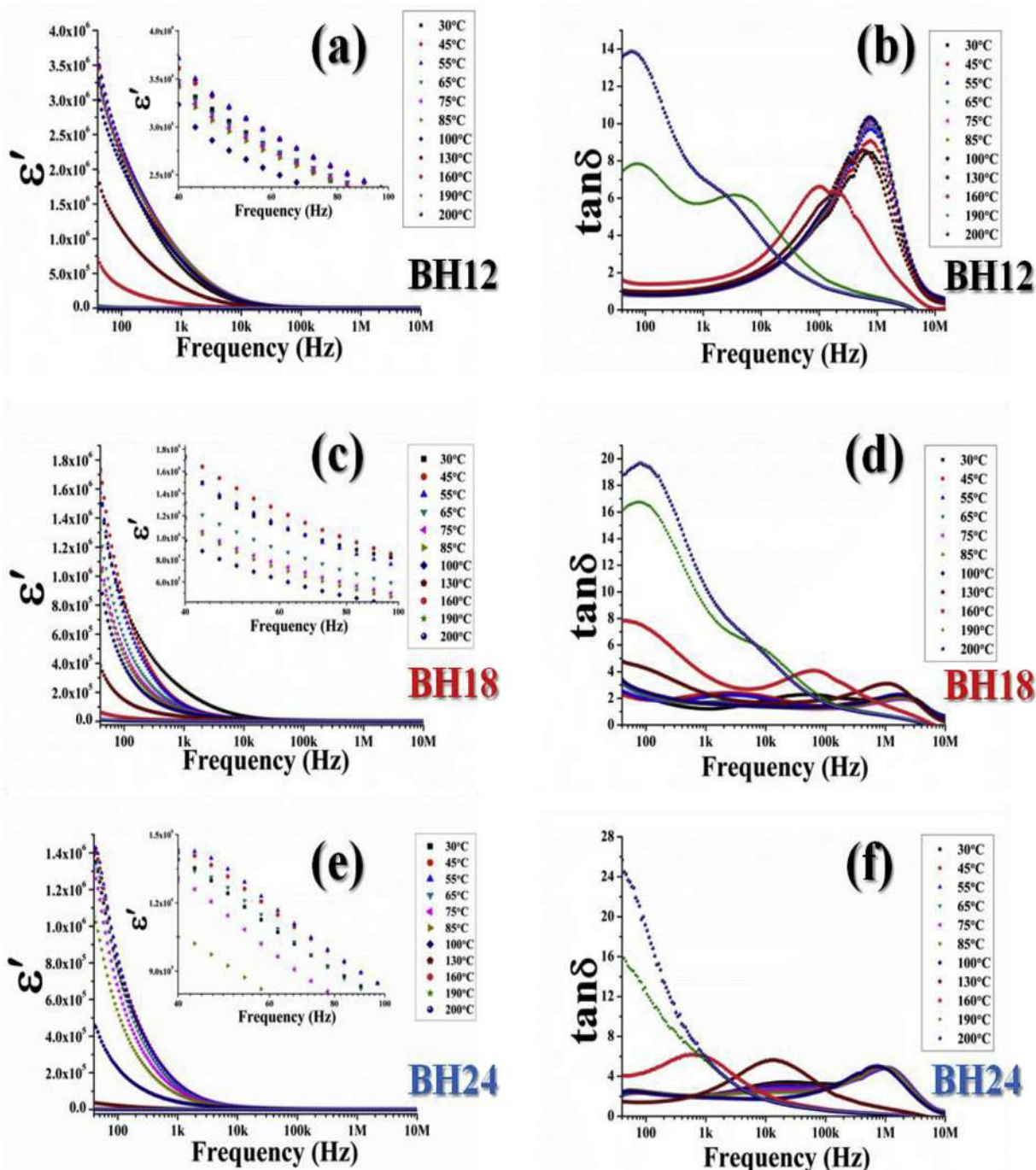
Fig. 8. Variation of Dielectric constant with frequency for the samples (a) BH12, (c) BH18, (e). BH24 and tangent loss (tanδ) of the samples (b) BH12, (d) BH18, (f) BH24.

addition, from the temperature dependent dielectric plots of our samples (Fig. 9 (a–c)), it could be noticed that in the case of BH12 the value of dielectric constant remains almost stable and quite high up to 110 °C which might be beneficial for making high capacity storage devices.

Fig. 10(a–c) shows the dependence of ac conductivity of the samples with frequency at different temperatures. We obtain low values and almost frequency independent ac conductivities for all

the samples at lower frequency region of the applied field. Below 10^4 Hz frequency highly resistive grain boundary restricts hopping mechanism of the free charge carriers [34]. But in a higher frequency domain, charge carriers become more energetic and their hopping frequency increases, which results in enhancement of ac conductivity toward high-frequency region [35]. Similar findings were reported by S. Das et al. [29]. In the case of BH12, when measuring temperature reaches above the room temperature ac
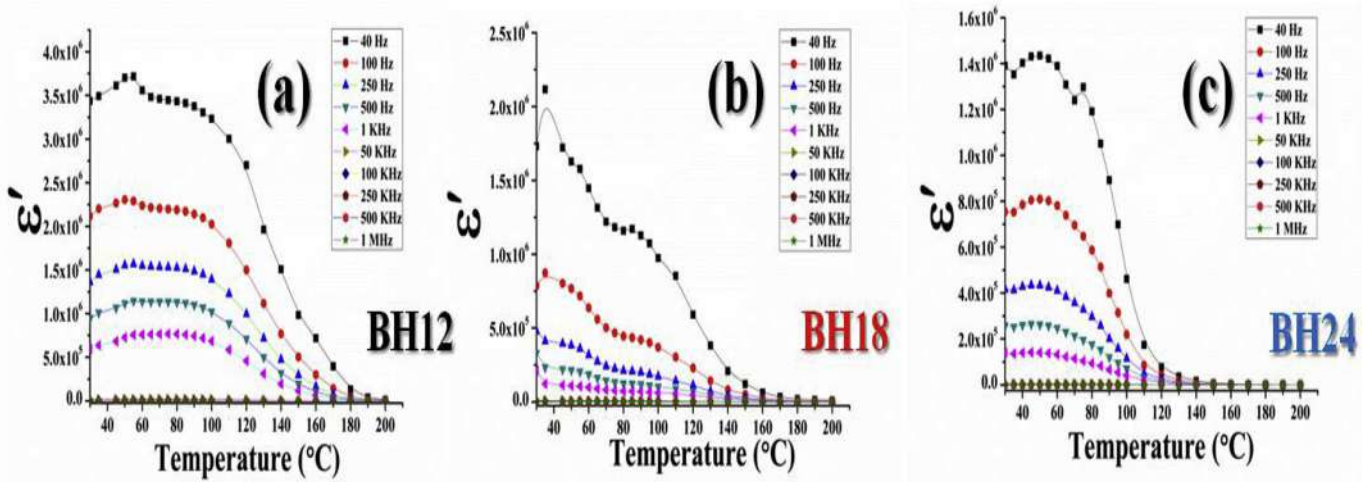
Fig. 9. Variation of Dielectric constant with temperature for the samples (a) BH12, (b) BH18 and (c) BH24.
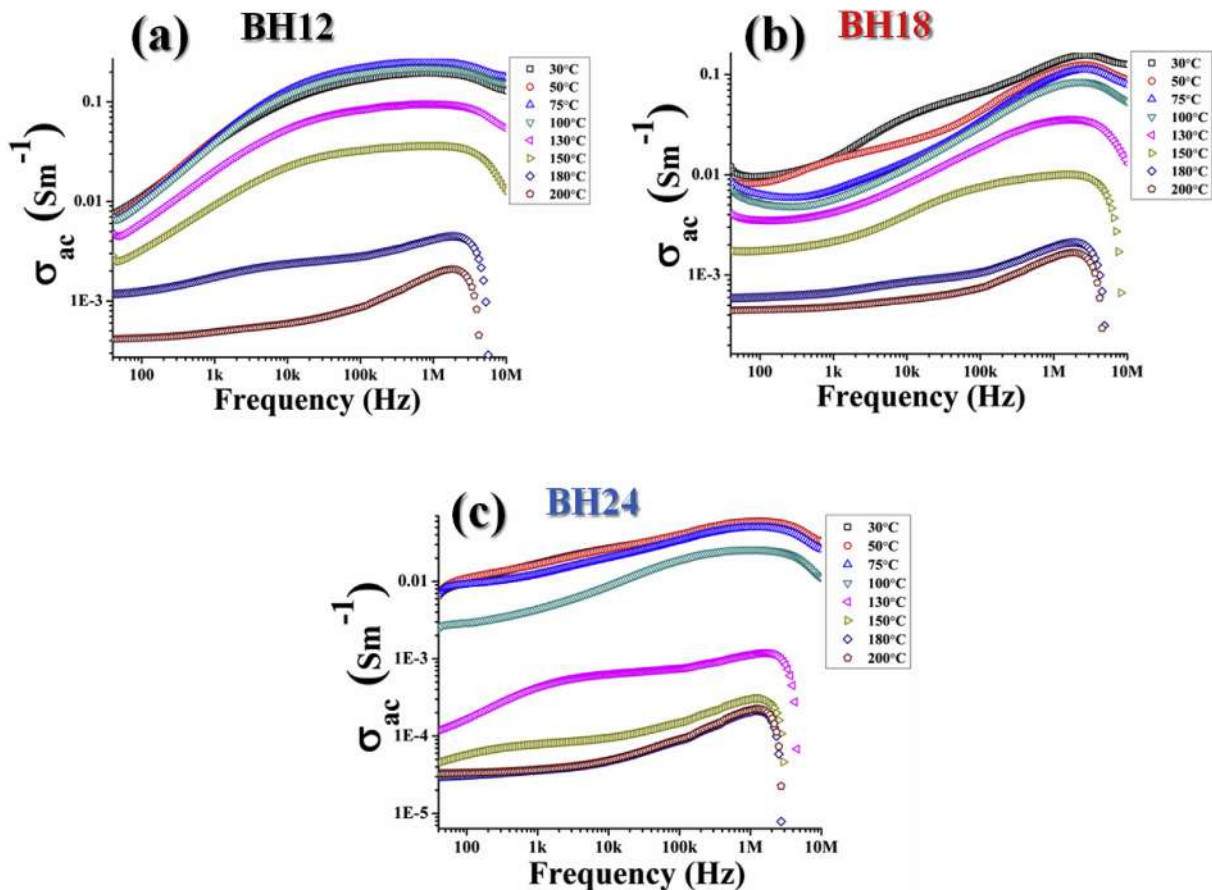
Fig. 10. Variation of ac electrical conductivity with frequency for the samples (a) BH12, (b) BH18, (c) BH24.
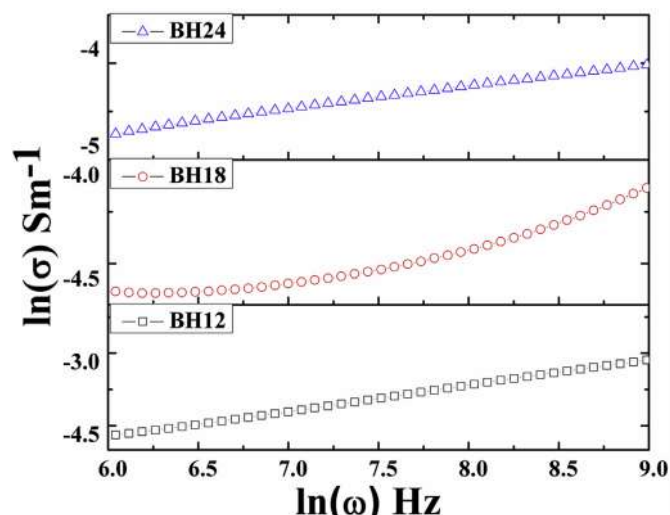
Fig. 11. Jonscher's plot for the samples BH12, BH18 and BH24.

conductivity gets increased and beyond 75°C, it starts to fall down again. This actually occurred due to the hopping mechanism of released free charge carriers within the grain due to the introduction of cationic/anionic vacancy defects. For other two samples, the ac conductivity falls down with the increasing temperature. However, when the temperature of the sample increases, it causes a transition from γ-boehmite to γ*- boehmite, which has more oxygen vacancies than that of γ-boehmite [36]. Thus, the trapping of free charge carriers at the defect zones restricts the hopping mechanism and hence as a consequence a decrease in ac conductivity can be observed. Dependence of ac conductivity on frequency is also studied through Jonscher's universal power law [37].

$$\sigma_{ac} = B\omega^n \qquad (4)$$

where 'B' and 'n' are constants. B has the units of conductivity and n is dimensionless. In the present work, the nonzero value of 'n' refers to the frequency dependent conduction mechanism [38]. The exponent 'n' has been calculated for each sample by plotting $\ln\sigma$ vs $\ln\omega$, shown in Fig. 11 The estimated values of the 'n' are found to vary between 0.4499 and 0.1875 (Table 3) which indicates that our samples are not perfectly Debye type (where n = 0) [39] and diffusion limited hopping involves the conduction phenomenon

[40]. Now to execute the hopping mechanism, charge carriers need activation energy to jump over a potential barrier. It can be estimated from the Arrhenius equation [39].

$$\sigma = \sigma_0 \exp(-E_a/K_B T) \qquad (5)$$

Here, σ_0 is the pre-exponential factor; E_a is the activation energy for conduction. Arrhenius plots were obtained from the conductivity data calculated at frequencies 100 Hz, 100 kHz and 1 MHz of the applied electric field and have been presented in Fig. 12(a−c). The activation energy is found to increase with the increasing frequency which is due to the increasing hopping mechanism of free carriers. A detailed description of activation energies of our samples is given in Table 3 . Therefore, it can be concluded that the crystal defects, more specifically, the crystallinity of the samples play an important role in all the electrical measurements.

4. Conclusion

This article, for the first time, reports the crystallinity driven optical and electrical properties of boehmite nanoparticles. Time-varied facile hydrothermal synthesis makes our synthesis procedure simple and cost effective which could be further useable in industries. Our boehmite samples have been characterized with the help of XRD, FESEM, TEM and FTIR. XRD data which confirms the orthorhombic phase as well as nanocrystallite sizes varying from 2.2 nm (BH12) to 4.9 nm (BH24). Lattice parameters are also being calculated using Bragg's law which depicts a directional growth with increasing hydrothermal reaction time. The morphological characteristics of the synthesized samples have been investigated using FESEM. The FESEM micrographs show spherical structures with nearly equal size for BH12 and BH18 samples although, an admixture of cubic and spherical particles is observed for BH24 sample. To further investigate the particle sizes we have employed TEM characterization. The particle sizes estimated from TEM shows that the BH12 sample has an average particle size of 3.19 nm whereas; BH18 and BH24 have the mean sizes of 4.10 and 4.82 nm respectively. These mean particle sizes are quite close to the values estimated from XRD data. Spherical morphology has been obtained in the case of our BH12 sample whereas, mixture of nanocubes along with the nanospheres have been seen in our TEM micrographs of BH18 and BH24. The nucleation and self assembly of synthesized boehmite nanoparticles has been illustrated and a qualitative discussion has also been given to establish the growth mechanism. Optical band gap for our samples has been measured from UV−Vis study where higher crystalline nanoparticles possess
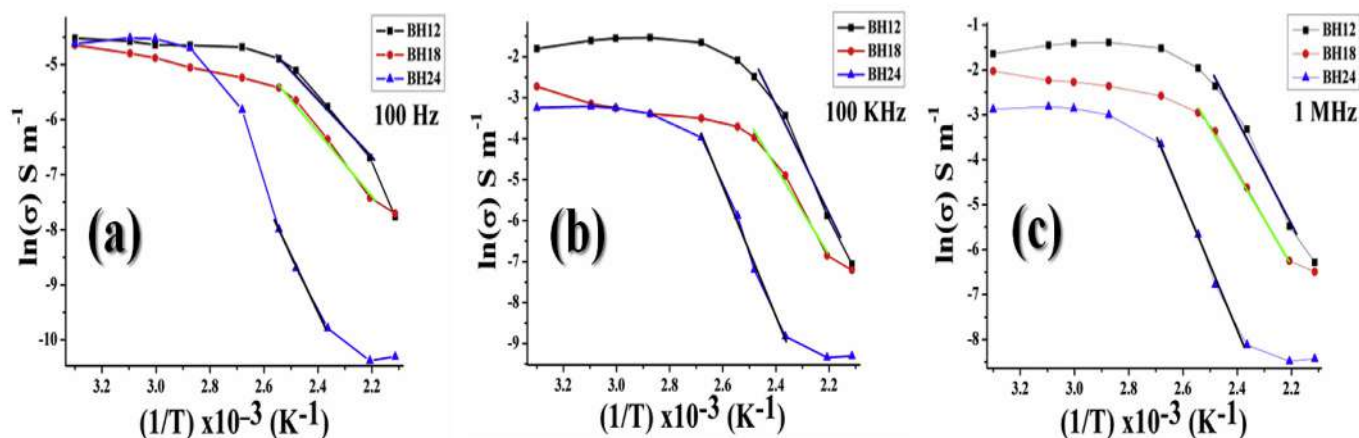
Fig. 12. Arrhenius plots for the samples (a) 100 Hz, (b) 100 KHz and (c) 1 MHz.

lower band gap values. The enhancement in the PL intensity of the larger nanostructures of boehmite indicates its optically active nature which has been further analyzed. We have observed a high emission in the blue and green region of the spectrum of our samples which makes our samples potential candidates for bio-imaging and bio-sensing applications. Here crystallinity plays a pivotal role in determining the electrical characteristics of the three boehmite nanostructures. The sample of lower crystalline nature exhibits high values of dielectric and ac conductivity with a minimal dielectric loss. Additionally, temperature-dependent variation of real part of the dielectric permittivity and ac conductivity of our samples are described here. The salient features of these materials lie in their remarkably high dielectric constant with a nominal dielectric loss which empowers it to serve as the potential separator material for supercapacitors and other energy harvesting devices.

Acknowledgment

References

[1] G. Mendoza-Damián, F. Tzompantzi, R. Pérez-Hernández, R. Gómez, A. Hernández-Gordillo, Photocatalytic properties of boehmite–SnO2composites for the degradation of phenol, Catal. Today 266 (2016) 82–89.

[2] Y. Hu, Z.L. Wang, Recent progress in piezoelectric nanogenerators as a sustainable power source in self-powered systems and active sensors, Nano Energy 14 (2015) 3–14.

[3] G. Li, Y. Liu, D. Liu, L. Liu, C. Liu, Synthesis of flower-like Boehmite (AlOOH) via a simple solvothermal process without surfactant, Mater. Res. Bull. 45 (2010) 1487–1491.

[4] Y. Liu, D. Ma, X. Han, X. Bao, W. Frandsen, D. Wang, D. Su, Hydrothermal synthesis of microscale boehmite and gamma nanoleaves alumina, Mater. Lett. 62 (2008) 1297–1301.

[5] G. Štefanić, S. Musić, Microstructural analysis of boehmite nanoparticles prepared by rapid hydrolysis of aluminum sec-butoxide, Croat. Chem. Acta 84 (2011) 481–485.

[6] S. Musić, O. Dragčević, S. Popovic, Hydrothermal crystallization of boehmite from freshly precipitated aluminium hydroxide, Mater. Lett. 40 (1999) 269–274.

[7] X. Bai, G. Caputo, Z. Hao, V.T. Freitas, J. Zhang, R.L. Longo, O.L. Malta, R.A.S. Ferreira, N. Pinna, Efficient and tuneable photoluminescent boehmite hybrid nanoplates lacking metal activator centres for single-phase white LEDs, Nat. Commun. 5 (2014) 5702.

[8] Y. Mathieu, B. Lebeau, V. Valtchev, Control of the morphology and particle size of boehmite nanoparticles synthesized under hydrothermal conditions, Langmuir 23 (2007) 9435–9442.

[9] S. Das, S. Das, D. Das, S. Sutradhar, Tailoring of room temperature ferromagnetism and electrical properties in ZnO by Co (3d) and Gd (4f) element co doping, J. Alloys Compd. 691 (2017) 739–749.

[10] S. Das, S. Das, S. Sutradhar, Enhanced dielectric behavior and ac electrical response in Gd- Mn-ZnO nanoparticles, J. Alloys Compd. 726 (2017) 11–21.

[11] K.V. Sankar, S. Shanmugapriya, S. Surendran, S.C. Jun, R.K. Selvan, Facile hydrothermal synthesis of carbon-coated cobalt ferrite spherical nanoparticles as a potential negative electrode for flexible supercapattery, J. Colloid Interface Sci. 513 (2018) 480–488.

[12] Y. Asakura, Y. Inaguma, K. Ueda, Y. Masubuchi, S. Yin, Synthesis of gallium oxynitride nanoparticles through hydrothermal reaction in the presence of acetylene black and their photocatalytic NOx decomposition, Nanoscale 10 (2018) 1837.

[13] N.K.V. Nadimpalli, R. Bandyopadhyaya, V. Runkana, Thermodynamic analysis of hydrothermal synthesis of nanoparticles, Fluid Phase Equil. 456 (2018) 33–45.

[14] A.A. Kokorina, E.S. Prikhozhdenko, N.V. Tarakina, A.V. Sapelkin, G.B. Sukhorukov, I.Y. Goryacheva, Dispersion of optical and structural properties in gel column separated carbon nanoparticles, Carbon 127 (2018) 541–547.

[15] H. Huang, L. Wang, Y. Cai, C. Zhou, Y. Yuan, X. Zhang, H. Wana, G. Guan, Facile

[16] fabrication of urchin-like hollow boehmite and alumina microspheres with a hierarchical structure via Triton X-100 assisted hydrothermal synthesis, CrystEngComm 17 (2015) 1318.

[16] P. Raybaud, M. Digne, R. Iftimie, W. Wellens, P. Euzen, H. Toulhoat, Morphology and surface properties of boehmite (γ-AlOOH): a density functional theory study, J. Catal. 201 (2001) 236–246.

[17] S. Das, S. Das, A. Roychowdhury, D. Das, S. Sutradhar, Effect of Gd doping concentration and sintering temperature on structural, optical, dielectric and magnetic properties of hydrothermally synthesized ZnO nanostructure, J. Alloys Compd. 708 (2017) 231–246.

[18] A. Zirehpour, A. Rahimpour, F. Seyedpour, M. Jahanshahi, Developing new CTA/CA- based membrane containing hydrophilic nanoparticles to enhance the forward osmosis desalination, Desalination 371 (2015) 46–57.

[19] W. Brostow, T. Datashvili, Chemical modification and characterization of boehmite particle, Chem. Chem. Technol. 2 (2008) 27–32.

[20] Z. Wu, Q. Zhuo, T. Sun, Z. Wang, Mechanical properties of epoxy resins reinforced with synthetic boehmite (AlOOH) nanosheets, J. Appl. Polym. Sci. (2015) 41409.

[21] Y. Hakuta, H. Ura, H. Hayashi, K. Arai, Effects of hydrothermal synthetic conditions on the particle size of γ-AlO(OH) in sub and supercritical water using a flow reaction system, Mater. Chem. Phys. 93 (2005) 466–472.

[22] D. Panias, P. Asimidis, I. Paspaliaris, Solubility of boehmite in concentrated sodium hydroxide solutions: model development and assessment, Hydrometallurgy 59 (2001) 15–29.

[23] D.K. Chanda, P.S. Das, A. Samanta, A. Dey, A.K. Mandal, K.D. Gupta, T. Maitya, A.K. Mukhopadhyay, Intertwined nanopetal assembly of Mg(OH)2 powders, Ceram. Int. 40 (2014) 11411–11417.

[24] D.K. Chanda, A. Samanta, A. Dey, P.S. Das, A.K. Mukhopadhyay, Nanoflower, nanoplatelet and nanocapsule Mg(OH)2 powders for adsorption of CO2 gas, J. Mater. Sci. (2017), https://doi.org/10.1007/s10853-016-0728-4.

[25] D. Panias, P. Asimidis, I. Paspaliaris, Solubility of boehmite in concentrated sodium hydroxide solutions: model development and assessment, Hydrometallurgy 59 (2001) 15–29.

[26] A. Alemi, Z. Hosseinpour, M. Dolatyari, A. Bakhtiari, Boehmite (γ-AlOOH) nanoparticles:Hydrothermal synthesis, characterization, pH-controlled morphologies, optical properties, and DFT calculations, Phys. Status Solidi B 249 (2012) 1264–1270.

[27] Z.Q. Yua, C.X. Wanga, X.T. Gub, C. Li, Photoluminescent properties of boehmite whisker prepared by sol-gel process, J. Lumin. 106 (2004) 153–157.

[28] K. Okabe, N. Inada, C. Gota, Y. Harada, T. Funatsu, S. Uchiyama, Intracellular temperature mapping with a fluorescent polymeric thermometer and fluorescence lifetime imaging microscopy, Nat. Commun. 3 (2012) 705–714.

[29] S. Das, S. Das, S. Sutradhar, Effect of Gd3+ and Al3+ on optical and dielectric properties of ZnO nanoparticle prepared by two step hydrothermal method, Ceram. Int. 43 (2017) 6932–6941.

[30] J. Liu, C.G. Duan, W.G. Yin, W.N. Mei, R.W. Smith, J.R. Hardy, Phys. Rev. B 70 (2004) 144106.

[31a] C.G. Koops, On the dispersion of resistivity and dielectric constant of some semiconductors at audiofrequencies, Phys. Rev. 83 (1951) 121.

[31b] L. Singh, W. Kim, B.C. Sin, K.D. Mandal, U.S. Rai, A. Ullah, H. Chung, Y. Lee, Dielectric studies of a nano-crystalline CaCu2.90Zn0.10Ti4O12 electroceramic by one pot glycine assisted synthesis from inexpensive TiO2for energy storage capacitors, RSC Adv. 4 (2014) 52770–52784.

[31c] P.K. Ghosh, M.K. Mitra, K.K. Chattopadhyay, ZnS nanobelts grown in a polymer matrix by chemical bath deposition, Nanotechnology 16 (2005) 107–112.

[32] K. Tsuji, H. Su Han, S. Guillemet-Fritschc, C.A. Randall, Dielectric relaxation and localized electron hopping in colossal dielectric (Nb,In)-doped TiO2 rutile nanoceramics, Phys. Chem. Chem. Phys. 19 (2017) 8568.

[33] Y. Rao, S. Ogitani, P. Kohl, C.P. Wong, Novel polymer–ceramic nanocomposite based on high dielectric constant epoxy formula for embedded capacitor application, J. Appl. Polym. Sci. 83 (2002) 1084–1090.

[34] W. Ling, L. Hongxia, J. Peihai, W. Tinga, L. Lizhu, The effects of TiC@AlOOH core–shell nanoparticles on the dielectric properties of PVDF based nanocomposites, RSC Adv. 6 (2016) 25015.

[35] S. Kabashima, T. Kawakubo, High frequency conductivity of NiO, J. Phys. Soc. Jpn. 24 (1968) 493–497.

[36] J.A. Wang, X. Bokhimi, A. Morales, O. Novaro, T. López, R. Gómez, Aluminum local environment and defects in the crystalline structure of sol-gel alumina catalyst, J. Phys. Chem. B 103 (1999) 299–303.

[37] A.K. Jonscher, A new understanding of the dielectric relaxation of solids, J. Mater. Sci. 16 (1981) 2037–2060.

[38] S.R. Majid, A.K. Arof, Electrical behavior of proton-conducting chitosan-phosphoric acid- based electrolytes, Physica B 390 (2007) 209–215.

[39] L.K. Sudha, S. Roy, K. Uma Rao, Evaluation of activation energy (Ea) profiles of nanostructured alumina polycarbonate composite insulation materials, Int. J. Mach. Mach. Mater. 2 (2014) 96–100.

[40] S.K. Saha, M.A. Rahman, M.R.H. Sarkar, M. Shahjahan, M.K.R. Khan, Effect of Co doping on structural, optical, electrical and thermal properties of nanostructured ZnO thin films, J. Semiconduct. 36 (2015), 033004.

CrystEngComm

Effects of various morphologies on the optical and electrical properties of boehmite nanostructures†

Shubham Roy, [ID][a] Anupam Maity,[ab] Paulami Mandal, [ID][a] Dipak Kr. Chanda, [ID][cd] Kunal Pal,[e] Souravi Bardhan[a] and Sukhen Das [ID] *[a]

The present article reports three different grain morphologies of boehmite nanoparticles: spherical (EBH), needle-shaped (UBH) and flower-like (HBH). EBH possesses the highest surface area, whereas HBH has the lowest. A novel synthesis route for spherical (EBH) boehmite nanostructures using ethylenediamine has been reported here. Moreover, we have compared the growth mechanisms and morphology-dependent changes in the optical and electrical properties of the three samples. The band gap energies were evaluated to be 5.30 eV, 5.44 and 5.87 eV for EBH, UBH and HBH, respectively. Strong photoluminescence (PL) emission for all the nanostructures, the highest for HBH, was noted. The lowest surface area of HBH provides a surface with fewer defects; this seals the possibility of energy loss *via* non-radiative recombination of electrons and holes, which enhances the PL intensity. The dielectric constants for EBH, UBH and HBH are 1.49×10^6, 1.14×10^5, and 7.14×10^4, respectively. Variations in the dielectric loss tangents and temperature-dependent electrical properties of the three morphologies were evaluated in support. Also, the ac conductivity and impedance analyses are in good accordance with our dielectric analysis. The present investigation may be highly beneficial in developing biosensors, bio-imaging, and fabricating cost-effective energy storage devices.

1. Introduction

Recent developments in the fields of nanotechnology and nanoscience have introduced potentially significant nanostructured materials with promising applications in the fields of electronics, pharmaceutics, catalysis, energy storage and medical science.[1–5] Nanocrystals possess unique physicochemical properties due to their nano-sized dimensions, which actually enhance their surface-to-volume ratios.[7] Current challenges in the synthesis of nanomaterials essentially include morphological control by controlling different reaction parameters, such as the pH of the reaction, incorporated capping agents, temperature, and reaction duration. Self-assembly of nanostructured building blocks has also attracted

significant interest in materials synthesis and device fabrication.[6] However, during the self-assembly, the crystalline lattice planes can be almost perfectly aligned or dislocated at the contact areas between the adjacent particles, where the latter leads to defects in the finally formed product[6] and the former produces a different morphology.[8,9] In progressive structures, a hierarchical nano-architecture assembled from nanoscale units provides higher functionality and performance due to these defects. Thus, self-assembly has become an important approach for the fabrication of nanostructures with various morphologies. For example, hierarchical ZnO and MnO₂, featherlike BaWO₄, 3D dendritic CuO and Fe₂O₃, and dandelion-like CuO and ZnO nanostructures have been successfully prepared, and various aspects of their application are now well established.[10,11]

Among various alumina phases, boehmite (γ-AlOOH), which is a non-toxic oxy-hydroxide aluminum compound, possesses a high surface area[12] and catalytic properties; thus, it is a significant precursor for the manufacturing of advanced catalysts,[13a] coatings and fillers in membranes.[14] Due to its significant biocompatibility, another important area of interest is the use of boehmite as an orthopedic or a dental material.[15] In recent decades, considerable efforts have been focused on the synthesis of boehmite nanostructures.[16a,b] Previous reports illustrate the syntheses of various morphologies of boehmite nanostructures, such as nanoparticles,

[a] *Department of Physics, Jadavpur University, S.C. Mullick Road, Kolkata-700032, India. E-mail: sdasphysics@gmail.com; Tel: +91 9433091337*
[b] *School of Materials Science, Indian Association for the Cultivation of Science, Kolkata-700032, India*
[c] *Advanced Materials and Mechanical Characterization Division, CSIR-Central Glass and Ceramics Research Institute, Kolkata-700032, India*
[d] *School of Materials Science and Nano Technology, Jadavpur University, Kolkata-700032, India*
[e] *Department of Life Science and Biotechnology, Jadavpur University, Kolkata-700032, India*
† Electronic supplementary information (ESI) available. See DOI: 10.1039/c8ce01171k

nanofibers, nanopetals, nanobelts, nanotubes and flowerlike 3D nano-architectures.[17,18a] However, to date, a very limited amount of interest has been shown in understanding the electrical and optical properties of boehmite nanostructures in detail, which has restricted their efficient application in the fields of energy storage, biosensing and bioimaging.

In our present study, we have introduced a new synthesis route of boehmite nanostructures using ethylenediamine as a starting material in addition to two other conventional synthesis procedures. Our investigation specifically focuses on understanding the optical and electrical properties of three different morphologies, spherical (EBH), needle-shaped (UBH) and flower-like (HBH) boehmite nanostructures, along with adopting novel synthesis procedures and characterizing different morphologies. We have examined the impedance properties of these three nanostructures by varying the temperature, which in turn reveals the contribution of conductive and non-conductive grain boundaries in detail. This elementary analysis supports Maxwell–Wagner's dielectric polarization model, which is the backbone of this study. The impedance analysis also provides a basic idea of the conduction mechanisms of these samples. This is the first time that we have successfully analyzed and interpreted the dielectric and impedance properties of boehmite nanostructures with various morphologies in a detailed manner. Moreover, our present comparative investigation revealed high dielectric constants with very low tangent losses and commendable photoluminescence intensities of our three samples; thus, they are suitable for fabricating energy storage devices and biosensors.

2. Experimental section

2.1. Materials

Aluminum nitrate nonahydrate $[Al(NO_3)_3 \cdot 9H_2O]$, extra pure urea crystals $[CH_4N_2O]$ and ethylenediamine $[C_2H_8N_2]$ were purchased from Merck, India. Hexamine (99% extra pure) was purchased from Loba Chemie Pvt. Ltd. All the reagents were used without further purification. Millipore water with a resistivity of at least 18 MΩ cm was used throughout the experiments. All glassware used in our experiments was cleaned with aqua regia solution followed by rinsing with ultrapure water.

2.2. Synthesis of nanostructures

Different morphological nanostructures of γ-AlOOH were prepared by a hydrothermal route. In a typical experiment,[18b,c] 0.1 M aluminum nitrate nanohydrate was dissolved in Millipore water using a magnetic stirrer to form a clear and transparent solution. The transparency of the solution indicates the formation of Al^{3+} ions. Later, this solution was basified using different precursors to achieve different nanostructures of boehmite. The entire solution was then divided into three different parts, namely part-A, part-B and part-C.

Ethylenediamine was added dropwise to the part-A solution, which resulted in a thick white precipitate. Ethyl-

enediamine was added until the pH of the solution reached 9.[27d] The use of ethylenediamine to obtain spherical boehmite nanoparticles is adopted for the first time here in our work. The white solution was left under stirring conditions for another 3 h.

Part-B was treated with hexamine powder[18b] under the same stirring conditions, maintaining a pH value of 5, to achieve the nucleation of nano-needles of boehmite.

Powdered urea crystals[18c] were added to the part-C solution under vigorous stirring, and the pH was adjusted to 7 to start the nucleation of flower-like boehmite.

All three treated solutions were then transferred into three different Teflon-lined stainless steel autoclaves and maintained in a dust-free oven at 160 °C for 16 h. After completion of the hydrothermal reaction, the autoclaves were allowed to cool naturally to room temperature; white precipitates were obtained in every case, which indicates the formation of boehmite nanoparticles. The hydrothermally treated part-A sample was found to have a spherical nanostructure and was named EBH, whereas part-B and part-C had nano-needle and nanoflower forms, respectively, and were correspondingly named HBH and UBH. The precipitates were collected by centrifugation at 10 000 RPM for 10 minutes, washed several times with distilled water and then dried under vacuum for 24 h to develop dry powders[18d] of the various morphologies. The samples were then marked and used for further characterization.

2.3. Material characterization

The XRD patterns of all the samples were recorded using a powder X-ray diffractometer (Model D8, BRUKER AXS) with Cu-Kα radiation (λ = 1.5405 Å) in the range of 2θ from 10° to 80°. The scan speed was set at 0.02 with a tube voltage of 35 kV and 35 mA. The Fourier transform infrared spectroscopy study was performed using a Shimadzu FTIR-8400S in the wavenumber range from 400 cm^{-1} to 4000 cm^{-1}. A total of 60 individual scans were merged together to evaluate the final spectra of each sample. The synthesized samples were mixed with KBr in a ratio of 1 : 50 to perform the FT-IR analysis. An INSPECT F50 field emission scanning electron microscope (FESEM) (FEI, Netherlands) was employed for the morphological studies. A minute amount of powder was placed in a carbon-coated grid to perform the FESEM and EDX analyses. The accelerating voltage of the electron gun was set between 10 and 20 kV and the magnification was set between 50 000× and 100 000× for our samples. The EDX analyses of the synthesized samples were investigated on a Supra 55 (ZEISS). The TEM characterization of EBH, UBH and HBH was performed using a Jeol 2000 FX transmission electron microscope. Small amounts of samples were first dissolved in HPLC-grade acetone and then ultra-sonicated for 2 h to form homogenous solutions. The solutions were then casted dropwise on carbon-coated copper grids (300 mesh) and then dried under ultra high vacuum for further analysis. Surface area measurements of the samples were performed by the

Brunauer–Emmett–Teller (BET) method using N_2 gas adsorption–desorption. A twin surface area analyzer (Quantachrome Instruments, USA) was employed for this purpose. The pore size distributions were evaluated from the BJH (Barrer–Joyner–Halenda) calculations of the desorption isotherms. The degassing temperature was set at 90 °C for all the samples. The boehmite samples were dissolved in spectroscopic grade ethanol at 1 mg ml^{-1} concentration to perform the spectroscopic studies. Ultraviolet visible spectra (UV-vis) of the samples were recorded using a Perkin Elmer Lambda-365 spectrophotometer. The photoluminescence spectroscopy studies were performed using a Cary Eclipse fluorescence spectrophotometer, Agilent Technologies, with an excitation wavelength (λ_{ex}) of 389 nm. Dielectric measurements, electrical conduction mechanisms and impedance measurements were performed using an Agilent 4294A precision impedance analyzer. The bias voltage was set at 500 mV throughout the experiments.

3. Results and discussion

3.1. Structural and morphological analysis

To characterize the three boehmite nanostructures, XRD analysis was performed. Fig. 1 demonstrates the XRD patterns of our entire sample set, *i.e.* EBH, HBH and UBH. The formation of orthorhombic γ-AlOOH phases of all the samples is indicated by the XRD peaks, which are well matched with JCPDS card no. 21-1307. The absence of unwanted peaks in the XRD data reveals the high purity of the samples. Also, in our XRD data, no extra peak was observed due to unreacted Al(OH)$_3$ or any other alumina phases, implying complete transformation of the entire Al(OH)$_3$ precursor into γ-AlOOH after the hydrothermal treatment. Moreover, our whole sample set possesses sharp diffraction peaks corresponding to the (020) plane, indicating that the growth units of the γ-AlOOH nano structures are abundant along the (020) plane. The nano-crystallite diameters of the different nano-

structures of γ-AlOOH have been estimated using the Debye–Scherrer equation:[19]
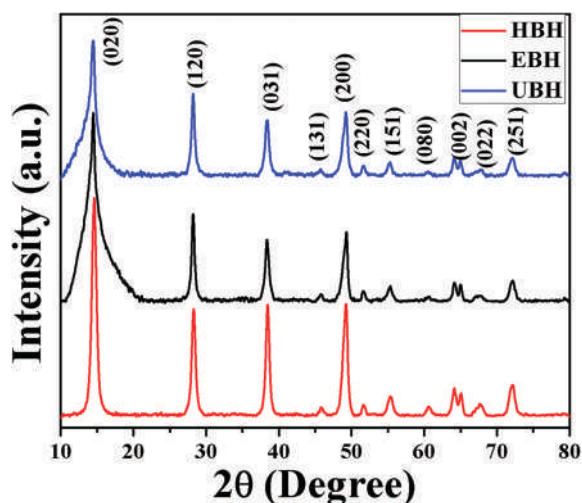
$$\langle D \rangle_{020} = 0.9\lambda/(\beta_{1/2} \cos \theta) \tag{1}$$

here, D is the average crystallite size, λ is the wavelength of the incident X-ray beam, θ is the corresponding Braggs angle, and $\beta_{1/2}$ is the full width at half maximum (FWHM) of the (020) peak. It can be shown by the Debye–Scherrer equation that the average crystallite size of γ-AlOOH varies from 4.868 nm (EBH) to 11.012 nm (HBH) depending on the different morphologies and different reaction phenomena. The lattice parameters of the synthesized γ-AlOOH nanostructures were calculated using the Braggs equation and are presented in Table 1.

The FT-IR spectra of γ-AlOOH with different nanostructures are presented in Fig. 2. The absorption bands observed at 3286, 3090, 1640, 1159, 889, 758 and 629 cm^{-1} are in good agreement with values reported in the literature,[13a] confirming the formation of γ-AlOOH nano-structures. The peak at 1385 cm^{-1} is attributed to stretching vibrations of the nitrate.[20] Two strong bands located at 3286 and 3090 cm^{-1} are due to the asymmetric vibrations of (Al)O–H and the symmetric (Al)O–H stretching vibrations, respectively.[21] The bands located at 1071 and 1159 cm^{-1} are attributed to the v_{sym}Al–O–H and v_{asym}Al–O–H modes of boehmite, respectively.[13a] The stretching of Si–O and –OH deformation linked to aluminum ions are also observed in the spectra at 1016 and 953 cm^{-1}.[13b] The torsional modes at 758 and 634 cm^{-1} of boehmite are also observed in our samples, which are due to AlO$_6$ vibrations.[13a] The band at around 1640 cm^{-1} can be assigned to the stretching mode of surface-adsorbed moisture.[6] Therefore, our FTIR analysis is quite consistent with the XRD results, revealing the formation of boehmite crystalline phases.

To further support the characterization of our three synthesized samples, FESEM and EDX studies were also performed. Different morphologies of the synthesized γ-AlOOH nanostructures were examined by FESEM micrographs (Fig. 3). It can be observed from Fig. 3(a) that EBH possesses a nearly spherical morphology. Due to the small size of the EBH nanoparticles, this sample has the highest amount of cohesive force between the grains, which may be the reason for the high agglomeration in EBH. Earlier reports suggested that when the pH of the reaction is very high, no particle formation occurs, probably due to the high solubility of γ-AlOOH particles at high

Fig. 1 XRD patterns of the EBH, UBH and HBH samples.

Table 1 Structural parameters of the different boehmite samples calculated from XRD data: nanocrystallite sizes (D), full widths at half maximum (FWHM) and lattice parameters (a, b, c)

Sample	D (nm)	FWHM (rad)	a (Å)	b (Å)	c (Å)
UBH	7.275	0.0192	3.6993	12.2253	2.8679
HBH	11.012	0.0127	3.6966	12.1212	2.8634
EBH	4.868	0.0287	3.6924	12.2389	2.8668
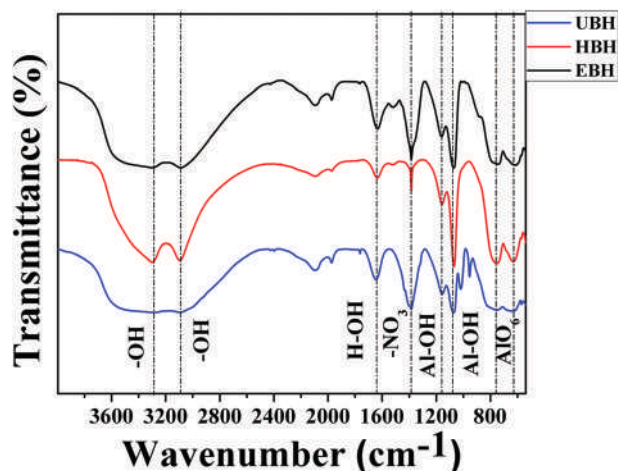
Fig. 2 FTIR spectra of the EBH, UBH and HBH samples.

pH.[22,23] However, we obtained boehmite particles at a higher pH value of 9 (for EBH) by a surfactant-free hydrothermal technique.

Fig. 3(b) reveals that the use of hexamine in the aluminum nitrate precursor at pH 5 results in nano-needles (HBH) of boehmite. Moreover, some of the needles stick together to form hierarchical structures of boehmite.

The nano-flower morphology (UBH) of boehmite was obtained using urea as a precursor material and is depicted in Fig. 3(c).

The micrograph demonstrates an equal distribution of nano-flowers with an average length and breadth of nearly 600 and 400 nm, respectively. The high resolution image (Fig. SD2†) shows surface roughness, indicating the aggregation of smaller particles to form the hierarchical nano-

flower structure of boehmite. This image also depicts that the nano-flowers consist of thin nano-petals linked together side by side. Each nano-petal has a thickness of 15 to 20 nm.

EDX measurements revealed the elemental constituents of the different nanostructures of γ-AlOOH (Fig. 3(d–f)). The EDX spectra of the different morphologies of boehmite confirm the presence of aluminium and oxygen, which further confirms the purity of our samples.

TEM micrographs (Fig. 4) allowed us to determine the sizes and the morphologies of the nano-structured samples in greater detail. In the TEM image of EBH, spherical particles are observed. The high resolution image of EBH depicts perfect spherical particles with a size range of 9 to 10 nm. Nano-needles are observed in the TEM images of the HBH sample, with an average length and breadth of 45 to 50 nm and 8 to 10 nm, respectively. The TEM image of UBH shows the agglomeration of nanorods and nanoneedles to form a hierarchical nano-flower architecture.

3.2. Surface areas and pore size distributions of the synthesized nanostructures

The data corresponding to the nitrogen (N_2) adsorption–desorption isotherms and the corresponding pore size distributions are shown in Fig. 5(a and b) for the γ-AlOOH nanopowders with different morphologies. For a given sample, the volumes of adsorbed and desorbed N_2 are very similar to each other, as shown in Fig. 5a. The type IV isotherms suggest the presence of mesopores[24,25] in our samples. H4-type hysteresis loops were observed for all of our boehmite nanostructures, indicating the formation of narrow slit-like pores.[24,25] EBH and HBH nanopowders possess average
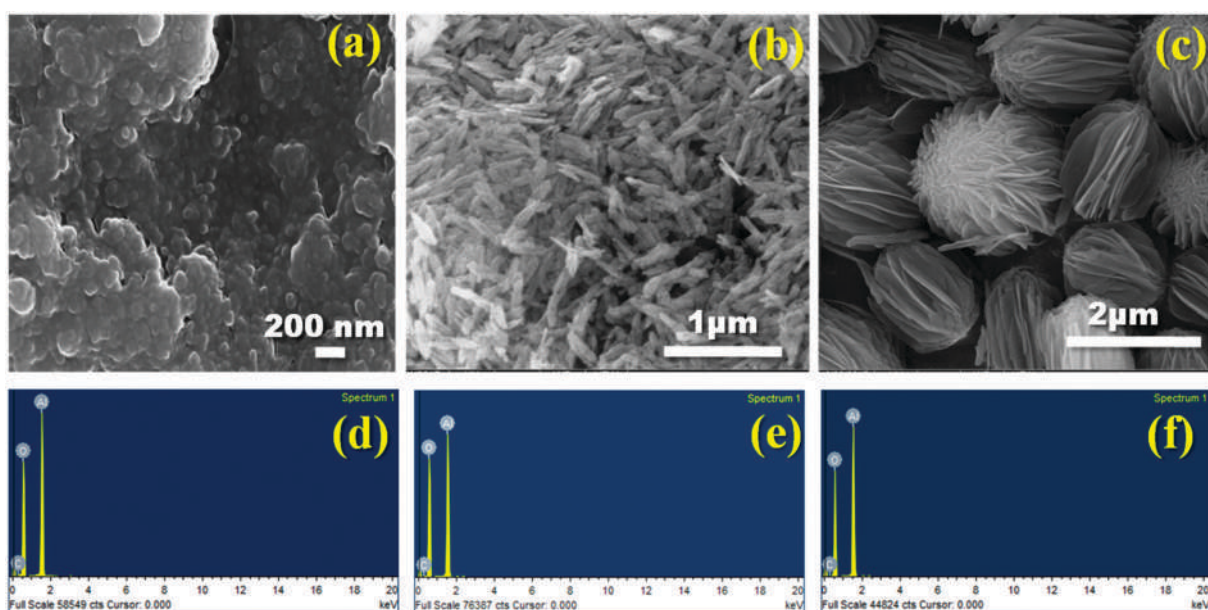
Fig. 3 FESEM images of the (a) EBH, (b) UBH, and (c) HBH samples and elemental analysis (EDX) of the (d) EBH, (e) UBH, and (f) HBH samples.
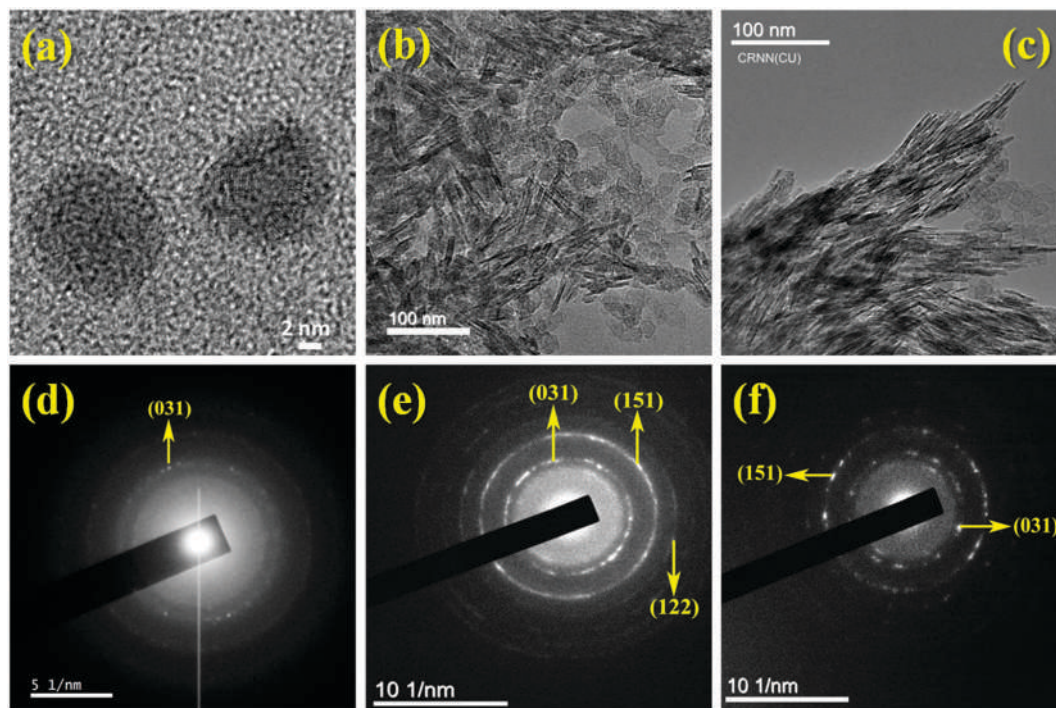
Fig. 4 TEM micrographs (a–c) and SAED (d–f) patterns of EBH, UBH and HBH.
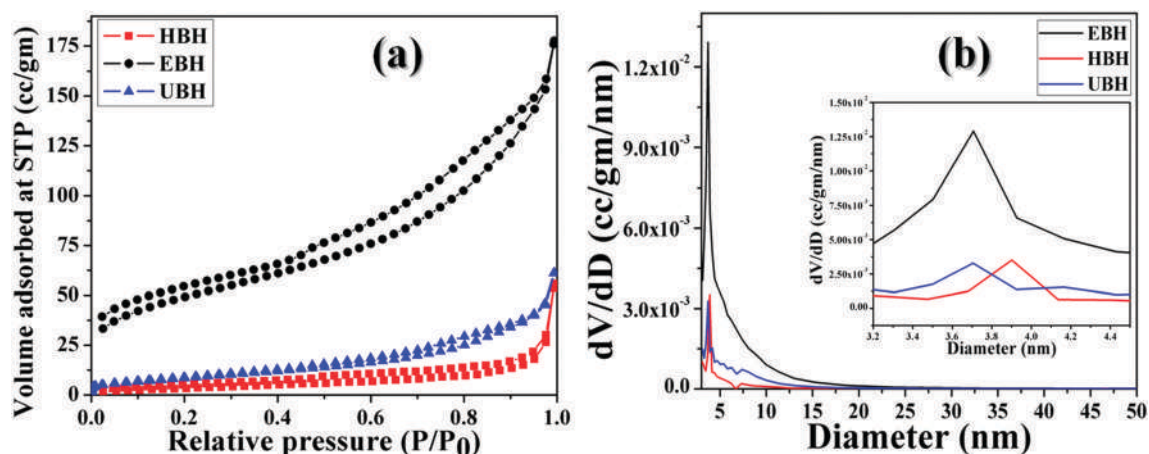
Fig. 5 (a) N$_2$ adsorption/desorption isotherms and (b) pore size distribution data for the different boehmite nanostructures.

mesopores sizes of ~3.9 and 3.8 nm, respectively, while UBH has mesopores ~3.7 nm in size (Fig. 5b).

The average Brunauer–Emmett–Teller (BET) surface areas of the EBH, HBH and UBH powders were evaluated to be 176.8, 12.81 and 31.64 m^2 g^{-1}, respectively (Table 2).

Table 2 Estimated BET surface area, pore radius and pore volume data of the different boehmite samples

Sample name	Surface area (m^2 g^{-1})	Pore size (nm)	Pore volume (cc g^{-1})
HBH	12.81	3.9	8.628×10^{-2}
EBH	176.8	3.8	2.746×10^{-1}
UBH	31.64	3.7	9.486×10^{-2}

3.3. Qualitative model for the formation of different nano-architectures of boehmite

Based on the results obtained from XRD, FT-IR and FESEM studies of the boehmite samples with different morphologies (Fig. 6(a–r)), here, we propose formation mechanisms of the self-assembled nanoparticles (Fig. 6(a–f)), nano-needles (Fig. 6(g–l)) and nano-flowers (Fig. 6(m–r)). There are three stages in the formation of a nanostructure. These are nucleation, growth, and self-assembly to produce different morphologies.[26,27a]

Initially, dissolution of aluminum nitrate salt in water produces [Al(H$_2$O)$_6$]$^{3+}$ ions, which further transform into [Al(H$_2$O)$_5$OH]$^{2+}$ due to hydrolysis of the O–H bonds. This 'olation' reaction also forms an extra proton (H$^+$), which
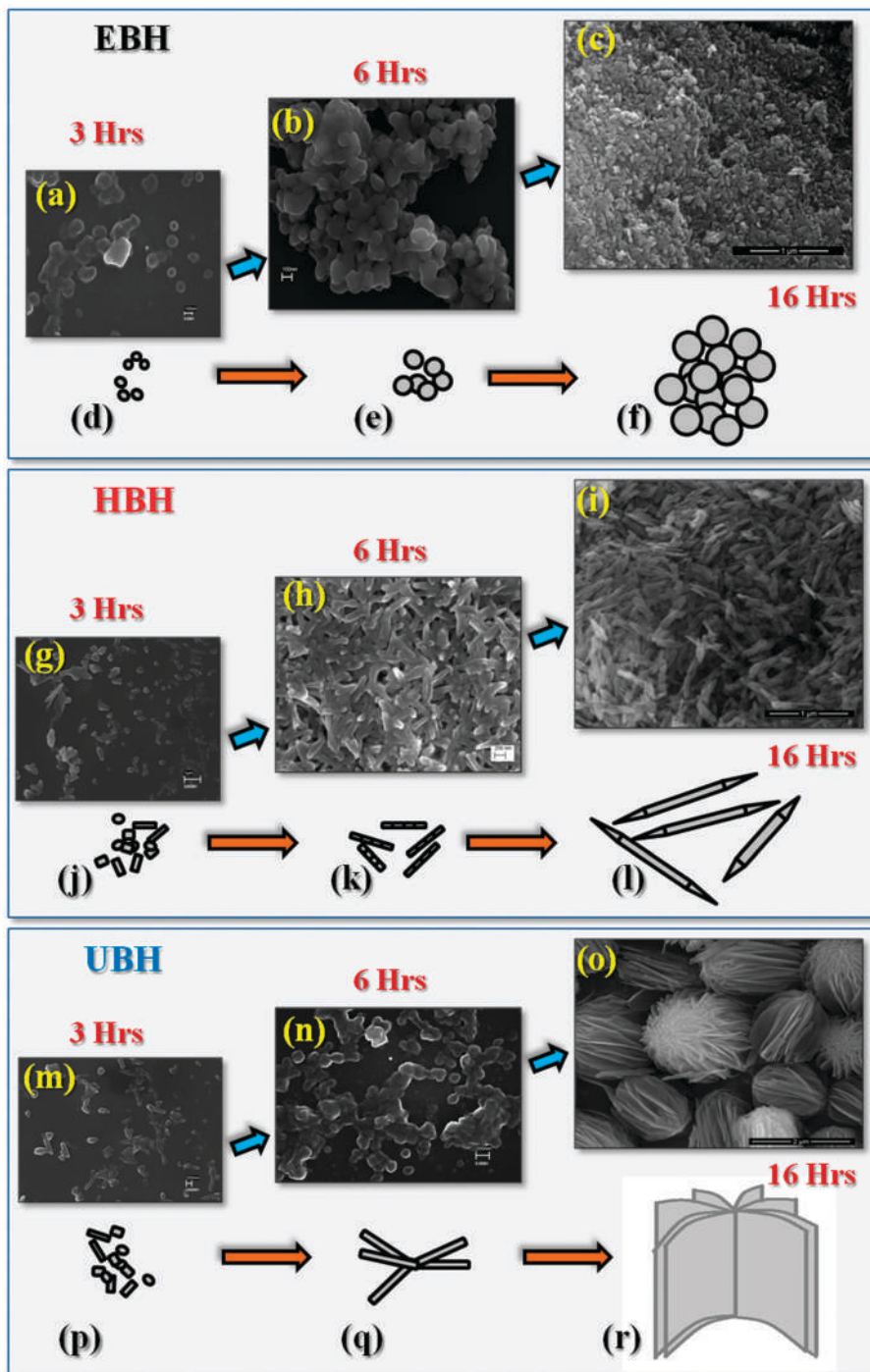
Fig. 6 Mechanisms of formation of the different boehmite nano-architectures.

decreases the pH level of the solution to 2 from neutral pH. As the amine/amide (R–NH$_2$)-containing precursor is added to the solution, this proton is 'accepted' by the amine/amide-containing reagent, which results in R–NH$_3^+$.[27b] After accepting the proton, the pH of the solution increases rapidly; this leads to the Ostwald ripening process,[16a] forming aluminum hydroxide Al(OH)$_3$ as a white precipitate. The R–NH$_3^+$ ions are basic in nature and are further adsorbed by the [Al(H$_2$O)$_5$OH]$^{2+}$ ions. Here, the pH level of the solution is

an indicator of this adsorption mechanism. A higher pH level indicates a higher amount of R–NH$_3^+$ ion adsorption.

$$Al(NO_3)_3 + H_2O \rightarrow [Al(H_2O)_6]^{3+}$$

$$[Al(H_2O)_6]^{3+} \rightarrow [Al(H_2O)_5OH]^{2+} + H^+$$
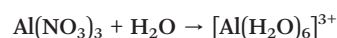
Smaller amines, such as ethylenediamine,[27c,d] have relatively shorter chain lengths. In this case, adsorption takes place rapidly, even at ambient pressure and temperature; this results in the formation of $Al(OH)_3$ at a high pH value of 9. Nonlinear amines/amides, such as hexamine and urea, have relatively complex structures with longer non-linear chains. This complexity results in lower adsorption and less or no precipitation during the nucleation.[27h] The pH levels are also low in the cases of these two basifying agents, which corroborates our proposed nucleation mechanism.

Under typical hydrothermal conditions, $Al(OH)_3$ releases one water molecule at high pressure and temperature, which results in the formation of γ-AlOOH.

$$Al(OH)_3 - H_2O \rightarrow AlOOH$$
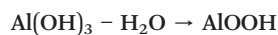
In summary, here in our study, we used three different basifying agents, ethylenediamine, hexamine and urea, in our reactions; these not only acted as 'pH controllers' but also delivered three different morphologies depending upon their chemical structures. Being the simplest amine, ethylenediamine produced a spherical morphology. This happened due to the fact that in a hydrothermal environment, EBH undergoes no preferential growth. Therefore, at higher pressure and temperature, $Al(OH)_3$ not only eliminates a water molecule from its structure but also creates a spherical structure.

Although there is less precipitation due to insufficient adsorption of $R-NH_3^+$ ions, after the hydrothermal reaction, HBH consists of a thick white precipitate of boehmite nano-needles. Under hydrothermal conditions, $R-NH_3^+$ adsorption into the precursor nuclei began and water elimination took place simultaneously, resulting in preferential growth of the HBH sample.[27e] This phenomenon was supported by our FESEM and XRD data (Fig. SD2(b)†).

Urea has internal covalent bonds which will not split into ions in a water medium. Instead, there will be a large number of associations between water molecules and urea[27f] via hydrogen bonds. When the hydrothermal ageing begins, the presence of a strong cationic environment and excess pressure creates rod-like structures[27i,j] as the electronegative part (C=O group) of urea chelates with the aluminum ions, resulting in unidirectional growth. Here, urea acts as a capping agent. During the hydrothermal ageing, the nano-rods become more agglomerated and form nano-petals, undergoing preferential growth. Next, these nano-petals are superposed on each other to form localized self-assemblies of nano-flowers.[27g]

In our case, different boehmite nanostructures were developed at different pH values. Previous literature reported that at lower pH values, the probability of nano-needle/nanorod formation is quite high, but at higher pH values, nano-spheres are formed. This phenomenon is quite analogous to our case. We achieved nanoneedles of boehmite at pH 5, whereas nanospheres were formed at pH 9.

The time-varied FT-IR data of the different morphologies suggest that the aluminium hydroxide precursor and other mixed alumina phases are totally converted to boehmite after completion of the hydrothermal reaction, thereby establishing the purity of our final products.

3.4. Optical and spectroscopic studies

UV-vis absorption spectroscopy is another useful tool to characterize both organic and inorganic materials. In our investigation, we employed this technique in the evaluation of the band gap energies of the three morphologies of boehmite nano-structures. The absorption spectra of the boehmite nanostructures with different morphologies are displayed in Fig. 7(a). It is apparent from Fig. 7(a) that the spectrum of HBH contains a broad absorption band at 226 nm, whereas for UBH and EBH, the absorption peaks are located at 214 and 213 nm, respectively; this indicates a prominent blue shift of the absorption band position for the three samples with increasing particle size.

Next, the corresponding band gaps of the boehmite nanostructures were evaluated from the absorption band positions using the following Tauc plot relation:[29]

$$\alpha E = A(E - E_g)^n \tag{2}$$

where E and E_g are the photon energy and the optical band gap energy in eV, respectively. The other two terms, α and A, are the absorption coefficient and a constant term, respectively. From the Tauc plot (Fig. 7(b)), the band gap energy is estimated by extrapolating the linear region of the curve to the energy axis. The calculated values of the band gap energies for EBH, UBH and HBH are 5.30 eV, 5.44 and 5.87 eV, respectively, showing that the band gap increases with increasing particle size.

In addition to characterization, in order to explore the optical quality of our nano-materials, we used photoluminescence spectroscopy. Fig. 7(c) shows the photoluminescence spectra of the synthesized boehmite nanostructures with different morphologies at an excitation wavelength of 389 nm. From the figure, four sharp and strong emission bands at about 438, 461, 486 and 530 nm are apparent. A broad band is also visible at 668 nm. The luminescence peak centered at 486 nm (2.55 eV) can be assigned to hydroxyl groups bound to surface aluminum (Al–OH) centers.[30] The peak positions in the emission spectra of our samples are not strongly dependent on the morphology of the samples. However, the PL emission intensities of the boehmite samples with three different morphologies are different under identical conditions. The needle-like HBH has the highest emission intensity, while the spherical EBH exhibits the lowest intensity. In general, the surface area of materials increases as the size decreases. Herein, the surface area of HBH is smaller than those of EBH and UBH (obtained from BET analysis). The structure of the EBH sample has a greatly increased surface area. The large surface area introduces a large number of 'defects' into the
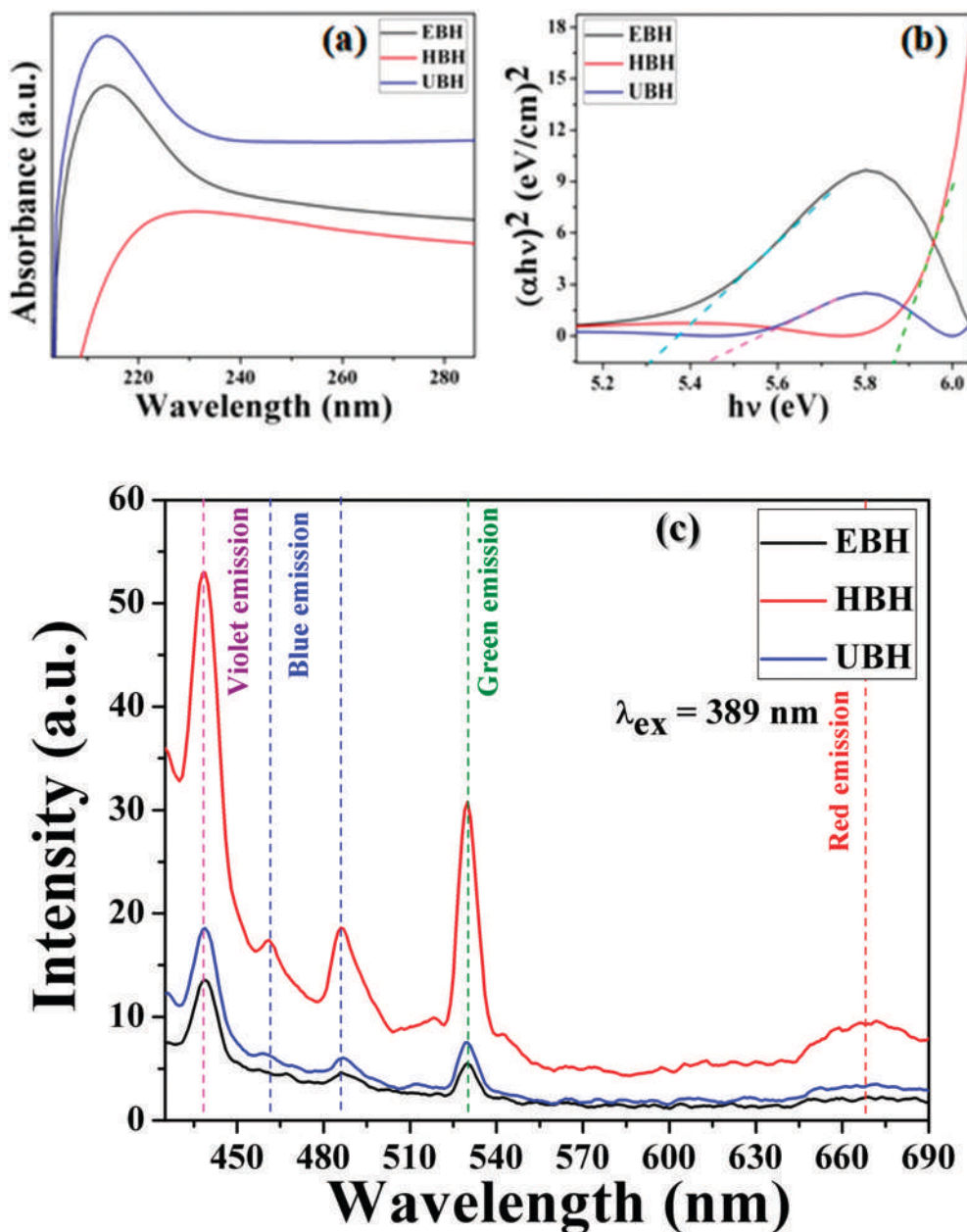
Fig. 7 (a) UV-vis spectra and (b) Tauc plots for band gap analysis of the samples. (c) Photoluminescence spectra of EBH, UBH and HBH.

crystal. In general, defects are introduced in a crystal during its growth. In our investigation, the crystal defects were introduced during the hydrothermal reaction process due to dislocation and imperfection of the alignments in two neighboring crystals. Morphology plays a pivotal role in mediating such defect states. During the crystal growth and alignment process, different morphologies initiate different defect densities. These defects decrease the PL intensity because they provide non-radiative recombination for electrons and holes,[31,32] which may be the reason for the lowest relative emission intensity of EBH. However, as the surface area of a material is decreased, the surface contains fewer defects, leading to PL intensity enhancement;[31] this may cause the highest PL intensity of HBH.

3.5. Investigation of dielectric permittivity and tangent loss

Dielectric studies were performed on our three morphologies to evaluate the dielectric permittivities and tangent losses of our synthesized nanostructures. The dielectric properties of materials depend on many parameters, such as the frequency of the applied electric field, temperature, chemical composition, and grain size. The dielectric response of a material can be described using the relation

$$\varepsilon = \varepsilon' + j\varepsilon'' \tag{3}$$

where ε' and ε'' are the real and imaginary part of the relative dielectric constant, respectively. The real part of the dielectric

constant (ε') contributes to the amount of energy stored in the material due to polarization effects, whereas the imaginary part (ε'') is associated with the dissipation of energy within the material. The real part of the dielectric constant can be calculated using the relation

$$\varepsilon' = (C \cdot d)/(\varepsilon_0 A) \tag{4}$$

where C is the capacitance of the sample, d and A are thickness and surface area of the sample, respectively, and ε_0 is the permittivity of free space (8.85×10^{-12} F m^{-1}). Variations of the real part of the dielectric constant (ε') with applied field frequency (ranging from 40 Hz to 10 MHz) for all the samples at different temperatures (from 30 °C to 190 °C) are shown in Fig. 8(a–c).

At lower frequencies, high dielectric values were observed; this is due to the Maxwell–Wagner interfacial polarization effect,[19–29] which obeys Koop's theory.[33] After a certain frequency, the real part of the dielectric constant falls off gradually.

Generally, a dielectric medium consists of conducting grains that are separated by non-conducting grain bound-aries which were formed during the hydrothermal reaction process.[34] At lower frequencies, the effects of these grain boundaries are more dominant. Free charge carriers trapped in these grain boundaries result in dipoles, producing a polarization effect.[35,36] Oscillating dipoles can easily follow the external field at lower frequencies; however, in high frequency domains, the dipoles cannot withstand rapid changes in the applied frequency, which causes a gradual decrease in the dielectric values for our entire sample set. The variations of the dielectric loss tangents of our samples are in good agreement with the high dielectric values (Fig. 8(g–i)). In the low frequency region and at low temperature, the losses are low for the all samples, resulting in high values of the dielectric constant. In contrast, high losses at low frequency and higher temperatures were observed for our samples. At higher temperature, γ-AlOOH is converted into γ*-AlOOH, which contains more oxygen vacancies in its structure.[37] These crystal defects contribute to higher values of the loss tangent in a low-frequency domain and at high temperature. At lower temperatures and at high frequency, the high value of the loss tangent indicates a mismatch of the
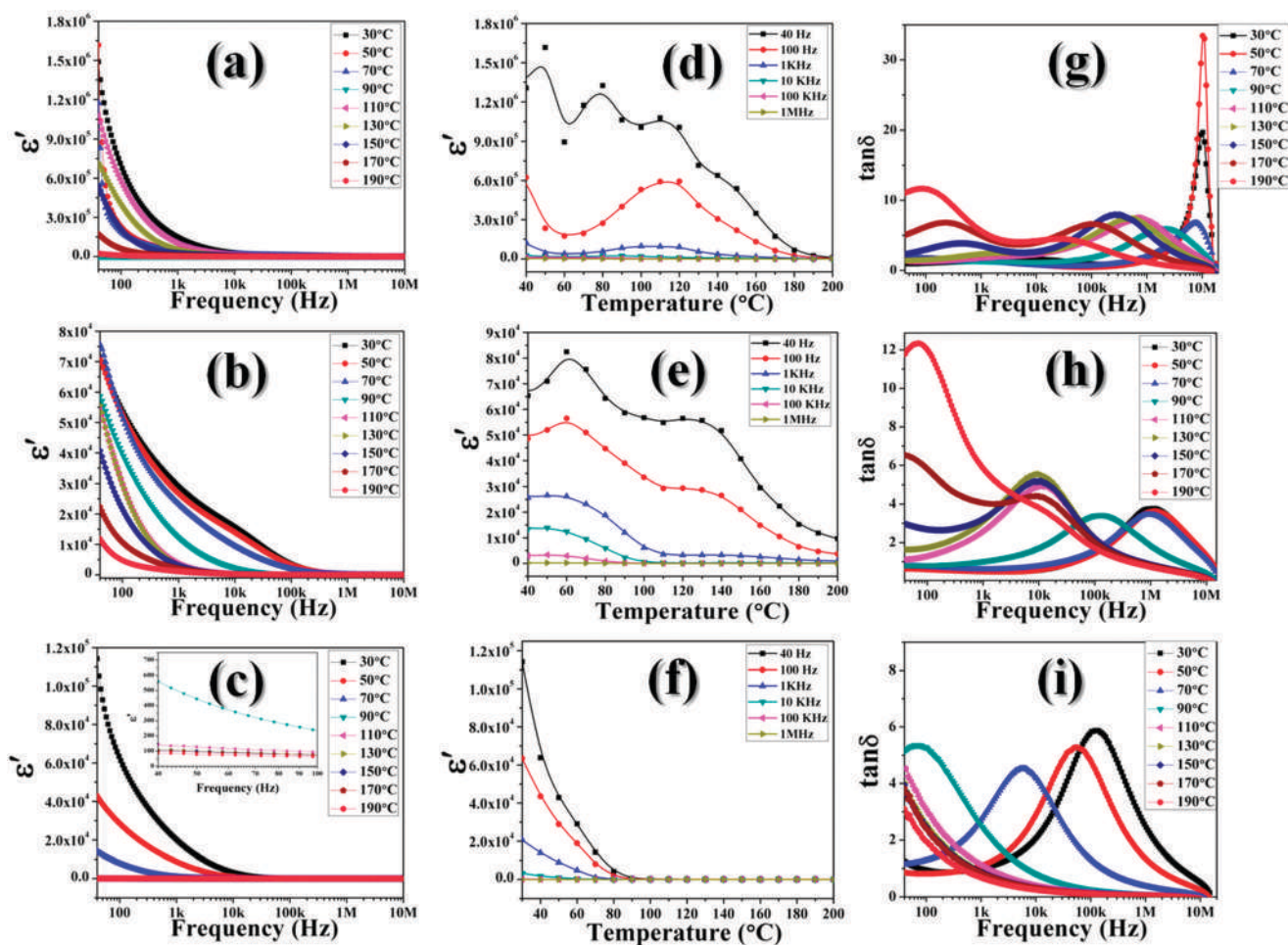
Fig. 8 Variation of the dielectric constants with frequency (a–c), temperature (d–f) and tangent loss (g–i) for the EBH, HBH and UBH samples, respectively.

external field frequency with the frequency of the oscillating nano-dipoles, which is also reflected in the real part of the dielectric values (ε') for the sample set.

From the dielectric measurement data, we calculated the dielectric constants for the total sample set. At room temperature and 40 Hz frequency, the dielectric constants for the three samples EBH, UBH and HBH were found to be 1.49×10^6, 1.14×10^5, and 7.14×10^4, respectively. As mentioned previously, EBH has the highest surface-to-volume ratio (from BET analysis), indicating that the num-

ber of dipoles per unit volume is also the highest for EBH. This may be the key reason that EBH possesses the highest dielectric properties among the three morphologies. Conversely, HBH has the lowest surface-to-volume ratio, which justifies its lowest dielectric response among the three samples.

In order to obtain an idea of the changes in dielectric behavior with temperature, we also plotted temperature response graphs (Fig. 8(d–f)) for the real parts of the dielectric constant for the different morphologies. From the graph, it
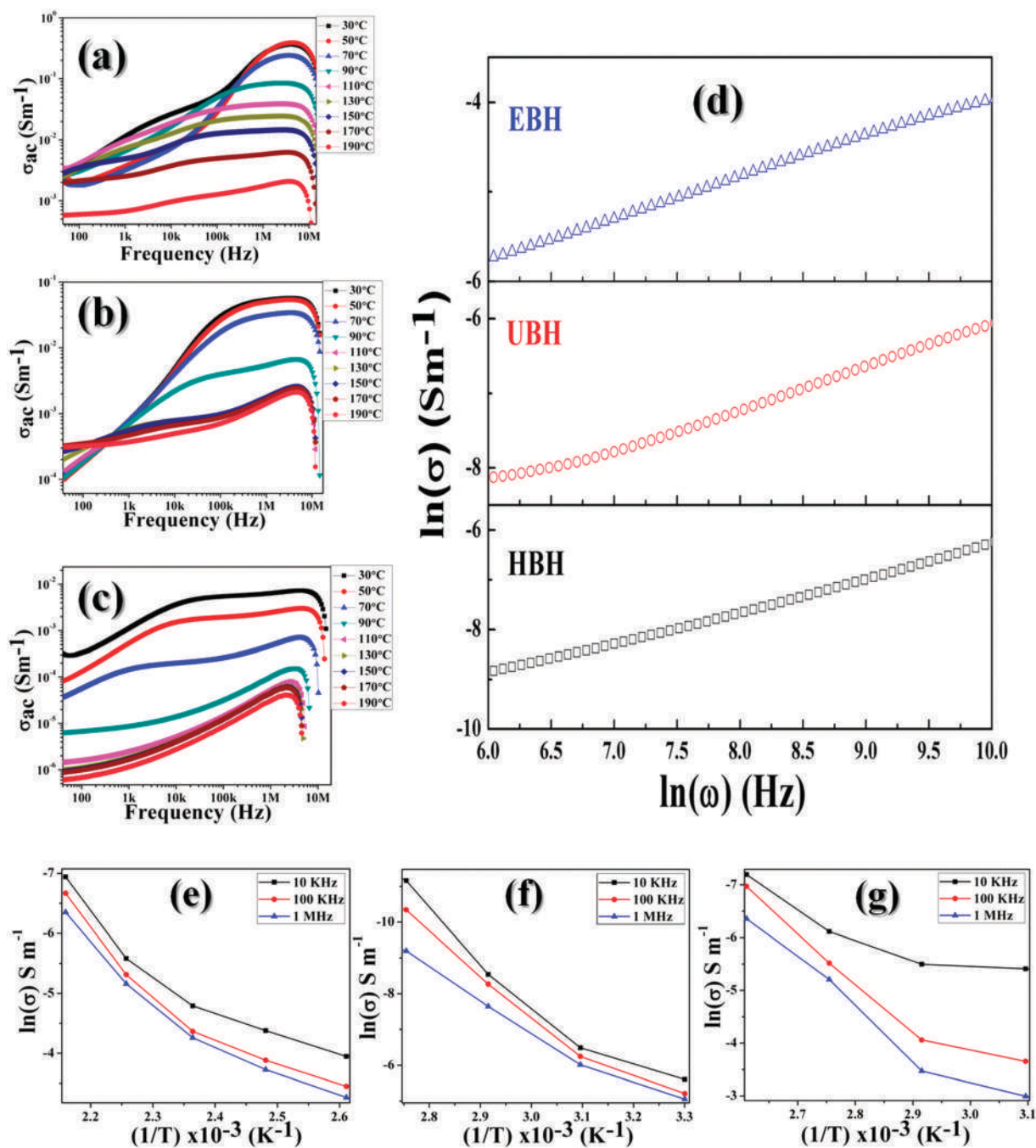
Fig. 9 Variation of the ac electrical conductivity with frequency for the (a) EBH, (b) UBH, and (c) HBH samples and (d) Jonscher's plots for the samples. Arrhenius plots for the (e) EBH, (f) UBH, and (g) HBH samples in different frequency domains.

Table 3 Calculated activation energies from the Arrhenius plots for the different morphological distributions of boehmite nanostructures

Sample	Frequency	Activation energy (eV)
UBH	10 kHz	1.2565
	100 kHz	1.0374
	1 MHz	0.5551
HBH	10 kHz	0.4742
	100 kHz	0.8367
	1 MHz	0.8788
EBH	10 kHz	0.8734
	100 kHz	0.9691
	1 MHz	0.8839

can be observed that for HBH, the dielectric constant rapidly decreases with the initial temperature (30 °C). In contrast, for both EBH and UBH, the dielectric constants were found to decrease slowly from 130 °C. At lower temperatures, the energy of the nano-dipoles is not sufficient to overcome the inter-dipolar frictional force, leading to the high dielectric values of our samples in this temperature range. Thus, our

investigation reveals that dielectric behavior depends upon the surface morphology for the three nano γ-AlOOH derivatives.

3.6. Ac conductivity studies

To further explore the electrical conductivity of the three nanostructures, we performed ac conductivity studies. Fig. 9(a–c) displays the dependence of ac conductivity of γ-AlOOH of the different morphologies on frequency at different temperatures. In the low frequency domain of the applied field, low values and a frequency-independent nature of the ac conductivity for all the samples was observed. Below 10 kHz frequency, the highly resistive grain boundary restricts the hopping mechanism of the free charge carriers.[19] When the external field approaches the high frequency region, the electrons become more energetic and their mobility increases, which results in enhancement of the ac conductivity. Beyond 5 MHz frequency, the value of the ac conductivity decreases sharply due to the transformation of
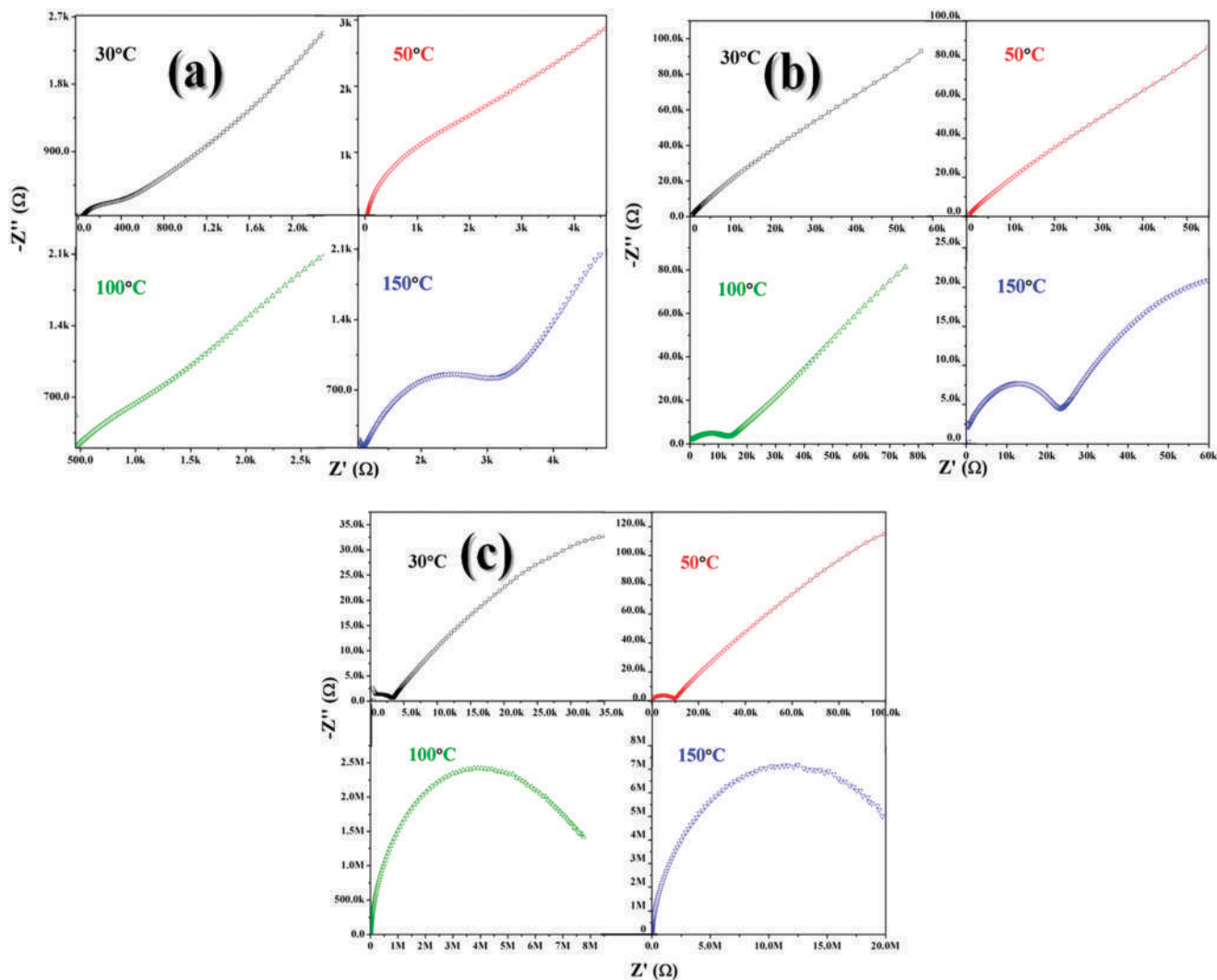
Fig. 10 Nyquist plots for the (a) EBH, (b) UBH and (c) HBH samples.

γ-AlOOH into γ*-AlOOH; it has more interstitial defects trapping free charge carriers during the hopping mechanism, leading to the sharp decreases in ac conductivity in the high frequency region.[37]

The frequency response of ac conductivity was also studied through Jonscher's power law,[38]

$$\sigma_{ac} = B\omega^n \qquad (5)$$

where 'B' and 'n' are constants. B has the unit of conductivity, and n is a dimensionless constant. The value of 'n' was estimated for each sample by plotting $\ln\sigma$ vs. $\ln\omega$ followed by applying eqn (5) above, as shown in Fig. 9(d). The estimated values of 'n' in our case were found to vary between 0.4709 and 0.6487, which indicates that our samples are not perfectly Debye type (where $n = 0$)[39] and diffusion-limited hopping is involved in the conduction phenomenon.[40] The charge carriers require activation energy to overcome the potential barrier to initiate the charge hopping mechanism, resulting in higher conduction. This can be calculated from the Arrhenius equation.[39]

$$\sigma = \sigma_0 \exp(-E_a/K_B T) \qquad (6)$$

where σ_0 is the pre-exponential factor, E_a is the activation energy, K_B is the Boltzmann constant and T is the absolute temperature. Arrhenius plots were obtained from the conductivity data calculated at frequencies of 100 Hz, 100 kHz and 1 MHz of the applied external field and are shown in Fig. 9(e–g). A detailed description of the activation energies is given in Table 3.

Our results indicate that the morphology plays a crucial role in the ac conductivity values of γ-AlOOH. Here, among the three morphologies, EBH has the smallest grain size and highest grain concentration, resulting in the highest degree of conductivity. In contrast, the ac conductivity of HBH was found to be the lowest because it possesses the highest grain size. These results further corroborate our previously calculated band gap energies, where we obtained the smallest band gap for EBH, resulting in the highest conductivity among the three morphologies.

3.7. Impedance analysis of the nanostructures

Impedance spectroscopy is a useful technique to understand the contribution of grains and non-conducting grain boundaries. It can also provide information related to the interactions between a sample and conducting electrodes.[35] The impedance characteristics of our samples were investigated using Nyquist plots,[41] where the X-axis denotes the real part (Z′) and the Y-axis consists of the imaginary part (Z″) of the impedance, as depicted in Fig. 10. In our case, all the samples possessed higher contributions of grain boundaries at lower temperatures (defined by the straight lines), while at higher temperatures, the effect of the conducting grains was prominent (denoted by semicircles).[35] Among the three mor-

phologies, EBH has a complex impedance of 9.1 kΩ at 1 kΩ resistance, whereas UBH and HBH have complex impedances of 4.9 kΩ and 1.29 kΩ, respectively, at the same resistance value.

From a morphological point of view, EBH has the highest number of grain boundaries because it has the highest surface area; therefore, the value of the complex impedance is the highest in this case. On the other hand, it was found to be the lowest for HBH, as reflected in the Nyquist plots. Our impedance results therefore support our previous dielectric and conductivity measurements very well.

4. Conclusion

In summary, different nanostructures of boehmite have been synthesized and characterized using X-ray diffraction (XRD), Fourier transform infrared spectroscopy (FT-IR), field emission scanning electron microscopy (FESEM), energy dispersive X-ray (EDX) analysis, transmission electron microscopy (TEM), and Brunauer–Emmett–Teller (BET) measurements. The growth mechanisms of the different morphologies of the boehmite nanostructures have been illustrated by examining their nucleation, growth, and self-assembly to produce different morphologies, such as the spherical morphology for EBH, nano-needle shape for HBH and nano-flower morphology for UBH. UV-vis absorption and photoluminescence spectra show that our three samples exhibit strong luminescence emissions in the green and blue regions of the spectrum with different intensities, which has potential applications in the fields of bio-imaging and bio-sensing. The temperature-dependent dielectric permittivities and ac conductivities of the different boehmite nanostructures reveal that the synthesized nanostructures have remarkably high dielectric constants with very low losses. Due to their high dielectric constants and low dielectric losses, the boehmite nanostructures may be useful for fabricating high energy storage devices.

Conflicts of interest

There are no conflicts to declare.

Acknowledgements

References

1 J. Li, C. Papadopoulos, J. M. Xu and M. Moskovits, *Appl. Phys. Lett.*, 1999, 75, 367–369.

2 L. H. Reddy, J. L. Arias, J. Nicolas and P. Couvreur, *Chem. Rev.*, 2012, **112**, 5818–5878.

3 G. Mendoza-Damiána, F. Tzompantzia, R. Pérez-Hernándezb, R. Gómeza and A. Hernández-Gordilloc, *Catal. Today*, 2016, **266**, 82–89.

4 Y. Hua and Z. L. Wang, *Nano Energy*, 2015, **14**, 3–14.

5 A. Ito, M. Shinkai, H. Honda and T. Kobayashi, *J. Biosci. Bioeng.*, 2005, **100**, 1–11.

6 J. Zhang, S. Liu, J. Lin, H. Song, J. Luo, E. M. Elssfah, E. Ammar, Y. Huang, X. Ding, J. Gao, S. Qi and C. Tang, *J. Phys. Chem. B*, 2006, **110**, 14249–14252.

7 B. Martínez, X. Obradors, L. Balcells, A. Rouanet and C. Monty, *Phys. Rev. Lett.*, 1998, **80**, 181–184.

8 J. Liang, X. Gao, J. Guo, C. Chen, K. Fan and J. Ma, *Sci. China Mater.*, 2017, **61**(1), 30–38.

9 J. Liang, C. Yuan, H. Li, K. Fan, Z. Wei, H. Sun and J. Ma, *Nano-Micro Lett.*, 2018, **10**–21.

10 Z. Zhang, X. Shao, H. Yu, Y. Wang and M. Han, *Chem. Mater.*, 2005, **17**, 332–336.

11 H. Shi, L. Qi, J. Ma and H. Cheng, *J. Am. Chem. Soc.*, 2003, **125**, 3450–3451.

12 S. Musić, O. Dragčević and S. Popović, *Mater. Lett.*, 1999, **40**, 269–274.

13 (*a*) A. Dandapat and G. De, *J. Mater. Chem.*, 2010, **20**, 3890–3894; (*b*) B. J. Saikia and G. Parthasarathy, *J. Mod. Phys.*, 2010, **1**, 206–210.

14 C. Esposito Corcione and M. Frigione, *Prog. Org. Coat.*, 2012, **74**, 781–787.

15 V. Vatanpoura, S. S. Madaenia, L. Rajabib, S. Zinadinia and A. A. Derakhshan, *J. Membr. Sci.*, 2012, **401–402**, 132–143.

16 (*a*) S. Shen, W. Kiong Ng, L. S. Onn Chia, Y. C. Dong and R. B. Hee Tan, *Cryst. Growth Des.*, 2012, **12**, 4987–4994; (*b*) T. Z. Ren, Z. Y. Yuan and B. L. Su, *Langmuir*, 2004, **20**, 1531–1534.

17 J. Yang and R. L. Frost, *Res. Lett. Inorg. Chem.*, 2008, **1**, 1–4.

18 (*a*) X. Y. Chen, H. S. Huh and S. W. Lee, *Nanotechnology*, 2007, **18**, 285608; (*b*) J. R. Wen, M. H. Liub and C. Y. Mou, *CrystEngComm*, 2015, **17**, 1959; (*c*) M. A. Pagano, C. Forano and J. P. Besse, *J. Mater. Chem.*, 2003, **13**, 1988–1993; (*d*) B. Huang, C. Huang, J. Chen and X. Sun, *J. Alloys Compd.*, 2017, **712**, 164–171.

19 S. Roy, S. Bardhan, K. Pal, S. Ghosh, P. Mandal, S. Das and S. Das, *J. Alloys Compd.*, 2018, **763**, 749–758.

20 A. Zirehpour, A. Rahimpour, F. Seyedpour and M. Jahanshahi, *Desalination*, 2015, **371**, 46–57.

21 W. Brostow and T. Datashvili, *Chem. Chem. Technol.*, 2008, **2**, 27–32.

22 Y. Hakuta, H. Ura, H. Hayashi and K. Arai, *Mater. Chem. Phys.*, 2005, **93**, 466–472.

23 D. Panias, P. Asimidis and I. Paspaliaris, *Hydrometallurgy*, 2001, **59**, 15–29.

24 D. K. Chanda, P. S. Das, A. Samanta, A. Dey, A. K. Mandal, K. D. Gupta, T. Maitya and A. K. Mukhopadhyay, *Ceram. Int.*, 2014, **40**, 11411–11417.

25 D. K. Chanda, A. Samanta, A. Dey, P. S. Das and A. K. Mukhopadhyay, *J. Mater. Sci.*, 2017, **52**(9), 4910–4922.

26 H. Cao, H. Zheng, K. Liu and J. H. Warner, *ChemPhysChem*, 2010, **11**, 489.

27 (*a*) X. L. Li, C. X. Wang and G. W. Yang, *Prog. Mater. Sci.*, 2014, **64**, 121–199; (*b*) A. A. Anderson, S. P. Yurel and M. V. Shymanska, *J. Chromatogr.*, 1974, **95**, 91–101; (*c*) K. L. Cheng, *Anal. Chem.*, 1955, **27**, 1165–1166; (*d*) M. G. Ma and Y. J. Zhu, *Mater. Lett.*, 2008, **62**, 2512–2515; (*e*) A. Sugunan, H. C. Warad, M. Boman and J. Dutta, *J. Sol-Gel Sci. Technol.*, 2006, **39**, 49–56; (*f*) C. Fong, D. Wells, I. Krodkiewska, P. G. Hartley and C. J. Drummond, *Chem. Mater.*, 2006, **18**, 594–597; (*g*) J. Gao, W. Kong, L. Zhou, Y. He, L. Ma, Y. Wang, L. Yin and Y. Jiang, *Chem. Eng. J.*, 2017, **309**, 70–79; (*h*) L. Zhua, Y. Li and W. Zeng, *Appl. Surf. Sci.*, 2018, **427**, 281–287; (*i*) Z. G. Zhao and M. Miyauchi, *J. Phys. Chem. C*, 2009, **113**, 6539–6546; (*j*) D. Ma, G. Shi, H. Wang, Q. Zhang and Y. Li, *J. Mater. Chem. A*, 2013, **1**, 684.

28 K. Ballschmiter and J. J. Katz, *J. Am. Chem. Soc.*, 1969, **91**, 2661–2677.

29 S. Das, S. Das, A. Roychowdhury, D. Das and S. Sutradhar, *J. Alloys Compd.*, 2017, **708**, 231–246.

30 A. Amirsalari and S. FarjamiShayesteh, *Superlattices Microstruct.*, 2015, **82**, 507–524.

31 G. Li, C. Peng, C. Li, P. Yang, Z. Hou, Y. Fan, Z. Cheng and J. Lin, *Inorg. Chem.*, 2010, **49**, 1449–1457.

32 N. Talebian, S. M. Amininezhad and M. Doudi, *J. Photochem. Photobiol., B*, 2013, **120**, 66–73.

33 C. G. Koops, *Phys. Rev.*, 1951, **83**, 121–124.

34 K. Halder, D. Roy and S. Das, *J. Mater. Sci.: Mater. Electron.*, 2015, **26**, 5803–5811.

35 S. Das, S. Das and S. Sutradhar, *J. Alloys Compd.*, 2017, **726**, 11–21.

36 A. S. Lanje, S. J. Sharma, R. S. Ningthoujam, J. S. Ahn and R. B. Pode, *Adv. Powder Technol.*, 2013, **24**, 331–335.

37 J. A. Wang, X. Bokhimi, A. Morales, O. Novaro, T. López and R. Gómez, *J. Phys. Chem. B*, 1999, **103**, 299–303.

38 A. K. Jonscher, *J. Mater. Sci.*, 1981, **16**, 2037–2060.

39 L. K. Sudha, S. Roy and K. Uma Rao, *Int. J. Mater., Mech. Manuf.*, 2014, **2**, 96–100.

40 S. K. Saha, M. A. Rahman, M. R. H. Sarkar, M. Shahjahan and M. K. R. Khan, *J. Semicond.*, 2015, **36**, 033004.

41 Q. Wang, J. E. Moser and M. Gratzel, *J. Phys. Chem. B*, 2005, **109**, 14945–14953.

Gd(III)-Doped Boehmite Nanoparticle: An Emergent Material for the Fluorescent Sensing of Cr(VI) in Wastewater and Live Cells

Shubham Roy,[†] Kunal Pal,[‡] Souravi Bardhan,[†] Shilpa Maity,[†] Dipak Kr. Chanda,[§] Saheli Ghosh,[†] Parimal Karmakar,[‡] and Sukhen Das*,[†]

[†]Department of Physics, [‡]Department of Life Science and Biotechnology, and [§]School of Materials Science and Nano Technology, Jadavpur University, Kolkata 700032, India

S Supporting Information

ABSTRACT: This article reports the effect of Gd(III) doping on the structure, microstructure, and optical properties of boehmite nanoparticles. The bright-blue fluorescence along with a long lifetime makes our material an efficient candidate for optical applications. Our material particularly targets and eliminates hexavalent chromium ions (Cr(VI)) from aqueous media, which turns it into a multifunctional fluorescent nanosensor (MFNS). The development of an efficient hexavalent chromium ion (Cr(VI)) sensor to detect and quantify Cr(VI) ions is still a serious issue worldwide. Thus, this work will be very beneficial for various environmental applications. No such work has been reported so far which includes cost-effective and biocompatible boehmite nanoparticles in this field. Detailed synthesis and characterization procedures for the MFNS have been incorporated here. The biocompatibility of the MFNS has also been studied rigorously by performing cell survivability assay (MTT) and cellular morphology assessments. Our extensive research confirmed that the "turn-off" sensing mechanism of this sensor material is based on a collisional quenching model which initiates the photoinduced electron transfer (PET) process. High selectivity and sensitivity ($\sim 1.05 \times 10^{-5}$ M) of the MFNS toward hexavalent chromium ions even in real life wastewater samples have been confirmed, which makes this fluorescent probe a potential candidate for new age imaging and sensing technologies.
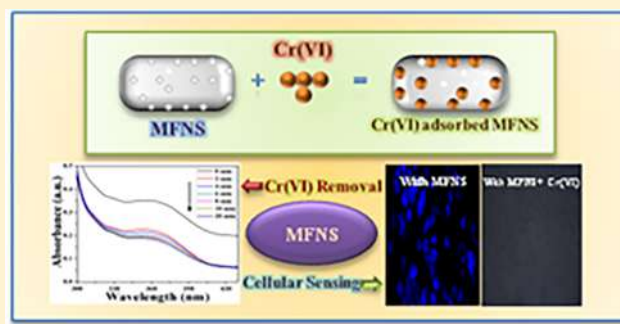
1. INTRODUCTION

The development of new-generation fluorescent sensors is currently of great research interest because they play a crucial role in detecting and quantifying various infections and diseases in biological systems.[1,2] Sometimes, they can locate and entrap an infection on the cellular level.[3] Not only biological systems but also these sensors can provide important information regarding any type of chemical contamination by modulating its fluorescence level.[4,5] Researchers and scientists are working to enhance the limit of detection (LOD) and the fluorescence properties of these sensors. Thus, the fabrication of biocompatible, efficient fluorosensors is an emerging research topic.

Recent studies on hazardous ion sensors such as heavy metal ions (Hg(II), Cd(II), Cr(III), etc.)[6−8] and toxic anions (nitrate, dichromate, etc.)[9,10] dominate the studies on all other fluorosensors because of their huge applicability and excessive demand. Moreover, various diseases, such as congestive heart failure,[11] liver infarction,[12] and lung cancer,[13] can occur in the presence of such toxic ions. Some essential metal ions, including Fe^{2+}, Cu^{2+}, Mn^{2+}, and Co^{2+}, can also be toxic at higher doses.[14−17] In addition, other heavy metal ions, such as Hg^{2+}, Cd^{2+}, Pb^{2+}, and As^{3+}, are extremely toxic to humans and aquatic species even at lower concentrations, and the bioaccumulation of these metal ions can culminate in severe health hazards.[18−21]

Hexavalent chromium (Cr(VI)) is a well-known carcinogen[13] that is rapidly spreading as a result of its wide applications in leather tanning, metallurgy, chromium electroplating, and pigment production.[22,23] Because of its enormously harmful nature to human health and the environment, its detection and segregation from water streams have become immensely challenging.[11−13] Apart from these, the accumulation of Cr(VI) in aquatic living varieties can cause biomagnifications.[24] Therefore, developing selective and sensitive methods to detect and remove Cr(VI) ions for environmental monitoring, medical diagnostics, and food safety is of considerable importance.

We have synthesized a novel material, Gd(III)-doped boehmite nanoparticles, which has not been reported previously to the best of our knowledge. Thus, proper characterization has been done along with microstructural analysis by using the Rietveld refinement method to understand the effect of Gd doping into the boehmite matrix.[25,26] Interestingly, gadolinium incorporation enhances the optical

quality and surface area of the synthesized sensor material. The photoluminescence spectrum shows a high fluorescence intensity of the doped sample, which establishes the fact that this material could be used for fluorescence applications. Our material can detect the hazardous Cr(VI) ion through fluorescence techniques and can capture it through multilayer adsorption, which has been examined by absorption spectroscopy and EDX. Moreover, upon addition of Cr(VI), the emission intensity of the MFNS has been greatly quenched by ~11-fold. The plausible cause of the fluorescence quenching has been justified using the Stern−Volmer quenching model.[27,28] A real life tannery wastewater sample (the industrial source of Cr(VI)) has been used in our sensing experiments to prove the efficacy of our sensor material. This fluorescent sensor also exhibits cell permeability and intracellular Cr(VI) ion sensing in breast cancer cells (MDA-MB-468). Intercellular functionalities of our MFNS could be very beneficial for the detection of Cr(VI) ions in living systems, which could help us in biomagnifications studies. The main advantage of this sensor is its facile synthesis procedure that is not only economical but also industrially feasible. A highly selective and accurate Cr(VI) ion sensing capacity along with a very low limit of detection value (in the ppm range) makes this multifunctional MFNS a new age technology for the detection and removal of hazardous metal ions.

2. MATERIALS AND METHODS

2.1. Materials. Aluminum nitrate nonahydrate ($Al(NO_3)_3 \cdot 9H_2O$, MW 375.13), acetone (HPLC grade), ethanol (HPLC grade), and aqueous ammonia solution (25%) were purchased from Merck, India. Gadolinium oxide (Gd_2O_3, MW 362.50) was obtained from SRL, India. All purchased reagents are of analytical grade and were used without further purification. Deionized (Millipore) water was used throughout the experiment with a resistivity of at least 18 MΩ·cm. All of the glassware used in our experiments was cleaned with aqua regia solution followed by rinsing with ultrapure water.

2.2. Synthesis Procedure. Various compositions of Gd-doped boehmite nanoparticles were obtained by a facile hydrothermal reaction method. In a typical synthesis procedure, aluminum nitrate was mixed with 70 mL of Millipore water under vigorous stirring conditions at room temperature. After the proper dissolution of the aluminum salt, gadolinium oxide was added to the salt solution to maintain the proper gadolinium to aluminum weight ratios (0, 0.5, and 1%) as mentioned in Table.1.

Table 1. Preparation of Different Doping Percentages of Gd-Doped Boehmite Samples

sample name	aluminum nitrate amount (g)	gadolinum oxide amount (mg)	water amount (mL)
GBH0	2.539	0	70
GBH0.5	3.732	18.125	70
GBH1	3.713	36.250	70

After the formation of a clear and transparent solution, liquid ammonia was added to the solution dropwise until the pH reached 10. At this pH, thick white precipitates were formed, indicating the formation of Gd-incorporated $Al(OH)_3$. The stirring was continued another 3 h for the completion of the reaction.

In a separate glass container, a similar procedure was performed, but in this case, gadolinium oxide was not added.

After the completion of reaction, the samples were transferred into separate Teflon-lined stainless steel autoclaves and placed in a dust-free hot air oven at 180 °C for 16 h. The solid white precipitates were collected from the bottom of the Teflon jacket and washed several times with water. The washed precipitates were dried in vacuum at

room temperature first and then at 60 °C for another 24 h. Dried samples were further ground in a mortar, marked, and sent for characterization.

3. RESULTS AND DISCUSSION

3.1. Structural and Morphological Analyses of the Samples. X-ray diffraction (XRD) is an important characterization tool to determine the crystallographic structure, phase purity, and crystallite size of the sample.[29] It can also provide major crystallographic information regarding the incorporation of any foreign element into the phase-pure crystal and crystal growth directions. Here, Figure 1a shows the XRD patterns of synthesized nanostructures of pure boehmite and Gd^{3+}-doped boehmite nanostructures that have been recorded by using a D8 Bruker AXS powder X-ray diffractometer with Cu-Kα radiation (λ = 1.5405 Å) in the range of 2θ from 10 to 70°. The scan speed was set at 0.02 with a tube voltage of 35 kV at 35 mA. All of the peaks have been assigned by using the JCPDS (card no. 21-1307). The absence of any undesired diffraction maxima in our XRD diffractograms confirms that the entire aluminum hydroxide precursor had been completely converted to boehmite (or Gd^{3+}-doped boehmite) during the hydrothermal treatment. It is evident from the XRD patterns that the doping of Gd^{3+} ions even up to 1% does not change the standard boehmite orthorhombic structure. This further confirms the successful incorporation of Gd^{3+} ions into the boehmite's nanostructure. The mean nanocrystallite sizes of the entire sample set have been calculated from the broadening of the (020) peak by using the Debye−Scherrer equation[30] and are depicted in Table 2

$$\langle D \rangle_{(020)} = 0.9\lambda / (\beta_{1/2} \cos \theta) \tag{1}$$

where D is the average crystallite size, $\beta_{1/2}$ is the full width at half-maximum (fwhm) of the (020) peak, λ is the wavelength of the incident X-ray beam, and θ is the corresponding Bragg angle. The average crystallite diameters (D) for different doped samples were found to be within the range of 3.2−2.2 nm.

To determine the phase purity and microstructural and structural characteristics of the doped and undoped samples, Rietveld refinement was performed using Rietveld-based software package MAUD v2.8 (material analysis using diffraction). The XRD pattern of the individual samples was superimposed with corresponding Miller indices and matched with the standard database (JCPDS card no. 21-1307). Figure S1 shows the well-matched experimental and computed patterns of the samples. In our case, we have observed that microstrain inside the crystals gradually increases with increasing doping concentration (Table.2), which might be due to the substitution by larger Gd^{3+} ions (0.94 Å) with smaller Al^{3+} ions (0.53 Å) inside the orthorhombic sites of γ-AlOOH crystals.[31] Thus, the structural analysis corroborates that the cationic dopant, having larger radii than that of the host cation, creates difficulty in accommodating the inside of the lattice structure of the host crystal. However, the amount of dopants that has been successfully accommodated inside the host lattice structure is good enough to create a sufficient number of structural defects for the modulation of various physical properties.[31] The results obtained after the final cycle regarding structural, microstructural, and reliability parameters of the samples are provided in Table 2.

Vesta v3.4.3 (visualization for electronic and structural analysis) software has been employed to analyze the structural
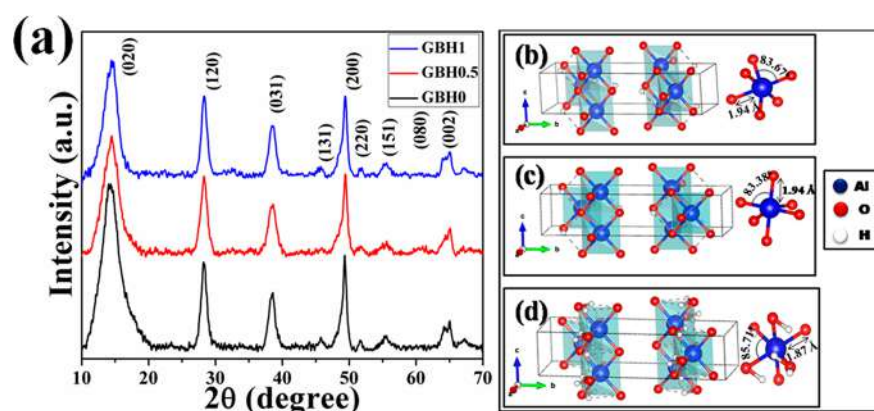
Figure 1. (a) XRD patterns of samples GBH0, GBH0.5, and GBH1. Corresponding microstructural diagrams of (b) GBH0, (c) GBH0.5, and (d) GBH1.

Table 2. Structural and Microstructural Parameters of the Samples Obtained from Rietveld Analysis of the XRD Pattern

parameters	GBH0	GBH0.5	GBH1
a (Å)	3.6971173 ± 0.003350923	3.6826758 ± 0.0034330236	3.6910741 ± 0.004538715
b (Å)	12.199201 ± 0.022052469	12.230068 ± 0.022432782	12.1S66799 ± 0.032643557
c (Å)	2.8673484 ± 0.0025944936	2.8599763 ± 0.0026292377	2.8682199 ± 0.003596273
nanocrystallite size (nm)	3.2278	2.5642	2.2532
strain	2.7673983×10^{-7} ± 89.18558	1.7377633×10^{-5} ± 0.051312458	2.825615×10^{-5} ± 0.12719534
χ^2	1.5863	1.4646	1.7543
R_p (%)	0.08718333	0.09335655	0.11429352
R_{wp} (%)	0.10980562	0.112979405	0.15138145
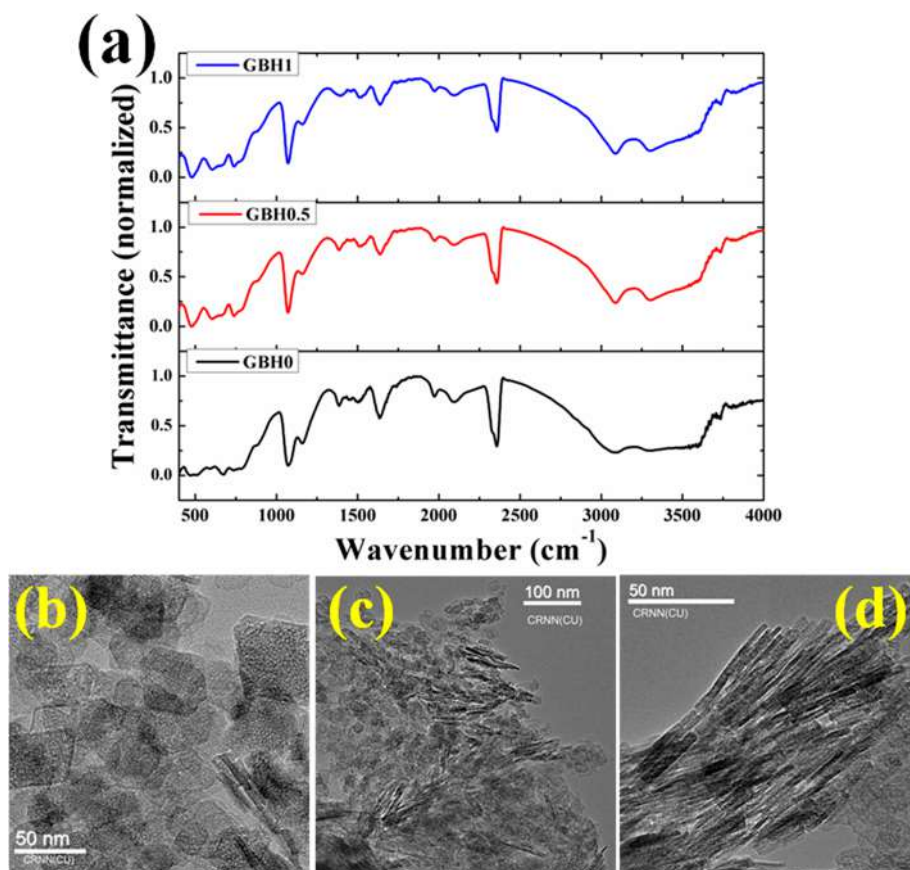
Figure 2. (a) FTIR spectra of samples GBH0, GBH0.5, and GBH1. Corresponding TEM micrographs of samples (b) GBH0, (c) GBH0.5, and (d) GBH1, respectively.

properties and bonding networks of the samples, as depicted in Figure 1b−d. In our case, three AlO_6 polyhedra stacked together to form the orthorhombic phase of boehmite. The incorporation of Gd ions does not change this structural symmetry but changes the bond angle and bond lengths slightly, which has been depicted in Charts S1−S3.

FT-IR spectra of the samples presented in Figure 2a have been recorded using a Shimadzu FTIR-8400S in the wavenumber range from 400 to 4000 cm⁻¹. Absorption bands observed in our GBH0 sample are in good agreement with the values reported in the literature, confirming the formation of boehmite nanostructure. The characteristic absorption bands located at 480, 758, and 634 cm⁻¹ of boehmite are observed in our sample, which occurred as a result of the AlO_6 vibration.[30a−c] The small absorption band at 1385 cm⁻¹ is attributed to the stretching vibration of the nitrate.[32] Two sharp bands located at 3286 and 3090 cm⁻¹ are due to the asymmetric vibration of O−H and symmetric O−H stretching vibrations, respectively.[33] The stretching of Si−O and the −OH deformation linked to aluminum ions are also observed in the spectra at 1016 and 953 cm⁻¹.[34] ν_{sym}Al−O−H and ν_{asym}Al−O−H modes are attributed to the bands located at 1071 and 1159 cm⁻¹, respectively.[35] The surface-adsorbed moisture causes[36] the vibration at around 1640 cm⁻¹. Furthermore, our GBH0.5 and GBH1 samples show similar kinds of absorption bands, which leads to the fact that the incorporation of the Gd^{3+} ion does not alter any bond structure inside the nanocrystalline boehmite phase, which is in accordance with our XRD results.

The morphology and particle sizes of the synthesized samples have been characterized using a Jeol 2000 FX transmission electron microscope. A very small amount of powdered nanosamples was dissolved in acetone and then casted on carbon-coated copper grids (300 mesh) after ultrasonication for 1 h to obtain the TEM microscopy results. The TEM micrograph of the undoped boehmite sample (i.e., GBH0 (Figure 2b)) shows a mixture of rhombic and hexagonal particles. These particles have lengths of between 20 and 40 nm with a large number of pores on their surfaces. Although GBH0 has a mixture of rhombic and hexagonal, GBH0.5 shows (Figure 2c) the coexistence of rhombic particles and nanorods. Interestingly, the presence of these rodlike particles is highest in our GBH1 sample (Figure 2d). The incorporation of Gd^{3+} ions inside the pure boehmite matrix creates various interstitial defects that introduce further lattice strain into the crystal.[31] This lattice strain may be responsible for this type of morphological evolution upon the addition of foreign ions inside the boehmite matrix.

The elemental composition of the as-synthesized samples were analyzed by EDX (Figure S2), where GBH1 contained a minute quantity of Gd and GBH0 shows the presence of Al and O only. Furthermore, to confirm the presence of Gd in the structure of our sample, XRF (X-ray fluorescence) measurements have been made using Axios, a PANalytical X-ray fluorescence spectrometer (Figure S3), along with elemental analysis (Table S1).

The pore size distribution and surface area analysis of the nanostructures have been investigated by the Brunauer−Emmett−Teller (BET) and Barrer−Joyner−Halenda (BJH) methods using N_2 gas adsorption−desorption values. A Twin Surface Area Analyzer from Quanta-chrome Instruments (USA) was employed for this purpose. Figure S4 depicts the data corresponding to the nitrogen (N_2) adsorption−

desorption isotherms and the corresponding pore size distributions for our nanopowders with different doping concentrations. Figure S4a also shows that, for a specific sample, the adsorbed and desorbed volumes of nitrogen are similar to each other. The type IV isotherms suggest the presence of mesopores in our samples, which is an indication of a good industrial adsorbent material.[37,38] The H4-type hysteresis loop suggests that our samples have narrow slitlike pores.[37,38] Surface area data shows that our GBH1 sample has the highest surface area (92.174 m²·g⁻¹) whereas undoped GBH0 has the lowest surface area (74.96 m²·g⁻¹) among the three samples. The plausible cause of this surface area enhancement is due to the morphological evolution (from cubic to nanorod) caused by the incorporation of Gd^{3+} ions, which is in good accordance with our TEM results. The pore size also varies with doping concentration in our case. GBH0 has a pore diameter of 5.84 nm, whereas GBH0.5 and GBH1 have pore diameters of 5.76 and 5.03 nm, respectively (Figure S4b). This decrement in pore diameter with increasing doping concentration is due to the entrapment of dopant inside the mesopores of the pure boehmite matrix. Although the pore diameter decreases with increasing dopant volume, the pore volume increase significantly (Table 3), which makes our GBH1 sample highly mesoporous with the highest surface area among the three synthesized nanosamples.

Table 3. Estimated BET Surface Area, Pore Radius, and Pore Volume Data of Boehmite Samples Loaded with Various Gd Concentrations

sample name	surface area (m²/g)	pore size (nm)	pore volume (mL/g)
GBH0	74.960	5.84	0.248
GBH0.5	91.663	5.76	0.278
GBH1	92.174	5.03	0.299

3.2. Photoluminescence Performance and Fluorescence Quantum Yield of the MFNS. To understand the optical quality and fluorescence properties of our samples, photoluminescence spectroscopy has been performed at room temperature using a Cary Eclipse fluorescence spectrophotometer from Agilent Technologies with an excitation wavelength (λ_{ex}) of 375 nm (Figure S5). The PL spectra of our synthesized samples show luminescent maxima centered at 430 nm that further indicate the near-blue emission of our samples. A crystal-defect mediated radiative transition is responsible for this kind of emission.[29,30] Our GBH1 sample shows the highest fluorescence intensity caused by the maximum amount of Gd doping. Normally, a higher amount of doping increases the number of defect states (mainly oxygen vacancies), which has already been justified by microstrain analysis. These defect states enhance the fluorescence intensity of a sample. A similar phenomenon has also been reported by Liu et al.[39] for ZnO quantum dots. Thus, highly fluorescent GBH1 could be used in optical imaging and sensing applications, and it can act as a fluorescent nanosensor (MFNS).

The fluorescence quantum yield of the GBH1 sample has been calculated using the following relation[40a]

$$QY_{sample} = QY_{ref} \frac{A_{ref} I_{sample} \eta_{sample}^2}{A_{sample} I_{ref} \eta_{ref}^2}$$

(2)
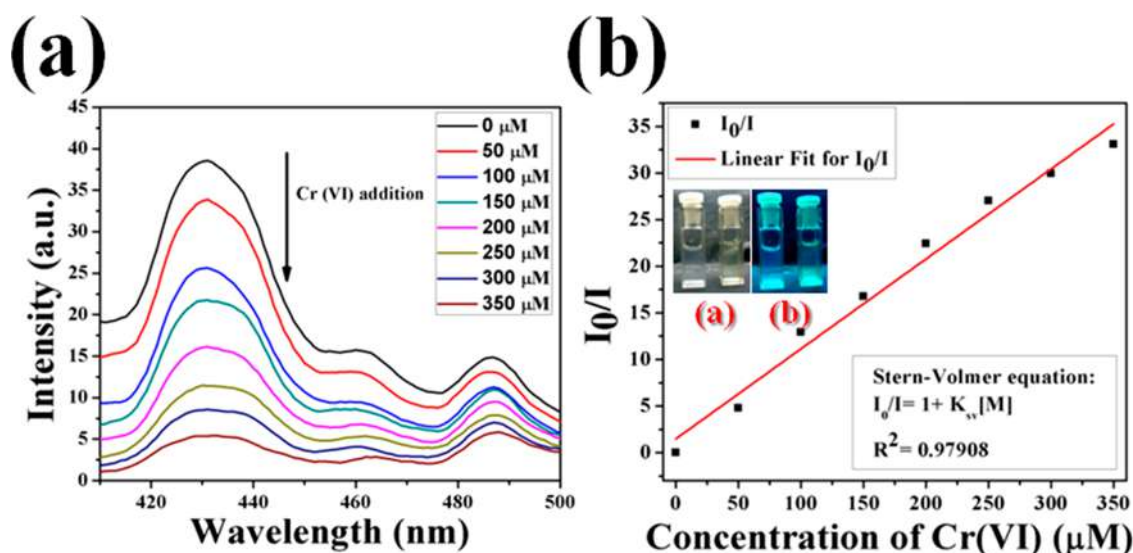
Figure 3. (a) Fluorescence titration data for the GBH1 sample using Cr(VI) as the quencher. (b) Stern−Volmer fitting of the corresponding fluorescence quenching data. Naked eye observation of the fluorescence quenching of GBH1 upon Cr(VI) addition (inset).

where I is the area under the emission spectral curve, A is the optical density of the sample at the excitation wavelength, and η is the refractive index of the solvent. Here the value of QY_{ref} is taken to be 0.52 (quinine sulfate). GBH1 shows a high quantum yield value of 0.692 with the highest fluorescence intensity, which justifies the fact that gadolinium ion incorporation successfully enhances the optical quality of boehmite nanoparticles.

3.3. Cr(VI) Ion-Sensing Properties of the MFNS. Boehmite-based GBH1 has a promising optical property, thus it has been applied as a fluorescent sensor. To test the efficacy of GBH1 as a sensor for Cr(VI), the fluorescence of GBH1 was monitored in an aqueous medium. Initially, a 1 mg·mL^{-1} aqueous solution of GBH1 was prepared and ultrasonicated for 20 min to form a homogeneous solution. The PL spectra of the as-prepared solution were recorded and found to be quite high (at 430 nm) upon 375 nm excitation. Different concentrations of the Cr(VI) ion (0−350 μM) were then added to the solution and measured in the same manner (Figure 3a). From Figure 3a, one can observe that the characteristic emission maxima of GBH1, centered at 430 nm, have been reduced drastically upon the addition of hexavalent chromium. The quenching effects can be visualized by the naked eye under a normal UV lamp (excited at 365 nm) (Figure 3b, inset). Quantitatively, the quenching effect can be analyzed by the linear Stern−Volmer quenching model, expressed as[40b,41]

$$\frac{I_0}{I} = 1 + K_{SV}[M] \tag{3}$$

where I_0 and I are the fluorescence intensities before and after the addition of Cr(VI), respectively, $[M]$ is the concentration of the chromium ion, and K_{SV} is the Stern−Volmer quenching constant.

Figure 3b shows that the fluorescence quenching upon the addition of chromium ion follows the Stern−Volmer model of quenching with a linear fit coefficient of 0.97908. The high K_{SV} value (0.0966 × 10^6) suggests that the quenching efficacy of the nanosensor (GBH1) is quite high with a low detection limit (1.05 × 10^{-5} M). The limit of detection (LOD) has been evaluated using the relation[41]

$$LOD = \frac{3\sigma}{K_{SV}} \tag{4}$$

where σ is the standard deviation of at least 10 measurements of the fluorescence intensities of the pure GBH1 sample.

Apart from hexavalent chromium, other cations and anions have also been studied in a similar way with a 350 μM concentration of the guest ion (Figure 4) to test the selectivity of the MFNS.[42] It can be shown from Figure 4 that the fluorescence intensities after the addition of various cations and anions are nearly the same as for our MFNS, but in the case of Cr(VI), it is drastically quenched.

3.4. Real Life Sensing of Cr(VI) in Tannery Wastewater. To evaluate the efficacy of our sensor material (GBH1), the sensing experiments have been performed by using real life tannery wastewater samples. Tannery wastewater has been collected and kept at 4 °C before performing the experiment. Initially, the chromium content of the wastewater sample has been measured using ICP (inductively coupled plasma) and has been found to be higher than the LOD value of our sensor material. Traces of other elements such as lead and iron have also been found in the ICP results (Table 4). The collected wastewater was added to the sensor material, and the emission spectrum was recorded (Figure 5). Figure 5 shows that the fluorescence intensity of GBH1 was quenched significantly after wastewater addition, which justifies the fact that our sensor material can sense chromium in a real environment and in the presence of other disturbing elements.

3.5. Mechanism of Cr(VI) Detection. To investigate the quenching mechanism, we have employed time-resolved fluorescence techniques as well as steady state fluorescence and absorption experiments. The ground-state fluorescence data (PL) shows a reduction in fluorescence intensity upon Cr(VI) addition, whereas the same behavior has been obtained in excited-state fluorescence experiments (Table S2). The average lifetime of the fluorophores decreased drastically upon hexavalent chromium addition (Figure S6). The linear Stern−Volmer plot and the reduced lifetimes of the fluorophores suggest the collisional quenching mechanism.[43] This type of quenching happens when collisions take place between the quencher and the fluorophores in the excited state.
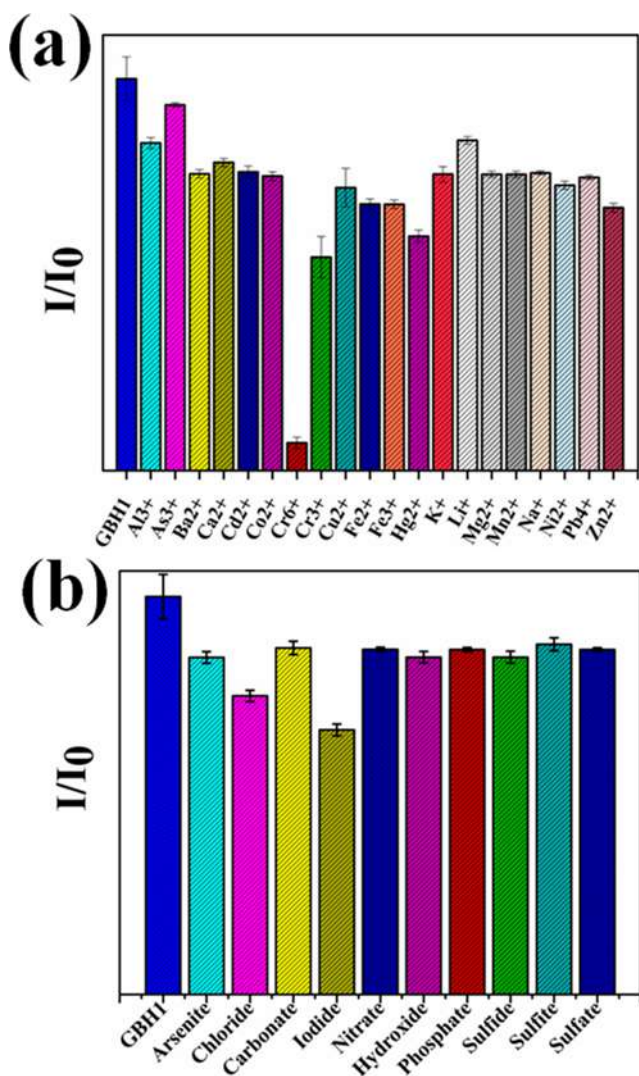
Figure 4. Selectivity studies of the MFNS by using various (a) cations and (b) anions.

Table 4. Inductively Coupled Plasma Data of the Collected Wastewater Sample

constituents	amount (ppm)
cadmium (Cd)	not detected
lead (Pb)	0.10
chromium (Cr)	20.58
iron (Fe)	4.84

Initially, the Cr(VI) ions with small ionic radii ($\sim$0.3−0.4 Å) get adsorbed into the vacant sites of mesoporous MFNS (average pore diameter $\sim$5 nm), which has already been proven by various spectroscopic techniques and EDX data. Adsorption makes the distance between the quencher and the fluorophores short (<10 nm), which is responsible for the charge transfer between the fluorophores and the quencher molecules. This phenomenon is known as photoinduced electron transfer (PET).[40b]

Here, Gd acts as the foreign element that creates interstitial defects in the boehmite matrix, which then makes our sensor material highly fluorescent. This mechanism has been depicted in detail in our XRD analysis. Furthermore, boehmite (γ-
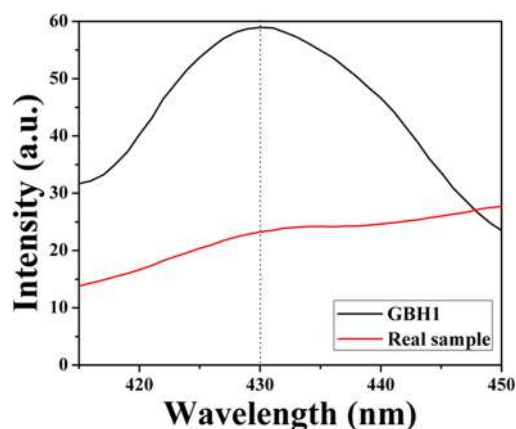
Figure 5. Fluorescence quenching result of a real life tannery wastewater sample under 375 nm excitation.

AlOOH) in water creates $Al(OH)_4^-$ species, which in turn produce protons (H^+).[40c]

$$AlOOH + 2H_2O \rightarrow Al(OH)_4^- + H^+$$
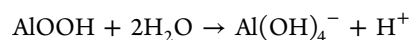
The proton released from the sensor material is accepted by the hexavalent chromium species that further converts it to trivalent chromium.[40d]

$$2Cr_2O_7^{2-} + 16H^+ + h\nu \rightarrow 4Cr^{3+} + 8H_2O + O_2$$
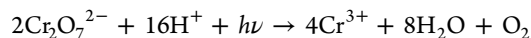
In this work, the amount of Cr(III) formation is very low compared to that of Cr(VI), thus the signal in the absorption spectra of Cr-adsorbed GBH1 is very feeble, which is depicted in Figure S7. Additionally, to ascertain that no leaching of Gd(III) ions occurs while Gd-loaded boehmite is dissolved in water, time-dependent UV−visible spectroscopy was carried out using GBH1. Figure S8 clearly shows that no Gd is released from GBH1.

During the PET mechanism, the fluorophores of MFNS in the ground state absorb the given UV energy (375 nm) and jump into the excited state where they collide with the quencher, resulting in nonradiative decay and jumping to the ground state without emitting any fluorescence. This type of collisional or dynamic quenching is illustrated herein (Figure 6).

3.6. Adsorption Uptake Studies. It is well known that the adsorption process of heavy-metal ions in porous material relies on multiple factors such as the shape, pore size, pore
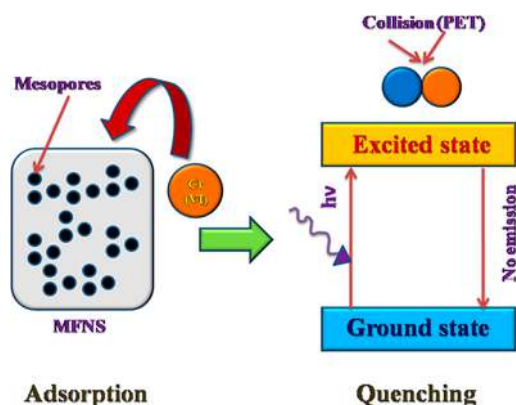
Figure 6. Fluorescence quenching mechanism of the MFNS.
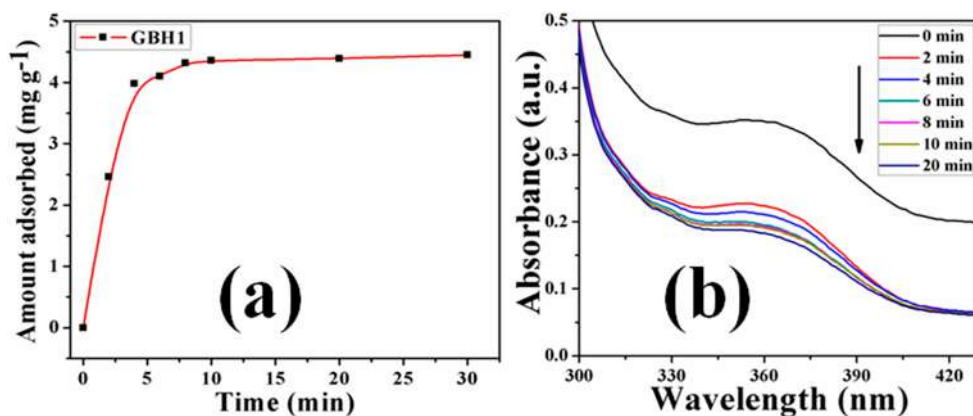
Figure 7. Adsorption kinetics study for the GBH1 sample in terms of (a) the time-based UV−vis technique and (b) time-dependent adsorption uptake using the Cr(VI) ion as the adsorbate.
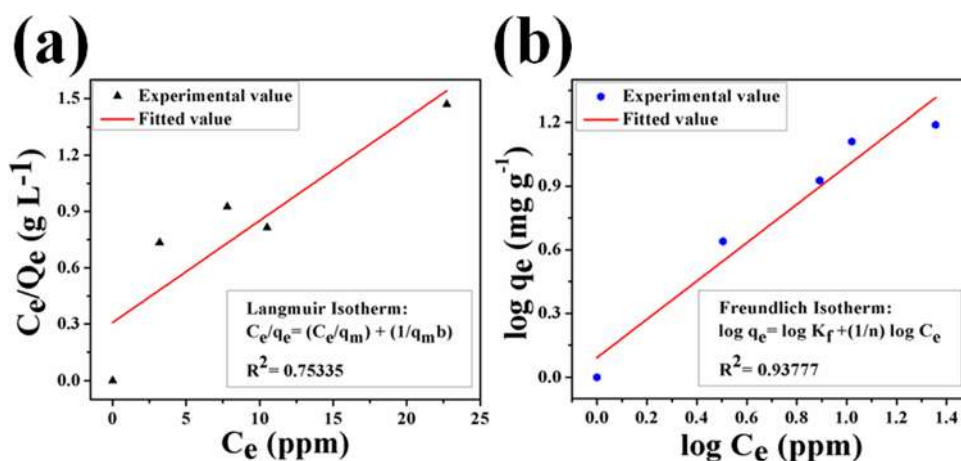
Figure 8. (a) Langmuir and (b) Freundlich adsorptive isotherm fittings for the GBH1 sample using the Cr(VI) ion as an adsorbate at 25 °C.

volume, and surface area of adsorbents.[40b] To evaluate the efficiency of the adsorbate, adsorption uptake studies have been carried out. A Biotek 96-well UV−vis plate reader was employed for this purpose. Ten milligrams of each sample (i.e., GBH0, GBH0.5, and GBH1) was separately added to 50 ppm of Cr(VI) solution and stirred using a magnetic stirrer for 2 h. Then it was kept in the dark for another 24 h before performing the spectrometry.

The adsorption uptake is calculated using the following equation[44]

$$uptake(\%) = ((C_0 - C_e)/C_0) \times 100 \qquad (5)$$

where C_0 and C_e are the initial and equilibrium concentrations of the Cr(VI) ion. Figure S9a shows that the adsorption uptake capacity of our GBH1 sample is highest (80.05%) among the three samples. This is due to the highest surface area of GBH1. On the basis of these results, GBH1 was selected as the most suitable sample for other adsorption experiments. The EDX analysis of the adsorbed GBH1 sample was performed (Figure S9b,c), which shows the traces of chromium in the sample, while the unadsorbed sample does not have any traces of chromium. This further shows that GBH1 adsorbs the Cr(VI) ion into its slitlike pores.

3.7. Adsorption Kinetics of the Sample. The adsorption of Cr(VI) from aqueous solution onto GBH1 as a function of the contact time was monitored by UV−vis spectroscopy.[28,44] Figure 7 shows that the intensity of the absorption peak of

Cr(VI) in solution at 353 nm quickly decreases within 20 min of Cr(VI) solution and GBH1 contact. More than 80% of the initial Cr(VI) amount (50 ppm) was adsorbed by GBH1 in less than 5 min, which corroborates that the encapsulation of Cr(VI) by GBH1 was extremely fast.

The rapid removal of Cr(VI) ion is reasonably due to the high pore volume of GBH1, which adsorbs the ion more quickly. The high surface area of GBH1 gives rise to the fact that the contact area of the adsorbent and the Cr(VI) ion is fairly high in our case, which is another cause of the rapid entrapment of the hazardous Cr(VI) ion. On the basis of these results, 20 min was selected as the contact time to ensure full equilibrium in our following experiments.

3.8. Adsorption Isotherms. To confirm the Cr(VI) ion adsorption capacity, adsorption isotherms were evaluated at 25 °C. The adsorption isotherms for the Cr(VI)-adsorbed GBH1 sample were studied according to standard Langmuir and Freundlich isotherm models,[44−46] which are usually used to describe the adsorption process between an adsorbent and an adsorbate. Figure 8a,b shows the adsorption isotherms of our GBH1 sample. Linear forms of the Langmuir (eq 6) and Freundlich (eq 7) isotherm models can be expressed as[44]

$$\frac{C_e}{q_e} = \frac{C_e}{q_m} + \frac{1}{q_m b} \qquad (6)$$

$$\log q_e = \log K_f + \frac{1}{n} \log C_e \tag{7}$$

where q_e is the amount of Cr(VI) adsorbed on the adsorbent at equilibrium (mg g^{-1}), C_e is the equilibrium concentration in the solution (mg L^{-1}), q_m is the maximum adsorption capacity (mg g^{-1}), and b and K_f are the Langmuir constant and the Freundlich constant, respectively, reflecting the affinity of the binding sites (L mg^{-1}) for the energy of adsorption.

From Figure 8, it is evident that GBH1 specifically follows the Freundlich isotherm model ($R^2 = 0.93777$), which indicates the multilayer adsorption of the chromium ion onto a heterogeneous surface of GBH1.[47]

3.9. Biocompatibility Assessment of the Sensor. The in vitro cytotoxicity of the MFNS is estimated to check the biocompatibility with the WI38 cell line. The cells were treated with five different concentrations (20, 40, 60, 80, and 100 μM·mL^{-1}) of GBH1 for 24 h, followed by the MTT assay (Figure 9).[48] It is observed that GBH1 exhibited no significant toxicity
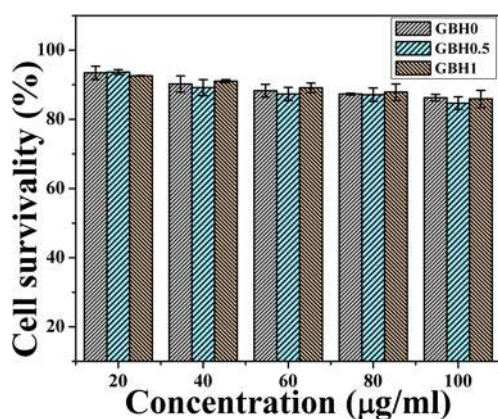
Figure 9. Cellular survival assay of the human WI38 cell line upon MFNS addition at various concentrations.

even at the highest concentration of 100 μM. Therefore, we can conclude that the MFNS has commendable biocompatibility and is ideal for biological application. As Figure S10 suggests, the cell survivability decreases when we use a 1.5% Gd-doped boehmite sample. Because of this biocompatibility issue, GBH1 has been selected as the MFNS.

WI38 cells were treated with 500 μg·mL^{-1} MFNS and kept for 7 days to envisage any change in the cellular morphology.[48] It is observed that the number of cells increases after 7 days, and the cells exhibit their normal morphologies without any anomalies during this time span of 7 days as shown in Figure 10. Therefore, it is positive proof of the nontoxicity of MFNS toward WI38 human lung fibroblast cells.

3.10. Cellular Imaging and Sensing with the MFNS. A cell imaging experiment is performed with MDA-MB 468 cells in order to demonstrate the efficacy of the MFNS to serve as a luminescent bioprobe.[42] The MDA-MB 468 cells are fluorescently labeled by the MFNS, and immediately after the treatment, the cells emit a strong blue fluorescent signal under the microscope (Figure 11). Thus, the MFNS is permeable to the cells and becomes saturated within 1 h of treatment because no increase in fluorescence is evident after 1 h. The cells also retain the fluorescence signal even after 12 h of treatment. Furthermore, no apparent morphological anomalies of the cells were observed because the MFNS is considerably biocompatible, as we have already observed from
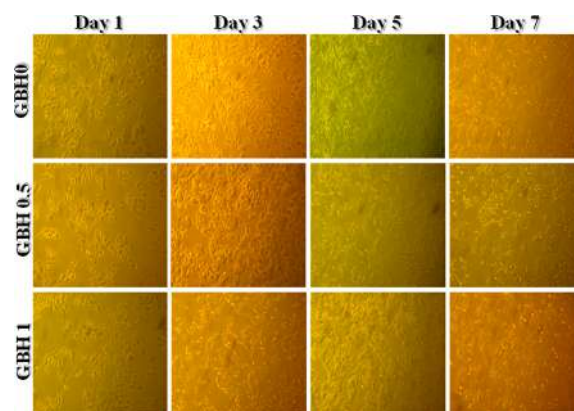
Figure 10. Assessment of cellular morphology upon MFNS addition.
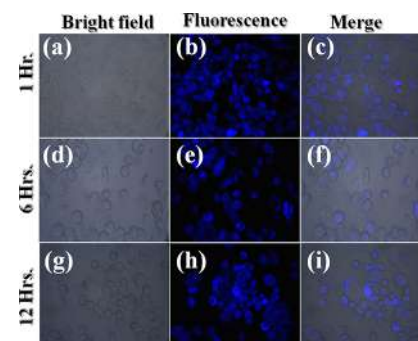
Figure 11. Bioimaging capacity and cellular permeability studies of a human breast cancer cell line (MDA-MB 468) by using the MFNS.

the MTT assay and cell morphology studies. The mock-treated cells exhibited no fluorescence, but immediately after the addition of the Cr(VI) ion to the labeled cells, the cells no longer emit any signal as a result of the quenching of the fluorescence signal by the Cr(VI) ion (Figure 12). Hence, we can conclude that our synthesized MFNS has the ability to detect Cr(VI) ions within the cellular milieu of MDA-MB 468 cancerous cells.
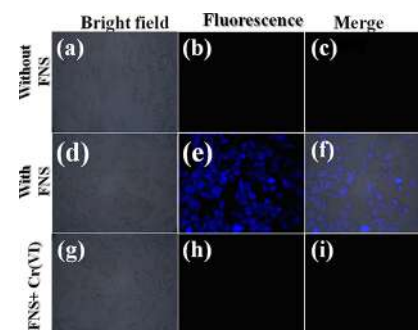
Figure 12. Sensing of Cr(VI) ions in a human breast cancer cell line (MDA-MB 468) by using the MFNS.

4. CONCLUSIONS

Here we present a novel gadolinium ion-doped boehmite-based fluorescent nanosensor (MFNS) that can detect the hexavalent chromium ion using fluorescence quenching and eliminate it through an adsorption technique. This is the first time that we have presented Gd-tailored boehmite as a

fluorescent nanosensor (Table S3). Trivalent Gd doping into an orthorhombic boehmite matrix is also a new phenomenon that we have used in a detailed manner. This nanosensor has a great capability to detect Cr(VI) ion at the cellular level, which has been shown herein. This MFNS provides us with promising blue fluorescence with a quantum yield of 0.692 that in turn is quenched upon the addition of the hexavalent chromium ion. Moreover, it exhibits high selectivity toward Cr(VI) even in the presence of a high concentration of disturbing ions. The selectivity and sensitivity of the sensor material have also been examined in a real life wastewater sample which has been collected from industrial tannery wastes. This fluorescence quenching mechanism is well explained on the basis of photoinduced electron transfer. Adsorption-based removal of the chromium ion happens mainly as a result of the high surface area of our material. Multilayered adsorption (Freundlich model) is adopted herein to explain the adsorption mechanism that has an extremely high adsorption rate (K_f = 0.903). The MTT assay and cellular morphology studies have been performed to ensure the biocompatibility of our sensor material. Finally, our material has been applied to human cells to confirm the cellular permeability and biosensing capacity. Strong blue fluorescence has been seen, which is quenched significantly upon the addition of the chromium ion. This makes our sensor material (MFNS) a promising candidate for the detection and segregation of Cr(VI) at the cellular level.

■ ASSOCIATED CONTENT

Ⓢ Supporting Information

The Supporting Information is available free of charge on the ACS Publications website at DOI: 10.1021/acs.inorg-chem.9b00425.

> Microstructural analysis of the samples, EDX data, BET and BJH analyses, time-resolved fluorescence data, spectroscopic data of adsorbed and pure MFNS, stability of the MFNS, proof of Cr(VI) adsorption, comparative fluorescence analysis of our samples, MTT data, comparative study of our work with the available literature, and biological tools and methods (PDF)

■ AUTHOR INFORMATION

Corresponding Author
*E-mail: sdasphysics@gmail.com. Phone: +91 94330 91337.

ORCID
Shubham Roy: 0000-0001-5245-3229
Dipak Kr. Chanda: 0000-0003-0147-4972
Sukhen Das: 0000-0001-8372-3076

Notes
The authors declare no competing financial interest.

■ ACKNOWLEDGMENTS

■ REFERENCES

(1) Liu, B.; Tang, B. Z. Fluorescent Sensors. *Macromol. Rapid Commun.* **2013**, *34*, 704.

(2) Gao, M.; Tang, B. Z. Fluorescent Sensors Based on Aggregation-Induced Emission: Recent Advances and Perspectives. *ACS Sens.* **2017**, *2* (10), 1382−1399.

(3) Zhu, A.; Qu, Q.; Shao, X.; Kong, B.; Tian, Y. Carbon-Dot-Based Dual-Emission Nanohybrid Produces a Ratiometric Fluorescent Sensor for In Vivo Imaging of Cellular Copper Ions. *Angew. Chem., Int. Ed.* **2012**, *51* (29), 7185−7189.

(4) Qian, X.; Xu, Z. Fluorescence Imaging of Metal Ions Implicated in Diseases. *Chem. Soc. Rev.* **2015**, *44*, 4487−4493.

(5) Liu, K.; Xu, Z.; Yin, M.; Yang, W.; He, B.; Wei, W.; Shen, J. A. Multifunctional Perylenediimide Derivative (DTPDI) can be used as a Recyclable Specific Hg²⁺ Ion Sensor and an Efficient DNA Delivery Carrier. *J. Mater. Chem. B* **2014**, *2*, 2093−2096.

(6) de Souza, A. P. R.; Foster, C. W.; Kolliopoulos, A. V.; Bertotti, M.; Banks, C. E. Screen-Printed Back-to-Back Electroanalytical Sensors: Heavy Metal Ion Sensing. *Analyst* **2015**, *140*, 4130−4136.

(7) Qin, W.; Dou, W.; Leen, V.; Dehaen, W.; Auweraer, M. V. D.; Boens, N. A Ratiometric, Fluorescent BODIPY-Based Probe for Transition and Heavy Metal Ions. *RSC Adv.* **2016**, *6*, 7806−7816.

(8) Neupane, L. N.; Oh, E. T.; Park, H. J.; Lee, K. H. Selective and Sensitive Detection Selective and Sensitive Detection of Heavy Metal Ions in 100% Aqueous Solution and Cells with a Fluorescence Chemosensor Based on Peptide Using Aggregation-Induced Emission. *Anal. Chem.* **2016**, *88* (6), 3333−3340.

(9) Gale, P. A.; Caltagirone, C. Anion Sensing By Small Molecules and Molecular Ensembles. *Chem. Soc. Rev.* **2015**, *44*, 4212−4227.

(10) Lee, M.; Jo, S.; Lee, D.; Xu, Z.; Yoon, J. A New Naphthalimide Derivative as a Selective Fluorescent and Colorimetric Sensor for Fluoride, Cyanide and CO₂. *Dyes Pigm.* **2015**, *120*, 288−292.

(11) Moniz, S.; Hodgkinson, S.; Yates, P. Cardiac Transplant due to Metal Toxicity Associated with Hip Arthroplasty. *Arthroplast Today* **2017**, *3* (3), 151−153.

(12) Abdel-Gadir, A.; Berber, R.; Porter, J. B.; Quinn, P. D.; Suri, D.; Kellman, P.; Hart, A. J.; Moon, J. C.; Manisty, C.; Skinner, J. A. Detection of Metallic Cobalt and Chromium Liver Deposition Following Failed Hip Replacement Using T2* and R2Magnetic Resonance. *Journal of Cardiovascular Magnetic Resonance* **2016**, *18*, 29.

(13) Urbano, A. M.; Ferreira, L. M.; Alpoim, M. C. Molecular and Cellular Mechanisms of Hexavalent Chromium-Induced Lung Cancer: An Updated Perspective. *Curr. Drug Metab.* **2012**, *13* (3), 284−305.

(14) Zhang, Y.; Wang, Y. P.; Liu, P.; Song, J. M.; Xu, G. D.; Zheng, G. H. Effect of Toxic Fe²⁺ Levels on the Biological Characteristics of Rice Root Border Cells. *Russ. J. Plant Physiol.* **2012**, *59*, 766.

(15) Strauch, S. M.; Richter, P. R.; Haag, F. W. M.; Krüger, M.; Krüger, J.; Azizullah, A.; Breiter, R.; Lebert, M. Delayed Fluorescence, Steady State Fluorescence, Photosystem II Quantum Yield as Endpoints for Toxicity Evaluation of Cu²⁺ and Ag⁺. *Environ. Exp. Bot.* **2016**, *130*, 174−180.

(16) Huang, X.; Shabala, S.; Shabala, L.; Rengel, Z.; Wu, X.; Zhang, G.; Zhou, M. Linking Waterlogging Tolerance with Mn²⁺ Toxicity: A Case Study for Barley. *Plant Biol.* **2015**, *17* (1), 26−33.

(17) Teodoro, F. S.; Ramos, S. N.D.C.; Elias, M. M. C.; Mageste, A. B.; Ferreira, G. M. D.; Silva, L. H. M. D.; Gil, L. F.; Gurgel, L. V. A. Synthesis and Application of a New Carboxylated Cellulose Derivative. Part I: Removal of Co²⁺, Cu²⁺ And Ni²⁺ from Monocomponent Spiked Aqueous Solution. *J. Colloid Interface Sci.* **2016**, *483*, 185−200.

(18) Naushad, M.; Ahamad, T.; Sharma, G.; Al-Muhtaseb, A. H.; Albadarin, A. B.; Alam, M. M.; ALOthman, Z. A.; Alshehri, S. M.; Ghfar, A. A. Synthesis and Characterization of a New Starch/SnO₂ Nanocomposite For Efficient Adsorption of Toxic Hg²⁺ Metal Ion. *Chem. Eng. J.* **2016**, *300*, 306−316.

(19) Nair, A. R.; Lee, W. K.; Smeets, K.; Swennen, Q.; Sanchez, A.; Thévenod, F.; Cuypers, A. Glutathione and Mitochondria Determine Acute Defense Responses and Adaptive Processes in Cadmium-Induced Oxidative Stress and Toxicity of the Kidney. *Arch. Toxicol.* **2015**, *89* (12), 2273−2289.

(20) Naushad, M.; ALOthman, Z. A. Separation of Toxic Pb^{2+} Metal from Aqueous Solution Using Strongly Acidic Cation-Exchange Resin: Analytical Applications for the Removal of Metal Ions from Pharmaceutical Formulation. *Desalin. Water Treat.* **2015**, *53* (8), 2158−2166.

(21) Kim, J. H.; Kang, J. C. The Arsenic Accumulation and Its Effect on Oxidative Stress Responses in Juvenile Rockfish, *Sebastes Schlegelii*, Exposed to Waterborne Arsenic (As^{3+}). *Environ. Toxicol. Pharmacol.* **2015**, *39* (2), 668−676.

(22) Berger, L. M. Application of Hardness as Thermal Spray Coatings. *Int. J. Refract. Hard Met.* **2015**, *49*, 350−364.

(23) Daure, J. L.; Carrington, M. J.; Shipway, P. H.; McCartney, D. G.; Stewart, D. A. A Comparison of the Galling Wear Behavior Of PVD Cr and Electroplated Hard Cr Thin Films. *Surf. Coat. Technol.* **2018**, *350*, 40−47.

(24) Herath, I.; Iqbal, M. C. M.; Al-Wabel, M. I.; Abduljabbar, A.; Ahmad, M.; Usman, A. R. A.; Ok, Y. S.; Vithanage, M. Bioenergy-Derived Waste Biochar for Reducing Mobility, Bioavailability, and Phytotoxicity of Chromium in Anthropized Tannery Soil. *J. Soils Sediments* **2017**, *17* (3), 731−740.

(25) Titus, A. T. S.; Sudandararaj, S.; Sathish Kumar, G.; Dhivya, M.; Eithiraj, R. D.; Shameem Banu, I. B. Band Structure Calculation and Rietveld Refinement of Nanoscale $GdFeO_3$ with Affirmation of Jahn Teller's Distortion on Electric and Magnetic Properties. *J. Alloys Compd.* **2019**, *783*, 393−398.

(26) Zibrov, I. P.; Filonenko, V. P. Heavily Boron Doped Diamond Powder: Synthesis and Rietveld Refinement. *Crystals* **2018**, *8*, 297.

(27) Van de Weert, M.; Stella, L. Fluorescence quenching and ligand binding: A Critical Discussion of a Popular Methodology. *J. Mol. Struct.* **2011**, *998*, 144−150.

(28) Geethanjali, H. S.; Nagaraja, D.; Melavanki, R. M.; Kusanur, R. A. Fluorescence Quenching of Boronic Acid Derivatives by Aniline In Alcohols − A Negative Deviation from Stern-Volmer Equation. *J. Lumin.* **2015**, *167*, 216−221.

(29) Roy, S.; Bardhan, S.; Pal, K.; Ghosh, S.; Mandal, P.; Das, S.; Das, S. Crystallinity Mediated Variation in Optical and Electrical Properties of Hydrothermally Synthesized Boehmite (γ-AlOOH) Nanoparticles. *J. Alloys Compd.* **2018**, *763*, 749−758.

(30) (a) Roy, S.; Maity, A.; Mandal, P.; Chanda, D. K.; Pal, K.; Bardhan, S.; Das, S. Effects of Various Morphologies on the Optical and Electrical Properties of Boehmite Nanostructures. *CrystEngComm* **2018**, *20*, 6338−6350. (b) Zhang, X.; Zhang, X.; Graham, T. R.; Pearce, C. I.; Mehdi, B. L.; N'Diaye, A. T.; Kerisit, S.; Browning, N. D.; Clark, S. B.; Rosso, K. M. Fast Synthesis of Gibbsite Nanoplates and Process Optimizationusing Box-Behnken Experimental Design. *Cryst. Growth Des.* **2017**, *17*, 6801−6808. (c) Alex, T. C.; Kumar, R.; Roy, S. K.; Mehrotra, S. P. Leaching behaviour of high surface area synthetic boehmite in NaOH solution. *Hydrometallurgy* **2013**, *137*, 23−32.

(31) Das, S.; Das, S.; Das, D.; Sutradhar, S. Tailoring of Room Temperature Ferromagnetism and Electrical Properties in ZnO By Co (3d) and Gd (4f) Element Co-Doping. *J. Alloys Compd.* **2017**, *691*, 739−749.

(32) Zirehpour, A.; Rahimpour, A.; Seyedpour, F.; Jahanshahi, M. Developing New CTA/CA-Based Membrane Containing Hydrophilic Nanoparticles to Enhance the Forward Osmosis Desalination. *Desalination* **2015**, *371*, 46−57.

(33) Brostow, W.; Datashvili, T. Chemical Modification and Characterization of Boehmite Particles. *Chem. Chem. Technol.* **2008**, *2*, 27−32.

(34) Saikia, B. J.; Parthasarathy, G. Fourier Transform Infrared Spectroscopic Characterization of Kaolinite from Assam and Meghalaya, Northeastern India. *J. Mod. Phys.* **2010**, *1*, 206−210.

(35) Dandapat, A.; De, G. Nanorods Assembly of Mesoporous Boehmite Film on Glass: An Efficient Catalyst for Permanganate Reduction to MnO_2 Nanoparticles. *J. Mater. Chem.* **2010**, *20*, 3890−3894.

(36) Zhang, J.; Liu, S.; Lin, J.; Song, H.; Luo, J.; Elssfah, E. M.; Ammar, E.; Huang, Y.; Ding, X.; Gao, J.; Qi, S.; Tang, C. Self-Assembly of Flowerlike AlOOH (Boehmite) 3D Nanoarchitectures. *J. Phys. Chem. B* **2006**, *110*, 14249−14252.

(37) Chanda, D. K.; Das, P. S.; Samanta, A.; Dey, A.; Mandal, A. K.; Gupta, K. D.; Maitya, T.; Mukhopadhyay, A. K. Intertwined Nanopetal Assembly of $Mg(OH)_2$ Powders. *Ceram. Int.* **2014**, *40*, 11411−11417.

(38) Chanda, D. K.; Samanta, A.; Dey, A.; Das, P. S.; Mukhopadhyay, A. K. Nanoflower, Nanoplatelet and Nanocapsule $Mg(OH)_2$ Powders for Adsorption of CO_2 Gas. *J. Mater. Sci.* **2017**, *52* (9), 4910−4922.

(39) Liu, Y.; Ai, K.; Yuan, Q.; Lu, L. Fluorescence-Enhanced Gadolinium-Doped Zinc Oxide Quantum Dots for Magnetic Resonance and Fluorescence Imaging. *Biomaterials* **2011**, *32*, 1185−1192.

(40) (a) Brouwer, A. M. Standards for Photoluminescence Quantum Yield Measurements in Solution (IUPAC Technical Report)*. *Pure Appl. Chem.* **2011**, *83* (12), 2213−2228. (b) Lin, Z. J.; Zheng, H. Q.; Zheng, H. Y.; Lin, L. P.; Xin, Q.; Cao, R. Efficient Capture and Effective Sensing of $Cr_2O_7^{2-}$ from Water Using a Zirconium Metal−Organic Framework. *Inorg. Chem.* **2017**, *56*, 14178−14188. (c) Castet, S.; Dandurand, J. L.; Schott, J.; Gout, R. Boehmite solubility and aqueous aluminum speciation in hydrothermal solutions (90−350°C): Experimental study and modeling. *Geochim. Cosmochim. Acta* **1993**, *57* (20), 4869−4884. (d) Barrera-Díaz, C. E.; Lugo-Lugo, V.; Bilyeu, B. A review of chemical, electrochemical and biological methods for aqueous Cr(VI) reduction. *J. Hazard. Mater.* **2012**, *223−224*, 1−12.

(41) Hussain, S.; Malik, A. H.; Afroz, M. A.; Iyer, P. K. Ultrasensitive Detection of nitroexplosive−Picric Acid Via a Conjugated Poly-electrolyte in Aqueous Media and Solid Support. *Chem. Commun.* **2015**, *51*, 7207−7210.

(42) Mandal, J.; Ghorai, P.; Pal, K.; Karmakar, P.; Saha, A. 2-Hydroxy-5-Methylisophthalaldehyde Based Fluorescent-Colorimetric Chemosensor for Dual Detection of Zn2+ And Cu2+ with High Sensitivity and Application in Live Cell Imaging. *J. Lumin.* **2019**, *205*, 14−22.

(43) van de Weert, M.; Stella, L.V. D. Fluorescence Quenching and Ligand Binding: A Critical Discussion of a Popular Methodology. *J. Mol. Struct.* **2011**, *998*, 144−150.

(44) Vijayakumar, G.; Tamilarasan, R.; Dharmendirakumar, M. Adsorption, Kinetic, Equilibrium and Thermodynamic Studies on the Removal of Basic Dye Rhodamine-B from Aqueous Solution by the Use of Natural Adsorbent Perlite. *J. Mater. Environ. Sci.* **2012**, *3* (1), 157−170.

(45) Chung, H. K.; Kim, W. H.; Park, J.; Cho, J.; Jeong, T. Y.; Park, P. K. Application of Langmuir and Freundlich Isotherms to Predict Adsorbate Removal Efficiency or Required Amount of Adsorbent. *J. Ind. Eng. Chem.* **2015**, *28*, 241−246.

(46) Putro, J. N.; Santoso, S. P.; Ismadji, S.; Ju, Y. H. Investigation of Heavy Metal Adsorption in Binary System by Nanocrystalline Cellulose- Bentonite Nanocomposite: Improvement on Extended Langmuir Isotherm Model. *Microporous Mesoporous Mater.* **2017**, *246*, 166−177.

(47) Karthikeyan, T.; Rajgopal, S.; Miranda, L. R. Chromium(VI) Adsorption from Aqueous Solution by *Hevea Brasilinesis* Sawdust Activated Carbon. *J. Hazard. Mater.* **2005**, *124* (1−3), 192−199.

(48) Zhang, C.; Fu, Y. Y.; Zhang, X.; Yu, C.; Zhao, Y.; Sun, S. K. BSA-Directed Synthesis of CuS Nanoparticles as a Biocompatible Photothermal Agent for Tumor Ablation In Vivo. *Dalton Trans.* **2015**, *44*, 13112−13118.

PAPER

Cu(II) and Gd(III) doped boehmite nanostructures: a comparative study of electrical property and thermal stability

Shubham Roy[1] ⬚ , **Souravi Bardhan**[1], **Dipak Kr Chanda**[2] ⬚, **Anupam Maity**[3], **Saheli Ghosh**[1], **Dhananjoy Mondal**[1], **Subhankar Singh**[1] **and Sukhen Das**[1] ⬚

1 Department of Physics, Jadavpur University, Kolkata-700032, India
2 Advanced Materials and Mechanical Characterization Division, CSIR-Central Glass and Ceramics Research Institute, Kolkata- 700032, India
3 School of Materials Science, Indian Association for the Cultivation of Science, Kolkata- 700032, India

E-mail: sdasphysics@gmail.com

Abstract

The present article reports the effect of transition (Cu^{2+}) and rare earth metal (Gd^{3+}) ion doping on structural, microstructural and electrical properties of boehmite nanoparticles. Rietveld refinement is adopted here to refine the x-ray diffractograms for further analyzing the microstructural details and their alteration due to the incorporation of foreign cations. This is probably the first time when dielectric properties of these doped boehmite samples having been reported herein. These samples show remarkably high dielectric constant values which corroborate that doping enhances the microstrain values inside the orthorhombic structure and results in higher crystallographic defects. Enhancement in defect sites causes the augmentation of relative permittivity and ac conductivity. Temperature stability has also been enhanced significantly in our Cu-doped sample. The present study enables us to determine a relationship between crystalline deformation and electrical properties of nanomaterials which may be highly beneficial in fabricating cost-effective energy harvesting devices.

1. Introduction

Advancement of humankind put its giant footmark in every branch of science and technology and comes out with flourishing results like nanoscience and nanotechnology which enables us to go to any extent in material research that is still undiscovered. Nanotechnology and nanoscience is the pioneer of producing significantly promising nano-materials with applications in various fields of electronics [1, 2], catalysis [3–6], energy storage [7, 8], pharmaceutics and medical sciences [9–13]. Nowadays, researchers particularly focuses on multifunctional or hybrid nanomaterials those are having multiple areas of application. However, these multifunctional materials are either multi-crystalline or form a composite [7, 8]. Thus, a considerable amount of interest has been given nowadays for fabricating such nanocomposite or doped nanomaterial [14–16].

In spite of that, biocompatibility and bioavailability are major issues that determines the potential areas of application which is the main reason for the replacement of hazardous nanoparticles with biocompatible ones [17]. In recent times, some studies show that the researchers are focussing on biocompatible nano-systems to fabricate efficient and cost-effective organic solar cells [18], heavy metal sensors [19–21], gas sensors [22] and energy harvesting devices such as nanogenerators [23] and supercapacitors [24–26]. These next-generation nano-systems and nano-devices are capable to reduce environmental pollution and delivers greater efficiency [27, 28].

Boehmite (γ-AlOOH) is a typical oxy-hydroxide compound of aluminum with a layered orthorhombic structure [29, 30]. Previously, extensive research has been done on different synthesis pathways of this nanomaterial [31, 32]. Some research is based on different properties such as optical [33], electrical [34], mechanical properties [35] of boehmite those are showing its multi-dimensional usability. Biocompatibility is another major advantage of selecting boehmite for any application [36]. Boehmite was reported as a promising dental and orthopedic material due to its biocompatibility and bioavailability [37, 38]. Nonetheless, a very limited amount of interest has been paid on hybrid or doped boehmite nanostructure.

In this study, we have developed a transition metal (Cu(II)) and another rare earth metal (Gd(III)) derived boehmite nano-systems that are capable of producing remarkably high electrical permittivity and greater temperature stability (in case of the copper doped sample). The foreign metal ions are doped into the orthorhombic structure of boehmite matrix in a very small quantity (1% weight) and characterized by using x-ray Diffraction (XRD), FT-IR (Fourier Transform Infrared Spectroscopy), TEM (Transmission Electron Microscopy) and Brunauer–Emmett–Teller (BET). A detailed crystallographic analysis of the samples was done by refining the XRD patterns of the samples by using a Rietveld based software package MAUD and analyzed herein. Comprehensive dielectric and ac conductivity studies have been performed and analyzed to ascertain the alteration of electrical quality of the samples as a function of crystallographic deformation created by foreign metal ion mediated doping. Increasing temperature stability, extensively high dielectric value with a very low tangent loss makes these doped boehmite samples potential candidates for energy harvesting applications.

2. Experimental section

2.1. Materials

Aluminum nitrate nonahydrate [$Al(NO_3)3 \cdot 9H_2O$], aqueous ammonia solution (25%), copper acetate, acetone (HPLC grade) and ethanol (HPLC grade) were purchased from Merck, India while gadolinium oxide was purchased from SRL, India. All the reagents used were of analytical grade and were used without any further purification. Millipore water with a resistivity of at least 18.2 MΩ.cm was used throughout our experiments.

2.2. Synthesis

Nanostructures of doped and undoped boehmite samples were synthesized by a facile two step hydrothermal process. Undoped boehmite nanoparticles (NBH) were obtained by dissolving aluminum nitrate in 70 ml Millipore water using magnetic stirrer at room temperature followed by the drop-wise addition of ammonia solution until the pH reached at 10. In case of copper-doped boehmite (CBH) and gadolinium-doped boehmite (GBH), copper acetate and gadolinium oxide were added respectively into the solutions, maintaining the weight ratios of Cu and Gd to be 1%, followed by pH adjustment at 10 using ammonia solution. After proper dissolution through vigorous stirring for 3 h, the solutions were transferred into separate Teflon lined stainless steel autoclaves which were then placed in a dust free hot air oven at180 °C for 18 h.

The solid precipitates were collected from the bottom of each Teflon jacket, washed several times with Millipore water, dried in vacuum at room temperature, then ground using a mortar, marked and sent for further characterizations.

3. Results and discussion

3.1. Structural and microstructural analysis

X-Ray Diffraction (XRD) is an efficient and significant characterization tool for the determination of crystal size, structure, microstructure along with detection and quantification of phase purity [39]. To determine the crystallinity of our samples, an x-ray powder Diffractometer (XRD) (D8, Bruker AXS, Winconsin, USA) was employed using Cu-Kα target at the wavelength of 1.5418 Å and operated at 35 kV, 35 mA with a scan speed of 2 s/step and 2θ range from 15°–60°. Structural and microstructural parameters were studied through the refinement of the obtained samples using Rietveld based MAUD program (version: 2.8), and the refined structures were theoretically constructed using the VESTA program (version: 3.4.3). Figure 1 depicts the XRD patterns of the synthesized samples superimposed with corresponding miller indices, which are found to be in good agreement with the Joint Committee on Powder Diffraction Standards (JCPDS) card no.21–1307. Absence of any extra undesirable peak confirms their purity and ascertain that both Gd^{3+} and Cu^{2+} ions in the case of GBH and CBH respectively do not alter the orthorhombic structure of boehmite even up to 1% doping and are successfully incorporated into the structure.

Rietveld refinement was performed for the undoped (NBH) and doped (CBH and GBH) samples to analyze their microstructural and structural characteristics [40]. There is a subsequent increase in microstrain on the addition of foreign Gd^{3+} and Cu^{2+} ions, which might be due to the substitution of smaller Al^{3+} ions (0.53 Å) by larger Gd^{3+} ions (0.94 Å) or Cu^{2+} ions (0.71 Å) into the orthorhombic unit cells [41]. Besides that, entry of larger cation inside the lattice structure causes internal homogeneous lattice stress which is evident from the slight shifting of diffraction maxima towards the higher diffraction angle in the case of CBH and GBH [42]. Thus the dopants have created structural defects that can alter various physicochemical properties of boehmite. All structural and microstructural data obtained from the refinement for all the three samples are illustrated in table 1.

Detailed analysis of structural and bond properties was done by using Vesta v3.4.3 (Visualization for Electronic and Structural Analysis) software and have been depicted in figure 1. Incorporation of Gd^{3+} and
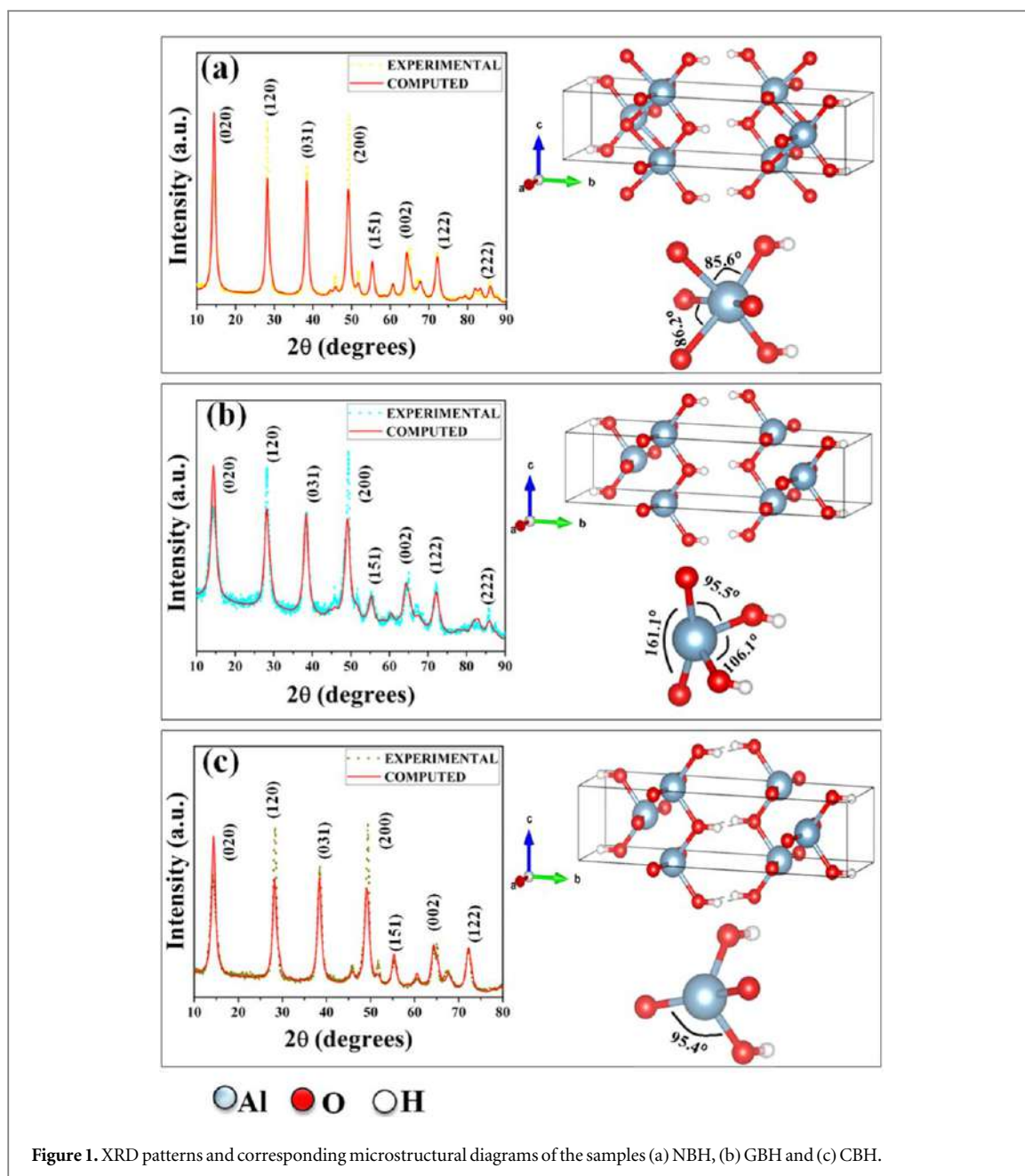
Figure 1. XRD patterns and corresponding microstructural diagrams of the samples (a) NBH, (b) GBH and (c) CBH.

Table 1. Structural and microstructural parameters of the samples obtained from Rietveld refinement of XRD diffractograms.

Parameters	NBH	GBH	CBH
a (Å)	$3.69205 \pm 7.694 \times 10^{-4}$	$3.6949866 \pm 0.0013171516$	$3.688224 \pm 8.923 \times 10^{-4}$
b (Å)	$12.210675 \pm 0.0033434944$	$12.242514 \pm 0.0064571705$	$12.226487 \pm 0.004935658$
c (Å)	$2.8641748 \pm 5.9727 \times 10^{-4}$	$2.8604217 \pm 0.0010346824$	$2.8592756 \pm 7.333 \times 10^{-4}$
nanocrystallite size (nm)	12.583597 ± 1.2386371	7.7872505 ± 0.72373766	11.0133644 ± 1.0858079
strain	1.3950×10^{-9}	1.7313×10^{-5}	4.6784×10^{-6}
χ^2	1.6206	1.7689	1.6984
R_p (%)	0.16076866	0.094971605	0.12739837
R_{wp} (%)	0.20466273	0.12631688	0.16602717

Cu^{2+} ion does not alter the structural symmetry but the stress created from substitution by larger ions (Gd^{3+} and Cu^{2+}) changes the bond angle (table 3) and bond lengths (table 2) slightly in case of GBH and CBH.

In order to ensure successful incorporation of Gd^{3+} and Cu^{2+} into the orthorhombic structure of boehmite, FT-IR spectroscopy was performed (figure 2) in a Shimadzu FTIR-8400S spectrometer in the wavenumber range from 400 cm^{-1} to 4000 cm^{-1} and 80 individual scans were taken and merged together to obtain the final spectra for
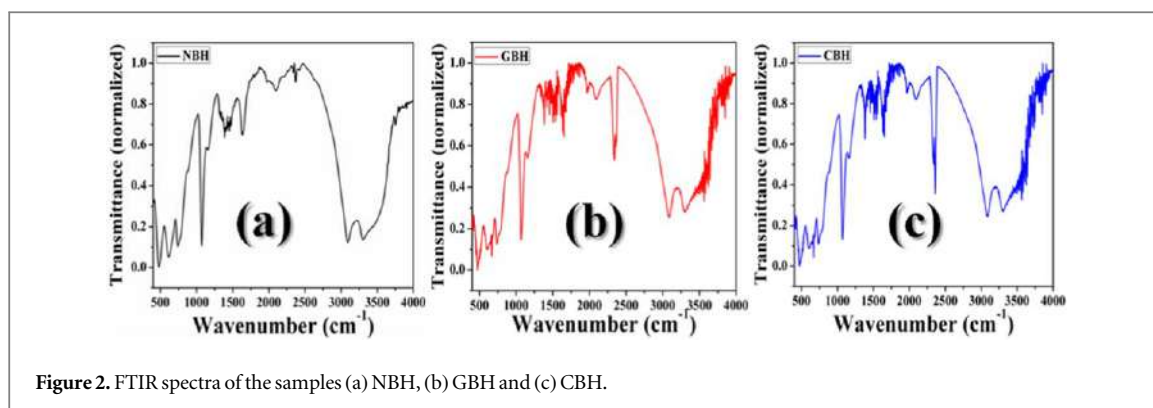
Figure 2. FTIR spectra of the samples (a) NBH, (b) GBH and (c) CBH.

Table 2. Variation of the bond lengths of pure and doped boehmite samples.

Nature of the bond	NBH (Å)	GBH(Å)	CBH(Å)
Al–O (O$_1$)	1.87386	1.87285	1.86532
Al–OH (O$_2$)	1.83549	1.78957	1.83252

Table 3. Variation of the bond angles of pure and doped boehmite samples.

Angle between	NBH (degree)	GBH(degree)	CBH(degree)
OH–Al–O	85.5992	95.6575	95.3984
OH–Al–OH	102.5614	106.1062	102.5486
O–Al–O	86.2401	161.1207	162.7013

each sample. 2 mg of each sample was homogenized with 100 mg KBr (at 1:50 ratio) and the mixtures were pressed for 5 min at 5 ton in a hydraulic hand press to form a 10 mm pellet which was dried at 80 °C for 4 h before measurement in order to remove excess moisture. Figure 2 depicts the FTIR spectra of as-synthesized nanostructures.

In the case of normal boehmite (NBH), the absorption peaks were located at 480, 758, and 634 cm^{-1}, which are the characteristic peaks of boehmite [43]. Small peaks located at 1069 and 1158 cm^{-1} respectively were due to Al-O-H vibration [44]. Absorption bands located at 3095 and 3305 cm^{-1} are due to symmetric and asymmetric O–H vibrations respectively [45]. The absorption band at 1634 cm^{-1} is due to moisture adsorbed on the surfaces of the samples [46]. Moreover, GBH and CBH samples show a similar type of absorption band pattern which signifies that incorporation of the Gd^{3+} and Cu^{2+} neither alter any bond structure nor create any bonding network inside the boehmite phase, which agrees with our XRD results.

Detailed morphological features were analyzed by using a JEOL JEM-2000 transmission electron microscope (TEM) with an operating voltage of 200 kV. A minute amount of sample was well-dispersed in acetone, sonicated till the homogenous solution was formed, and then drop-casted on carbon-coated copper grids of 300 mesh for microscopy.

Doping-dependant alteration in morphological features of the three samples was investigated using TEM analysis which confirmed that there is a change in particle morphology resulting from subsequent addition of Gd^{3+} and Cu^{2+} ions in the structure (figure 3). In the case of the undoped sample (NBH), the particles appeared to be hexagonal with a sponge-like porous structure. Copper doped boehmite (CBH) sample shows highly porous rhomboidal morphology with a mean pore diameter of 2–4 nm. Rare earth gadolinium doped GBH particles appeared to be rod-like. Previously, we have mentioned in our article [38] that increasing microstrain changes the particle morphology significantly by virtue of crystal defects which contribute toward this morphological evolution [41]. Here, in the case of CBH, the ionic radius of copper ions is quite smaller than that of gadolinium ions. Thus, the microstrain created inside the orthorhombic structure of the host material in the case of CBH is also lower than that of GBH. Henceforth, the morphology has drastically been changed into rod-shaped, whereas, CBH sample has been completely transformed into rhomboidal particles. Moreover, the incorporation of foreign cations inside the pure boehmite matrix have been examined and justified by using Energy Dispersive x-ray spectroscopy (EDX) (figure 4). The traces of Gd and Cu inside the orthorhombic phase
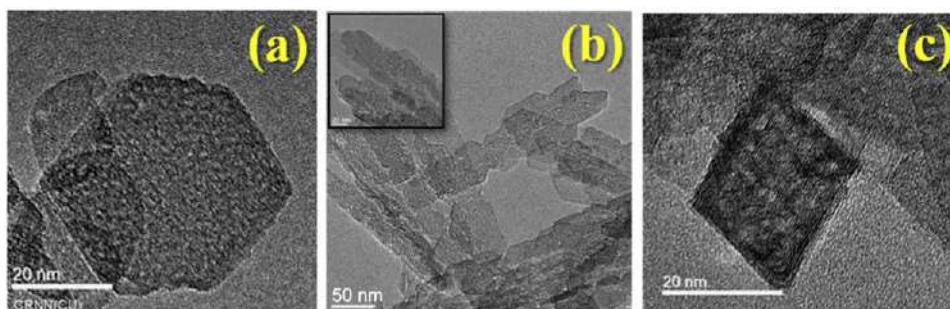
Figure 3. TEM micrographs of as-synthesized (a) NBH, (b) GBH and (c) CBH.
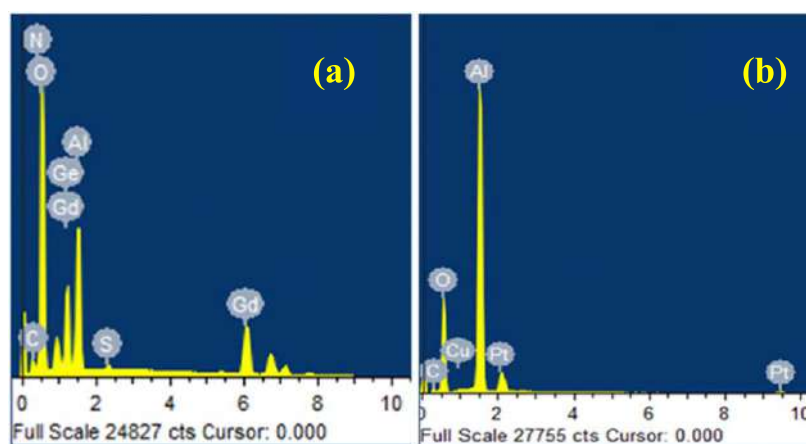
Figure 4. EDX spectra of (a) GBH and (b) CBH samples those are showing the traces of Gd and Cu respectively in the boehmite (γ-AlOOH) matrix.
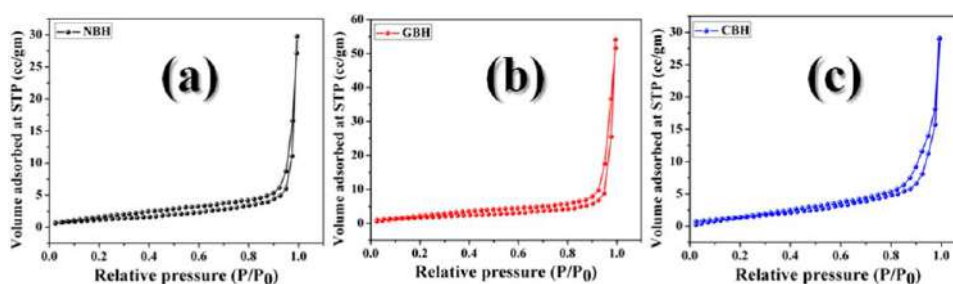
Figure 5. N$_2$ adsorption/desorption isotherm of (a) NBH, (b) GBH and (c) CBH.

of boehmite can be observed in EDX data which corroborates that the foreign impurities have been properly incorporated in the boehmite samples.

3.2. Surface area and porosity analysis

The pore size distribution and surface area of the as-synthesized nanostructures have been analyzed through Brunauer–Emmett–Teller (BET) and Barrer-Joyner-Halenda (BJH) methods by using N$_2$ gas adsorption-desorption values by employing a Twin Surface Area Analyzer from Quanta-chrome Instruments (USA).

Surface areas of the synthesized nanostructures corresponding to the nitrogen (N$_2$) adsorption-desorption isotherms and their corresponding pore size distributions are illustrated in figure 5. The type-IV isotherm (figure 6) obtained from the data indicates that the undoped (NBH) sample is mesoporous, having a pore diameter of 3.53 nm in our samples [47, 48]. H4-type hysteresis loops were obtained for all the samples,
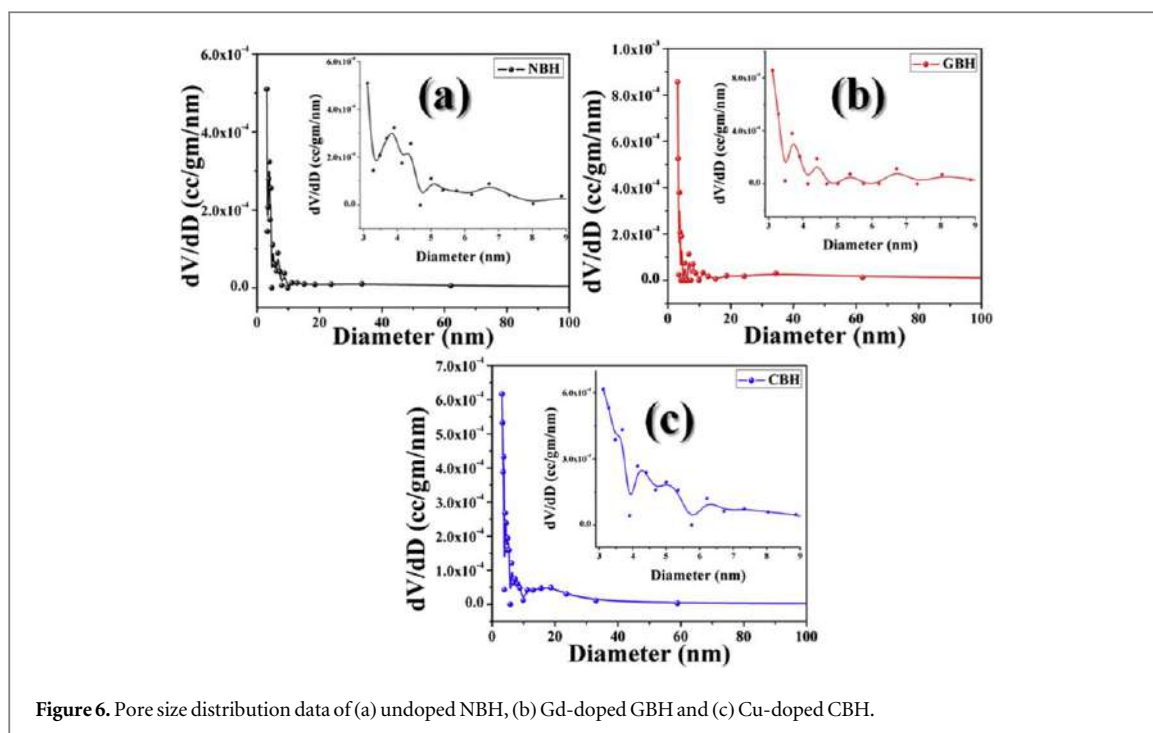
Figure 6. Pore size distribution data of (a) undoped NBH, (b) Gd-doped GBH and (c) Cu-doped CBH.

Table 4. Estimated BET surface area, pore radius and pore volume of pure and doped boehmite nanostructures.

Sample name	Surface area (m^2/g)	Pore size (nm)	Pore volume (cc./g)
NBH	4.473	3.530	4.292×10^{-2}
GBH	6.406	3.113	9.532×10^{-2}
CBH	5.282	3.113	4.514×10^{-2}

indicating the formation of slit-like pores [47, 48]. From the BET data, it is quite evident that the surface areas of the doped boehmite samples enhanced quite significantly. The surface area for NBH was found to be 4.473 m^2 g^{-1} while the surface area of CBH and GBH was found to be 5.282 m^2 g^{-1} and 6.406 m^2 g^{-1} respectively (table 4). This surface area enhancement could be beneficial for producing high dielectric materials.

3.3. Dielectric permittivity analysis

Electrical properties (dielectric constant and electrical conduction mechanism) were determined by using an Agilent 4294 A Precision Impedance Analyzer operating at 0.5 V bias voltages set at a frequency range from 40 Hz to 10 MHz. Solid pellets of the samples were prepared to compact them in the Hydraulic press system at 5 tons for 5 min, using small metallic sample holders and the sent for electrical characterizations.

Dielectric properties of a material can be described using the relation [49],

$$\varepsilon = \varepsilon' + j\,\varepsilon'' \tag{1}$$

where, ε' and ε'' are the real and imaginary part of the relative dielectric constant respectively, and ε' contributes to the quantity of energy stored in the material due to polarization effect and often referred as dielectric constant, whereas the imaginary part (ε'') is related to the energy dissipated by the material. The real part of the dielectric constant can be calculated using the relation:

$$\varepsilon' = \frac{C.d}{\varepsilon_0 \mathrm{A}} \tag{2}$$

where, C is the capacitance of the sample, d and A are thickness and surface area of the sample respectively and ε_0 is the permittivity of free space (8.85×10^{-12} F m^{-1}). Doping dependent variation of the real part of the dielectric constant (ε') with applied field frequency (ranging from 40 Hz to 10 MHz) at different temperatures ranging from 30 °C to 150 °C has been shown in figures 7(a)–(c).
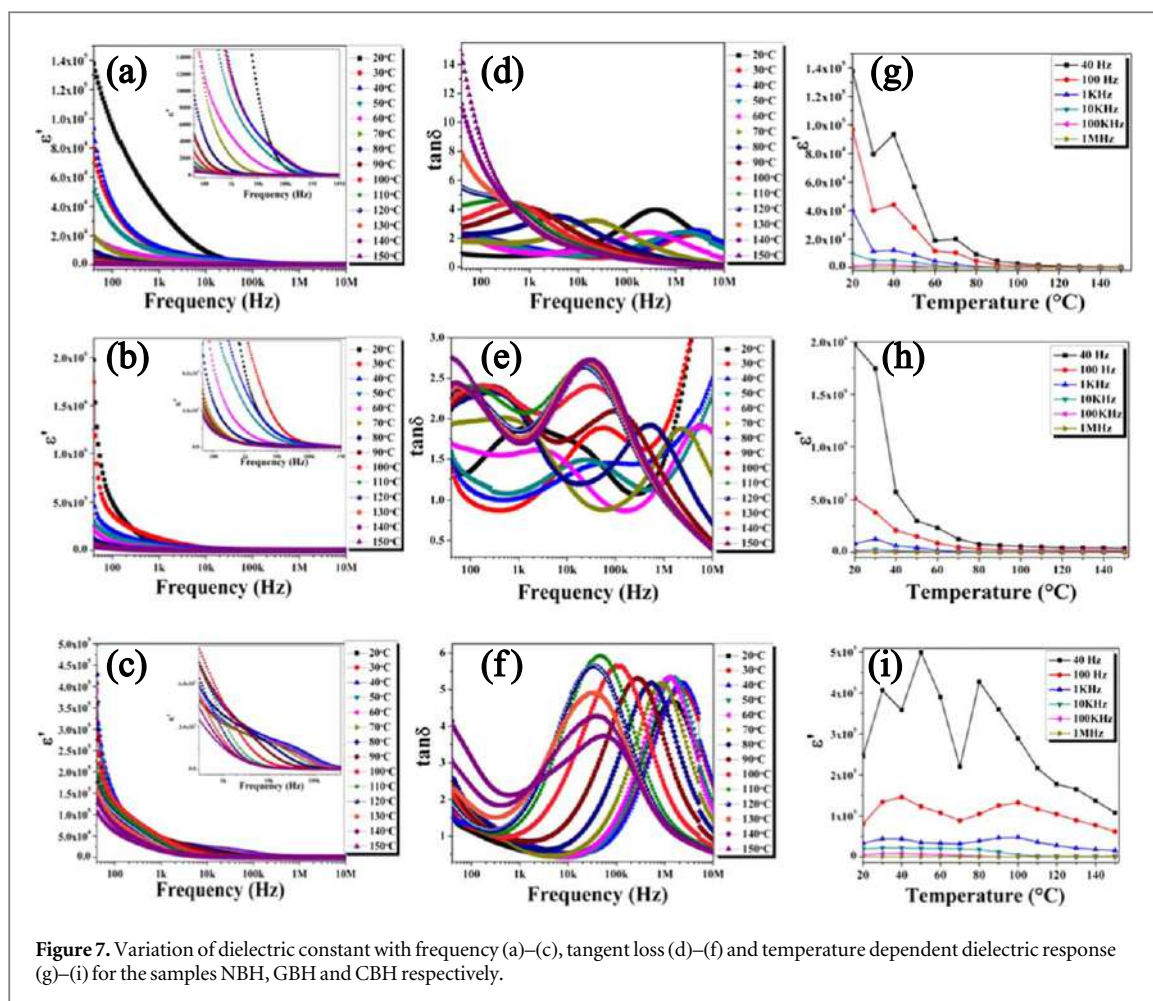
Figure 7. Variation of dielectric constant with frequency (a)–(c), tangent loss (d)–(f) and temperature dependent dielectric response (g)–(i) for the samples NBH, GBH and CBH respectively.
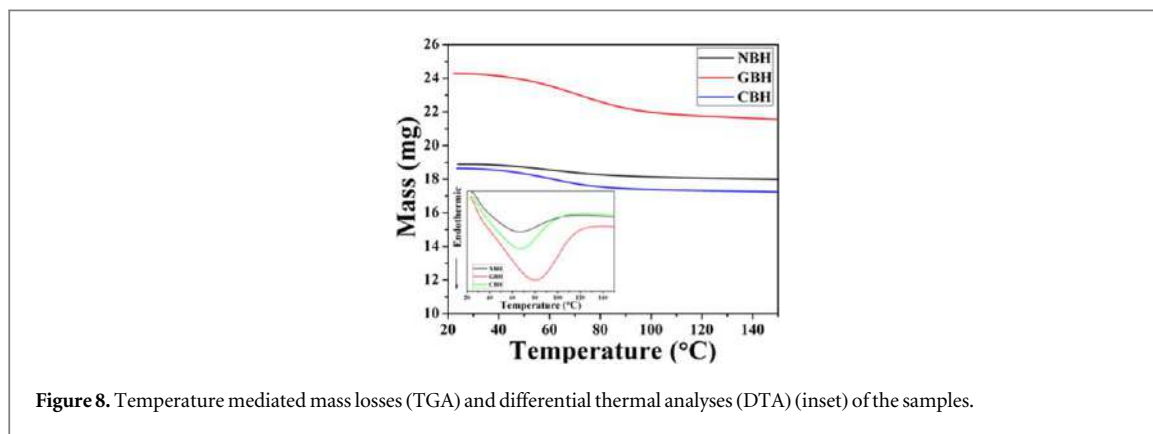
Figure 8. Temperature mediated mass losses (TGA) and differential thermal analyses (DTA) (inset) of the samples.

In all three samples, there was a drastic reduction of dielectric constant value with increasing frequency. The values of the dielectric constant at lower frequency were considerably higher due to the Maxwell-Wagner interfacial polarization effect [50, 51], which is in good agreement with Koop's theory [52]. As per this theory, the conducting grains of the dielectric medium are separated by poorly conducting grain boundaries which are formed due to imperfection in crystal alignment. Doping of larger sized ions like Gd^{3+} and Cu^{2+} causes crystal defects, as evident from our XRD results. These defects generate space charge distributions at the interfaces. Space charge comes under the influence of the external field and trapped at interfacial defects centers on grain boundary during their movement and converted into dielectric species that result in high dielectric constant in our doped samples [53, 54].

On the other hand, incorporation of larger sized Gd-ions into the boehmite matrix causes higher stress, resulting in nearly rod-shaped morphology that enhances the surface to volume ratio and results in the highest value for dielectric constant (1.973×10^6) at room temperature and 40 Hz frequency. A lower amount of
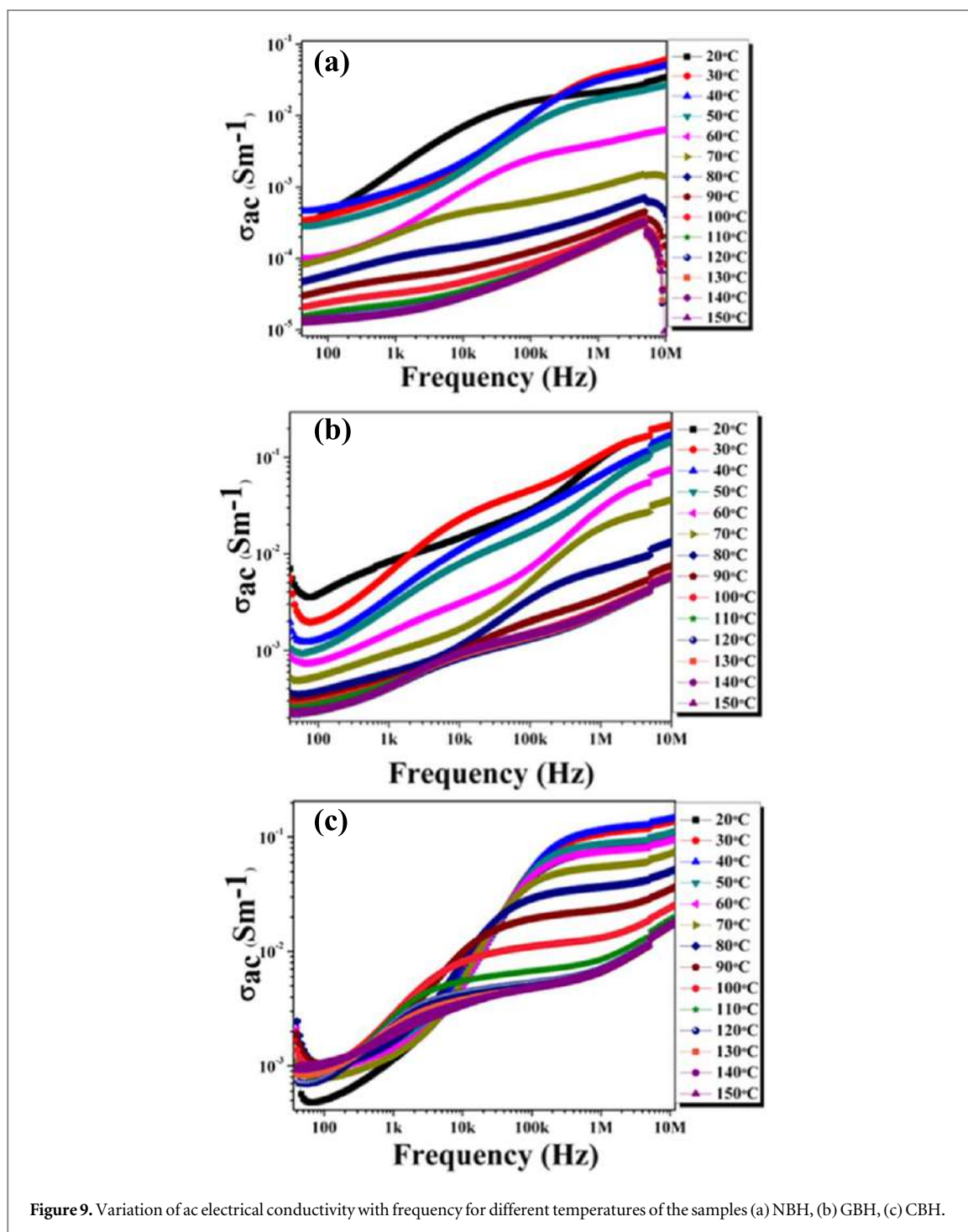
Figure 9. Variation of ac electrical conductivity with frequency for different temperatures of the samples (a) NBH, (b) GBH, (c) CBH.

microstrain developed due to the incorporation of copper ions which further creates rhomboidal particles with a surface area of 5.282 m^2 g^{-1} and causes a dielectric constant of 4.07 $\times$ 10^5, while for NBH, it was found to be lowest (1.37 $\times$ 10^5).

In reality, the enhanced surface to volume ratio can accommodate a higher number of electric dipoles dielectric species that further can enhance the permittivity value as we have mentioned herein. Henceforth, the dielectric constant of our doped samples enhanced not only due to the crystal defects but also due to the higher surface to volume ratios.

Tangent losses of our synthesized nanostructures are in good agreement with high dielectric values. In every case, the peaks of the loss tangent shift toward the lower frequency sides with increasing temperatures (figures 7(d)–(f)). This is because, at higher temperatures γ-AlOOH (boehmite) turns into another unstable phase (γ*-AlOOH) that has more oxygen vacancies [55]. These vacancy defects contribute to higher values of the tangent loss in the low-frequency regions and at high temperatures.
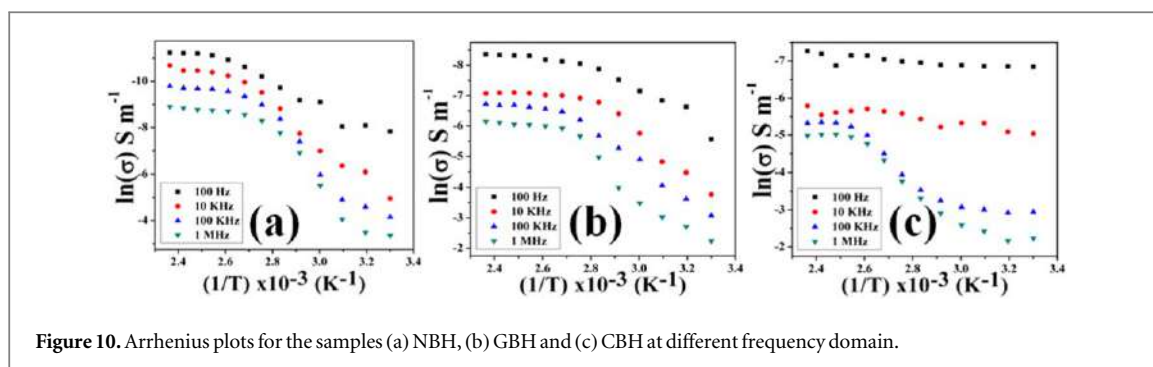
Figure 10. Arrhenius plots for the samples (a) NBH, (b) GBH and (c) CBH at different frequency domain.

Table 5. Calculated Activation energies (E_a) from Arrhenius plots.

Sample name	Frequency	E_a(eV)
NBH	100 hz	0.5135
	10 kHz	0.7301
	100 kHz	0.9028
	1 MHz	0.9728
GBH	100 hz	0.2658
	10 KHz	0.6803
	100 KHz	0.7248
	1 MHz	0.784
CBH	100 Hz	0.0428
	10 KHz	0.0976
	100 KHz	0.4001
	1 MHz	0.5281

The permittivity graphs plotted against varying temperatures have been depicted in figures 7(g)–(i) which illustrates that the dielectric value is quite high for NBH and GBH up to 70°–80 °C temperatures and then slowly decreases. Thermo-gravimetric analysis (TGA) and Differential Thermal Analysis (DTA) have been performed to investigate this phenomenon (figure 8). Very small amount of samples have been placed into platinum crucibles and the TGA-DTA were performed in presence of N2 gas as the medium. A DTG-60H, Shimadzu was employed for this purpose with a constant heating rate of 10 °C min^{-1}.

TGA-DTA data shows that the mass loss in case of NBH is around 4.796% with an endothermic peak centered at 66.67 °C, whereas, it is 11.157% and 7.453% with peaks centered at 79.92 and 67.17 °C for GBH and CBH respectively. As par our dielectric data suggest, the electrical permittivity also decreases slowly in this particular region due to the release of adsorbed moisture from the surface of the samples. Nonetheless, low mass losses indicate that our samples are quite stable up to 150 °C and applicable for capacitive applications and incorporation of foreign cations increases the thermal stability of our doped samples.

3.4. Electrical conduction mechanism

The electrical conductivity of the three nanostructures is investigated to explore the conduction mechanism. From figure 9 it is quite evident that the lower frequency region (<10 kHz) contributes low values of ac conductivity for all the samples as the grain boundary restricts the hopping of the free charge carriers [56]. Beyond the 10 kHz field frequency, the samples exhibit high values of ac conductivities. In the high-frequency domain, charge carriers get their activation energies (E_a) to overcome the potential barrier and results in higher values of electrical conductivities. The activation energies of the entire sample set have been calculated by using the Arrhenius equation as follows [57],

$$\sigma = \sigma_0 \, e^{\frac{-E_a}{K_B T}}$$

(3)

where E_a is the activation energy, σ_0 be the pre-exponential factor, K_B is Boltzmann constant and T is the absolute temperature. Arrhenius plots were estimated from the ac conductivity data calculated at field frequencies 100 Hz, 10 kHz, 100 kHz and 1 MHz (figure 10). A detailed depiction of activation energies is given in table 5.

Among the three samples, GBH shows the highest conductivity values at higher frequency region and NBH has the lowest value of ac conductivity among these three samples. In reality, doped samples (GBH and CBH) have a higher surface area and a higher number of free charge carriers which makes them easier to perform hopping from one grain to another under the external electric field frequency. Henceforth, doped boehmite samples, especially GBH have the potential to produce good conduction among the three.

4. Conclusion

Here we synthesized transition metal (Cu(II)) and rare earth metal (Gd(III)) decorated boehmite nanostructures and analyzed their structural, microstructural and electrical properties based on crystallographic deformation. This is the first time when the dielectric and conductivity properties of these doped samples along with pure boehmite nanostructure have been performed and compared. Rietveld refinement enables us to perform microstructural analyses that make a crucial impact to study the dielectric and ac conductivity of these nanostructures. Increasing microstrain not only generates crystal defects but also enhances the electrical properties significantly by modulating surface area and morphology. Temperature-dependent variation of electrical parameters of these nanostructures shows that particularly doped samples are electrically stable which was further investigated by using TGA-DTA. Among these three nanostructures, GBH shows a promising value of dielectric constant (1.97×10^6 at 40 Hz frequency in room temperature) with a very low tangent loss whereas, copper doped CBH has a high dielectric permittivity with remarkably high-temperature stability. Due to their colossal permittivity, high-temperature stability and negligible tangent loss, these doped boehmite samples could be used as potential materials in energy harvesting devices.

Acknowledgments

Notes

The authors declare no conflict of interest.

Synopsis

This work demonstrates how incorporation of infinitesimally small amounts of transition metal Cu(II) and rare earth metal Gd(III) alters the crystallographic properties of doped boehmite samples and results in the enhancements of temperature stability and electrical properties of the doped boehmite samples.

ORCID iDs

Shubham Roy ⓘ https://orcid.org/0000-0001-5245-3229
Dipak Kr Chanda ⓘ https://orcid.org/0000-0003-0147-4972
Sukhen Das ⓘ https://orcid.org/0000-0001-8372-3076

References

[1] Shipway A N, Katz E and Willner I 2000 *Chem. Phys. Chem.* **1** 18–52
[2] Sarkar S and Chattopadhyay K K 2012 *Physica E* **44** 1742–6
[3] Mendoza-Damián G, Tzompantzi F, Pérez-Hernández R, Gómez R and Hernández-Gordillo A 2016 *Catalysis Today* **266** 82–9
[4] Maity A and Panda S K 2018 *AIP Conf. Proc.* (https://doi.org/10.1063/1.5028688)
[5] Yang Y *et al* 2019 *Chinese Chemical Letters* **30** 2065–88
[6] Yang Y *et al* 2019 *Chinese Chemical Letters* **30** 2089–109
[7] Hu Y and Wang Z L 2015 *Nano Energy* **14** 3–14
[8] Xu B, Qi S, Li F, Peng X, Cai J, Liang J and Ma J 2019 *Chinese Chemical Letters* **31** 217–22
[9] Lead J R, Batley G E, Alvarez P J, Croteau M N, Handy R D, McLaughlin M J, Judy J D and Schirmer K 2018 *Environmental toxicology and chemistry* **37** 2029–63
[10] Carretero M I and Pozo M 2009 *Applied Clay Science* **46** 73–80
[11] Oun A A, Shankar S and Rhim J W 2019 *Critical Reviews in food Science and Nutrition* 1–26
[12] Guo S, Dong S and Wang E 2009 *Chem. Eur. J.* **15** 2416–24
[13] Liu J, Ma Q, Huang Z, Liu G and Zhang H 2019 *Adv. Mater.* **31** 1800696

[14] Zhao P, Yao M, Ren H, Wang N and Komarneni S 2019 *Appl. Surf. Sci.* **463** 931–8

[15] Maity A, Samanta S, Chatterjee S, Maiti R, Biswas D, Saha S K and Chakravorty D 2018 *Journal of Physics D: Applied Physics* **51** 245301

[16] Samanta S, Maity A, Chatterjee S, Maiti R, Biswas D, Giri S and Chakravorty D 2019 *Transactions of the Indian Institute of Metals* **72** 1963–9

[17] Ovais M, Khalil A T, Raza A, Islam N U, Ayaz M, Saravanan M, Ali M, Ahmad I, Shahid M and Shinwari Z K 2018 *Appl. Microbiol. Biotechnol.* **102** 4393–408

[18] Hou J, Inganäs O, Friend R H and Gao F 2018 *Nat. Mater.* **17** 119

[19] Gan X, Zhao H, Schirhagl R and Quan X 2018 *Microchimica Acta* **185** 478

[20] Liu X, Yao Y, Ying Y and Ping J 2019 *Trends Anal. Chem.* **115** 187–202

[21] Tsai W T, Nguyen M H, Lai J R, Nguyen H B, Lee M C and Tseng F G *Sens. Actuators, B* **265** 75–83

[22] Dey A 2018 *Mater. Sci. Eng. B* **229** 206–17

[23] Hoque N A, Thakur P, Biswas P, Saikh M M, Roy S, Bagchi B, Das S and Ray P P 2018 *J. Mater. Chem. A* **6** 13848–58

[24] Chen C, Zhang Y, Li Y, Dai J, Song J, Yao Y, Gong Y, Kierzewski I, Xie J and Hu L 2017 *Energy Environ. Sci.* **10** 538–45

[25] He S *et al* 2017 *Carbon* **122** 162–7

[26] Wu D, Zhang W, Feng Y and Ma J 2020 *Journal of Materials Chemistry A.* (https://doi.org/10.1039/C9TA12859J)

[27] Cicciù M, Fiorillo L, Herford A S, Crimi S, Bianchi A, D'Amico C, Laino L and Cervino G 2019 *Biomedicines* **7** 12

[28] Grumezescu A and Oprea A E (ed) 2017 *Nanotechnology Applications in Food: Flavor, Stability, Nutrition and Safety* (New York: Academic)

[29] Štefanić G and Musić S 2011 *Croat. Chem. Acta* **84** 481–5

[30] Haghnazari N, Abdollahifar M and Jahani F 2014 *J. Mex. Chem. Soc.* **58** 95–8

[31] Musić S, Dragčević Đ and Popović S 1999 *Mater. Lett.* **40** 269–74

[32] Bai X, Caputo G, Hao Z, Freitas V T, Zhang J, Longo R L, Malta O L, Ferreira R A and Pinna N 2014 *Nat. Commun.* **5** 5702

[33] Kirchner S, Teychené S, Boualleg M, Dandeu A, Frances C and Biscans B 2015 *Chem. Eng. J.* **280** 658–69

[34] Abram A, Eršte A, Dražić G and Bobnar V 2016 *J. Mater. Sci: Mater. Electron* **27** 10221–5

[35] Wu Z, Zhuo Q, Sun T and Wang Z 2015 *J. Appl. Polym. Sci.* **132** 41409

[36] Solovev Y V, Prilepskii A Y, Krivoshapkina E F, Fakhardo A F, Bryushkova E A, Kalikina P A, Koshel E I and Vinogradov V V 2019 *Sci. Rep.* **9** 1176

[37] Liu G H, Li Z, Li X B, Qi T G, Peng Z H and Zhou Q S 2017 *Int. J. Miner, Metall Mater.* **24** 954–63

[38] Roy S, Pal K, Bardhan S, Maity S, Chanda D K, Ghosh S, Karmakar P and Das S 2019 *Inorg. Chem.* **58** 8369–78

[39] Bunaciu A A, UdriŞTioiu E G and Aboul-Enein H Y 2015 *Crit. Rev. Anal. Chem.* **45** 289–99

[40] Serafini A, Lutterotti L, Gross S and Gialanella S 2017 *Powder Diffr.* **32** S63–8

[41] Das S, Das S, Roychowdhury A, Das D and Sutradhar S 2017 *J. Alloys Compd.* **708** 231–46

[42] Ateia E E, Ahmed M A, Salah L M and El-Gamal A A 2014 *Phys. B* **445** 60–7

[43] Zirehpour A, Rahimpour A, Seyedpour F and Jahanshahi M 2015 *Desalination* **371** 46–57

[44] Brostow W and Datashvili T 2008 *Chem. Chem. Technol.* **2** 27–32

[45] Dandapat A and De G 2010 *J. Mater. Chem.* **20** 3890–4

[46] Zhang J *et al* 2006 *J. Phys. Chem. B* **110** 14249–52

[47] Chanda D K, Das P S, Samanta A, Dey A, Mandal A K, Gupta K D, Maity T and Mukhopadhyay A K 2014 *Ceram. Int.* **40** 11411–7

[48] Chanda D K, Samanta A, Dey A, Das P S and Mukhopadhyay A K 2017 *J. Mater. Sci.* **52** 4910–22

[49] Usha V, Kalyanaraman S, Vettumperumal R and Thangavel R 2017 *Physica B* **504** 63–8

[50] Chuprinko D and Titov K 2017 *Geophys. J. Int.* **209** 186–91

[51] Das S, Das S, Roychowdhury A, Das D and Sutradhar S 2017 *J. Alloys Compd.* **708** 231–46

[52] Koops C G 1951 *Phys. Rev.* **83** 121–4

[53] Hassan A, Mustafa G M, Abbas S K, Atiq S, Saleem M, Riaz S and Naseem S 2019 *Ceram. Int.* **45** 14576–85

[54] Qi X, Sun E, Zhang R, Yang B, Li S and Cao W 2017 *Ceram. Int.* **43** 16819–26

[55] Wang J A, Bokhimi X, Morales A, Novaro O, Lopez T and Gomez R 1999 *J. Phys. Chem. B* **103** 299–303

[56] Kabashima S and Kawakubo T 1968 *J. Phys. Soc. Jpn* **24** 493–7

[57] Sudha L K, Sukumar R and Uma Rao K 2014 *Int. J. Mach. Mach. Mater.* **2** 96–100

PAPER
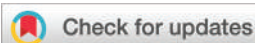
Development of a Cu(II) doped boehmite based multifunctional sensor for detection and removal of Cr(VI) from wastewater and conversion of Cr(VI) into an energy harvesting source†

Shubham Roy, [ID] [a] Souravi Bardhan, [ID] [a] Dipak Kr. Chanda, [b] Saheli Ghosh, [a] Dhananjoy Mondal, [a] Jhilik Roy [c] and Sukhen Das [ID] *[a]

This article reports a copper doped boehmite (CBH) based nano-material which is capable of detecting and removing hexavalent chromium simultaneously. Basic characterization has been performed to determine its phase purity, particle size (~20 nm), morphology and surface properties (surface area 15.29 m^2 g^{-1} and pore diameter 3.9 nm) by using some basic characterization tools. The Rietveld refinement method has been adopted to analyze the microstructural details of the synthesized nanostructure. Photoinduced electron transfer (PET) based quenching of fluorescence is mainly responsible for chromium sensing in this case. This nanosensor is exceptionally sensitive (limit of detection ~ 6.24 μM) and merely selective towards hexavalent chromium ions. Industrial wastewater samples have also been used here to demonstrate the real life applicability of this material, which shows the same trend. This fluorosensor gains its multi-functionality when it comes to the adsorption based removal of Cr(VI) from wastewater. The synthesized material shows a remarkably high adsorption rate (~85% in just 5 minutes) due to its sponge-like porous structure. Adsorption of hexavalent chromium from wastewater enhances the dielectric constant of this material significantly (~7.93 times). Ionic polarization-dependent enhancement of the dielectric constant resulting from industrial wastewater treatment is a quite unmarked approach. Very low tangent loss with augmented dielectric permittivity makes this nano-material desirable for energy harvesting applications. Previously many articles have reported the sensing and removal of various industrial effluents. Keeping this in mind, this work has been designed and, apart from sensing and removal, it provides a new insight into energy harvesting from wastewater.

1. Introduction

Heavy metal contamination is an alarming problem worldwide.[1] Industrial effluents and fertilizers at agricultural sites cause this type of contamination.[2] The global demand for potable water has already become a mass issue and many precautionary measures have been taken to combat its severe effects.[3a,b] Our society is still struggling to get rid of potable water pollution. Industrial discharges of heavy metal ions like Hg^{2+}, Cd^{2+}, Pb^{2+}, and As^{3+} are highly toxic to humans and aquatic species even at very lower concentrations.[4–6] Even

some essential ions, such as Fe^{2+}, Cu^{2+}, Mn^{2+}, and Co^{2+}, can also be toxic above a critical dose rate which can culminate in diseases like heart failure, liver infection, and lung cancer.[7–10a] Apart from heavy metals various organic compounds are also responsible for such contaminations.[10b–f]

Hexavalent chromium (Cr(VI)) is a well-known toxic heavy metal ion and can be extremely harmful even at a very low concentration.[11] Leather tanneries,[12] electroplating industries,[13] steel industries,[14] and pigment production factories[15] are mainly responsible for discharging Cr(VI) into our environment resulting in various diseases such as nasal and dermal irritation, ulcer formation, eardrum perforation, and lung cancer.[16–18] Thus, proper detection and removal of Cr(VI) from wastewater is an important task.

In this work, a porous nanostructure of Cu-doped boehmite (CBH) has been successfully synthesized and characterized. High fluorescence intensity establishes the fact that this material could be used in fluorescence applications. Photoinduced electron transfer (PET) between the fluoro-

[a]Department of Physics, Jadavpur University, Raja S.C. Mullick Road, Kolkata-700032, India. E-mail: sdasphysics@gmail.com; Tel: +91 9433091337
[b]Advanced Materials and Mechanical Characterization Division, CSIR-Central Glass and Ceramics Research Institute, Kolkata-700032, India
[c]Department of Physics, Techno India University, Kolkata-700091, India

phores of the synthesized material and hexavalent chromium reduces the fluorescence intensity radically (~23 times) which is responsible for the selective sensing of Cr(vi) at a very low concentration. The Stern–Volmer quenching model has been adopted here to justify the fluorescence sensing method. The adsorption based removal of chromium is caused due to the mesoporous "sponge-like structure" of this material. The adsorption mechanism has been confirmed by using the standard Freundlich model. Around 85% of hexavalent chromium has been removed in 5 minutes, which ensures the high removal rate of this MFNS. The dielectric properties and the ac conductivities have also been analyzed for pure and Cr(vi) adsorbed CBH samples, showing a commendable enhancement in the dielectric constant of the adsorbed sample in the high-frequency domain with a nominal tangent loss. Such a high dielectric constant makes our chromium adsorbed sample a potential candidate for energy harvesting applications.

Detection and removal of heavy metal ions from the aqueous medium is a well-established field in science and technology.[19–21c] Various methods have been previously used to detect or remove heavy metals from water,[22–24] but simultaneous sensing and removal is a quite new approach. Previously, we have reported this type of simultaneity elsewhere and coined the term "MFNS".[25] This time, we present a copper doped boehmite based MFNS that not only can detect and segregate hexavalent chromium in aqueous medium but can also be used in energy harvesting devices after entrapping Cr(vi) from wastewater. This is the first time a toxic industrial effluent is used as an energy harvesting source and hence this copper-based MFNS can be regarded as a "waste to wealth converter".

2. Experimental section

The nanostructure of copper doped boehmite (CBH) was synthesized by using a two-step facile hydrothermal technique. First, 3.71 g of aluminum nitrate nonahydrate (Merck, India) and 0.0199 g of copper acetate (Merck, India) were dissolved in 60 ml of Millipore water (resistivity ~ 18 MΩ cm) and mixed vigorously for 30 min. After the complete dissolution of the salts, aqueous ammonia solution (Merck, India) was added dropwise until the pH of the solution reached 9. The enhanced pH level results in the formation of thick purple precipitates. The stirring was continued for another 4 h to ensure the completion of the reaction and the resultant solution was then transferred and sealed in a Teflon lined stainless steel autoclave. After putting the autoclave into an electric oven the temperature was set to 180 °C for 16 h. The solid purple precipitates were collected from the bottom of the Teflon jacket and washed several times with Millipore water. The washed precipitates were dried in a vacuum at room temperature. Dried samples were further ground in a mortar, marked as CBH and sent for characterization (illustrated in the supplementary file).

3. Results and discussion

3.1 Selectivity and sensitivity analysis of the MFNS

The functionality of a sensor lies in its sensitivity and selectivity towards a specific target. Herein, the selectivity experiment has been performed by using various cations and anions along with hexavalent chromium, which in this case is the target material for our multifunctional fluorescent nanosensor (MFNS). A stock solution of the sensor material (CBH) was prepared (1 mg ml^{-1}) and different anions and cations of the same concentration were added separately to the stock solution and monitored in a Cary Eclipse Fluorescence Spectrophotometer, Agilent Technology at 428 nm upon excitation at 375 nm. The results of the selectivity test have been plotted in a column graph and are depicted in Fig. 1. Fig. 1 shows a drastic change in fluorescence intensity in the case of the hexavalent chromium ion only, whereas no significant alteration has been observed for other ions. This phenomenon establishes the fact that our nano-sensor material is merely selective. The overall fluorescence quenching in the case of our nano-sensor is about 23 times which makes our material (CBH) a good Cr(vi) sensor.

Initially, 1 mg ml^{-1} aqueous solution of the sensor material (CBH) was prepared and sonicated vigorously for 10 minutes.
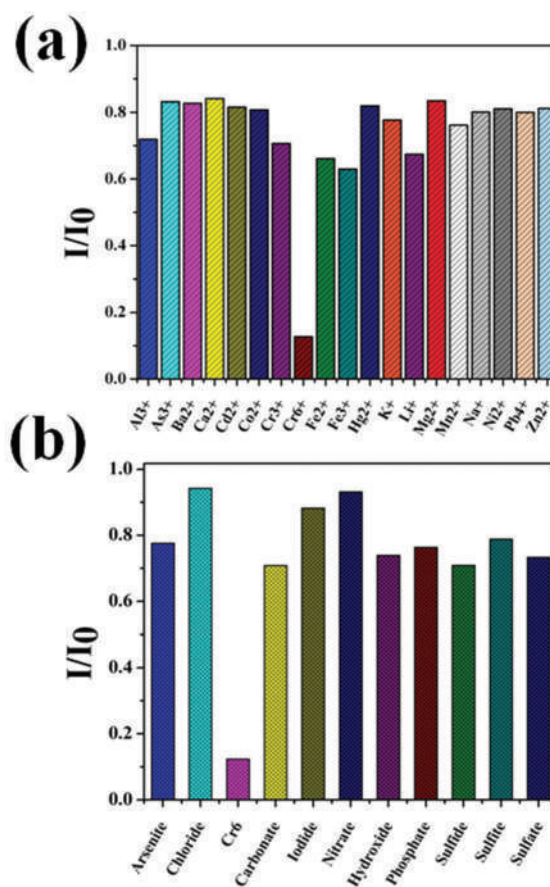
Fig. 1 Selectivity studies of the MFNS by using various (a) cations and (b) anions.
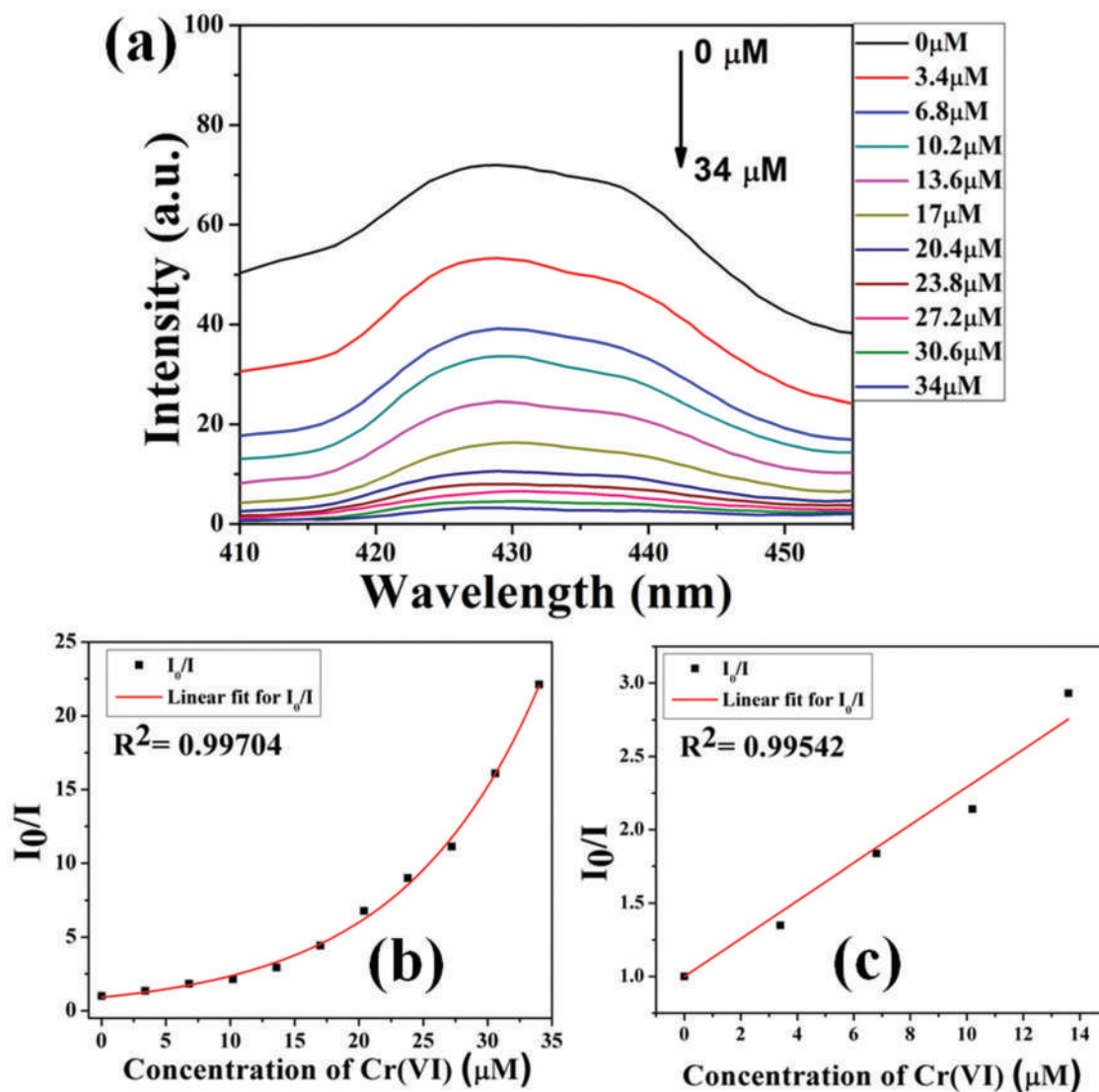
Fig. 2 (a) Fluorescence titration data for the CBH sample using Cr(vi) as the quencher; (b) exponential and (c) linear Stern–Volmer plots of CBH with varying concentration of Cr(vi).

The PL spectra of the as-prepared solution of CBH were measured and found to be quite high at 428 nm upon irradiation at a 375 nm excitation wavelength. Next, aqueous solutions of Cr(vi) of different molarity (0–34 μM) were prepared in different aliquot tubes and then added to the sensor solution separately maintaining the molar ratio and measured in a similar manner (Fig. 2(a)). Fig. 2(a) illustrates that the fluorescence maximum of the sensor material centered at 428 nm has been greatly reduced due to the addition of chromium ions. In our case, the Stern–Volmer (S–V) plot shows an upward increment of I_0/I with varying quencher (Cr(vi)) concentration. The nonlinear S–V plot (Fig. 2(b)) has been fitted well with the exponential quenching equation with a fit coefficient of 0.99704.

To ascertain the quenching mechanism at lower concentrations of the quencher, the concentration dependent

quenching data have been fitted with a linear Stern–Volmer equation (Fig. 2(c)) expressed as $\frac{I_0}{I} = 1 + K_{SV}[M]$,[26] which gave a fit coefficient of 0.99542, where I_0 and I are the fluorescence intensities before and after the addition of Cr(vi), respectively, [M] is the concentration of the chromium ion and K_{SV} is the Stern–Volmer quenching constant. Generally, linear S–V plots along with reduction in the fluorescence lifetime occur due to collisional quenching between the fluorophores and the quencher.[27] To get a clearer picture of the sensing mechanism, excited state fluorescence data are shown in Fig. 3. Fig. 3 suggests that the addition of hexavalent chromium also reduces the fluorescence lifetime which was also found in our steady-state fluorescence experiments. The pure CBH sample has a lifetime of 4.728995 ns, whereas addition of 10 μM chromium ions reduces it to 0.811854 ns (Table S6†). This
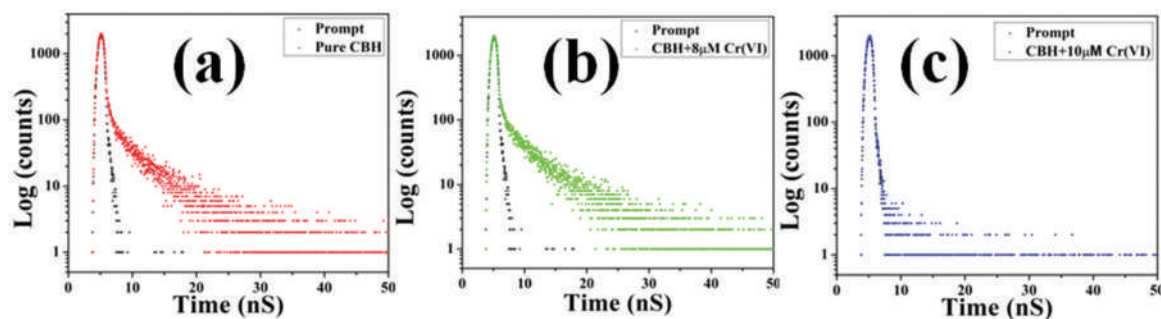
Fig. 3 Time resolved fluorescence spectra (lifetime) of (a) pure CBH and CBH added with (b) 8 μM and (c) 10 μM Cr(VI) ions indicating the reduction of fluorescence lifetimes with increasing Cr(VI) concentration which demonstrates the electron transfer mechanism between CBH and Cr(VI) ions.
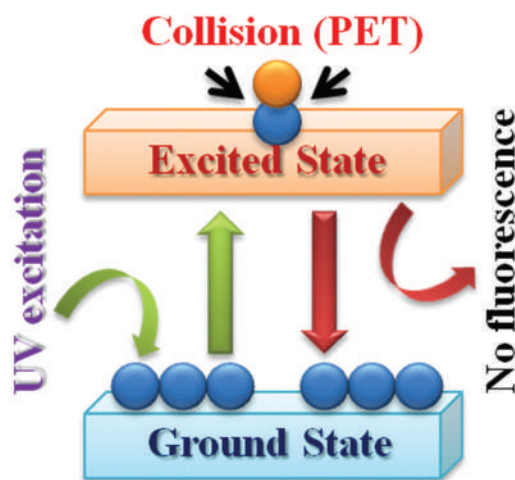
Fig. 4 Collisional/dynamic quenching mechanism of the synthesized MFNS.

reduction in the fluorescence lifetime suggests that the fluorophores of CBH undergo collisional/dynamic quenching (Fig. 4) in the excited state at lower concentration (<200 μM).[28] At higher quencher concentrations (>200 μM), the S–V plot shows an exponential growth which is attributed to the Inner filter Effect (IFE).[29] This type of plot is quite common and occurs when some of the fluorophores are less accessible than others.[30]

A linear Stern–Volmer plot shows a high value of quenching constant (0.163×10^6 M^{-1}) which dramatically enhances the sensitivity of our nano-sensor that has been calculated using the following expression,[31a]

$$\text{LOD} = \frac{3\sigma}{K_{SV}} \qquad (1)$$

where σ is the standard deviation obtained by performing at least ten measurements of the fluorescence intensities of the pure sensor material without the presence of any quencher and K_{SV} is the quenching constant. In this case, the LOD of the MFNS is around 6.24 μM.

3.2 Sensing of Cr(VI) in real life industrial wastewater

Real life industrial wastewater has been collected from a local tannery industry and the compositional analysis has been

Table 1 ICP-AES data for the collected wastewater sample

Constituents	Amount (ppm)
Arsenic (As)	Not detected
Lead (Pb)	0.14
Chromium (Cr)	20.67
Iron (Fe)	4.94

performed by using the ICP-AES (inductively coupled plasma atomic emission spectroscopy) method (Table 1). ICP-AES analysis shows an alarming trend of chromium (20.67 ppm) in the collected wastewater sample. The chromium containing water was exposed to the as-synthesized MFNS and the fluorescence intensity was recorded upon excitation at 375 nm (Fig. 5(a)).

The recorded spectrum shows the drastic quenching of fluorescence intensity upon the addition of the chromium containing industrial wastewater sample. This quenching phenomenon suggests that the synthesized nano-sensor material can detect chromium even in the presence of other interfering elements and in the real life environment.

Moreover, real life water samples have been taken from various sources (tap, pond and waste water) and exposed to the MFNS. Water samples were filtered using filter papers (pore size 11 μm) and preserved at 4 °C before conducting the experiment. In order to test the physical parameters of the collected water samples, a portable pH/EC/TDS/temperature meter, Hanna instruments was employed. A detailed result of the pH, resistivity, and TDS is given in Table 2.

After measuring the physical parameters of the water samples, the synthesized sensor material was added (maintaining 1 mg ml^{-1} concentration) and fluorescence intensity was checked using an excitation wavelength of 375 nm. These solutions were then spiked with 10 μM Cr(VI) and again checked with the same excitation wavelength (Fig. 5(b)). Addition of Cr(VI) causes the rapid quenching of fluorescence intensity in all cases which further confirms that the sensor material can show the same efficiency in any type of water sample even in the presence of other interfering elements in the real life samples.
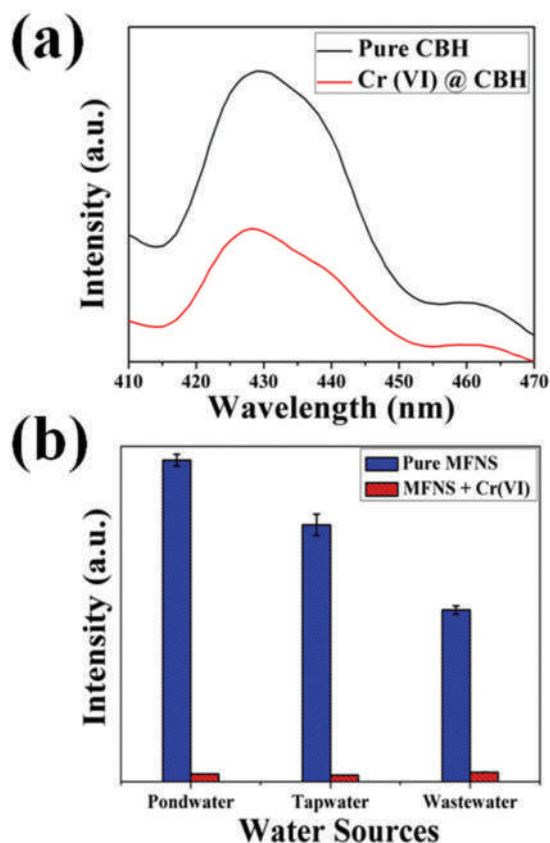
Fig. 5 (a) Fluorescence quenching results of the real life tannery waste-water sample under 375 nm excitation; (b) sensing of Cr(VI) in different water samples.

Table 2 Physical parameters of the collected water samples

Type of water	pH	TDS (ppm)
Tap	7.88	1031
Pond	7.78	1001
Waste	3.04	1590

3.3 Adsorption based removal experiments of Cr(VI)

3.3.1 Adsorption uptake study. The adsorption based removal of heavy metals is a non-toxic and eco-friendly pathway to achieve clearer water.[31b–d] It is a well-studied and experimented field.[32–35] Herein, the adsorption based removal technique has been used as our sample is mesoporous with a high surface area.

In order to determine the hexavalent chromium removal capacity of our sample, the adsorption experiments were carried out. The adsorption of Cr(VI) has been ensured by using EDX spectra (Fig. 6), which show traces of chromium in the adsorbed CBH sample. Adsorption uptake studies were performed to show the adsorption efficacy of our sample.[36] Initially, 10 mg of CBH was added into 40 ppm chromium solution and stirred vigorously for 3 h and kept in the dark for another 24 h before performing the uptake study (Fig. 7(a and b)).
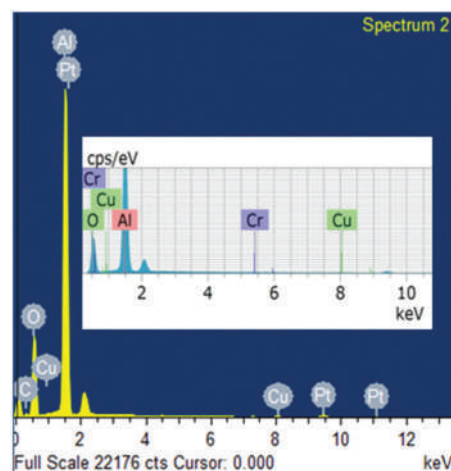
Fig. 6 EDX spectra of pure CBH and Cr(VI) adsorbed CBH (inset).

The adsorption uptake is calculated using the following equation,[37a]

$$\text{Uptake } (\%) = ((C_0 - C_e)/C_0) \times 100 \qquad (2)$$

where C_0 and C_e are the initial and equilibrium concentrations of Cr(VI) ions. High porosity makes our sample capable enough to adsorb hexavalent chromium ions. In our case, around 85.225% of chromium is removed from the aqueous solution.

In order to determine the effect of pH on adsorption uptake, a pH dependent adsorption study has been performed (Fig. S6†). This experiment was performed by varying the pH of the solution from pH 2.0 to pH 10. It is evident from Fig. S6† that the pH of the solution influences Cr(VI) adsorption to some extent. At lower pH values (pH < 4), the percentage uptake is higher than that at pH > 4. Similar phenomena have been reported elsewhere.[37b,c] At lower pH values, due to the low concentration of –OH ions in the solution, the –OH groups in the adsorbent surface tend to move toward the solution, which results in the creation of positive ions on the adsorbent. This phenomenon starts the adsorption process (as the contaminant is negatively charged in this pH range). By increasing the pH, the concentration of –OH groups ascends, and thus the –OH groups on the adsorbent surface are not released, which in turn causes lower adsorption uptake.[37b,c]

3.3.2 Kinetics of the adsorption phenomena. The adsorption kinetics of an adsorbent enables us to determine how fast the adsorption process occurs.[38] In our case, adsorption of Cr(VI) onto CBH nanoparticles as a function of contact time was measured by using absorption spectroscopy. The peak of the absorption spectra located at 348 nm (Fig. 7(a)) drastically quenches upon Cr(VI) addition. Around 85% of Cr(VI) has been adsorbed by CBH in less than 5 min which ensures the rapid removal of hexavalent chromium. On the basis of the above results, 20 min was selected as the contact time to reach the full equilibrium which we have used in our following experiments.
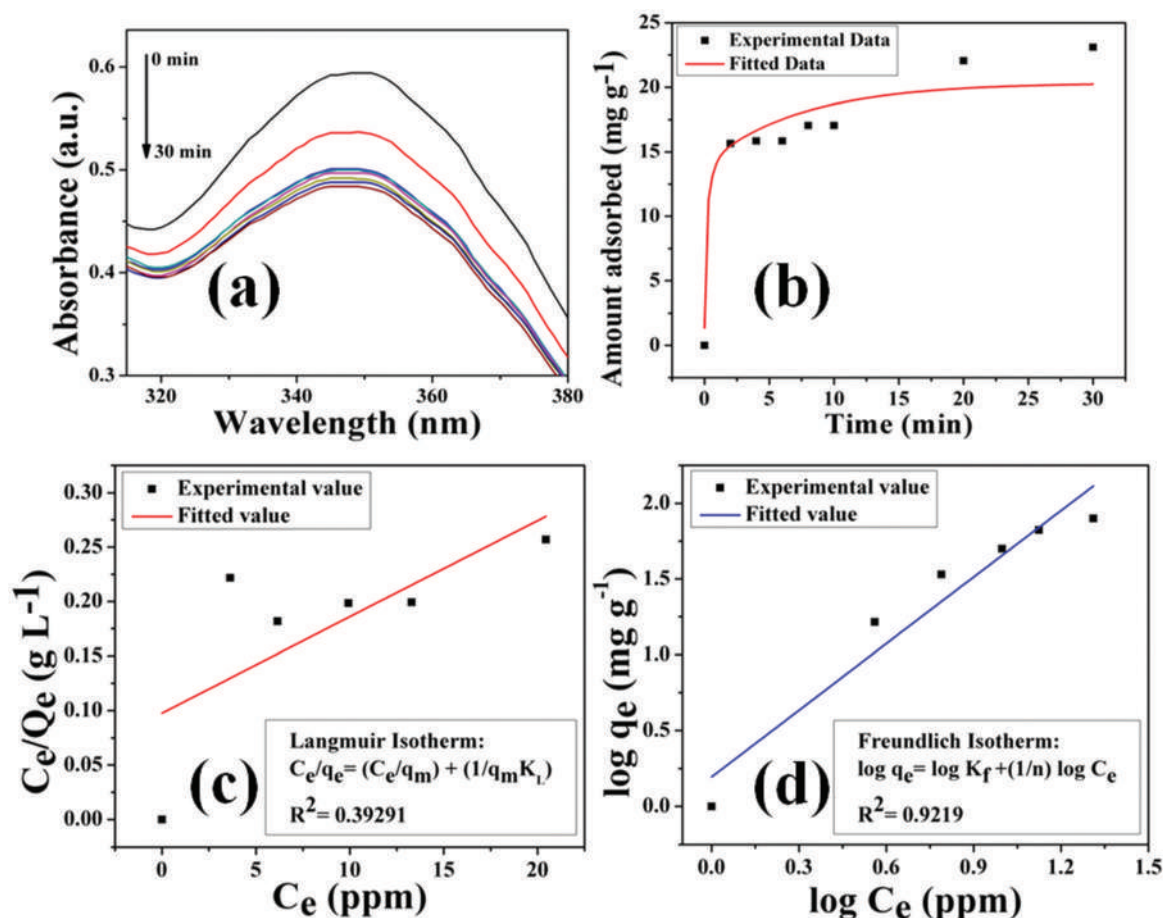
Fig. 7 Adsorption kinetics study of the CBH sample in terms of (a) the time based UV-vis technique and (b) time dependent adsorption uptake using the Cr(VI) ion as the adsorbate; (c) Langmuir and (d) Freundlich adsorptive isotherm fittings for the CBH sample using the Cr(VI) ion as the adsorbate at 25 °C.

3.3.3 Adsorption isotherm study. In order to ascertain the Cr(VI) adsorption pathway along with adsorption capacities, adsorption isotherms were studied at 25 °C.[39] The adsorption isotherm data for Cr(VI) adsorbed CBH nanoparticles were fitted with standard Langmuir and Freundlich isotherm models (Fig. 7(c and d)).[37–39] Linear forms of the Langmuir (eqn (3)) and Freundlich (eqn (4)) isotherm models can be expressed as:[37–39]

$$\frac{C_e}{q_e} = \frac{C_e}{q_m} + \frac{1}{q_m K_L} \qquad (3)$$

$$\log q_e = \log K_F + \frac{1}{n} \log C_e \qquad (4)$$

where C_e is the equilibrium concentration of the solution (mg L^{-1}), q_e is the amount of Cr(VI) adsorbed at equilibrium (mg g^{-1}), q_m is the maximum capacity of adsorption (mg g^{-1}), and K_L and K_F are the Langmuir and Freundlich constants respectively. As the fitting coefficients suggest, our sample specifically follows the Freundlich isotherm model ($R^2 = 0.9219$) which in turn implies that the adsorption of chromium ions takes place on the multilayered heterogeneous sur-

faces of sponge-like CBH nanoparticles.[40] This multilayered adsorption is responsible for such a quick removal (<5 min) of hexavalent chromium ions from aqueous medium. The maximum monolayer coverage (q_m), as per the Langmuir model, is found to be 113.12 mg g^{-1} for CBH. Precise calculations propose that the Freundlich constant (K_F), which is analogous to the adsorption capacity of a multilayered adsorbent, is around 1.564 with an 'n' value of 0.683 suggesting it to be a good adsorbent material for hexavalent chromium.

3.3.4 Adsorption of Cr(VI) from real life samples. The sorption experiment in real life water samples has been performed by spiking 100 ppm Cr(VI) in each of the collected water samples in order to test the effect of interfering ions on Cr(VI) adsorption. The collection process and various physical parameters of the collected water samples are mentioned in Table 2.

Fig. S7† depicts the % uptake of Cr(VI) in the presence of interfering ions. It is evident from Fig. S7† that there is no such alteration in % uptake for other interfering ions in real life water samples. In fact, a heavily contaminated wastewater sample shows a satisfactory result (% uptake ∼ 79) in this regard. Thus, it can be concluded that the interfering ions

have no effect on the sorption mechanism of Cr(vi) in the case of CBH.

3.3.5 Plausible adsorption mechanism of CBH.
The adsorption properties of an adsorbent depend on various factors like surface properties, porosity, pH and surface charge. The BET results of CBH confirm that the sample is mesoporous (pore diameter 3.9 nm) having a large surface area ($\sim$15.3 m^2 g^{-1}). The type-IV hysteresis loop of the adsorption–desorption cycle ensures the slit like porosity, which is further confirmed by TEM data. These slit like pores make CBH a promising adsorbent material.

On the other hand, the surface charge of CBH has been measured (Fig. S8†) and it is found to be highly positive ($\sim$16). This positive surface charge electrostatically binds to the negatively charged $HCrO_4$ and $Cr_2O_7^{2-}$ species of chromium resulting in higher adsorption.[37b,c]

The adsorption of Cr(vi) on CBH is a synergistic effect of these two factors. While the electrostatic binding of the adsorbate and the contaminant initiates the sorption process, surface porosity enhances the sorption rate remarkably.

3.4 Dielectric response of the Cr(vi) adsorbed MFNS

This study not only deals with the sensing or removal of hexavalent chromium, but this work is also directed towards the waste to wealth conversion. Therefore, room temperature dielectric properties along with tangent loss and ac conductivity have also been measured for the pure and Cr(vi) adsorbed CBH samples.

After adsorbing the toxic hexavalent chromium ion from the aqueous medium, the adsorbed CBH sample has been collected by centrifugation at 5000 rpm for 5 minutes and then dried in a vacuum desiccator for 48 h. The dried powder is then pressed in a hydraulic press system to form a solid pellet. In order to investigate the change in electrical properties, two such pellets have been made. One is the pure CBH sample, and the other one is hexavalent chromium adsorbed CBH. The amount of the powder taken in both cases is equal, *i.e.* 100 mg, so that any error can be eliminated during the comparison of their electrical properties.

Generally, the dielectric constant of a material depends on various parameters, such as frequency of the applied electric field, temperature, composition, *etc*.[41,42] The following equation describes the response of a dielectric material:[43]

$$\varepsilon = \varepsilon' + j\varepsilon'' \qquad (5)$$

where ε' and ε'' are the real and imaginary parts of the dielectric constant respectively. The real part of the dielectric constant can be expressed as follows:[43]

$$\varepsilon' = (C \cdot d)/(\varepsilon_0 A) \qquad (6)$$
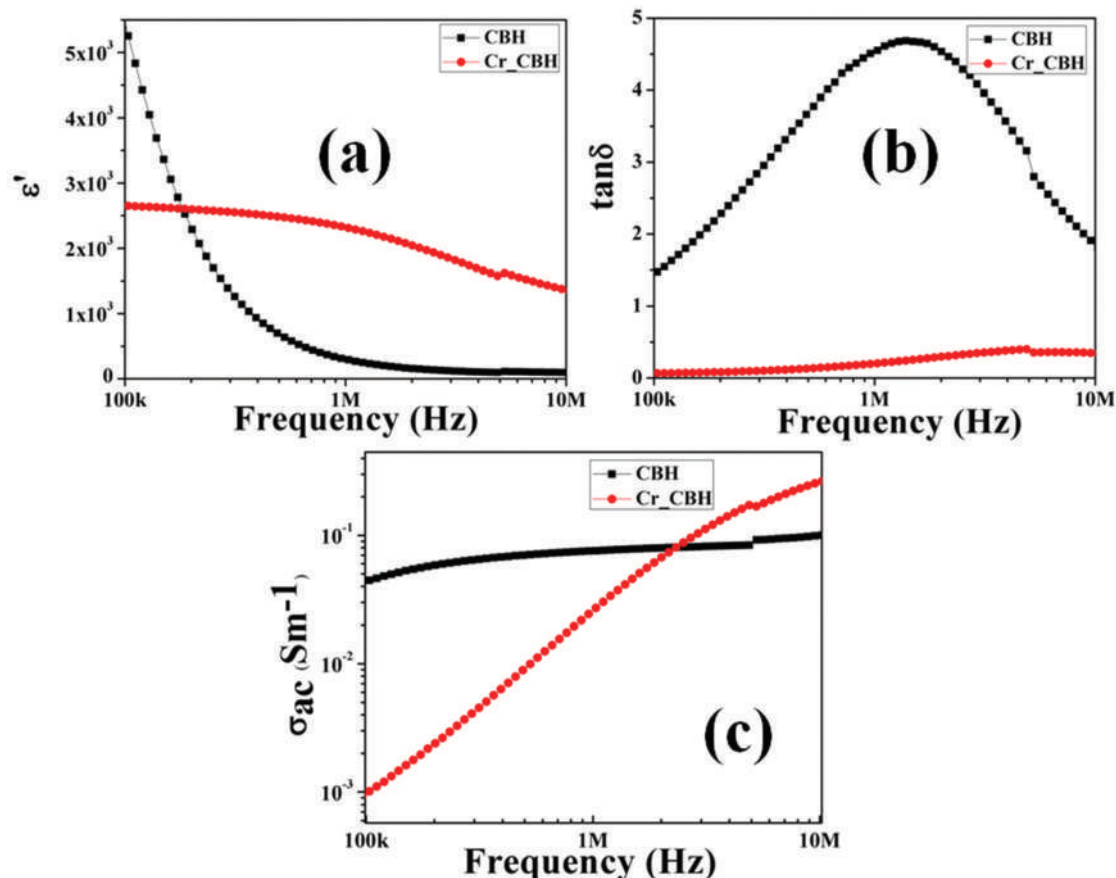
Fig. 8 Comparative analysis of (a) the dielectric constant, (b) tangent loss and (c) ac conductivity of pure CBH and Cr(vi) adsorbed CBH.

where C is the capacitance of the sample, d and A are the thickness and surface area of the solid pellets respectively and ε_0 is the free space permittivity (8.85×10^{-12} F m^{-1}).

As depicted in Fig. 8(a), the dielectric constant of chromium adsorbed CBH is much higher than that of pure CBH nanoparticles. In a lower frequency domain (~100 kHz), the dielectric permittivity of pure CBH is quite higher than that of adsorbed CBH. However, when the external field frequency approaches a higher value (~1 MHz), the adsorbed CBH sample shows better permittivity. The pure CBH sample has a room temperature dielectric constant of 283, whereas Cr(vi) adsorbed CBH shows a dielectric constant of 2315 at a frequency level of 1 MHz. This augmentation in the dielectric constant in a high-frequency domain is mainly due to the contributions of electronic and ionic polarizations.[44,45] In this high-frequency domain, the adsorbed chromium ions get polarized which elevates the dielectric constant of our adsorbed CBH sample. The tangent loss has also been investigated for both the samples and it is in good agreement with the high dielectric data, which has been depicted in Fig. 8(b).

Fig. 8(c) also shows the dependence of ac electrical conductivities of the samples with a varying field frequency. The ac conductivity is almost frequency independent for pure CBH, whereas chromium adsorbed CBH shows a sharp increment beyond 1 MHz field frequency. This type of relaxation is quite common and it is mainly due to the excitation of free charge carriers in a higher frequency domain.[46] The Cr(vi) adsorbed sample has more free ionic charge transport units than the pure CBH which causes this type of drastic increment of ac conductivity in the higher frequency side.

The adsorption of hexavalent chromium on the surface of CBH enhances its dielectric constant and ac conductivity significantly at a very high-frequency maintaining a very low tangent loss, which makes this sample a potential candidate for energy harvesting applications.

4. Conclusions

In summary, a novel Cu-tailored boehmite based MFNS has been synthesized by using a two-step facile hydrothermal technique and characterized by using some basic characterization tools. High fluorescence intensity makes this nanostructured sample desirable for sensing applications. Its remarkably high sensitivity and selectivity towards hexavalent chromium make it a good Cr(vi) sensor. 'Turn off' based sensing of our nanosensor is attributed to the dynamic quenching of fluorescence. The dynamic quenching is well supported herein by steady-state and excited-state fluorescence data. Detection of chromium in real-life industrial wastewater has also been performed here to justify its real-life applicability. In addition, this MFNS can segregate and remove Cr(vi) from wastewater by a facile adsorption technique. The mesoporous structure of this MFNS is capable of adsorbing toxic Cr(vi) ions which has been justified using the standard Freundlich model. An extremely fast removal rate has been reported herein and justified

using multilayered adsorption theory. The synthesized MFNS plays a vital role in converting the toxic hexavalent chromium into an energy harvesting source. The adsorption of Cr(vi) onto the surface of this MFNS enhances its dielectric permittivity in a high-frequency domain. This type of dielectric relaxation is due to the ionic polarization of the adsorbed Cr(vi) ions. Therefore, chromium adsorption from wastewater not only makes the water clean but also enhances the charge storage capacity of the MFNS. Hence, one can argue that this copper-based MFNS is really a "waste to wealth converter".

Conflicts of interest

The authors declare no conflict of interest.

Acknowledgements

References

1 A. P. R. de Souza, C. W. Foster, A. V. Kolliopoulos, M. Bertotti and C. E. Banks, *Analyst*, 2015, **140**, 4130–4136.

2 T. Weldeslassie, H. Naz, B. Singh and M. Oves, *Modern Age Environmental Problems and their Remediation*, Springer, 2018, pp. 1–22.

3 (*a*) M. A. Hanjra and M. E. Qureshi, *Food Policy*, 2010, **35**, 365–377; (*b*) N. Nasseh, L. Taghavi, B. Barikbin and M. A. Nasseri, *J. Cleaner Prod.*, 2018, **179**, 42–54.

4 W. Qin, W. Dou, V. Leen, W. Dehaen, M. Van der Auweraer and N. Boens, *RSC Adv.*, 2016, **6**, 7806–7816.

5 L. N. Neupane, E. T. Oh, H. J. Park and K. H. Lee, *Anal. Chem.*, 2016, **88**, 3333–3340.

6 C. Liu, T. Wu, P. C. Hsu, J. Xie, J. Zhao, K. Liu, J. Sun, J. Xu, J. Tang and Z. Ye, *ACS Nano*, 2019, **13**(6), 6431–6437.

7 Y. Zhang, Y. Wang, P. Liu, J. Song, G. Xu and G. Zheng, *Russ. J. Plant Physiol.*, 2012, **59**, 766–771.

8 S. M. Strauch, P. R. Richter, F. W. Haag, M. Krüger, J. Krüger, A. Azizullah, R. Breiter and M. Lebert, *Environ. Exp. Bot.*, 2016, **130**, 174–180.

9 X. Huang, S. Shabala, L. Shabala, Z. Rengel, X. Wu, G. Zhang and M. Zhou, *Plant Biol.*, 2015, **17**, 26–33.

10 (*a*) M. Naushad, T. Ahamad, G. Sharma, H. Ala'a, A. B. Albadarin, M. M. Alam, Z. A. ALOthman, S. M. Alshehri and A. A. Ghfar, *Chem. Eng. J.*, 2016, **300**, 306–316; (*b*) S. Chavoshan, M. Khodadadi, N. Nasseh, A. H. Panahi and A. Hosseinnejad, *Environ. Health Eng. Manage. J.*, 2018, **5**(4), 187–196; (*c*) N. Nasseh, A. H. Panahi, M. Esmati, N. Daglioglu, A. Asadi, H. Rajati and F. Khodadoost, *J. Mol. Liq.*, 2020, 112434; (*d*) N. Nasseh, T. J. Al-Musawi, M. R. Miri, S. Rodriguez-Couto and

A. H. Panahi, *Environ. Pollut.*, 2020, **261**, 114127; (*e*) S. Chavoshan, M. Khodadadi and N. Nasseh, *J. Environ. Health Sci. Eng.*, 2020, **18**, 1–11; (*f*) N. Nasseh, F. S. Arghavan, S. Rodriguez-Couto, A. H. Panahi, M. Esmati and T. J. A-Musawi, *Adv. Powder Technol.*, 2019, **31**(2), 875–885.

11 S. Elabbas, L. Mandi, F. Berrekhis, M. N. Pons, J. P. Leclerc and N. Ouazzani, *J. Environ. Manage.*, 2016, **166**, 589–595.

12 M. Fontaine, Y. Clement, N. Blanc and C. Demesmay, *J. Hazard. Mater.*, 2019, **368**, 811–818.

13 F. V. Hackbarth, D. Maass, A. A. U. de Souza, V. J. Vilar and S. M. G. U. de Souza, *Chem. Eng. J.*, 2016, **290**, 477–489.

14 J. Li, B. Liu, Y. Zeng, Z. Wang and Z. Gao, *Environ. Monit. Assess.*, 2017, **189**, 113.

15 C. H. Lin, C. H. Lai, Y. P. Peng, P. C. Wu, K. Y. Chuang, T. Y. Yen and Y. K. Xiang, *Environ. Sci. Pollut. Res.*, 2018, 1–11.

16 S. Mishra and R. N. Bharagava, *J. Environ. Sci. Health, Part C: Environ. Carcinog. Ecotoxicol. Rev.*, 2016, **34**, 1–32.

17 V. Madhavi, A. V. B. Reddy, K. G. Reddy, G. Madhavi and T. Prasad, *Res. J. Recent Sci.*, 2013, **2277**, 2502.

18 R. Chandra, R. N. Bharagava, A. Kapley and H. J. Purohit, *Bioresour. Technol.*, 2011, **102**, 2333–2341.

19 H. Sis and T. Uysal, *Appl. Clay Sci.*, 2014, **95**, 1–8.

20 A. Mittal, M. Naushad, G. Sharma, Z. ALothman, S. Wabaidur and M. Alam, *Desalin. Water Treat.*, 2016, **57**, 21863–21869.

21 (*a*) J. E. Efome, D. Rana, T. Matsuura and C. Q. Lan, *ACS Appl. Mater. Interfaces*, 2018, **10**, 18619–18629; (*b*) M. Kamranifara, M. H. Moslehib, N. Nasseh, M. Ghadiriand and S. M. Rahimie, *Desalin. Water Treat.*, 2019, **165**, 203–211; (*c*) N. Nasseh, I. Nasseh, M. Khodadadi, A. Beirami and M. Kamranifar, *Ann. Mil. Health. Sci. Res.*, 2017, **15**(3), 1–7.

22 D. Vilela, J. Parmar, Y. Zeng, Y. Zhao and S. Sánchez, *Nano Lett.*, 2016, **16**, 2860–2866.

23 P. A. Kobielska, A. J. Howarth, O. K. Farha and S. Nayak, *Coord. Chem. Rev.*, 2018, **358**, 92–107.

24 M. Kumari, C. U. Pittman Jr. and D. Mohan, *J. Colloid Interface Sci.*, 2015, **442**, 120–132.

25 S. Roy, K. Pal, S. Bardhan, S. Maity, D. K. Chanda, S. Ghosh, P. Karmakar and S. Das, *Inorg. Chem.*, 2019, **58**, 8369–8378.

26 Z. J. Lin, H. Q. Zheng, H. Y. Zheng, L. P. Lin, Q. Xin and R. Cao, *Inorg. Chem.*, 2017, **56**, 14178–14188.

27 S. Hussain, A. H. Malik, M. A. Afroz and P. K. Iyer, *Chem. Commun.*, 2015, **51**, 7207–7210.

28 M. Van de Weert and L. Stella, *J. Mol. Struct.*, 2011, **998**, 144–150.

29 Q. Hu, L. Gao, S. Q. Rao, Z. Q. Yang, T. Li and X. Gong, *Food Chem.*, 2019, **280**, 195–202.

30 M. Mittal and S. Sapra, *ChemPhysChem*, 2017, **18**, 2509–2516.

31 (*a*) J. Mandal, P. Ghorai, K. Pal, P. Karmakar and A. Saha, *J. Lumin.*, 2019, **205**, 14–22; (*b*) M. Kamranifar, M. Khodadadi, V. Samiei, B. Dehdashti, M. N. Sepehr, L. Rafati and N. Nasseh, *J. Mol. Liq.*, 2018, **255**, 572–577; (*c*) N. Nasseh, B. Barikbin, L. Taghavi and M. A. Nasseri, *Composites, Part B*, 2019, **159**, 146–156; (*d*) N. Nasseh, L. Taghavi, B. Barikbin, M. A. Nasseri and A. Allahresani, *Composites, Part B*, 2019, **166**, 328–340.

32 D. K. Chanda, D. Mukherjee, P. S. Das, C. K. Ghosh and A. K. Mukhopadhyay, *Mater. Res. Express*, 2018, **5**, 075027.

33 M. Premkumar, K. Thiruvengadaravi, P. S. Kumar, J. Nandagopal and S. Sivanesan, *Environmental Contaminants*, Springer, 2018, pp. 317–360.

34 T. V. Charpentier, A. Neville, J. L. Lanigan, R. Barker, M. J. Smith and T. Richardson, *ACS Omega*, 2016, **1**, 77–83.

35 G. Vilardi, J. M. Ochando-Pulido, N. Verdone, M. Stoller and L. Di Palma, *J. Cleaner Prod.*, 2018, **190**, 200–210.

36 M. H. Dehghani, D. Sanaei, I. Ali and A. Bhatnagar, *J. Mol. Liq.*, 2016, **215**, 671–679.

37 (*a*) G. Vijayakumar, R. Tamilarasan and M. Dharmendirakumar, *J. Mater. Environ. Sci.*, 2012, **3**, 157–170; (*b*) N. Nasseh, L. Taghavi, B. Barikbin and M. Khodadadi, *Int. J. Environ. Sci. Technol.*, 2017, **14**(2), 251–562; (*c*) N. Nasseh, L. Taghavi, B. Barikbin and A. R. Harifi-Mood, *J. Water Reuse Desalin.*, 2017, 7(4), 449–460.

38 H. K. Chung, W. H. Kim, J. Park, J. Cho, T. Y. Jeong and P. K. Park, *J. Ind. Eng. Chem.*, 2015, **28**, 241–246.

39 J. N. Putro, S. P. Santoso, S. Ismadji and Y. H. Ju, *Microporous Mesoporous Mater.*, 2017, **246**, 166–177.

40 T. Karthikeyan, S. Rajgopal and L. R. Miranda, *J. Hazard. Mater.*, 2005, **124**, 192–199.

41 U. Ghodake, R. C. Kambale and S. Suryavanshi, *Ceram. Int.*, 2017, **43**, 1129–1134.

42 A. M. Mohammad, S. M. A. Ridha and T. H. Mubarak, *Int. J. Appl. Eng. Res.*, 2018, **13**, 6026–6035.

43 V. Usha, S. Kalyanaraman, R. Vettumperumal and R. Thangavel, *Phys. B*, 2017, **504**, 63–68.

44 A. Hassan, G. M. Mustafa, S. K. Abbas, S. Atiq, M. Saleem, S. Riaz and S. Naseem, *Ceram. Int.*, 2019, **45**, 14576–14585.

45 X. Qi, E. Sun, R. Zhang, B. Yang, S. Li and W. Cao, *Ceram. Int.*, 2017, **43**, 16819–16826.

46 S. Kabashima and T. Kawakubo, *J. Phys. Soc. Jpn.*, 1968, **24**, 493–497.

Contents lists available at ScienceDirect

Materials Today: Proceedings

journal homepage: www.elsevier.com/locate/matpr

Waste capacitor: A fresh approach to detect and remove Cr(VI) from water and making it an energy harvesting material

Shubham Roy [a], Souravi Bardhan [a], Jhilik Roy [b], Sukhen Das [a],*

[a] Department of Physics, Jadavpur University, Kolkata, 700032, India
[b] Department of Physics, Techno India University, Kolkata, 700091, India

ABSTRACT

The large scale amplification of industrial discharge in the modern era is resulting in widespread water pollution, especially from various industrial effluents and wastewater containing heavy metals, posing a severe threat to our environment. In order to combat such problems, this work aims on Multifunctional Fluorescent Nano-Sensor (MFNS) mediated simultaneous detection and removal of hexavalent chromium from real life wastewater which further converts it into an energy harvesting material, namely, "Waste capacitor". This smart material can detect the presence of the targeted heavy metal (Cr(VI)) in the wastewater and can entrap it by using a facile adsorption process. Thereafter, it will change its microstructure which further enhances its dielectric properties. Morphology, microstructure and optical properties of the synthesized material have been studied thoroughly and a turn-off based fluorescence sensing has been reported herein. Photoinduced electron transfer (PET) based fluorescence quenching is mainly responsible for this sensing mechanism. The selectivity and sensitivity of the material during fluorescence sensing have also been studied by using standard Stern-Volmer method showing that the synthesized material is tremendously selective and sensitive towards the specific target ion. High surface area with slit-like porous structure enhances the adsorption based removal of the contaminant. Nearly 76% of contaminants have been removed by using this smart material. After adsorbing specified target, this MFNS changes its microstructure and results in superior dielectric constant with a minimal tangent loss. Tremendous sensitivity (in nM range), selectivity towards the specific contaminant and adsorption of toxic heavy metal and converting it into a green energy harvesting material (waste capacitor) makes this smart multifunctional material a real waste to wealth converter.

© 2021 Elsevier Ltd. All rights reserved.
Selection and Peer-review under responsibility of the scientific committee of the Third International Conference on Materials Science (ICMS2020).

1. Introduction

Energy and environment are the two main pillars of human civilization. Limited amount of fossil fuel desperately increases the search for alternative energy sources, whereas, energy producing industries are continuously damaging our eco-system by using various harmful chemicals and solid waste materials [1–3]. In other words, energy and environment are knotted together to serve the humankind. Imbalance in any of which can cause severe harm to the environment [4].

Industrial discharges from various industries, such as, pigment production industries [5], battery industries [6], leather industries [7–8] are continuously polluting potable water as these are con-

nected to the local canals and rivers [9]. This type of industrial discharge generally contains harmful heavy metals like, lead, chromium, mercury, arsenic etc. These heavy metals are tremendously harmful for aquatic species and neighboring biota. Moreover, these harmful metal ions are detrimental even at very lower concentrations causing various diseases like skin cancer, lung cancer, brain tumor etc [10–12]. Thus, proper detection and removal is much needed in this regard. Beside these, increasing demand of energy enhances the usage of these harmful materials. Though battery and capacitor producing industries are using various 'green materials' [13–14] nowadays to overcome these issues but the general awareness and waste management [15] is still a blazing concern.

Henceforth, this work proposes a multifunctional fluorescence based nano-material, which can detect one of the most harmful

* Corresponding author.

heavy metal ion (hexavalent chromium) by modulating its fluorescence level and simultaneously it can remove the contamination by using a facile adsorption technique. Apart from that, this material can change its microstructure after adsorbing the chromium ions directly from the wastewater which further enhances its dielectric permittivity and ac conductivity. Moreover, this work introduces a new insight into the term 'Waste capacitor'. In reality, our material uses hexavalent chromium ions from wastewater and converts it into a superior dielectric material. Hence, these chromium adsorbed samples could be highly beneficial for capacitor industries and energy harvesting applications as these are not leaching the adsorbed chromium ions to the environment.

Boehmite (γ-AlOOH) is a typical oxy-hydroxide compound of aluminum, is quite known for its porous sponge-like morphology [16–18]. Here, three different morphologies of boehmite have been prepared and well characterized. The promising fluorescence property of the needle shaped HBH sample somehow shows better selectivity and sensitivity among the other morphologies (spherical EBH and flower shaped UBH). Highest adsorption uptake also establishes the fact that the needle shaped HBH is the best candidate among these three samples in this regard. Thus, further studies have been carried out using the needle-like boehmite nanostructure which makes this sample a potential candidate for 'Waste capacitor' application.

2. Experimental section

2.1. Materials

Aluminum nitrate nonahydrate, extra pure urea crystals, ethylenediamine and hexamine were purchased from Merck, India. All the reagents were used without further distillation and purification. Ultrapure water was used throughout the experiment with resistivity at least 18.2 MΩ.cm. The glass-wares used in our experiments were cleaned with aqua regia solution followed by rinsing with ultrapure water.

2.2. Synthesis of nanostructures

γ-AlOOH of different morphologies have been synthesized by using a facile hydrothermal route. 0.1(M) aluminum nitrate nonahydrate was dissolved in Millipore water first. Later, the solution was basified using different ammonia containing precursors to achieve different nanostructures of boehmite. The entire solution was then divided into three different parts.

Ethylenediamine was added drop-wise until the pH of the solution reached to 9 and marked as part-A, which results in thick white precipitation. Part-B solution was treated with hexamine under vigorous stirring condition maintaining a pH value of 5. Urea crystals were added to the part-C solution and the pH was adjusted to 7 to start flower like nucleation.

These basified solutions were then transferred into three different Teflon lined stainless steel autoclaves and kept in a hot air oven at 170 °C for 18 h. The autoclaves were then allowed to cool naturally after completion of the hydrothermal treatment. Precipitates were obtained from the bottom of the Teflon jackets for all samples. Hydrothermally treated part-A sample was named as EBH, whereas, part-B and part-C were named as HBH and UBH respectively. The precipitates were collected by centrifugation at 10,000 RPM for 10 min and washed several times and then dried in vacuum for 48 h. The samples were then marked and sent for further characterizations.

3. Results and discussion

3.1. Basic characterizations of the synthesized nanostructures

X-ray diffraction is an important characterization tool to ensure the purity and phase identification of a sample. A Bruker Advanced D-8 Diffractometer has been used to evaluate the diffraction patterns [19] of the as synthesized boehmite samples. Small amounts of powdered samples were directly mounted on the sample holder and the scan rates were set to 0.02 steps/ sec for the entire sample set. The samples were scanned from 2θ = 10° to 80° in these experiments which has been depicted in Fig. 1.

It is quite evident from Fig. 1 that the orthorhombic boehmite phases are formed indicating the high purity of the samples. The XRD patterns were further matched with JCPDS card no. 21–1307 which specifies the complete transformation of aluminum hydroxide into pure boehmite. Absence of any unwanted phases in the diffraction data confirms the purity of the as-synthesized samples. A sharp diffraction maxima located at 2θ = 14.5° corresponding to (0 2 0) plane suggests that the growth units of nano-structured boehmite are abundant along (0 2 0) plane. The crystallite diameters for all the samples have been estimated using Scherrer equation [20]:

$$< D >_{(020)} = 0.9\lambda / \left(\beta_{1/2} cos\theta \right) \qquad (1)$$

Here, λ is the wavelength of the incident X-ray, D is the mean crystallite diameter, θ is the corresponding Braggs angle, $\beta_{1/2}$ is the full width at half maximum (FWHM) of the (0 2 0) peak. The Scherrer equation reveals that the average crystallite diameter of synthesized boehmite nanostructures varies from 4.7 nm (EBH) to 11.1 nm (HBH) depending on the different morphology and different reaction conditions (Table 1).

Furthermore, the different morphologies of the synthesized samples have been studied by using an INSPECT F50 (FEI, Netherland) field emission scanning electron microscope (FESEM). Very small amount of boehmite nano-powders have been placed over the carbon meshes for this experiment. The accelerating voltages of the instrument were set between 5 and 20 kV to evaluate the microstructural details.

It could be observed from the FESEM micrographs that EBH (Fig. 2(a)) possesses nearly spherical morphology. These smaller sized nano-structures of EBH are leading to very high amount of inter-granular cohesive forces which results in the agglomeration of this sample.
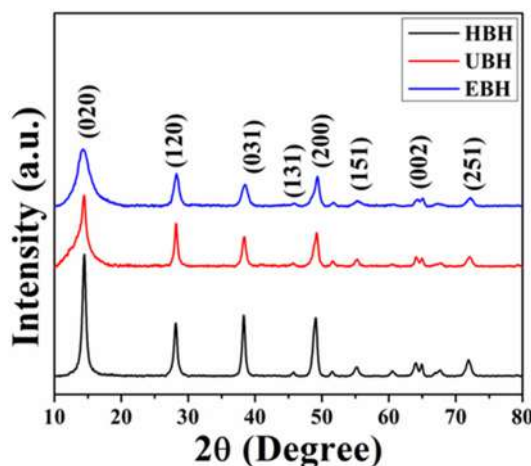
Fig. 1. XRD patterns of the synthesized samples.

Table 1
Microstructural parameters from XRD analysis.

Sample	FWHM corresponding to (0 2 0) plane (rad)	Crystallite diameter (nm)
EBH	0.0297	4.7
HBH	0.0126	11.1
UBH	0.0191	7.3

Boehmite prepared using hexamine as a reducing agent shows needle shaped nano-morphology (Fig. 2(b)) whereas it is flower like for the UBH sample. Henceforth, FESEM images reveal an interesting alteration of morphology of boehmite nanostructures due to different basifying reagents.

In order to evaluate the optical quality of the materials, room temperature photoluminescence spectroscopy has been performed by using a Cary Eclipse Fluorescence Spectrophotometer, Agilent Technologies with an excitation wavelength (λ_{ex}) of 375 nm (Fig. 3).

It has been observed from the PL data that the fluorescence intensity is highest for the needle-like HBH sample, whereas, it is lowest for spherical EBH. This type of phenomena is due to the difference in defect densities reported previously [17]. The highest fluorescence intensity of HBH among the three samples makes this needle-shaped HBH a potential candidate for sensing and imaging applications.

3.2. Sensing of Cr(VI) in aqueous medium and real life wastewater

In order to confirm the sensing ability of the needle-shaped boehmite material, the selectivity and sensitivity experiments have been carried out. Various cations and anions along with the targeted hexavalent chromium have been added separately to the HBH in aqueous medium. In each case, 500 μM of ions were added to the aqueous solution of HBH. Each time the fluorescence spectrum is recorded at 428 nm upon an excitation wavelength of 375 nm. The results of the selectivity tests have been plotted in a column graph and are depicted in Fig. 4.

Fig. 4 depicts a drastic quenching of fluorescence intensity in case of Cr(VI), whereas other anions and cations does not alters the fluorescence level of the nanosensor (HBH). The fluorescence quenching attributed to Cr(VI) is about 99%, which makes our material a good Cr(VI) sensor.

Moreover, to rationalize the performance of the nanosensor, the detection limit (LOD) of the sensor material is computed by fitting the concentration dependent fluorescence data with the linear Stern-Volmer equation [21–22]. Initially, 1 mg.ml^{-1} aqueous solution of the sensor material has been prepared and aqueous solutions of Cr (VI) of different molarity (0–34 μM) were added to the sensor solution separately. In each case, fluorescence spectrum of the sample has been recorded (Fig. 5(a)) by giving an excitation energy equivalent to 375 nm wavelength.
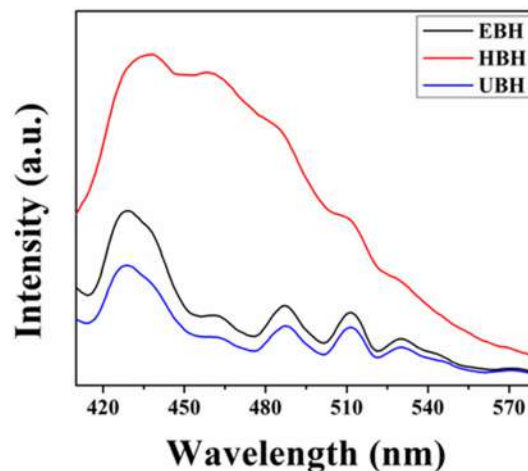
Fig. 3. Comparative fluorescence spectra of synthesized boehmite samples.

Fig. 5(a) shows an apparent reduction in florescence intensity with increasing Cr(VI) concentration.

The fluorescence intensities recorded at 428 nm at various Cr (VI) concentrations have been plotted against the Cr(VI) concentration itself and fitted with the linear Stern-Volmer equation [21–22] as mentioned below:

$$I_0/I = 1 + K_{SV}[M] \tag{2}$$

where, I_0 and I are fluorescence intensities of pure HBH sample and HBH with Cr(VI) at various concentrations of Cr(VI), K_{SV} is the Stern-Volmer coefficient. As these fitted parameters suggest, the value of K_{SV} in this case is 24.255×10^6 with a fitting coefficient of 0.96414. This high K_{SV} value of HBH sample reduces greatly its detection limit to 0.42 nM. Hence, one can argue that the tremendously high detection limit and remarkable selectivity makes this HBH sample a good candidate for making fluorescence based nanosensors.

The extent of this nanosensor in real life conditions has been verified by using a real life tannery wastewater sample containing 23.4 ppm of chromium with other common industrial effluents. The collected wastewater sample was filtered using a filter paper and then preserved at 4 °C temperature before use. The sample was then added to the sensor material (HBH) and the fluorescence spectra was recorded and depicted in Fig. 6.

Fig. 6 shows a dramatic reduction in fluorescence intensity at 428 nm when the wastewater sample is added to the sensor, which in turn proves the real life applicability of this nanosensor.

3.3. Mechanism of Cr(VI) sensing

In general, fluorescence quenching occurs due to various reasons. Among them, Inner Filter Effect (IFE), Photoinduced Electron
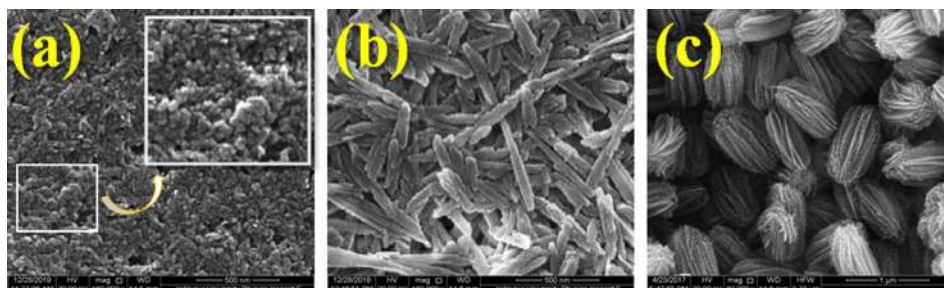
Fig. 2. FESEM micrographs of different boehmite nanostructures.
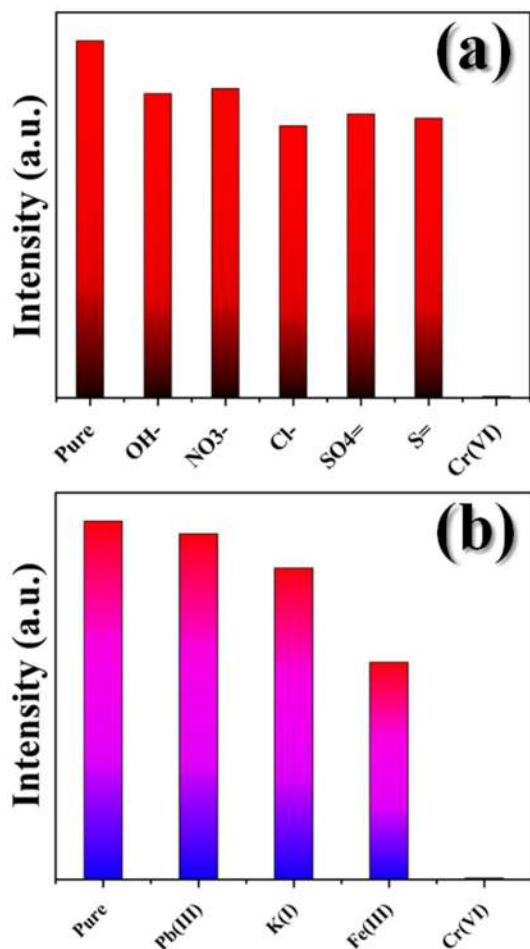
Fig. 4. Selectivity data of the HBH sample at various ionic environments.

Transfer (PET) and Energy Transfer (ET) routes are quite common [23–24]. In this case, neither absorption and emission spectra overlaps nor the absorption maxima alters its position after Cr(VI) addition, thus ET and IFE routes of quenching could be excluded. Moreover, the linearity of Stern-Volmer plot gives rise to the fact that the fluorophores of HBH makes collision with the quenching molecules in the excited state and causes this type of drastic fluorescence quenching [25]. Henceforth, it can be argued that the quenching of fluorescence is primarily occurs due to the PET in the excited state.

3.4. Removal of hexavalent chromium

Adsorption based contamination removal technique is less harmful and rapid than other filtration techniques [26–27]. Herein, the removal of hexavalent chromium by the multifunctional boehmite sample is based on this surface adsorption technique. The adsorption efficacy, i.e. the uptake of adsorption is measured for all three nanostructures of boehmite (EBH, HBH, UBH). Initially, aqueous solutions of the three boehmite samples were prepared (500 μM) and Cr(VI) was added separately to this samples at a concentration of 100 ppm. The Cr(VI) added boehmite samples were stirred by using magnetic stirrers for 6 h and then the absorption characteristics were recorded (Fig. 7) by employing a λ-25, Perkin Elmer UV–Vis Spectrophotometer. The characteristic absorbance maximum centered at 351 nm due to the hexavalent chromium has been greatly reduced after adding the HBH sample. The absorption peak do not alters significantly for the other two nanostruc-
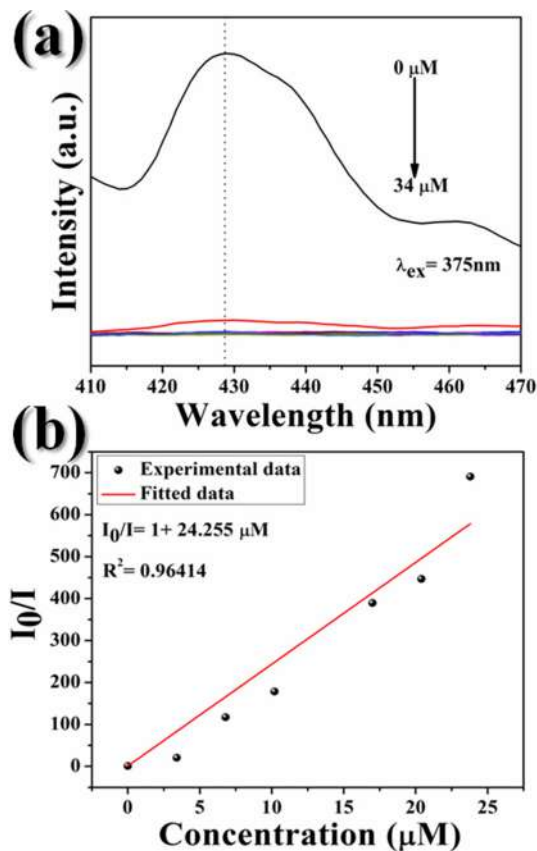
Fig. 5. (a) Fluorescence quenching data, (b) Stern-Volmer plot.
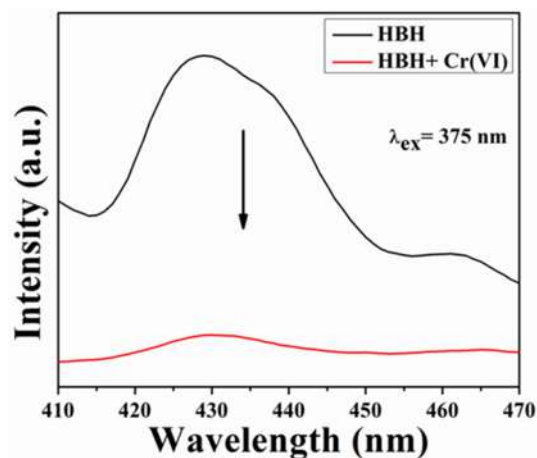
Fig. 6. Sensing experiment in real life industrial wastewater sample.

tures of boehmite (EBH, UBH), which suggests that the adsorption uptake is maximum for the synthesized HBH sample. The uptake is calculated using the following equation [28],

$$Uptake(\%) = ((C_0 - C_e)/C_0)x\ 100 \qquad (3)$$

Here, C_0 and C_e are initial and equilibrium concentrations of Cr (VI) ion. It is estimated from equation (3) that the percentage uptake for HBH is around 76%, whereas it is 48% for EBH and 64% for UBH. Thus, HBH has been selected for other adsorption experiments as this has the highest uptake value among the three samples.

Previously, the surface areas and mean porosities of these three nanostructures were estimated and reported elsewhere by using
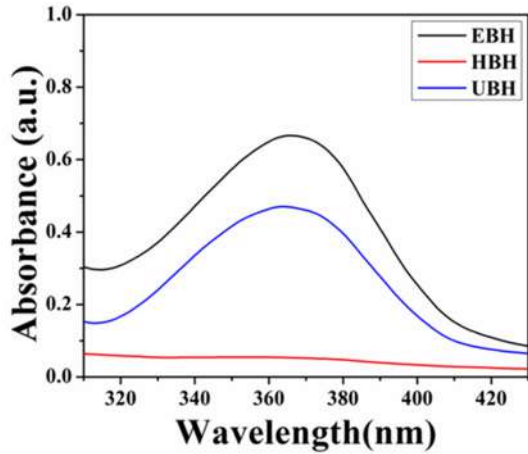
Fig. 7. Adsorption uptake studies for synthesized boehmite samples.

BET-BJH analysis [17]. The previously reported data ensures the fact that the HBH is having the highest pore diameter among the three samples which could be the rationale of the highest uptake value of HBH.

In order to ensure the adsorption equilibrium and overall removal performance, adsorption kinetics study has been carried out. In a typical experiment, 80 ppm Cr(VI) solution was exposed to the HBH sample and a time varied absorption spectra was recorded from 0 to 10 min.

The adsorption kinetics has been depicted in Fig. 8, where it can be observed that the characteristic absorbance maximum centered at 352 nm gradually reduces with time. It has also been observed that the Cr(VI) concentration remarkably decreases just in 10 min after the addition of HBH. This type of rapid removal is mainly due to the multilayered adsorption as mentioned elsewhere [29–30].

3.5. Electrical studies and proposal of waste capacitor

Charge storage capacity of a material depends primarily on dielectric permittivity. Previously, we have reported the dielectric constant of HBH is around 6.2×10^4 at 40 Hz field frequency in room temperature [17]. The reported permittivity value was attributed to the Maxwell-Wagner interfacial polarization. This time, the electrical permittivity has been elevated to a value of 2.7×10^6 for the same sample when it is exposed to the hexavalent chromium.

Initially, 100 mg of pure HBH powder was added to the 10 ml, 100 ppm Cr(VI) aqueous solution and stirred by using a magnetic stirrer for 3 h. The chromium adsorbed HBH sample was then centrifuged and dried in a dust free oven for 12 h at 60 °C. The dried sample was then pressed in a hydraulic press system to make a solid pellet. A pellet of pure HBH was prepared in a same manner to understand the alteration of electrical properties due to the adsorption of hexavalent chromium on to the surface of HBH sample.

The electrical properties of these solid pellets were then estimated by employing an Agilent 4294A precision impedance ana-
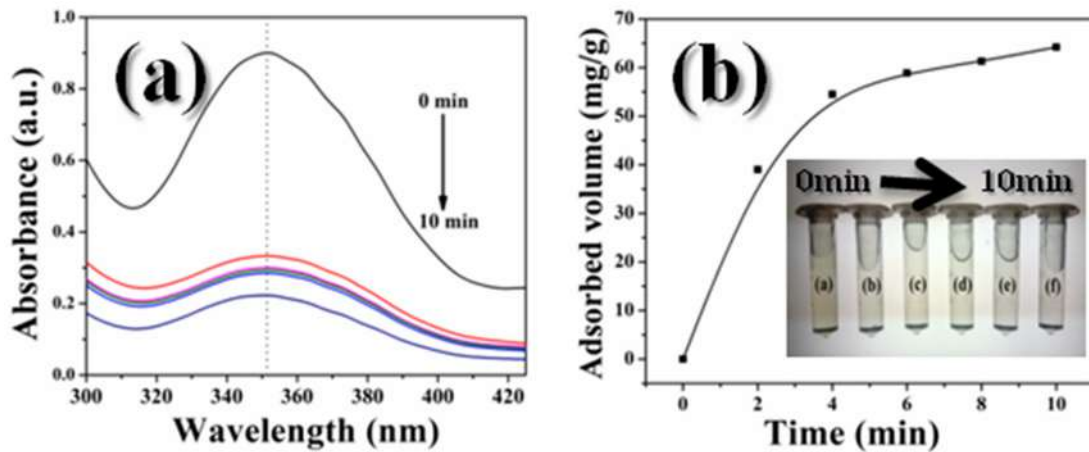
Fig. 8. Adsorption kinetics study for needle like HBH sample.
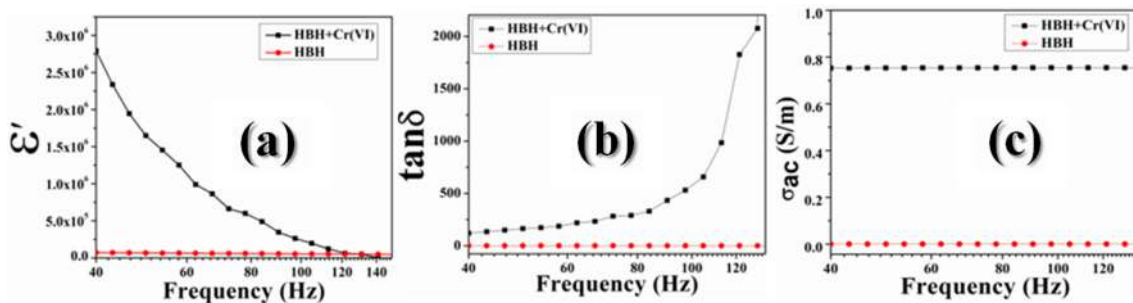
Fig. 9. Electrical properties of pure and Cr(VI) adsorbed HBH samples.

lyzer in a fixed bias voltage of 0.5 V in the frequency ranges from 40 Hz to 150 Hz.

The dielectric permittivity of the samples is depicted in Fig. 9(a), which shows that the surface adsorption of Cr(VI) drastically enhances the permittivity value of the chromium adsorbed sample. This type of dielectric relaxation is caused due to the interfacial polarization effect [31]. In reality, the number of conductive grains in Cr(VI) adsorbed sample is higher than that of pure HBH. Thus, the numbers of interfacial dipoles are also greater in chromium adsorbed sample, which in turn elevates the dielectric constant of the adsorbed HBH.

The ac conductivity of the Cr(VI) adsorbed boehmite is also greater than its pure fraction, which could be due to the augmentation in the number of charge carriers. These free charge carriers introduce hopping from one grain boundary to another that further improves the value of ac conductivity of the chromium adsorbed sample [32]. Hence, the enhanced electrical properties of chromium adsorbed boehmite (HBH) make this sample a potential agent for fabricating waste capacitors.

4. Conclusion

In summary, three different nanostructures of boehmite have been synthesized and characterized. The needle-like HBH sample is having promising fluorescence intensity and highest adsorption capacity among the three nanostructures and it is selected for further experiments. The drastic quenching of fluorescence intensity of the HBH upon Cr(VI) addition is found to be momentary with a detection limit of 0.42 nM. Linear Stern-Volmer plot and other spectroscopic data suggest that the fluorescence quenching is due to the PET effect. The sensing performance of the HBH has also been examined in real life industrial wastewater sample, which agrees with other sensing data quite well. Ultra low detection limit and remarkable selectivity make this material a superior Cr(VI) sensor. Apart from sensing, this material can remove hexavalent chromium very quickly from chromium containing water. The rapid removal of hexavalent chromium has been justified by using the adsorption kinetics data of HBH. Around 76% of the total contamination has been eliminated from the aqueous solution of chromium in just 10 min. Adsorbed chromium ions onto the porous structure of boehmite is not only usable for sensing and removal applications but also this phenomenon drastically changes the dielectric permittivity and ac conductivity of the chromium adsorbed sample. At least 43 time increment in dielectric constant makes our multifunctional needle-shaped boehmite nanostructure a budding candidate for fabricating 'waste capacitors'.

CRediT authorship contribution statement

Shubham Roy: Conceptualization, Methodology, Writing - original draft. **Souravi Bardhan:** Data curation. **Jhilik Roy:** Data curation, Investigation. **Sukhen Das:** Writing - review & editing, Supervision.

Declaration of Competing Interest

The authors declare that they have no known competing financial interests or personal relationships that could have appeared to influence the work reported in this paper.

Acknowledgments

References

[1] N. Hossain, M.A. Bhuiyan, B.K. Pramanik, S. Nizamuddin, G. Griffin, Waste materials for wastewater treatment and waste adsorbents for biofuel and cement supplement applications: a critical review, J. Cleaner Prod. 120261 (2020).

[2] Y. Xu, J. Li, Q. Tan, A.L. Peters, C. Yang, Global status of recycling waste solar panels: A review, Waste Manage. 75 (2018) 450–458.

[3] M.R. Maghami, H. Hizam, C. Gomes, M.A. Radzi, M.I. Rezadad, S. Hajighorbani, Power loss due to soiling on solar panel: A review, Renew. Sustain. Energy Rev. 59 (2016) 1307–1316.

[4] X. Liu, S. Zhang, J. Bae, The nexus of renewable energy-agriculture-environment in BRICS, Appl. Energy 204 (2017) 489–496.

[5] A. Dave, Performance Evaluation of Effluent Treatment Plant for Pigment industry and reuse of waste Aluminum Hydroxide as coagulant, Perform. Eval. 4 (12) (2017).

[6] V.V. Kulkarni, A.K. Golder, P.K. Ghosh, Critical analysis and valorization potential of battery industry sludge: Speciation, risk assessment and metal recovery, J. Cleaner Prod. 171 (2018) 820–830.

[7] Hutton M., Shafahi M. Water pollution and leather industry-A review. (2018).

[8] M.M. Abdul, S.M. Ali, R. Rajesh, S.K. Paul, Modeling the interrelationships among barriers to sustainable supply chain management in leather industry, J. Cleaner Prod. 181 (2018) 631–651.

[9] P. Wang, J. Yao, G. Wang, F. Hao, S. Shrestha, B. Xue, G. Xie, Y. Peng, Exploring the application of artificial intelligence technology for identification of water pollution characteristics and tracing the source of water quality pollutants, Sci. Total Environ. 693 (2019) 133440.

[10] W. Qin, W. Dou, V. Leen, W. Dehaen, M. Van der Auweraer, N. Boens, A ratiometric, fluorescent BODIPY-based probe for transition and heavy metal ions, RSC Adv. 6 (10) (2016) 7806–7816.

[11] L.N. Neupane, E.T. Oh, H.J. Park, K.H. Lee, Selective and sensitive detection of heavy metal ions in 100% aqueous solution and cells with a fluorescence chemosensor based on peptide using aggregation-induced emission, Anal. Chem. 88 (6) (2016) 3333–3340.

[12] C. Liu, T. Wu, P.C. Hsu, J. Xie, J. Zhao, K. Liu, J. Sun, J. Xu, J. Tang, Z. Ye, Direct/ Alternating Current Electrochemical Method for Removing and Recovering Heavy Metal from Water Using Graphene Oxide Electrode, ACS Nano (2019).

[13] Y. An, H. Fei, G. Zeng, L. Ci, S. Xiong, J. Feng, Y. Qian, Green, scalable, and controllable fabrication of nanoporous silicon from commercial alloy precursors for high-energy lithium-ion batteries, ACS Nano 12 (5) (2018) 4993–5002.

[14] P. Hu, H. Wang, Y. Yang, J. Yang, J. Lin, L. Guo, Renewable-biomolecule-based full lithium-ion batteries, Adv. Mater. 28 (18) (2016) 3486–3492.

[15] C.H. Chang, S.H. Chung, A. Manthiram, Transforming waste newspapers into nitrogen-doped conducting interlayers for advanced Li-S batteries, Sustainable Energy Fuels 1 (3) (2017) 444–449.

[16] Minaei S., AbdollahifarM., Shojaeimehr T., Kumar D. Micro/mesoporous quasi-zero-dimensional AlOOH and Al2O3 nanoparticles. Inorg. Nano-Metal Chem. 50(3) (2020) 170-177.

[17] S. Roy, A. Maity, P. Mandal, D.K. Chanda, K. Pal, S. Bardhan, S. Das, Effects of various morphologies on the optical and electrical properties of boehmite nanostructures, CrystEngComm 20 (40) (2018) 6338–6350.

[18] J.L. Contreras-Larios, A. Infantes-Molina, L.A. Negrete-Melo, J.M. Labadie-Suárez, H.T. Yee-Madeira, M.A. Autie-Pérez, E. Rodríguez-Castellón, Separation of N-C5H12-C9H20 Paraffins Using Boehmite by Inverse Gas Chromatography, Appl. Sci. 9 (9) (2019) 1810.

[19] S. Roy, S. Bardhan, K. Pal, S. Ghosh, P. Mandal, S. Das, S. Das, Crystallinity Mediated Variation in Optical and Electrical Properties of Hydrothermally Synthesized Boehmite (γ-AlOOH) Nanoparticles, J. Alloys Compd. 763 (2018) 749–758.

[20] S. Das, S. Das, A. Roychowdhury, D. Das, S. Sutradhar, Effect of Gd doping concentration and sintering temperature on structural, optical, dielectric and magnetic properties of hydrothermally synthesized ZnO nanostructure, J. Alloys Compd. 708 (2017) 231–246.

[21] S. Hussain, A.H. Malik, M.A. Afroz, P.K. Iyer, Ultrasensitive Detection of nitroexplosive-Picric Acid Via a Conjugated Polyelectrolyte in Aqueous Media and Solid Support, Chem. Commun. 51 (2015) 7207–7210.

[22] Z.J. Lin, H.Q. Zheng, H.Y. Zheng, L.P. Lin, Q. Xin, R. Cao, Efficient Capture and Effective Sensing of $Cr_2O_7^{2-}$ from Water Using a Zirconium Metal-Organic Framework, Inorg. Chem. 56 (2017) 14178–14188.

[23] M. van de Weert, L.V.D. Stella, Fluorescence quenching and ligand binding: a critical discussion of a popular methodology, J. Mol. Struct. 998 (2011) 144–150.

[24] C.E. Barrera-Díaz, V. Lugo-Lugo, B. Bilyeu, A review of chemical, electrochemical and biological methods for aqueous Cr(VI) reduction, J. Hazard. Mater. 223–224 (2012) 1–12.

[25] Sun X., Kong C., Zhang H. Sensing mechanism of a fluorescent probe for thiophenols: Invalidity of excited-state intramolecular proton transfer mechanism. Spectrochim. Acta Part A: Mol. Biomol. Spect. (2020) 118129.

[26] A. Abbas, A.M. Al-Amer, T. Laoui, M.J. Al-Marri, M.S. Nasser, M. Khraisheh, M.A. Atieh, Heavy metal removal from aqueous solution by advanced carbon

nanotubes: critical review of adsorption applications, Sep. Purif. Technol. 157 (2016) 141–161.

[27] A. Azimi, A. Azari, M. Rezakazemi, M. Ansarpour, Removal of heavy metals from industrial wastewaters: a review, ChemBioEng Rev. 4 (1) (2017) 37–59.

[28] G. Vijayakumar, R. Tamilarasan, M. Dharmendirakumar, Adsorption, Kinetic, Equilibrium and Thermodynamic Studies on the Removal of Basic Dye Rhodamine-B from Aqueous Solution by the use of Natural Adsorbent Perlite, J. Mater. Environ. Sci. 3 (1) (2012) 157–170.

[29] S. Roy, K. Pal, S. Bardhan, S. Maity, D.K. Chanda, S. Ghosh, P. Karmakar, S. Das, Gd (III)-Doped Boehmite Nanoparticle: An Emergent Material for the Fluorescent Sensing of Cr (VI) in Wastewater and Live Cells, Inorg. Chem. 58 (2019) 8369–8378.

[30] S. Roy, S. Bardhan, D.K. Chanda, S. Ghosh, D. Mondal, J. Roy, S. Das, Development of Cu(II) Doped Boehmite Based Multifunctional Sensor for Detection, Removal of Cr(VI) from Wastewater and Conversion into an Energy Harvesting Material, Dalton Trans. (2020), https://doi.org/10.1039/D0DT00888E.

[31] S. Bardhan, S. Roy, D.K. Chanda, S. Das, K. Pal, A. Chakraborty, R. Basu, S. Das, Microstructure and Dielectric Properties of Naturally Formed Microcline and Kyanite: A Size-Dependent Study, Cryst. Growth Des. 19 (8) (2019) 4588–4601.

[32] S. Das, S. Das, S. Sutradhar, Enhanced dielectric behavior and ac electrical response in Gd- Mn-ZnO nanoparticles, J. Alloys Compd. 726 (2017) 11–21.

In Situ-Grown Cdot-Wrapped Boehmite Nanoparticles for Cr(VI) Sensing in Wastewater and a Theoretical Probe for Chromium-Induced Carcinogen Detection

Shubham Roy, Souravi Bardhan, Dipak Kr. Chanda, Jhilik Roy, Dhananjoy Mondal, and Sukhen Das*

ACCESS | Metrics & More | Article Recommendations | SI Supporting Information

ABSTRACT: In modern society, massive industrialization escalates environmental degradation by liberating various contaminants into the environment. Hexavalent chromium is a heavy metal that is being discharged from tannery and other industries, resulting in various carcinogenic diseases. This study reports a carbon dot (cdot)-based fluorometric probe for detecting hexavalent chromium in water. This is the very first time that cdots are tailored over the boehmite nanoparticle's surface using an *in situ* approach. Validation of formation of the nanocomposite has been discussed in detail employing the Rietveld refinement-based X-ray crystallography method. Vibrational spectroscopy and electron microscopy of the sample authenticate the nucleation process and the growth mechanism. The Stern−Volmer approach and time-resolved fluorescence measurements justify the sensitivity of the sensor (∼58 nM), and selectivity is analyzed by exposing the material to different ionic environments. Density functional theory (DFT) is applied herein to analyze the origin of fluorescence and the sensing mechanism of the probe, which shows that photoinduced electron transfer is responsible for the turn-off-based sensing of Cr(VI). The molecular docking simulation is carried out to ensure the binding of cdots to the binding pocket of the glutathione enzyme, which is responsible for treating reactive oxygen species-mediated DNA damage due to elements such as hexavalent chromium. Time-dependent density functional calculations show that the fluorometric probe is capable of detecting Cr(VI) in living cells making it an early stage chromium-mediated carcinogen detector.

KEYWORDS: *Rietveld refinement, density functional theory, molecular docking, fluorescent sensor, carbon dot*
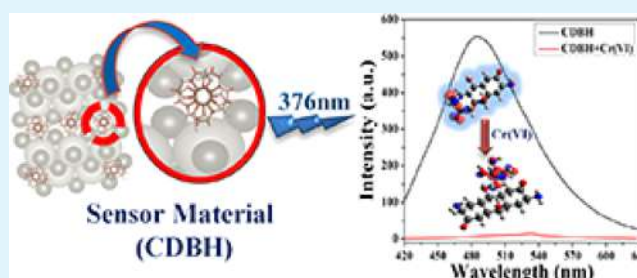
1. INTRODUCTION

Industrial discharge into water contaminates the local environment enormously and pollutes the biota.[1] Several health issues, such as skin disease, lung disease, and chronic bowel problems, are directly associated with water pollution.[2−4] Various carcinogenic diseases can also occur if the level of contamination is reasonably escalated.[5] Recent works allegedly relate heavy-metal pollution with various carcinogenic symptoms.[6,7] Among a range of heavy metals, hexavalent chromium [Cr(VI)] has gained importance because of its severe toxicity.[8] A minute dose of Cr(VI) (∼1 ppm) can harm living cells.[9] In reality, hexavalent chromium is cytotoxic, genotoxic, and carcinogenic and does not directly react with the DNA.[10,11] Its genotoxicity is attributed to oxidative DNA damage.[12] Thus, fast and accurate detection of Cr(VI) is much needed to combat its severe toxicity. There are various reasonable detection techniques, such as inductively coupled plasma atomic emission spectroscopy (ICP-AES), ICP−mass spectrometry, and spectroscopic detection techniques, to detect Cr(VI) in an aqueous medium.[13−15] However, they lack effectiveness on site because of their bulk size machineries and high cost. Hence, fluorometric detection is a good alternative in this regard. Fluorometric detection of contaminants is a relatively new approach and is gaining importance because of their biocompatibility, sensitivity, and low cost.[16−18] Generally, a fluorescent probe can "sense" a target molecule either by modulating its fluorescence intensity (turn on/turn off) or by changing its color.[19,20] Henceforth, it is obvious to have a promising fluorescent material in order to detect contaminants in this manner. Various new-generation materials, such as graphene quantum dots, metal ions, and rare earth ions-doped metal−oxide nanosystems, and some perovskite materials are gaining interest because of their selectivity and promising fluorescence property, but synthesis, high-cost, and stability issues restrict their usage in real-life situations.

Carbon quantum dots (cdots) are a relatively new and promising nanomaterial because of its outstanding fluorescence property.[21,22] This zero-dimensional nanosystem is quantum mechanically confined because of its tiny size (<10 nm). In reality, cdots possess exceptional "tunable" fluorescence property upon excitation.[23] Biocompatibility and a higher degree of fluorescence quantum yield already made this nanomaterial a potential candidate for various imaging and sensing applications.[24−26] Still, most of the researchers faced difficulties in restricting the agglomeration, which greatly influences the fluorescence emission of this nanosystem.[27−29] Recently, researchers used different polymers, natural nano-materials, and metal−oxide compounds as the substrate of cdots in order to stabilize and escalate the fluorescence emission of the system.[30−32] However, most of the cases dealt with the *ex situ* growth of cdots, which were somewhat time consuming and costly. *In situ* growth is very useful as both cdots and the substrate system can be grown simultaneously in this method. It lowers the production cost and radically minimizes the preparation time maintaining similar phys-icochemical properties.

This work reports a fluorescent probe for hexavalent chromium with a nanomolar detection limit using *in situ*-grown cdots on a boehmite nanoparticles' (γ-AlOOH) surface. This is probably the first time that cdots have been grown *in situ* on a nanoparticle surface. The synthesized nanosystem has been characterized using basic characterization techniques, and the probable structure of the nanocomposite [cdots−boehmite (CDBH)] has been determined by the X-ray crystallography method. Enhanced emission intensity and fluorescence stability have been confirmed and on-site activity of this fluorometric probe has been carried out using standard emission spectros-copy techniques. Additionally, the origin of fluorescence and the fluorometric detection mechanism of the synthesized nanocomposite have been investigated using the standard Stern−Volmer (SV) equation and density functional theory (DFT), revealing the photoinduced electron transfer (PET) between the quencher and fluorophores. Molecular docking simulation discloses the binding affinity of the synthesized probe toward the glutathione protein, which might be responsible for the biosensing activity of the nanocomposite when exposed to Cr(VI). This biosensing activity has been modeled and theorized accordingly using time-dependent DFT (TDDFT), justifying the synthesized material to be a novel fluorometric probe for early stage cancer detection in living cells.

2. MATERIALS AND METHODS

2.1. Materials. Aluminum nitrate nonahydrate and anhydrous citric acid (Merck) were used as main precursor materials for boehmite and cdots, respectively. Ethylenediamine (Merck) was used as a precipitation agent for the nanocomposite. It also caused nitrogen doping into the cdot structure. Potassium bromide (Merck) was used as the substrate material for Fourier-transform infrared (FTIR) spectroscopy. Aqua regia and ethanol (Merck) were used for cleaning the glassware. A 5% hydrochloric acid solution (Merck) was prepared for cleaning the quartz sample holders before spectroscopic measurements. All the chemicals were of analytical grade and used without further purification. Millipore water (resistivity of at least 18 MΩ cm) was used throughout the experiments.

2.2. Synthesis of the CDBH Nanocomposite. In a typical synthesis, 3.56 g of aluminum nitrate was dissolved in 70 mL Millipore water along with 0.096 g of citric acid. The solution was stirred using a magnetic stirrer until complete dissolution of added

precursors took place. Afterward, ethylenediamine was added drop by drop into the solution in order to raise the pH to 12 that results in nucleation of the CDBH nanocomposite. At this point, stirring was continued for another 3 h to complete the reaction process. After completion of stirring, the thick, white solution was put into a Teflon-lined stainless-steel autoclave and subject to hydrothermal treatment at 170 °C for 20 h. The autoclave was then cooled down to room temperature slowly and a brown solution was collected, which was then washed properly using the centrifugation technique and finally dried in a vacuum chamber for 48 h. The dried clusters were ground into fine particles using an agate mortar and subject to further characterization.

2.3. Computational Methods. The crystallographic phase parameters of the sample were ascertained by refining the experimental X-ray pattern of CDBH using the Rietveld-based software package MAUD v2.94.[33] The crystallographic information file of boehmite (COD file no. 9015088) was used to refine the experimental diffraction pattern of the nanocomposite. Initially, the instrumental broadening parameters and Caglioti PV functions were refined along with the background function of the diffractogram.[34] In this case, the interpolated background model was adopted for a greater accuracy. The unit cell parameters and atomic positions were also refined to produce a plausible theoretical model of the sample. The crystal texture and the size−strain model were refined using an arbitrary texture model and Popa rules, respectively.[35] Finally, the output file was saved in the crystallographic information file (.cif) format and further visualized using the VESTA v3.5.2 program.[36] The bond lengths and bond angles were calculated using this visualization software tool in order to capture the theoretical model of the synthesized nanostructure.

The DFT calculations were carried out using a hybrid Becke, 3-parameter, Lee−Yang−Parr (B3LYP) functional associated with the continuum aqueous solvent mode (CPCM).[37] The entire set of DFT and TDDFT calculations was performed using the Orca v4.2 package and modeled with the Avogadro v1.2 program.[38,39] The 6-31G** basis set along with the RIJCOSX auxiliary basis function was implemented to describe the elements (C, H, O, and N) and the Cr(VI) ion, respectively.[40] The frequency optimization of the cdot was carried out at the same theoretical level depicting the absence of any imaginary frequency. The TDDFT method was used to evaluate the theoretical absorbance spectra and electronic transitions of the complexes.

The molecular docking study between cdots and glutathione was carried out in order to envisage the binding affinity between these two molecules. Initially, Autodock Tools v.1.5.6 was employed to prepare the protein by removing the water molecule and adding polar hydrogen and Kollman charges.[41] Autodock vina v.1.1.2 was used to check the binding affinity of the said protein−ligand complex.[42] The exact binding pocket was identified and visualized using the PyMol v.2.0.7 program.[43]

3. RESULTS AND DISCUSSION

3.1. Structural Analysis and Formation Mechanism of the Sensor Material. X-ray crystallography is a useful technique to examine the purity by fingerprinting the material. Information regarding structural details and bonding networks could also be analyzed using this characterization technique.[44] The X-ray diffractogram of the material was examined using a D8, Bruker AXS diffractometer, Wisconsin, USA, equipped with a Cu Kα target of 1.5418 Å and operated at a 35 kV, 35 mA bias with a scan speed of 2 s/step. The diffractogram of the sample was further analyzed using the standard Rietveld refinement method superposing the experimental data with the COD file no. 9015088 (crystallographic open database), which shows the absence of any undesired diffraction maxima revealing the phase purity of the material.[45] It is also observed that the experimental data fitted quite well (fitting coefficient, $\chi^2 = 1.59$) with the theoretical data confirming the curve fitting

to be reasonable (Table 1). The refined diffractogram along with the experimental data and the difference plot are depicted

Table 1. Microstructural Parameters of the Sensing Probe Obtained from Rietveld Refinement

parameters	CDBH
a (Å)	3.6862557
b (Å)	12.160722
c (Å)	2.8536618
V (Å^3)	127.9243
size (Å)	68.23992
microstrain	1.4809×10^{-4}
R_p (%)	7.745
R_{wp} (%)	9.751
χ^2	1.59
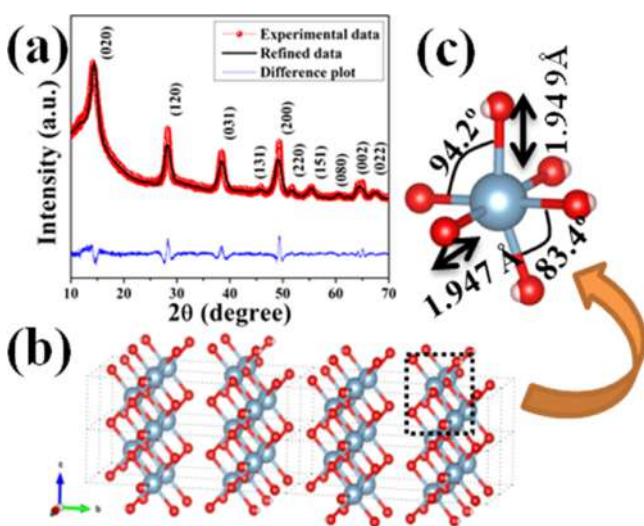
Figure 1. (a) Refined X-ray diffractogram, (b) microstructure, and (c) bonding network analysis of CDBH.

in Figure 1. The microstructural analysis of the sample has been performed, which shows the AlO$_6$ polyhedra of boehmite stacked together with the −OH radicals facing outward giving an orthorhombic structure to the sample. The mean Al−O and Al−OH bond lengths are found to be 1.947 and 1.949 Å causing angular displacements of 94.2° (O−Al−OH) and 83.4° (OH−Al−OH), respectively. Although cdots do not bind with the boehmite crystals, they develop microstrain inside the orthorhombic phase of the material. The Popa size−strain model-based refinement reveals the microstrain value to be 1.481×10^{-4} with a crystal size of 6.82 nm, revealing the formation of a CDBH nanocomposite.

FTIR spectroscopy was performed using a FTIR-8400S, Shimadzu in the wave number ranges between 400 and 4000 cm^{-1} to get an idea of the coexistence of cdots and boehmite in the synthesized sample. The FTIR spectrum in Figure 2 depicts the presence of AlO$_6$ radicals in the sample as the vibrations occur in the range from 590 to 780 cm^{-1}.[44] The −OH deformation linked to aluminum ions has also been observed (896 cm^{-1}). These bands below 1000 cm^{-1} ascertain the formation of boehmite.[46] The symmetric and asymmetric bands found at 1071 and 1154 cm^{-1}, respectively, are characteristic Al−O−H vibrations.[44] There are small bands
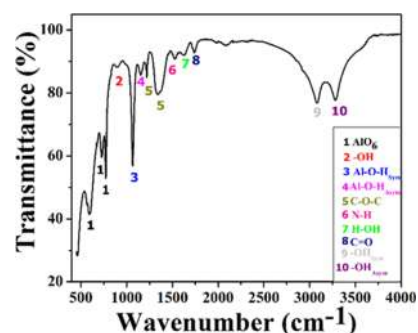
Figure 2. FTIR spectrum of the synthesized sensing probe.

located at 1223, 1336, and 1746 cm^{-1}, which are due to the C−O−C stretching and C=O vibrations confirming the presence of cdots in the sample.[47,48] A vibrational maximum seen at 1526 cm^{-1} is assigned to the N−H vibration ascribed to the formation of nitrogenous cdots.[49] The symmetric and asymmetric −OH vibrations (3081 and 3285 cm^{-1}, respectively) and surface-adsorbed moisture (1624 cm^{-1}) have also been observed in the spectrum.[46] Hence, it can be said that the synthesized nanocomposite has been successfully formed and there is no evidence of strong bond formation between boehmite and cdots, which alternatively corroborates the crystallographic data.

The morphology and particle size of the sensor material (CDBH) have been estimated using a JEOL JEM-2000 transmission electron microscope (TEM) operated at 200 kV. The overall particle morphology is spherical with a diameter ranging between 80 and 100 nm (Figure 3). A similar phenomenon has been reported in our previous work where ethylenediamine results in spherical morphology of boehmite nanoparticles when added to aluminum nitrate salt.[44] The
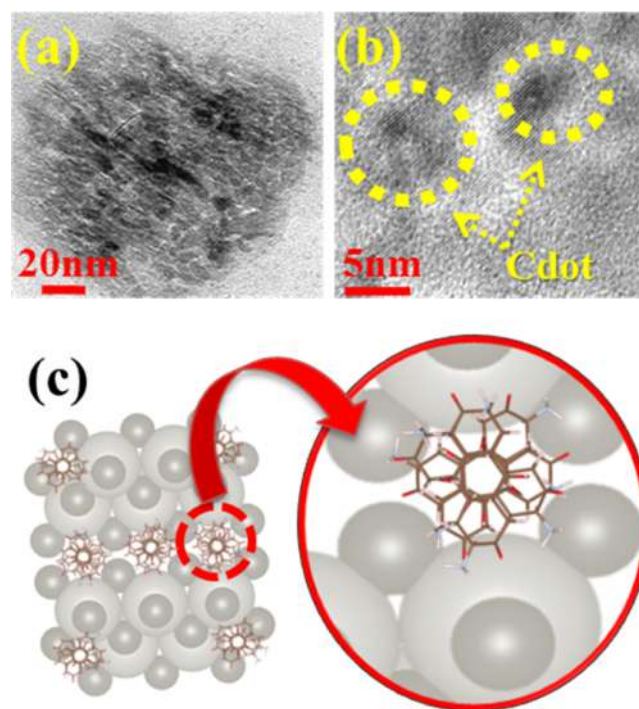
Figure 3. (a) TEM and (b) high-resolution TEM micrographs; (c) plausible structure of the sample showing cdots capturing the pores of boehmite on its surface.
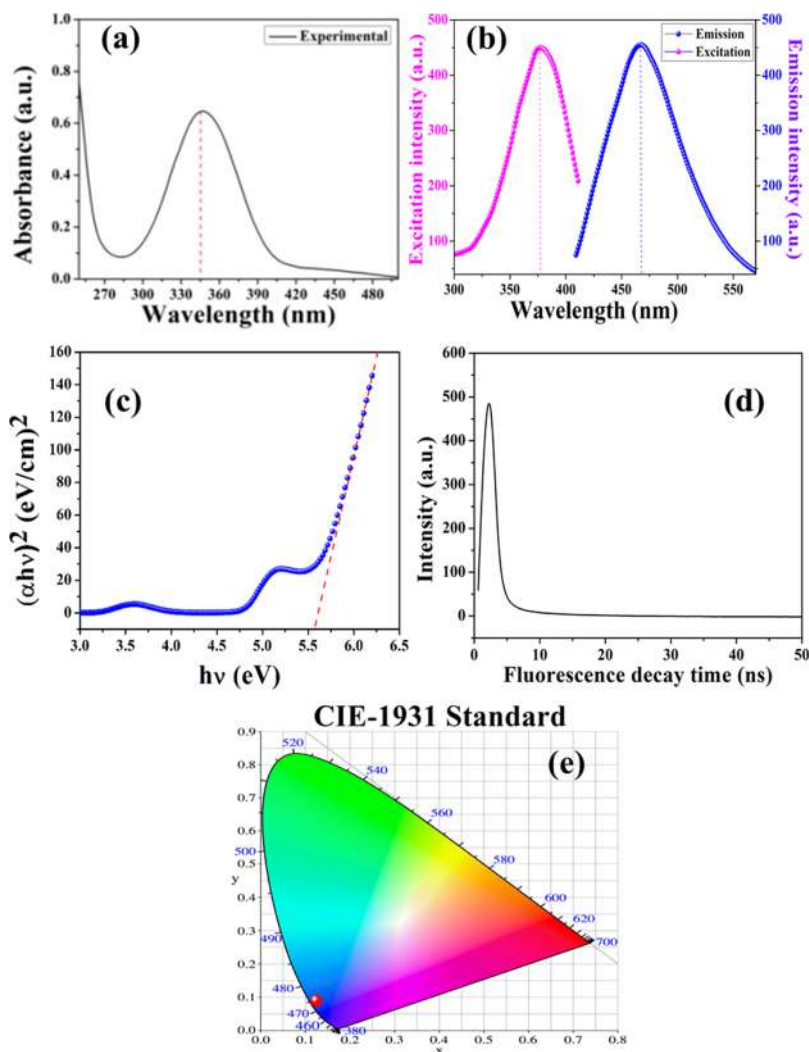
Figure 4. (a) Absorbance spectrum of the probe; (b) excitation and emission spectra of the sample; (c) Tauc plot of the probe; (d) time-resolved fluorescence decay pattern and (e) CIE-1931 color space analysis of the sensor material.

sphere of the boehmite is pretty rough and wrapped with relatively smaller spheres of nearly 3−5 nm diameter. These smaller spheres endorse the formation of cdots on the spherical boehmite surface. A schematic diagram (Figure 3) is demonstrated for realization of the entire structure of the nanocomposite.

Based on physical characterization results, it is quite evident that the dissolution of the aluminum precursor produces $[Al(H_2O)_6]^{3+}$ ions, which further transforms into $[Al(H_2O)_5OH]^{2+}$ due to hydrolysis of the O−H bonds and starts producing H^+ ions.[44] This extra proton (H^+) chelates with ethylenediamine, which increases the pH to a higher value (12, in this case) and starts precipitation due to Ostwald ripening.

$$Al(NO_3)_3 + H_2O \rightarrow [Al(H_2O)_6]^{3+} \tag{1}$$

$$[Al(H_2O)_6]^{3+} \rightarrow [Al(H_2O)_5OH]^{2+} + H^+ \tag{2}$$
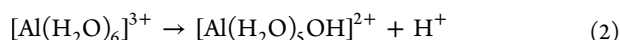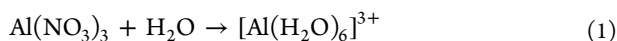
Citric acid also follows a similar pathway for dissolution in water and produces protons. The amine here also acts as a proton acceptor.

$$C_6H_8O_7 + H_2O \rightarrow C_6H_5O_7^{-3} + H^+ \tag{3}$$
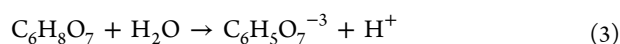
Individually, nucleation starts for these two elements, but during the hydrothermal treatment both aluminum and citrate ions start growing. As the shapes of both cdots and boehmite are nearly spherical, it can be argued that no preferential growth happens during the selfassembly of these two nanostructures. Previous studies suggest that boehmite is a mesoporous material having a pore diameter from 3 to 8 nm. These pores in our case entrap the cdots on its surface and finally produce the CDBH nanocomposite.

3.2. Study of Optical Properties and Origin of Fluorescence of the Sensor. The optical quality of a material can be validated by its absorption and emission spectra.[50] Initially, the absorption spectrum of the sample was measured on a PerkinElmer λ-25 spectrometer. In all the spectroscopic measurements, 500 μM solution of the sample was taken. The absorption spectrum is centered at 352 nm with an optical band gap of 5.52 eV (Figure 4). This band gap value has been calculated using Tauc's equation (eq 4)[51a]

$$\alpha E = A(E - E_g)^n \tag{4}$$

where E, E_g, α, and A are the photon energy, optical band gap energy in eV, absorption coefficient, and a constant term, respectively. In the Tauc plot (Figure 4), $(ah\nu)^2$ is plotted
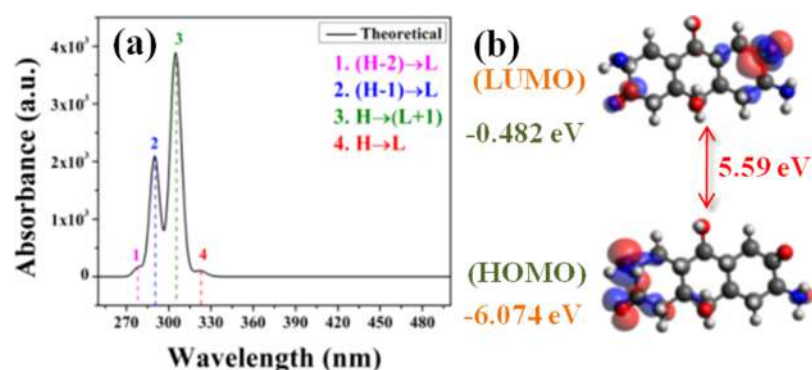
Figure 5. (a) Theoretical absorbance spectrum of the sample calculated from the TDDFT study and (b) TDDFT-based electronic transition pattern of the fluorophores for the CDBH sample.
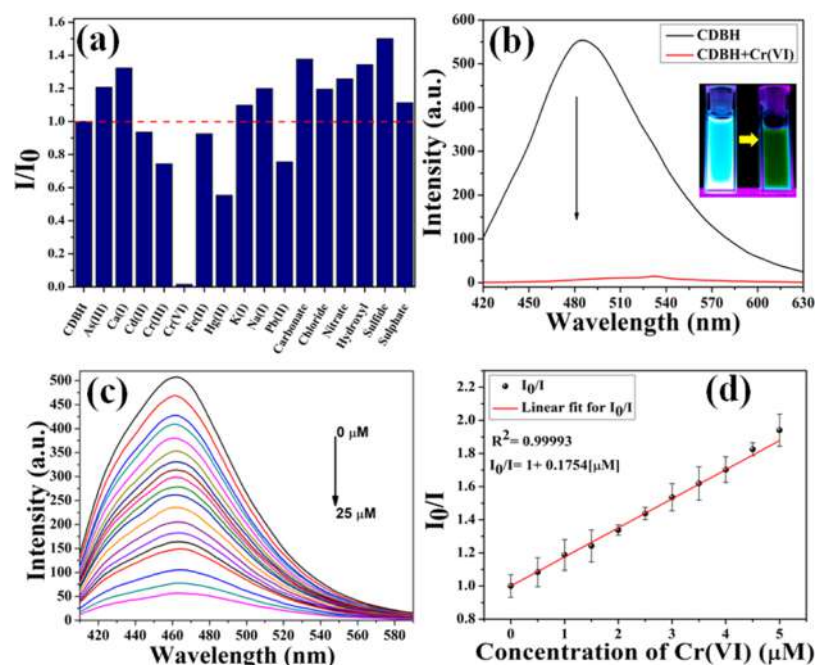
Figure 6. (a) Selectivity study of the sensor toward various anions and cations; (b) fluorescence quenching experiment of CDBH upon 50 μM Cr(VI) addition and (inset) naked eye detection of fluorescence quenching; (c) concentration-dependent fluorescence quenching of the sensor; and (d) linear SV plot of the probe.

against photon energy $h\nu$, and the band gap energy is calculated by extrapolating the linear region and intersecting the linear portion of the curve to the energy axis.

Herein, the excitation and emission spectra of the sensor material (CDBH) were recorded employing a Cary Eclipse Fluorescence spectrometer, Agilent Technologies with a slit size of 5 nm. The broad emission spectrum is centered at 462 nm showing excellent fluorescence intensity in the blue region of the spectrum. The excitation-dependent emission spectra are also depicted in Figure S1, which shows that the probable excitation lies somewhere between 370 and 380 nm. Finally, the excitation spectrum has been taken for 462 nm emission showing a broad peak centered at 375 nm (Figure 4). In order to ensure the real-life applicability of the sample as a sensor material, the CIE-1931 color space is used to compute the color temperature and color coordinates for the fluorescence spectrum of CDBH (Figure 4).[52] The color temperature is found to be 3372 K with the coordinates ($x = 0.12484$, $y = 0.09432$) lying in the bright blue region of the color space

enlightening the material to be acceptable for sensing and imaging applications.

Previously, a brief discussion has been made on the fluorescence stability of the cdot. It can be seen in the TEM micrographs that the cdot molecules are distinctly small and far apart on the boehmite's surface. This somewhat restricts the agglomeration of cdot molecules causing a better fluorescence stability (>20 min) in our sample (Figure S2). In this way, boehmite acts as a brilliant substrate for cdot molecules.

The time-resolved fluorescence decay of CDBH was estimated using a Cary Eclipse Fluorescence spectrometer employing a 5 nm emission slit width and a single pulse with 1 μs gate time. The emission and excitation wavelengths were set to 462 and 376 nm, respectively. The fitted fluorescence decay data are depicted in Figure 4 showing a decay time of 3.58 ns, which is reasonably high and effective for fluorometric applications.

In order to ensure the origin of fluorescence in our sample, theoretical DFT calculation has been applied.[51b−e] Nitrogenous cdots are well-known fluorophores.[49] Thus, this part of

the nanocomposite was taken to perform the quantum chemical calculations. Initially, the geometry of the cdot molecule has been optimized and no imaginary frequency value was found, which ensures the validity of the model. Afterward, the TDDFT approach was applied to compute the absorbance spectrum and electronic-transition probabilities theoretically. The frontier molecular orbitals are depicted along with the theoretical absorbance spectrum in Figure 5. The highest occupied molecular orbital (HOMO)−lowest unoccupied molecular orbital (LUMO) gap is found to be 5.59 eV, which is quite close to the experimental band gap value (5.52 eV) of the sample (Figure 5). The theoretical absorbance spectrum shows four distinct electronic transitions located at 278, 291, 305, and 323 nm, among which λ_{max} is situated at 323 nm and responsible for the majority of electronic transitions (it is also close to the experimental absorbance maximum). In reality, the λ_{max} transition occurs between the HOMO (−6.074 eV) and the LUMO (−0.482). Previously, various research works reported that the C−N bond in cdots introduces charge dislocation and promotes electron-transfer ability, which enhances the fluorescence property of the sample.[53] In our case, fluorophores situated at the C−N moiety of the cdot in the HOMO partially transferred to the C=O-carrying part in the LUMO, resulting in a π-stacking between these two states (Figure 5). Henceforth, it can be said that the TDDFT formalism successfully captures the mechanism of fluorescence for the sensing probe.

3.3. Estimation of Selectivity and Sensitivity of the Sensor Material.

The performance of a sensor material is judged by its selectivity and sensitivity toward a specific target molecule. Herein, CDBH acts as a fluorometric probe to determine the presence of hexavalent chromium in the aqueous medium and biological species. In order to verify the selectivity of the material, 50 μM solutions of various cations and anions were prepared and were separately added to a CDBH solution of 500 μM concentration.

Apart from Cr(VI), in each case, the fluorescence spectra do not alter or even the fluorescence intensity does not change significantly. However, when added to Cr(VI), the fluorescence intensity of the synthesized sensor material rapidly quenches (Figure 6). A similar type of phenomenon occurs when a UV light of 390 nm is irradiated on the sensor material before and after the addition of hexavalent chromium. The bright blue fluorescent signal has been drastically quenched upon Cr(VI) addition, which is visible even through the naked eye (Figure 6).

In order to estimate the sensitivity of the probe, various concentrations of Cr(VI) (0−25 μM) were added to 500 μM solution of CDBH, and the responses are depicted in Figure 6. It shows a gradual decrement of fluorescence intensity of the sensor material upon Cr(VI) addition, which has been fitted using the linear SV equation (Figure 6)[54]

$$I_0/I = 1 + K_{SV}[M] \tag{5}$$

where I_0 and I are the fluorescence intensities before and after the addition of Cr(VI), respectively, $[M]$ is the concentration of the ions, and K_{SV} is the SV quenching constant. The SV plot is taken up to 5 μM concentration of Cr(VI) to ensure the linearity of the plot, showing a fitting coefficient (R^2) of 0.99993. Beyond this value, the graph shows an upward increment (Figure S3), which might be due to the inner filter effect (IFE).[55]

The limit of detection (LOD) of the sensing probe is estimated using the following formula (eq 6)[54]

$$LOD = 3\sigma/K_{SV} \tag{6}$$

where σ and K_{SV} are the standard deviation of at least 10 measurements of the fluorescence intensities of pure CDBH without the presence of any quencher and the quenching constant, respectively. The LOD of the probe is found to be 58.1 nM, which is lesser than most of the previous reports mentioned in Table S1.

The interaction between the fluorophores and the quencher ions [Cr(VI)] has also been estimated in the excited state by employing time-resolved fluorescence decay measurements (Figure S4). The decay time of the fluorophores reduced tremendously when exposed to the quencher ion presenting the fact that the quenching phenomenon occurs in the excited state.

3.4. Detection Mechanism of the Sensor Material.

Fluorophore−quencher interaction can happen in various ways. IFE, energy transfer, and PET are well-established pathways among them.[56,57] Initially, it has been observed from the electrostatic potential mapping analysis (Figure S5) that the surface of the fluorophore (i.e., cdots) is highly negative, which is responsible for attracting hexavalent chromium ions to the surface of the sensor. Additionally, a mesoporous site of boehmite accepts relatively smaller chromium ions (∼0.4 Å) into its pores, resulting in a better binding affinity between the sensor and the quencher molecules.

Time-resolved fluorescence data suggest that the quenching phenomenon might occur in the excited state, which is further justified using the DFT formalism. The DFT study ensures Cr(VI) to be in close proximity (∼4 Å) to the fluorophore (Figure 7). Initially, the geometry optimization has been done, which depicts the absence of any undesired imaginary frequency and validates the theoretical model. The TDDFT study of the cdot−Cr(VI) complex shows that the main electronic transition of the complex happens in the 628 nm
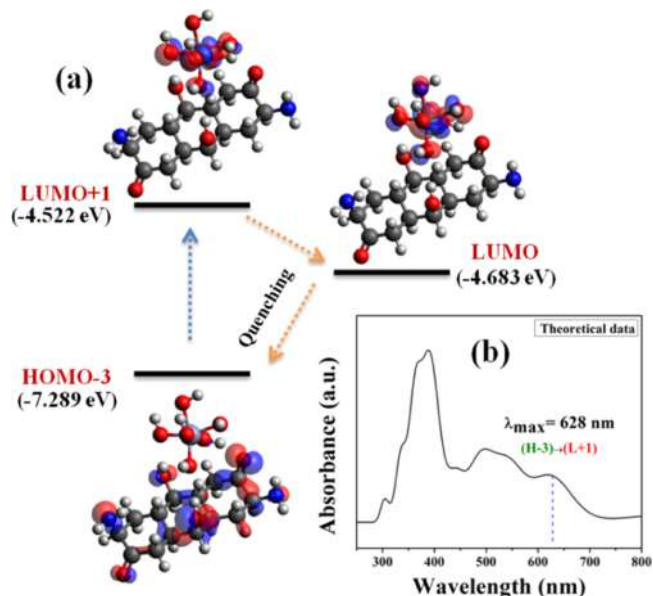
Figure 7. (a) PET-based fluorescence "turn off" mechanism analysis for CDBH using TDDFT; (b) TDDFT-based theoretical absorbance spectrum of CDBH.

wavelength range (Figure 7). This electronic transition occurs between HOMO − 3 (−7.289 eV) and LUMO + 1 (−4.522 eV). The electronic charges at HOMO − 3 situated at the cdot end of the complex have completely been transferred to the quencher in the LUMO + 1 state.

According to Kasha's rule, the distribution on the excited state (LUMO + 1) would decay to the LUMO state (−4.683 eV) momentarily through the internal conversion process causing a nonradiative decay and finally to the ground state, which is mainly a radiative pathway (Figure 7).[58] This type of charge transfer between the fluorophore and the quencher in the excited state establishes the fact that the fluorescence quenching mechanism herein follows the PET process.

3.5. Effect of Ambient Conditions on Sensing Efficiency.

3.5.1. Dependence on pH. The fluorescence stability of the sensing probe and the efficiency of sensing at different pH values have been examined and incorporated (Figure 8). It can be observed from Figure 8 that the
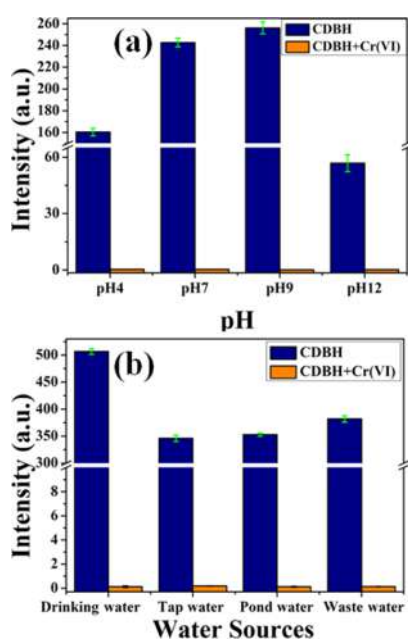
Figure 8. Detection efficiency testing at (a) varying pH and (b) different water conditions.

fluorescence intensity is relatively higher in a moderate pH range (7−9). Otherwise, the fluorescence quality reaches lower values at extreme pH conditions (4 and 12). This is due to the IFE as HCl and NaOH were added to control the pH during the experiment. IFE is a fluorescence quenching process where some of the fluorophores are less accessible than others because of the presence of quencher ions/molecules. At extreme pH values, a significant number of H^+ and OH^- ions are present in the sensing environment, which "block" the photons coming from the fluorophores that in turn result in fluorescence quenching. This type of quenching is absent at moderate pH values because of the absence of excess H^+ and OH^- ions. Although the fluorescence intensity alters, the sensitivity of the probe remains the same at varying pH conditions as the sensor material does not select H^+ and OH^- ions for the PET process, which approves the applicability of the sensor material at any pH condition.

3.5.2. Dependence on Water Quality. In order to study the sensing efficiency of the synthesized material in different water

qualities, spectroscopic studies have been initiated for four different water samples collected from diverse sources. In reality, drinking water was collected from the water purifier adjacent to our laboratory, tap water was collected from our laboratory tap, pond water was collected from a nearby pond situated inside our university campus, and wastewater was collected from a drainage output within our institute area. The collected water samples were filtered using membrane filters (0.45 μm), followed by spiking with 50 μM Cr(VI) in each case. The physical parameters of the collected water samples have been measured using a portable pH/TDS/temperature meter, Hanna (HI991300) and are depicted in Table 2.

Table 2. Physical Parameters of the Collected Water Samples

type of water	pH	TDS (ppm)
drinking	6.53	41
tap	7.44	>2000
pond	8.29	1012
waste	3.05	1996

In all cases, the fluorescence intensity of the sensor (at 462 nm) drastically quenches upon Cr(VI) addition (Figure 8), revealing the efficiency of the sensor for real-life water samples. Unlike the pH of the solution, the total dissolved solids (TDS) also cause IFE that quenches the fluorescence of the sensing probe. However, no effect of TDS and other physical parameters of water affect the sensing efficiency of the sensor as they do not take part in the PET process.

3.5.3. Real-Life Sensing of Cr(VI) in Tannery Wastewater. The tannery wastewater was collected from a canal adjacent to a local tannery industry. The collected water was initially filtered using a membrane filter (0.45 μm) and subject to ICP-AES to determine the elemental composition (Table 3). The amount of chromium was found to be around 18 ppm in the tannery wastewater sample, which was further added to the sensor material (CDBH) for the fluorescence study.

Table 3. ICP-AES Data of the Collected Tannery Wastewater Sample

constituents	amount (ppm)
arsenic (As)	not detected
lead (Pb)	0.31
chromium (Cr)	18.24
iron (Fe)	5.94

It is found that the addition of tannery wastewater significantly quenches the fluorescence intensity of the sensor material, as previously seen in other sensing experiments (Figure S6). There are several other elements present in the wastewater sample along with chromium. However, the sensing efficiency was not affected by the interfering element, which proves the real-life detection capacity of the sensor.

3.6. Theoretical Sensing of the Model of Cr(VI) in Living Cells.

3.6.1. Interaction between Fluorophores and Living Cells: a Molecular Docking Study. Hexavalent chromium is both genotoxic and cytotoxic at the same time, as evident from various studies.[10] The insertion of this contaminant into the living cells directly binds it with different enzymes, such as glutathione that can be found in virtually every human cell and even in microbes. Glutathione is an

antioxidant capable of preventing cellular damage because of heavy metals and reactive oxygen species.[59] It is quite surprising that hexavalent chromium transformed into Cr(III) *via* reactive intermediates [such as Cr(IV) and Cr(V)] in the presence of enzymes, such as cytochrome $b5$ and glutathione.[60] The Cr(III) residue forms reactive species through "Fenton-like" reactions that the transcription and replication at the DNA level are affected, leading to cancer development.[61] Thus, it is evident that detection of hexavalent chromium in close proximity to enzymes such as glutathione could be beneficial for early stage cancer detection.

Thenceforth, molecular docking simulation has been carried out to visualize the interaction between the sensing probe and glutathione. The docking study between cdots and glutathione (PDB ID: 1PKW) predicts nine different poses, in which the binding affinity of the first pose (Table S2) was minimum (−8.7 kcal/mol) and thus taken for further analyses. This pose reveals the weak hydrogen bonding between glutathione and cdots (Figure 9). Amino acids such as serine (SER-18) and
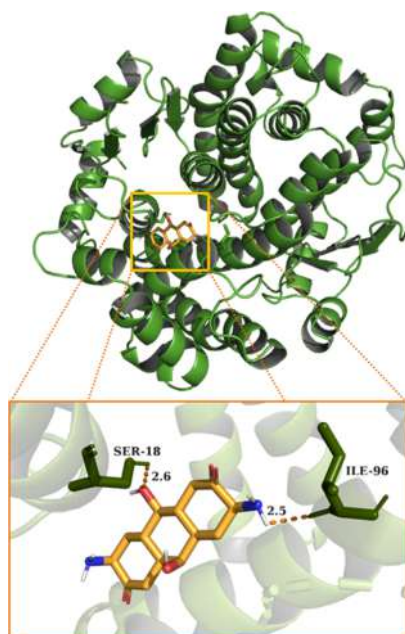
Figure 9. Molecular docking simulation showing cdot binding with glutathione.

isoleucine (ILE-96) forms bond with the C−O and N−H moieties of the cdots confirming the successful binding of the fluorophore with the binding pocket.

3.6.2. Theoretical Imaging Study of the Probe in Living Cells. The interaction between the fluorophore of the sensor and glutathione creates a positive impact on the bioimaging efficiency of the synthesized sensor material, which has been theoretically justified using the TDDFT approach (Figure 10). The model was prepared as predicted in the docking study. The theoretical absorbance spectrum suggests the λ_{max} at 313 nm. This electronic transition occurs between the HOMO (−6.081 eV) and the LUMO (−0.483 eV) maintaining a band gap value of 5.59 eV, which is quite close to that of the pure CDBH sample (5.52 eV). The molecular orbital in the ground state situated over the N−H moiety completely transferred to the C═O part of the cdot in the excited state. There is no evidence for any energy or charge transfer to the amino acids being taken into consideration, implying that the fluorometric
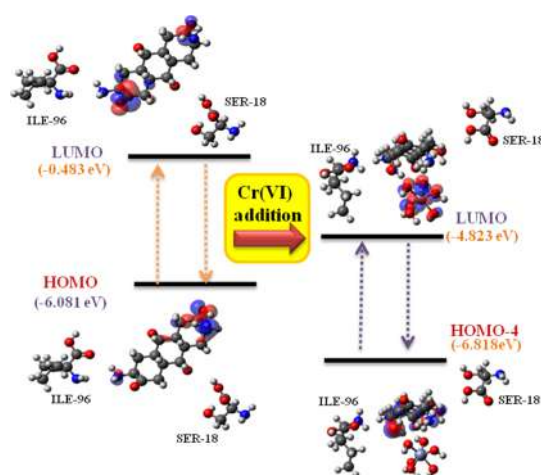
Figure 10. TDDFT-based theoretical model for studying the detection capacity of the sensing probe in living cells showing that CDBH initiates electron transfer when Cr(VI) is added to glutathione.

probe is capable of producing fluorescence in glutathione. This makes the synthesized sensor material a potential bioimaging agent.

3.6.3. Theoretical Model of Cr(VI) Detection in Living Cells. As previously mentioned, glutathione is one of those few enzymes that directly interacts with hexavalent chromium and transforms it into Cr(III).[60,61] Thus, detection of hexavalent chromium in glutathione would be beneficial for early stage cancer detection. The bioimaging of the glutathione has already been done theoretically showing that CDBH can image glutathione. Hence, Cr(VI) has been incorporated in the said theoretical model to study the interaction using the standard TDDFT formalism. The TDDFT study shows that the λ_{max} in this case is situated at 632 nm. This transition takes places between HOMO − 4 (−6.818 eV) and LUMO (−4.823 eV), which shows significant electron transfer between cdots and Cr(VI) (Figure 10). A similar phenomenon has already been observed for wastewater, where the molecular orbital shifted from cdots to Cr(VI) causing tremendous fluorescence quenching. The mobilization of molecular orbitals to Cr(VI) shows that the electrons of CDBH after absorbing photons in the ground state instantaneously traveled to the excited state and jumps to Cr(VI) in the excited state as it is energetically favorable (as seen in TDDFT analysis). This electron transfer is known as PET that quenches the fluorescence intensity drastically. In the absence of Cr(VI), no such "orbital shifting" or PET takes place even in the presence of glutathione (Figure 10). Henceforth, it can be said that no fluorescence quenching will occur if the sensor material is exposed to glutathione only, but in the presence of Cr(VI), the fluorescence alteration can happen because of the PET. Thus, it can be said that the theoretical model predicts a turn-off-based fluorescence sensing in living cells when exposed to hexavalent chromium.

4. CONCLUSIONS

In summary, the *in situ* growth of cdots on a spherical boehmite matrix has been achieved successfully that enables the detection of hexavalent chromium in wastewater. Initially, the X-ray crystallography study along with vibrational spectroscopy (FTIR) and morphological analysis (TEM) of the synthesized probe shows the purity and formation mechanism

of the nanocomposite. The plausible architecture of the sensing probe has also been computed by employing the Rietveld refinement method, which depicts the spherical cdot structures "wrapped" over the boehmite surface significantly. The absence of any agglomeration in cdots due to the presence of boehmite leads to promising fluorescence activity along with higher stability and better decay time. The sensitivity of the probe has been estimated using the linear SV equation depicting that the sensitivity lies in the nanomolar range (58.1 nM). The fluorometric probe is found to be enormously selective toward Cr(VI) and does not alter its sensing efficiency under varying ambient conditions. PET between the fluorophore and the contaminant is primarily responsible for such selective and sensitive fluorometric detection, which is justified using a theoretical TDDFT approach. The molecular docking study reveals the binding affinity of the sensor toward the glutathione enzyme, which acts as an antioxidant in almost all living cells. The TDDFT study finds that the fluorescence activity of the synthesized probe does not change even after the cdots—glutathione interaction and is greatly quenched when the said model is exposed to Cr(VI). This theoretical study approves the fact that the sensor material is capable of detecting chromium in living cells using its turn-off-based fluorescence mechanism, which could be beneficial for early stage cancer detection.

ASSOCIATED CONTENT

Supporting Information

The Supporting Information is available free of charge at https://pubs.acs.org/doi/10.1021/acsami.0c13433.

> Excitation wavelength and time-dependent emission spectra of the probe, SV plot for higher concentrations, fluorescence decay, electrostatic potential mapping of the fluorophore, sensing efficiencies of the probe at different pHs and water qualities, detection of Cr(VI) in real-life tannery wastewater, comparative study of various Cr(VI) sensors, molecular dynamics results, refinement data of the composite, and DFT-optimized structure of the fluorophore (PDF)

AUTHOR INFORMATION

Corresponding Author

Sukhen Das — *Department of Physics, Jadavpur University, Kolkata 700032, India;* orcid.org/0000-0001-8372-3076; Phone: +91 94330 91337; Email: sdasphysics@gmail.com

Authors

Shubham Roy — *Department of Physics, Jadavpur University, Kolkata 700032, India;* orcid.org/0000-0001-5245-3229

Souravi Bardhan — *Department of Physics, Jadavpur University, Kolkata 700032, India;* orcid.org/0000-0003-0944-2940

Dipak Kr. Chanda — *Advanced Materials and Mechanical Characterization Division, CSIR-Central Glass and Ceramics Research Institute, Kolkata 700032, India;* orcid.org/0000-0003-0147-4972

Jhilik Roy — *Department of Physics, Techno India University, Kolkata 700091, India*

Dhananjoy Mondal — *Department of Physics, Jadavpur University, Kolkata 700032, India*

Complete contact information is available at:
https://pubs.acs.org/10.1021/acsami.0c13433

Notes
The authors declare no competing financial interest.

ACKNOWLEDGMENTS

REFERENCES

(1) Jin, W.; Zhang, H. Q.; Liu, S. S.; Zhang, H. B. Technological Innovation, Environmental Regulation, and Green Total Factor Efficiency of Industrial Water Resources. *J. Clean. Prod.* **2019**, *211*, 61−69.

(2) Yajima, I.; Kumasaka, M. Y.; Iida, M.; Oshino, R.; Tanihata, H.; Al Hossain, A.; Ohgami, N.; Kato, M. Arsenic-Mediated Hyperpigmentation in Skin Via NF-Kappa B/Endothelin-1 Signaling in an Originally Developed Hairless Mouse Model. *Arch. Toxicol.* **2017**, *91*, 3507−3516.

(3) Gogoi, K.; Manna, P.; Dey, T.; Kalita, J.; Unni, B. G.; Ozah, D.; Baruah, P. K. Circulatory Heavy Metals (Cadmium, Lead, Mercury, and Chromium) Inversely Correlate with Plasma GST Activity and GSH Level in COPD Patients and Impair NOX_4/Nrf2/GCLC/GST Signaling Pathway in Cultured Monocytes. *Toxicol. In Vitro* **2019**, *54*, 269−279.

(4) Abraham, B. P.; Ahmed, T.; Ali, T. Inflammatory Bowel Disease: Pathophysiology and Current Therapeutic Approaches. Gastrointestinal Pharmacology. *Handbook of Experimental Pharmacology*; Springer, 2017; Vol. 239, pp 115−146.

(5) Xu, C.; Xing, D.; Wang, J.; Xiao, G. The Lag Effect of Water Pollution on the Mortality Rate for Esophageal Cancer in a Rapidly Industrialized Region in China. *Environ. Sci. Pollut. Res.* **2019**, *26*, 32852−32858.

(6) Vigneri, R.; Malandrino, P.; Gianì, F.; Russo, M.; Vigneri, P. Heavy Metals in the Volcanic Environment and Thyroid Cancer. *Mol. Cell. Endocrinol.* **2017**, *457*, 73−80.

(7) Saher, N. U.; Kanwal, N. Assessment of Some Heavy Metal Accumulation and Nutritional Quality of Shellfish with Reference to Human Health and Cancer Risk Assessment: A Seafood Safety Approach. *Environ. Sci. Pollut. Res.* **2019**, *26*, 5189−5201.

(8) Tripathi, M.; Upadhyay, S. K.; Kaur, M.; Kaur, K. Toxicity Concerns of Hexavalent Chromium from Tannery Waste. *J. Adv. Biotechnol. Bioeng.* **2018**, *2*, 40−44.

(9) Kauermann, G.; Becher, H.; Maier, V. Exploring the Statistical Uncertainty in Acceptable Exposure Limit Values for Hexavalent Chromium Exposure. *J. Exposure Sci. Environ. Epidemiol.* **2018**, *28*, 69−75.

(10) Speer, R. M.; Wise, S. S.; Croom-Perez, T. J.; Aboueissa, A.-M.; Martin-Bras, M.; Barandiaran, M.; Bermúdez, E.; Wise Sr, J. P. A Comparison of Particulate Hexavalent Chromium Cytotoxicity and Genotoxicity in Human and Leatherback Sea Turtle Lung Cells from a One Environmental Health Perspective. *Toxicol. Appl. Pharmacol.* **2019**, *376*, 70−81.

(11) Wise, S. S.; Wise, C.; Xie, H.; Guillette, L. J., Jr; Zhu, C.; Wise, J. P., Jr; Wise Sr, J. P. Hexavalent Chromium is Cytotoxic and Genotoxic to American Alligator Cells. *Aquat. Toxicol.* **2016**, *171*, 30−36.

(12) Kart, A.; Koc, E.; Dalginli, K. Y.; Gulmez, C.; Sertcelik, M.; Atakisi, O. The Therapeutic Role of Glutathione in Oxidative Stress and Oxidative DNA Damage Caused by Hexavalent Chromium. *Biol. Trace Elem. Res.* **2016**, *174*, 387−391.

(13) Mihai, O.; Kawamoto, M. S.; LeBlanc, K. L.; Grinberg, P.; de Araújo Nogueira, A. R.; Mester, Z. Determination of Chromium Picolinate and Trace Hexavalent Chromium in Multivitamins and Supplements by HPLC-ICP-QQQ-MS. *J. Food Compos. Anal.* **2020**, *87*, 103421.

(14) Zewdu, F.; Amare, M. Determination of the Level of Hexavalent, Trivalent, and Total Chromium in the Discharged

Effluent of Bahir Dar Tannery using ICP-OES and UV-Visible Spectrometry. *Cogent Chem.* **2018**, *4*, 1534566.

(15) Ismail, M.; Khan, M.; Akhtar, K.; Khan, M. A.; Asiri, A. M.; Khan, S. B. Biosynthesis of Silver Nanoparticles: A Colorimetric Optical Sensor for Detection of Hexavalent Chromium and Ammonia in Aqueous Solution. *Phys. E* **2018**, *103*, 367−376.

(16) Roy, S.; Bardhan, S.; Roy, J.; Das, S. Waste Capacitor: A Fresh Approach to Detect and Remove Cr (VI) from Water and Making it an Energy Harvesting Material. *Mater. Today: Proc.* **2020**, DOI: 10.1016/j.matpr.2020.04.770.

(17) Feng, D.-Q.; Zhu, W.; Liu, G.; Wang, W. Dual-Modal Light Scattering and Fluorometric Detection Of Lead Ion by Stimuli-Responsive Aggregation of BSA-stabilized Copper Nanoclusters. *RSC Adv.* **2016**, *6*, 96729−96734.

(18) Vaishanav, S. K.; Korram, J.; Pradhan, P.; Chandraker, K.; Nagwanshi, R.; Ghosh, K. K.; Satnami, M. L. Green Luminescent CdTe Quantum Dot Based Fluorescence Nano-Sensor for Sensitive Detection of Arsenic (III). *J. Fluoresc.* **2017**, *27*, 781−789.

(19) Malek, A.; Bera, K.; Biswas, S.; Perumal, G.; Das, A. K.; Doble, M.; Thomas, T.; Prasad, E. Development of a Next-Generation Fluorescent Turn-on Sensor to Simultaneously Detect and Detoxify Mercury in Living Samples. *Anal. Chem.* **2019**, *91*, 3533−3538.

(20) Makwana, B. A.; Vyas, D. J.; Bhatt, K. D.; Darji, S.; Jain, V. K. Novel Fluorescent Silver Nanoparticles: Sensitive and Selective Turn off Sensor for Cadmium Ions. *Appl. Nanosci.* **2016**, *6*, 555−566.

(21) Bhattacharya, S.; Phatake, R. S.; Nabha Barnea, S.; Zerby, N.; Zhu, J. J.; Shikler, R.; Lemcoff, N. G.; Jelinek, R. Fluorescent Self-Healing Carbon Dot/Polymer Gels. *ACS Nano* **2019**, *13*, 1433−1442.

(22) Kalytchuk, S.; Wang, Y.; Poláková, K. i.; Zbořil, R. Carbon Dot Fluorescence-Lifetime-Encoded Anti-Counterfeiting. *ACS Appl. Mater. Interfaces* **2018**, *10*, 29902−29908.

(23) Wang, C.; Lin, H.; Xu, Z.; Huang, Y.; Humphrey, M. G.; Zhang, C. Tunable Carbon-Dot-Based Dual-Emission Fluorescent Nanohybrids for Ratiometric Optical Thermometry in Living Cells. *ACS Appl. Mater. Interfaces* **2018**, *8*, 6621−6628.

(24) Tian, Y.; Ran, Z.; Yang, W. Carbon Dot-Silica Composite Nanoparticle: An Excitation-Independent Fluorescence Material with Tunable Fluorescence. *RSC Adv.* **2017**, *7*, 43839−43844.

(25) Jiao, J.; Liu, C.; Li, X.; Liu, J.; Di, D.; Zhang, Y.; Zhao, Q.; Wang, S. Fluorescent Carbon Dot Modified Mesoporous Silica Nanocarriers for Redox-Responsive Controlled Drug Delivery and Bioimaging. *J. Colloid Interface Sci.* **2016**, *483*, 343−352.

(26) Li, H.; Yan, X.; Lu, G.; Su, X. Carbon Dot-Based Bioplatform for Dual Colorimetric and Fluorometric Sensing of Organophosphate Pesticides. *Sens. Actuators, B* **2018**, *260*, 563−570.

(27) Rezaei, B.; Hassani, Z.; Shahshahanipour, M.; Ensafi, A. A.; Mohammadnezhad, G. Application of Modified Mesoporous Boehmite (γ-AlOOH) with Green Synthesis Carbon Quantum Dots for a Fabrication Biosensor to Determine Trace Amounts of Doxorubicin. *Luminescence* **2018**, *33*, 1377−1386.

(28) Sobhani, R.; Rezaei, B.; Shahshahanipour, M.; Ensafi, A. A.; Mohammadnezhad, G. Simple and Green Synthesis of Carbon Dots (CDs) from Valerian Root and Application of modified Mesoporous Boehmite (AlOOH) with CDs as a Fluorescence Probe for Determination of Imipramine. *Anal. Bioanal. Chem.* **2019**, *411*, 3115−3124.

(29) Zhai, Y.; Bai, X.; Cui, H.; Zhu, J.; Liu, W.; Zhang, T.; Dong, B.; Pan, G.; Xu, L.; Zhang, S. Carbon Dot/Polyvinylpyrrolidone Hybrid Nanofibers with Efficient Solid-State Photoluminescence Constructed using an Electrospinning Technique. *Nanotechnology* **2017**, *29*, 025706.

(30) Zhang, D.; Jiang, W.; Zhao, Y.; Dong, Y.; Feng, X.; Chen, L. Carbon Dots Rooted PVDF Membrane for Fluorescence Detection of Heavy Metal Ions. *Appl. Surf. Sci.* **2019**, *494*, 635−643.

(31) Bardhan, S.; Roy, S.; Chanda, D. K.; Ghosh, S.; Mondal, D.; Das, S.; Das, S. Nitrogenous Carbon Dot Decorated Natural Microcline: An Ameliorative Dual Fluorometric Probe for Fe^{3+} and Cr^{6+} Detection. *Dalton Trans.* **2020**, *49*, 10554−10566.

(32) Unnikrishnan, B.; Wu, C.-W.; Chen, I.-W. P.; Chang, H. T.; Lin, C.-H.; Huang, C. C. Carbon Dot-Mediated Synthesis of Manganese Oxide Decorated Graphene Nanosheets for Super-capacitor Application. *ACS Sustainable Chem. Eng.* **2016**, *4*, 3008−3016.

(33) Karimi, S.; Kameli, P.; Ahmadvand, H.; Salamati, H. Effects of Zn-Cr-Substitution on the Structural and Magnetic Properties of $Ni_{1−x}Zn_xFe_{2−x}Cr_xO_4$ Ferrites. *Ceram. Int.* **2016**, *42*, 16948−16955.

(34) Lutterotti, L. Quantitative Rietveld Analysis in Batch Mode with Maud. *Structures of Minute Crystallites with Exceptional Properties and Frontiers of Powder Diffraction*; University of Trento, 2011.

(35) Balzar, D.; Audebrand, N.; Daymond, M.; Fitch, A.; Hewat, A.; Langford, J.; Le Bail, A.; Louër, D.; Masson, O.; McCowan, C. N. Size-Strain Line-Broadening Analysis of the Ceria Round-Robin Sample. *J. Appl. Crystallogr.* **2004**, *37*, 911−924.

(36) Momma, K.; Izumi, F. VESTA: A Three-Dimensional Visualization System for Electronic and Structural Analysis. *J. Appl. Crystallogr.* **2008**, *41*, 653−658.

(37) Perry, J. K.; Tahir-Kheli, J.; Goddard, W. A., III Antiferromagnetic Band Structure of La2CuO4: Becke-3−Lee-Yang-Parr Calculations. *Phys. Rev. B: Condens. Matter Mater. Phys.* **2001**, *63*, 144510.

(38) Neese, F.; Wennmohs, F.; Becker, U.; Riplinger, C. The ORCA Quantum Chemistry Program Package. *J. Chem. Phys.* **2020**, *152*, 224108.

(39) Hanwell, M. D.; Curtis, D. E.; Lonie, D. C.; Vandermeersch, T.; Zurek, E.; Hutchison, G. R. Avogadro: An Advanced Semantic Chemical Editor, Visualization, and Analysis Platform. *J. Cheminf.* **2012**, *4*, 17.

(40) Del Bene, J. E.; Person, W. B.; Szczepaniak, K. Properties of Hydrogen-Bonded Complexes Obtained from the B3LYP Functional with 6-31G (d,p) and 6−31+ G (d,p) Basis Sets: Comparison with MP2/6−31+ G (d,p) Results and Experimental Data. *J. Chem. Phys.* **1995**, *99*, 10705−10707.

(41) Morris, G. M.; Huey, R.; Olson, A. J. Using Autodock for Ligand-Receptor Docking. *Curr. Protoc. Bioinf.* **2008**, *24*, 8−14.

(42) Trott, O.; Olson, A. J. AutoDock Vina: improving the Speed and Accuracy of Docking with a New Scoring Function, Efficient Optimization, and Multithreading. *J. Comput. Chem.* **2010**, *31*, 455−461.

(43) DeLano, W. L. Pymol: An Open-Source Molecular Graphics Tool. *CCP4 Newsletter on Protein Crystallography*. 2002; Vol. *40*(1), pp 82−92.

(44) Roy, S.; Maity, A.; Mandal, P.; Chanda, D. K.; Pal, K.; Bardhan, S.; Das, S. Effects of Various Morphologies on the Optical and Electrical Properties of Boehmite Nanostructures. *CrystEngComm* **2018**, *20*, 6338−6350.

(45) Roy, S.; Bardhan, S.; Chanda, D. K.; Maity, A.; Ghosh, S.; Mondal, D.; Singh, S.; Das, S. Cu (II) and Gd (III) Doped Boehmite Nanostructures: A Comparative Study of Electrical Property and Thermal Stability. *Mater. Res. Express* **2020**, *7*, 025020.

(46) Roy, S.; Bardhan, S.; Pal, K.; Ghosh, S.; Mandal, P.; Das, S.; Das, S. Crystallinity Mediated Variation in Optical and Electrical Properties of Hydrothermally Synthesized Boehmite (γ-AlOOH) Nanoparticles. *J. Alloys Compd.* **2018**, *763*, 749−758.

(47) Zhao, L.; Di, F.; Wang, D.; Guo, L.-H.; Yang, Y.; Wan, B.; Zhang, H. Chemiluminescence of Carbon Dots under Strong Alkaline Solutions: A Novel Insight into Carbon Dot Optical Properties. *Nanoscale* **2013**, *5*, 2655−2658.

(48) Ma, Z.; Ming, H.; Huang, H.; Liu, Y.; Kang, Z. One-Step Ultrasonic Synthesis of Fluorescent N-Doped Carbon Dots from Glucose and their Visible-Light Sensitive Photocatalytic Ability. *New J. Chem.* **2012**, *36*, 861−864.

(49) Su, Y.; Zhou, X.; Long, Y.; Li, W. Immobilization of Horseradish Peroxidase on Amino-Functionalized Carbon Dots for the Sensitive Detection of Hydrogen Peroxide. *Microchim. Acta* **2018**, *185*, 114.

(50) Janke, E. M.; Williams, N. E.; She, C.; Zherebetskyy, D.; Hudson, M. H.; Wang, L.; Gosztola, D. J.; Schaller, R. D.; Lee, B.;

Sun, C. Origin of Broad Emission Spectra in InP Quantum Dots: Contributions from Structural and Electronic Disorder. *J. Am. Chem. Soc.* **2018**, *140*, 15791−15803.

(51) (a) Coulter, J. B.; Birnie, D. P., III Assessing Tauc Plot Slope Quantification: ZnO Thin Films as a Model System. *Phys. Status Solidi B* **2018**, *255*, 1700393. (b) Zhou, T.; Wang, M.; Zang, Z.; Fang, L. Stable Dynamics Performance and High Efficiency of ABX3-type Super-Alkali Perovskites First Obtained by Introducing H_5O_2 Cation. *Adv. Energy Mater.* **2019**, *9*, 1900664. (c) Zhou, T.; Zhang, Y.; Wang, M.; Zang, Z.; Tang, X. Tunable Electronic Structures and High Efficiency Obtained by Introducing Superalkali and Superhalogen into AMX3-type Perovskites. *J. Power Sources* **2019**, *429*, 120−126. (d) Yan, D.; Shi, T.; Zang, Z.; Zhou, T.; Liu, Z.; Zhang, Z.; Du, J.; Leng, Y.; Tang, X. Ultrastable CsPbBr$_3$ Perovskite Quantum Dot and their Enhanced Amplified Spontaneous Emission by Surface Ligand Modification. *Small* **2019**, *15*, 1901173. (e) Zhou, T.; Wang, M.; Zang, Z.; Tang, X.; Fang, L. Two-Dimensional Lead-Free Hybrid Halide Perovskite using Superatom Anions with Tunable Electronic Properties. *Sol. Energy Mater. Sol. Cells* **2019**, *191*, 33−38.

(52) Fairman, H. S.; Brill, M. H.; Hemmendinger, H. How the CIE 1931 Color-Matching Functions were derived from Wright-Guild data. *Color Res. Appl.* **1997**, *22*, 11−23.

(53) Schneider, J.; Reckmeier, C. J.; Xiong, Y.; von Seckendorff, M.; Susha, A. S.; Kasák, P.; Rogach, A. L. Molecular fluorescence in citric acid-based carbon dots. *J. Phys. Chem. C* **2017**, *121*, 2014−2022.

(54) Roy, S.; Pal, K.; Bardhan, S.; Maity, S.; Chanda, D. K.; Ghosh, S.; Karmakar, P.; Das, S. Gd (III)-Doped Boehmite Nanoparticle: An Emergent Material for the Fluorescent Sensing of Cr(VI) in Wastewater and Live Cells. *Inorg. Chem.* **2019**, *58*, 8369−8378.

(55) Kubista, M.; Sjöback, R.; Eriksson, S.; Albinsson, B. Experimental Correction for the Inner-Filter Effect in Fluorescence Spectra. *Analyst* **1994**, *119*, 417−419.

(56) Slocum, J. D.; Palmer, A. E.; Jimenez, R. Intramolecular Fluorescent Protein Association in a Class of Zinc FRET Sensors Leads to Increased Dynamic Range. *J. Phys. Chem. B* **2019**, *123*, 3079−3085.

(57) Mohandoss, S.; Stalin, T. A New Fluorescent PET Sensor Probe for Co^{2+} Ion Detection: Computational, Logic Device and Living Cell Imaging Applications. *RSC Adv.* **2017**, *7*, 16581−16593.

(58) Nenov, A.; Borrego-Varillas, R.; Oriana, A.; Ganzer, L.; Segatta, F.; Conti, I.; Segarra-Marti, J.; Omachi, J.; Dapor, M.; Taioli, S. UV-light-induced Vibrational Coherences: The Key to Understand Kasha Rule Violation in Trans-Azobenzene. *J. Phys. Chem. Lett.* **2018**, *9*, 1534−1541.

(59) Grahn, E.; Novotny, M.; Jakobsson, E.; Gustafsson, A.; Grehn, L.; Olin, B.; Madsen, D.; Wahlberg, M.; Mannervik, B.; Kleywegt, G. J. New Crystal Structures of Human Glutathione Transferase A1-1 Shed Light on Glutathione Binding and the Conformation of the C-Terminal Helix. *Acta Crystallogr., Sect. D: Biol. Crystallogr.* **2006**, *62*, 197−207.

(60) DesMarias, T. L.; Costa, M. Mechanisms of Chromium-Induced Toxicity. *Curr. Opin. Toxicol.* **2019**, *14*, 1−7.

(61) Mazzer, P. A.; Maurmann, L.; Bose, R. N. Mechanisms of DNA Damage and Insight into Mutations by Chromium (VI) in the Presence of Glutathione. *J. Inorg. Biochem.* **2007**, *101*, 44−55.

Contents lists available at ScienceDirect

Sensors and Actuators: B. Chemical

journal homepage: www.elsevier.com/locate/snb

Polymeric carbon dot/boehmite nanocomposite made portable sensing device (Kavach) for non-invasive and selective detection of Cr(VI) in wastewater and living cells

Shubham Roy [a,1], Souravi Bardhan [a,2], Dhananjoy Mondal [a], Ishita Saha [b], Jhilik Roy [a], Solanky Das [c], Dipak Kr. Chanda [d,3], Parimal Karmakar [b], Sukhen Das [a,*,4]

[a] *Department of Physics, Jadavpur University, Raja S.C. Mullick Road, Kolkata 700032, India*
[b] *Department of Life Science and Biotechnology, Jadavpur University, Kolkata 700032, India*
[c] *Department of Geological Sciences, Jadavpur University, Kolkata 700032, India*
[d] *School of Materials Science and Nano Technology, Jadavpur University, Kolkata 700032, India*

ARTICLE INFO

ABSTRACT

This work reports a handheld fluorometric probe, namely 'Kavach' for monitoring hexavalent chromium in industrial wastewater and living systems. Kavach is capable to detect chromium contamination in a rapid and facile way. The device is made of a thin layer (~1 mm) of carbon dot decorated boehmite nanostructure (BH@CD) incorporated in a layer of poly vinylidene fluoride-co-hexafluoropropylene (PVDF-HFP) membrane. The doped membrane has an excellent blue fluorescence upon UV excitation (355 nm) and alters its fluorescence level when exposed to Cr(VI). In reality, tiny carbon dots leach out from the nano-matrices to produce secondary contamination. Incorporation of the BH@CD into the polymeric matrix of PVDF-HFP significantly reduces such contamination and makes this material a potential sensing probe. This photoinduced electron transfer (PET) based sensor is tremendously selective and sensitive (LOD ~66 nM) towards aqueous chromium. The performance of the probe remains unaltered in different pH and water qualities. Additionally, this material can sense chromium in living cells, which has been validated theoretically using molecular docking and observed experimentally using fluorescence microscopy. Kavach is truly a handheld, reusable and non-invasive sensing probe against Cr(VI), which can be employed for on-site low-cost detection.

1. Introduction

The toxic industrial effluents are enormously causing harm to the water bodies. These effluents, such as Cr(VI), Fe(III), Pb(II), *etc.* are mostly carcinogenic and mutagenic in nature [1a]. Such toxins are not only polluting water and water bodies but also cause severe harm to the environment and thus need proper detection and removal. Traditionally, various detection techniques, like inductively coupled plasma mass spectroscopy (ICP-MS), atomic absorption (AAS) are well adopted in detecting such heavy metals in water [1a]. But, recently fluorometric sensors have gained enormous interest due to their tremendous sensitivity and rapid detection of various ions, molecules and biological elements [1b]. Biocompatible fluorescent materials have been used widely for fabricating such excellent sensing materials, but a well-devised handheld sensor is yet to be achieved. Mostly, fabrication of a fluorescent sensor device is difficult due to the limited availability of free-standing, flexible and reusable sensing materials, when it comes to heavy metal detection in aqueous media [2]. Several heavy metal sensors have been developed recently, among them carbon dot and its derivatives are showing great potential in this field [3–5].

Carbon dot (c-dot) is a nanostructure made of sp^2- hybridized carbon atoms known for excellent fluorescence properties [6a]. The

fluorescence emission of carbon dot is tunable and greatly varies with its particle size [6b]. Additionally, carbon dots have the inherent ability to transfer electrons, which is required for any promising fluorometric sensing probe [6b]. Thus, carbon dots are widely considered as a potential material for pollutant sensing, biosensing and bioimaging, bio-monitoring, targeted drug delivery, photonic and electro-optical material synthesis, catalysis and fabrication of fluorescent devices [7–11]. Besides, carbon dot has a diverse use as nano-fillers [12,13].

Bare carbon dot loses its fluorescence property when subjected to a normal atmosphere for a long period. In reality, these quantum dots agglomerate rapidly in the air at normal pressure and temperature, resulting in fluorescence quenching [2]. Thus, various nanomaterials have been used to stabilize the system for fluorometric applications. Nowadays, carbon dot-tailored nano-systems have been used extensively [14–17] in wastewater treatment and water-related experiments. Hence, widespread efforts have been made on the *ex-situ* and *in-situ* growth of c-dot in the host nanostructure [18]. Mostly, fluorescent carbon dots have been grafted on the host material to restrict agglomeration [19]. In some cases, weak hydrogen bonds have been produced by modifying the surface structure of the host element [20,21]. Due to such weak bonding and perhaps uncontrolled grafting, the leaching of carbon dots can occur into the solvents. Such an important issue must be addressed carefully while working with c-dots. Leaching could also affect the experimental results. Proper quantification and recovery studies could not be possible if this happens.

Henceforth, this article proposes a facile strategy to restrict c-dot leaching from boehmite-carbon dot nanocomposite for fabricating a fluorometric sensor device to detect hexavalent chromium in water. Herein, the boehmite-carbon dot nanocomposite (BH@CD) has been encapsulated within the polymeric matrix of PVDF-HFP (poly (vinylidene fluoride-co-hexafluoropropylene)). In reality, the $-CF_2$ moiety attracts the positive surface of the boehmite-cdot nanocomposite and restricts the c-dot leaching. This encapsulation not only provides the nanocomposite (BH@CD) a flexible and solid substrate but also promotes the stability, fluorescence intensity and Cr(VI) sensing efficacy in water and living cells. Various theoretical tools have been used to validate the fluorometric sensing mechanism, such as TDDFT and molecular docking. These theoretical approaches substantiate not only the sensing mechanism but also illustrate the binding affinities for identifying the *in-vitro* Cr(VI) detection pathways.

2. Material and methods

The BH@CD nanocomposite was prepared by an *in-situ* hydrothermal technique as mentioned previously by Roy et al. [22]. Herein, the BH@CD nano-powder was incorporated inside the PVDF-HFP polymer and the detailed synthesis process of the polymeric encapsulation (PV/BH@CD) is mentioned in the supplementary section of this article.

Further, the membrane was utilized to fabricate the handheld fluorometric sensor device (Kavach). In a typical fabrication process, the PV/BH@CD membrane of nearly 1 mm thickness was cut into small pieces (preferably, 2×4 cm). A plastic frame having a hole at the center was taken to fix the membrane rigidly to avoid any damage. The membrane was fixed in such a way that it can completely cover the hole and named as 'sample stage'. The rest of the plastic frame was then covered by aluminum foil to block any direct/ transmitted light beam as shown in Fig. 1. A small drop of the test sample in the sample stage could detect the presence of Cr(VI) in the test sample if the stage is illuminated by UV radiation (~340–370 nm).

3. Results and discussion

3.1. Optical characteristics of the sensing probe

The experiments on the device were performed by extracting the membrane from the device. All the experiments were executed on this
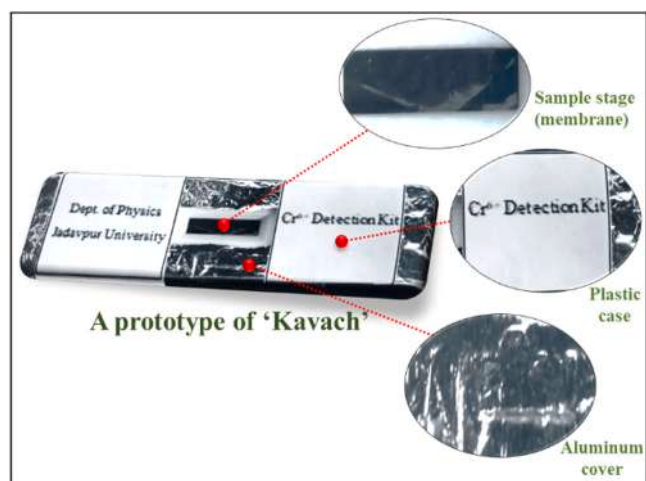
Fig. 1. A single prototype of Kavach with its various parts.

membrane only. Initially, the absorption and emission spectra of the as-prepared membrane have been studied rigorously to determine the optical characteristics of the sample. The absorption spectrum of the sample has been recorded in a UV-1900i, Shimadzu in a varying wavelength ranging between 250 and 450 nm to ascertain the excitation energy. It is observed that a broad absorption maximum (ranging between 300 and 360 nm) is centered at 325 nm in this case (Fig. 2). This broadband occurred due to the π-electron stacking [23] of the c-dot moiety.

Furthermore, the membrane was excited in a varying wavelength, ranging from 340 to 375 nm to predict the exact excitation energy. The emission spectrometry was performed in a Cary Eclipse, Agilent Technologies with a slit width of 5 nm (both emission and excitation). It is found that the excitation energy corresponds to 355 nm wavelength produces the highest fluorescence intensity (Fig. S3). Thus, 355 nm wavelength was chosen to excite the sample for further fluorometric experiments. A separate excitation spectrum of the sample has also been recorded (Fig. 2) showing a broad excitation ranging between 340 and 360 nm making a good agreement with the absorption spectrum.

The emission of the membrane is quite promising. The spectrum is centered at 467 nm and showing outstanding blue fluorescence intensity (Fig. 2). It is observed that the fluorescence emission does not alter with the excitation wavelength, which could be beneficial for making a fluorometric sensing probe.

3.2. Fluorescence stability assays of the membrane

3.2.1. Fluorescence stability as a function of time

Fluorescence stability is an important measure for any fluorometric probe. It can be determined by varying the ambient conditions. Herein, the fluorescence stability of the membrane has been measured by changing the temperature and time. It is found that the fluorescence intensity remains stable even after hundred days of rigorous use (Fig. 3). In reality, the membrane was used in various fluorometric studies and sensing applications in these hundred days and kept in normal ambient conditions (25–30 ºC) without any vacuum desiccation. But the fluorescence intensity remains unaltered. Previously, it was observed that the fluorescence intensity of c-dot has been quenched due to moisture adsorption [24]. This problem could be eliminated by using this PV/BH@CD membrane.

3.2.2. Thermal stability of the fluorescent membrane

The temperature response of the membrane in terms of fluorescence intensity has been investigated (Fig. 3). The temperature was varied between 10 and 70 ºC using a Cary Single cell Peltier Accessory, Agilent
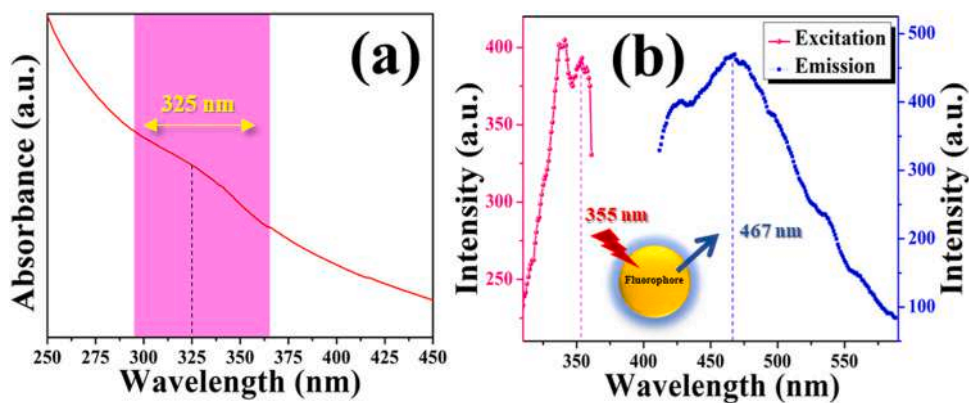
Fig. 2. (a) Absorbance and (b) excitation and emission spectra of the sample.
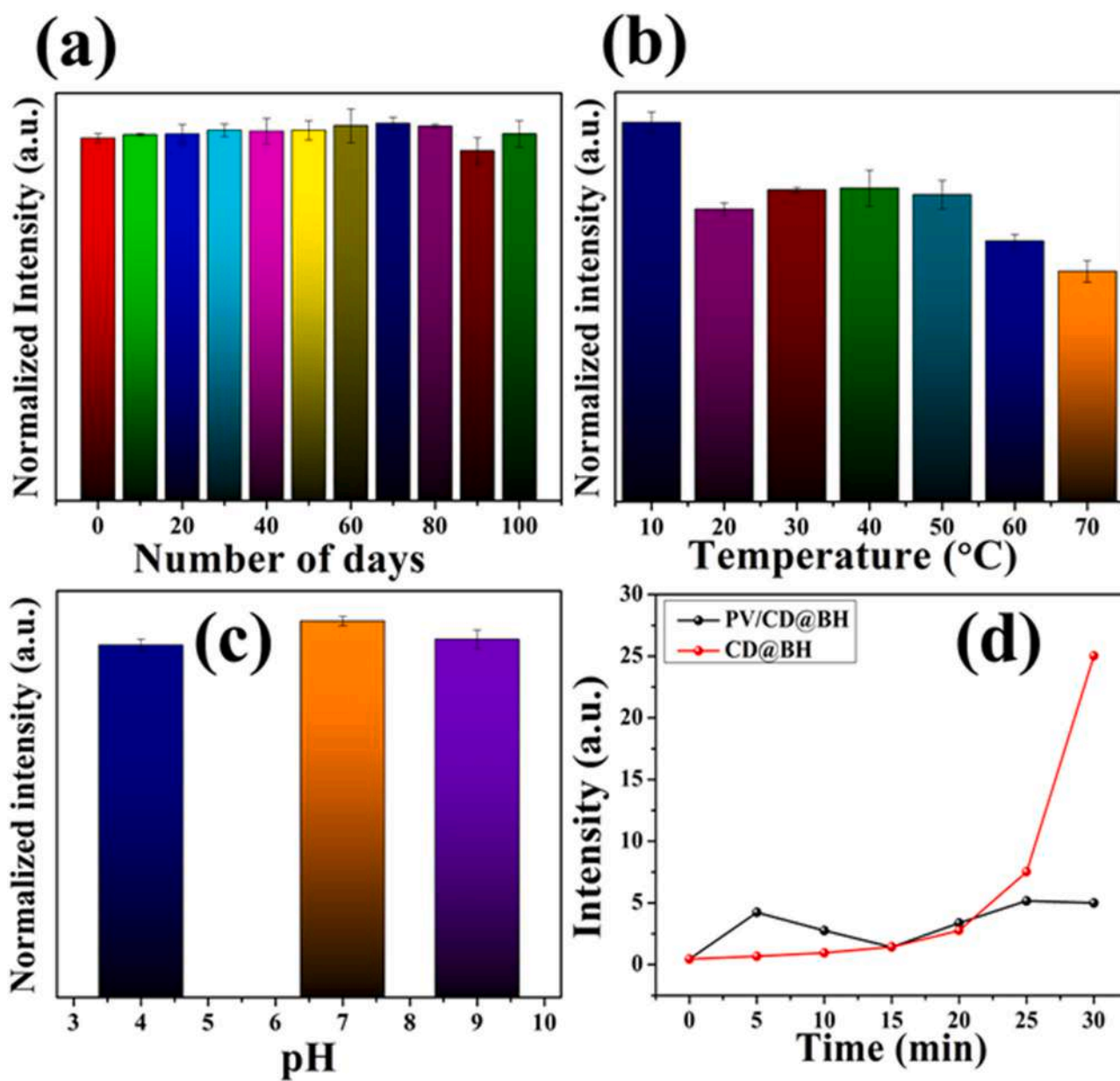
Fig. 3. Fluorescence stability of the sample as functions of (a) time, (b) temperature, and (c) pH; (d) c-dot leaching from the bare BH@CD and PVDF modified BH@CD as a function of time.

equipped with the fluorescence spectrometer. It can be argued from Fig. 3 that, the fluorescence intensity quenches a little at the higher temperatures due to excess collisional quenching between the fluorophores at the excited state [25]. The optimum intensity has been found around 30 ºC revealing the membrane could be used in a varied temperature range. Although the fluorescence of the membrane has been tested up to 70 ºC, it was further exposed to 200 ºC in a DTG-60H, Shimadzu to analyze the DTA-TGA thermograms. A very small amount of sample (~10 mg) was kept in a platinum sample holder and heated under N_2 environment (50 mL/min) to avoid any contamination during heat treatment. The rate of heating was set at 10 ºC/min for this purpose. It is observed that the membrane is thermally stable up to 153 ºC temperature (Fig. S4). Beyond this, an endothermic transition occurs [26]. Previous studies suggest the melting of PVDF-HFP at this high temperature [2]. Apart from this, there is a very nominal mass loss (~0.66%) has been recorded during the TGA analysis, which in other words validates the membrane to be stable enough up to 153 ºC temperature.

3.2.3. pH dependent fluorometric analysis

The fluorescent membrane was further placed in a varying pH range (pH 4–9) to estimate the fluorescence stability (Fig. 3). HCl and NaOH were used to control the pH of the media. It is observed that there is a slight reduction of fluorescence at pH 4 and pH 9 (~3–5%), which is due to the inner filter effect caused by excess H^+ and OH^- ions [27]. The presence of such ions in media would block the fluorescence path of the fluorophores and the intensity gets reduced. Such a minute amount of quenching is immaterial in this regard.

3.2.4. Structural stability of the fluorophores

As mentioned earlier, tiny c-dot particles are difficult to fix over any nanoparticle's surface and hence leaching occurs. The *In-situ* grown BH@CD is having a similar tendency to leach out c-dot into the solvent, which un-stabilizes the system and restricts its reusability. Thus, a comparative study was initiated, where time varied leaching of c-dot has been studied for both BH@CD and the PV/BH@CD membrane.

The leaching study shows that the c-dot has been drastically leached out from BH@CD nanocomposite (11.2% in 30 min) compromising the stability of the material, while an insignificant amount of c-dot leaching from the membrane surface has been found (less than 3.7% in 30 min) (Fig. 3). This would make the fluorescent membrane structurally stable and reusable.
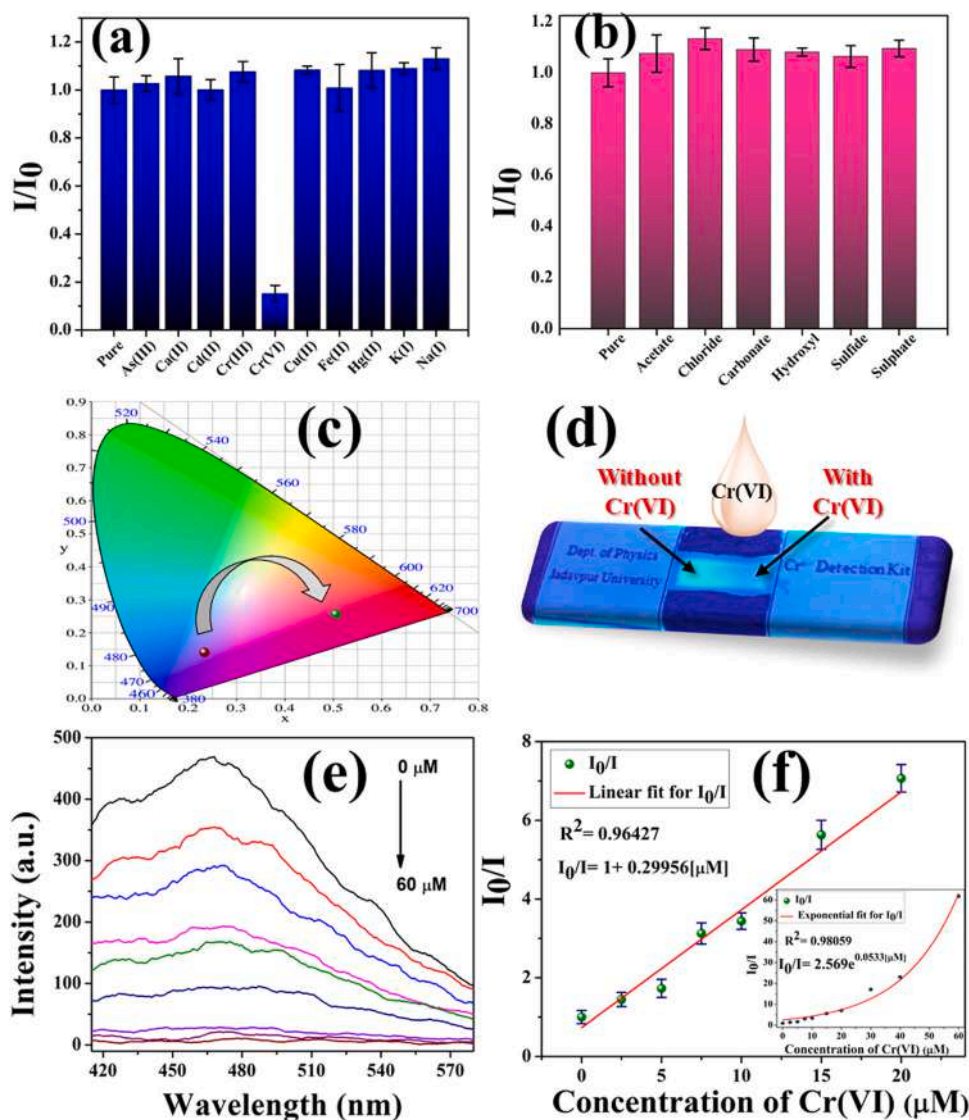
Fig. 4. Selectivity study of the probe among various (a) cations and (b) anions; (c) CIE-1931 plot of the probe showing color difference upon chromium addition; (d) naked eye visualization of the device under UV rays upon partial Cr(VI) addition on its sample stage; (e) UV fluorescence quenching experiment of the sensor upon Cr (VI) addition; (d) subsequent linear Stern-Volmer plot of the probe with exponential S-V plot (inset).

3.3. BH@CD incorporated PVDF-HFP membrane as a fluorometric Cr (VI) sensor

3.3.1. Selectivity and sensitivity analyses

Fluorometric sensors are tremendously sensitive and selective to the target ion/molecule [28]. To test the selectivity of the PV/BH@CD membrane, a series of cationic and anionic solutions (1 mg mL^{-1}) were prepared in small aliquot tubes and further diluted 10 times by adding Millipore water in each case. The sensor membrane was immersed into the solutions separately and excited at 355 nm to record the fluorescence of the sample at 467 nm. The result of selectivity analysis has been depicted in Fig. 4, which shows an abrupt change in fluorescence intensity when the sensor membrane is immersed in hexavalent chromium solution. Otherwise, no significant changes have been observed. To make detection more convenient, an anti-interference study was conducted using certain common ions of water. Fig. S5 shows efficient performance in Cr(VI) detection irrespective of the presence of various interfering ions that validate the selectivity of the membrane towards hexavalent chromium only.

Additionally, the CIE-1931 color space [29] has been used to ensure the changes in optical temperature and color coordinates (Fig. 4). It is observed that the pure membrane emits 'bluish' fluorescence (x = 0.2342, y = 0.14505) having a color temperature of 3751 K, while in presence of Cr(VI) it emits a dark orange color (x = 0.50548, y = 0.26047) with a color temperature of 3534 K. This type of fluorescence quenching along with a significant color change definitely makes this membrane a dedicated Cr(VI) sensor.

Limit of detection (LOD) and limit of quantitation (LOQ) are two major parameters to study the sensitivity of any sensor. Herein, LOD and LOQ are determined by taking a series of Cr(VI) solutions in varying concentrations (0–60 μM) and the membrane was immersed in each case before recording the fluorescence data. Such concentration-dependent fluorometric analysis shows the gradual reduction of the fluorescence intensity of the sensor membrane with an increasing concentration of Cr (VI). Further, this fluorometric data have been fitted with both linear and exponential Stern-Volmer's equations [30a,30b] and depicted in Fig. 4.

$$I_0/I = 1 + K[M] \tag{1}$$

$$I_0/I = Ae^{K[M]} \tag{2}$$

where, I_0 and I are the fluorescence intensities before and after the addition of Cr(VI) respectively, [M] is the concentration of the ions and K is the Stern-Volmer quenching constant and A is a constant term. The linearity of the plot is found to be quite high (up to 20 μM) with a K value of 0.29956×10^6 M^{-1} (fitting coefficient 0.96427) revealing the broad range applicability of the sensing probe. Similarly, the exponential plot depicts a K value of 0.0533×10^6 M^{-1} with a fitting coefficient of 0.98059. The LOD and LOQ have been calculated using the following relations [31a] (Eqs. 3 and 4),

$$LOD = 3\sigma/K \tag{3}$$

$$LOQ = 10\sigma/K \tag{4}$$

where, σ and K are the standard deviation by taking at least ten measurements of the fluorescence intensities of the pure membrane and the quenching constant respectively. The LOD and LOQ are found to be 66 nM and 220 nM respectively for hexavalent chromium in the linear range. Such a low detection limit portrays the membrane to be an efficient Cr(VI) sensor in recent times (Table S1). Table S1 depicts numerous Cr(VI) sensors with their sensitivities. These chromium sensors are rapid and very efficient in detecting chromium ions in water. In some cases, the sensitivity reaches a few nanomolar range. Though these sensitive probes are offering lower LOD values, the non-invasive sensing platform is still an important task to perform [31b,31c]. Mostly these sensors are in powder/ liquid form, thus fabrication of a complete and

portable device is quite difficult. Henceforth, PVDF-HFP modified BH@CD could play a crucial role in this field.

Qualitative detection of hexavalent chromium has already been done by using the fluorescence quenching of the membrane. But this sample is also capable to quantify the amount of chromium contamination in water. To validate this, the recovery study has been performed using the membrane. In this study, the SV plot of the membrane (Fig. 4) has been used as the calibration graph of the sensing probe. Further, 1.5, 5 and 20 μM Cr(VI) samples were prepared and tested using the sensor (Table S2). It is found that the Cr(VI) recovery percentages (RR %) are significantly high (95–101%) for this probe illustrating the significance of detection.

3.3.2. Cr(VI) detection mechanism

Fluorometric sensors involve different mechanisms and pathways to detect the target molecule/ions. Among them, Photoinduced Electron Transfer (PET), Energy Transfer (FRET and DRET), and Inner Filter Effect (IFE) routes [32,33] are quite common.

This study provides an insight into the detection mechanism by using the Density Functional Theory (DFT) method and fluorescence lifetime decay analysis of the probe in Cr(VI) environment. The fluorescence decay profile of the probe has been studied in a Cary-Eclipse, Agilent spectrometer. The decay lifetimes were considered by varying the Cr(VI) concentration and have been depicted in Fig. S6. The decay profiles show a gradual decrease in fluorescence lifetimes when the membrane has been exposed to varying concentrations of Cr(VI) and thus reveals the fluorescence quenching to be held at the excited state of the system [34].

As the fluorescence quenching phenomenon happens at the excited state, the Time-Dependent Density functional study (TDDFT) has been carried out (Fig. 5). To minimize the complexity of the calculation, the fluorophore part (*i.e.*, c-dot) has been taken herein to interact with the hexavalent chromium ion. The quencher (chromium) and the fluorophore (c-dot) have been placed at a distance of 5 Å to interact. The TDDFT study suggests the molecular orbitals be held at the fluorophore moiety at the HOMO-5 state, which upon excitation goes to the LUMO+ 2 state and after a non-radiative internal conversion jump to the LUMO state of the complex system. Interestingly, the entire molecular orbital shifts to the quencher moiety during these transitions and depicts electron transfer between fluorophore and quencher. Finally, a radiative transition occurs from LUMO to HOMO-5 resulting in the fluorescence quenching as there is a drastic orbital shifting towards the quencher moiety. This phenomenon is referred to as photoinduced electron transfer or PET [35], which generally occurs in the excited state due to collision between the fluorophore and the quencher resulting in a gradual decay in fluorescence lifetime as observed herein.

Additionally, the sensing mechanism has been characterized at higher Cr(VI) concentrations (> 20 μM). As mentioned previously at higher quencher concentrations, the calibration plot (S-V plot) shows an upward increment. This type of fluorometric relaxation generally refers to a synergistic effect of static and dynamic quenching. In reality, the presence of excess Cr(VI) ions block the fluorescence path of the fluorophores and quenching occurs [27].

3.3.3. Detection of Cr(VI) in different conditions

Previously, the fluorescence stability of the pure sensor membrane has been established. It showed an insignificant fluorescence alteration in a varying pH range (pH 4–9). Similarly, Cr(VI) sensing efficiency of the membrane has been studied. Initially, Cr(VI) solutions (500 μM) of different pH have been prepared and the membrane was exposed to the as-prepared solutions separately for measuring the fluorescence spectra. It is found that the fluorescence intensity centered at 467 nm drastically quenches upon Cr(VI) addition. Thus, the fluorometric detection efficacy of the membrane is said to be unaffected even in different pH levels of the solvent (Fig. S7).

The real-life applicability of the sensor and interference of other ions
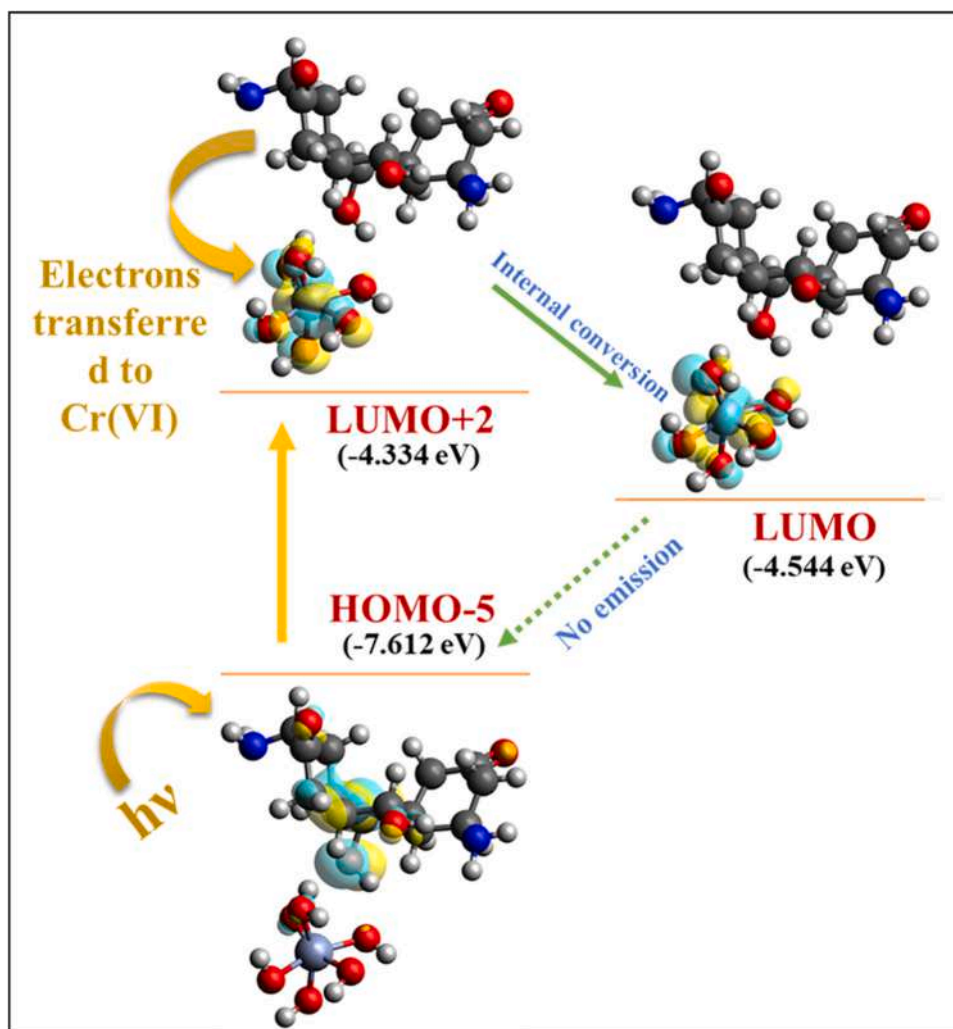
Fig. 5. (a) PET based fluorescence 'turn off' mechanism analysis using TDDFT formalism.

has been evaluated by using it in four different water samples. The water samples were taken from distinct sources, such as laboratory tap (tap water), from a nearby canal connected to a local tannery (wastewater), a nearby pond situated inside the university campus (pond water) and from the water purifier placed adjacent to the laboratory (drinking water). The samples were passed through separate filter papers (0.45 μm) and then taken for TDS, pH and resistivity analyses (Table S3). Further, the water samples were divided into two parts, of which one part was spiked with chromium (500 μM). The membrane was immersed in each of the water samples separately and exposed to a 355 nm wavelength for fluorometric studies. The fluorescence data shows significant quenching of fluorescence intensity when the Cr(VI) spiked samples have been used (Fig. S7). Otherwise, in pure water samples no fluorescence quenching has been detected. This phenomenon reveals that the sensor membrane is capable to detect Cr(VI) in real life water samples when other interfering elements are present.

Additionally, detailed inter-day and intra-day batch studies have been performed by taking various water samples from different sources to confirm the sensing performance of the device in real world. These studies reveal very low relative standard deviations (0.8–3.19%) with promising recovery rates (87–108%) (Table S4). This not only amplifies the analytical aspects of the sensing probe but also reveals its applicability in different water qualities.

Reusability is another major advantage of this fluorometric probe. The membrane was immersed in water and thereafter Cr(VI) repetitively contained water to record the fluorescence intensity. It shows no

alteration or quenching of the fluorescence even after repetitive use of the single membrane over a few cycles (Fig. S7). Henceforth, implying the reusability of the membrane in fluorometric sensing of Cr(VI) in aqueous media.

3.4. Detection of 'early stage Cr(VI) induced carcinogenic effect' in living cells

Hexavalent chromium is a genotoxic element and can cause severe harm in biological systems [36]. Thus, sensitive biosensors and molecular probes are required to detect the presence of such a heavy metal in living systems. It is very important to locate the pathway of contamination to detect it in an early stage. It is established that Cr(VI) uses the sulphur transport channel to enter a living cell [37]. After passing through the cell membrane, it goes directly to the proteins, such as glutathione and cytochrome b5 and reduces its valent state. In reality, Cr(VI) reduces to Cr(III) in presence of glutathione and produces Reactive Oxygen Species (ROS), which blocks the physicochemical activities of the infected cell and causes DNA damage [38]. Such activity leads to cancer development and could be probed if dedicated sensors are deployed in this contamination pathway [39].

It is observed that the sensor-treated cells emit bright blue fluorescence when exposed to UV radiation (Fig. 6). This validates the successful adhesion of the cells over the fluorescent membrane. Interestingly, the fluorescent signal gets quenched completely in the presence of Cr(VI). This phenomenon corroborates that the Cr(VI) ions
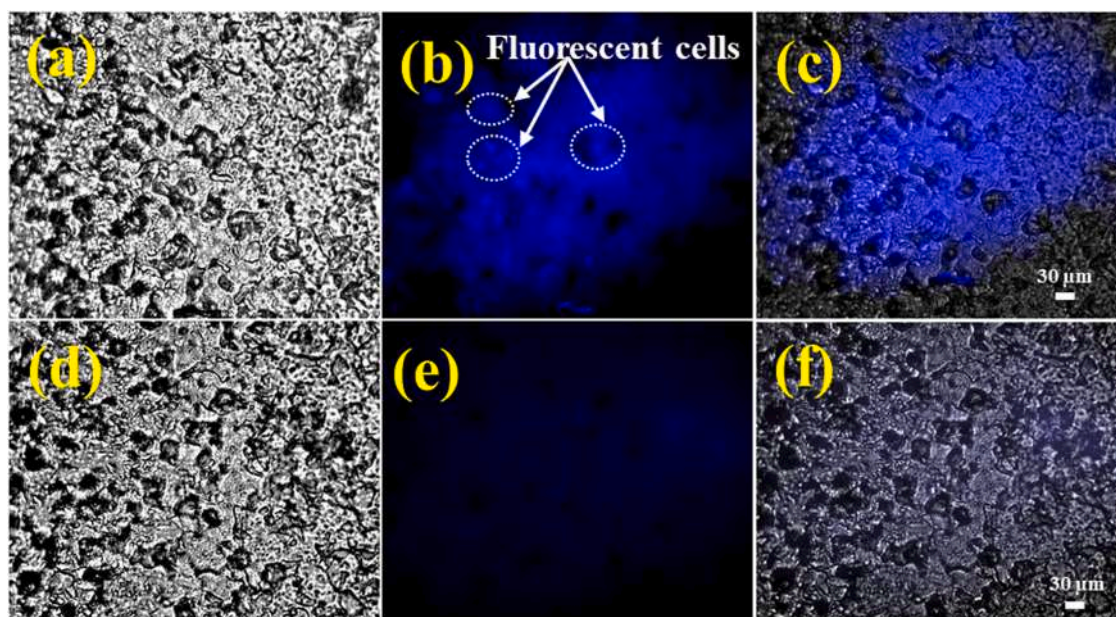
Fig. 6. Sensing of Cr(VI) ion in HELA cells by using the sensing probe showing excellent fluorescence quenching upon Cr(VI) addition, where, (b) fluorescent cells turn off their fluorescence (e) upon Cr(VI) addition. (a), (d) and (c), (f) are showing bright and merged fields.

inside the cell interact with the fluorophores (c-dot) of the as-prepared membrane sample (PV/CD@BH) and gets quenched. This also refers to the migration of the fluorophores through the cell membrane.

Herein, the molecular docking approach has been adopted to validate such an interesting issue. The binding affinities between the synthesized membrane (especially, the fluorophore part) and several

Fig. 7. Molecular docking analyses of the sensing probe showing interactions between fluorophore of the probe and (a) sulphur channel protein (5IOF), (b) glutathione (1PKW).

proteins of the chromium contamination pathway have been determined (Fig. 7) to ensure the fact. Initially, an SLC26Dg transporter protein (PDB: 5IOF) has been used to test the binding affinity of the synthesized probe at the cell membrane. Similarly, to check the affinity at the interior of the cell, glutathione (PDB: 1PKW) has been selected [40]. Binding affinities between the proteins and the ligand were determined using molecular docking.

In both cases, the protein-ligand docking is found to be successful (Table S5). The binding affinity between c-dot and SLC26Dg transporter protein is − 7.0 kcal/M, whereas, it is − 8.3 kcal/M for c-dot and glutathione. A closer look suggests that the possibility of binding Glycine (GLY-286, GLY-79) and Glutamic acid (GLU-241) with the c-dot is more favorable than any other parts of the SLC26Dg. Similarly, promising binding affinity is found between c-dot and Threonine (THR-68), Serine (SER-18), when it comes to glutathione. Hence, it is possible that the fluorophore (c-dot) part of the sample can bind with the entire Cr(VI) pathway inside the living cells and determine the chromium contamination at an early stage.

Such a dramatic fluorometric bio-sensing activity inside human cells is quite significant. As stated previously, this membrane is capable to detect the presence of Cr(VI) at an early stage in living cells and thus could be employed as an 'early-stage Cr(VI) induced carcinogen detector'.

4. Conclusions

Herein, a reusable and low-cost fluorometric sensing probe, namely, Kavach has been developed that can detect hexavalent chromium in all types of water. The PVDF-HFP coating restricts the c-dot leaching from the boehmite's surface. This flexible membrane has a great potential to sense chromium in living cells as well. Such an efficient sensor (detection limit~ 66 nM with a linear range of 0–20 μM) could be used in industrial wastewater monitoring systems and biomagnification studies. The fluorescence lifetime gets quenched upon Cr(VI) addition suggesting the PET-based sensing mechanism, which has also been validated by employing DFT-based calculations. The thermal stability of the sensor with apathetic pH behavior makes this device usable in extreme weather conditions and harsh industrial exposures. Kavach is capable to sense chromium qualitatively in all water quality and does not alter its sensing

efficacy in different ambient conditions. Additionally, various batch experiments have been performed on an inter-day and intra-day basis, showing excellent stability of the device with very promising recovery rates (~87–108%). The molecular docking studi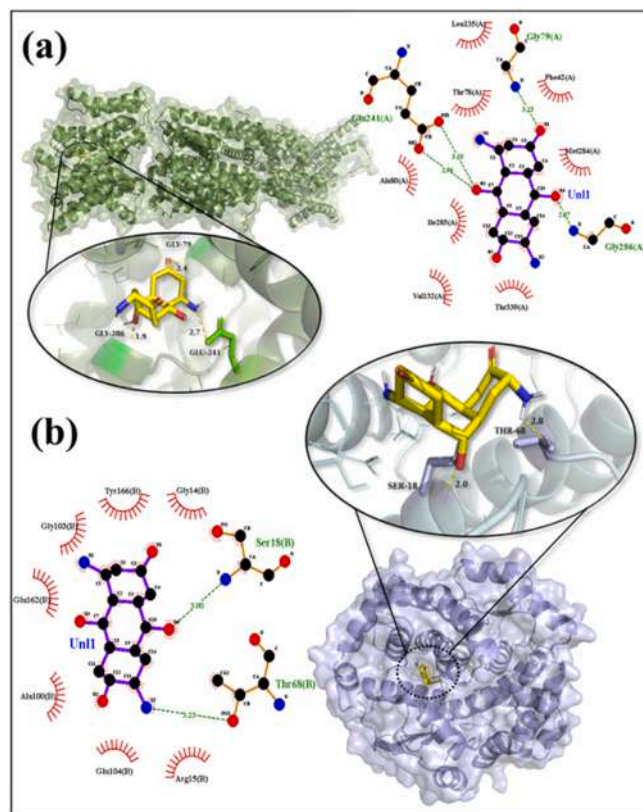es show a promising binding affinity between the sensor and various chromium receptors (glutathione and SLC26Dg transporter protein) in living cells and validates the experimental biosensing mechanism of Cr(VI). This handheld device could be a promising alternative in wastewater plants and wastewater monitoring systems shortly if properly improvised.

CRediT authorship contribution statement

Shubham Roy: Conceptualization, Methodology, Computation, Writing – original draft preparation. **Souravi Bardhan:** Writing - Assistance, Conceptualization, Investigation. **Dhananjoy Mondal:** Data curation, Investigation. **Ishita Saha:** Investigation. **Jhilik Roy:** Data curation, Software. **Solanky Das**: Data curation. **Dipak Kr. Chanda:** Writing - Assistance. **Parimal Karmakar:** Writing – review & editing, Resources. **Sukhen Das:** Supervision, Funding acquisition.

Declaration of Competing Interest

The authors declare that they have no known competing financial interests or personal relationships that could have appeared to influence the work reported in this paper.

Acknowledgments

Appendix A. Supporting information

Supplementary data associated with this article can be found in the online version at doi:10.1016/j.snb.2021.130662.

References

[1] (a) S. Roy, S. Bardhan, J. Roy, S. Das, Waste capacitor: a fresh approach to detect and remove Cr(VI) from water and making it an energy harvesting material, Mater. Today.: Proc. 46 (2021) 6223–6229;
(b) R. Bandi, R. Dadigala, B.R. Gangapuram, F.K. Sabir, M. Alle, S.H. Lee, V. Guttena, N-Doped carbon dots with pH-sensitive emission, and their application to simultaneous fluorometric determination of iron (III) and copper (II), Microchim. Acta 187 (1) (2020) 1–10.

[2] S. Bardhan, S. Roy, D.K. Chanda, D. Mondal, S. Das, S. Das, Flexible and reusable carbon dot decorated natural microcline membrane: a futuristic probe for multiple heavy metal induced carcinogen detection, Microchim. Acta 188 (4) (2021) 1–12.

[3] V.A. Ansi, N.K. Renuka, Table sugar derived carbon dot–a naked eye sensor for toxic Pb^{2+} ions, Sens. Actuators B-Chem. 264 (2018) 67–75.

[4] A. Chandra, N. Singh, Biocompatible fluorescent carbon dots for ratiometric intracellular pH sensing, ChemistrySelect 2 (20) (2017) 5723–5728.

[5] Z. Liu, W. Jin, F. Wang, T. Li, J. Nie, W. Xiao, Q. Zhang, Y. Zhang, Ratiometric fluorescent sensing of Pb^{2+} and Hg^{2+} with two types of carbon dot nanohybrids synthesized from the same biomass, Sens. Actuators B: Chem. 296 (2019), 126698.

[6] (a) P. Zuo, X. Lu, Z. Sun, Y. Guo, H. He, A review on syntheses, properties, characterization and bioanalytical applications of fluorescent carbon dots, Microchim. Acta 183 (2) (2016) 519–542;
(b) C. Wang, H. Lin, Z. Xu, Y. Huang, M.G. Humphrey, C. Zhang, Tunable carbon-dot-based dual-emission fluorescent nanohybrids for ratiometric optical thermometry in living cells, ACS Appl. Mater. Interfaces 8 (2016) 6621–6628.

[7] P. Das, M. Maruthapandi, A. Saravanan, M. Natan, G. Jacobi, E. Banin, A. Gedanken, Carbon dots for heavy-metal sensing, pH-sensitive cargo delivery, and antibacterial applications, ACS Appl. Nano Mater. 3 (12) (2020) 11777–11790.

[8] R.K. Singh, K.D. Patel, C. Mahapatra, M.S. Kang, H.W. Kim, C-dot generated bioactive organosilica nanospheres in theranostics: multicolor luminescent and photothermal properties combined with drug delivery capacity, ACS Appl. Mater. Interfaces 8 (37) (2016) 24433–24444.

[9] M. Zheng, Y. Li, S. Liu, W. Wang, Z. Xie, X. Jing, One-pot to synthesize multifunctional carbon dots for near infrared fluorescence imaging and photothermal cancer therapy, ACS Appl. Mater. Interfaces 8 (36) (2016) 23533–23541.

[10] M.J. Cho, S.Y. Park, Carbon-dot-based ratiometric fluorescence glucose biosensor, Sens. Actuators B-Chem. 282 (2019) 719–729.

[11] S. Miao, K. Liang, B. Kong, Förster resonance energy transfer (FRET) paired carbon dot-based complex nanoprobes: versatile platforms for sensing and imaging applications, Mater. Chem. Front. 4 (1) (2020) 128–139.

[12] P.R. Sreenath, S. Mandal, H. Panigrahi, P. Das, K.D. Kumar, Carbon dots: fluorescence active, covalently conjugated and strong reinforcing nanofiller for polymer latex, Nano-Struct. Nano-Objects 23 (2020), 100477.

[13] M.E. Yibowei, J.G. Adekoya, A.A. Adediran, O. Adekomaya, Carbon-based nano-filler in polymeric composites for supercapacitor electrode materials: a review, Environ. Sci. Pollut. Res. 28 (2021) 26269–26279.

[14] C. Long, Z. Jiang, J. Shangguan, T. Qing, P. Zhang, B. Feng, Applications of carbon dots in environmental pollution control: a review, Chem. Eng. J. 406 (2021), 126848.

[15] M. Jani, J.A. Arcos-Pareja, M. Ni, Engineered zero-dimensional fullerene/carbon dots-polymer based nanocomposite membranes for wastewater treatment, Molecules 25 (21) (2020) 4934.

[16] Y. Zhou, Y. Liu, Y. Li, Z. He, Q. Xu, Y. Chen, J. Street, H. Guo, M. Nelles, Multicolor carbon nanodots from food waste and their heavy metal ion detection application, RSC Adv. 8 (42) (2018) 23657–23662.

[17] A. Selim, S. Kaur, A.H. Dar, S. Sartaliya, G. Jayamurugan, Synergistic effects of carbon dots and palladium nanoparticles enhance the sonocatalytic performance for Rhodamine B degradation in the absence of light, ACS Omega 5 (35) (2020) 22603–22613.

[18] B.B. Chen, M.L. Liu, C.M. Li, C.Z. Huang, Fluorescent carbon dots functionalization, Adv. Colloid Interface Sci. 270 (2019) 165–190.

[19] S. Bardhan, S. Roy, D.K. Chanda, S. Ghosh, D. Mondal, S. Das, S. Das, Nitrogenous carbon dot decorated natural microcline: an ameliorative dual fluorometric probe for Fe^{3+} and Cr^{6+} detection, Dalton Trans. 49 (2020) 10554–10566.

[20] H. Liu, J. Yang, Z. Li, L. Xiao, A.A. Aryee, Y. Sun, R. Yang, H. Meng, L. Qu, Y. Lin, X. Zhang, Hydrogen-bond-induced emission of carbon dots for wash-free nucleus imaging, Anal. Chem. 91 (14) (2019) 9259–9265.

[21] C.M. Carbonaro, D. Chiriu, L. Stagi, M.F. Casula, S.V. Thakkar, L. Malfatti, K. Suzuki, P.C. Ricci, R. Corpino, Carbon dots in water and mesoporous matrix: chasing the origin of their photoluminescence, J. Phys. Chem. C 122 (44) (2018) 25638–25650.

[22] S. Roy, S. Bardhan, D.K. Chanda, J. Roy, D. Mondal, S. Das, In situ-grown cdot-wrapped boehmite nanoparticles for Cr (VI) sensing in wastewater and a theoretical probe for chromium-induced carcinogen detection, ACS Appl. Mater. Interfaces 12 (39) (2020) 43833–43843.

[23] R. Jalili, A. Khataee, M.R. Rashidi, R. Luque, Dual-colored carbon dot encapsulated metal-organic framework for ratiometric detection of glutathione, Sens. Actuators B: Chem. 297 (2019), 126775.

[24] M.J. Molaei, Principles, mechanisms, and application of carbon quantum dots in sensors: a review, Anal. Methods 12 (10) (2020) 1266–1287.

[25] C. Pérez-Rodríguez, L.L. Martín, S.F. León-Luis, I.R. Martín, K.K. Kumar, C. K. Jayasankar, Relevance of radiative transfer processes on Nd^{3+} doped phosphate glasses for temperature sensing by means of the fluorescence intensity ratio technique, Sens. Actuators B Chem. 195 (2014) 324–331.

[26] S. Samanta, A. Maity, S. Roy, S. Giri, D. Chakravorty, Effect of microstructure on ionic transport in silica-based sodium containing nanoconfined systems and their electrochemical performance as electrodes, Phys. Chem. C 124 (38) (2020) 21155–21169.

[27] G. Gabor, D.R. Walt, Sensitivity enhancement of fluorescent pH indicators by inner filter effects, Anal. Chem. 63 (8) (1991) 793–796.

[28] S. Roy, K. Pal, S. Bardhan, D.K. Chanda, S. Ghosh, P. Karmakar, S. Das, Gd (III)-doped boehmite nanoparticle: an emergent material for the fluorescent sensing of Cr(VI) in wastewater and live cells, Inorg. Chem. 58 (13) (2019) 8369–8378.

[29] T. Liang, P. Yang, T. Wu, M. Shi, X. Xu, T. Qiang, X. Sun, A general strategy to quantify analytes through fluorescence chromaticity and luminosity, Chin. Chem. Lett. 31 (11) (2020) 2975–2979.

[30] (a) S. Roy, S. Bardhan, D.K. Chanda, S. Ghosh, D. Mondal, J. Roy, S. Das, Development of a Cu (II) doped boehmite based multifunctional sensor for detection and removal of Cr (VI) from wastewater and conversion of Cr(VI) into an energy harvesting source, Dalton Trans. 49 (20) (2020) 6607–6615;
(b) J. Carvalho, P. Nottelet, J.L. Mergny, J.A. Queiroz, G.F. Salgado, C. Cruz, Study of the interaction between indole-based compounds and biologically relevant G-quadruplexes, Biochimie 135 (2017) 186–195.

[31] (a) M. Pajewska-Szmyt, B. Buszewski, R. Gadzała-Kopciuch, Sulphur and nitrogen doped carbon dots synthesis by microwave assisted method as quantitative analytical nano-tool for mercury ion sensing, Mater. Chem. Phys. 242 (2020), 122484;
(b) Y. Zhang, X. Fang, H. Zhao, Z. Li, A highly sensitive and selective detection of Cr(VI) and ascorbic acid based on nitrogen-doped carbon dots, Talanta 181 (2018) 318–325;
(c) Y.S. Lin, T.C. Chiu, C.C. Hu, Fluorescence-tunable copper nanoclusters and their application in hexavalent chromium sensing, RSC Adv. 9 (2019) 9228–9235.

[32] F. Zu, F. Yan, Z. Bai, J. Xu, Y. Wang, Y. Huang, X. Zhou, The quenching of the fluorescence of carbon dots: a review on mechanisms and applications, Microchim. Acta 184 (7) (2017) 1899–1914.

[33] D. Kukkar, K. Vellingiri, V. Kumar, A. Deep, K.H. Kim, A critical review on the metal sensing capabilities of optically active nanomaterials: limiting factors, mechanism, and performance evaluation, TrAC Trends Anal. Chem. 109 (2018) 227–246.

[34] M. van de Weert, L.V.D. Stella, Fluorescence quenching and ligand binding: a critical discussion of a popular methodology, J. Mol. Struct. 998 (2011) 144–150.

[35] Z.J. Lin, H.Q. Zheng, H.Y. Zheng, L.P. Lin, Q. Xin, R. Cao, Efficient capture and effective sensing of $Cr_2O_7^{2-}$ from water using a zirconium metal-organic framework, Inorg. Chem. 56 (2017) 14178–14188.

[36] A.M. Standeven, K.E. Wetterhahn, Chromium (VI) toxicity: uptake, reduction, and DNA damage, J. Am. Coll. Toxicol. 8 (7) (1989) 1275–1283.

[37] S. Mishra, R.N. Bharagava, Toxic and genotoxic effects of hexavalent chromium in environment and its bioremediation strategies, J. Environ. Sci. Health C. 34 (1) (2016) 1–32.

[38] X. Shi, Reduction of chromium(VI) and its relationship to carcinogenesis, J. Toxicol. Environ. Health B Crit. Rev. 2 (1) (1999) 87–104.

[39] J.A. Alcedo, K.E. Wetterhahn, Chromium toxicity and carcinogenesis, Int. J. Clin. Exp. Pathol. 31 (1990) 85–108.

[40] P. Ruzza, A. Calderan, Glutathione transferase (GST)-activated prodrugs, Pharmaceutics 5 (2) (2013) 220–231.

Shubham Roy *Jadavpur University, Kolkata, India* Shubham Roy obtained his Bachelor's degree in Physics from University of Calcutta in 2013 and acquired his Master's degree in the same discipline from Madurai Kamaraj University in the year 2015. He is presently pursuing his Doctoral degree under the supervision of Prof. Sukhen Das from the Department of Physics, Jadavpur University, India. His research area involves synthesis and characterization of nanomaterials for fabricating low cost fluorometric sensor to combat wastewater mediated heavy metal pollution. Mr. Roy has published numerous papers on multifunctional fluorometric sensors and their contamination removal techniques.

Souravi Bardhan, *Jadavpur University, Kolkata, India,* Souravi Bardhan is currently pursuing her Ph.D. degree from the Department of Physics, Jadavpur University, India. She pursued her graduation and post-graduation in Environmental Science from University of Calcutta, India. Prior to join the PhD program she worked in a project on biogeochemistry of core regions of Indian Sundarbans with School of Environmental Science, Jawaharlal Nehru University, India. Her present research-work involves enhancement of optical, electrical and biological properties of natural minerals in their nano- regime in order to design natural-multifunctional sensors for wastewater treatment.

Dhananjoy Mondal, *Jadavpur University, Kolkata, India,* Dhananjoy Mondal is currently pursuing Ph.D. degree from Department of Physics, Jadavpur University, Kolkata, India. He has received graduation and post-graduation degree in Physics from the same department. His research interest involves biocompatible materials-based sensors and actuators along with piezo-responsive catalysts. He is presently working as a junior research fellow under DST-SERB funded project in Jadavpur University, India.

Ishita Saha, *Jadavpur University, Kolkata, India,* Ishita Saha is currently working on wound healing activities of various biopolymers at the Department of Life Science and Biotechnology, Jadavpur University, India. She has several journal publications on wound healing and biocompatibility analyses of nanomaterials. Ms. Saha is trained in cell culture and various fluorometric applications on bio-systems.

Jhilik Roy, *Jadavpur University, Kolkata, India,* Jhilik Roy is presently doing her research in Materials science from the Department of Physics, Jadavpur University, Kolkata, India. She has obtained both B.Sc and M.Sc degrees in Physics from University of Calcutta and Techno India University respectively. Ms. Roy has an excellent command on theoretical molecular docking analysis and other *in silico* studies. She has published several research papers recently on fluorometric sensors and their interaction with living systems.

Solanky Das, *Jadavpur University, Kolkata, India,* Solanky Das is presently doing her research on natural mineral based sensors and actuators. She is working as a research scholar at the Department of Geology, Jadavpur University, India. Ms. Das has a specialization in the field of mineralogy and environmental geology. She has received her Bachelor's degree from University of Calcutta and completed her Master's degree in Geology from Jadavpur University. The research interest of Ms. Das involves magnetic properties of minerals in natural rocks.

Dr. **Dipak Kr. Chanda**, *Jadavpur University, Kolkata, India,* Dr. Dipak Kr. Chanda is a Research Associate at the School of Materials science and Nano Technology, Jadavpur University, Kolkata. He has completed his M. Tech (Materials Engineering) in 2014, M. Sc (Chemistry) in 2010 and B.Sc. (Chemistry) in 2008 from IIEST (Shibpur), Guru Ghasidas University and Burdwan University respectively. He has obtained his Ph.D. degree from Jadavpur University on 2019. Dr. Chanda has an exceptional command on material characterization and synthesis. He has published several articles in various reputed journals.

Prof. **Parimal Karmakar**, *Jadavpur University, Kolkata, India,* Prof. Parimal Karmakar is a senior professor in the Department of Life Science and Biotechnology, Jadavpur University, India. Prof. Karmakar has more than 150 journal publications in the field of cell biology and biotechnology. He has guided several doctoral and post-doctoral scholars beside teaching. His recent works on wound healing and biocompatible sensors gained much interest.

Prof. **Sukhen Das**, *Jadavpur University, Kolkata, India,* Prof. Sukhen Das is currently the Head of Department of Physics, Jadavpur University, India. He has guided several doctoral and post-doctoral fellows and has more than 200 research publications in reputed journals. He has been working as a Scientist in CSIR-CGCRI, India in his initial years before joining Jadavpur University. Other than Jadavpur University, Prof. Sukhen Das has also been appointed as a Visiting Professor at University of Virginia, USA; North Virginia Community college, USA and New York University, USA. He is also the recipient of "UGC Research Award 2012–2014". Prof. Das's research area includes development of ceramics, polymeric materials, antimicrobial bio-ceramics and nanomaterials for the development of piezoelectric probes and sensors. Recently, he and his group have done extensive research on fluorometric sensors to combat wastewater pollution. He and his team comprising of Souravi Bardhan and Shubham Roy has also received award at National level of ANVESHAN 2019-Student Research Convention organized by Association of Indian Universities (A.I.U.) under category of Basic sciences for their research work in wastewater remediation.

A Brief Review on Carbon-Based Nanosystems for Detection of Pollutants in Industrial Wastewater and Living Cells and Their Subsequent Removal Strategies

Shubham Roy[1], Souravi Bardhan[1], Nur Amin Hoque[2] and Sukhen Das[1]*

[1] Department of Physics, Jadavpur University, Kolkata - 700032, India
[2] Department of Marine Information Technology, Zhejiang University,
   Zhoushan - 316021, PR China

1. Introduction

In ancient days, people were aware of water pollution. Shreds of evidence suggest that Indus Valley (2600-1700 BCE) was far advanced in wastewater management (Lofrano and Brown 2010). They used separate channels for drainage water, which was passed through tapered terra-cotta pipelines into small sumps (Feo et al. 2014). The sumps collected the solid wastes using the sedimentation process and the freshwater was further used from above. Similarly, Egyptian, Greek, and Roman civilizations were also equipped with their wastewater management systems (Angelakis and Spyridakis 2010).

Things changed when the Roman era collapsed. It is known as the sanitary Dark Age (476-1800) (Lofrano and Brown 2010). During this period, the culture of wastewater treatment and water resource management was abandoned (Yannopoulos et al. 2017). Lack of concern regarding hygiene and health along with rumors spreading and convictions probably caused this. Urbanization and the evolution of technology during the mid-nineteenth century bought industrial wastes into the game (Geels 2006). Nowadays, water pollution is occurring in numerous pathways, and among them industrial water pollution is causing severe harm to the environment. Various industries, like textile, leather, steel, chemical, fertilizer, etc., are discharging hazardous contaminants directly into the water through pipelines and small canals

Corresponding author: sdasphysics@gmail.com

(Yadav et al. 2019). Industrial contaminants, such as chromium, arsenic, lead and mercury, are enormously harmful to human health even at lower doses (Duruibe et al. 2007) and some of them, iron, nitrate and sulfate can also damage water bodies above a critical limit (Du et al. 2020). Long-time exposure to these contaminants results in various diseases, such as chronic diarrhea, various bowel syndromes and improper pigmentation of the skin (Fernandez-Luqueno et al. 2013), besides several carcinogenic diseases (Fasinu and Orisakwe 2013) like cirrhosis of the liver, lung cancer, skin cancer, etc., which could be minimized if the proper wastewater management system is employed. Recent advancements in materials science, especially nanotechnology, enable us with various nanostructures capable of determining contaminants rapidly and removing them from water in a facile manner (Liu et al. 2019). Thus, comprehensive and exhaustive knowledge is much needed to implement proper wastewater management systems on-site.

The present study is contemplated to discuss different carbon-based nanomaterials for wastewater treatment. Initially, this work includes a brief overview of various carbonaceous nanostructures and their applications in numerous fields. Detection of pollutants in wastewater is the preliminary step toward wastewater management. Hence, special attention has been given to fluorometric sensing using carbon nanotechnology. Numerous applications of bioimaging and biosensing using carbonaceous nanomaterials have been incorporated in this work to study the toxicological aspects of industrial contaminants. Adsorption-based remediation and modern piezo-catalysis techniques employing various carbon-based nanostructures and polymer-nanocomposites have been discussed here in a detailed manner, which portrays the importance of carbonaceous nanomaterials in this field.

2. Carbon-Based Nano Systems: A New Era in Nanotechnology

Carbon nanomaterials are gaining importance for applications in various fields, such as superconductors (Tang et al. 2001), electronic materials (Dai et al. 2012), reinforcement material in composites (Esawi and Farag 2007), drug delivery systems (Hosnedlova et al. 2019), biosensors and biomedical applications (Mohajeri et al. 2019). Carbon nanomaterials exhibit a unique combination of physicochemical properties, such as remarkably high electrical conductivity (Chen and Dai 2013), mechanical strength (Hayashi et al. 2007), optical absorption and emission properties (Dekaliuk et al. 2014) and thermal stability (Bannov et al. 2020). These unique properties of carbon nanomaterials significantly vary with their dimension and structure. The synthesis of such carbon nanostructures is quite facile and industrially feasible (Huczko et al. 2014).

Earlier studies show that fluorescent carbon dot (CD) is a dimensionless promising imaging and fluorometric sensing agent for the detection of various contaminants (Molaei 2020) in aqueous media. Surprisingly, the size-dependent tuneability of optical emission enhances the applicability of this novel fluorometric probe (Kailasa et al. 2019). This zero-dimensional carbon nanomaterial is one of the newest and most promising candidates in the carbon nanotechnology era.
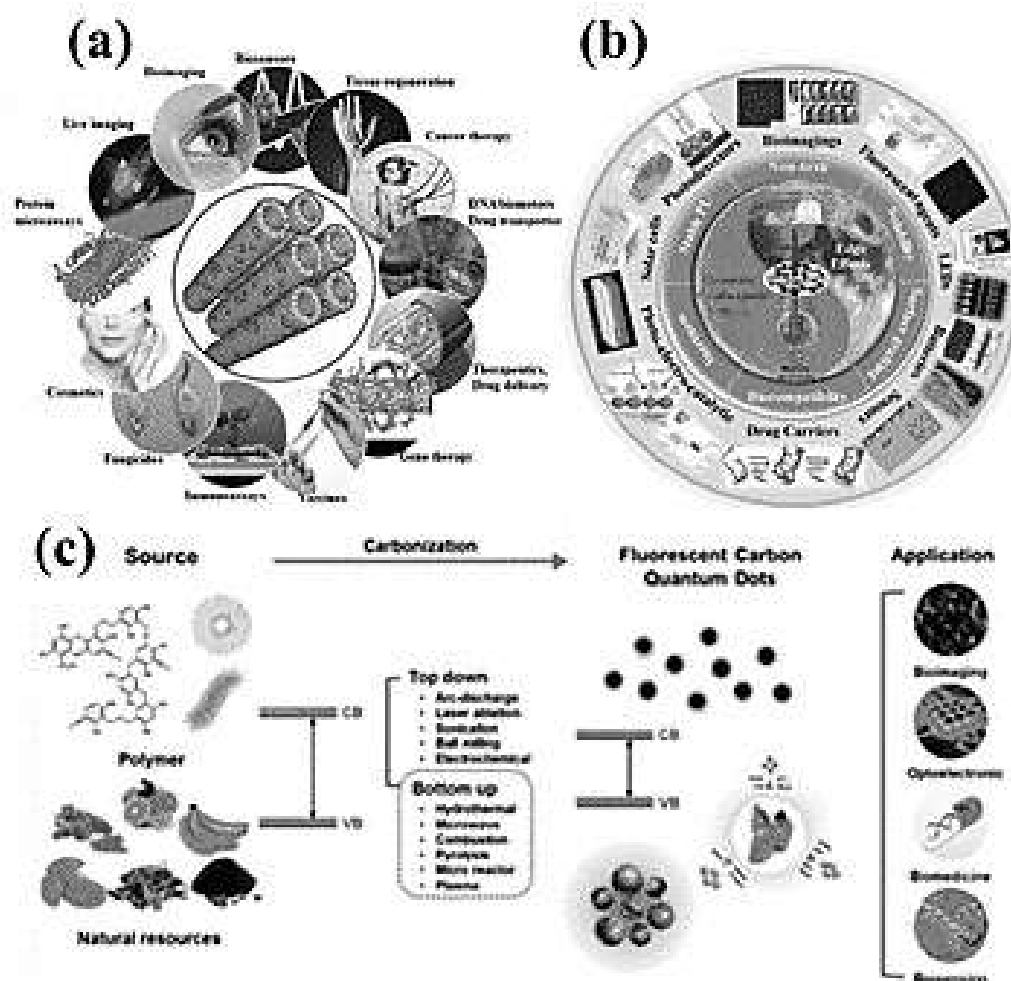
Figure 1. Applications of various carbon-based nanostructures in modern days showing: (a) CNT as a next generation advanced nanomaterial. Reproduced from Merum et al. 2017. Copyright 2017 with permission from Elsevier. (b) Some fluorometric and colorimetric applications of GQD. Reproduced from Tian et al. 2018. Copyright 2018 with permission from Elsevier. (c) Synthesis and numerous physicochemical applications of carbon quantum dots. Reproduced from Mazrad et al. 2018. Copyright 2018 with permission from Royal Society of Chemistry

On the other hand, 1D carbon nanotube (CNT) is an excellent electronic material having a great contribution to piezoelectric nanogenerators and electrodes (Vilatela and Marcilla 2015). High electrical conductivity and electrical stability make this material desirable for the electrode (Liu et al. 2012) and capacitor applications. A few studies have been initiated with CNT and CNT polymer nanocomposites, which show an enhanced thermoelectric figure (An et al. 2017) of merit upon CNT addition. The 2D graphene is quite popular in adsorption-based wastewater treatment due to its high adsorption capacities (Yap et al. 2018). Graphene is a lightweight and hard nanomaterial having a high surface area (Jiang and Fan 2014). It has uniform porosity, a large aspect ratio and hollow pores, making it a promising adsorbent for wastewater treatment applications.

Recently, researchers are working on the waste-based synthesis of carbon nanomaterials. Thus, various biomaterials and waste products have been used extensively to synthesize functionalized carbon nanostructures (Deng et al. 2016). In reality, the use of such natural materials and waste products not only minimizes the production cost but also sustainably decreases environmental pollution.

3. Water Quality Assessment with Carbon-Based Nanosystems

3.1 Limitations of Conventional Systems and Rise of Fluorometric Probes

Water quality assessment is generally based on chemical, physical and bacteriological parameters. Escalating technological demand liberates enormous amounts of metals, ions and complexes into the water causing physical and chemical damage to the water quality. Hence, water quality assessment, i.e. detection of such foreign elements is necessary to combat industrial water pollution.

Several techniques have been employed, such as atomic absorption spectroscopy, cyclic voltammetric method, potentiometry, light scattering method and liquid chromatography for water quality assessment (Conti et al. 2002, Ammann 2002). But these conventional methods have their limitations. In reality, these methods are site and sample, specifically having limited range and long measurement times (Bardhan et al. 2020). Henceforth, recently developed fluorometric sensors are gaining importance for their fast and accurate response (Bandi et al. 2020).

A fluorophore is a fluorescent chemical compound or a part of any chemical compound that can re-emit light upon light excitation (Bachmann et al. 2006). Generally, the interaction between fluorophore and contaminant alters the overall fluorescence property of the fluorophore (Xu et al. 1996). This simple photophysical phenomenon is known as fluorometric sensing. These fluorometric sensors are way more sensitive (Wang et al. 2018) than other conventional sensors, including colorimetric sensors. The fluorescence intensity is measured directly without any reference beam, which makes this technique selective and sensitive.

3.2. Carbonaceous Nanomaterials as Fluorometric Probes: Theory and Pathways

Carbon nanostructures are a class of novel nanomaterials that are widely used in various fluorometric applications, such as fluorometric sensors, biomarkers and bioimaging agents (Pirsaheb et al. 2019). Predominantly, carbon dot and graphene quantum dot show significant fluorescence emission than other carbon-based nanosystems. The emission peak position of these quantum dots is related to their excitation wavelength (Zhu et al. 2015), which may result from the wide distribution of differently sized particles, different emissive traps and surface chemistry that make these carbonaceous nanostructures fluorescent. An extensive study of functionalized CD and GQD shows that the incorporation of nitrogen and sulfur creates C=N

and C=S moieties, respectively (Ouyang et al. 2019), which results in surface functionalization of these nanodots.

Thus, it incorporates new energy levels and emits better fluorescence than the undoped quantum dots. Surprisingly, CNT show promising near-infrared (NIR) fluorescence when encapsulated into a polymer matrix (Wolfbeis 2015) and becomes a striking fluorescent probe for metal ions, proteins and small biological species, including glucose, H_2O_2, ATP and NO (Kruss et al. 2013).

Carbonaceous nanomaterials undergo numerous pathways that are involved in fluorescence-based contaminant detection; among them Inner Filter Effect (IFE), Photoinduced Electron Transfer (PET) and Förster Resonance Energy Transfer (FRET) routes are quite popular.

3.2.a Inner Filter Effect (IFE)

It is observed that when fluorophores interact with foreign elements (quencher in this case), such as ions, molecules, complexes with a relatively higher concentration and some quenchers 'block' the emission of the fluorophore (Chen et al. 2018). In this case, some fluorophores are less accessible than others and result in fluorometric quenching (turn off). In other words, fluorescence quenching suggests the presence of the targeted quencher in the sample (Zheng et al. 2013).
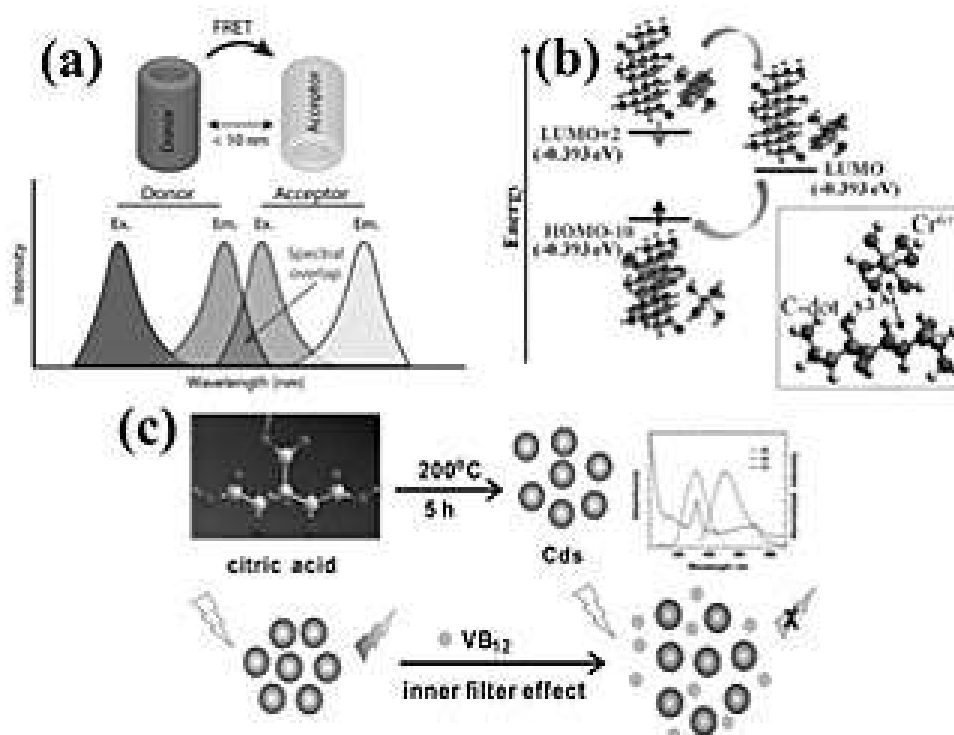
Figure 2. Different fluorometric sensing pathways depicting: (a) FRET based sensing technique. Reproduced from Broussard and Green 2017. Copyright 2017 with permission from Elsevier. (b) DFT based determination of PET based sensing with CDs. Reproduced from Bardhan et al. 2020. Copyright 2020 with permission from Royal Society of Chemistry. (c) Inner Filter Effect using carbon dots showing fluorescence quenching. Reproduced from Ding et al. 2018. Copyright 2018 with permission from Elsevier.

IFE is a steady-state phenomenon that usually occurs in the ground state. Studies suggest that carbon dot undergoes IFE in various cases to detect silver nanoparticles in cosmetics, biomarkers like alkaline phosphatase, hexavalent chromium and ascorbic acid in wastewater (Zheng et al. 2013). IFE can happen in other carbon nanostructures, like CNT and graphene quantum dot (GQD). Zhao et al. (2010) reported the behavior of Bovine Serum Albumin adsorbed onto CNT through IFE. Similarly, GQD depicts its efficacy in detecting artemisinin, cyanide and blood glucose using the inner filter effect (Zhu et al. 2019).

3.2.b Photoinduced Electron Transfer (PET)

In PET, donors are nearby (<10 nm) with acceptors get excited when photons are irradiated (Roy et al. 2019). This donor-acceptor pair in an excited state collides with each other and electrons get transported to the acceptor moiety, causing a rapid alteration of the fluorescence intensity. This phenomenon is known as photoinduced electron transfer. Fluorescence lifetimes get changed in this phenomenon as the PET occurs in the excited state. Lan et al. in their 2015 paper proposed a carbon dot-based turn-on sensor (sensitivity 84 nM) for hydrogen peroxide following the PET mechanism. In this case, the carbon dot acts as an electron acceptor. A similar phenomenon has been reported by Pan et al. showing detection of mercury ions using PET-based technique. Carbon nanotube undergoes PET as well (Baskaran et al. 2019). Phthalocyanines-CNT complex shows significant photoinduced electron transfer as reported by Ballesteros et al. in their 2007 paper.

3.2.c Förster Resonance Energy Transfer (FRET)

FRET is the radiationless energy transmission from the donor molecule to the acceptor molecule. The donor molecule is the fluorophore that initially absorbs the energy and the acceptor is the molecule to which the energy is subsequently transferred. In order to achieve a decent FRET system, the distance between the donor and the acceptor must be less than 5-10 nm (Mondal et al. 2013). The efficacy of this energy transfer is inversely proportional to the sixth power of the distance between donor and acceptor, which makes FRET extremely sensitive to a little alteration in distance (Dennis and Bao 2008). Currently, FRET-based sensing probes are quite popular due to their sensitivity. Bu et al. developed a carbon dot-gold nanoparticle FRET system for polybrominated biphenyl detection with a sensitivity of 0.039 µg/ml. FRET-based ammonia sensor with carbon dot as a sensing probe (Ganiga and Cyriac 2016) has also been reported recently showing a 3 ppm detection limit.

3.3   Carbonaceous Fluorometric Probes for Detection of Contaminants in Wastewater

Industrial wastewater largely contains heavy metal ions and metal complexes. Thus, detection of industrial heavy metals is necessary to assess the water quality. Fluorescent carbon-based nanosystems have been widely used in the past few years to detect heavy metal ions in wastewater.

3.3.a Carbon Quantum Dot (CD)

In their recent paper, Bardhan et al. showed nitrogenous CD doped in natural microcline nanoparticles can detect Cr(VI) and Fe(III) simultaneously. The detection limit, in this case, is very low. Besides, Ma et al. reported a novel CD nanocomposite for Cu(II) ion detection. A dual-mode colorimetric and fluorometric sensor based on CD has also been proposed by Kalaiyarasan et al. for copper ion detection with a detection limit of 3.8 nM. Low dimensionality causes a higher probability of these quantum dots to agglomerate and lose their fluorescence. This could be eliminated by employing the *in-situ* growth technique of CD in other nanostructures. Roy et al. proposed this unique technique and detected Cr(VI) in real-life wastewater using CD-doped boehmite nanoparticles. The detection limit was found to be 58 nM in this case. Other heavy metal ions, such as mercury, arsenic, selenium, zinc and lead, have also been detected using CD in quite a similar manner (Devi et al. 2019), making it a promising fluorometric agent for industrial usage.

3.3.b Graphene Quantum Dot (GQD)

Promising biocompatibility, fluorescence and chemical stability makes GQD a potential candidate for fluorometric sensing. GQD is capable to detect hazardous heavy metal ions, like As(V) and Hg(II) using the FRET mechanism (Chini et al. 2019) when attached to carbon dots with very low detection limits. Nitrogen-doped GQD was used to sense Fe(III) ions with a detection limit of 90 nM (Ju and Chen 2014). Similarly, sulfur-doped GQD was found to be a promising fluorometric probe for Ag(I) ions in water (Bian et al. 2017). Shtepliuk et al. developed a theoretical strategy to detect Cd, Hg and Pb in water using GQD-based nanoprobe. They used density functional methods (DFT) to understand the sensing capability of this novel probe.

3.3.c Carbon-Based Fluorescent Nanofibers and Polymers

Recently, emphasis has been given to optically active carbonaceous polymers and nanofibers for fluorometric detection of industrial contaminants in wastewater. Primarily, Hg(II), Ni(II), Cu(II), Al(III) and Fe(III) ions have been detected (Ramdzan et al. 2020) using these fluorescent nanosystems. Polymers like, Polycaprolactone (PCL), polyaniline (PANI), poly(vinyl alcohol) (PVA) and ethyl cellulose (EC), have been widely used to fabricate innovative optically active fluorometric probes (Terra et al. 2017) for this purpose. In several reports, it has been shown that multiple heavy metal detection is possible using these fluorometric probes (Kailasa et al. 2019, Bandi 2020). Wang et al. detected Cr(III) and Cu(II) simultaneously using electrospun 1,4-DHAQ-doped cellulose nanofiber films. Similarly, Wei et al. in their 2014 paper showed PVA nanofibrous membrane modified with spirolactam-rhodamine derivatives for simultaneous detection of Fe(III), Cr(III) and Hg(II). These polymeric sensing probes are way more stable and reusable than aqueous nano-sensors. In reality, these polymers do not inherit fluorescence properties. Thus, loaded with fluorophores (Tao et al. 2017) such as dyes, conjugated polymers, carbon-based nanomaterials, and nanoparticles produce fluorescent detection systems.

4. Toxicity Assessment of Industrial Wastewater Using Carbon-Based Nanostructures

Carbon nanoparticles having the benefit of biocompatibility with additional fluorescence quality created a large domain in the field of toxicological and nano theranostics study (Molaei 2019). Both *in-vitro* and *in-vivo* applications of such nanomaterials are widely explored (Molaei 2018) to seek new avenues for advanced bio-sensing and bio-monitoring of industrial wastewater. Although most of the toxicologic studies involve short-term indicators of toxicity or alteration of cellular functions or interfere with metabolic pathways, carbon nanostructures have reported overcoming such drawbacks and can be modified accordingly for even sub-chronic exposure assays or various pathologic reactions for *in-vivo* experiments without causing a secondary modification of host cells (Hurt et al. 2006).

Bio-sensing and bio-imaging techniques involving the detection of specific molecules or pollutants in wastewater have colossal significance in environmental safety and health care, hence there is a huge demand for detecting pollutants at the cellular or genetic level (Gao et al. 2014). The fluorescence technique emerged as one of the feasible, time-saving and reliable methods to fulfill such prerequisites. The intrinsic fluorescence properties of carbon-based nanostructures, especially nitrogen or sulfur-doped CDs and GQDs, make them potential candidates for bio-sensors and bio-imaging agents.

Moreover, these quantum dots can be conjugated with various small molecules, antibodies and nanoparticles to detect cancer cells, conduct targeted sensing and can be used as biomarkers (Simpson et al. 2018). They can even be useful in detecting the presence of various molecules or heavy metals (Deshmukh et al. 2018), such as Hg(II), Pb(II), Cu(II), Fe(III), Cr(VI) within live cells, thus possessing a great role in biomagnification study. Even the electroactive properties of graphene facilitate the synthesis of electro-chemiluminescent and fluorescent biosensors (Pumera 2011).

Another benefit of carbon nanostructure, especially CDs is that they have remarkable photostability and high resistance toward metabolic degradation, making them preferable for *in-vivo*/*in-vitro* bioimaging applications with relatively lower chances of cytotoxicity as compared to other quantum dots (CdSe, CdTe) (Li et al. 2017). Other than fluorescence turn-on and turn-off biosensors, various carbon nanostructure-based colorimetric biosensors have exhibited promising potential toward targeted detection at very low concentrations compared to conventional colorimetric biosensors developed from silver or gold nanoparticle or metallic QDs (Sabela et al. 2017).

Bhunia et al. 2013 chemically designed functionalized carbon nanoparticle-based nanoprobes with tunable emission paving the path for the advancement of carbon nanostructure-based bioimaging probes. Recent researches to explore new fluorescent markers in cell imaging proved carbon nanoparticles as a suitable candidate due to their high fluorescence and low cytotoxicity (Song et al. 2018) since they can instantly detect the presence of a very low concentration of specific pollutants or heavy metals in human cell or microorganism by the fluorescent turn-on-off method (Pirsaheb et al. 2019, Sharma et al. 2016).
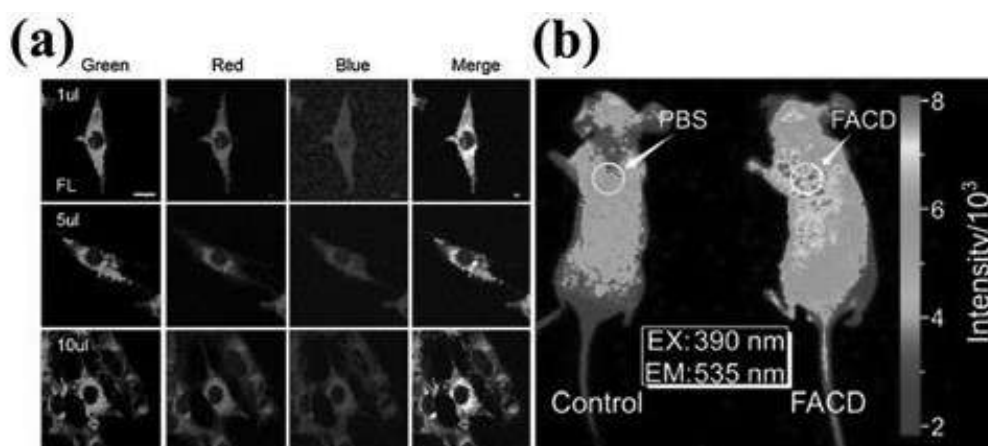
Figure 3. Bioimaging studies using carbon based nano systems showing: (a) N-isopropylacrylamide passivated carbon dots for multicolor *in-vitro* bioimaging applications. Reproduced from Kim et al. 2018. Copyright 2018 with permission from Elsevier. (b) Aspirin based CDs for *in-vivo* bioimaging in mice. Adapted from Xu et al. 2016. Copyright 2016 with permission from American Chemical Society

In the quest for fabricating next-generation probes for *in-vivo* fluorescent imaging, Yang et al. (2009) were the first to inject mice with carbon dots to explore feasibility. After the success, further similar investigations were performed by coupling carbon nanomaterials with other active molecules for various *in-vivo* applications, such as cancer diagnostics (Luo et al. 2013) which can validate the *in-vitro* assessments on cancer cells.

Hence, there are future endeavors of development of more advanced carbon nanostructure-based biosensors and modifying the bio-imaging techniques to detect even minute quantity of specific molecule or heavy metal even in live cells and animal models to combat environmental pollution and maintain health safety along with the determination of pathway for biomagnification, thus preventing health hazards from industrial water pollution.

5. Remediation of Industrial Wastewater Using Carbon-Based Nanostructures

Removal of toxic pollutants and heavy metals, both from the wastewater and living cells has attracted huge attention because of its high significance in healthcare and the environment. Various techniques for pollutant removal, such as adsorption, ion exchange, reverse osmosis, coagulation, electrochemical and solvent extraction, were reported (Dąbrowski et al. 2004) but most of them suffered drawbacks. A few of these techniques are costly. Particularly, ion exchange suffers recyclability and electrical techniques require high energy consumption (Fiyadh et al. 2019).

5.1 Adsorption-Based Removal of Heavy Metals Using Carbonaceous Nanomaterials

The adsorption-based removal of contaminants has widely proved to be effective

(Wingenfelder et al. 2005) and is now practiced extensively because of its simplicity, ease of use, convenience, low energy consumption, scope for regeneration and high level of effectiveness even when pollutants are present at low concentration. Carbon nanomaterials undergo both adsorption processes, which makes them promising adsorbents for heavy metal removal from wastewater. Although various organic and inorganic adsorbents and bio-adsorbents are still used, carbon-based nanomaterials are now gaining popularity due to their surface properties, high stability and inertness and in many cases due to their porous structure (Khezami and Capart 2005). Moreover, the incorporation of various functional groups on their surface or tailoring their physical and chemical properties enhanced their sorption capacities (Yoon et al. 2007). The adsorptive capacity of these carbon-based nanomaterials was evaluated using isotherm models like pseudo-second-order rate equation, Langmuir, Freundlich, Redlich-Peterson and Dubinin-Radushkevich models (Xu et al. 2018).

5.1.a   Carbon Nanotubes

CNTs have emerged as a potential next-generation adsorbent because of their remarkable structural, physical and chemical properties and very high adsorption capacity which attributes to the presence defects, functional groups, outside surfaces, grooves and interstitial regions between nanotube bundles (Thostenson et al. 2001). Although they are highly stable, they are not a good adsorbent themselves, hence requires surface functionalization, such as the acid modification or grafting of functional groups like $-NH_2$ or $-SH$, increasing the number of pre-existing groups like $-COOH$ or $-OH$ or by coating with specific nanomaterials to achieve high selectivity and excellent adsorbing capacity of heavy metals. Various reports proved that functionalized multi-walled CNTs can effectively tackle toxic heavy metals, like As^{3+}, Hg^{2+}, Cd^{2+}, Cr^{6+}, Pb^{2+}, Ni^{2+} in an aqueous medium (Fiyadh et al. 2019, Abbas et al. 2016). The metal ions interact with the CNT surface and are adsorbed via various mechanisms, mainly by physical adsorption, sorption-precipitation, electrostatic attraction lowering the metal ion concentration from an aqueous medium. The mechanism followed and affinity of functionalized CNTs toward heavy metal ions depend on various factors, like pH, temperature, surface area and charge, concentration and ionic strength and hence various affinity orders are reported in different studies. Rao et al. (2007) reported the following affinity order $Cd^{2+} < Cu^{2+} < Zn^{2+} < Ni^{2+} < Pb^{2+}$, while Stafiej and Pyrzynska (2007) reported $Mn^{2+} < Zn^{2+} < Co^{2+} < Pb^{2+} < Cu^{2+}$. In most of these cases, the adsorption model follows the Langmuir equation, which applies to adsorption on homogeneous surfaces, while in some cases it follows Freundlich equations, which mainly represent adsorption on the heterogeneous surface (Abbas et al. 2016). CNTs are also reported to successfully remove organic pollutants such as dyes from wastewater due to their tendency to interact by non-covalent forces like hydrogen bonding, π–π stacking and van der Waals forces (Gupta and Saleh 2013).

5.1.b   Graphene and Its Derivatives

Graphene and graphene-based nanostructure are used for the past few years as an economical adsorbent for wastewater treatment because of the desirable surface properties and functional sites (Tabish et al. 2018), which can be further enhanced by
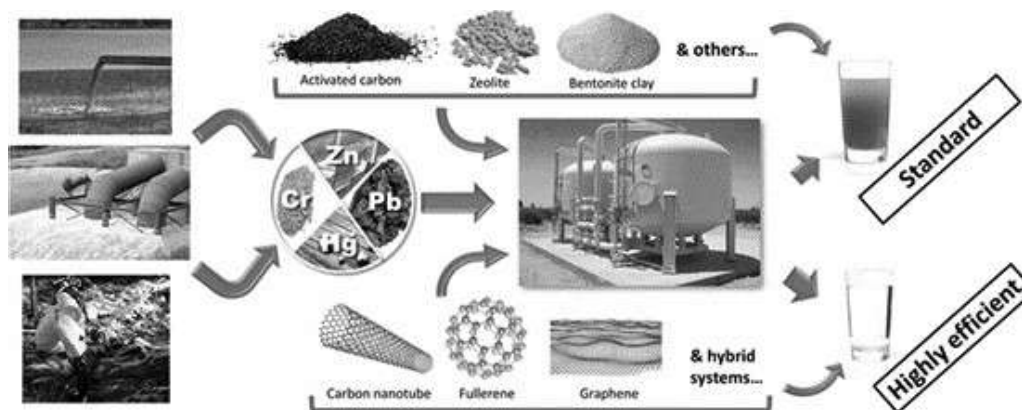
Figure 4. A brief comparison between conventional adsorbents and futuristic nano-adsorbents showing their efficacy in real life condition. Reproduced from Burakov et al. 2018. Copyright 2018 with permission from Elsevier.

the oxidation method. The negative charge on graphene or graphene oxide surface facilitates the electrostatic attraction of heavy metal ions. Moreover, the presence of functional groups like –COOH or –OH attributes to ion exchange or surface complex formation. Although graphene has poor adsorption selectivity, the specificity can be improved by functionalization, adsorbent thickness maintenance and desired ambient conditions, which also increases the adsorption capacity, thus facilitating heavy metal removal. Affinity order for heavy metals was found to be $Ca^{2+} \approx Sr^{2+} < Zn^{2+} \approx Ni^{2+} \approx Cd^{2+} < Cu^{2+} < Pb^{2+}$, which can be correlated with their electronegativity and standard reduction potential (Peng et al. 2017). In the case of anionic pollutants of wastewater, like fluoride, chromate, arsenate and arsenite, as reported by Reyes Bahena et al. (2002), under low pH ligand exchange reactions can take place as the anions can displace –OH groups from graphene surface.

5.1.c Carbon-Based Polymer Nanocomposites

Scientists are now giving more emphasis on carbon nanostructure-doped polymer adsorbents (Zhao et al. 2018) for their multiple benefits, like practicability, feasible regeneration, mechanical stability and durability, adjustable surface functional groups, benign nature and the polymeric matrix provides greater surface area for adsorption or specific interaction. An obvious feature of carbon-polymer nanocomposites for heavy metal removal is their high sorption ability (Wu et al. 2011) and reduction of the potential risk of release of pollutants back to the environment after they interact with the polymer matrix. Modifications of such polymeric membranes with improved regeneration capacity and multiple-use facilities to curb wastage have become a new challenge for scientists. Presently, the removal of heavy metals from living cells using carbon-based nanostructures is gaining popularity, mainly due to its biocompatibility.

5.2 Piezo-Catalytic Removal of Contaminants from Aqueous Media

Removal of organic pollutants from wastewater is of utmost importance. Various strategies like photocatalysis and membrane separation have been widely introduced

to combat this. But lack of selectivity, high cost in membrane separation and rapid electron-hole pair recombination are the common difficulties that limit semiconductor-based photocatalysis and membrane separation.

Piezo-catalysis is a relatively new concept of eliminating these drawbacks demonstrating unique catalytic properties as a result of the creation of the built-in electric field by the dipole polarization. This dipolar polarization delivers a driving force to move the photoinduced charge carriers enabling their separation (Liang et al. 2019).

The era of piezocatalysis has begun with piezoelectric crystals, like $BaTiO_3$, $PbTiO_3$ and $NaNbO_3$ (Wang et al. 2019). Later, Lin et al. (2014) incorporated zirconium into the lead titanate crystals and achieved better piezocatalytic activity. Similarly, Sharma et al. (2020) co-doped cerium and calcium into standard barium titanate crystals to clean dye/pharmaceutical wastewater. ZnO/Al_2O_3 nanosheet-based ultrasonic catalyst was prepared by Nie et al. very recently, which is capable of removing methyl orange dye from an aqueous medium.

Carbon and its nanostructures are unexplored in this field until now. A few works report the enhancement of piezocatalytic activity when carbon nanomaterials were added to piezo-electric materials. Chen et al. in their recent paper reported novel barium titanate/carbon hybrid nanocomposites for piezocatalytic degradation of dye in wastewater (Chen et al. 2020). In this work, the authors achieved the best results for 2% carbon-doped barium titanate crystal, which rapidly eliminates around 75.5% of rhodamine-B dye under ultrasonic vibration in wastewater. This enhancement can be ascribed to the action of carbon's charge transfer, which promotes the effective separation of the piezoelectrically induced charges in this case. Thus, the application of carbonaceous nanostructures in piezocatalytic removal of pollutants is still a futuristic domain, which could be a game-changer in the next few years.
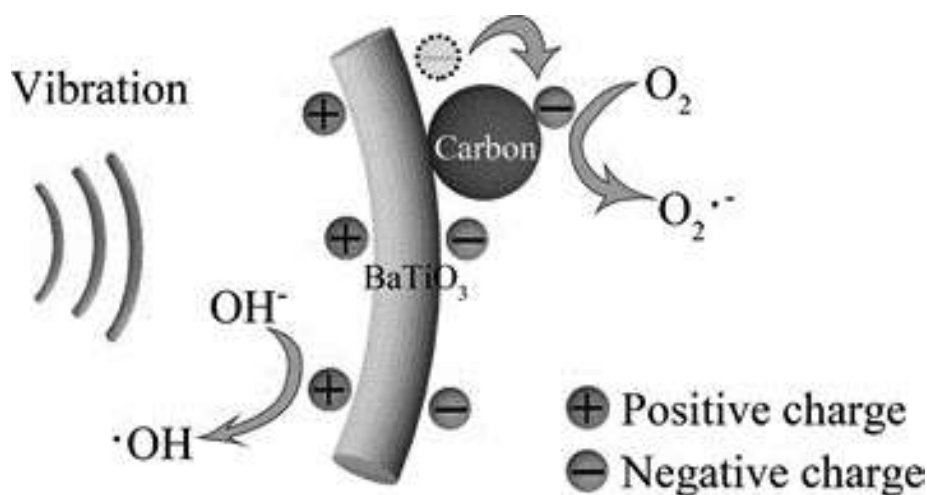

Figure 5. The working mechanism of $BaTiO_3$/carbon piezocatalytic nanocomposite showing charge separation process under vibration. Reproduced from Chen et al. 2020. Copyright 2020 with permission from Elsevier.

6. Prospective and Summary - Conclusions and Outlook

In this review, the importance of wastewater treatment has been discussed in great depth with various solution strategies. Initially, the role of materials science, especially, carbon-nanotechnology in wastewater treatment is discussed and two distinct (sensing of industrial contaminants and their removal) branches of wastewater remediation have been elaborated. The development of carbon nanotechnology enables us with numerous quantum dots (CD and GQD) and carbon nanostructures (CNT and graphene); those are having exceptionally remarkable physicochemical properties to detect and remove industrial contaminants from wastewater. In reality, fluorometric detection of carbonaceous nanostructures has been discussed and their potential applicability of toxicological analysis has been depicted, which could be the next-generation sensor technology for wastewater treatment plants.

Apart from that, plausible remediation strategies involving classical adsorption-based contaminant removal and novel piezocatalytic removal have also been discussed in a detailed manner. Carbon nanomaterials with high aspect ratios have already emerged as promising adsorbent materials, but carbon nanomaterials mediated piezocatalysis is a relatively new approach, which could be thoroughly studied in near future.

In summary, carbon nanostructures have emerged as next-generation wastewater monitoring and remediation materials for combating environmental pollution and wastewater-related health hazards.

Conflict of Interests

The authors declare no conflict of interest.

References

Abbas, A., Al-Amer, A.M., Laoui, T., Al-Marri, M.J., Nasser, M.S., Khraisheh, M. and Atieh, M.A. 2016. Heavy metal removal from aqueous solution by advanced carbon nanotubes: critical review of adsorption applications. Sep. Purif. Technol. 157: 141-161.

Ammann, A.A. 2002. Speciation of heavy metals in environmental water by ion chromatography coupled to ICP–MS. Anal. Bioanal. Chem. 372(3): 448-452.

An, C.J., Kang, Y.H., Song, H., Jeong, Y. and Cho, S.Y. 2017. High-performance flexible thermoelectric generator by control of electronic structure of directly spun carbon nanotube webs with various molecular dopants. J. Mater. Chem. A 5(30): 15631-15639.

Angelakis, A.N. and Spyridakis, D.S. 2010. A brief history of water supply and wastewater management in ancient Greece. Water Science and Technology: Water Supply 10(4): 618-628.

Bachmann, L., Zezell, D.M., Ribeiro, A.D.C., Gomes, L. and Ito, A.S. 2006. Fluorescence spectroscopy of biological tissues—a review. Appl. Spectrosc. Rev. 41(6): 575-590.

Ballesteros, B., de la Torre, G., Ehli, C., Aminur Rahman, G.M., Agulló-Rueda, F., Guldi, D.M. and Torres, T. 2007. Single-wall carbon nanotubes bearing covalently linked phthalocyanines–photoinduced electron transfer. J. Am. Chem. Soc. 129(16): 5061-5068.

Bandi, R., Dadigala, R., Gangapuram, B.R., Sabir, F.K., Alle, M., Lee, S.H. and Guttena, V. 2020. N-doped carbon dots with pH-sensitive emission, and their application to simultaneous fluorometric determination of iron (III) and copper (II). Microchim. Acta 187(1): 30.

Bannov, A.G., Popov, M.V. and Kurmashov, P.B. 2020. Thermal analysis of carbon nanomaterials: advantages and problems of interpretation. J. Therm. Anal. Calorim. 142(1): 349-370.

Bardhan, S., Roy, S., Chanda, D.K., Ghosh, S., Mondal, D., Das, S. and Das, S. 2020. Nitrogenous carbon dot decorated natural microcline: an ameliorative dual fluorometric probe for Fe^{3+} and Cr^{6+} detection. Dalton Trans. 49(30): 10554-10566.

Baskaran, D., Mays, J.W., Zhang, X.P. and Bratcher, M.S. 2005. Carbon nanotubes with covalently linked porphyrin antennae: photoinduced electron transfer. J. Am. Chem. Soc. 127(19): 6916-6917.

Bhunia, S.K., Saha, A., Maity, A.R., Ray, S.C. and Jana, N.R. 2013. Carbon nanoparticle-based fluorescent bioimaging probes. Sci. Rep. 3(1): 1-7.

Bian, S., Shen, C., Qian, Y., Liu, J., Xi, F. and Dong, X. 2017. Facile synthesis of sulfur-doped graphene quantum dots as fluorescent sensing probes for Ag^+ ions detection. Sens. Actuators, B 242: 231-237.

Broussard, J.A. and Green, K.J. 2017. Research techniques made simple: methodology and applications of Förster Resonance Energy Transfer (FRET) microscopy. J. Invest. Dermatol. 137(11): 185-191.

Bu, D., Zhuang, H., Yang, G. and Ping, X. 2014. An immunosensor designed for polybrominated biphenyl detection based on fluorescence resonance energy transfer (FRET) between carbon dots and gold nanoparticles. Sens. Actuators, B 195: 540-548.

Burakov, A.E., Galunin, E.V., Burakova, I.V., Kucherova, A.E., Agarwal, S., Tkachev, A.G. and Gupta, V.K. 2018. Adsorption of heavy metals on conventional and nanostructured materials for wastewater treatment purposes: a review. Ecotoxicol. Environ. Saf. 148: 702-712.

Chen, L., Jia, Y., Zhao, J., Ma, J., Wu, Z., Yuan, G. and Cui, X. 2021. Strong piezocatalysis in barium titanate/carbon hybrid nanocomposites for dye wastewater decomposition. J. Colloid Interface Sci. 586: 758-765.

Chen, S., Yu, Y.L. and Wang, J.H. 2018. Inner filter effect-based fluorescent sensing systems: a review. Anal. Chim. Acta 999: 13-26.

Chen, T. and Dai, L. 2013. Carbon nanomaterials for high-performance supercapacitors. Mater. Today 16(7-8): 272-280.

Chini, M.K., Kumar, V., Javed, A. and Satapathi, S. 2019. Graphene quantum dots and carbon nano dots for the FRET based detection of heavy metal ions. Nano-Struct. Nano-Objects 19: 100347.

Conti, M.E., Tudino, M.B., Muse, J.O. and Cecchetti, G. 2002. Biomonitoring of heavy metals and their species in the marine environment: the contribution of atomic absorption

spectroscopy and inductively coupled plasma spectroscopy. Res. Trends Appl. Spectros. 4: 295-324.

Dąbrowski, A., Hubicki, Z., Podkościelny, P. and Robens, E. 2004. Selective removal of the heavy metal ions from waters and industrial wastewaters by ion-exchange method. Chemosphere 56(2): 91-106.

Dai, L., Chang, D.W., Baek, J.B. and Lu, W. 2012. Carbon nanomaterials for advanced energy conversion and storage. Small 8(8): 1130-1166.

De Feo, G., Antoniou, G., Fardin, H.F., El-Gohary, F., Zheng, X.Y., Reklaityte, I. et al. 2014. The historical development of sewers worldwide. Sustainability 6(6): 3936-3974.

Dekaliuk, M.O., Viagin, O., Malyukin, Y.V. and Demchenko, A.P. 2014. Fluorescent carbon nanomaterials: "quantum dots" or nanoclusters? Phys. Chem. Chem. Phys. 16(30): 16075-16084.

Deng, J., You, Y., Sahajwalla, V. and Joshi, R.K. 2016. Transforming waste into carbon-based nanomaterials. Carbon 96: 105-115.

Dennis, A.M. and Bao, G. 2008. Quantum dot–fluorescent protein pairs as novel fluorescence resonance energy transfer probes. Nano Lett. 8(5): 1439-1445.

Deshmukh, M.A., Shirsat, M.D., Ramanaviciene, A. and Ramanavicius, A. 2018. Composites based on conducting polymers and carbon nanomaterials for heavy metal ion sensing. Crit. Rev. Anal. Chem. 48(4): 293-304.

Devi, P., Rajput, P., Thakur, A., Kim, K.H. and Kumar, P. 2019. Recent advances in carbon quantum dot-based sensing of heavy metals in water. TrAC, Trends Anal. Chem. 114: 171-195.

Ding, L., Yang, H., Ge, S. and Yu, J. 2018. Fluorescent carbon dots nanosensor for label-free determination of vitamin B12 based on inner filter effect. Spectrochim. Acta, Part A 193: 305-309.

Du, L., Wu, A., Liu, G., Li, H., Yu, B. and Wang, X. 2020. Green autofluorescence eleocytes from earthworm as a tool for detecting environmental iron pollution. Ecol. Indic. 108: 105695.

Duruibe, J.O., Ogwuegbu, M.O.C. and Egwurugwu, J.N. 2007. Heavy metal pollution and human biotoxic effects. Int. J. Phys. Sci. 2(5): 112-118.

Esawi, A.M. and Farag, M.M. 2007. Carbon nanotube reinforced composites: potential and current challenges. Mater. Design 28(9): 2394-2401.

Fasinu, P.S. and Orisakwe, O.E. 2013. Heavy metal pollution in sub-Saharan Africa and possible implications in cancer epidemiology. Asian Pac. J. Cancer Prev. 14(6): 3393-3402.

Fernandez-Luqueno, F., López-Valdez, F., Gamero-Melo, P., Luna-Suárez, S., Aguilera-González, E.N., Martínez, A.I., et al. 2013. Heavy metal pollution in drinking water – a global risk for human health: a review. Afr. J. Environ. Sci. Technol. 7(7): 567-584.

Fiyadh, S.S., AlSaadi, M.A., Jaafar, W.Z., AlOmar, M.K., Fayaed, S.S., Mohd, N.S., Hin, L.S. and El-Shafie, A. 2019. Review on heavy metal adsorption processes by carbon nanotubes. J. Clean. Prod. 230: 783-793.

Ganiga, M. and Cyriac, J. 2016. FRET based ammonia sensor using carbon dots. Sens. Actuators, B 225: 522-528.

Gao, X., Ding, C., Zhu, A. and Tian, Y. 2014. Carbon-dot-based ratiometric fluorescent probe for imaging and biosensing of superoxide anion in live cells. Anal. Chem. 86(14): 7071-7078.

Geels, F.W. 2006. The hygienic transition from cesspools to sewer systems (1840–1930): the dynamics of regime transformation. Research Policy 35(7): 1069-1082.

Gupta, V.K. and Saleh, T.A. 2013. Sorption of pollutants by porous carbon, carbon nanotubes and fullerene – an overview. Environ. Sci. Pollut. Res. 20(5): 2828-2843.

Hayashi, T., Kim, Y.A., Natsuki, T. and Endo, M. 2007. Mechanical properties of carbon nanomaterials. Chemphyschem 8(7): 999-1004.

Hosnedlova, B., Kepinska, M., Fernandez, C., Peng, Q., Ruttkay-Nedecky, B., Milnerowicz, H. and Kizek, R. 2019. Carbon nanomaterials for targeted cancer therapy drugs: a critical review. Chem. Rec. 19(2-3): 502-522.

Huczko, A., Dąbrowska, A., Łabędź, O., Soszyński, M., Bystrzejewski, M., Baranowski, P. et al. 2014. Facile and fast combustion synthesis and characterization of novel carbon nanostructures. Phys. Status Solid B 251(12): 2563-2568.

Hurt, R.H., Monthioux, M. and Kane, A. 2006. Toxicology of carbon nanomaterials: status, trends, and perspectives on the special issue. Carbon 44(6): 1028-1033.

Jiang, L. and Fan, Z. 2014. Design of advanced porous graphene materials: from graphene nanomesh to 3D architectures. Nanoscale 6(4): 1922-1945.

Ju, J. and Chen, W. 2014. Synthesis of highly fluorescent nitrogen-doped graphene quantum dots for sensitive, label-free detection of Fe (III) in aqueous media. Biosens. Bioelectron. 58: 219-225.

Kailasa, S.K., Ha, S., Baek, S.H., Kim, S., Kwak, K. and Park, T.J. 2019. Tuning of carbon dots emission color for sensing of Fe^{3+} ion and bioimaging applications. Mater. Sci. Eng. C 98: 834-842.

Kalaiyarasan, G. and Joseph, J. 2019. Efficient dual-mode colorimetric/fluorometric sensor for the detection of copper ions and vitamin C based on pH-sensitive amino-terminated nitrogen-doped carbon quantum dots: effect of reactive oxygen species and antioxidants. Anal. Bioanal. Chem. 411(12): 2619-2633.

Khezami, L. and Capart, R. 2005. Removal of chromium (VI) from aqueous solution by activated carbons: kinetic and equilibrium studies. J. Hazard. Mater. 123(1-3): 223-231.

Kim, M.C., Yu, K.S., Han, S.Y., Kim, J.J., Lee, J.W., Lee, N.S., Jeong, Y.G. and Kim, D.K. 2018. Highly photoluminescent N-isopropylacrylamide (NIPAAM) passivated carbon dots for multicolor bioimaging applications. Eur. Polym. J. 98: 191-198.

Kruss, S., Hilmer, A.J., Zhang, J., Reuel, N.F., Mu, B. and Strano, M.S. 2013. Carbon nanotubes as optical biomedical sensors. Adv. Drug Deliv. Rev. 65(15): 1933-1950.

Lan, M., Di, Y., Zhu, X., Ng, T.W., Xia, J., Liu, W., Meng, X., Wang, P., Lee, C.S. and Zhang, W. 2015. A carbon dot-based fluorescence turn-on sensor for hydrogen peroxide with a photo-induced electron transfer mechanism. ChemComm 51(85): 15574-15577.

Li, M., Yu, C., Hu, C., Yang, W., Zhao, C., Wang, S. et al. 2017. Solvothermal conversion of coal into nitrogen-doped carbon dots with singlet oxygen generation and high quantum yield. Chem. Eng. J. 320: 570-575.

Liang, Z., Yan, C.F., Rtimi, S. and Bandara, J. 2019. Piezoelectric materials for catalytic/ photocatalytic removal of pollutants: recent advances and outlook. Appl. Catal. B 241: 256-269.

Lin, H., Wu, Z., Jia, Y., Li, W., Zheng, R.K. and Luo, H. 2014. Piezoelectrically induced mechano-catalytic effect for degradation of dye wastewater through vibrating Pb $(Zr_{0.52}Ti_{0.48})O_3$ fibers. Appl. Phys. Lett. 104(16): 162907.

Liu, L., Luo, X.B., Ding, L. and Luo, S.L. 2019. Application of nanotechnology in the removal of heavy metal from water. *In*: Nanomaterials for the Removal of Pollutants and Resource Reutilization. pp. 83-147. Elsevier.

Liu, X.M., Dong Huang, Z., Woon Oh, S., Zhang, B., Ma, P.C., Yuen, M.M. and Kim, J.K. 2012. Carbon nanotube (CNT)-based composites as electrode material for rechargeable Li-ion batteries: a review. Compos. Sci. Technol. 72(2): 121-144.

Lofrano, G. and Brown, J. 2010. Wastewater management through the ages: a history of mankind. Sci. Total Environ. 408(22): 5254-5264.

Luo, P.G., Sahu, S., Yang, S.T., Sonkar, S.K., Wang, J., Wang, H., LeCroy, G.E., Cao, L. and Sun, Y.P. 2013. Carbon "quantum" dots for optical bioimaging. J. Mater. Chem. B 1(16): 2116-2127.

Ma, X., Lin, S., Dang, Y., Dai, Y., Zhang, X. and Xia, F. 2019. Carbon dots as an "on-off-on" fluorescent probe for detection of Cu (II) ion, ascorbic acid, and acid phosphatase. Anal. Bioanal. Chem. 411(25): 6645-6653.

Mazrad, Z.A.I., Lee, K., Chae, A., In, I., Lee, H. and Park, S.Y. 2018. Progress in internal/ external stimuli responsive fluorescent carbon nanoparticles for theranostic and sensing applications. J. Mater. Chem. B 6(8): 1149-1178.

Merum, S., Veluru, J.B. and Seeram, R. 2017. Functionalized carbon nanotubes in bio-world: applications, limitations and future directions. Mater. Sci. Eng. B 223: 43-63.

Mohajeri, M., Behnam, B. and Sahebkar, A. 2019. Biomedical applications of carbon nanomaterials: drug and gene delivery potentials. J. Cell. Physiol. 234(1): 298-319.

Molaei, M.J. 2019. A review on nanostructured carbon quantum dots and their applications in biotechnology, sensors, and chemiluminescence. Talanta 196: 456-478.

Molaei, M.J. 2020. Principles, mechanisms, and application of carbon quantum dots in sensors: a review. Anal. Methods 12(10): 1266-1287.

Mondal, S., Das, T., Ghosh, P., Maity, A., Mallick, A. and Purkayastha, P. 2013. FRET-based characterisation of surfactant bilayer protected core-shell carbon nanoparticles: advancement toward carbon nanotechnology. ChemComm 49(69): 7638-7640.

Nie, Q., Xie, Y., Ma, J., Wang, J. and Zhang, G. 2020. High piezo-catalytic activity of ZnO/ Al_2O_3 nanosheets utilizing ultrasonic energy for wastewater treatment. J. Clean. Prod. 242: 118532.

Ouyang, Z., Lei, Y., Chen, Y., Zhang, Z., Jiang, Z., Hu, J. and Lin, Y. 2019. Preparation and specific capacitance properties of sulfur, nitrogen co-doped graphene quantum dots. Nanoscale Res. Lett. 14(1): 219.

Pan, X., Zhang, Y., Sun, X., Pan, W. and Wang, J. 2018. A green emissive carbon-dot-based sensor with diverse responsive manners for multi-mode sensing. Analyst 143(23): 5812-5821.

Peng, W., Li, H., Liu, Y. and Song, S. 2017. A review on heavy metal ions adsorption from water by graphene oxide and its composites. J. Mol. Liq. 230: 496-504.

Pirsaheb, M., Mohammadi, S. and Salimi, A. 2019. Current advances of carbon dots based biosensors for tumor marker detection, cancer cells analysis and bioimaging. TrAC Trends Analyt. Chem. 115: 83-99.

Pirsaheb, M., Mohammadi, S., Salimi, A. and Payandeh, M. 2019. Functionalized fluorescent carbon nanostructures for targeted imaging of cancer cells: a review. Microchim. Acta 186(4): 1-20.

Pumera, M. 2011. Graphene in biosensing. Mater. Today 14(7-8): 308-315.

Ramdzan, N.S.M., Fen, Y.W., Anas, N.A.A., Omar, N.A.S. and Saleviter, S. 2020. Development of biopolymer and conducting polymer-based optical sensors for heavy metal ion detection. Molecules 25(11): 2548.

Rao, G.P., Lu, C. and Su, F. 2007. Sorption of divalent metal ions from aqueous solution by carbon nanotubes: a review. Sep. Purif. Technol. 58(1): 224-231.

Reyes Bahena, J.L., Robledo Cabrera, A., López Valdivieso, A. and Herrera Urbina, R. 2002. Fluoride adsorption onto α-Al_2O_3 and its effect on the zeta potential at the alumina-aqueous electrolyte interface. Sep. Sci. Technol. 37(8): 1973-1987.

Roy, S., Bardhan, S., Chanda, D.K., Roy, J., Mondal, D. and Das, S. 2020. In situ-grown Cdot-wrapped boehmite nanoparticles for Cr (VI) sensing in wastewater and a theoretical probe for chromium-induced carcinogen detection. ACS Appl. Mater. Interfaces 12(39): 43833-43843.

Roy, S., Pal, K., Bardhan, S., Maity, S., Chanda, D.K., Ghosh, S., Karmakar, P. and Das, S. 2019. Gd (III)-doped boehmite nanoparticle: an emergent material for the fluorescent sensing of Cr (VI) in wastewater and live cells. Inorg. Chem. 58(13): 8369-8378.

Sabela, M., Balme, S., Bechelany, M., Janot, J.M. and Bisetty, K. 2017. A review of gold and silver nanoparticle-based colorimetric sensing Assays. Adv. Eng. Mater. 19(12): 1700270.

Sharma, M., Halder, A. and Vaish, R. 2020. Effect of Ce on piezo/photocatalytic effects of $Ba_{0.9}Ca_{0.1}Ce_xTi_{1-x}O_3$ ceramics for dye/pharmaceutical waste water treatment. Mater. Res. Bull. 122: 110647.

Sharma, V., Saini, A.K. and Mobin, S.M. 2016. Multicolour fluorescent carbon nanoparticle probes for live cell imaging and dual palladium and mercury sensors. J. Mater. Chem. B 4(36): 6154-6154.

Shtepliuk, I., Caffrey, N.M., Iakimov, T., Khranovskyy, V., Abrikosov, I.A. and Yakimova, R. 2017. On the interaction of toxic heavy metals (Cd, Hg, Pb) with graphene quantum dots and infinite graphene. Sci. Rep. 7(1): 1-17.

Simpson, A., Pandey, R.R., Chusuei, C.C., Ghosh, K., Patel, R. and Wanekaya, A.K. 2018. Fabrication characterization and potential applications of carbon nanoparticles in the detection of heavy metal ions in aqueous media. Carbon 127: 122-130.

Song, J., Ma, Q., Zhang, S., Liu, H., Guo, Y. and Feng, F. 2018. S, N-Co-doped carbon nanoparticles with high quantum yield for metal ion detection, IMP logic gates and bioimaging applications. New J. Chem. 42(24), 20180-20189.

Stafiej, A. and Pyrzynska, K. 2007. Adsorption of heavy metal ions with carbon nanotubes. Sep. Purif. Technol. 58(1): 49-52.

Tabish, T.A., Memon, F.A., Gomez, D.E., Horsell, D.W. and Zhang, S. 2018. A facile synthesis of porous graphene for efficient water and wastewater treatment. Sci. Rep. 8(1): 1-14.

Tang, Z.K., Zhang, L., Wang, N., Zhang, X.X., Wen, G.H., Li, G.D., et al. 2001. Superconductivity in 4 angstrom single-walled carbon nanotubes. Science 292(5526): 2462-2465.

Tao, S., Zhu, S., Feng, T., Xia, C., Song, Y. and Yang, B. 2017. The polymeric characteristics and photoluminescence mechanism in polymer carbon dots: a review. Mater. Today Chem. 6: 13-25.

Terra, I.A., Mercante, L.A., Andre, R.S. and Correa, D.S. 2017. Fluorescent and colorimetric electrospun nanofibers for heavy-metal sensing. Biosensors 7(4): 61.

Thostenson, E.T., Ren, Z. and Chou, T.W. 2001. Advances in the science and technology of carbon nanotubes and their composites: a review. Compos. Sci. Technol. 61(13): 1899-1912.

Tian, P., Tang, L., Teng, K.S. and Lau, S.P. 2018. Graphene quantum dots from chemistry to applications. Mater. Today Chem. 10: 221-258.

Vilatela, J.J. and Marcilla, R. 2015. Tough electrodes: carbon nanotube fibers as the ultimate current collectors/active material for energy management devices. Chem. Mater. 27(20): 6901-6917.

Wang, C., Li, Z., Pan, Z. and Li, D. 2018. Development and characterization of a highly sensitive fluorometric transducer for ultra low aqueous ammonia nitrogen measurements in aquaculture. Comput. Electron. Agric. 150: 364-373.

Wang, S., Wu, Z., Chen, J., Ma, J., Ying, J., Cui, S., Yu, S., Hu, Y., Zhao, J. and Jia, Y. 2019. Lead-free sodium niobate nanowires with strong piezo-catalysis for dye wastewater degradation. Ceram. Int. 45(9): 11703-11708.

Wang, Z.X. and Ding, S.N. 2014. One-pot green synthesis of high quantum yield oxygen-doped, nitrogen-rich, photoluminescent polymer carbon nanoribbons as an effective fluorescent sensing platform for sensitive and selective detection of silver (I) and mercury (II) ions. Anal. Chem. 86(15): 7436-7445.

Wei, Z., Zhao, H., Zhang, J., Deng, L., Wu, S., He, J. and Dong, A. 2014. Poly(vinyl alcohol) electrospun nanofibrous membrane modified with spirolactam–rhodamine derivatives for visible detection and removal of metal ions. RSC Adv. 4(93): 51381-51388.

Wingenfelder, U., Hansen, C., Furrer, G. and Schulin, R. 2005. Removal of heavy metals from mine waters by natural zeolites. Environ. Sci. Technol. 39(12): 4606-4613.

Wolfbeis, O.S. 2015. An overview of nanoparticles commonly used in fluorescent bioimaging. Chem. Soc. Rev. 44(14): 4743-4768.

Wu, A., Jia, J. and Luan, S. 2011. Amphiphilic PMMA/PEI core–shell nanoparticles as polymeric adsorbents to remove heavy metal pollutants. Colloids Surf. A 384(1-3): 180-185.

Xu, C., Williams, R.M., Zipfel, W. and Webb, W.W. 1996. Multiphoton excitation cross-sections of molecular fluorophores. Bioimaging 4(3): 198-207.

Xu, J., Cao, Z., Zhang, Y., Yuan, Z., Lou, Z., Xu, X. and Wang, X. 2018. A review of functionalized carbon nanotubes and graphene for heavy metal adsorption from water: preparation, application, and mechanism. Chemosphere 195: 351-364.

Xu, X., Zhang, K., Zhao, L., Li, C., Bu, W., Shen, Y., Gu, Z., Chang, B., Zheng, C., Lin, C. and Sun, H. 2016. Aspirin-based carbon dots, a good biocompatibility of material applied for bioimaging and anti-inflammation. ACS Appl. Mater. Interfaces 8(48): 32706-32716.

Yadav, V.B., Gadi, R. and Kalra, S. 2019. Clay based nanocomposites for removal of heavy metals from water: a review. J. Environ. Manage. 232: 803-817.

Yang, S.T., Cao, L., Luo, P.G., Lu, F., Wang, X., Wang, H. et al. 2009. Carbon dots for optical imaging in vivo. J. Am. Chem. Soc. 131(32): 11308-11309.

Yannopoulos, S., Yapijakis, C., Kaiafa-Saropoulou, A., Antoniou, G. and Angelakis, A.N. 2017. History of sanitation and hygiene technologies in the Hellenic world. Journal of Water, Sanitation and Hygiene for Development 7(2): 163-180.

Yap, P.L., Kabiri, S., Tran, D.N. and Losic, D. 2018. Multifunctional binding chemistry on modified graphene composite for selective and highly efficient adsorption of mercury. ACS Appl. Mater. Interfaces 11(6): 6350-6362.

Yoon, H., Ko, S. and Jang, J. 2007. Nitrogen-doped magnetic carbon nanoparticles as catalyst supports for efficient recovery and recycling. Chem. Commun. (14): 1468-1470.

Zhao, G., Huang, X., Tang, Z., Huang, Q., Niu, F. and Wang, X. 2018. Polymer-based nanocomposites for heavy metal ions removal from aqueous solution: a review. Polym. Chem. 9(26): 3562-3582.

Zhao, X., Liu, R., Chi, Z., Teng, Y. and Qin, P. 2010. New insights into the behavior of bovine serum albumin adsorbed onto carbon nanotubes: comprehensive spectroscopic studies. J. Phys. Chem. B 114(16): 5625-5631.

Zheng, M., Xie, Z., Qu, D., Li, D., Du, P., Jing, X. and Sun, Z. 2013. On-off-on fluorescent carbon dot nanosensor for recognition of chromium (VI) and ascorbic acid based on the inner filter effect. ACS Appl. Mater. Interfaces 5(24): 13242-13247.

Zhu, S., Song, Y., Zhao, X., Shao, J., Zhang, J. and Yang, B. 2015. The photoluminescence mechanism in carbon dots (graphene quantum dots, carbon nanodots, and polymer dots): current state and future perspective. Nano Res. 8(2): 355-381.

Zhu, S., Yan, X., Sun, J., Zhao, X.E. and Wang, X. 2019. A novel and sensitive fluorescent assay for artemisinin with graphene quantum dots based on inner filter effect. Talanta 200: 163-168.

Certificates of conferences and seminars

ANVESHAN

National Student Research Convention

March 12-14, 2019

Certificate of Participation

This is to Certify that Mr / Ms. **Shubham Roy,.**

affiliated with **Jadavpur University, Kolkata**

has participated in Anveshan: **National**

Student Research Convention organized by **Association of Indian Universities, New Delhi** and hosted by **Ganpat University, Gujarat** during

March 12-14, 2019. He/She presented a Research Project titled **NATURAL PLANT RESIN GUM ACACIA BASED MULTIFUNCTIONAL NANO- DEVICE FOR HEAVY METAL DETECTION AND REMEDIATION: "FROM THE NATURE FOR THE NATURE"**

under the category of **Basic Science**

Dr. Amarendra Pani
Chief Convener
Director(I/c), Research
Association of Indian Universities, New Delhi

Dr. Satyen Parikh
Anveshan Coordinator
Dean, Faculty of Computer Applications
Ganpat University

Dr. Mahendra Sharma
Director General
Ganpat University

ASSOCIATION OF INDIAN UNIVERSITIES

GANPAT UNIVERSITY
|| विद्या समाजोत्कर्षः ||

Association of Indian Universities, New Delhi
&
Central University of Jharkhand, Ranchi

ANVESHAN - 2018

Student Research Convention (Eastern Zone)

Certificate

This is to certify that Mr/Ms/Dr _____ Shubham Roy _____ enrolled in _____ Ph.D _____ of

S/o / Daughter of Shri _____ Jhuma Roy _____

Department / Faculty of _____ Physics _____

_____ Jadavpur _____ University / Institute participated in

Eastern Zone Student Research Convention held at Central University of Jharkhand, Ranchi during February 18-19, 2019.

His / Her Proposal / project entitled _Natural Plant Resin Gum --- for the Nature_

under the category of _____ Basic Sciences _____ .

Dr. Amarendra Pani
Joint Director & Head Research
Association of Indian Universities, New Delhi

Dr. Ajai Singh
Zonal Co-ordinator
Central University of Jharkhand

Prof. Nand Kr. Yadav 'Indu'
Vice-Chancellor
Central University of Jharkhand

DST-SERB Sponsored

One Day Workshop on Material Synthesis & Characterization Techniques

Organized by: Department of Physics, Jadavpur University, Kolkata-700032
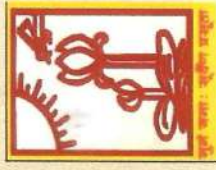
Certificate of Presentation

This Certificate is awarded to

Mr./ Ms. Shubham Roy .... for successfully presenting a paper entitled ...Multifunctional Nanosensors.................... in the Workshop organized by Department of Physics, Jadavpur University, Kolkata on 29th February 2020.

29/02/2020

Head, Department of Physics, Jadavpur University

National Seminar on

New Directions in Physical Sciences 2020 (NDPS 2020)

Organised by

Department of Physics, Jadavpur University
In association with
Indian Photobiology Society
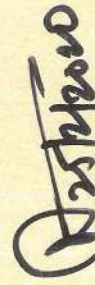
Certificate of Participation

This is to certify that Prof./Dr./Mr./Ms. _Sukham Roy_ of _Jadavpur University_ has participated/ presented a poster entitled _Multifunctional Fluorescence based Nanosensor for detection and_ _Removal of Cr(VI)_ at the seminar on 'New Directions in Physical Sciences 2020' at Jadavpur University, Kolkata on February 25, 2020.

Dr. Soumen Mondal
Convener, NDPS 2020

Prof. Mitali Mondal
Convener, NDPS 2020

Prof. Sukhen Das
Head, Dept. of Physics

Third International Conference
on
Material Science
(ICMS2020)

04-06 March, 2020

Organized by

Department of Physics
Tripura University (A Central University)
Suryamaninagar-799022, Tripura, India

Certificate of Participation

Certified that Prof./Dr./Mr./Ms. _Shubham Roy_

has participated / presented a paper entitled " _Waste Capacitor : A fresh approach... An energy harvesting material._ " in the **Third International Conference on Material Science (ICMS2020)** organized by **Department of Physics, Tripura University (A Central University)**

during 04-06 March, 2020.

(Prof. Debajyoti Bhattacharjee)
Chairman
Local Organizing Committee

(Dr. Syed Arshad Hussain)
Convener
Local Organizing Committee

NATIONAL SEMINAR

On

Physics at Surfaces and Interfaces of Soft Materials **(PSISM-2019)**

Organised by Condensed Matter Physics Research Centre, Department of Physics, Jadavpur University, Kolkata – 700032.

CERTIFICATE OF PARTICIPATION

This is to certify that Mr./Mrs./Dr./Prof. ...... Shubham Roy ....

Has participated/presented (oral/poster) a paper entitled ...... Boehmite based 'MFNS' for ..... A waste

...... to wealth conversion. ...... In the seminar on

Physics at surfaces and interfaces of soft materials (PSISM-2019) during 26-27st September, 2019 held at

Department of Physics, Jadavpur University, Kolkata – 700032.
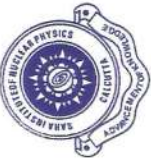
Prof. B. D. Chattopadhyay

Dr. Sanat Karmakar
(Conveners)

Materials Research Society of India (MRSI)

(Kolkata Chapter)

Certificate of Participation

This is to certify that .... Shubham Roy .... of

JU

has participated at the

"Young Scientists' Colloquium 2019"

Organised by

Materials Research Society of India (MRSI), Kolkata Chapter

On Tuesday, September 17, 2019

at SAHA INSTITUTE OF NUCLEAR PHYSICS, Kolkata

Prof. N. R. Bandyopadhyay
Chairman, MRSI, Kolkata

Prof. Satyajit Hazra
Chairman, YSC 2019

Dr. Arijit Sinha
Secretary, MRSI, Kolkata

International Conference on

EMERGING TRENDS IN CHEMICAL SCIENCES (ETCS-2018)

DEPARTMENT OF CHEMISTRY, DIBRUGARH UNIVERSITY

Dibrugarh, Assam, India.

Certificate

This is to certify that Prof./Dr./Mr./Ms. **Shubham Roy** ....

of .... Jadavpur University .... attended/presented research paper

(Invited lecture/Oral/Poster) in the International Conference "Emerging Trends in

Chemical Sciences" held during 26 -28 February, 2018.

(P. Das)
Convener

(S. Konwer)
Co-Convener

(A. Baruah)
Co-Convener

CIRE

CENTRE FOR INTERDISCIPLINARY RESEARCH AND EDUCATION

404B, Jodhpur Park, Kolkata – 700068

25th March, 2017

CERTIFICATE OF PARTICIPATION

This is to certify that

Shubham Roy

has contributed through Lecture / Oral Presentation / Poster Presentation / Participation to the success

of the One Day National Symposium on Nanotechnology:

From Materials to Medicine and their Social Impact held on 25th March, 2017

at Birla Industrial and Technological Museum, Kolkata.

Prof Sanjib Sarkar
President, CIRE

Certificates of awards

Institute of Scholars

An ISO 9001:2015 certified Institute by International Accurate Certification, Accredited by UASL

Bringing ideas into reality...........

InSc
Unit of SDPL

www.insc.in

Certificate

InSc Awards 2020

Young Achiever Award 2020

awarded to

Shubham Roy

M.Sc (Physics); Ph.D. (Pursuing)
Ph.D. Scholar
Department of Physics,
Jadavpur University,
Kolkata, West Bengal

For the work with following details:

Publication Type: Journal
Paper Title: In Situ-Grown Cdot-Wrapped Boehmite Nanoparticles for Cr (VI) Sensing in Wastewater and a Theoretical Probe for Chromium-Induced Carcinogen Detection
Journal Name: ACS Applied Materials and Interfaces
Volume: 12
Issue No. : 39
Month of Publication: September
Year: 2020
Page No. : 43833-43843
ISSN: 1944-8252

Nanjesh Bennur

Nanjesh Bennur
Director, InSc

ANVESHAN

National Student Research Convention
March 12-14, 2019

Certificate

This is to Certify that Mr / Ms / Dr. _____ Shubham Roy _____

affiliated with _____ Jadavpur University, Kolkata _____

participated in Anveshan: National Student Research

Convention organized by Association of Indian Universities, New Delhi and hosted by Ganpat University, Gujarat during March 12-14, 2019.

His/Her research project titled _Natural plant resin gum acacia based multifunctional nano- device for heavy metal detection and remediation: "From the nature, for the nature"_

_____ under the category of **Basic Sciences** has won **SECOND PRIZE.**

Dr. Amarendra Pani
Chief Convener
Director(I/c), Research
Association of Indian Universities, New Delhi

Dr. Satyen Parikh
Anveshan Coordinator
Dean, Faculty of Computer Applications.
Ganpat University

Dr. Mahendra Sharma
Director General
Ganpat University

Association of Indian Universities, New Delhi

&

Central University of Jharkhand, Ranchi

ANVESHAN - 2018

Student Research Convention (Eastern Zone)

Certificate

This is to certify that Mr/Ms/Dr _Shubham Bey_ enrolled in _PhD_

S/o / Daughter of Shri _Jhuma Bey_ of

Department / Faculty of _Physics_

Jadavpur University / Institute participated in

Eastern Zone Student Research Convention held at Central University of Jharkhand, Ranchi during February 18-19, 2019.

His / Her Proposal / project entitled _Natural Plant Resorufum locacia – from the Nature_

under the category of _Basic Sciences_ and secured _First Position_

Dr. Amarendra Pani
Joint Director & Head Research
Association of Indian Universities, New Delhi

Dr. Ajay Singh
Zonal Co-ordinator
Central University of Jharkhand

Prof. Nand Kr. Yadav 'Indu'
Vice-Chancellor
Central University of Jharkhand